Bitlis Eren Üniversitesi
Fen Bilimleri Dergisi

Bitlis Eren University
Journal of Science

ISSN : 2147-3129
e-ISSN : 2147-3188

Cilt / *Volume*: 12 Sayı / *Number*: 1 Yıl / *Year*: 2023

Yazışma Adresi

Bitlis Eren Üniversitesi
Lisansüstü Eğitim Enstitüsü
13000, Merkez, Bitlis/TÜRKİYE
Tel: 0 (434) 2220071

https://dergipark.org.tr/tr/pub/bitlisfen

BEU FBD

Bitlis Eren Üniversitesi Fen Bilimler Dergisi

Bitlis Eren University Journal of Science

Yıl/*Year:* 2023 - Cilt/*Volume:* 12 - Sayı/*Number:* 1

Editör (Yayın) Kurulu / *Editorial Board*

Danışma Kurulu / *Advisory Board*

Dergi Hakkında / *About Journal*

Bitlis Eren Üniversitesi Fen Bilimleri Dergisi, mühendislik ve temel bilimler alanlarındaki gelişmeleri ve yenilikleri takip etmek, meslek kuruluşlarının, araştırmacıların ve bireylerin ulusal ve uluslararası gelişimlerine katkıda bulunmak ve bu alanlarda elektronik bir kaynak oluşturmak amacıyla yayımlanmaktadır. Derginin yazım dili Türkçe veya İngilizcedir. Fen Bilimleri Dergisi, Bitlis Eren Üniversitesi Lisansüstü Eğitim Enstitüsü yayını olup, 2012 yılından bu yana ücretsiz ve açık erişimli olarak yayın hayatına devam etmektedir. Mühendislik ve temel bilimlerin bilgi tabanına ve teknolojik gelişmelere ışık tutması amacıyla bu alanlarda yapılmış deneysel ve teorik ilerlemeleri konu alan özgün araştırma makalelerine yer verilmektedir. Dergiye gönderilen çalışmaların benzerlik oranı %25'i geçmemelidir. Yazım kurallarına uymayan makaleler, hakemlere gönderilmeden önce düzeltilmek üzere yazara geri gönderilir. Bu nedenle, derginin yazım kuralları dikkate alınmalıdır. Ayrıca, editörlerden yazarlara iletilen düzeltmelere veya taleplere 30 gün içerisinde cevap verilmediği takdirde ilgili makaleler reddedilir. Makaleler şekiller ve tablolar dâhil 20 sayfayı geçmemelidir. Dergiye yayın için gönderilen makaleler en az iki hakem tarafından değerlendirilir. Yazarlardan hakem önerisi talep edilmemektedir. Makalelerin dergide yayımlanabilmesi için hakemler tarafından olumlu görüş bildirilmesi gerekmektedir. Dergi Editör Kurulu, hakem raporlarını (*en aziki hakemin değerlendirmeleri geldikten sonra*) dikkate alarak makalelerin yayımlanmak üzere kabul edilip edilmemesine karar verir. Fen Bilimleri Dergisi, yılda dört defa (*Mart, Haziran, Eylül, Aralık*) yayımlanmaktadır. **Dergimiz Tübitak-Ulakbim Mühendislik ve Temel Bilimler Veri Tabanı Dergi Listesinde taranmaktadır.**

B.E.Ü. Fen Bilimleri Dergisi 12(1), 2023 / *B.E.U. Journal of Science 12(1), 2023*
İÇİNDEKİLER / *CONTENTS*

Bitlis Eren Üniversitesi Fen Bilimleri Dergisi
BİTLİS EREN UNIVERSITY JOURNAL OF SCIENCE
ISSN: 2147-3129/e-ISSN: 2147-3188
VOLUME:12 NO: 1 PAGE: 1-9 YEAR: 2023
DOI:10.17798/bitlisfen.1057385

The Physical Concepts on Special Tube Surfaces Generated by Normal Curves in Galilean 3-Space

Fatma ALMAZ[1*], Mihriban ALYAMAÇ KÜLAHCI[1]

[1]*Firat University, Science of Faculty, Department of Mathematics, Elazığ/TÜRKİYE*
(ORCID: 0000-0002-1060-7813) (ORCID: 0000-0002-8621-5779)

Keywords: Galilean space, tube surfaces, Clairaut's theorem, normal curves, the specific kinetic energy, the specific angular momentum.

Abstract
In this study, we examine the tube surfaces formed by normal curves in Galilean 3-space, and we give Clairaut's theorem on the tube surfaces using geodesic normal curves. Also, we attempted to explain why the specific kinetic energy and angular momentum of particles may be on tube surfaces.

1. Introduction

The development of partial differential equations plays an important role in mathematics. A geodesic is a locally length-minimizing curve. The geodesic equation is expressed by establishing a one of the necessary theoretical foundations of relativity.

A Lagrangian formulation of the geodesic deviation equations is constructed for particle interpretations of quantum. The constants of motion that are of course constant along a geodesic are expressed by the geodesic equations. This constant is the result of one-parameter group of symmetries on the surface, and the surface is invariant under any one-parameter group of symmetries. In mathematical language, this quantity is a constant obtained by Clairaut for geodesic movement on a surface defined in a coordinate system adapted to this one-parameter group of symmetries [19].

Many studies of tube surfaces, including rectifying curves, the Darboux frame, the geodesic curve, the Mean curvature, the Gaussian curvature, have received much attention from our researchers. Among them, we can cite our work [2], in which we described the rotational surfaces using curves and matrices in Galilean 4-space. We examined the tube surfaces generated by special curves in G_3 and gave certain conditions describing the geodesics on the surfaces [3,5]. We studied Weingarten, HK-quadric, harmonic tubular surfaces, the conditions of geodesic on this surface using the help of Clairaut's theorem in G_3 [4]. We expressed the specific kinetic energy, the specific angular momentum, and the conditions of being geodesic on a rotational surface generated by a magnetic curve with the Killing magnetic field [6].

The tubular surface and the characterizations of the parameter curves of this surface have been investigated in Euclidean space, see [1,10-11]. In [8], the author defined the tubular surfaces in Galilean space and the differential features of tubular surfaces. In [12], they analyzed the problem of constructing a family of surfaces from a given space-like (or time-like) geodesic curve using the Frenet frame of the curve in Minkowski space and they expressed the family of surfaces as a linear combination of the components of this frame and the necessary and sufficient conditions for the coefficients to satisfy both the geodesic and the isoparametric requirements were given by the authors. In [6], the authors investigated some curves on a plane and in space and they stated the position vectors and gave some theorems about such curves in the Galilean plane G_2. Furthermore, the slant helices were given in G_3. In [20], the theory of the curves in Galilean space was studied. Also, some results were studied on surfaces in G_3 [9,13,18,22,25].

According to references [23, 24], the specific energy of the particle is constant because of its motion in space, which is very important in terms of its specific energy and angular momentum.

In this paper, the speed being constant along a geodesic is shown on the tube surface using Clairaut's

*Corresponding author: *fb_fat_almaz@hotmail.com*
Received: 13.01.2022, Accepted: 24.02.2023

theorem. Furthermore, the geodesic formulae are given using some parameters. Also, the energy and angular momentum on these surfaces that generated normal curves in G_3 are expressed.

2. Preliminaries

The classical context of Euclidean space is the origin of results that could be transferred to some other geometries. One way of defining new geometries is through Cayley-Klein spaces. They are expressed as projective spaces P_nR with an absolute figure, a subset of P_nR originating of a sequence of quadrics and planes 1. By means of the absolute figure, metric connections are also well defined, and they are invariant under the group of movements.
The scalar product and cross product of the vectors $U=(u_1,u_2,u_3)$, $V=(v_1,v_2,v_3)$ in G_3 is defined as

$$\langle U,V\rangle=\begin{cases}u_1v_1, & if\ \ u_1\ \neq 0 \text{ or } v_1\ \neq 0\\ u_2v_2+u_3v_3, & if\ \ u_1\ =0, v_1\ =0\end{cases} \tag{1}$$

and

$$U\times V=\begin{cases}\begin{pmatrix}0,\\ v_1u_3-v_3u_1,\\ v_2u_1-v_1u_2\end{pmatrix}, & \text{if } u_1\neq 0 \text{ or } v_1\ \neq 0\\ \begin{pmatrix}v_3u_2-v_2u_3,\\ 0,\\ 0\end{pmatrix}, & \text{if } u_1\ =0, v_1=0\end{cases} \tag{2}$$

[14].

Let $\varrho: I\subset\mathbb{R}\to G_3$ be a curve given by

$\varrho(s)=(s,y(s),z(s))$.

The vectors of the Frenet-Serret frame are defined by $t(s)=\big(1,y'(s),z'(s)\big);\ n(s)=\frac{t'(s)}{\kappa(s)};b(s)=\frac{n'(s)}{\tau(s)}$,

where the real valued functions $\kappa(s)=\|\,t'(s)\,\|$ is defined as the first curvature the curve and $\tau(s)=\|\,n'(s)\,\|$ is said to be as the second curvature function. Frenet-Serret equations are given by

$$t'=\kappa n, n'=\tau b, b'=-\tau n. \tag{3}$$

Let the equation of a surface $\Gamma=\Gamma(s,v)$ in G_3 be given by

$$\Gamma(s,v)=\big(x(s,v),y(s,v),z(s,v)\big), \tag{4}$$

and the unit normal vector field η on $\Gamma(s,v)$ is given by

$$\eta=\frac{\Gamma_{,1}\times\Gamma_{,2}}{\|\Gamma_{,1}\times\Gamma_{,2}\|}, \tag{5}$$

and the partial differentiations according to s and v are expressed by

momentum on these surfaces generated normal curves in G_3 are expressed.

$$\Gamma_{,1}=\frac{\partial\Gamma(s,v)}{\partial s};\Gamma_{,2}=\frac{\partial\Gamma(s,v)}{\partial v}. \tag{6}$$

Also, δ is written as

$$\delta=\frac{x_{,2}\Gamma_{,1}-x_{,1}\Gamma_{,2}}{w}, \tag{7}$$

where $x_{,1}=\frac{\partial x(s,v)}{\partial s}$, $x_{,2}=\frac{\partial x(s,v)}{\partial v}$ and $w=\|\Gamma_{,1}\times\Gamma_{,2}\|$.

Let us define

$$g_1=x_{,1}, g_2=x_{,2}, g_{ij}=g_ig_j; g^{\,1}=\frac{x_{,2}}{w},$$

$$g^{\,2}=\frac{x_{,1}}{w}, g^{ij}=g^ig^j; i,j=1,2; \tag{8}$$

$$h_{11}=\langle\Gamma^*_{,1},\Gamma^*_{,1}\rangle; h_{12}=\langle\Gamma^*_{,1},\Gamma^*_{,2}\rangle;\ \ h_{22}=\langle\Gamma^*_{,2},\Gamma^*_{,2}\rangle, \tag{9}$$

where $\Gamma^*_{,1}$ and $\Gamma^*_{,2}$ are the projections of the vectors $\Gamma_{,1}$ and $\Gamma_{,2}$ on the yz-plane, respectively, and the corresponding matrix of the first fundamental form ds^2 of the surface $\Gamma(s,v)$ is given by

$$ds^2=ds_1^2+ds_2^2=(g_1ds+g_2dv)^2+\ \ \varepsilon(h_{11}ds^2+2h_{12}dsdv+h_{22}dv^2) \tag{10}$$

where

$$\varepsilon=\begin{cases}0, & dw: dv_1\text{non}-\text{isotropic}\\ 1, & dw: dv_1\text{isotropic}\end{cases},\ \ [19]. \tag{11}$$

In this case, the coefficients of ds^2 are defined as g^*_{ij}. That is, it can be given in terms of g_i and h_{ij} by

$$w^2=g_1^2h_{22}-2g_1g_2h_{12}+g_2^2h_{11}.$$

The Gaussian and mean curvatures are expressed by means of the coefficients of L_{ij}, they are the normal components of $\Gamma_{,i,j}(i,j=1,2)$. That is,

$$\Gamma_{,i,j}=\sum^{2}\Gamma^k_{ij}\Gamma_{,k}+L_{ij}\eta, \tag{12}$$

where L_{ij} are written by

$$L_{ij}=\frac{1}{g_1}\langle g_1\Gamma^*_{,i,j}-g_{i,j}\Gamma^*_{,1},\eta\rangle$$
$$=\frac{1}{g_2}\langle g_2\Gamma^*_{,i,j}-g_{i,j}\Gamma^*_{,2},\eta\rangle, \tag{13}$$

and the curvatures K and H of the surface are wtitten as follows

$$K=\frac{L_{11}L_{22}-L_{12}^2}{w^2},\ H=\frac{g_2^2L_{11}-2g_1g_2L_{12}+g_1^2L_{22}^2}{w^2}, \tag{14}$$

[21].

Definition 1. A surface generated by the rotation of a regular parametrized plane curve $\varrho(s) = (h(s), 0, h(s))$ around an z-axis in its plane. Then, the position vector of the rotational surface is

$$\sigma(s, v_i) = \big(\rho(s)\cos v_i, \rho(s)\sin v_i, h(s)\big); \quad (15)$$

$$s \in I, 0 \le v_i \le 2\pi, x = \rho(s) > 0, z = h(s),$$

where ρ is the distance between a point on the surface and the z-axis of rotation and v_i is the angle of rotation, [14, 19].

Definition 2. Let $\varrho: I \subset \mathbb{R} \to M$ be a curve given as

$$\varrho(s) = \big(x(w(s), v_i(s)), y(w(s), v_i(s)), z(w(s), v_i(s))\big),$$

which is an arc-length parametrized geodesic on an rotational surface for differential equations given by $(w(s), v_i(s))$. By using the Lagrangian, the line element of the rotational surface is:

$$L = \dot{w}^2 + \rho^2 \dot{v_i}^2,$$

and

$$\frac{\partial}{\partial s}\left(\frac{\partial L}{\partial \frac{\partial w}{\partial s}}\right) = \frac{\partial L}{\partial w}; \quad \frac{\partial}{\partial s}\left(\frac{\partial L}{\partial \frac{\partial v_i}{\partial s}}\right) = \frac{\partial L}{\partial v_i};$$

$$\ddot{w} = \rho\rho' \dot{v_i}^2; \frac{d}{ds}(\rho \dot{v_i}^2) = 0 \quad (16)$$

so that is a constant of the motion and the previous equations are said to be as Euler-Lagrange equations, [14,19].

Definition 3. A vector $x = (x_1, x_2, x_3)$ is called a non-isotropic if $x_1 \neq 0$. All unit isotropic vectors are of the form $x = (1, x_2, x_3)$. For isotropic vectors $x_1 = 0$ hold, [14].

Theorem 1. (Clairaut's Theorem)Let M be a surface of rotation and let ϱ be a geodesic in M. Also, let ρ be the distance from the curve to axis of rotation and let θ express the angle between ϱ' and the longitudinal curve through ϱ. Then, if ϱ is a geodesic $\rho sin\theta$ is constant along the curve. On the contrary, if $\rho sin\theta$ is a constant, then the curve ϱ is a geodesic, [19].

Definition 4. A one-parameter group of diffeomorphisms of a manifold M is a smooth map $\psi: M \times \mathbb{R} \to M$, such that $\psi_t(x) = \psi(x, t)$, where

1) $\psi_t: M \to M$ *is a diffeomorphism*,
2) $\psi_o = id$.
3) $\psi_{s+t} = \psi_s o \psi_t$.

This group is associated with a vector field W given by $\frac{d}{dt}\psi_t(x) = W(x)$.

If a one-parameter group of isometries is formed by a vector field W and this vector is said to be as Killing vector field, [15].

3. Some Characteristics of Normal Curves in G_3

In this section, normal curves in G_3 are described using the components of their position vectors.

Theorem 2. Let $\varrho_i: I \subset \mathbb{R} \to G_3$ be a regular isotropic normal curve with curvatures $\kappa(w) \geq 0, \tau$ in $G_3, i = 1,2$. Then, the position vectors of ϱ_i hold following equalities*:*

1) If $\tau(w)$ =constant, the normal curve is given by

$$\varrho_1(w) = (2\eta_1 cos\tau w)\overleftarrow{n} - (2\eta_1 sin\tau w)\overleftarrow{b};\ \eta_i \in \mathbb{R}, i \in \{1,2\}.$$

2) If $\tau(w)$ ≠constant, the normal curve is given by

$$\varrho_2(w) = \gamma_3 e^{\frac{-\dot{\tau}}{2\tau}w}\left(cosh\left(\sqrt{\left(\frac{\dot{\tau}}{2\tau}\right)^2 - \tau^2}w\right)\right)\overleftarrow{n} + \frac{\gamma_3 e^{\frac{-\dot{\tau}}{2\tau}w}}{\tau}\left(\begin{array}{l}\left(\frac{-\dot{\tau}}{2\tau}w\right)_w cosh\left(\sqrt{\left(\frac{\dot{\tau}}{2\tau}\right)^2 - \tau^2}w\right) \\ +\left(\sqrt{\left(\frac{\dot{\tau}}{2\tau}\right)^2 - \tau^2}w\right)_w sinh\left(\sqrt{\left(\frac{\dot{\tau}}{2\tau}\right)^2 - \tau^2}w\right)\end{array}\right)\overleftarrow{b},$$

where $\gamma_3, \eta_1, \eta_2 \in \mathbb{R}_0$.

Proof. Assume that $\varrho(w)$ is an normal curve with the curvature functions $\kappa(w)$, $\tau(w)$ in G_3 as follows

$$\varrho(w) = \Sigma_0\overleftarrow{n} + \Sigma_1\overleftarrow{b}, \quad (17)$$

for some differentiable functions $\Sigma_0(w)$, $\Sigma_1(w)$. Thus, differentiating (17) with respect to w and using (3), we get

$$\overleftarrow{t} = \big(\dot{\Sigma}_0 - \tau\Sigma_1\big)\overleftarrow{n} + (\tau\Sigma_0 + \dot{\Sigma}_1)\overleftarrow{b}, \quad (18)$$

by multipling both sides of (3.2) by t, n, b, we have

$$\dot{\Sigma}_0 - \tau\Sigma_1 = 0; \tau\Sigma_0 + \dot{\Sigma}_1 = 0, \quad (19)$$

respectively and using (19) and making necessary calculations, we can write

1) if $\tau(w)$ ≠constant, we get

$$\Sigma_0 = e^{\frac{-\dot{\tau}}{2\tau}w}\begin{pmatrix} \gamma_1 e^{\sqrt{\left(\frac{\dot{\tau}}{2\tau}\right)^2-\tau^2}w} \\ +\gamma_2 e^{-\sqrt{\left(\frac{\dot{\tau}}{2\tau}\right)^2-\tau^2}w} \end{pmatrix}, \quad (20)$$

and taking $\gamma_1 = \gamma_2 = \frac{\gamma_3}{2}$, we get

$$\Sigma_0 = \gamma_3 e^{\frac{-\dot{\tau}}{2\tau}w}(\cosh(\sqrt{\left(\frac{\dot{\tau}}{2\tau}\right)^2-\tau^2}w)) \quad (21)$$

and using the equation $\dot{\Sigma_0} = \tau\Sigma_1$, we obtain

$$\Sigma_1 = \frac{\gamma_3}{\tau}e^{\frac{-\dot{\tau}}{2\tau}w}\begin{pmatrix} (\frac{-\dot{\tau}}{2\tau}w)_w\cosh(\sqrt{\left(\frac{\dot{\tau}}{2\tau}\right)^2-\tau^2}w) \\ +(\sqrt{\left(\frac{\dot{\tau}}{2\tau}\right)^2-\tau^2}w)_w\sinh(\sqrt{\left(\frac{\dot{\tau}}{2\tau}\right)^2-\tau^2}w) \end{pmatrix}. \quad (22)$$

Hence, from (21) and (22), the position vector is obtained.

2) if $\tau(w)$ =constant, we get

$$\Sigma_0 = (\eta_1+\eta_2)\cos\tau w + i(\eta_1-\eta_2)\sin\tau w; \quad (23)$$

$$\Sigma_1 = i\big((\eta_1-\eta_2)\cos\tau w + i(\eta_1+\eta_2)\sin\tau w\big) \quad (24)$$

and taking $\eta_1 = \eta_2$, we have

$$\varrho_1(w) = (2\eta_1\cos\tau w)\overleftarrow{n} - (2\eta_1\sin\tau w)\overleftarrow{b},$$

where $\eta_i, \gamma_i \in \mathbb{R}, i \in \{1,2,3\}$.

4. The Special Tube Surfaces Formed by Normal Curves in Galilean 3-space

In this part, special tube surfaces formed by a normal curve have been examined mathematically.

A canal surface is defined as a one-parameter set of spheres whose centres are described by a radius function ρ and the orbit $\varrho_i(w)$(spine curve), in addition to parametrizing the spine curve via the Frenet frame. If the radius function ρ is constant, the canal surface is said to be the tube or pipe surface [9].

Let us denote by ρ the vector connecting the point from the parametrized curve $\varrho_i(w)$ with the point from the surface. Afterwards, we have the position vector R of a point on the surface as

$$R = \varrho_i(w) + \rho = \varrho_i(w) + A\left(\cos v\vec{n} + \sin v\vec{b}\right), \quad (25)$$

where A is a constant radius of Euclidean circle of Frenet frame in G_3, v is the angle between n and ρ that ρ lies in the Euclidean normal plane of the curve $\varrho_i(w)$.

4.1 The Clairaut's Theorem on Special Tube Surface Formed by Normal Curve in G_3

In this subsection, using the Clairaut's theorem, the specific tube surfaces with normal curve are characterized. Also, the general equation of geodesics on the tube surfaces is given in G_3.

Theorem 3. Let $\varrho_i: I \subset \mathbb{R} \to G_3$ be a regular isotropic curve for $\kappa(w) \geq 0, \tau$ in $G_3, i = 1,2$ and let $\Gamma^i(w,v)$ be the tube surface formed by the normal curve. Then, the following statements hold:

a) If $\tau(w)$ =constant, there is no the tube surface generated by the normal curve.

b) If $\tau(w)$ ≠constant, the tube surface generated by the normal curve is given by

$$\Gamma^2(w,v) = (\gamma_3 e^f\cosh g + A\cos v)\overleftarrow{n} + \left\{\frac{\gamma_3 e^f}{\tau}(f_w\cosh g + g_w\sinh g) + A\sin v\right\}\overleftarrow{b}$$

and $A = \frac{-\gamma_3\rho(w)\cos v}{\tau(w)}$, where $\gamma_3 \in \mathbb{R}$ and for isotropic vectors, the first fundamental form is given by

$$I = \begin{pmatrix} \tau^2(w)A^2 + \gamma_3^2\rho^2(w) \\ +2\gamma_3\tau(w)\rho(w)A\cos v \end{pmatrix}\dot{w}^2 + A^2\dot{v}^2.$$

b_1) For the equation $2\int E(w,v)\partial w = c_2 s + c_3$, $\varrho_2(w)$ is a geodesic on $\Gamma^2(w,v)$ necessary and sufficient condition the following equations satisfied

$$A^2\ddot{v} + A2\tau(w)\gamma_3\sin v\dot{w}^2 = 0;$$

$$v = \arccos\left(\frac{\tau\tau_w A^2 + \rho\rho_w}{A\gamma_3(\tau_w\rho + \tau\rho_w)}\right); w = \int \cos\theta ds,$$

where

$$\xi^1 = e^f\cosh g, \xi^2 = f_w\cosh g + g_w\sinh g,$$

$$\xi^3 = e^f\xi^2 = \xi^1_w; h(w) = \frac{d}{dw}\left(\frac{\xi^3}{\tau}\right);$$

$$\rho(w) = \tau(w)\xi^1(w) + h(w);$$

$$f = \frac{-\dot{\tau}}{2\tau}w, g = \cosh(\sqrt{(\frac{\dot{\tau}}{2\tau})^2 - \tau^2}w).$$

Proof. The specific tube surface generated by normal curve $\varrho_2(w)$ is parametrized by

$$\Gamma^2(w,v) = \varrho_2(w) + A(\cos v\overleftarrow{n} + \sin v\overleftarrow{b}). \quad (26)$$

$i)$ For $\tau(w) \neq$constant, by using the following equation

$$\varrho_2(w) = (\gamma_3 e^{f(w)}\cosh g(w))\overleftarrow{n} + \\ + \frac{\gamma_3 e^{f(w)}}{\tau}(f_w\cosh g(w) + g_w\sinh g(w))\overleftarrow{b}, \quad (27)$$

where

$$f(w) = -\frac{\dot{\tau}}{2\tau}w; g(w) = \sqrt{\left(\frac{\dot{\tau}}{2\tau}\right)^2 - \tau^2 w},$$

we can write the tube surface as

$$\Gamma^2(w,v) = \begin{matrix}\{\gamma_3 e^{f(w)}\cosh g(w) + A\cos v\}\overleftarrow{n} \\ + \left\{\frac{\gamma_3 e^{f(w)}}{\tau}\begin{pmatrix} f_w\cosh g(w) \\ + g_w\sinh g(w) \\ + A\sin v\end{pmatrix}\right\}\overleftarrow{b},\end{matrix} \quad (28)$$

where v is the angle between $\overleftarrow{n}$ and $\overleftarrow{A}$, we can write the equation

$$A = \frac{-\gamma_3\rho(w)\cos v}{\tau(w)}, \quad (29)$$

where

$$\xi^1 = e^f\cosh g, \xi^2 = f_w\cosh g + g_w\sinh g,$$

$$\xi^3 = e^f\xi^2 = \xi^1_w;$$

$$h(w) = \frac{d\left(\frac{e^f}{\tau}(f_w\cosh g + g_w\sinh g)\right)}{dw} = \frac{d\left(\frac{\xi^3}{\tau}\right)}{dw};$$

$$\rho(w) = \tau(w)\xi^1(w) + h(w).$$

Recall, since $\tau \neq 0$, we can write

$$\Gamma^2_w = (-\tau A\sin v)\overleftarrow{n} + \{\gamma_3\rho(w) + \tau A\cos v\}\overleftarrow{b}) = N_w;$$

$$\Gamma^2_v = A(-\sin v\overleftarrow{n} + \cos v\overleftarrow{b}) = AN_v,$$

it follows that the vector cross product of these vectors is found out by

$$\Gamma^2_w \times \Gamma^2_v = A\gamma_3\rho(w)\sin v\overleftarrow{t} \quad (30)$$

and from (30) , the unit normal vector η of $\Gamma^2(w,v)$ is found as follows

$$\eta = \overleftarrow{t}. \quad (31)$$

Furthermore, from (7), we get

$$\delta = \frac{-\Gamma^2_v}{A} = \sin v\overleftarrow{n} - \cos v\overleftarrow{b}.$$

For the isotropic vectors $\overleftarrow{n}$ and $\overleftarrow{b}$ and by using the Frenet frame in Galilean space, we can find

$$x(w,v) = 0; x_w = g_1 = 0, x_{v_2} = g_2 = 0;$$

$$g_{11} = g_{12} = g_{22} = 0; g^1 = 0, g^2 = 0; \quad (32)$$

$$h_{11} = E(w,v) = \tau^2(w)A^2 + \gamma_3^2\rho^2(w) + \\ 2\gamma_3\tau(w)\rho(w)A\cos v; \quad (33)$$

$$h_{12} = 0, h_{22} = A^2. \quad (34)$$

Then, we substitute (33) and (34), (32) into the equation (10). Hence, the first fundamental form of the tube surface by generated normal curve in Galilean space can be written as

$$I = E(w,v)dw^2 + A^2dv^2. \quad (35)$$

Furthermore, since $\tau \neq 0$, we obtain the first fundamental form with two variable parameter. Hence, we write orthogonal coordinates of parametrization. So, by considering the first fundamental form, the Lagrangian can be written as

$$E(w,v)\dot{w}^2 + A^2\dot{v}^2 = L \quad (36)$$

and we know that a geodesic on the surface $\Gamma^2(w,v)$ can be found by using the Euler-Lagrangian equations

$$\frac{\partial}{\partial s}\left(\frac{\partial L}{\frac{\partial w}{\partial s}}\right) = \frac{\partial L}{\partial w}; \frac{\partial}{\partial s}\left(\frac{\partial L}{\frac{\partial v}{\partial s}}\right) = \frac{\partial L}{\partial v}. \quad (37)$$

$a)$ If $\tau(w) \neq$constant, for the equation given by

$$A^2\ddot{v} + 2\tau(w)A\gamma_3\sin v\dot{w}^2 = 0, \quad (38)$$

the second Lagrangian equation is given by $\frac{\partial}{\partial s}\left(\frac{\partial L}{\frac{\partial v}{\partial s}}\right) = \frac{\partial L}{\partial v} \neq 0$ and for the equation

$$v = \arccos\left(\frac{\tau\tau_w A^2 + \rho\rho_w}{A\gamma_3(\tau_w\rho + \tau\rho_w)}\right),$$

the equation $\frac{\partial}{\partial s}\left(\frac{\partial L}{\frac{\partial w}{\partial s}}\right) = \frac{\partial L}{\partial w} = 0$ holds. Thus, we can write $\frac{\partial L}{\frac{\partial w}{\partial s}} = 2E(w,v)\dot{w} =$ constant and which means

$$2\int E(w,v)\partial w = c_2 s + c_3 \quad (39)$$

and let $\varrho_2(w)$ be a geodesic on the surface of $\Gamma^2(w,v)$, so it is given by $(w(s),v(s))$. Also, let θ be the angle between $\dot{\varrho}_2$ and a meridian and N_w is the vector pointing along meridians of Γ^2; N_v is the vector pointing along parallels of Γ^2. Hence, we can say that orthonormal basis $\{N_w, N_v\}$ and $\dot{\varrho}_2$ is found out as

$$\dot{\varrho}_2 = N_w\cos\theta + N_v\sin\theta = \dot{w}\Gamma_w^2 + \dot{v}\Gamma_v^2 = \dot{w}N_w + \dot{v}AN_v.$$

We see that $\dot{w} = \cos\theta$, so we can write as $2E(w,v)\dot{w} = 2E(w,v)\cos\theta$=constant along $\varrho_2(w)$. Conversely, $\varrho_2(w)$ is the normal curve with $2E(w,v)\cos\theta$ = constant. Hence, the second Euler Lagrange equation is held. If the differential of the L value is taken and added to the first equation we have

$$w = \int \cos\theta ds. \tag{40}$$

b) For τ =constant, the tube surface generated by the curve ϱ_1 is parametrized by

$$\Gamma^1(w,v) = \varrho_1(w) + A_1(\cos v\overleftarrow{n} + \sin v\overleftarrow{b}), \tag{41}$$

where v is angle between the isotropic vectors $\overleftarrow{n}$ and $\overleftarrow{A_1}$. Clearly,

$$\Gamma^1(w,v) = (2\eta\cos\tau w + A_1\cos v)\overleftarrow{n} + (-2\eta\sin\tau w + A_1\sin v)\overleftarrow{b}. \tag{42}$$

Recall, we can write

$$\Gamma_w^1 = (-\tau A_1\sin v)\overleftarrow{n} + \tau A_1\cos v\overleftarrow{b} = \tau A_1 N_w;$$

$$\Gamma_v^1 = A_1(-\sin v\overleftarrow{n} + \cos v\overleftarrow{b}) = A_1 N_v.$$

Therefore, we have $\Gamma_w^1 \times \Gamma_{v_1}^1 = 0$, that means there is no such surface in G_3.

Theorem 4. The general equations of geodesics on the tube surface Γ^2 formed by the normal curve in G_3, for the special parameters $w = \int cos\theta ds$(or $2\int E(w,v)\partial w = c_2 s + c_3$) and $v = arccos\left(\frac{\tau\tau_w A^2 + \rho\rho_w}{A\gamma_3(\tau_w\rho + \tau\rho_w)}\right)$, are given by

$$\frac{dv}{dw} = \frac{c_{11}E(w,v)}{A}\sqrt{L - \frac{c_{10}}{E(w,v)}};$$

$$\frac{dv}{dw} = \frac{1}{A\cos\theta}\sqrt{L - E(w,v)\cos^2\theta}, \tag{43}$$

where $c_i \in \mathbb{R}_0$.

Proof. We consider the Euler-Lagrange equations in (4.13) for the general equation of geodesics. For $w = \int \cos\theta ds$ or $2\int E(w,v)\partial w = c_2 s + c_3$, we explain the equation of geodesic, solving the equation in $\frac{\partial}{\partial s}\left(\frac{\partial L}{\frac{\partial w}{\partial s}}\right) = \frac{\partial L}{\partial w} = 0$, we obtain

$$\dot{w} = \frac{c_2}{2E(w,v)}; \dot{w} = \cos\theta.$$

If we put the value of $\dot{w}$ at the Lagrange equation,

$$E(w,v)\left(\frac{dw}{ds}\right)^2 + A^2\left(\frac{dv}{dw}\frac{dw}{ds}\right)^2 = L.$$

Hence, we obtain the general equation of geodesics on Γ^2 as

$$\frac{dv}{dw} = \frac{c_{11}E(w,v)}{A}\sqrt{L - \frac{c_{10}}{E(w,v)}}.$$

Furthermore, according to the parameters

$$w = \int \cos\theta ds, v = \arccos\left(\frac{\tau\tau_w A^2 + \rho\rho_w}{A\gamma_3(\tau_w\rho + \tau\rho_w)}\right),$$

the geodesic equation on G_3 is given as

$$\frac{dv}{dw} = \frac{1}{A\cos\theta}\sqrt{L - E(w,v)\cos^2\theta},$$

where $c_i \in \mathbb{R}$.

5. A Physical Study on the Special Tube Surface with Normal Curve in G_3

In this article, we have carried out experiments to explain why the specific kinetic energy and angular momentum of particles, following a path called the trajectory of the particle.

Let $\Gamma^2(w(s),v(s))$ be a curve on the surface and we can write the position vector of this curve as

$$\Gamma^2(w(s),v(s) = (\gamma_3\xi^1(w(s)) + A\cos v(s))\overleftarrow{n} + (\frac{\gamma_3}{\tau(w(s))}\xi^3(w(s)) + A\sin v(s))\overleftarrow{b}.$$

Calculating the derivative of this tangent vector along the curve on Γ^2 and using the product and chain rules. Thus, the tangent vector is obtained by

$$\frac{d\Gamma^2(w(s),v(s))}{ds} = \frac{dw(s)}{ds}\Gamma_w^2 + \frac{dv(s)}{ds}\Gamma_v^2; \tag{44}$$

$$\dot{\varrho}_2 = N_w\cos\theta + N_v\sin\theta = \dot{w}\Gamma_w^2 + \dot{v}\Gamma_v^2 = \dot{w}N_w + \dot{v}AN_v. \tag{45}$$

The tangent vector of the geodesic curve is said to be as the velocity given as

$$\overleftarrow{W} = \frac{d\Gamma^2(w(s),v(s))}{ds} = W^w\Gamma_w^2 + W^v\Gamma_v^2 \quad (46)$$

and the norm of W is called as the speed. Take into account that $W^{w^*} = \sqrt{E(w,v)}\ .W^w = W\cos\theta$ is the radial velocity and W^v is the horizontal angular velocity. Hence, $W^{v^*} = AW^v = W\sin\theta$ is the horizontal component of the velocity vector.

Physically, the role of the radial variable in this velocity plane can be explained by the speed: the angle θ is expressed the side of the velocity in accordance with $\Gamma_{w^*}^2$, and the physical properties such as energy and momentum that have the mass as a proportional element can be taken instead of the specific statements obtained by partitioning out the mass. So, we can write the specific kinetic energy E_{energy} as

$$E_{energy} = \frac{\left(\sqrt{2E_{energy}}\cos\theta\right)^2 + \left(\sqrt{2E_{energy}}\sin\theta\right)^2}{2} = \frac{W^2}{2} = \frac{1}{2}(W^2\cos^2\theta + W^2\sin^2\theta)$$

$$= \frac{1}{2}E(w,v)\left(\frac{dw}{ds}\right)^2 + \frac{1}{2}A^2\left(\frac{dv}{ds}\right)^2, \quad (47)$$

from the right side of equ. (5.4) the specific energy and speed are constant along geodesic. Physically, the specific energy is constant on account of attribute of its motion, it is thought perpendicular to the surface. Therefore, the specific energy E_{energy} and the speed $W = \sqrt{2E_{energy}}$ have to be constant along a geodesic. Therefore, we can give following theorems in respect to previous expressions that we explain.

Theorem 5. Let $\Gamma^2(w,v)$ be the tube surface generated by the normal curve. Then, for the parameters

$$v = \arccos\left(\frac{\tau\tau_w A^2 + \rho\rho_w}{A\gamma_3(\tau_w\rho + \tau\rho_w)}\right),$$

$$w = \int \cos\theta ds (or \int E(w,v)\partial w = c_2 s + c_3)$$

and the equation $A^2\ddot{v} + 2\tau(w)A\gamma_3\sin v\dot{w}^2 = 0$, the specific angular momentum ℓ is given by

$$\ell = \sqrt{\tau^2A^2 + \gamma_3^2\rho^2 + 2\gamma_3\tau\rho A\cos v}W\cos\theta,$$

where $\rho = \tau(e^f\cosh g) + \frac{d}{dw}\left(\frac{(e^f\cosh g)_w}{\tau}\right)$ and the specific energy E_{energy} is given by

$$E_{energy} = \frac{1}{2}\left(\frac{\ell^2}{\tau^2A^2 + \gamma_3^2\rho^2 + 2\gamma_3\tau\rho A\cos v} + \frac{\gamma_3^2\rho^2\cos^2 v}{\tau^2}\left(\frac{dv}{ds}\right)^2\right),$$

$$E_{energy} = \frac{\ell}{\sqrt{2}\cos\theta},$$

where the curve $\varrho_2(w)$ is a geodesic on the surface Γ^2.

Proof. For the equations

$$v = \arccos\left(\frac{\tau\tau_w A^2 + \rho\rho_w}{A\gamma_3(\tau_w\rho + \tau\rho_w)}\right),$$

$$w = \int \cos\theta ds \text{ (or } 2\int E(w,v)\partial w = c_2 s + c_3)$$

and

$$A^2\ddot{v} + 2\tau(w)A\gamma_3\sin v\dot{w}^2 = 0,$$

we can write

$$2\sqrt{E(w,v)}\dot{w} = 2\sqrt{E(w,v)}\cos\theta \quad (48)$$

being constant along $\varrho_2(w)$. Also, we may consider as in the case of circular movement round an axis with radius $\|\overleftarrow{R}\| = \sqrt{E(w,v)}$ or $\overleftarrow{R} = -\sqrt{E(w,v)}\overleftarrow{e_2}$, and the velocity $W^{w^*} = \sqrt{E(w,v)}W^w = W\cos\theta = \sqrt{E(w,v)}\frac{dw}{ds} = \sqrt{2E_{energy}}\cos\theta$ in the angular direction multiplied by the radius $\sqrt{E(w,v)}$ of the circle. From the first geodesic equation ℓ is constant along geodesic and the specific angular momentum ℓ can be taken down as following equation

$$\ell = \overleftarrow{e_3}.\left(\overleftarrow{R} \times_{G_3} \overleftarrow{W}\right) = \sqrt{E(w,v)}W\cos\theta, \quad (49)$$

where $E(w,v) = \tau^2A^2 + \gamma_3^2\rho^2 + 2\gamma_3\tau\rho A\cos v$ and $\rho = \tau(e^f\cosh g) + \frac{d}{dw}\left(\frac{(e^f\cosh g)_w}{\tau}\right)$ and since $\sqrt{E(w,v)}\frac{dw}{ds} = W\cos\theta$, we can write $E(w,v)\frac{dw}{ds} = \sqrt{E(w,v)}W\cos\theta$, and ℓ is constant along geodesic. Hence, one gets

$$\ell = E(w,v)\frac{dw}{ds} \Rightarrow \frac{dw}{ds} = \frac{\ell}{E(w,v)}$$

$$\text{or } \ell = \sqrt{E(w,v)}\sqrt{2E_{energy}}\cos\theta. \quad (50)$$

Hence, using (50) from the radial motion and another constant of the motion the specific energy E_{energy} can be written by

$$E_{energy} = \frac{1}{2}(E(w,v)\left(\frac{dw}{ds}\right)^2 + A^2\left(\frac{dv}{ds}\right)^2);$$

$$E_{energy} = \frac{1}{2}\left(\begin{matrix}\frac{\ell^2}{\tau^2(w)A^2+\gamma_3^2\rho^2(w)+2\gamma_3\tau(w)\rho(w)A\cos v} \\ +\frac{\gamma_3^2\rho^2(w)\cos^2 v_2}{\tau^2(w)}\left(\frac{dv}{ds}\right)^2\end{matrix}\right) \quad (51)$$

6. Conclusion

In this study, the special tube surface formed by a normal curve is investigated, and certain results of describing geodesics on the tube surface are expressed. One important conclusion of our analysis is that the specific energy and the specific angular momentum on free particles of the tube surfaces can be considered in Galilean 3-space. We have carried out to research explain the conditions of being a geodesic normal curve.

Acknowledgment

The authors wish to express their thanks to the authors of literatures for the supplied scientific aspects and idea for this study.

and from $\ell = \sqrt{E(w,v)}\,\sqrt{2E_{energy}}\cos\theta$, we find

$$\frac{\ell^2}{2E(w,v)\cos^2\theta} = E_{energy}.$$

Contributions of the authors

FA put forward the first idea on the stated title and wrote, analyzed and commented on data. MAK analyzed the data and reinterpreted it in a well-organized for. All authors read and approved the final manuscript.

Conflict of Interest Statement

The study is complied with research and publication Ethics

Statement of Research and Publication Ethics

The study is complied with research and publication ethics

References

[1] M. Akyigit, K. Eren, and H.H. Kosal. "Tubular surfaces with modified orthogonal frame in Euclidean 3-space." *Honam Mathematical Journal*, vol. 43, no. 3, pp.453–63, 2021.

[2] F. Almaz and M.A. Külahcı, "The notes on rotational surfaces in Galilean space," *International Journal of Geometric Methods in Modern Phys.*, vol. 18, no. 2, 2021.

[3] F. Almaz and M.A. Külahcı, "A survey on tube surfaces in Galilean 3-space," *Journal of Polytechnic*, vol. 25, no. 3, pp.1033-1042, 2022.

[4] F. Almaz and M.A. Külahcı, "Some characterizations on the special tubular surfaces in Galilean space," *Prespacetime J.*, vol. 11, no. 7, 2020.

[5] F. Almaz and M.A. Külahcı, "A different interpretation on magnetic surfaces generated by special magnetic curve in $Q^2 \subset E_1^3$," *Adiyaman University Journal of Sci.*, vol. 10, no. 12, 2020.

[6] F. Almaz and M.A. Külahcı, "The geodesics on special tubular surfaces generated by Darboux frame in G_3," 18th International Geometry Symposium, 2021.

[7] A.T. Ali, "Position vectors of curves in the Galilean space G_3," *Matematicki Vesnik*, vol. 64, no. 3, pp.200-210, 2012.

[8] A.V. Aminova, "Pseudo-Riemannian manifolds with common geodesics," *Uspekhi Mat. Nauk*., vol. 48, pp.107-16, 1993.

[9] M. Dede, "Tubular surfaces in Galilean space", *Math. Commun*., vol. 18, pp.209-217, 2013.

[10] K. Eren, "On the harmonic evolute surfaces of tubular surfaces in Euclidean 3-space," *Journal of Science and Arts*, vol. 21, no. 2, pp.449–460, 2021.

[11] K. Eren, Ö.G. Yıldız, M. Akyiğit, "Tubular surfaces associated with framed base curves in Euclidean 3-space", *Math. Meth. Appl. Sci.*, pp.1- 9, 2021, https://doi.org/10.1002/mma.7590.

[12] E. Kasap and F.T. Akyildiz, "Surfaces with a Common Geodesic in Minkowski 3 −space," *App. Math. and Comp.*, vol. 177, pp.260-270, 2006.

[13] M. K. Karacan and Y. Yayli, " On the geodesics of tubular surfaces in Minkowski 3 −Space", *Bull. Malays. Math. Sci. Soc.*, vol. 31, pp.1-10, 2008.

[14] W. Kuhnel, *Differential Geometry Curves-Surfaces and Manifolds*. Second Edition, Providence, RI, United States, American Math. Soc., 2005.

[15] D. Lerner, *Lie Derivatives, Isometries, and Killing Vectors*. Department of Mathematics, University of Kansas, Lawrence, Kansas 66045-7594, 2010.

[16] Z. Milin-Šipuš and B. Divjak, "Surfaces of constant curvature in the pseudo-Galilean space," *Int. J. Math. Math. Sci.*, 2012, Art. ID 375264.

[17] J. W. Norbury, *General Relativity & Cosmology for Undergraduates.* Physics Department University of Wisconsin-Milwaukee P.O. Box 413 Milwaukee, WI 53201, 1997.

[18] H.B. Öztekin and S. Tatlipinar, "On some curves in Galilean plane and 3-dimensional Galilean space," *J. Dyn. Syst. Geom. Theor.*, vol. 10, no. 2, pp.189-196, 2012.

[19] A. Pressley, *Elementary Differential Geometry*. Second Edition. London, UK. Springer-Verlag London Limited, 2010.

[20] O. Röschel, *Die Geometrie des Galileischen Raumes.* Forschungszentrum Graz ResearchCentre, Austria, 1986.

[21] O. Röschel, *Die Geometrie des Galileischen Raumes, Bericht der Mathematisch Statistischen Sektion in der Forschungs-Gesellschaft Joanneum.* Bericht Nr. 256, Habilitationsschrift, Leoben, 1984.

[22] A. Saad and R.J. Low, "A generalized Clairaut's theorem in Minkowski space," *J. Geometry and Symmetry in Phys.*, vol. 35, pp.103-111, 2014.

[23] J.D. Walecka, *Introduction to General Relativity.* World Scientific, Singapore, 2007.

[24] J.D. Walecka, *Topics in Modern Physics: Theoretical Foundations.* World Scientific, 2013.

[25] D.W. Yoon, "Surfaces of Revolution in the three Dimensional Pseudo-Galilean Space," *Glasnik Math.*, vol. 48, no. 68, pp.415-428, 2013.

Bitlis Eren Üniversitesi Fen Bilimleri Dergisi
BİTLİS EREN UNIVERSITY JOURNAL OF SCIENCE
ISSN: 2147-3129/e-ISSN: 2147-3188
VOLUME:12 NO:1 PAGE: 10-16 YEAR: 2023
DOI:10.17798/bitlisfen.1146682

Investigation of Solid Formation Enthalpy and Molecular Mechanics Energies of Amino Acids via Force Field Approach

Levent SONGUR[1*], Oğuzhan ORHAN[2], Soner ÖZGEN [3]

[1]*Address (T.R. Ministry of Health Gaziantep Sehitkamil State Hospital,27500 Gaziantep, Turkey)*
[2]*Address (Firat University, Faculty of Arts and Sciences, Physics Department, 23119 Elazıg, Turke)*
(ORCID: 0000-0001-6393-5207) (ORCID: 0000-0003-2049-053X) (ORCID: 0000-0003-4292-9187)

Keywords: Solid Formation Enthalpy, Molecular Mechanics Energies, Amino Acids, Molecular Dynamics

Abstract

Amino acids which are organic compounds directly affect gene expression and control of the function of proteins. Their enthalpy values and molecular mechanical energies of them profoundly influence the protein folding mechanism. Molecular modeling simulations are one of the methods used to obtain their properties. In this study, the enthalpy values and molecular mechanics parameters of 17 amino acids have been investigated by the classical molecular dynamics simulation based on the force-field potential approach. Enthalpy values obtained from the simulation study for ALA, ASN, ASP, CYS, LYS, and PHE are in good agreement with the experimental data. In addition, molecular mechanics parameters such as Coulomb, bond, angle, dihedral, and Van der Waals have been calculated for all amino acids. It is represented that the Coulomb energy is quite low compared to the rest of the molecular mechanical energies. Their enthalpy and molecular energy values are crucial for molecular biology studies such as electronic interaction in protein-lipid modification, ligand binding to the cell surface, and correct protein localization.

1. Introduction

Amino acids are organic compounds that are consisted of Amino (COOH) (-COOH) which is basic and Carboxyl (COOH) (-COOH) which is possessed an acidic character. They have directly affected gene expression and control of the function of proteins [1].Proteins are linear polymers that fold into specific and ordered three-dimensional conformations based on their amino acid sequences[2], [3]. Their folding is a vital parameter that determines protein effectiveness in biological processes and this folding process is driven by thermodynamic stability. It is directly related to the enthalpy value that is dependent on the thermodynamic properties of both individual amino acids and their interactions among them[4], [5]. These enthalpy values can be obtained by both experimental methods and theoretical approaches[5]–[7]. Using this thermodynamic parameter, their probable folding concerning the protein sequence that is consist of amino acids can be predicted by approaches such as deep learning[8]. However, for these predictions to be accurate and reliable, it is necessary to find the enthalpy values of the amino acids.

To understand the effects of amino acids on biological activity, studies investigating thermochemical data are carried out extensively.Considering the literature, there are experimental studies on the thermodynamic properties of amino acids. For instance, Cole et al. have determined the enthalpy of the solid formation of alanine as -134.5 Kcal/mole experimentally [9]. Nguon (1977) et al., [10]have calculated it as -133.72 Kcal/mole, and Contineanu and Marchidan[11]have found out it as -134±0.41. This has also been studied by Petrauskas et al. using isothermal titration calorimetry to determine the average standard values of the thermodynamic parameters (Gibbs free energy, enthalpy, entropy, and heat capacity) of the interaction between positively charged amino acid homopolymers[12]. Hossian and colleagues have examined the current solubility of amino acids in different binary solvent systems and their thermodynamic behavior with different salt and organic solvent concentrations [13]. Pandit and De

*Corresponding author:levent.songur@saglik.gov.tr
Received: 21.07.2022, Accepted:.12.2022

have investigated the trends in thermodynamic properties in the interaction of amino acids and graphene oxide and conducted a study showing the correlation between enthalpy-entropy compensation analysis and flexibility [14]. Gheorghe et al. have calculated the enthalpy value of tryptophan by the calorimetric method [15].

The application of computer-based models using analytical potential energy functions within the framework of classical and quantum mechanics has proven its power to used in biochemistry and organic chemistry studies. Classical MD,ab-initio MD, and Monte Carlo methods are used for energy minimization on analytical potential energy surfaces in molecular mechanics applications[16]. These methods have been used to study a wide variety of phenomena, including the internal tension of organic molecules, the structure and dynamics of simple and complex liquids, the thermodynamics of ligand binding to proteins, and conformational transitions in nucleic acids [18]. Physical events in biological systems occur on a wide time scale, from 10-12 seconds to 10-18 seconds. For instance, in fully folded protein structures, bond vibrations take place in the femtosecond, while their side-chain rotamers occur in nanoseconds.Gas formation enthalpy of amino acids has been investigated by Dorofeeva and Ryzhova via the ab-initio study [17]. It has been exhibited that the calculated enthalpies of 10 out of 14 corresponded with experimental. In addition, Nie et al. theoretically have computed the evaporation enthalpies of 20 amino acids with Molecular Dynamics (MD) simulation[18].

In this study, the thermodynamic parameters of 17 amino acids have been obtained by the MD Simulation method. Force field approach, which is frequently used for biomolecules and allows us to produce the parameters very close to the experimental results, has been employed in this study. Finally, MD results have been compared with the experimental data. It is concluded that they are in agreement.

2. Material and Method

In this study, the classical MD method is employed to obtain the enthalpy values and molecular mechanical energies of amino acids[16]. The interactions of the atoms constituting amino acids have been described by the force-field potential. The equation of molecular mechanical force field potential and its parameters are given in equation 1. It consists of bond, angle, improper, torsion among the atoms of molecules, as well as, Lennard-Jones (LJ) and Coulomb energy coming from its electrical charge [19].

$$\cup = \sum_{\text{bounds}} k_i^{\text{bound}} (r_i - r_0)^2 + \sum_{\text{angles}} k_i^{\text{angle}} (\theta_i - \theta_0)^2 + \sum_{\text{improper}} k_\varphi (\varphi - \varphi_0)^2 + \sum_{\text{torsions}} k_i^{\text{torsion}} \left[1 + \cos\left(n_i \phi_i + \delta_i\right)\right] + \sum_i \sum_{j \neq i} 4\varepsilon_{ij} \left[\left(\frac{\sigma_{ij}}{r_{ij}}\right)^{12} - \left(\frac{\sigma_{ij}}{r_{ij}}\right)^{6}\right] + \sum_i \sum_{j \neq i} \frac{q_i q_j}{\varepsilon r_{ij}} \quad (1)$$

20 essential amino acids structure information in cartesian coordinates has been obtained from the Protein Data Bank (PDB) [20]. All simulations carry out via LAMMPS [21] software since it can calculate physical properties more efficiently than other counterparts. Their potential files have been generated by applying CHARMM topology (CHARMM36) to the Visual Molecular Dynamics (VMD) program [22]–[25]. However, 3 amino acids (Glutamine, Glutamate, and Glycine) have been not included in this study since potential parameters generated for them via CHARMM36 are problematic. To avoid surface interactions, the periodic boundary condition has been applied in all simulations. The Nosé-Hoover thermostat [26], [27], and Parrinello-Rahman [28]barostathave been employed to control both temperature and pressure. In the study, simulations have been made for each of the amino acids separately and no solvent was employed in them. System temperatures have been set to 298 K. Also, all models have been run for 0.5 nanoseconds to reach thermal equilibrium and 1 nanosecond to obtain the thermodynamics parameter with 0.2 femtoseconds time steps.

3. Results and Discussion

Protein chains can self-organize and transform into their natural structures in the appropriate environment. Thermodynamic investigations are excellent tools to explain these biological processes macroscopically [5]. Although thermodynamic control is widely accepted as the default behavior for correct folding, it is still difficult to understand in detail how the forces and atomic interactions involved in thermodynamic control relate the amino acid sequence to the folding and stability of the native structure [29]. Spectroscopic and calorimetric experiments have revealed that the increase in stability in protein folding, which is directly depend on amino acids, is mainly driven by enthalpy [30]. Enthalpy values are significant parameters for chemical reactions. The solid-state enthalpy of formation, calculated by MD simulation, is relational

energy, i.e. internal energy, based on the force field term [31]. The enthalpy values derived from the simulations and the measured values in the literature [32] are comparatively represented in Table 1. All enthalpies obtained from simulations have been averaged over the total simulation time that is 1 nanosecond. Although temperatures of the systems have fluctuated between 297K and 299K, the average temperature is around 298 K. It is concluded that the fluctuation of temperature results of potential energy functions. As it can be demonstrated in Table 1, the enthalpy of cysteine resulting from MD calculation is -124.37 Kcal/mole and the experimental value is -127.65 Kcal/mole[32]. The discrepancy between them is approximately 2.57%. While the enthalpy value obtained for alanine is -128.88 Kcal/mole, the value measured by the experimental method is -134.45 and the difference between them is 4.14%. In addition, the MD simulation and experimental enthalpy values for Phenylanin are -103.03 Kcal/mole, and -110.09 Kcal/mole, respectively. The enthalpy data of all amino acids included in the study are given in Table 1. Less than 10% difference between simulation results and experimental measurements supports the accuracy of simulation results. Weiss et al.[33] found that, with the thermochemical experimental approach, the enthalpy of solid-state formation is -127.63 Kcal/mole for Cysteine, -232.55 Kcal/mole for Aspartate, -188.58 Kcal/mol for Arginine, -148.9 Kcal/mole for Arginine, for Histidine, -111.62. However, for Prolinethere is quite a difference between the experimental and the simulation values. It is considered that below 10% difference between simulation results and experimental measurements can be acceptable. The difference between simulation and experimental results greater than %10 will be due to the potential energy parameters (CHARMM36) which cannot be acceptable.

Recent studies in cell biology and biophysics have created a new paradigm in protein targeting and function. The electrostatic charge on the surface of a biological membrane is emerging as a key determinant of signal protein localization and activity [34]. Therefore, electronic interaction is important for protein-lipid modification studies for ligand binding and accurate protein localization to the cell surface. Moreover, molecular mechanical energy directly influences the enthalpy and structural properties of amino acids. These energies are bond strain, angular, and torsional energies, which are the parameters of intramolecular interactions. Coulomb and Van der Waals energies are effective in intermolecular interaction. Van der Waals energy represents the long and short-distance electronic effect and is known as the electrodynamic energy used to explain bonding. Van der Waals terms utilizing theoretical protein-ligand binding calculations are defined by Lennard-Jones's potential approach [38]. Figure 1 indicates Van der Waals interaction. Thermodynamic parameters given in Table 2 are important parameters manipulated in protein design, bioengineering, and drug-vaccine studies. The molecular energy value is between the bonding atoms of the molecule, and it describes the energies required to bind related molecules in computational studies. Figure 1 shows the Coulomb interaction energy that allows proteins to approach the ligand or membrane surface.

The molecular mechanical energy values of the amino acids obtained in this study are presented in Table 2.It is concluded that the tertiary structures of proteins are affected by hydrophobic and Van der Waals interactions. Long-range Coulomb interactions, short-range Van der Waals interactions, and quantum mechanical repulsion between charged amino and carboxyl groups produce functional potential energy of proteins [35]. Protein folding will continue until the minimum energy level is reached [36], [37]. Moreover, the study of the time-dependent variation of these energy parameters is critical for determining the conformations of these molecules. It isdemonstrated that the molecular mechanical energy values of Alanine, Cysteine, Phenylalanine, and Lysine are compatible with the experimental results presented in Figure 1. It is exhibited that the molecular mechanical energies of ALA, CYS, LYS, and PHE fluctuate around the results given in Table 2 throughout the simulation. In addition, the Coulomb energy is quite low compared to the bond, angle, dihedral, and Van der Waals energies. Therefore, it is concluded that the remarkable negative energy in Coulomb energy is critical in preserving the natural structure of amino acids.

Table 1. Comparison of enthalpy as a result of MD simulations at 298 K temperature with experimental values [32].

Amino Acid	MD Result (Kcal/mole)	Experimental (Kcal/mole)	Error (%)
Alanine	-128.88	-134.45	4.14
Arginine	**-167.89**	**-149.04**	**12.65**
Asparagine	-205.72	-188.58	9.09
Aspartate	-237.66	-262.63	9.51
Cysteine	-124.37	-127.65	2.57
Histidine	-92.90	-105.60	12.03
Isoleucine	-100.17	-153.12	34.58
Leucine	-124.45	-154.60	19.50
Lysine	-175.97	-162.20	8.49
Methionine	-112.08	-138.0	18.78
Phenylalanine	-103.03	-110.09	6.41
Proline	-62.62	-121.30	48.38
Serine	-126.40	-175.13	27.83
Threonine	-124.90	-185.54	32.68
Tryptophan	-76.51	-97.18*	21.27
Tyrosine	-120.88	-163.86	26.23
Valine	-107.45	-150.30	28.51

*for Tryptophan [14]

Table 2. Molecular mechanical average energy values (Kcal/mol) were obtained as a result of the simulation of amino acids at 298K temperature. E_K, kinetic energy, E_P, potential energy, H, enthalpy, E_D, dihedral energy, E_A, angular energy, E_B, bond energy, E_{VDW}, Van der Waals energy, E_C, Coulomb energy, E_M, molecular energy

Amino Acid	E_K	E_P	H	E_D	E_A	E_B	E_{VDW}	E_C	E_M
Alanine	10.65	-139.19	-128.88	2.66	23.83	4.89	7.97	-116.52	31.80
Arginine	23.09	-191.30	-167.89	8.43	19.77	11.30	11.00	-242.43	40.13
Asparagine	14.23	-219.51	-205.28	9.33	25.71	5.28	6.12	-156.50	41.58
Aspartate	12.45	-249.29	-237.66	7.21	10.29	4.55	14.49	-95.17	22.84
Cysteine	11.59	-135.27	-124.37	3.18	8.01	5.37	8.73	-94.61	16.83
Histidine	16.89	-110.14	-92.90	12.03	20.67	7.37	5.18	-155.68	40.36
Isoleucine	18.55	-117.10	-100.17	9.99	23.04	7.24	9.11	-77.12	41.69
Leucine	18.65	-142.39	-124.45	10.63	24.66	7.26	4.59	-99.78	43.81
Lysine	21.24	-196.07	-175.97	6.34	15.62	7.09	8.82	-94.43	29.35
Methionine	16.91	-128.26	-112.08	4.83	15.28	7.03	5.71	-74.93	28.11
Phenylalanine	19.53	-122.27	-103.03	12.42	21.85	9.11	17.04	-96.19	44.27
Proline	14.26	-76.73	-62.62	7.50	11.63	4.82	1.12	-31.79	24.31
Serine	11.57	-138.67	-126.40	2.94	10.05	5.86	13.22	-54.50	19.13
Threonine	14.19	-138.53	-124.90	7.16	11.73	5.24	11.31	-51.41	24.43
Tryptophan	23.07	-99.04	-76.51	6.19	16.70	10.89	15.22	-29.55	34.06
Tyrosine	20.42	-140.93	-120.88	8.71	13.13	9.72	11.62	-75.49	31.86
Valine	16.05	-122.97	-107.45	2.73	13.07	6.06	8.54	-60.64	22.12

4. Conclusions and Suggestions

In this study, the enthalpy of solid formation for 17 amino acids and their molecular mechanical energies were calculated using the classical force-field approach. It has been observed that there is less than 10% error between the solid formation enthalpy calculated for ALA, ASN, ASP, CYS, LYS, and PHE and their corresponding experimental enthalpies. The improvement of models with a high error rate (referring to the experimental solid formation enthalpy) will be possible by improving the force field parameters.

These calculated enthalpy values will contribute to the determination of the thermodynamic stability of protein folding. Besides, it has been investigated that long-range interaction is more dominant than short-range interaction in amino acids. Since protein sequences are composed of amino acids, it is considered that long-range interaction is critical in the formation of these sequences and in preserving their natural structure. Furthermore, the obtained molecular mechanical energy values can be used in protein-lipid modification studies for electronic interaction, ligand binding to the cell surface, and accurate protein localization.

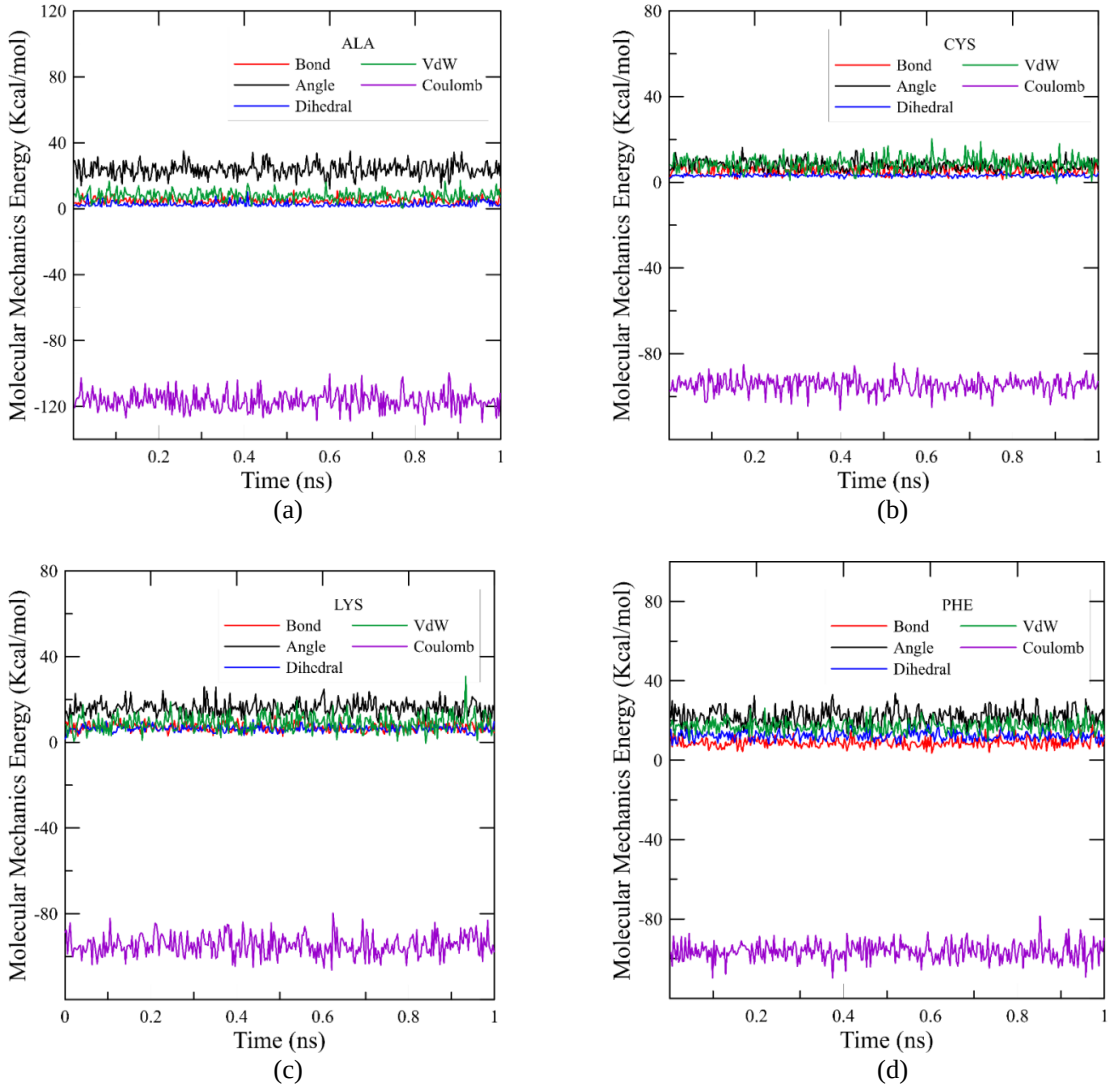

Figure 1. Molecular mechanical energy changes for amino acids (a) ALA, (b) CYS, (c) LYS, and (d) PHE, whose enthalpy values are close to the experimental measurements.

Acknowledgment

This work was supported by the Management Unit of Scientific Research projects of Firat University (FÜBAP)(Project Number: FF.16.28).

Contributions of the Authors

Levent Songur performed the potential energy file generation process by applying the CHARMM topology (CHARMM36). Oguzhan Orhan carried out MD simulations with LAMMPS software. Levent Songur and Soner OZGEN commented on the results obtained from the study. All authors contributed to the writing of the article.

Conflict of Interest Statement

There is no conflict of interest between the authors.

Statement of Research and Publication Ethics

The study is complied with research and publication ethics

References

[1] C. Kamble, R. Chavan, and V. Kamble, "A Review on Amino Acids," *Res. Rev. A J. Drug Des. Discov.*, vol. 8, no. 3, pp. 19–27, 2021.

[2] M. AlQuraishi, "End-to-End Differentiable Learning of Protein Structure," *Cell Syst.*, vol. 8, no. 4, pp. 292-301.e3, 2019, doi: 10.1016/j.cels.2019.03.006.

[3] A. V. Yakubovich, *Theory of Phase Transitions in Polypeptides and Proteins*, no. July. Berlin, Heidelberg: Springer Berlin Heidelberg, 2011.

[4] A. V. Finkelstein and O. V. Galzitskaya, "Physics of protein folding," *Phys. Life Rev.*, vol. 1, no. 1, pp. 23–56, 2004, doi: 10.1016/j.plrev.2004.03.001.

[5] S. A. Shirdel and K. Khalifeh, "Thermodynamics of protein folding: methodology, data analysis and interpretation of data," *Eur. Biophys. J.*, no. 0123456789, 2019, doi: 10.1007/s00249-019-01362-7.

[6] T. Schlick, *Molecular Modeling and Simulation: An Interdisciplinary Guide (Interdisciplinary Applied Mathematics, Volume 21), 2nd Edition*. 2010.

[7] P. Singh, D. Kumar, S. Pal, K. Kumari, and I. Bahadur, "L-amino-acids as immunity booster against COVID-19: DFT, molecular docking and MD simulations," *J. Mol. Struct.*, vol. 1250, p. 131924, 2022, doi: 10.1016/j.molstruc.2021.131924.

[8] M. Eisenstein, "Artificial intelligence powers protein-folding predictions," *Nature*, vol. 599, no. 7886, pp. 706–708, 2021, doi: 10.1038/d41586-021-03499-y.

[9] J. O. Hutchens, A. G. Cole, and J. W. Stout, "Heat Capacities from 11 to 305° K, Entropies, Enthalpy, and Free Energy of Formation of l-Serine," *J. Biol. Chem.*, vol. 239, no. 12, pp. 4194–4195, Dec. 1964, doi: 10.1016/S0021-9258(18)91154-3.

[10] S. Nguon Ngauv, R. Sabbah, and M. Laffitie, "Thermodynamique de composes azotes III. Etude Thermochimique de la glycine et de la l-α-alanine," *Thermochim. Acta*, vol. 20, no. 3, pp. 371–380, 1977, doi: 10.1016/0040-6031(77)85091-0.

[11] O. V. Dorofeeva and O. N. Ryzhova, "Revision of standard molar enthalpies of formation of glycine and l-alanine in the gaseous phase on the basis of theoretical calculations," *J. Chem. Thermodyn.*, vol. 41, no. 4, pp. 433–438, 2009, doi: 10.1016/j.jct.2008.12.001.

[12] V. Petrauskas, E. Maximowitsch, and D. Matulis, "Thermodynamics of Ion Pair Formations Between Charged Poly(Amino Acid)s," *J. Phys. Chem. B*, vol. 119, no. 37, pp. 12164–12171, 2015, doi: 10.1021/acs.jpcb.5b05767.

[13] A. Hossain, S. Roy, and B. K. Dolui, "Effects of thermodynamics on the solvation of amino acids in the pure and binary mixtures of solutions: A review," *J. Mol. Liq.*, vol. 232, pp. 332–350, 2017, doi: 10.1016/j.molliq.2017.02.080.

[14] S. Pandit and M. De, "Interaction of amino acids and graphene oxide: Trends in thermodynamic properties," *J. Phys. Chem. C*, vol. 121, no. 1, pp. 600–608, 2017, doi: 10.1021/acs.jpcc.6b11571.

[15] D. Gheorghe, A. Neacşu, I. Contineanu, S. Tănăsescu, and Ş. Perişanu, "A calorimetric study of l-, d- and dl-isomers of tryptophan," *J. Therm. Anal. Calorim.*, vol. 130, no. 2, pp. 1145–1152, 2017, doi: 10.1007/s10973-017-6396-z.

[16] M. Feig, *Modeling Solvent Environments: Applications to Simulations of Biomolecules*. 2010.

[17] O. V. Dorofeeva and O. N. Ryzhova, "Gas-phase enthalpies of formation and enthalpies of sublimation

of amino acids based on isodesmic reaction calculations," *J. Phys. Chem. A*, vol. 118, no. 19, pp. 3490–3502, 2014, doi: 10.1021/jp501357y.

[18] B. Nie, R. Li, Y. Wu, X. Yuan, and W. Zhang, "Theoretical Calculation of the Thermodynamic Properties of 20 Amino Acid Ionic Liquids," *J. Phys. Chem. B*, vol. 122, no. 46, pp. 10548–10557, 2018, doi: 10.1021/acs.jpcb.8b06813.

[19] K. Vanommeslaeghe, E. Prabhu Raman, and A. D. MacKerell, "Automation of the CHARMM General Force Field (CGenFF) II: Assignment of Bonded Parameters and Partial Atomic Charges," *J Chem Inf Model*, vol. 52, no. 12, pp. 3155–3168, 2013, doi: 10.1021/ci3003649.

[20] H. M. Berman, "The Protein Data Bank," *Nucleic Acids Res.*, vol. 28, no. 1, pp. 235–242, Jan. 2000, doi: 10.1093/nar/28.1.235.

[21] A. P. Thompson *et al.*, "LAMMPS - a flexible simulation tool for particle-based materials modeling at the atomic, meso, and continuum scales," *Comput. Phys. Commun.*, vol. 271, p. 108171, 2022, doi: 10.1016/j.cpc.2021.108171.

[22] R. B. Best *et al.*, "Optimization of the additive CHARMM all-atom protein force field targeting improved sampling of the backbone φ, ψ and side-chain χ1 and χ2 Dihedral Angles," *J. Chem. Theory Comput.*, vol. 8, no. 9, pp. 3257–3273, 2012, doi: 10.1021/ct300400x.

[23] A. D. MacKerell *et al.*, "All-atom empirical potential for molecular modeling and dynamics studies of proteins," *J. Phys. Chem. B*, vol. 102, no. 18, pp. 3586–3616, 1998, doi: 10.1021/jp973084f.

[24] S. Jo *et al.*, "CHARMM-GUI 10 years for biomolecular modeling and simulation," *J. Comput. Chem.*, vol. 38, no. 15, pp. 1114–1124, 2017, doi: 10.1002/jcc.24660.

[25] W. Humphrey, A. Dalke, and K. Schulten, "VMD - Visual Molecular Dynamics," *J. Molec. Graph.*, vol. 14, pp. 33–38, 1996.

[26] S. Nosé, "A unified formulation of the constant temperature molecular dynamics methods," *J. Chem. Phys.*, vol. 81, no. 1, pp. 511–519, 1984, doi: 10.1063/1.447334.

[27] W. G. Hoover, "Canonical dynamics: Equilibrium phase-space distributions," *Phys. Rev. A*, vol. 31, no. 3, pp. 1695–1697, Mar. 1985, doi: 10.1103/PhysRevA.31.1695.

[28] M. Parrinello and A. Rahman, "Polymorphic transitions in single crystals: A new molecular dynamics method," *J. Appl. Phys.*, vol. 52, no. 12, pp. 7182–7190, 1981, doi: 10.1063/1.328693.

[29] J. O. Wrabl, S. A. Larson, and V. J. Hilser, "Thermodynamic propensities of amino acids in the native state ensemble: Implications for fold recognition," *Protein Sci.*, vol. 10, no. 5, pp. 1032–1045, 2001, doi: 10.1110/ps.01601.

[30] S. Pal, P. Pyne, N. Samanta, S. Ebbinghaus, and R. K. Mitra, "Thermal stability modulation of the native and chemically-unfolded state of bovine serum albumin by amino acids," *Phys. Chem. Chem. Phys.*, vol. 22, no. 1, pp. 179–188, 2019, doi: 10.1039/c9cp04887a.

[31] F. Peccati and G. Jiménez-Osés, "Enthalpy-Entropy Compensation in Biomolecular Recognition: A Computational Perspective," *ACS Omega*, vol. 6, no. 17, pp. 11122–11130, 2021, doi: 10.1021/acsomega.1c00485.

[32] P. J. Linstrom and W. G. Mallard, "The NIST Chemistry WebBook: A chemical data resource on the Internet," *J. Chem. Eng. Data*, vol. 46, no. 5, pp. 1059–1063, 2001, doi: 10.1021/je000236i.

[33] I. M. Weiss, C. Muth, R. Drumm, and H. O. K. Kirchner, "Thermal decomposition of the amino acids glycine, cysteine, aspartic acid, asparagine, glutamic acid, glutamine, arginine and histidine," *BMC Biophys.*, vol. 11, no. 1, pp. 1–15, 2018, doi: 10.1186/s13628-018-0042-4.

[34] N. M. Goldenberg and B. E. Steinberg, "Surface charge: A key determinant of protein localization and function," *Cancer Res.*, vol. 70, no. 4, pp. 1277–1280, 2010, doi: 10.1158/0008-5472.CAN-09-2905.

[35] C. Clementi and S. S. Plotkin, "The effects of nonnative interactions on protein folding rates: Theory and simulation," *Protein Sci.*, vol. 13, no. 7, pp. 1750–1766, 2004, doi: 10.1110/ps.03580104.

[36] E. G. Asmus, "Protein Structure," *Am. Biol. Teach.*, vol. 69, no. 1, pp. 38–40, 2007.

[37] V. Raicu and A. Popescu, *Integrated Molecular and Cellular Biophysics*, no. July. Dordrecht: Springer Netherlands, 2008.

Bitlis Eren Üniversitesi Fen Bilimleri Dergisi
BİTLİS EREN UNIVERSITY JOURNAL OF SCIENCE
ISSN: 2147-3129/e-ISSN: 2147-3188
VOLUME: 12 NO: 1 PAGE: 17-24 YEAR: 2023
DOI:10.17798/bitlisfen.1155725

Predictive Analysis Using Web Scraping for the Real Estate Market in Gaziantep

Ali Can ÜZÜMCÜ[1], Nazmiye ELİGÜZEL[2*]

[1] *Gaziantep University, Industrial Engineering, 27310 Gaziantep, Turkey*
[2] *Gaziantep Islam Science and Technology University, Industrial Engineering, 27010 Gaziantep, Turkey (ORCID: 0000-0002-8089-2285) (ORCID: 0000-0001-6354-8215)*

Keywords: Gaziantep, Machine learning, Real estate, Web scraping.

Abstract
For investors and people who want to own a property, real estate is a crucial industry. Real estate includes land and any enduring construction, whether natural or artificial, such as houses, residences, apartments, and commercial structures. In Turkey, it is common to believe that owning property makes you live comfortably. Therefore, house ownership is a common aspiration among Turkish families. However, a variety of factors, such as a country's economic structure, inflation, world events, politics, etc., have an impact on the real estate market. In addition, the location, neighborhood, size, and number of rooms of a house can all affect how much it costs to live there. Gaziantep city is considered for analysis in the proposed study. The goal of this study is to predict which neighborhood, given a prospective buyer's financial status and specific property attributes, someone can afford to live in. As a result, web scraping is used to collect real estate data from the website. Once the data has been gathered, forecasting the neighborhood of a house is done using machine learning algorithms including decision trees, random forest, and extra trees. The results demonstrate that all algorithms produce good results with a performance accuracy of over 80%. However, among these algorithms, decision tree classification offers the best performance.

1.Introduction

Gaziantep city is located in South-Eastern Anatolian Region in Turkey. The province's 6554 km2 territorial area represents about 1% of Turkey's total land area and there are about 2130432 people living there[2]. It has nine districts. Gaziantep is also one of the Turkey's most expensive cities. One of the most important investments in most people's portfolios is real estate. Real estate includes land and any enduring construction, whether natural or artificial, such as houses, apartments, commercial structures, and fences [1]. In 2021, there were 1491856 housing sales in Turkey, a 0.5 percent decline from the previous year. With 276223 homes and 18.5 percent of the market, Istanbul had the biggest percentage of house sales. Ankara, with 144104 house sales and a 9.7 percent market share, and Izmir, with 86722 house sales and a 5.8 percent market share, followed Istanbul in that order. The provinces with the lowest number of house sales were Hakkari (267), Ardahan (377), and Bayburt (871), in that order. Gaziantep, on the other hand, ranked 10th with 35610 houses [3]. Figure 1 provides information regarding 2021 housing sales data. House prices in Gaziantep have increased significantly, from just 145661TL/m^2

* Corresponding author: nazmiye.eliguzel@gibtu.edu.tr
Received: 04.08.2022, Accepted: 01.03.2023

[2] http://www.gaziantep.gov.tr/

[3]https://data.tuik.gov.tr

in 2014 to over 721839 TL/m^2 in 2022[4]. In Figure 2, the trend of change in house prices is given.

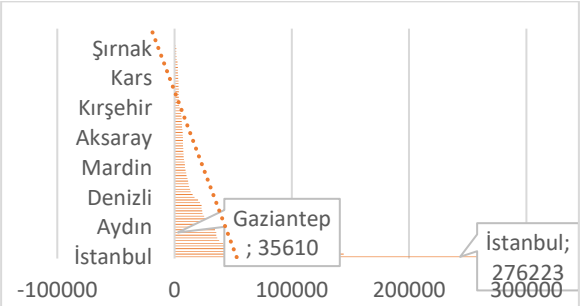

Figure 1. Housing sales in 2021 by provinces (TÜİK)

One of the biggest cities in Turkey, Gaziantep, has experienced significant housing inflation in recent years. Despite this, it has a high rank in terms of housing sales. Housing serves as a place to live as well as a significant investment that has an impact on life quality. The neighborhood of a house is very important to its stakeholders (investors, homeowners, developers, appraisers, and others) [2]. Therefore, it's critical for people to choose the neighborhood in which they can buy the house that has the features they want for their budget.

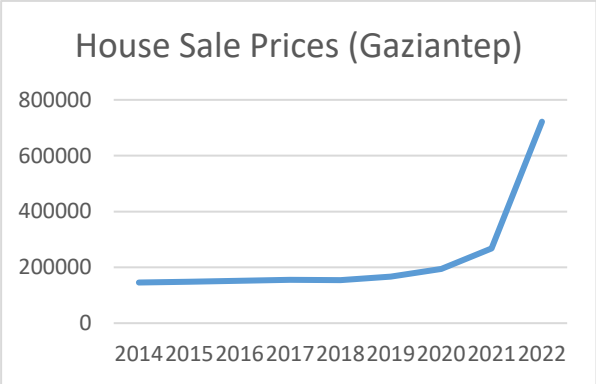

Figure 2. Change of house prices per square meter in Gaziantep by years

A rise in housing costs can be attributed to numerous things. The price of housing can alter due to a variety of factors, including a nation's economic structure, inflation, global events, politics, etc. These are the external variables. Other aspects of houses, such as the area, neighborhood, the size, and the number of rooms, can also have an impact on household pricing. The square meter of the house, the number of rooms, the district, real estate type, and the price are taken into account in the proposed study to forecast a house's neighborhood. Accurate predictions are required for the real estate and housing markets. We can notice a pattern that appears in the purchasing and selling of properties: for most people, owning a house is a lifelong ambition [3]. For various classification and regression problems, methods like the decision tree [4], extra trees [5], and random forest [6] are also frequently utilized. Machine learning algorithms were proposed by the authors as a reliable way to predict real estate property values. To increase prediction accuracy, they also examined feature importance and other data analysis techniques. In their research, they used linear regression, decision trees, XGBoost, extra trees, and random forests [7].

The objective of this study is to predict the neighborhood that a potential home buyer can afford to live in given her financial situation and certain property characteristics. Therefore, real estate data is taken from the website via web scraping. Machine learning methods like decision trees (DT), random forest (RF), and extra trees (ET) are used to forecast a house's neighborhood once the data has been collected.

The remainder of this paper is structured as follows: The literature review is presented in section 2, the research methodology is shown in section 3, and the findings and outcomes are presented in section 4. In section 5, the study is completed.

2. Literature Review

In order to assess real estate, there are some traditional approaches [2] in the literature such as cost approach [8] and income approach [9]. However, many machine learning-based methods have been utilized in recent years to forecast real estate values because they can identify functional relationships in past data.

The hedonic model, machine learning model, and geographically and temporally weighted regression (GTWR) were combined by Hu et al. [10]. They illustrated a novel method for segmenting the housing market. They then applied it to analyze the dynamics of the selling and renting submarkets in Shanghai, China, from 2018 to 2020. The method offered a useful and

[4] https://www.zingat.com/gaziantep-bolge-raporu

effective tool for segmenting the urban housing market.

Another study proposed by Xue and Yao [11] used a RF model to assess the significance and consequences of the physical environment, commute distance, housing costs, living area, and domestic socioeconomic and demographic factors on the housing relocation activity of members of the family with commuter employees or students. Their purpose was to offer baseline data for designers and real estate construction firms to use when planning and developing linked land, as well as to assist urban planners and directors in statistically examining the impact of causal factors on housing relocation activity.

Using data gathered from 24 randomly chosen Turkish cities, a Bayesian network driven by machine learning was created through a constrained structural learning method by Sevinç [12]. The information included various characteristics such as sales prices, details about each apartment's features, including its amount of bedrooms, the age of the building, whether a balcony is there, the net area, the heating system, mortgageability, the amount of bathrooms, seller type, and floor position.

Chou et al. [2] proposed a research that a brief overview of machine learning methods for forecasting home prices. The actual price registration system of Taiwan's Interior Ministry was used to gather information on housing transaction prices in Taipei City. Baseline and ensemble models were created using four popular artificial intelligence methods: Linear Regression, Artificial Neural Networks, Classification and Regression Trees, Support Vector Machines. Additionally, a hybrid model was created, and both baseline and ensemble methods were utilized to assess its prediction performance to that of the separate models.

Louati et al. [13] developed a collection of machine learning algorithms to perform analysis that could improve the accuracy of estimating land prices. The DT, RF, and linear regression are some of the machine learning methods used in their work. They gathered information from 5946 lands located in Riyadh, Saudi Arabia. Modern performance criteria, such as mean absolute error, median squared error, and mean squared error were utilized to assess the performance of the constructed models. According to the experiments, the RF-based model performs better than the other models.

Another research [14] that examined into the reasons Taiwanese home prices have risen steadily for the past ten years. Data relating to real estate gathered from publicly available websites was clustered employing a double-bottom map particle swarm optimization analytical technique. Population, rent and the money availability are three crucial elements that could impact real estate value trends, and they were highlighted in their assessment on the clustering results.

Instead of using different machine learning techniques to predict the transactions or list cost of real estate assets without distinguishing the building and land costs, Kim et al. [15] proposed a study that estimated cost of land utilizing a significant amount of land-utilization data information gathered from variety of building and land-related datasets. The RF and XGBoost algorithms were utilized to forecast 52,900 land costs in Seoul, South Korea, from January 2017 through December 2020. Additionally, the models underwent separate training for various land utilization and time periods. The overall findings showed that XGBoost produces a greater forecasting accuracy.

Some of the studies considered web scrapping technology in order to predict real estate [16]–[19]. Web scraping is a method for obtaining data from the Internet. The process of gathering data from websites and transferring them to a more convenient and more flexible form so that they can be examined and checked with ease is also referred to as web scraping, sometimes web crawling or data scraping, and sometimes data mining or text mining [16].

Web scraping and machine learning techniques are both utilized in the proposed study. While some studies focused solely on a few regions, others neglected crucial factors that affected real estate values, like the amount of rooms, neighborhood, and area. The studies' most typical drawback is that they estimate real estate prices in a limited region with few features. Even though the proposed study is focused on a particular area, it differs from prior studies in that it estimates neighborhood values rather than prices and deals with different real-estate features such as the square meter of real estate, the number of rooms, district, neighborhood, real estate type, and price. It is predicted where people can dwell based on a set of parameters and the amount of money they hold.

3. Material and Method

There are two parts to the planned study. Data is gathered in the first step using a web scraping technique. Utilizing machine learning techniques, the result is predicted in the second stage. The crucial steps in the use of web scraping and machine learning algorithms are presented in this section. First of all, web scraping is conducted to obtain data. The sequential procedures and methodologies for the web scrapping are shown in Figure 3.

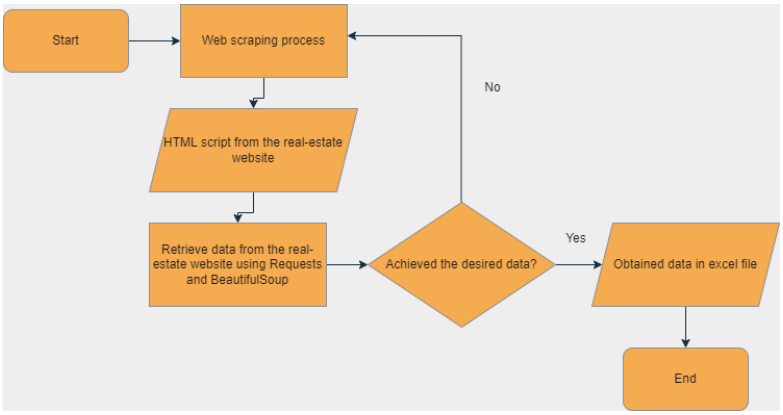

Figure 3. The structure of the proposed web scraping

Web scraping is a method of obtaining information from webpages using software. By utilizing low-level Hypertext Transfer Protocol (HTTP), this sort of software program simulates human browsing or investigation of the World Wide Web [20]. Python software is used for the web scraping. The steps of web scraping are given as follows:

- First of all, “EmlakBuluyoruz.Com” is chosen as real estate website[5].
- Search is conducted by considering Gaziantep city[6]. Houses for sale are considered in this study.
- In Python, Requests module is used to reach Hypertext Markup Language (HTML) contents of the website.
- The BeautifulSoup module is used to parse the contents of the HTML document and then discover elements using the "HTML class name" in the subsequent phase.
- After the mentioned processes, the data is obtained by utilizing the related class name.
- Finally, a excel file is created and data is saved for the next processes.

Through web scraping, a total of 548 pieces of data were collected on June 25, 2022. In Table 1, a sample of data is demonstrated. In the proposed study, to predict an house's neighborhood, the square meter of the house, the number of rooms, the district, real estate type, and the price are considered. Table 2 demonstrates the definition and data types of the variables. Scikit-learn supervised learning algorithms such as DT, RF, and ET are used to predict the neighborhood of a real estate.

[5] https://www.emlakbuluyoruz.com/

[6] https://www.emlakbuluyoruz.com/satilik/konut

Table 1. A sample data

The square meter, The number of rooms, District, Neighborhood, Real estate type, Price
170,3+1,Şehitkamil,Değirmiçem,Apartment,1275000
155,3+1,Şahinbey,Güneykent,Apartment,955000
195,3+1,Şehitkamil,İbrahimli,Apartment,2550000
250,4+1,Oğuzeli,Körkün,Cottage,3500000
120,2+1,Şahinbey,Kıbrıs,SingleHouse,400000
200,4+1,Şehitkamil,Onbeştemmuz,Apartment,2300000
175,3+1,Şehitkamil,İbrahimli,Apartment,1890000

In the proposed study, the target is to classify the target class, there are 75 classes available. neighborhood. Given that the neighborhood is

Table 2. Definition and data types of the variables

	Definition	Data Type
The square meter	Side x side = area of a square is the formula for calculating a square's surface area.	Integer
The number of rooms	Consists of rooms that may be occupied, such as bedrooms, kitchens, dining rooms, and living rooms.	String
District	A district is a particular kind of administrative division that the local government oversees in some countries.	String
Neighborhood	A neighborhood is a place where people reside and socialize.	String
Real estate type	Type of buildings	String
Price	Value of real estate	Integer

The collected data is processed via above mentioned machine learning techniques. These techniques are explained as follows:

3.1. Decision tree

DTs are one of the widely utilized techniques among classification algorithms. It is a non-parametric technique. DTs have nodes that form a rooted tree. That is, it is a directed tree without incoming edges at the root node. Each of the other nodes has just one incoming edge. Internal or test nodes are the name given to outgoing edges. Finally, the remaining nodes are known as leaves. [21]. Making a model that predicts the target value variable based on a variety of input factors is the aim of DT learning [22]. It is a graphical representation of decisions and their probable outcomes.

3.2 Random forest

One of the classifier algorithms used in it is composed of a number of DTs, each of which is created by putting an algorithm into practice. A majority vote is used to estimate the RF, rather than individual tree estimates [23]. Each tree in the ensemble is built individually utilizing a sample taken with substitution from the training set. As a result, RF is used to tackle mentioned problem due to its randomness [24].

3.3 Extra trees

ET, highly random trees based on the ensemble approach, lessen the weak generalization property and propensity for overfitting of conventional standalone DTs [25]. A meta-predictor that is fitted with several randomized DTs is utilized in this class. [26].

3.4. Evaluation

In the proposed study, the machine learning classification algorithms such as DT, RF, and ET are utilized. The Python programming language's Sklearn library is used. Classification accuracy (ACC) and F-measure are the metrics that are utilized for evaluation.

Evaluation metrics are computed by the given equations [27]:

ACC: Classifier accuracies are evaluated by using confusion matrices.

$$ACC = \frac{True\ Negatives + True\ Positives}{True\ Positives + False\ Positives + False\ Negatives + True\ Negatives} \quad (1)$$

F-measure: The other frequently used method for assessing the effectiveness of classification algorithms is the F-measure. It is a classification algorithm's harmonic mean of precision and recall. Improved predictive performance is indicated by higher F-measure values. The average F-measure for all one-versus-all classes is employed in this study as the macro-averaged F-measure.

$$\text{Macro} - \text{averaged F} - \text{measure} = \frac{1}{n}\sum_{i=1}^{n} \frac{2 * Precisioni * Recalli}{Preciisoni + Recalli} \quad (2)$$

$$\text{Precision} = \frac{True\ Positives}{True\ Positives + False\ Positives} \quad (3)$$

$$\text{Recall} = \frac{True\ Positives}{True\ Positives + False\ Negatives} \quad (4)$$

4. Results and Discussions

The results of the algorithms are given in Table 3.

Table 3. Results of the applied machine learning algorithms

Algorithm	ACC	F-measure	Precision	Recall
DT	0.878	0.869	0.90	0.879
RF	0.848	0.845	0.879	0.848
ET	0.863	0.860	0.892	0.864

As can be shown from Table 3, all algorithms offer satisfactory outcomes of more than 84 percent when both ACC and F-measure are taken into account. However, DT provides better performance when compared with the other algorithms. ETs come after DT. The worst performance is provided by RF. The technologies of web scraping and machine learning are used to conduct this investigation. By considering DT algorithm, the neighborhood of a real estate can be predicted. Finally, the following are the implications of the proposed study:

- Web scraping technique is used to mine real estate data from a real estate website.
- Performances of various machine learning algorithms such as DT, RF, and ET are compared.
- While all algorithms perform well, DT produces the best results.
- An accurate prediction is given for determining a house's neighborhood.
- The proposed study can be beneficial for both people, investors, and government.

5. Conclusion

Recently, utilizing machine learning models with publicly available data has helped research on predicting real estate value. Unlike studies that make price estimations, the proposed study aims to predict the neighborhood of a house by using machine learning techniques such as DT, RF, and ET. We make an estimation of the Gaziantep real estate market. Based on a number of criteria and the amount of money they own, it is estimated where people can live. The data is retrieved from a real estate website via web scraping. The planned study includes an investigation into the city of Gaziantep. The real estate market is impacted by a number of variables, including a nation's economic structure, inflation, global events, politics, etc. These are the external factors. In addition, a house's size, number of rooms, neighborhood, and location can all determine how much it costs to live there as internal factors. In the proposed study, internal factors are considered to predict the neighborhood of a house. Based on the study, all algorithms provided good performance by estimating the neighborhood of a house.

However, DT provides the best results. These results can help decision-makers choose the neighborhood they want to live in or invest in. As we concentrated on Gaziantep for the regional study, data gathering was a constraint of our study. Conducting an analysis of Turkey is a potential direction for future research. In addition, data from other real estate websites can be gathered and analyzed for the future work.

Acknowledgment

This research did not receive any specific grant from funding agencies in the public, commercial, or not-for-profit sectors.

Contributions of the Authors

The model and computational framework were developed by Ali Can ÜZÜMCÜ and Nazmiye ELİGÜZEL, who also carried out the experiments. The manuscript was written by Nazmiye ELİGÜZEL. Each author contributed ideas that helped refine the study, analysis, and article.

Conflict of Interest Statement

There is no conflict of interest between the authors.

Statement of Research and Publication Ethics

The study is complied with research and publication ethic

References

[1] J. Ratcliffe, M. Stubbs;, and M. Keeping, *Urban Planning and Real Estate Development*. Routledge, 2021.

[2] J. S. Chou, D. B. Fleshman, and D. N. Truong, *Comparison of machine learning models to provide preliminary forecasts of real estate prices*, no. 0123456789. Springer Netherlands, 2022.

[3] A. S. Ravikumar, *Real Estate Price Prediction Using Machine Learning*. 2017.

[4] M. F. Lee, G. S. Chen, S. P. Lin, and W. J. Wang, "A Data Mining Study on House Price in Central Regions of Taiwan Using Education Categorical Data, Environmental Indicators, and House Features Data," *Sustain.*, vol. 14, no. 11, 2022, doi: 10.3390/su14116433.

[5] C. H. Cheng and M. C. Tsai, "An Intelligent Homogeneous Model Based on an Enhanced Weighted Kernel Self-Organizing Map for Forecasting House Prices," *Land*, vol. 11, no. 8, 2022, doi: 10.3390/land11081138.

[6] Y. Ahn and C. K. Uejio, "Modeling Air Conditioning Ownership and Availability," *SSRN Electron. J.*, vol. 46, no. October, p. 101322, 2022, doi: 10.2139/ssrn.4211073.

[7] M. Cekic, K. N. Korkmaz, H. Mukus, A. A. Hameed, A. Jamil, and F. Soleimani, "Artificial Intelligence Approach for Modeling House Price Prediction," pp. 1–5, 2022, doi: 10.1109/icmi55296.2022.9873784.

[8] D. Kulikauskas, "The user cost of housing in the Baltic states," *J. Eur. Real Estate Res.*, vol. 10, no. 1, pp. 17–34, 2017, doi: 10.1108/JERER-11-2015-0042.

[9] G. J. Rangel, J. W. J. Ng, T. T. Murugasu, and W. C. Poon, "Measuring Malaysian housing affordability: the lifetime income approach," *Int. J. Hous. Mark. Anal.*, vol. 12, no. 5, pp. 966–984, 2019, doi: 10.1108/IJHMA-02-2019-0023.

[10] L. Hu, S. He, and S. Su, "A novel approach to examining urban housing market segmentation: Comparing the dynamics between sales submarkets and rental submarkets," *Comput. Environ. Urban Syst.*, vol. 94, no. January, p. 101775, 2022, doi: 10.1016/j.compenvurbsys.2022.101775.

[11] F. Xue and E. Yao, "Adopting a random forest approach to model household residential relocation behavior," *Cities*, vol. 125, no. May 2021, p. 103625, 2022, doi: 10.1016/j.cities.2022.103625.

[12] V. Sevinç, "Determining the Flat Sales Prices by Flat Characteristics Using Bayesian Network Models," *Comput. Econ.*, vol. 59, no. 2, pp. 549–577, 2022, doi: 10.1007/s10614-021-10099-5.

[13] A. Louati, R. Lahyani, A. Aldaej, A. Aldumaykhi, and S. Otai, "Price forecasting for real estate using machine learning: A case study on Riyadh city," *Concurr. Comput. Pract. Exp.*, vol. 34, no. 6, pp. 1–16, 2022, doi: 10.1002/cpe.6748.

[14] C. H. Yang, B. Lee, and Y. Da Lin, "Effect of Money Supply, Population, and Rent on Real Estate: A Clustering Analysis in Taiwan," *Mathematics*, vol. 10, no. 7, pp. 1–17, 2022, doi: 10.3390/math10071155.

[15] J. Kim, J. Won, H. Kim, and J. Heo, "Machine-learning-based prediction of land prices in Seoul, South Korea," *Sustain.*, vol. 13, no. 23, pp. 1–14, 2021, doi: 10.3390/su132313088.

[16] T. G. D. Souza, F. D. R. Fonseca, V. D. O. Fernandes, and J. C. Pedrassoli, "Exploratory spatial analysis of housing prices obtained from web scraping technique," *Int. Arch. Photogramm. Remote Sens. Spat. Inf. Sci. - ISPRS Arch.*, vol. 43, no. B4-2021, pp. 135–140, 2021, doi: 10.5194/isprs-archives-XLIII-B4-2021-135-2021.

[17] H. Salem and M. Mazzara, "ML-based Telegram bot for real estate price prediction," *J. Phys. Conf. Ser.*, vol. 1694, no. 1, 2020, doi: 10.1088/1742-6596/1694/1/012010.

[18] A. Grybauskas, V. Pilinkienė, and A. Stundžienė, "Predictive analytics using Big Data for the real estate market during the COVID-19 pandemic," *J. Big Data*, vol. 8, no. 1, 2021, doi: 10.1186/s40537-021-00476-0.

[19] H. Ahmed, T. A. Jilani, W. Haider, S. N. Hasany, M. A. Abbasi, and A. Masroor, "Producing standard rules for smart real estate property buying decisions based on web scraping technology and machine learning techniques," *Int. J. Adv. Comput. Sci. Appl.*, vol. 11, no. 3, pp. 498–505, 2020, doi: 10.14569/ijacsa.2020.0110363.

[20] V. S. Katti and S. H. N, "Patents and Publications Web Scraping," *IJCSN Int. J. Comput. Sci. Netw.*, vol. 5, no. 2, pp. 2277–5420, 2016, [Online]. Available: www.IJCSN.org.

[21] L. Rokach and O. Maimon, "DECISION TREES," in *DATA MINING AND KNOWLEDGE DISCOVERY HANDBOOK*, no. January, 2005, pp. 165–192.

[22] M. A. Jun and J. C. P. Cheng, "Selection of target LEED credits based on project information and climatic factors using data mining techniques," *Adv. Eng. Informatics*, vol. 32, pp. 224–236, 2017, doi: 10.1016/j.aei.2017.03.004.

[23] S. Shalev-Shwartz and S. Ben-David, *Understanding machine learning: From theory to algorithms*. New York: Cambridge University, 2013.

[24] G. Khanvilkar and D. Vora, "Product Recommendation using Sentiment Analysis of Reviews : A Random Forest Approach," *Int. J. Eng. Adv. Technol.*, no. January, 2019.

[25] S. Galelli and A. Castelletti, "Assessing the predictive capability of randomized tree-based ensembles in streamflow modelling," *Hydrol. Earth Syst. Sci.*, vol. 17, no. 7, pp. 2669–2684, 2013, doi: 10.5194/hess-17-2669-2013.

[26] M. W. Ahmad, J. Reynolds, and Y. Rezgui, "Predictive modelling for solar thermal energy systems : A comparison of support vector regression , random forest , extra trees and regression trees," *J. Clean. Prod.*, vol. 203, pp. 810–821, 2018, doi: 10.1016/j.jclepro.2018.08.207.

[27] A. Onan, "Biomedical Text Categorization Based on Ensemble Pruning and Optimized Topic Modelling," *Comput. Math. Methods Med.*, vol. 2018, 2018, doi: 10.1155/2018/2497471.

Bitlis Eren Üniversitesi Fen Bilimleri Dergisi
BİTLİS EREN UNIVERSITY JOURNAL OF SCIENCE
ISSN: 2147-3129/e-ISSN: 2147-3188
VOLUME: 12 NO: 1 PAGE: 25-32 YEAR: 2023
DOI:10.17798/bitlisfen.1170647

A new characterization of the Aminov surface with regards to its Gauss map in $\mathbb{E}^4$

Sezgin BÜYÜKKÜTÜK[1*], Günay ÖZTÜRK[2]

[1]*Kocaeli University, Gölcük Vocational School of Higher Education , Kocaeli, Turkey*
[2]*İzmir Democracy University, Arts and Science Faculty, Department of Mathematics, İzmir, Turkey*
(ORCID: 0000-0002-1845-0822) (ORCID: 0000-0002-1608-0354)

Keywords: Aminov surface, Gauss map, Monge patch.

Abstract

In this study, we focus on the Aminov surface with regard to its Gauss map in $\mathbb{E}^4$. Firstly, we write the covariant derivatives according to linear combinations of orthonormal vectors and separate the equalities using the Gauss and Weingarten formulas. Then, we get the Laplacian of the Gauss map. After giving some conditions, we yield the following results: Aminov surfaces can not have a harmonic Gauss map and can not have a pointwise one-type Gauss map of the first kind in $\mathbb{E}^4$. Further, we give an example of a helical cylinder which is also congruent to an Aminov surface. Lastly, we obtain the conditions of having a pointwise one-type Gauss map of the second kind.

1. Introduction

Surfaces given with Monge patch which are also called digital graph surfaces have many advantages by means of visualization. These types of surfaces can be covered by just a few atlas that are produced with Monge patches. The presentation of $3-$dimensional form is $\varphi(u,v)=(u,v,g(u,v))$ where g is a differentiable function [7].

Digital graph surfaces (Monge surfaces) in $4-$dimensional spaces have also attracted attention as $3-$dimensional spaces. These surfaces are given by $z=g(u,v), w=h(u,v)$ where u,v,z,w are the cartezian coordinates [1,3]. Some of them are translation surfaces, factorable (homothetical) surfaces, $TF-$type surfaces etc.[13, 14]. In particular, translation surface has many applications in architecture. They have a quadrilateral form and thanks to this property, they are used for free form glass structures [8].

The idea of finite (limited) type submanifolds was announced by Chen in the 1970s and has grown into a widely used concept in studies of Euclidean and semi-Euclidean spaces. This concept has been extended to differentiable transformations, especially to the Gauss map of submanifolds.The condition for a surface (or a submanifold) to have a pointwise one-type Gauss map is

$$\Delta G=\lambda\left(G+\vec{C}\right) \qquad (1)$$

where λ is a differentiable function and $\vec{C}$ is a constant vector in the $n-$dimensional Euclidean (or semi-Euclidean) space. If $\vec{C}=0$, the surface is said to have a pointwise one-type Gauss map of the first kind, otherwise the second kind [6].

One of the popular surfaces, Aminov surface, can be represented by a Monge patch

$$z(u,v)=r(u)\cos v, \quad w(u,v)=r(u)\sin v, \quad (2)$$

where $r(u)$ is a differentiable function [1, 3]. In [3, 4], the authors handled Aminov surfaces according to their curvatures in $4-$dimensional Euclidean and Minkowski spaces. The other studies about some surfacesin $\mathbb{E}^4$can be found in [9, 10, 11, 12].

In this study, we evaluate Aminov surfaces with regards to their Gauss maps in $\mathbb{E}^4$. In section 3, we obtain the covariant derivatives of

*Corresponding author: sezgin.buyukkutuk@kocaeli.edu.tr
Received: 06.10.2022, Accepted: 20.03.2023

orthonormal vectors on the surface and arrange them in accordance with the Gauss and Weingarten formulas. We write the shape operator matrices of the surface. In Section 4, we compute the Laplacian of the Gauss map of these surfaces. Then, we prove that Aminov surfaces can not have a harmonic Gauss map and can not have a pointwise one-type Gauss map of the first kind in $\mathbb{E}^4$. In an example, we get the Laplace transform of the Gauss map of a helical cylinder. Further, we present the conditions for Aminov surfaces to have a pointwise one-type Gauss map of the second kind.

2. Basic Concepts

Let $M:\varphi(u,v)$ denote a surface patch in Euclidean $4-$space $\mathbb{E}^4$. $\{\varphi_u,\varphi_v\}$ spans the tangent space of M. The first fundamental form coefficients are calculated by $F=\langle\varphi_u,\varphi_v\rangle, E=\langle\varphi_u,\varphi_u\rangle, G=\langle\varphi_v,\varphi_v\rangle$. Hence, M is known as regular in case of $W^2=EG-F^2\neq 0.$

Euclidean $4-$space can be considered as a decomposition of tangential and normal component of M for each point p:

$$\mathsf{E}^4=T_pM\oplus T_p^{\perp}M.$$

Let the orthonormal tangent vectors and normal vector field of the surface be represented by φ_1,φ_2 and η, respectively. $\tilde{\nabla}$ and ∇ denotes the Levi-Civita connections, then the Weingarten and Gauss formulas are known as

$$\tilde{\nabla}_{\varphi_1}\eta=-A_\eta\varphi_1+D_{\varphi_1}\eta, \qquad (3)$$

$$\tilde{\nabla}_{\varphi_1}\varphi_2=\nabla_{\varphi_1}\varphi_2+h(\varphi_1,\varphi_2),$$

where A_η is the shape operator, D is the normal connection and h is the second fundamental tensor [2, 5].

Assuming that $\varphi_u=\dfrac{\partial}{\partial u}\varphi(u,v)$ and $\varphi_v=\dfrac{\partial}{\partial v}\varphi(u,v)$ are orthogonal, the orthonormal tangent vectors are

$$\varphi_1=\frac{\varphi_u}{E},\quad \varphi_2=\frac{\varphi_v}{G} \qquad (4)$$

The normal frame field $\{\eta_1,\eta_2\}$ is chosen as $\langle\eta_1,\eta_1\rangle=1,\langle\eta_2,\eta_2\rangle=1,\langle\eta_1,\eta_2\rangle=0,$ and the quadruple $\{\varphi_1,\varphi_2,\eta_1,\eta_2\}$ is positively oriented in $\mathbb{E}^4$. Thus, according to orthogonal tangent vectors φ_1 and φ_2, the second fundamental form is written as follows

$$\begin{aligned} h(\varphi_1,\varphi_1)&=h_{11}^1\eta_1+h_{11}^2\eta_2,\\ h(\varphi_1,\varphi_2)&=h_{12}^1\eta_1+h_{12}^2\eta_2, \qquad (5)\\ h(\varphi_2,\varphi_2)&=h_{22}^1\eta_1+h_{22}^2\eta_2, \end{aligned}$$

where $h_{ij}^k\,(i,j,k=1,2)$ are the coefficients of the second fundamental form.

With the help of Gauss and Weingarten formulas, $K=det(A_{\eta_1})+det(A_{\eta_2})$ gives the Gauss curvature of M and $H=\dfrac{trh}{2}$ gives the mean curvature. Therefore, the surface M is known as minimal (flat), if mean curvature (Gauss curvature) vanishes[5].

In $n-$dimensional Euclidean space, let $\{e_1,e_2\}$ be tanget vector fields of a surface, and the normal vectors denoted by $\{e_3,\ldots,e_n\}$, for the orthonormal frame $\{e_1,e_2,...,e_n\}$. Then, Gauss map of the surface is given by

$$G(p)=(e_1\wedge e_2)(p), \qquad (6)$$

and the Laplace of any differentiable function ψ on M is known as

$$\Delta\psi=-\left(\tilde{\nabla}_{\varphi_i}\tilde{\nabla}_{\varphi_i}\psi-\tilde{\nabla}_{\nabla_{\varphi_i}\varphi i}\psi\right). \qquad (7)$$

(see, [5]).

3. Aminov Surfaces in $4-$dimensional Euclidean Space

Definition 1: Let $M:\varphi(u,v)$ be a regular surface in $\mathbb{E}^4$. If M is parametrized by the Monge patch

$$\varphi(u,v)=(u,v,r(u)\cos v,r(u)\sin v), \qquad (8)$$

where $r(u)$ is a differentiable function, then this surface is called as Aminov surface in $\mathbb{E}^4$[1, 3].

Assume that M is an Aminov surface in four-dimensional Euclidean space. Then, the vector fields

$$\varphi_u=(1,0,r'(u)\cos v,r'(u)\sin v),$$

$$\varphi_v=(0,1,-r(u)\sin v,r(u)\cos v),$$

are tangent to M. Thus, the coefficients of first fundamental form are

$$E = (r')^2 + 1, \quad (9)$$
$$F = 0,$$
$$G = r^2 + 1.$$

We set $W^2 = EG - F^2 = EG = (r^2+1)((r')^2+1) \neq 0$, i.e., it is regular.
Since these vectors are orthogonal, the orthonormal tangent vectors are written as

$$\varphi_1 = \frac{1}{\sqrt{E}}\varphi_u = \frac{1}{\sqrt{(r')^2+1}}(1,\ 0,\ r'(u)\cos v, r'(u)\sin v), \quad (10)$$
$$\varphi_2 = \frac{1}{\sqrt{G}}\varphi_v = \frac{1}{\sqrt{r^2+1}}(0,\ 1,\ -r(u)\sin v,\ r(u)\cos v).$$

and the vectors

$$\eta_1 = \frac{1}{\sqrt{\tilde{E}}}(-r'\cos v,\ r\sin v,\ 1,\ 0), \quad (11)$$
$$\eta_2 = \frac{1}{\sqrt{\tilde{E}EG}}(-r'G\sin v,\ -rE\cos v,\ -\tilde{F},\ \tilde{E})$$

are obtained as unit normal vector fields, where

$$\tilde{E} = 1 + r'^2\cos^2 v + r^2\sin^2 v,$$
$$\tilde{F} = \cos v \sin v(r'^2 - r^2).$$

Furthermore, with the help of Weingarten and Gauss formulas, we get

$$\tilde{\nabla}_{\varphi_1}\varphi_1 = k_1\eta_1 + k_2\eta_2,$$
$$\tilde{\nabla}_{\varphi_1}\varphi_2 = -k_6\eta_1 + k_7\eta_2,$$
$$\tilde{\nabla}_{\varphi_2}\varphi_1 = k_3\varphi_2 - k_6\eta_1 + k_7\eta_2,$$
$$\tilde{\nabla}_{\varphi_2}\varphi_2 = -k_3\varphi_1 - k_4\eta_1 - k_5\eta_2, \quad (12)$$
$$\tilde{\nabla}_{\varphi_1}\eta_1 = -k_1\varphi_1 + k_6\eta_1 + k_8\eta_2,$$
$$\tilde{\nabla}_{\varphi_2}\eta_1 = k_6\varphi_1 + k_4\varphi_2 - k_9\eta_2,$$
$$\tilde{\nabla}_{\varphi_1}\eta_2 = -k_2\varphi_1 - k_7\varphi_2 - k_8\eta_1,$$
$$\tilde{\nabla}_{\varphi_2}\eta_2 = -k_7\varphi_1 + k_5\varphi_2 + k_9\eta_1,$$

where the differentiable functions $k_i\ (i = 1,...,9)$ satisfy

$$k_1 = \frac{r''\cos v}{E\sqrt{\tilde{E}}},\ k_2 = \frac{r''G\sin v}{E\sqrt{\tilde{E}EG}},\ k_3 = \frac{r'r}{G\sqrt{E}},$$
$$k_4 = \frac{r\cos v}{G\sqrt{\tilde{E}}},\ k_5 = \frac{r\sin v}{\sqrt{\tilde{E}EG}},\ k_6 = \frac{r'\sin v}{\sqrt{\tilde{E}EG}}, \quad (13)$$
$$k_7 = \frac{r'\cos v}{G\sqrt{\tilde{E}}},\ k_8 = \frac{r'\cos v\sin v(r''G - rE)}{\tilde{E}E\sqrt{G}},$$
$$k_9 = \frac{EG - \tilde{E}}{\tilde{E}G\sqrt{E}}.$$

Thus, these relations can be decompose into tangent and normal components as

$$\begin{aligned} &\nabla_{\varphi_1}\varphi_1 = 0, && A_{\eta_1}\varphi_1 = k_1\varphi_1 - k_6\varphi_2,\\ &\nabla_{\varphi_2}\varphi_2 = -k_3\varphi_1, && A_{\eta_1}\varphi_2 = -k_6\varphi_1 - k_4\varphi_2,\\ &\nabla_{\varphi_1}\varphi_2 = 0, && A_{\eta_2}\varphi_1 = k_2\varphi_1 + k_7\varphi_2,\\ &\nabla_{\varphi_2}\varphi_1 = k_3\varphi_2, && A_{\eta_2}\varphi_2 = k_7\varphi_1 - k_5\varphi_2, \end{aligned} \quad (14)$$

and

$$\begin{aligned} &h(\varphi_1,\varphi_1) = k_1\eta_1 + k_2\eta_2, && D_{\varphi_1}\eta_1 = k_8\eta_2,\\ &h(\varphi_1,\varphi_2) = -k_6\eta_1 + k_7\eta_2, && D_{\varphi_1}\eta_2 = -k_8\eta_1,\\ &h(\varphi_2,\varphi_2) = -k_4\eta_1 - k_5\eta_2, && D_{\varphi_2}\eta_1 = -k_9\eta_2,\\ & && D_{\varphi_2}\eta_2 = k_9\eta_1. \end{aligned} \quad (15)$$

Moreover, with the help of (5) and (15), we obtain the coefficients h_{ij}^k:

$$h_{11}^1 = \frac{r''\cos v}{E\sqrt{\tilde{E}}},\quad h_{11}^2 = \frac{r''G\sin v}{E\sqrt{\tilde{E}EG}},$$
$$h_{12}^1 = \frac{-r'\sin v}{\sqrt{\tilde{E}EG}},\quad h_{12}^2 = \frac{r'\cos v}{G\sqrt{\tilde{E}}}, \quad (16)$$
$$h_{22}^1 = \frac{-r\cos v}{G\sqrt{\tilde{E}}},\quad h_{22}^2 = \frac{-r\sin v}{\sqrt{\tilde{E}EG}}.$$

Lemma 2: Let the equality (8) respresent an Aminov surface in $\mathbb{E}^4$. Then, the shape operator matrices are given by

$$A_{\eta_1}=\begin{pmatrix} \dfrac{r^{''}\cos v}{E\sqrt{\tilde{E}}} & \dfrac{-r^{'}\sin v}{\sqrt{\tilde{E}EG}} \\ \dfrac{-r^{'}\sin v}{\sqrt{\tilde{E}EG}} & \dfrac{-r\cos v}{G\sqrt{\tilde{E}}} \end{pmatrix}, \quad (17)$$

$$A_{\eta_2}=\begin{pmatrix} \dfrac{r^{''}G\sin v}{E\sqrt{\tilde{E}EG}} & \dfrac{r^{'}\cos v}{G\sqrt{\tilde{E}}} \\ \dfrac{r^{'}\cos v}{G\sqrt{\tilde{E}}} & \dfrac{-r\sin v}{\sqrt{\tilde{E}EG}} \end{pmatrix}.$$

Theorem 3:[3]Let M be an Aminov surface in $\mathbb{E}^4$ given by the Monge patch (8). Then, the Gaussian curvature and the mean curvature vectors are

$$K=\frac{-r''rG-(r')^2E}{W^4} \quad (18)$$

and

$$H=\frac{\cos v(r''G-rE)}{2\sqrt{\tilde{E}}W^2}\eta_1+\frac{\sin v(r''G-rE)}{2E\sqrt{\tilde{E}}W}\eta_2 \quad (19)$$

respectively.

Proof. With the help of Lemma 2, and the Gaussian curvature of a surface in $\mathbb{E}^4$ $\left(K=det(A_{\eta_1})+det(A_{\eta_2})\right)$; we yield

$$K=\frac{1}{EG}\left[\left(\frac{-r^{''}r\cos^2 v-r^{'2}\sin^2 v}{\tilde{E}}\right)+\left(\frac{-r^{''}rG^2\sin^2 v-r^{'2}E^2\cos^2 v}{\tilde{E}EG}\right)\right]$$

$$=\frac{\left(-r^{''}rG-r^{'2}E\right)\left(1+r^{'2}\cos^2 v+r^2\sin^2 v\right)}{\tilde{E}E^2G^2}$$

$$=\frac{-r^{''}rG-(r^{'})^2E}{W^4}.$$

In addition, with the help of the mean curvature vector of a surface $\left(H=\frac{trh}{2}\right)$, we compute

$$H=\frac{r^{''}G\cos v-rE\cos v}{2EG\sqrt{\tilde{E}}}\eta_1+\frac{r^{''}G\sin v-rE\sin v}{2E\sqrt{\tilde{E}EG}}\eta_2$$

$$=\frac{\cos v\left(r^{''}G-rE\right)}{2\sqrt{\tilde{E}}W^2}\eta_1+\frac{\sin v\left(r^{''}G-rE\right)}{2E\sqrt{\tilde{E}}W}\eta_2.$$

It completes the proof.

Corollary 4: Let the equality (8) represent an Aminov surface in $\mathbb{E}^4$. Then, it is minimal if and only if

$$r(u)=\frac{1}{2c_1}\left((c_1)^2e^{\pm\frac{2(u+c_2)}{c_1}}+(c_1)^2-1\right)e^{\pm\frac{(u+c_2)}{c_1}}, \quad (20)$$

where c_i, $(i=1,2)$ are real constants.

Proof. The surface is minimal, i.e., $H=0$ in (19) if and only if

$$-rE+r^{''}G=0.$$

Substituting the first fundamental form coefficients into (9), we get the differential equation

$$-r\left(1+(r')^2\right)+r^{''}\left(1+r^2\right)=0$$

which has the solution (20). It completes the proof.

Example 5: The surface

$$M:\varphi(u,v)=\left(u,\ v,\ e^u\cos v,\ e^u\sin v\right)$$

is congruent to minimal Aminov surface with $r(u)=e^u$ with the constants $c_i=1$ in (20). One can plot by Maple:

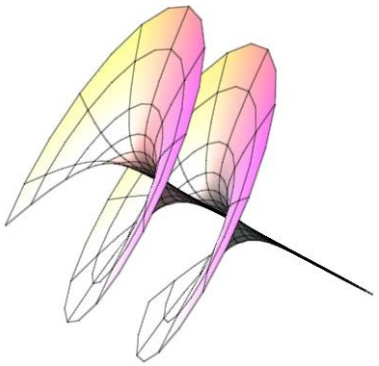

Figure 1: Minimal Aminov surface

4. A characterization of Aminov Surface with regards to its Gauss map in $\mathbf{E}^4$

Let $\{\varphi_1,\varphi_2,\eta_1,\eta_2\}$ denote the orthonormal frame of a regular surface $M:\varphi(u,v)$ in $\mathbb{E}^4$. Then, the Gauss map of the surface is

$$G=\varphi_1\wedge\varphi_2.$$

By the use of the relation (7), the Laplacian operator of this Gauss map in $\mathbb{E}^4$ can be written as

$$-\Delta G=\tilde{\nabla}_{\varphi_1}\tilde{\nabla}_{\varphi_1}G+\tilde{\nabla}_{\varphi_2}\tilde{\nabla}_{\varphi_2}G-\tilde{\nabla}_{\nabla_{\varphi_1}\varphi_1}G-\tilde{\nabla}_{\nabla_{\varphi_2}\varphi_2}G. \quad (21)$$

Theorem 6: Let M be an Aminov surface in $\mathbb{E}^4$ given by the Monge patch (8). Then, the Laplace of G of M is given by

$$\begin{aligned}-\Delta G=&\left(-(k_1)^2-(k_2)^2-(k_4)^2-(k_5)^2-2(k_6)^2-2(k_7)^2\right)\\&\varphi_1\wedge\varphi_2\\&+\left(-\varphi_1[k_6]-\varphi_2[k_4]-k_7k_8-k_5k_9-2k_3k_6\right)\varphi_1\wedge\eta_1\\&+\left(\varphi_1[k_7]-\varphi_2[k_5]-k_6k_8+k_4k_9+2k_3k_7\right)\varphi_1\wedge\eta_2 \quad (22)\\&+\left(-\varphi_1[k_1]+\varphi_2[k_6]+k_2k_8-k_1k_3-k_3k_4-k_7k_9\right)\varphi_2\wedge\eta_1\\&+\left(-\varphi_1[k_2]-\varphi_2[k_7]-k_1k_8-k_2k_3-k_3k_5-k_6k_9\right)\varphi_2\wedge\eta_2\\&+2\left(k_7(k_1+k_4)+k_6(k_2+k_5)\right)\eta_1\wedge\eta_2\end{aligned}$$

where $\varphi_i[k_j]$ are correspond to directional derivatives with respect to φ_i and the functions k_j $(j=1,...,9)$ are given by (13).

Proof. With the help of Gauss and Weingarten formulas and their components, the derivatives $\tilde{\nabla}_{\varphi_i}\tilde{\nabla}_{\varphi_i}G$ and $\tilde{\nabla}_{\nabla_{\varphi_i}\varphi_i}G$ $(i=1,2)$ are yielded as

$$\tilde{\nabla}_{\varphi_1}\tilde{\nabla}_{\varphi_1}G=\left(-(k_1)^2-(k_2)^2-(k_6)^2-(k_7)^2\right)\varphi_1\wedge\varphi_2$$

$$+\left(-\varphi_1[k_6]-k_7k_8\right)\varphi_1\wedge\eta_1+\left(\varphi_1[k_7]-k_6k_8\right)\varphi_1\wedge\eta_2$$

$$+\left(-\varphi_1[k_1]+k_2k_8\right)\varphi_2\wedge\eta_1+\left(-\varphi_1[k_2]-k_1k_8\right)\varphi_2\wedge\eta_2$$

$$+2\left(k_1k_7+k_2k_6\right)\eta_1\wedge\eta_2,$$

$$\tilde{\nabla}_{\varphi_2}\tilde{\nabla}_{\varphi_2}G=\left(-(k_4)^2-(k_5)^2-(k_6)^2-(k_7)^2\right)\varphi_1\wedge\varphi_2$$

$$+\left(-\varphi_2[k_4]-k_3k_6-k_5k_9\right)\varphi_1\wedge\eta_1$$

$$+\left(-\varphi_2[k_5]+k_3k_7+k_4k_9\right)\varphi_1\wedge\eta_2$$

$$+\left(\varphi_2[k_6]-k_3k_4-k_7k_9\right)\varphi_2\wedge\eta_1$$

$$+\left(-\varphi_2[k_7]-k_3k_5-k_6k_9\right)\varphi_2\wedge\eta_2$$

$$+2\left(k_4k_7+k_5k_6\right)\eta_1\wedge\eta_2,$$

$$\tilde{\nabla}_{\nabla_{F_1}F_1}G=0,$$

$$\tilde{\nabla}_{\nabla_{F_2}F_2}G=\left(k_3k_6\right)\varphi_1\wedge\eta_1-\left(k_3k_7\right)\varphi_1\wedge\eta_2$$

$$+\left(k_1k_3\right)\varphi_2\wedge\eta_1+\left(k_2k_3\right)\varphi_2\wedge\eta_2.$$

Then, substitute these derivatives into (21), we obtain the desired result.

Example 7: The helical cylinder

$$M:\varphi(u,v)=(0,v,\cos v,\sin v)+(u,0,0,0) \quad (23)$$

also corresponds to Aminov surface with $r(u)=1$ and the Laplace of G of M is calculated as

$$\Delta G=\left(\frac{1}{4}\right)\varphi_1\wedge\varphi_2-\frac{\sin v}{2\sqrt{2}}\left(\frac{1-2\sqrt{2}\cos^2 v}{(1+\sin^2 v)^{\frac{3}{2}}}\right)\varphi_1\wedge\eta_1$$

$$+\frac{\cos v}{4}\left(\frac{1-2\sqrt{2}\cos^2 v}{(1+\sin^2 v)^{\frac{3}{2}}}\right)\varphi_1\wedge\eta_2.$$

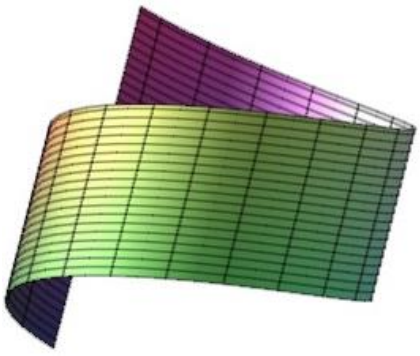

Figure 2: Aminov surface with r(u)=1

Theorem 8: Aminov surfaces can not have harmonic Gauss map in $\mathbb{E}^4$.

Proof. Let M be an Aminov surface in $\mathbb{E}^4$ given by the Monge patch (8). The Laplacian of Gauss map can be written as

$$\Delta G = \alpha_1(\varphi_1 \wedge \varphi_2) + \alpha_2(\varphi_1 \wedge \eta_1) + \alpha_3(\varphi_1 \wedge \eta_2) + \alpha_4(\varphi_2 \wedge \eta_1) + \alpha_5(\varphi_2 \wedge \eta_2) + \alpha_6(\eta_1 \wedge \eta_2),$$

where α_i (i=1,…,6) are indicated in (22). If M has a harmonic Gauss map, then $\Delta G = 0$, i.e., $\alpha_i = 0$. Then, we get

$$\alpha_1 = (k_1)^2 + (k_2)^2 + (k_4)^2 + (k_5)^2 + 2(k_6)^2 + 2(k_7)^2 = 0,$$

It means that $r(u) = 0$ in the surface parametrization (8). Hence, this contradicts with the regularity of the surface which completes the proof.

Theorem 9: Let M be an Aminov surface in $\mathbb{E}^4$ given by the representation (8). Then, M has pointwise one-type Gauss map of first kind if and only if

$$\frac{(k_1)^2 + (k_2)^2 + (k_4)^2 + (k_5)^2 + 2(k_6)^2 + 2(k_7)^2}{\lambda} - 1 = 0,$$

$$\frac{\varphi_1[k_6] + \varphi_2[k_4] + k_7k_8 + k_5k_9 + 2k_3k_6}{\lambda} = 0,$$

$$\frac{-\varphi_1[k_7] + \varphi_2[k_5] + k_6k_8 - k_4k_9 - 2k_3k_7}{\lambda} = 0, \quad (24)$$

$$\frac{\varphi_1[k_1] - \varphi_2[k_6] - k_2k_8 + k_1k_3 + k_3k_4 + k_7k_9}{\lambda} = 0,$$

$$\frac{\varphi_1[k_2] + \varphi_2[k_7] + k_1k_8 + k_2k_3 + k_3k_5 + k_6k_9}{\lambda} = 0,$$

$$\frac{-2k_7}{\lambda}(k_1 + k_4) + \frac{-2k_6}{\lambda}(k_2 + k_5) = 0,$$

where λ is a non-zero smooth function.

Proof. Let M be an Aminov surface in $\mathbb{E}^4$ given by Monge patch (8). With the help of (1) and (22), we can write

$$\lambda + \lambda\langle \vec{C}, \varphi_1 \wedge \varphi_2 \rangle = (k_1)^2 + (k_2)^2 + (k_4)^2 + (k_5)^2 + 2(k_6)^2 + 2(k_7)^2,$$

$$\lambda\langle \vec{C}, \varphi_1 \wedge \eta_1 \rangle = \varphi_1[k_6] + \varphi_2[k_4] + k_7k_8 + k_5k_9 + 2k_3k_6,$$

$$\lambda\langle \vec{C}, \varphi_1 \wedge \eta_2 \rangle = -\varphi_1[k_7] + \varphi_2[k_5] + k_6k_8 - k_4k_9 - 2k_3k_7,$$

$$\lambda\langle \vec{C}, \varphi_2 \wedge \eta_1 \rangle = \varphi_1[k_1] - \varphi_2[k_6] - k_2k_8 + k_1k_3 + k_3k_4 + k_7k_9,$$

$$\lambda\langle \vec{C}, \varphi_2 \wedge \eta_2 \rangle = \varphi_1[k_2] + \varphi_2[k_7] + k_1k_8 + k_2k_3 + k_3k_5 + k_6k_9,$$

$$\lambda\langle \vec{C}, \eta_1 \wedge \eta_2 \rangle = -2k_7(k_1 + k_4) - 2k_6(k_2 + k_5),$$

where λ is non-zero differentiable function. By using the equality (1), the constant vector $\overleftarrow{C}$ can be considered as

$$\vec{C} = C_1\varphi_1 \wedge \varphi_2 + C_2\varphi_1 \wedge \eta_1 + C_3\varphi_1 \wedge \eta_2 + C_4\varphi_2 \wedge \eta_1 + C_5\varphi_2 \wedge \eta_2 + C_6\eta_1 \wedge \eta_2 \quad (25)$$

where

$$C_1(u,v) = \frac{(k_1)^2 + (k_2)^2 + (k_4)^2 + (k_5)^2 + 2(k_6)^2 + 2(k_7)^2}{\lambda} - 1,$$

$$C_2(u,v) = \frac{\varphi_1[k_6] + \varphi_2[k_4] + k_7k_8 + k_5k_9 + 2k_3k_6}{\lambda},$$

$$C_3(u,v) = \frac{-\varphi_1[k_7] + \varphi_2[k_5] + k_6k_8 - k_4k_9 - 2k_3k_7}{\lambda}, \quad (26)$$

$$C_4(u,v) = \frac{\varphi_1[k_1] - \varphi_2[k_6] - k_2k_8 + k_1k_3 + k_3k_4 + k_7k_9}{\lambda},$$

$$C_5(u,v) = \frac{\varphi_1[k_2] + \varphi_2[k_7] + k_1k_8 + k_2k_3 + k_3k_5 + k_6k_9}{\lambda},$$

$$C_6(u,v) = \frac{-2k_7}{\lambda}(k_1 + k_4) + \frac{-2k_6}{\lambda}(k_2 + k_5)$$

are differentiable functions. If M has a pointwise one-type Gauss map of the first kind, then $C = 0$ in the equation (1). By the use of (25) and (26), we get the desired result.

Corollary 10: Aminov surfaces can not have a pointwise one-type Gauss map of the first kind in $\mathbb{E}^4$.

Proof. Assume that an Aminov surface M has a pointwise one-type Gauss map of the first kind in $\mathbb{E}^4$. Then, the equation system (24) is hold. By using the last equation in (24), we get

$$\frac{2r'(r''G+rE)}{\lambda E^2G^2}=0.$$

Hence, there are two cases: $r'(u)=0$ or $r''(u)G+r(u)E=0.$ Using the first one ($r=const.$) in the second equation of (24), we yield

$$\frac{-r\sin v}{\left(1+r^2\sin^2 v\right)^{\frac{3}{2}}}\left(1-\frac{r^2\cos^2 v}{\left(1+r^2\right)^{\frac{3}{2}}}\right)=0.$$

Using the second one, i.e., substituting $r''=-\frac{rE}{G}$ into the second equation in (24), we obtain

$$-\frac{(r')^2G^2+\left(2(r')^2+r^2\right)E^2}{E^2G^2}=0.$$

These relations are satisfied if and only if $r(u)=0,$ but it contradicts with the regularity of the surface. Thus, we get the desired result.

Theorem 11 Let M be Aminov surface in $\mathbb{E}^4$ given by the Monge patch (8). Then, M has a pointwise one-type Gauss map of the second kind if and only if

$$\begin{aligned}
&\varphi_1[C_1]+C_2k_6-C_3k_7+C_4k_1+C_5k_2=0,\\
&\varphi_1[C_2]-C_1k_6-C_3k_8+C_6k_2=0,\\
&\varphi_1[C_3]+C_1k_7+C_2k_8-C_6k_1=0,\\
&\varphi_1[C_4]-C_1k_1-C_5k_8+C_6k_7=0,\\
&\varphi_1[C_5]-C_1k_2+C_4k_8+C_6k_6=0,\\
&\varphi_1[C_6]-C_2k_2+C_3k_1-C_4k_7-C_5k_6=0
\end{aligned}\qquad(27)$$

and

$$\begin{aligned}
&\varphi_2[C_1]+C_2k_4+C_3k_5-C_4k_6+C_5k_7=0,\\
&\varphi_2[C_2]-C_1k_4+C_3k_9-C_4k_3+C_6k_7=0,\\
&\varphi_2[C_3]-C_1k_5-C_2k_9-C_5k_3+C_6k_6=0,\\
&\varphi_2[C_4]+C_1k_6+C_2k_3+C_5k_9-C_6k_5=0,\\
&\varphi_2[C_5]-C_1k_7+C_3k_3-C_4k_9+C_6k_4=0,\\
&\varphi_2[C_6]-C_2k_7-C_3k_6+C_4k_5-C_5k_4=0
\end{aligned}\qquad(28)$$

are satisfied, where $\varphi_i[C_j]$ are correspond to directional derivatives with respect to φ_i.

Proof. Let M be an Aminov surface in $\mathbb{E}^4$ which has a pointwise one-type Gauss map of second kind. It means that $\vec{C}$ is a constant in (1). With the help of the equation (25) and (12), the directional derivatives of the vector $\vec{C}$ are obtained as

$$\begin{aligned}
\tilde{\nabla}_{\varphi_1}C=&\left(\varphi_1[C_1]+C_2k_6-C_3k_7+C_4k_1+C_5k_2\right)\varphi_1\wedge\varphi_2\\
&+\left(\varphi_1[C_2]-C_1k_6-C_3k_8+C_6k_2\right)\varphi_1\wedge\eta_1\\
&+\left(\varphi_1[C_3]+C_1k_7+C_2k_8-C_6k_1\right)\varphi_1\wedge\eta_2\\
&+\left(\varphi_1[C_4]-C_1k_1-C_5k_8+C_6k_7\right)\varphi_2\wedge\eta_1\\
&+\left(\varphi_1[C_5]-C_1k_2+C_4k_8+C_6k_6\right)\varphi_2\wedge\eta_2\\
&+\left(\varphi_1[C_6]-C_2k_2+C_3k_1-C_4k_7-C_5k_6\right)\eta_1\wedge\eta_2
\end{aligned}$$

and

$$\begin{aligned}
\tilde{\nabla}_{\varphi_2}C=&\left(\varphi_2[C_1]+C_2k_4+C_3k_5-C_4k_6+C_5k_7\right)\varphi_1\wedge\varphi_2\\
&+\left(\varphi_2[C_2]-C_1k_4+C_3k_9-C_4k_3+C_6k_7\right)\varphi_1\wedge\eta_1\\
&+\left(\varphi_2[C_3]-C_1k_5-C_2k_9-C_5k_3+C_6k_6\right)\varphi_1\wedge\eta_2\\
&+\left(\varphi_2[C_4]+C_1k_6+C_2k_3+C_5k_9-C_6k_5\right)\varphi_2\wedge\eta_1\\
&+\left(\varphi_2[C_5]-C_1k_7+C_3k_3-C_4k_9+C_6k_4\right)\varphi_2\wedge\eta_2\\
&+\left(\varphi_2[C_6]-C_2k_7-C_3k_6+C_4k_5-C_5k_4\right)\eta_1\wedge\eta_2
\end{aligned}$$

Due to fact that the vector $\vec{C}$ is constant, these derivatives vanish and the equalities (27) and (28) are obtained. This completes the proof.
Now, we will also visualize the Aminov surface with the following example:

Example 12: Suppose that an Aminov surface is given by the parameterization (8). By taking $r(u)=\ln u$, one can plot the projection of this surface with the help of Maple command:

$$plot3d([u+v, \ln u \cos v, \ln u \sin v], u=-2*pi..2*pi, v=-2*pi..2*pi)$$

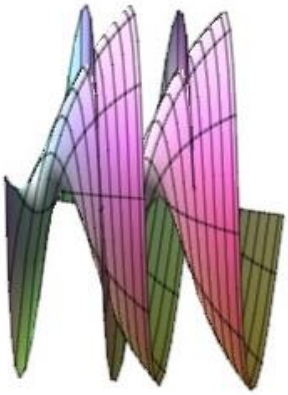

Figure 3: Aminov surface with r(u)=lnu

Conclusion

Aminov surfaces are the first described by Yu. A. Aminov in four-dimensional Euclidean space. In this paper, we calculate the Laplace of the Gauss map of these types of surfaces and examine them with respect to having pointwise one-type Gauss map.In future studies, this examination can be done for all surfaces given with Monge patch

.

References

[1] Y.A. Aminov, "Surfaces in E^4 with a Gaussian curvature coinciding with a Gaussian torsion up to sign," *Mathematical Notes*, vol. 56, pp. 1211-1215, 1994.

[2] Y.A. Aminov,*The Geometry of Submanifolds*. Singapore: Gordon and Breach Science Publishers, 2001.

[3] B. Bulca, K. Arslan, "Surfaces Given with the Monge Patch in E^4," *Journal of Mathematical Physics, Analysis, Geometry*, vol. 9, pp. 435-447, 2013.

[4] S. Büyükkütük, G. Öztürk, "A new type timelike surface given with Monge patch in E_1^4," *TWMS J. App. and Eng. Math.*, vol.11, 176–183, 2021.

[5] B.Y. Chen,*Geometry of Submanifolds*. New York: Dekker, 1973.

[6] B.Y. Chen, M. Choi, Y.H. Kim, "Surfaces of revolution with pointwise 1-type Gauss map.,"*J. Korean Math. Soc.*vol. 42, 447–455, 2005.

[7] A. Gray,"A Monge Patch.," *Modern Differential Geometry of Curves and Surfaces with Mathematica*, 2nd ed. Boca Raton. FL: CRC Press. pp. 398–401, 1997.

[8] J. Glymph, D. Schelden, C. Ceccato,J.Mussel, H. Schober, "A parametric strategy for free-form glass structures using quadrilateral planar facets,"*Automation in Construction*,vol.13, 187–202, 2004.

[9] E. Güler, Ö. Kişi,"The Second Laplace-Beltrami Operator on Rotational Hypersurfaces in the Euclidean 4-Space,"*Mathematica Aeterna*. Vol.8, 1–12, 2018.

[10] E. Güler, Ö. Kişi,"Weingarten Map of the Henneberg-Type Minimal Surfaces in 4-Space,*"Konuralp J Math.* Vol.9, 132–136, 2021.

[11] E. Güler, Ö. Kişi,C. Konaxis, "Implicit Equations of the Henneberg-Type Minimal Surface in the Four-Dimensional Euclidean Space,*"Mathematics*. Vol.9, 279, 2018.

[12] İ. Kişi, G. Öztürk, "A new type tubular surface having pointwise 1-type Gauss map in Euclidean 4-space E4,*"Journal of Korean Mathematical Society*. Vol.55, 923-938, 2018.

[13] E.A. Pamuk, B. Bulca,"Translation-Factorable Surfaces in 4-dimensional Euclidean Space,"*Konuralp Journal of Mathematics*. Vol.9, 193–200, 2021.

[14] L.Verstraelen,J.Walrave,S.Yaprak, "The Minimal Translation Surface in Euclidean Space," Soochow J. Math., vol.20, 77–82, 1994.

Bitlis Eren Üniversitesi Fen Bilimleri Dergisi
BİTLİS EREN UNIVERSITY JOURNAL OF SCIENCE
ISSN: 2147-3129/e-ISSN: 2147-3188
VOLUME: 12 NO: 1 PAGE: 33-37 YEAR: 2023
DOI:10.17798/bitlisfen.1184983

Topological Hoarded Graphs

Kadirhan POLAT[1*]

[1]*Department of Mathematics, Faculty of Science and Letter, Ağrı, 04100, Türkiye*
(ORCID: 0000-0002-3460-2021)

Keywords: Hoarded graph. Topological hoarded graph, Topology.

Abstract
In this paper, we first introduced the steps that need to be taken to get the set-family that goes with a hoarded graph, as well as an example of how these steps could be used. Then, we explained what a topological hoarded graph is and showed when a set-family induced by a topological hoarded graph is a topology on a set. We also presented some useful facts about topological hoarded graphs.

1. Introduction

A subfamily $\mathcal{S}_X^{(n)}$ $\left(\text{orshortly}\mathcal{S}^{(n)}\right)$ of n-times-iterated power set of a set X is called a *n-set-family on X*. In particular, we use the convention that the 0-set-family $\mathcal{S}^{(0)}$ is a subset of X. We denote m-times generalized union of a family $\mathcal{S}^{(n)}$ by $\bigsqcup^m \mathcal{S}^{(n)}$, that is,

$$\bigsqcup^m \mathcal{S}^{(n)} = \underbrace{\bigcup \cdots \bigcup}_{m \text{ times}} \mathcal{S}^{(n)} \qquad (1)$$

where $1 \leq m \leq n$. For simplicity, we adopt the convention $\bigsqcup^0 \mathcal{F}^{(n)} = \mathcal{F}^{(n)}$. Let I be a partially ordered set with the least element. An indexed family $\{A_i | i \in I\}$ whose the least-indexed element is empty, *i.e.*, in which $A_{i_0} = \emptyset$ where $i_0 = \min I$ is said to be *first-empty*. We denote the set of all integers $\geq k$ and $\leq n$ where $k, n \in \mathbb{Z}$ by I_n^k.

Given a digraph $G = (V, A)$. The sets of heads and tails of all arcs in G is denoted by $V_h(G)$ and $V_t(G)$, respectively. Hence the set $V(G)$ of its all endpoints is union of $V_t(G)$ and $V_h(G)$. Furthermore, we denote the set of all heads of all v-tailed arcs in G by $V_h(G; v)$, or in short $V_h(v)$; and similarly the sets of all tails of all v-headed arcs in G by $V_t(G; v)$, or in short $V_t(v)$. A path in G whose the first and last vertices are in V' and V'', respectively, where $V', V'' \subseteq V$, is denoted by $p_{V' \to V''}$. Especially, we prefer to use the element of that set in the notation if V' or V'' is a singleton, and the dot symbol is used instead of unknown sets in the notation $p_{V' \to V''}$. The set of last vertices of all directed paths $p_{v \to W}$ in G where $W \subseteq V$ is denoted by $V_l(v \to W; G)$, or in short $V_l(v \to W)$, and similarly the set of first vertices of all directed paths $p_{W \to v}$ in G by $V_f(W \to v; G)$, or in short $V_f(W \to v)$. We prefer to use the notation $V_l(v)$ and $V_f(v)$ instead if W is not particular. *The length of a directed path* in G is the number of arcs on it. A directed path with length n in G is called a *n-directed path*. Let $G[G']$ denote a subgraph G' of G. Also, we denote a *vertex-induced subgraph* by $V' \subseteq V$ of G by $G[V', \cdot]$, and denote an *edge-induced subgraph* by $A' \subseteq A$ of G by $G[\cdot, A']$ (for detailed information, see [1-3, 6-11]). The pair v, w of vertices in G is called *semiconnected* if G contains a directed path from v to w or vice versa; the pair is called *non-semiconnected* if they are not semiconnected (see [5]).

We introduced the notion of cumulative graph as a subclass of acyclic digraphs [4]. We recall that a n-cumulative graph $G = (\mathcal{V}, \mathcal{A}, \mathcal{B})$ with first-empty indexed families $\mathcal{V} = \{V_i\}_{i \in I_n^0}$, $\mathcal{A} = \{A_i\}_{i \in I_n^1}$ and $\mathcal{B} = \{B_i\}_{i \in I_n^1}$ is an acyclic digraph $G = (\bigcup \mathcal{V}, \bigcup(\mathcal{A} \cup \mathcal{B}))$ satisfying the following : (i) $V_n = V(G[\cdot, A_n]) \cup V_t(G[\cdot, B_n])$, and for every integer $1 \leq i < n$, $V_i = V(G[\cdot, A_i]) \cup V_t(G[\cdot, B_i]) \cup V_h(G[\cdot, B_{i+1}])$, (ii) for every $1 \leq i \leq n$, $vw \in A_i$ and $ws \in A_i \Rightarrow vs \notin A_i$, (iii) for every $1 \leq i \leq n$, $vw \in A_i$ and $ws \in B_i \Rightarrow vs \notin B_i$.

*Corresponding author: kadirhanpolat@agri.edu.tr
Received: 06.10.2022, Accepted: 15.03.2023

2. A Set-family Corresponding to A Hoarded Graph

We introduced the definition of a cumulative graph in our previous paper [4]. The main motivation for this definition was to specify a particular class of graphs that would correspond to a n-set-family. It is natural to ask for which class of graphs there is a set-family corresponding to any graph of that class. To answer this question, we give the following definition.

Definition 1. A *n-hoarded graph* $G = (\mathcal{V}, \mathcal{A}, \mathcal{B})$ with pairwise disjoint families $\mathcal{V} = \{V_i\}_{i\in I_n^1}$, $\mathcal{A} = \{A_i\}_{i\in I_n^2}$ *and* $\mathcal{B} = \{B_i\}_{i\in I_n^2}$ is an acyclic digraph $\mathrm{G} = \left(\cup\mathcal{V}, \cup(\mathcal{A}\cup\mathcal{B})\right)$ which satisfies the following conditions:

(1) For every $\boldsymbol{2 \le i \le n}$, the endpoints of every arc in $\boldsymbol{A_i}$ belong to $\boldsymbol{V_i}$ while tails of every arc in $\boldsymbol{B_i}$ belong to $\boldsymbol{V_i}$ and the set of heads of all arcs in $\boldsymbol{B_i}$ equals to $\boldsymbol{V_{i-1}}$.

(2) If a vertex in $\boldsymbol{V_i}$ precedes that in $\boldsymbol{V_j}$ on some directed path in $\boldsymbol{G}$, then $\boldsymbol{i \ge j}$.

(3) If $\boldsymbol{u_1u_2 \ldots u_m}$ with $\boldsymbol{m \ge 3}$ is a directed path in $\boldsymbol{G}$ every arc of which belongs to $\boldsymbol{A_i}$ for some $\boldsymbol{2 \le i \le n}$, then $\boldsymbol{u_1u_m \notin A_i}$.

(4) For every $\boldsymbol{2 \le i \le n}$, $\boldsymbol{vw \in A_i}$ and $\boldsymbol{ws \in B_i \Rightarrow vs \notin B_i}$.

For every distinct pair $\boldsymbol{u, v}$ of vertices in some $\boldsymbol{V_i}$ with $\boldsymbol{1 \le i \le n}$, there exists a vertex $\boldsymbol{w}$ such that $\boldsymbol{w}$ is the last vertex of some directed path with the first vertex $\boldsymbol{u}$ but not that of any directed path with the first vertex $\boldsymbol{v}$.

In the paper [4], we have shown the steps to obtain the $\boldsymbol{(n+1)}$-cumulative graph induced by a $\boldsymbol{n}$-set-family. Now we introduce the steps to be taken to get the $\boldsymbol{(n-1)}$-set-family corresponding to a $\boldsymbol{n}$-hoarded graph $\boldsymbol{G} = (\boldsymbol{\mathcal{V}}, \boldsymbol{\mathcal{A}}, \boldsymbol{\mathcal{B}})$.

Step 1 We set $\boldsymbol{\mathcal{F} = V_n}$.

Step 2 We perform the following steps from $\boldsymbol{i = n}$ to $\boldsymbol{i = 2}$,

Step 2.1 We substitute the set $\boldsymbol{v \cup \bigcup V_h(G[\cdot, A_i]; v)}$ for each vertex $\boldsymbol{v}$ occurring in $\boldsymbol{\mathcal{F}}$.

Step 2.2 We substitute the set $\boldsymbol{V_h(G[\cdot, B_i]; v)}$ for each vertex $\boldsymbol{v}$ occuring in $\boldsymbol{\mathcal{F}}$.

After performing the above steps, the resulting $\boldsymbol{\mathcal{F}}$ is the set-family corresponding to the hoarded graph $\boldsymbol{G}$.

Example 2. Let $\boldsymbol{G = (\mathcal{V}, \mathcal{A}, \mathcal{B})}$ be a $\boldsymbol{4}$-hoarded graph with $\boldsymbol{\mathcal{V} = \{V_i\}_{i\in I_4^1}}$, $\boldsymbol{\mathcal{A} = \{A_i\}_{i\in I_4^2}}$ and $\boldsymbol{\mathcal{B} = \{B_i\}_{i\in I_4^2}}$ where

$\boldsymbol{V_1 = \{v_1, \ldots, v_6\}, V_2 = \{v_7, \ldots, v_{10}\}}$,
$\boldsymbol{V_3 = \{v_{11}, \ldots, v_{14}\}, V_4 = \{v_{15}, v_{16}, v_{17}\}}$,
$\boldsymbol{A_2 = \{v_8v_7, v_9v_7, v_{10}v_8\}}$,
$\boldsymbol{A_3 = \{v_{13}v_{11}, v_{14}v_{11}, v_{14}v_{12}\}}$,
$\boldsymbol{A_4 = \{v_{16}v_{15}, v_{17}v_{16}\}}$,
$\boldsymbol{B_2 = \{v_8v_1, v_8v_3, v_8v_4, v_9v_1, v_9v_2, v_9v_3, v_9v_6, v_{10}v_5\}}$,
$\boldsymbol{B_3 = \{v_{11}v_7, v_{12}v_{10}, v_{13}v_9, v_{14}v_8\}}$,
$\boldsymbol{B_4 = \{v_{16}v_{11}, v_{16}v_{13}, v_{17}v_{12}, v_{17}v_{14}\}}$

as Figure 1.

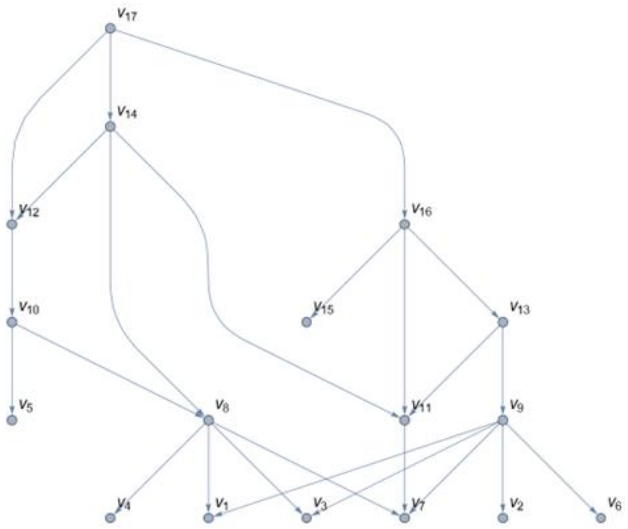

Figure 1. An example of a hoarded graph.

We first set $\mathcal{F} = V_4 = \{v_{15}, v_{16}, v_{17}\}$. For $i = 4$, we write $\mathcal{F} = \{v_{15}, v_{16} \cup v_{15}, v_{17} \cup v_{16} \cup v_{15}\}$ since

$$V_h(G[\cdot, A_4]; v_{15}) = v_{15} \cup \emptyset = v_{15},$$
$$V_h(G[\cdot, A_4]; v_{16}) = v_{16} \cup \bigcup \{v_{15}\} = v_{16} \cup v_{15},$$
$$V_h(G[\cdot, A_4]; v_{17}) = v_{17} \cup \bigcup \{v_{16}\} = v_{17} \cup v_{16} \cup v_{15}.$$

And since

$$V_h(G[\cdot, B_4]; v_{15}) = \emptyset,$$
$$V_h(G[\cdot, B_4]; v_{16}) = \{v_{11}, v_{13}\},$$
$$V_h(G[\cdot, B_4]; v_{17}) = \{v_{12}, v_{14}\},$$

we get $\mathcal{F} = \{\emptyset, \{v_{11}, v_{13}\}, \{v_{11}, v_{12}, v_{13}, v_{14}\}\}$. Then by performing Step 2 for $n = 3$, we get

$$V_h(G[\cdot, A_3]; v_{11}) = v_{11} \cup \emptyset = v_{11},$$
$$V_h(G[\cdot, A_3]; v_{12}) = v_{12} \cup \emptyset = v_{12},$$
$$V_h(G[\cdot, A_3]; v_{13}) = v_{13} \cup \bigcup \{v_{11}\} = v_{13} \cup v_{11},$$
$$V_h(G[\cdot, A_3]; v_{14}) = v_{14} \cup \bigcup \{v_{11}, v_{12}\} = v_{14} \cup v_{12} \cup v_{11}.$$

So, we obtain

$$\mathcal{F} = \{\emptyset, \{v_{11}, v_{13} \cup v_{11}\}, \{v_{11}, v_{12}, v_{13} \cup v_{11}, v_{14} \cup v_{12} \cup v_{11}\}\}.$$

Then we write

$$V_h(G[\cdot, B_3]; v_{11}) = \{v_7\},$$
$$V_h(G[\cdot, B_3]; v_{12}) = \{v_{10}\},$$
$$V_h(G[\cdot, B_3]; v_{13}) = \{v_9\},$$
$$V_h(G[\cdot, B_3]; v_{14}) = \{v_8\}$$

which yield

$$\mathcal{F} = \{\emptyset, \{\{v_7\}, \{v_7, v_9\}\}, \{\{v_7\}, \{v_{10}\}, \{v_7, v_9\}, \{v_7, v_8, v_{10}\}\}\}$$

Continuing Step 2, we rewrite

$$\mathcal{F} = \{\emptyset, \{\{v_7\}, \{v_7, v_9 \cup v_7\}\}, \{\{v_7\}, \{v_{10} \cup v_8 \cup v_7\}, \{v_7, v_9 \cup v_7\}, \{v_7, v_8 \cup v_7, v_{10} \cup v_8 \cup v_7\}\}\}$$

because

$$V_h(G[\cdot, A_2]; v_7) = v_7 \cup \emptyset = v_7,$$

$$V_h(G[\cdot, A_2]; v_8) = v_8 \cup \bigcup \{v_7\} = v_8 \cup v_7,$$

$$V_h(G[\cdot, A_2]; v_9) = v_9 \cup \bigcup \{v_7\} = v_9 \cup v_7,$$

$$V_h(G[\cdot, A_2]; v_{10}) = v_{10} \cup \bigcup \{v_8\} = v_{10} \cup v_8 \cup v_7.$$

In the sequel, we find as

$$V_h(G[\cdot, B_2]; v_7) = \emptyset,$$
$$V_h(G[\cdot, B_2]; v_8) = \{v_1, v_3, v_4\},$$
$$V_h(G[\cdot, B_2]; v_9) = \{v_1, v_2, v_3, v_6\},$$
$$V_h(G[\cdot, B_2]; v_{10}) = \{v_5\}$$

and hence we finally get

$$\mathcal{F} = \{\emptyset, \{\{\emptyset\}, \{\emptyset, \{v_1, v_2, v_3, v_6\}\}\}, \{\{\emptyset\}, \{\{v_1, v_3, v_4, v_5\}\}, \{\emptyset, \{v_1, v_2, v_3, v_6\}\}, \{\emptyset, \{v_1, v_3, v_4\}, \{v_1, v_3, v_4, v_5\}\}\}\}.$$

3. Topological Hoarded Graphs

We first introduce the definition of topological hoarded graph:

Definition 3. A 2-hoarded graph $G = (\mathcal{V}, \mathcal{A}, \mathcal{B})$ with $\mathcal{V} = \{V_1, V_2\}$, $\mathcal{A} = \{A_2\}$ and $\mathcal{B} = \{B_2\}$ is called a *topological hoarded graph* and denoted by $G = (V_1, V_2, A_2, B_2)$ if it satisfies the following conditions:
(1) There exists a vertex in V_2 that is the tail of no arc in G.
(2) For every vertex v in V_1, there exists a vertex $u \in V_2$ in which a directed path from itself to v exists.
(3) For any subset S of mutually two non-semiconnected vertices in V_2, there exists a vertex v in V_2 such that G contains a dipath from v to s for each vertex $s \in S$.
For any non-semiconnected pair u, w of vertices in V_2, if G contains pairs of directed paths with the first vertices u, w and the same last vertices in V_1, then there exists a vertex $v \in V_2$ such that G contains pairs of v-headed arcs with the tails u, w on these directed paths.

Theorem 4. If $G = (X, Y, A, B)$ be a topological hoarded graph, then X equipped with the 1-set-family τ corresponding to G is a topological space.

Proof. Let us first show that τ contains the empty set. From Definition 3(3), there exists a vertex y in Y such that y is not the tail of any arc in G. When we first perform Step 1 to obtain 1-set-family τ corresponding to G, we get $\tau = Y$. In Step 2.1, we write

$$y \cup \bigcup V_h(G[\cdot, A]; y) = y \cup \emptyset = y$$

instead of y in τ since y is not the tail of any arc in G. In Step 2.2, since y is not the tail of any arc in G, we replace y in τ with

$$V_h(G[\cdot, B]; y) = \emptyset$$

which means that τ contains $\emptyset$.
Now we show that τ contains the set X. Assume that $X \notin \tau$. It implies that $X \neq V_h(G[\cdot, B]; y)$ for every occurrence y in τ obtained by applying Step 2.1. Then for every occurrence y in τ obtained by applying Step 2.1, there exists a point $x \in X$ such that $x \notin V_h(G[\cdot, B]; y)$ which contradicts Definition 3(3). So $X \in \tau$.
Given a subfamily $\{U_i\}_{i \in I}$ of τ. Let's show that τ contains $\bigcup_{i \in I} U_i$. If $U_{i_0} = X$ for a particular $i_0 \in I$, then $\bigcup_{i \in I} U_i = X \in \tau$. If there exists a subset $J \subseteq I$ such that there exists an index $j \in J$ such that $U_i \subseteq U_j$ for every $i \in I \backslash J$, then $\bigcup_{i \in I} U_i = \bigcup_{i \in J} U_i$. In such a case, we show that $\bigcup_{i \in J} U_i$. In that case, $\{U_i\}_{i \in J}$ is a subfamily of τ such that U_i is neither a subset nor a superset U_j for every distinct indices $i, j \in J$. For each $i \in J$, U_i corresponding some vertex $v_i \in Y$ is obtained by performing Step 2.1 and Step 2.2. From Definition 3(3), there exists a vertex w in Y such that G contains a dipath from w to v_i for every $i \in J$. Just after applying Step 2.1 and Step 2.2, we obtain a set, say W, that corresponds $w \in Y$. Furthermore, $\bigcup_{i \in J} U_i = W \in \tau$.
Let U and V be members of τ. Finally, if we show that $U \cap V \in \tau$, then we complete the proof. If U does not intersect V, then $U \cap V = \emptyset \in \tau$. If $U \subseteq V$ or $V \subseteq U$, then it is clear that $U \cap V = U \in \tau$ or $U \cap V = V \in \tau$. In the other case, U and V corresponding some vertices $u, v \in Y$, respectively, are obtained by performing Step 2.1 and Step 2.2. Since $U \cap V \neq \emptyset$ and $U \not\subseteq V$ and $V \not\subseteq U$, G contains pair of directed paths with the first vertices u, v and the same last vertex w_p in X that corresponds to each point $p \in U \cap V$. From Definition 3(3), there exists a vertex w in Y such that G contains pairs of w_p-headed arcs with the tails u, v on these directed paths. Just after performing Step 2.1 and Step 2.2, we obtain a set, say W, that corresponds $w \in Y$. Furthermore, $U \cap V = W \in \tau$.

Example 5. Let $G = (X, Y, A, B)$ be a topological hoarded graph where

$X = \{v_1, \dots, v_6\}, Y = \{v_7, \dots, v_{19}\},$
$A = \{v_8v_7, v_9v_7, v_{10}v_8, v_{10}v_9, v_{11}v_9, v_{12}v_9, v_{13}v_{10},$
$v_{13}v_{11}, v_{14}v_{10}, v_{14}v_{12}, v_{15}v_{11}, v_{15}v_{12}, v_{16}v_{13},$
$v_{16}v_{14}, v_{16}v_{15}, v_{17}v_{14}, v_{18}v_{16}, v_{18}v_{17}, v_{19}v_{18}\},$
$B = \{v_8v_1, v_9v_2, v_{11}v_3, v_{12}v_5, v_{17}v_6, v_{19}v_4\}$
as Figure 5.

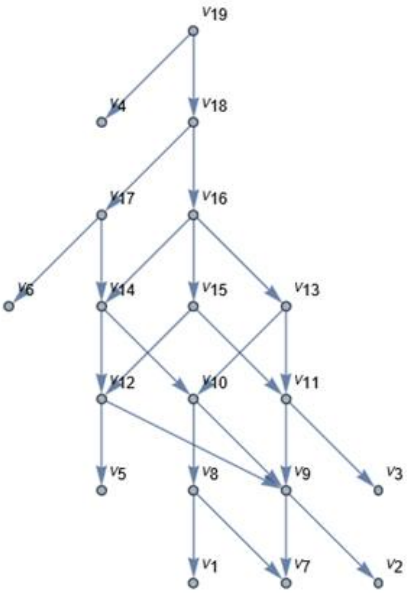

Figure 2. An example of a topological hoarded graph.

Indeed, it can be easily verified that G satisfies the conditions in Definition 3. We first set $\mathcal{F} = Y = \{v_7, \dots, v_{19}\}$. For $i = 2$, we write

$$\mathcal{F} = \{v_7, v_8 \cup v_7, v_9 \cup v_7, v_{10} \cup \dots \cup v_7, v_{11} \cup v_9 \cup v_7, v_{12} \cup v_9 \cup v_7, v_{13} \cup v_{11} \cup \dots \cup v_7, v_{14} \cup v_{12} \cup v_{10} \cup \dots \cup v_7, v_{15} \cup v_{12} \cup v_{11} \cup v_9 \cup v_7, v_{16} \cup \dots \cup v_7, v_{17} \cup v_{14} \cup v_{12} \cup v_{10} \cup \dots \cup v_7, v_{18} \cup \dots \cup v_7, v_{19} \cup \dots \cup v_7\}$$

since

$$V_h(G[\cdot, A_2]; v_7) = v_7 \cup \emptyset = v_7,$$
$$V_h(G[\cdot, A_2]; v_8) = v_8 \cup \bigcup \{v_7\} = v_8 \cup v_7,$$
$$V_h(G[\cdot, A_2]; v_9) = v_9 \cup \bigcup \{v_7\} = v_9 \cup v_7,$$
$$V_h(G[\cdot, A_2]; v_{10}) = v_{10} \cup \bigcup \{v_8, v_9\} = v_{10} \cup \dots \cup v_7,$$
$$V_h(G[\cdot, A_2]; v_{11}) = v_{11} \cup \bigcup \{v_9\} = v_{11} \cup v_9 \cup v_7,$$
$$V_h(G[\cdot, A_2]; v_{12}) = v_{12} \cup \bigcup \{v_9\} = v_{12} \cup v_9 \cup v_7,$$
$$V_h(G[\cdot, A_2]; v_{13}) = v_{13} \cup \bigcup \{v_{10}, v_{11}\} = v_{13} \cup v_{11} \cup v_{10} \cup v_9 \cup v_8 \cup v_7,$$
$$V_h(G[\cdot, A_2]; v_{14}) = v_{14} \cup \bigcup \{v_{10}, v_{12}\} = v_{14} \cup v_{12} \cup v_{10} \cup v_9 \cup v_8 \cup v_7,$$
$$V_h(G[\cdot, A_2]; v_{15}) = v_{15} \cup \bigcup \{v_{11}, v_{12}\} = v_{15} \cup v_{12} \cup v_{11} \cup v_9 \cup v_7,$$
$$V_h(G[\cdot, A_2]; v_{16}) = v_{16} \cup \bigcup \{v_{13}, v_{14}, v_{15}\} = v_{16} \cup \dots \cup v_7,$$
$$V_h(G[\cdot, A_2]; v_{17}) = v_{17} \cup \bigcup \{v_{14}\} = v_{17} \cup v_{14} \cup v_{12} \cup v_{10} \cup v_9 \cup v_8 \cup v_7,$$
$$V_h(G[\cdot, A_2]; v_{18}) = v_{18} \cup \bigcup \{v_{16}, v_{17}\} = v_{18} \cup \dots \cup v_7,$$
$$V_h(G[\cdot, A_2]; v_{19}) = v_{19} \cup \bigcup \{v_{18}\} = v_{19} \cup \dots \cup v_7.$$

And since

$V_h(G[\cdot, B_2]; v_7) = \emptyset, V_h(G[\cdot, B_2]; v_{14}) = \emptyset,$
$V_h(G[\cdot, B_2]; v_8) = \{v_1\}, V_h(G[\cdot, B_2]; v_{15}) = \emptyset,$
$V_h(G[\cdot, B_2]; v_9) = \{v_2\}, V_h(G[\cdot, B_2]; v_{16}) = \emptyset,$
$V_h(G[\cdot, B_2]; v_{10}) = \emptyset, V_h(G[\cdot, B_2]; v_{17}) = \{v_6\},$
$V_h(G[\cdot, B_2]; v_{11}) = \{v_3\}, V_h(G[\cdot, B_2]; v_{18}) = \emptyset,$
$V_h(G[\cdot, B_2]; v_{12}) = \{v_5\}, V_h(G[\cdot, B_2]; v_{19}) = \{v_4\},$
$V_h(G[\cdot, B_2]; v_{13}) = \emptyset,$

we get

$$\mathcal{F} = \{\emptyset, \{v_1\}, \{v_2\}, \{v_1, v_2\}, \{v_2, v_3\}, \{v_2, v_5\}, \{v_1, v_2, v_3\}, \{v_1, v_2, v_5\}, \{v_2, v_3, v_5\}, \{v_1, v_2, v_3, v_5\}, \{v_1, v_2, v_5, v_6\}, \{v_1, v_2, v_3, v_5, v_6\}, \{v_1, v_2, v_3, v_4, v_5, v_6\}\}$$

which can easily be proved to be a topology on X.

4. Conclusion and Suggestions

We first give a concept of a n-hoarded graph to which there exists a $(n-1)$-set family corresponding. We present the steps to be performed to get the corresponding set-family, and we have shown the results of these steps in an example. We then introduced the concept of a topological hoarded graph. Above all, we show that X equipped with the 1-set-family τ corresponding to a topological hoarded graph $G = (X, Y, A, B)$ is a topological space. And finally, we have confirmed this fact with an example.

References

[1] B. Bollobas, *Modern Graph Theory*. New York, NY: Springer, 2014.

[2] G. Chartrand, *A First Course in Graph Theory*. Mineola, NY: Dover Publications, 2012.

[3] J. L. Gross, J. Yellen, and P. Zhang, Eds., *Handbook of graph theory*, 2nd ed. London, England: CRC Press, 2018.

[4] K. Polat, "On cumulative graph representations of set-families", *Karamanoğlu Mehmetbey Üniversitesi Mühendislik ve Doğa Bilimleri Dergisi*, vol. 3, no. 2, pp. 74–78, 2022.

[5] K. S. Htay, K. A. Tint, and N. O. Htike, "Application of connectivity on graph theory", *International Journal of Scientific Engineering and Technology Research*, vol. 8, no. 1, pp. 525–530, 2019.

[6] K. R. Saoub, *Graph theory: An introduction to proofs, algorithms, and applications*. London, England: CRC Press, 2021.

[7] R. J. Trudeau, *Introduction to graph theory*. Pmapublishing.com, 2017.

[8] L.W. Beineke, "Derived graphs and digraphs", *In Beitrage zur Graphentheorie*, pp. 17-33, 1968.

[9] G. Chartrand, and L. Lesniak, *Graphs and Digraphs*, 2nd ed., Wadsworth, USA: Springer, 1986.

[10] F.R.K. Chung, "On partitions of graphs into trees", *Discrete Mathematics*, vol. 23 no. 1, pp. 23-30, 1978.

[11] J. Edmonds, "Paths, trees, and flowers", *Canadian Journal of Mathematics*, vol. 17, no. 1, pp. 449-467, 1965.

Bitlis Eren Üniversitesi Fen Bilimleri Dergisi
BİTLİS EREN UNIVERSITY JOURNAL OF SCIENCE
ISSN: 2147-3129/e-ISSN: 2147-3188
VOLUME: 12 NO: 1 PAGE: 38-50 YEAR: 2023
DOI:10.17798/bitlisfen.1185363

Determining and Spatial Analysis Biogas Energy Potentials from Agricultural - Animal Wastes in Isparta, Türkiye

Kazım KUMAŞ[1], Kerem HEPDENİZ[1], Ali AKYÜZ[1*]

[1]*Burdur Mehmet Akif Ersoy University, Burdur, Türkiye*
(ORCID: 0000-0002-2348-4664) (ORCID: 0000-0003-4182-5570) (ORCID: 0000-0001-9265-7293)

Keywords: Renewable energy, Biomass potential, Agricultural Waste, Animal Waste, Biogas Energy, Geographical Information Systems, ArcGIS

Abstract
Increasing energy need poses various problems in terms of energy supply security and environmental aspects for many countries. Therefore, energy policies are an important part of sustainable development plans, especially in developing countries. Türkiye is one of the developing countries and its need for energy is increasing day by day. In Türkiye, which generally meets its energy needs from fossil fuels, it is very important both economically and environmentally to reduce the use of these fuels, which are harmful to the environment and depend on foreign sources, and to use renewable energy sources. Considering Türkiye's potential in renewable energy resources, the energy production efficiency to be obtained from the investments to be made is quite high. In this study, a numerical map was created by determining the biogas and energy potentials that can be obtained depending on the agricultural and animal wastes of the province of Isparta, Türkiye. In determining the energy potential, 2018 agricultural and animal statistics of the Turkish Statistical Institute were used. In the calculation made for the province of Isparta, a total of 25831264.2 m^3/year of biogas can be obtained from animal wastes and the thermal value of this value is 586369.70 GJ/year and the total energy potential that can be obtained from some agricultural wastes is calculated as 3549790.42 GJ/year.

1. Introduction

Energy is one of the most important inputs of daily life and industry that determine the development levels of countries. Energy is obtained from renewable energy sources such as solar and wind as well as fossil-based resources. Biomass energy is also an important renewable energy source and is being developed day by day in terms of technology and use [1, 2, 3]. Population growth and industrialization in the world cause an increased need for energy. Biomass energy is one of the most important energy resources that are environmentally friendly and can meet energy needs sustainably. Accordingly, the European Commission sets some targets for the use of renewable energy to reduce fossil fuel consumption [4,5]. In Europe, it is aimed to increase renewable energy consumption from 5% to 20% by 2020. Türkiye is increasing rapidly in developing countries and is one of the priority objectives in the strategic plan, giving priority to local resources by ensuring the diversification of sources and the share of renewable energy sources in the energy supply. In this context, to reduce the external dependency ratio, the share of renewable energy sources in electricity generation is aimed to be at least 30% in 2023 [6,7]. Türkiye has different climate types, topographic structure, soil structure, and depth and due to these characteristics has rich plant diversity. When these characteristics are taken into consideration, a large number of cereals, industrial plants, fruit trees, and forest trees are grown in Türkiye in terms of biomass energy sources. Although there are large amounts of agricultural and vegetable residues in the country every year, the usage rates of these residues are very low. Agricultural residues constitute an important potential for fuel production. The main agricultural residues are

*Corresponding author: caakyuz@mehmetakif.edu.tr
Received: 06.10.2022, Accepted: 27.02.2023

sunflower, corn, cotton and grain straws, and pruning residues that occur in orchards If this potential is evaluated, an economic input can be provided in terms of energy, and rural development can be realized as a result of ensuring a sustainable quality environment by reducing harmful wastes in terms of the environment [8,9,10,11]. Türkiye can only produce an average of one-third of the energy it has consumed in recent years. This situation reveals the need for countries with high agricultural potential, such as Türkiye, to convert vegetable and animal waste into energy by using it more efficiently. Currently, these plant wastes are usually buried under the soil or burned, using them most inefficiently, leading to environmental pollution. The waste assessment is very important in terms of environmental pollution and energy needs [12]. Onurbaş and Türker (2012) calculated the total biogas energy potential of Türkiye as 2.18 Gm^3 using the numbers of cattle, small ruminants, and poultry for 2009. The study also stated that 68% of this potential is caused by cattle, 5% by small ruminants, and 27% by poultry, and found that Türkiye's biogas energy equivalent potential is about 49PJ (1170.4 ktoe) [13]. Akçay (2014) identified the biomass potential and energy value of paddy stalk in the Thrace region, Türkiye. For paddy stalk samples, the minimum thermal value was 3.4 cal/G, the power production was 39.39 GWh/year and the power production potential was 5.29 MWe. It is stated that this calculated amount corresponds to 0.019% of the total electricity consumption of Türkiye and 0.7% of the total electricity consumption of Tekirdag province [14]. Aybek et al (2015) determined and mapped the potential values of biogas and energy that can be obtained from total animal and grain waste based on agricultural regions of Türkiye for 2014. In the study, the amount of volatile dry matter that can be obtained from animal fertilizers is 33210.844 billion tons/year, the amount of volatile dry matter that can be obtained from grain waste is 7.17 billion tons/year and the biogas energy potential is approximately 331.87 PJ / year [15]. Aybek et al. (2015) calculated the biogas potential of animal and some plant wastes in Kahramanmaraş, Türkiye. In the calculation, it was determined that the annual total biogas energy potential that can be obtained from agricultural waste is 2.18 TJ/year [16]. Özsoy and Alibaş (2015) determined the biogas potential that can be obtained from animal waste in Bursa, Türkiye. The potential amount of biogas to be obtained from animal waste and the potential bio-electrical energy per capita were examined. It has been stated that if the biogas potential is utilized, 1.12% of the electricity consumption in Bursa can be met by transforming it into electricity from animal waste [17]. Demir et all. (2016) determined the equivalent potential of agricultural biomass energy in Erzincan, Türkiye between 2006 and 2015 and compared it proportionally with the data obtained for Türkiye and the eastern Anatolia region. Using the cultivated area values of sugar beets, cereals, fruits, vegetables, dry legumes, and forage crops, they calculated the energy potentials of average agricultural biomass in MW. They found that the 9.23 MW value obtained for Erzincan province is equal to 0.59% of the biomass energy potential of Türkiye and 5.76% of the Eastern Anatolia Region [18]. Salihoglu et all. (2019) determined the amount of biogas production that can be obtained from cattle and small ruminant wastes in Balıkesir, Türkiye for 2017 and calculated the energy potential. Different calculation approaches were used according to the amount of waste accepted per animal, and it was stated that 82815.60 m^3 of biogas and 1879914.12 MJ of energy can be produced from 5955.32 tons of waste annually in Balıkesir [19]. Akbaş (2019) calculated the energy equivalent potential of agricultural biomass for Aydın, Türkiye in MW using fruit, vegetable, grain, oilseeds, and dry legumes data between 2009-2018. It has been determined that a total of 40.59 MW of agricultural biomass energy can be obtained [20]. Avcioglu et all. (2019) developed a mathematical model for calculating the energy potential of agricultural biomass residues in Türkiye. The total amount of biomass residues obtained from field crops and garden plants in Türkiye was 59432 kilotons and 15652 kilotons, respectively. Energy potentials from agricultural biomass residues were found to be 298955 TJ for agricultural field crops and 65491 TJ for garden plants [21]. Türkiye has a high potential in terms of animal and vegetable production. However, wastes are buried in the soil for fertilizer purposes, collected around the production area, and directly burned or left to rot or stored to provide grass for animals [22]. In this study, the biomass potential of Isparta from animal and agricultural production was determined by using the data of the Turkish Statistical Institute (TUIK) in 2018 [23]. Different animal species were used in determining the potential of animal biomass. Agricultural biomass resources were evaluated

into four groups: field crops, vegetables, fruits, and ornamental crops. By determining the amount of production area belonging to product groups, the average annual amount of dry biogas and the energy equivalent of the biogas potential were calculated over these areas. In the light of the calculated data, the energy potentials of the province based on livestock and agricultural products were also created.

2. Material and Method

Isparta province is located between longitudes 30°01' and 31°33' east and latitudes 37°18' and 38°30' North. Its area is 8933 km^2 and its average altitude is 1050 m, located in the Mediterranean region. Isparta has twelve districts: Aksu, Atabey, Eğridir, Gelendost, Gönen, Keçiborlu, Senirkent, Sütçüler, Şarkikaraağaç, Uluborlu, Yalvaç and Yenişarbademli. The effects of the Mediterranean climate are observed in Sütçüler, Eğirdir, and partially Aksu and Merkez districts that form the southern part of Isparta lands. In these parts, winters are rainy and milder, while summers are hot and humid. Again, the same geography shows the geographical features of the Mediterranean Region [24]. The distribution sizes of agriculture, forest, meadow-pasture forest, and non-agricultural land of Isparta province and their % ratio are given in Table 1. Paragraphs following the first paragraph should begin with the paragraph indentation.

Table 1 Land distribution of Isparta [20]

Land type	Area size (ha)	Percentage (%)
Agricultural land	210078	28.13
Meadow - pasture land	17747	1.87
Forest land	386048	43.22
Other lands	279434	26.78
Total	893307	100

The number of animals in the districts is given in Table 2. The total number of animals in Isparta province is 1084621. Of the total number of animals, 45.32% consist of sheep-goats, 39.16% of chickens, 7.74% of dairy cattle, 5.63% of meat cattle, 1.91% of turkey-goose-duck, 0.24% of horse-donkey-mule. Considering the distribution of animals by district, the number of chickens and turkey-goose-duck are the most in the central district, while other animal species are located in the Yalvaç district. The formulas and parameters given in Figure 1 were used in the theoretical calculation of the biogas potential resulting from animal waste [24, 26]. The calorific value of animal wastes has been accepted as 22.7 MJ /m^3 [26]. The coefficients used in the calculation method have been obtained from various studies and are given in Table 3.

Table 2. Number of animals in Isparta [23]

District	Dairy Cattle	Meat Cattle	Horse-Donkey-Mule	Small ruminant	Turkey-Goose-Duck	Chicken
Aksu	3589	2532	273	6829	302	1950
Atabey	3462	2985	22	18389	200	3907
Eğirdir	8780	4720	180	59765	264	27000
Gelendost	3865	2824	75	28036	475	16500
Gönen	3303	2234	19	19982	785	7300
Keçiborlu	5201	4865	70	20947	92	9300
City center	11574	7628	224	84564	10042	294359
Senirkent	2566	1371	36	32013	83	775
Sütçüler	6253	4186	194	39770	265	10400
Uluborlu	600	1227	50	15013	82	1100
Yalvaç	17860	13177	893	98349	1700	45000
Yenişarbademli	864	420	28	2653	133	1750
Şarkikaraağaç	16070	12856	421	65240	6310	5500

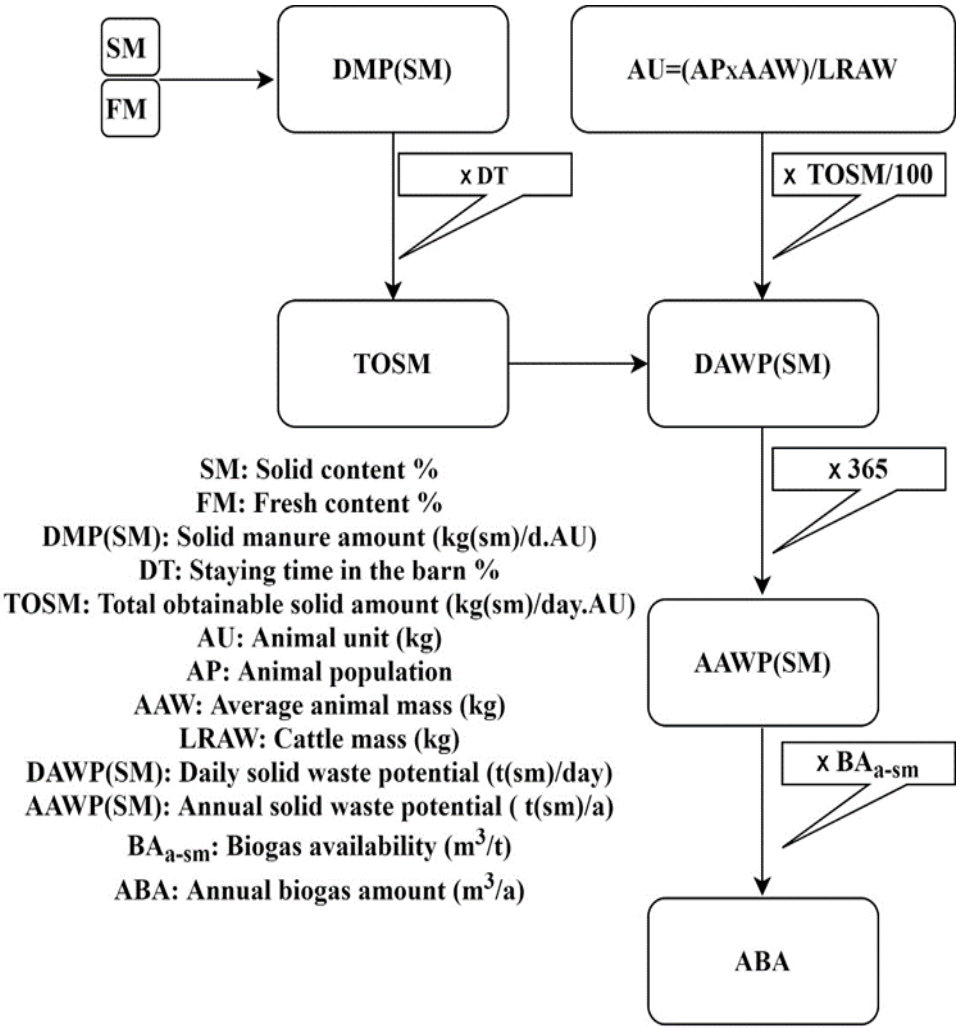

Figure 1. The theoretical calculation of the biogas potential [6, 12, 19]

Table 3 Parameters used in the calculation [6, 12, 19]

Animal	FM	SM	DMP	DT	TOSM	AAW	BAa-sm
Dairy cattle	33.33	12.7	4.233	65	2.7515	454	202
Meat cattle	34.68	11,6	4.023	25	1.0058	454	202
Horse-Donkey-Mule	37.71	21	7.9191	29	2.2965	250	300
Small ruminant	16.44	25	4.1100	13	0.5343	50	251
Turkey-Goose-Duck	26.61	25	6.654	68	4.5247	8	300
Chicken	25.29	25	6.323	99	6.2597	2	300

Data on the production areas of field crops were obtained using the statistics of plant production in the database of the Turkish Statistical Institute. Considering the distribution of agricultural areas by districts, Yalvaç has the highest area with approximately 25.34%. It is followed by Şarkikaraağaç (14.4%) and Gelendost (11.5%) districts, respectively. Approximately 60.81% of the cultivated areas in the province are composed of cereals and other herbal products, while 20.52% of them are fruits, beverages, and spice plants. Vegetables constitute 2.7% of the land and 0.03% of ornamental plants. Agricultural lands for Isparta are given in Table 4 [24, 25].

Table 4 Isparta agricultural areas (decares) [24, 25]

District	Fruits, beverages, spice herbs	Vegetables	Ornamental Plants	Cereals and other herbal products	Fallow field	Uncultivated area
City center	27170	7110	646	71328	43112	24870
Aksu	5811	3083	-	19882	14512	64120
Atabey	10441	3142	-	40343	16000	14730
Eğirdir	64627	1989	-	28352	40162	79770
Gelendost	60019	919	-	157655	14500	18090
Gönen	14445	1774	-	71708	48000	39810
Keçiborlu	12496	5080	-	123835	17767	26640
Senirkent	88563	12118	-	37328	7090	10890
Sütçüler	2466	2385	-	20835	60600	83980
Uluborlu	29512	44	-	5605	1475	22110
Yalvaç	77485	8706	-	385143	42000	66790
Yenişarbademli	5884	604	-	7385	11000	15660
Şarkikaraağaç	16822	9049	-	262339	5400	15090
Total	415.741	56.003	646	1.231.738	321.618	482.550

In Isparta, 440996 tons of field products were produced according to 2018 TUIK data. While sugar beet has the largest share in this production with 117986 tons, peanuts have the lowest share with 42 tons. Corn, barley, and wheat products follow sugar beet, respectively. The production amount of field products belonging to the Isparta center and districts are given in Table 5 [24, 25]. In 2018, 872452 tons of fruit, beverage, and garden plants were produced in Isparta center and its districts. Production amounts of grape, apple, cherry, peach, apricot, pear, almond, and hazelnut are given in Table 6 [24, 25]. While the most produced product was the apple, the least was hazelnuts. Table 7 is used for the theoretical biomass potential from agricultural product wastes. The formulas for the calculation are given at the bottom of the table [15, 16].

Table 5. Field crops production (tons) [24, 25]

District	Wheat	Barley	Corn	Rye	Oat	Bean	Sugar beet	Chickpea	Potato
City center	3088	8159	4451	100	119	454	2156	10	1130
Aksu	771	888	2117	-	-	2228	-	2	44
Atabey	108	6897	6958	-	538	221	29844	6	121
Eğirdir	3941	393	515	-	-	151	-	35	395
Gelendost	11634	11850	172	-	-	207	-	6542	-
Gönen	2194	9104	2669	-	53	42	4903	26	582
Keçiborlu	6119	11809	3444	-	-	226	110	45	-
Senirkent	1257	5781	3880	-	1625	1124	22056	5	76
Sütçüler	1437	533	59	-	13	271	-	18	57
Uluborlu	152	355	150	-	13	13	-	34	-
Yalvaç	32867	22222	16119	237	2100	1870	-	4971	5156
Yenişarbademli	255	97	2746	-	-	442	-	-	-
Şarkikaraağaç	26326	13698	63113	336	290	1825	58917	873	14
Total	90149	91786	106393	673	4751	9074	117986	12567	7575

Table 6. Horticultural crops production (tons) [24, 25]

District	Grape	Apple	Cherry	Peach	Apricot	Pear	Almond	Hazelnut
City center	10759	7246	3739	3438	132	183	131	2
Aksu	-	15532	65	96	-	4	-	-
Atabey	538	10793	1942	949	152	211	65	-
Eğirdir	266	364703	920	1282	74	733	120	-
Gelendost	529	182736	1536	819	732	71	78	-
Gönen	1957	4508	2580	96	80	135	49	17
Keçiborlu	6240	3225	878	140	190	207	787	-
Senirkent	26888	75001	15850	1062	2584	197	1051	-
Sütçüler	70	1501	292	259	-	171	22	-
Uluborlu	275	10381	5215	14	13	178	57	19
Yalvaç	35036	19648	1083	317	5018	1460	165	-
Yenişarbademli	323	2527	808	61	-	8	9	6
Şarkikaraağaç	6339	19600	1367	265	5018	463	166	-
Total	89220	717401	36275	8798	13993	4021	2700	44

Table 7. Waste type, moisture information, product waste rate, lower calorific value, and availability of selected field crops and horticultural crops [15, 18, 21]

Products	Waste type	Average Humidity (H) (%)	Product waste ratio (PWR)	Lower heating value (LHV) (MJ/kg)	Average availability (%) (AP)
Wheat	Straw	13	1.13	16.7	15
Barley	Straw	13	1.22	18.5	15
Corn	Handle	16	1.88	17	60
Rye	Stub	8	0.57	15.5	60
Bean	Straw	12	0.37	18.5	15
Sugar beet	Stem and leaf	5	1.45	14.7	15
Peanut	Stem and leaf	60	0.45	13.6	95
Grape	Pruning	45	0.42	18	80
Apple	Pruning	40	0.19	17.8	80
Cherry	Pruning	40	0.19	21.7	80
Peach	Pruning	40	0.40	18.2	80
Apricot	Pruning	40	0.19	20	80
Pear	Pruning	38	0.22	18.2	80

$$TBP = AA\ x\ PWR\ x\ [1 - 0.01xH]$$

$$AEP = TBP\ x\ LHV\ x\ AP$$

TBP: Theoretical biomass potential

AEP: Available energy potential

AA: Annual amount of products in tons

Geographical Information Systems provide the opportunity to geographically coordinate and store data, query, and analyze data. In this study, the Kriging interpolation method in the Spatial Analysis module of the ArcGIS 10 program was used. The purpose of using this method is that data collection for every point in the study area is very costly and laborious. This method enables the determination of the predictive values of the data obtained from the sampling points in the study area regarding the remaining areas in the field. Thus, it creates a continuous surface from sample points within the boundaries [27].

3. Results and Discussion

Isparta's 2018 animal numbers with the basis of its districts and the usable waste potential of animal origin are given in Table 8. The biogas energy values obtained from the waste potential by animal type are given in Table 9. According to Table 8, a total of 122392.81 tons of usable animal waste were obtained annually. The vast majority of usable waste is dairy cattle with 68.31% and meat cattle with 18.14%. The last usable waste was obtained from turkey-goose-duck-chicken with 0.4%.

Table 8. Animal Waste Potential (ton/year)

District	Dairy Cattle	Meat Cattle	Horse-Donkey-Mule	Small ruminant	Turkey-Goose-Duck	Chicken
Aksu	3572.6	921.3	126.0	146.7	8.8	19.6
Atabey	3446.2	1086.1	10.2	394.9	5.8	39.3
Eğirdir	8739.9	1717.4	83.1	1283.6	7.7	271.8
Gelendost	3847.4	1027.6	34.6	602.2	13.8	166.1
Gönen	3287.9	812.9	8.8	429.2	22.9	73.5
Keçiborlu	5177.3	1770.2	32.3	449.9	2.7	93.6
City center	11521.2	2775.6	103.4	1816.3	292.2	2962.8
Senirkent	2554.3	498.9	16.6	687.6	2.4	7.8
Sütçüler	6224.5	1523.1	89.5	854.2	7.7	104.7
Uluborlu	597.3	446.5	23.1	322.5	2.4	11.1
Yalvaç	17778.6	4794.6	412.2	2112.3	49.5	452.9
Yenişarbademli	860.1	152.8	12.9	57.0	3.9	17.6
Şarkikaraağaç	15996.7	4677.8	194.3	1401.2	183.6	55.4
Total	83604.0	22204.8	1147.1	10557.5	603.4	4276.1

According to Table 9, cattle account for 82.7% of the achievable biogas potential. Small ruminants compose 10.25% of the potential, chickens compose 4.9% and other species make up the rest. Dairy cattle make the greatest contribution to the biogas potential with 16888006.39 m^3/year, while the Central District plays the greatest role in the formation of this value. The district where biogas potential is highest is Şarkikaraağac with 4657960.83 m^3/year, and the district where it is least is Yenişarbademli with 229227.26 m^3/year (Table 9).

According to TUIK 2018 data, 331662.45 tons of products (Table 10) have been obtained from field products used in the study in Isparta and its districts [23]. The biomass potentials of selected field crops are given in Table 11. The highest biomass potential available from field crops is obtained from barley production with 97421.66 tons, and the lowest biomass potential is obtained from peanut production with 13.91 tons. About 72% of the total biomass potential in the province consists of barley, wheat, corn beans, and chickpeas, while 28% consists of the remaining agricultural products.

Table 9. Biogas potential from animal waste (m^3/year)

District	Dairy Cattle	Meat Cattle	Horse-Donkey-Mule	Small ruminant	Turkey-Goose-Duck	Chicken
Aksu	721671.9	186103.4	37803.7	36814.9	2636.6	5888.2
Atabey	696134.9	219399.1	3046.5	99134.3	1746.1	11797.5
Eğirdir	1765472.0	346922.5	24925.5	322190.6	2304.9	81528.7
Gelendost	777169.6	207565.5	10385.7	151140.9	4147.0	49823.1
Gönen	664163.3	164200.2	2631.0	107722.1	6853.5	22042.9
Keçiborlu	1045810.9	357580.1	9693.3	112924.4	803.2	28082.1
City center	2327286.2	560662.1	31018.5	455880.9	87671.9	888840.8
Senirkent	515968.2	100769.2	4985.1	172580.7	724.6	2340.2
Sütçüler	1257345.8	307673.2	26864.2	214398.4	2313.6	31403.6
Uluborlu	120647.3	90185.2	6923.8	80934.4	715.9	3321.5
Yalvaç	3591267.6	968516.6	123658.4	530195.3	14841.9	135881.1

Yenişarbademli	173732.1	30870.2	3877.3	14302.2	1161.2	5284.3
Şarkikaraağaç	3231336.5	944922.9	58298.1	351706.1	55089.6	16607.7
Total	16888006.4	4485370.2	344111.0	2649925.2	181009.8	1282841.7

Table 10. Field crops biomass potential (tons)

District	Wheat	Barley	Stalk	Corncob	Rye	Oat	Bean	Sugar beet	Chickpea	Potato
City center	3035.8	8659,9	3514.5	1167.0	84.2	38.7	625.4	70.0	11.1	203.4
Aksu	757.9	842.5	1671.6	555.0	-	-	3069.1	-	2.2	7.9
Atabey	106.2	7320.5	5494.0	1824.4	-	175.2	304.4	969.9	6.6	21.8
Eğirdir	3874.4	417.1	406.6	135.0	-	-	208.0	-	38.7	71.1
Gelendost	11437.4	12577.6	135.8	45.1	-	-	285.1	-	7228.9	-
Gönen	2156.9	9662.9	2107.4	699.8	-	17.3	57.9	159.3	28.7	104.8
Keçiborlu	6015.6	12534.1	2719.4	903.0	-	-	311.3	3.6	49.7	-
Senirkent	1235.8	6135.9	3063.6	1017.3	-	529.1	1548.3	716.8	5.5	13.7
Sütçüler	1412.7	565.7	46.6	15.5	-	4.2	373.3	-	19.9	10.3
Uluborlu	149.4	376.8	11844	39.3	-	4.2	17.9	-	37.6	-
Yalvaç	32311.6	23586.4	12727.5	4226.4	199.4	683.8	2575.9	-	5492.9	928.1
Yenişarbademli	250.7	102.9	2168.2	720.0	-	-	608.9	-	-	-
Şarkikaraağaç	25881.1	14539.1	49834.0	16548.2	282.7	94.4	2513.9	1914.8	904.7	2.5
Total	88625.5	97421.6	84007.9	27896.2	566.3	1546.9	12499.4	3834.5	13886.5	1363.5

Table 11 shows the biomass potential that can be obtained from garden products. The highest biomass potential originating from garden products is obtained from apples with 81783.71 tons and hazelnuts with at least 88.17 tons. When the total biomass potential of horticultural products is examined, the highest biomass potential was obtained from apples with 81783.71 tons and hazelnuts with at least 88.17 tons. Apple constitutes 70% of the total biomass potential and grapes 17%. When the biomass potential of apples is evaluated, Eğirdir is in the first place with 41576.14 tons, while Sütçüler is in the last place with 171.11 tons. When the total biomass potential of the grape is evaluated, Yalvaç was the district that made the most contribution and Aksu was the least.

Table 11. Horticultural biomass potential (tons)

District	Grape	Apple	Cherry	Peach	Apricot	Pear	Almond	Hazelnut
City center	2485.3	826.0	426.2	825.1	15.0	25.0	49.5	4.0
Aksu	-	1770.6	7.4	23.0	-	0.5	-	-
Atabey	124.3	1230.4	221.4	227.8	17.3	28.8	24.6	-
Eğirdir	61.4	41576.1	104.9	307.7	8.4	99.9	45.4	-
Gelendost	122.2	20831.9	175.1	196.6	83.4	9.7	29.5	-
Gönen	452.1	513.9	294.1	23.0	9.1	18.4	18.5	34.1
Keçiborlu	1441.4	367.6	100.1	33.6	21.7	28.2	297.6	-
Senirkent	6211.1	8550.1	1806.9	254.9	294.6	26.9	397.5	-
Sütçüler	16.2	171.1	33.3	62.2	-	23.3	8.3	-
Uluborlu	63.5	1183.4	594.5	3.4	1.5	24.3	21.6	38.1
Yalvaç	8093.3	2239.9	123.5	76.1	572.0	199.1	62.4	-
Yenişarbademli	74.6	288.1	92.1	14.6	-	1.1	3.4	12.0
Şarkikaraağaç	1464.3	2234.4	155.8	63.6	572.0	63.2	62.8	-
Total	20609.8	81783.7	4135.4	2111.5	1595.2	548.5	1021.1	88.2

The Kriging method, a geostationary method, is widely used to predict properties in non-measuring points or areas. In this method, weights are based not only on the distance between the measured points and the prediction location but also on the overall spatial arrangement of the measured points [27, 28]. In this study, Isparta provincial border was geographically coordinated and digitized using ArcGIS 10 program. 13 district boundaries were created within the provincial borders, and the values of animals and agricultural products for each district (energy potentials calculated using Figure 1 and Table 7) were recorded in the attribute table created in the program. Using the Kriging interpolation method in the ArcGIS spatial analysis module, spatial distribution maps of the values entered in the province were created. In Figure 2, the maps of the energy potentials that can be obtained from dairy cattle, horse-donkey-mule, sheep-goat, and chicken are given according to the amount of biogas potential obtained in Table 9. According to Figure 2, while the highest energy potential was obtained from dairy cattle, the least energy was obtained from horse-donkey-mule animal species. High values are shown on the map in colors close to red, while low values are shown in colors close to blue.

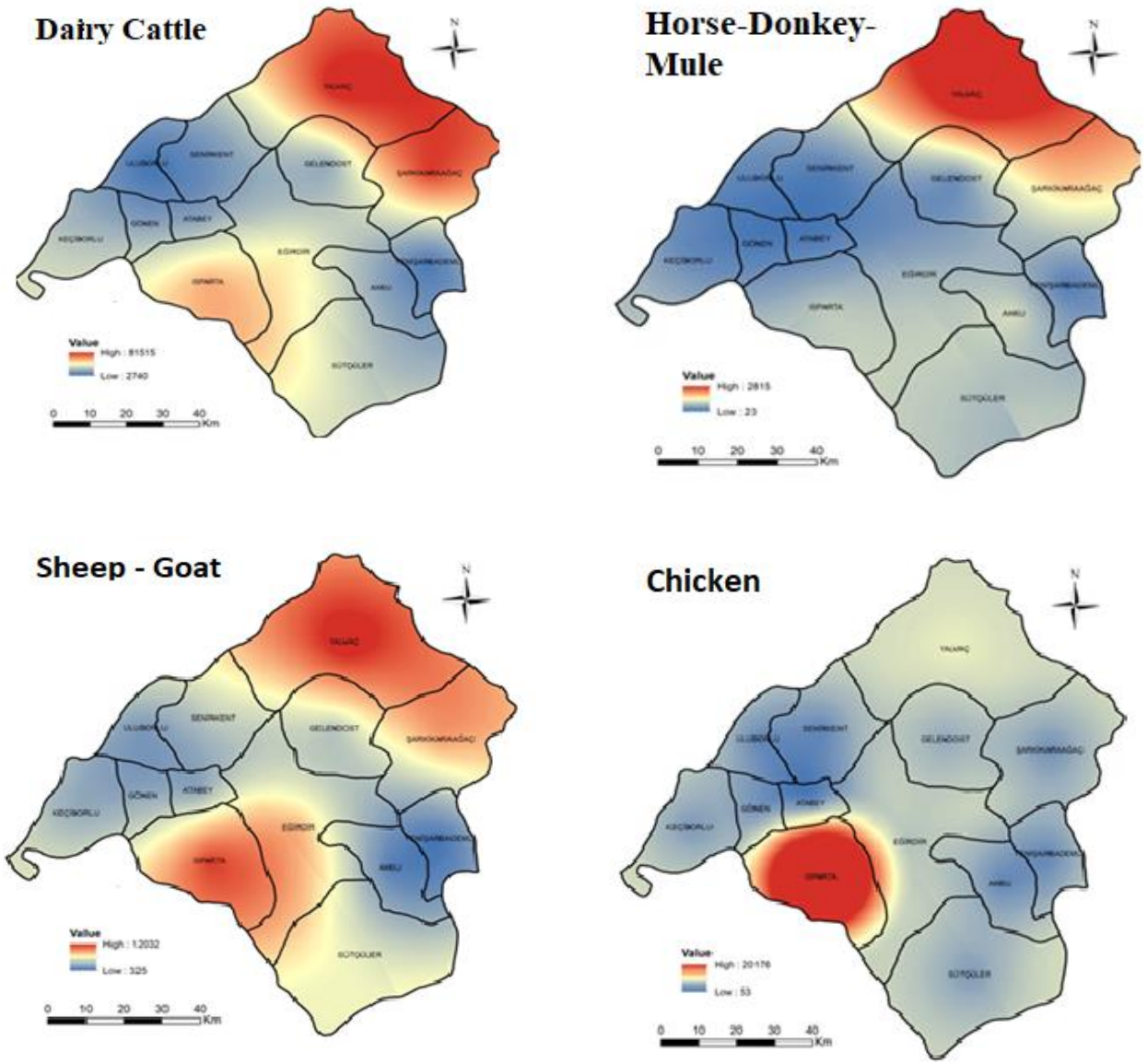

Figure 2. Energy potential according to animal species in Isparta

In Figure 3, the map of the energy potentials that can be obtained for wheat, barley, corn, and beans is given on a district basis. High values are shown on the map in colors close to red, while low values are shown in colors close to blue. When the energy potential of horticultural products is examined, it is seen that the highest energy potential is obtained from apples. The energy potential that can be obtained from all horticultural crops comes from apples the most and hazelnut the least. Rye and peanut from field crops could not be mapped due to the lack of biomass potential in each district. The energy potential of rye and peanuts has been calculated as 1478.12 GJ/year. A total of 71789.68 GJ/year, which can be obtained from the garden products cherry throughout the province, has been calculated (Figure 4). In figure 4, high values are shown on the map in colors close to red, while low values are shown in colors close to blue.

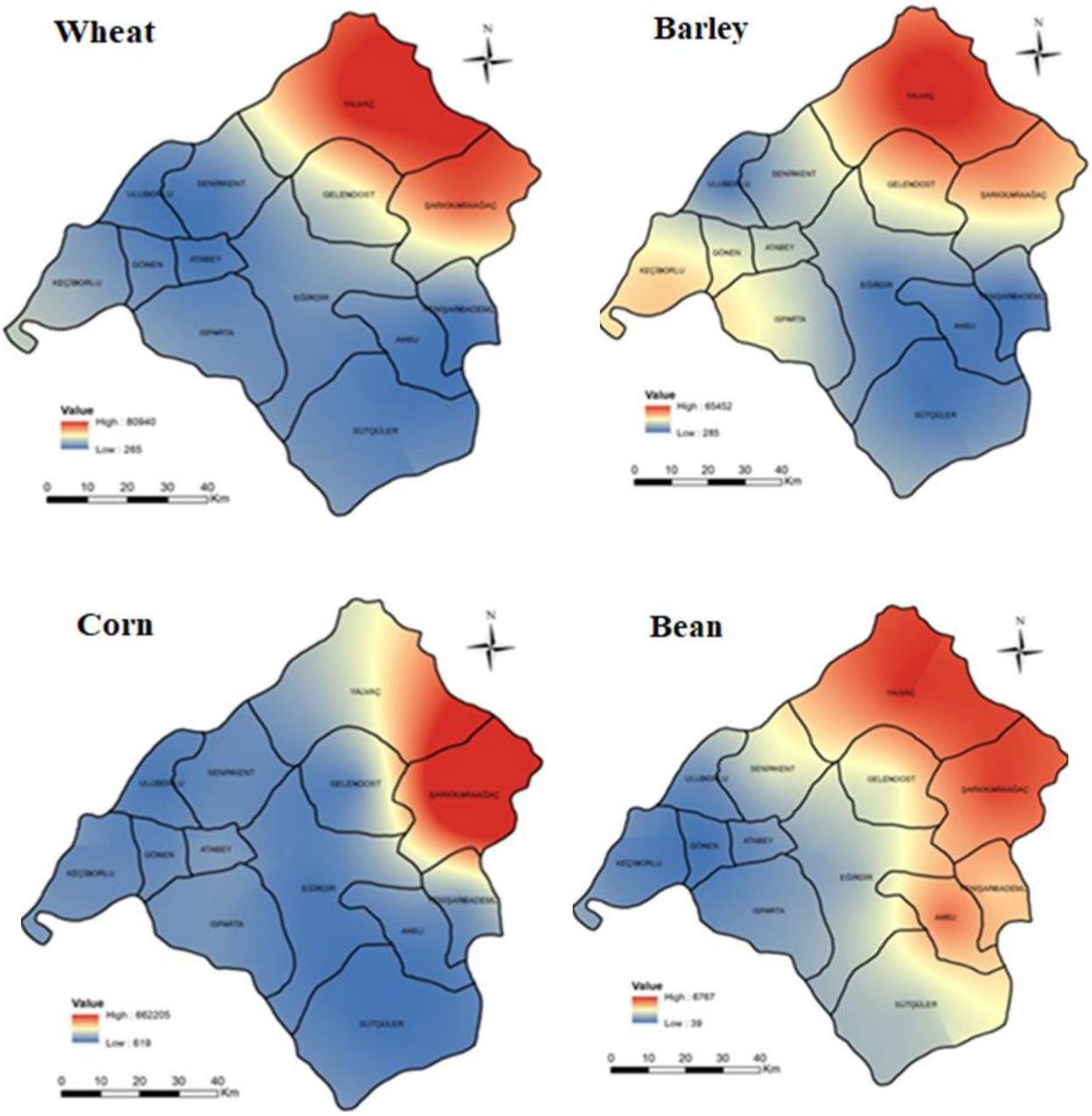

Figure 3. Energy potential that can be obtained from field products in Isparta

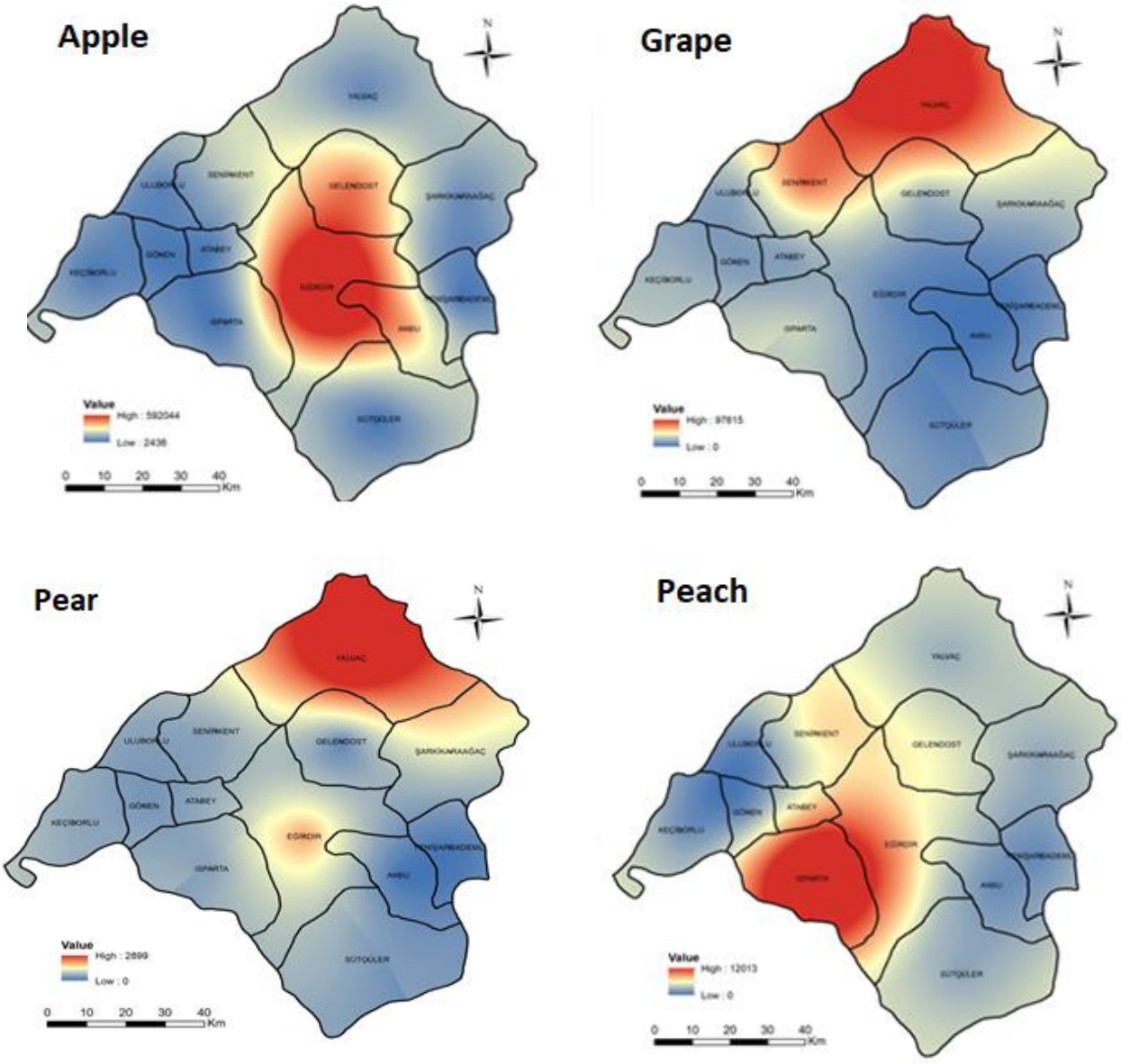

Figure 4.. Energy potential that can be obtained from horticultural products in Isparta

4. Conclusion and Suggestions

The energy competition between the countries has caused rapid oil consumption, global warming, and the deterioration of the ecosystem. It is necessary to turn to renewable energy sources to reduce oil over time, warming the world and not destroying ecosystems. To meet the general energy demand in Türkiye, it is tried to switch to renewable energy sources that can be used in the long term as much as possible. In this study, according to TUIK 2018 data, the biogas and energy potential of animal manure and agricultural wastes in Isparta were determined all the data and the results obtained were and digital maps were created. According to 2018 data in the center and
districts of Isparta, 443555.82 tons of biomass potential was determined from some agricultural (field and garden) products. The total thermal capacity of these wastes was determined to be 3549790.42 GJ/year. It has been calculated that a total of 25831264.2 m^3/year of biogas can be obtained from animal waste and the heating value of this value is 586369.70 GJ/year. Studies on biomass energy potential, energy use rate, and environmental effects in Türkiye will enable the creation of databases related to the field. With this study,

mapped thematically in GIS. Thus, the data differences between the districts and the visual observation of the obtained results were provided. The database obtained by the study will create a healthy resource for future studies on different subjects to be made throughout the province.

Contributions of the Authors

Kazım KUMAŞ: Conceptualization, methodology
Kerem KEPDENİZ: Conceptualization, methodology, investigation, visualization
Ali AKYÜZ: Conceptualization, writing - review & editing

Conflict of Interest Statement

There is no conflict of interest between the authors.

Statement of Research and Publication Ethics

The study is complied with research and publication ethics.

References

[1] B. Demir, Z. A. Kuş, H. A. İrik and N. Çetin, "Mersin İli Tarımsal Biyokütle Enerji Eşdeğer Potansiyeli," *Alinteri Journal of Agriculture Science*, vol. 29, no. 2, pp. 12-18, 2016.

[2] H. Şenol, E. A. Elibol, Ü. Açıkel and M. Şenol, "Türkiye'de Biyogaz Üretimi İçin Başlıca Biyokütle Kaynakları," *Bitlis Eren Üniversitesi Fen Bilimleri Dergisi*, vol. 6, no. 2, pp. 81-92, Dec. 2017, doi:10.17798/bitlisfen.315118.

[3] H. Yaka, M. A. Insel, O. Yucel, and H. Sadikoglu, "A comparison of machine learning algorithms for estimation of higher heating values of biomass and fossil fuels from ultimate analysis," *Fuel*, vol. 320, no. 123971, p. 123971, 2022. https://doi.org/10.1016/j.fuel.2022.123971.

[4] E. Toklu, "Biomass energy potential and utilization in Turkey," *Renew. Energy*, vol. 107, pp. 235–244, 2017. https://doi.org/10.1016/j.renene.2017.02.008

[5] E. Kalayc, G. Türker and E. Çağlarer, "Kırklareli İlinin Hayvansal Atık Potansiyelinin Biyogaz Üretimi Çerçevesinde Değerlendirilmesi ve Güncel Yapının Yorumlanması," Bitlis Eren Üniversitesi *Fen Bilimleri Dergisi*, vol. 8, no. 4, pp. 1489-1497, Dec. 2019, https://doi.org/10.17798/bitlisfen.593791

[6] K. Kumaş and A. Ö. Akyüz, "Methane, Diesel Fuel, Electrical Energy, CO_2 Emissions and Economical Equavialent from Animal Manure of Tokat, Turkey," *International Scientific and Vocational Studies Journal*, vol. 5, no. 2, pp. 144-153, 2021, https://doi.org/10.47897/bilmes.969372.

[7] G. Küsek, C. Güngör, H. H. Öztürk ve Ş. Akdemir , "Tarımsal Artıklardan Biyopelet Üretimi," *Uludağ Üniversitesi Ziraat Fakültesi Dergisi*, c. 29, sayı. 2, ss. 137-145, 2015.

[8] A. Horuz, A. Korkmaz and G. Akınoğlu, "Biyoyakıt Bitkileri ve Teknolojisi," *Toprak Bilimi ve Bitki Besleme Dergisi*, vol. 3, no. 2, pp. 69-81, 2015.

[9] K. Kumaş and A.Ö. Akyüz, "Biogas Potential, CO_2 Emission and Electrical Energy Equivalent from Animal Waste in Burdur, Turkey," *Akademia Doğa ve İnsan Bilimleri Dergisi*, vol 7, no 1, pp. 52-62, 2021. https://dergipark.org.tr/tr/pub/adibd/issue/60270/912682

[10] F. D. Tunçez "Ereğli İlçesinin Biyogaz Potansiyelinin Belirlenmesi," *Ulusal Çevre Bilimleri Araştırma Dergisi*, vol. 1, no.1, pp.1-7, 2018.

[11] O. A. Avcıoğlu, U. Türker, Z. Demirel Atasoy, D. Koçtürk, "Tarımsal Kökenli Yenilenebilir Enerjiler Biyoyakıtlar," *Nobel Akademik Yayıncılık*, 2011.

[12] M. Taşova and S. Yazarel, "Yozgat İli Hayvansal Kaynaklı Atıkların Biyogaz ve Enerji Potansiyellerinin Belirlenmesi," *International Journal of Life Sciences and Biotechnology*, vol. 2, no. 1, pp. 16–24, 2019.

[13] A. O. Avcioğlu and U. Türker, "Status and potential of biogas energy from animal wastes in Turkey," *Renew. Sustain. Energy Rev.*, vol. 16, no. 3, pp. 1557–1561, 2012. https://doi.org/10.1016/j.rser.2011.11.006

[14] T. Akçay, "Trakya bölgesinde çeltik sapının biyokütle potansiyeli ve enerji değerlerinin saptanması," *Namık Kemal Üniversitesi Fen Bilimleri Enstitüsü, Yüksek Lisans Tezi*, Tekirdağ, 2014.

[15] A. Aybek, S. Üçok, M. E. Bilgili, and M. A. İspir, "Kahramanmaraş İlinde Bazı Tarımsal Atıkların Biyogaz Enerji Potansiyelinin Belirlenerek Sayısal Haritalarının Oluşturulması," *Uludağ Üniversitesi Ziraat Fakültesi Dergisi,* vol. 29, no. 2, pp. 25–37, 2015.

[16] A. Aybek, S. Üçok, M. A. İspir and M. E. Bilgili, "Digital Mapping and Determination of Biogas Energy Potential of Usable Animal Manure and Cereal Straw Wastes in Turkey," *Journal of Tekirdag Agricultural Faculty*, vol. 12, no. 3, pp. 109-120, 2015.

[17] G. Ozsoy and I. Alibas, "GIS mapping of biogas potential from animal wastes in Bursa, Turkey," *Int. j. agric. biol. eng.*, vol. 8, no. 1, pp. 74–83, 2015.

[18] B. Demir, N. Çetin, Z. A. Kuş and E. Kuş, "Agricultural Originated Biomass Energy Equivalent Potential of Erzincan Province", *Uluslararası Erzincan Sempozyumu*, Erzincan, 28 September-1 October pp. 641-646, 2016.

[19] N. K. Salihoğlu, A. Teksoy, and K. Altan, "Büyükbaş ve Küçükbaş Hayvan Atıklarından Biyogaz Üretim Potansiyelinin Belirlenmesi: Balıkesir İli Örneği," *Ömer Halisdemir Üniv. Mühendis. Bilim. Derg.*, vol. 8, no. 1, pp. 31–47, 2019. https://doi.org/10.28948/ngumuh.516798

[20] T. Akbaş, "Determination of Agricultural Biomass Energy Equivalent Potential of Aydın Province", *2. Uluslararası Tarım, Çevre ve Sağlık Kongresi*, Aydın, 18-19 October, pp.1952-1964, 2019.

[21] A. O. Avcıoğlu, M. A. Dayıoğlu, and U. Türker, "Assessment of the energy potential of agricultural biomass residues in Turkey," *Renew. Energy*, vol. 138, pp. 610–619, 2019. https://doi.org/10.1016/j.renene.2019.01.053

[22] E. Tınmaz Köse, "Determination and digital mapping of biogas energy potential of animal manures in Thrace region," *Pamukkale Univ. J. Eng. Sci.*, vol. 23, no. 6, pp. 762–772, 2017.

[23] TUİK, Hayvansal istatistikleri. (2018). Accessed: 10.02.2022. [Online]. https://biruni.tuik.gov.tr/medas/?kn%C2%BC101&locale%C2%BCtr

[24] Anonim, Republic of Turkey Isparta Governorate. (2022). Accessed: 10.02.2022. [Online]. http://www.isparta.gov.tr/

[25]. TUİK, Bitkisel üretim istatistikleri. (2018). Accessed: 10.02.2022. [Online]. https://biruni.tuik.gov.tr/medas/?kn=92&locale=tr

[26] A. M. Omer and Y. Fadalla, "Biogas energy technology in Sudan," *Renew. Energy*, vol. 28, no. 3, pp. 499–507, 2003. https://doi.org/10.1016/S0960-1481(02)00053-8

[27] S. Yaprak and E. Arslan, "Kriging Yöntemi ve Geoit Yüksekliklerin Enterpolasyonu," *J. Geod. Geoinf.*, no. 98, pp. 36–42, 2008.

[28] Anonim, Arcmap desktop 10.3. (2020). Accessed: 10.06.2022. [Online]. https://desktop.arcgis.com/en/arcmap/10.3/tools/3d-analyst-toolbox/how-kriging-works.htm

Bitlis Eren Universitesi Fen Bilimleri Dergisi
BİTLİS EREN UNIVERSITY JOURNAL OF SCIENCE
ISSN: 2147-3129/e-ISSN: 2147-3188
VOLUME: 12 NO: 1 PAGE: 51-56 YEAR: 2023
DOI:10.17798/bitlisfen.1190004

Investigating Mechanical and Wear Properties of CaCO3 Filled PP Composite Filament Production for 3D Printer

Alp Eren SAHİN[1*]

Mechanical Engineering Department of Kocaeli University, Umuttepe Campus, İzmit/Kocaeli

(ORCID: 0000-0001-7313-2467)

Keywords: 3D Printer, Composite Filament, Polymer Composite.

Abstract

Recently, the interest in 3D printers, which is one of the polymer-based material production methods, and the amount of production in the sector are increasing day by day. It is clearly seen that 3D printers, which were used as hobby devices in the beginning, have evolved from being hobby devices to industrial production devices. When current studies are examined, it is clearly observed that not only pure polymers, but also composite materials are used in 3D printers. In this study, Pure PP and various weight filling ratio CaCO3 filled PP composite filaments were produced. Wear test and three-point bending test specimens were produced by 3D printer. When the mechanical test results were examined, it was determined that the flexural strength of the composite samples was affected adversely. The wear test results showed that the particle reinforcement reduced the friction coefficient by making a lubricating effect on the surface. The wear volume of the composite samples decreased by approximately 40% compared to pure PP. As a result, it has been seen that composite samples can be produced with some compromise in strength in applications requiring high wear resistance and low friction. Especially when it is considered that there is a ratio of approximately 1/10 between the prices of matrix and reinforcement materials, composite filament gains more importance in order to reduce the cost of the final product.

1. Introduction

The method of manufacturing with 3D printing, which initially appeared as a fast model production and design method, has found a large area of use for hobby purposes. However, the increase in the usage area of the produced products necessitated the production of stronger end products. [1-5]. The continuous development of 3D printing production technology has resulted in a significant increase in production speed, quality, and production reliability. However, the need for the production of structural parts and the use of high-quality materials has emerged [6,7]. While the production with 3D printer technology was initially carried out with pure and easy to produce polymers, the use of engineering polymers and composite materials was needed over time [1]. In this way, it was ensured that a product with higher properties was obtained. When current literature studies are examined, it is noteworthy that there are very few studies on composite filament production and its production in 3D printers [8,9].

One of the most widely used particle for polymer reinforcement is Calcium carbonate ($CaCO_3$). There is much more study on the effects of $CaCO_3$ particle filling for polymer matrix composites, and they are well-known in literature [11-14].

Polypropylene (PP) is one of the most popular thermoplastic polymers, with a wide area of use in industrial applications due to its lower price, high impact resistance and ductility, resistance to water and chemicals. Moreover, being recyclable and easy to process is among the main reasons that increase the interest in polypropylene. Due to the above-mentioned advantages, polypropylene is increasingly used in many application areas such as automotive,

*Corresponding author: alperensahin88@gmail.com
Received: 16.10.2022, Accepted: 29.12.2022

home furniture and appliances, toy industry, storage tanks, food packaging, medical equipment [16-18].

In this study, composite filaments were produced by reinforcing PP polymer with $CaCO_3$, which is one of the traditional particle reinforcements, at different weight rates (0, 1, 2, 4 wt%). The produced filaments were used in sample production in 3D printer and their mechanical and tribological properties were characterized. Thus, composite sample production was carried out with the up-to-date 3D technology and its applicability was evaluated in detail. It is aimed to improve the properties of the 3D printer filament with particle reinforcement and to reduce the cost of the final product.

2. Material and Method

2.1 Materials

Moplen HP500 brand name polypropylene granule was supplied from LyondellBasell Company. Filler material $CaCO_3$ particles were supplied from Omya Madencilik A.S. (Turkey). The particle used is in the average 100-250 micron size range and the optical microscope photograph is given in Figure 1.

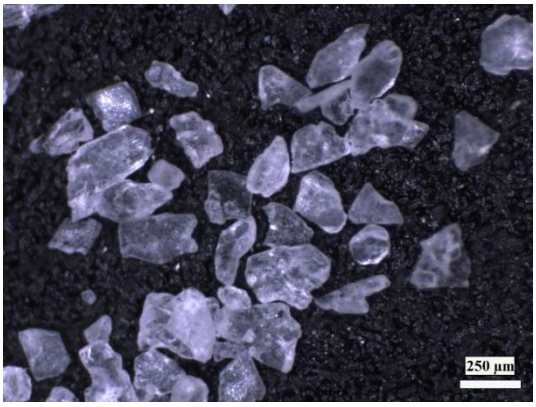

Figure1. Optic microscope photograph of $CaCO_3$ particle

2.2. Method

2.2.1. Sample Preparation

Before filament production, granular PP and $CaCO_3$ particles were kept in an oven at 80°C for 24 hours to dehumidify. Retsch PM100 brand name grinder was used for mechanical mixing of $CaCO_3$ particle and PP polymer granule. Then, pure PP and different mass ratios (1, 2, 4 wt%) of $CaCO_3$ reinforced composite filaments were produced by using the Arya Tech brand extruder and wrapper shown in Figure 3. Filament production was carried out at 200°C extruder temperature. T3 Dizayn brand name 3D printer was used for sample production and printing parameters are given at table 1. 10x80x4 mm and 20x20x5 mm dimension samples were produced for bending and wear test respectively. Photos of produced samples are given at Figure 2.

Table 1. 3D printing parameters

Nozzle Temperature	210°C
Table Temperature	100°C
Filling density	%100
Layer thickness	0.2 mm
Printing Speed	50 mm/s

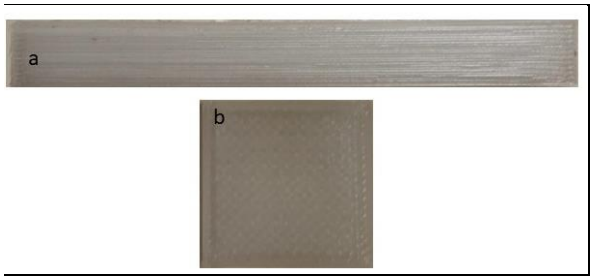

Figure 2. Produced test samples by 3D printer; a) 3 Point bending b) Wear

2.2.2. Bending Test

3-point bending tests were applied on the samples to characterize the mechanical properties of the samples. 3-point bending tests were applied according to ISO 178 with 5 mm/min cross head speed and 64 mm span distance by Instron brand name Universal Tester.

2.2.3. Wear Test

Nanovea T50 ball on disc test device was used to characterize the wear behavior of samples. ASTM G99 wear test standard was used for wear tests. Wear test parameters are given at table 2.

Figure 3. Flax brand name laboratory scale extruder and filament wrapper machine

Table 2. Test Paramaeers of Adhesive Wear Test

Normal Load	20 N
Velocity	250 rpm
Friction Radius	5 mm
Material of adhesive pin (ball)	Steel
Dimension of abradant ball	6 mm

The sample wear trace is given at Figure 4 and the calculation of the wear volume of worn surface was made according to formula (1). Here; V: wear volume, R friction radius, D: wear trace width (distance between two red lines), r: adhesive ball radius

$$V=\frac{\pi*R*D^3}{6*r} \quad (1)$$

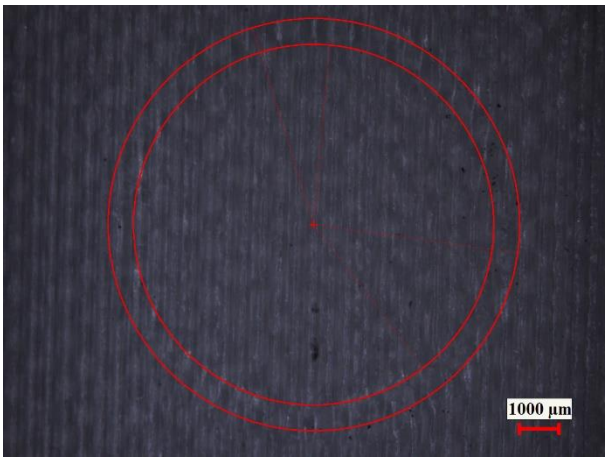

Figure 4. The sample wear trace

3. Results and Discussion

3.3.1. Three Point Bending Test

Three-point bending test results are given at Figure 5. Bending tests results show us that the addition of $CaCO_3$ particles in PP has a significantly negative effect on mechanical properties like bending strength of PP polymer. When Figure 5a is examined, it is seen that the strength of the composite samples is lower than pure PP and the increase of filling rate decreases the bending strength. The strength value of the 4 wt% particle reinforced composite decreased by approximately 50% compared to the pure PP. This situation could be explained by creating discontinuities in the sample due to the large size of the $CaCO_3$ particle. On the other hand, as it can be seen in Figure 1 surface of $CaCO_3$ is not very rough so the particle/matrix interface adhesion remains weak. As a result of this weakness particle reinforcement shows negative effect instead of positive effect. The decrease in strength with the increasing reinforcement ratio can be explained by agglomeration [20,21].

Although $CaCO_3$ is a rigid particle, even the modulus decreased with $CaCO_3$ particle reinforcement. Increasement of particle rate decreased the flexural modules of PP material. Finally flexural modules of the 4 wt% filled composite sample were approximately 46% worse than pure PP polymer. These results indicates that, particle matrix adhesion could not occur. In other words, it can be explained that the load on the matrix cannot be transferred to the particle, even the particles create discontinuity in the matrix and reduce the strength.

Considering the unit costs, PP polymer is 10 times more expensive than $CaCO_3$ particle. For this reason, if the decrease in mechanical strength is tolerable degree, it is possible to obtain a cheaper product with $CaCO_3$ addition.

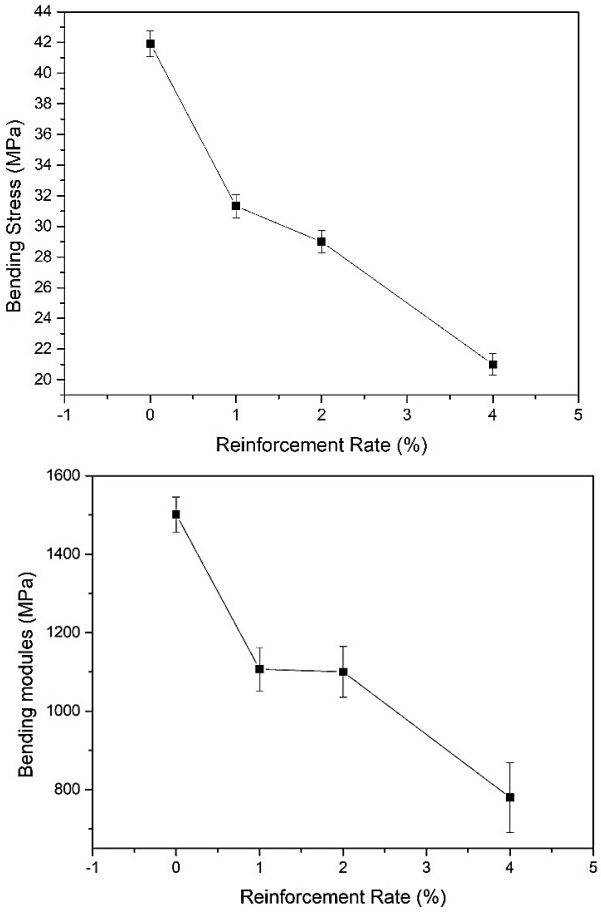

Figure 5. 3-point bending test results

3.3.2. Wear Test

Figure 6 shows the coefficient of friction values of pure PP and composite samples. While Figure 6a shows the coefficient of friction value of samples during sliding distance, Figure 6b shows the average coefficient of friction value of samples. 4 wt% $CaCO_3$ reinforced samples showed approximately 28% lower average coefficient of friction value compared to pure PP. It is clearly seen in the two graphs that the coefficient of friction value decreased by increasing the particle reinforcement rate. This situation could be explained by the reinforcement particles acting as a lubricant between the matrix and the abrasive tip.

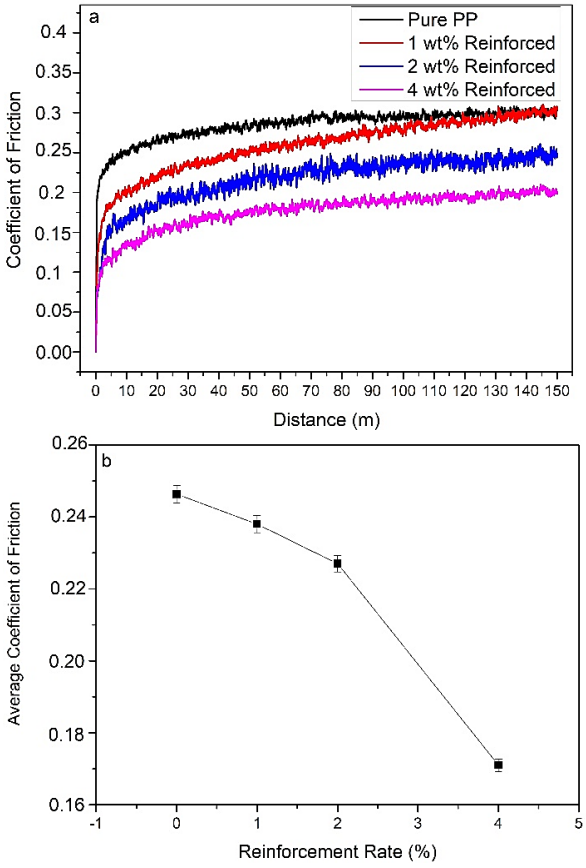

Figure 6. Coefficient of friction values a) during the wear test, b) average value

The wear volume results from the sliding wear test are given in Figure 7 and it is clearly seen that the wear volume decreases with particle reinforcement. In other words, the wear resistance of the samples increased with particle reinforcement. The wear resistance of PP improved about 40% by particle reinforcement. This situation could be explained by the rigid and hard structure of the $CaCO_3$ particles, which prevents the abradant ball from penetrating into the sample. Wear volume results were also supported by the coefficient of friction results [21].

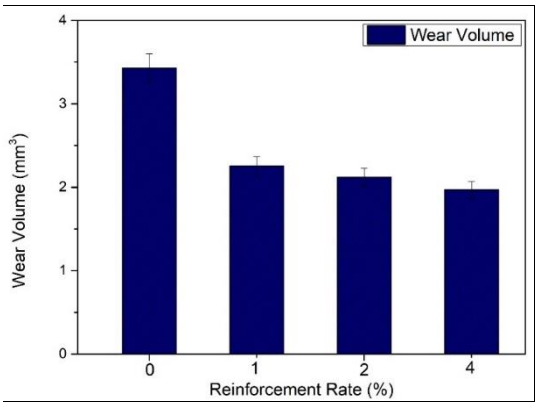

Figure 7. Wear volume results of worn samples

4. Conclusion and Suggestions

- It is demonstrated that $CaCO_3$ filled PP composite filament can be produced with this study.
- It is clearly seen that while $CaCO_3$ filling had negative effect on mechanical properties on PP, it positively affected the wear resistance. This shows that composite specimens can be used in applications that do not pose a problem in compromising mechanical strength to a certain extent but require low friction and wear resistance.
- When we compare the unit prices of polymer and reinforcement particles, PP polymer is 10 times more expensive than $CaCO_3$ particle. For this reason, the cost of the final product will be much more economical by $CaCO_3$ addition.
- The test results show that the particle-matrix interface adhesion is insufficient. For this reason, it has been seen that a compatibilizer should be used in future studies.

Acknowledgment

I would like to thank Dr. Özgür Kaplan and Mr. Beysim Çetin for their assistance during the filament production phase. Thanks to Kocaeli University for its support to the project.

Contributions of the Authors

All parts of manuscript were written by Assist. Prof. Alp Eren ŞAHİN

Conflict of Interest Statement

There is no conflict of interest between the authors.

Statement of Research and Publication Ethics

The study is complied with research and publication ethics

References

[1] K. Bulanda, M. Oleksy, R. Oliwa, G. Budzik, L. Przeszlowski, and A. Mazurkow, "Biodegradable polymer composites used in rapid prototyping technology by Melt Extrusion Polymers (MEP)," *Polimery*, vol. 65, no. 06, pp. 430–436, 2020.

[2] H. I. Medellin-Castillo and J. Zaragoza-Siqueiros, "Design and manufacturing strategies for fused deposition modelling in additive manufacturing: A review," *Chin. J. Mech. Eng.*, vol. 32, no. 1, 2019.

[3] E. Baran and H. Erbil, "Surface modification of 3D printed PLA objects by Fused Deposition Modeling: A review," *Colloids interfaces*, vol. 3, no. 2, p. 43, 2019.

[4] A. Valerga, M. Batista, J. Salguero, and F. Girot, "Influence of PLA filament conditions on characteristics of FDM parts," *Materials (Basel)*, vol. 11, no. 8, p. 1322, 2018.

[5] G. Alaimo, S. Marconi, L. Costato, F. Auricchio, "Influence of meso-structure and chemical composition on FDM 3D-printed parts". *Composites Part B*, vol.113, p. 371–380, 2017

[6] D. T. Pham and R. S. Gault, "A comparison of rapid prototyping technologies," *Int. J. Mach. Tools Manuf.*, vol. 38, no. 10–11, pp. 1257–1287, 1998.

[7] L. Paralı, A. Sarı, M. Esen, "Design of a 3D Printed Open Source Humanoid Robot," Bitlis Eren Üniversitesi Fen Bilimleri Dergisi, vol. 11 no. 2, pp. 411-420, 2022.

[8] C. S. Lee, S. G. Kim, H. J. Kim, and S. H. Ahn, "Measurement of anisotropic compressive strength of rapid prototyping parts," *J. Mater. Process. Technol.*, vol. 187–188, pp. 627–630, 2007.

[9] S. Kumar and J.-P. Kruth, "Composites by rapid prototyping technology," *Mater. Eng.*, vol. 31, no. 2, pp. 850–856, 2010.

[10] M. Seyedzavvar, C. Boğa, "A study on the effects of internal architecture on the mechanical properties and mixed-mode fracture behavior of 3D printed CaCO3/ABS nanocomposite samples." *Rapid Prototyping Journal*, 2022. DOI: 10.1108/RPJ-09-2021-0244

[11] F. P. L. Mantia, M. Morreale, R. Scaffaro, and S. Tulone, "Rheological and mechanical behavior of LDPE/calcium carbonate nanocomposites and microcomposites," *J. Appl. Polym. Sci.*, vol. 127, no. 4, pp. 2544–2552, 2013.

[12] W. Gao, X. Ma, Y. Liu, Z. Wang, and Y. Zhu, "Effect of calcium carbonate on PET physical properties and thermal stability," *Powder Technol.*, vol. 244, pp. 45–51, 2013.

[13] J.-Z. Liang, D.-R. Duan, C.-Y. Tang, C.-P. Tsui, and D.-Z. Chen, "Tensile properties of PLLA/PCL composites filled with nanometer calcium carbonate," *Polym. Test.*, vol. 32, no. 3, pp. 617–621, 2013.

[14] B. S. Tuen, A. Hassan, and A. Abu Bakar, "Thermal properties and processability of talc- and calcium carbonate-filled poly(vinyl chloride) hybrid composites," *J. Vinyl Addit. Technol.*, vol. 18, no. 2, pp. 87–94, 2012.

[15] H. Mao, B. He, W. Guo, L. Hua, Q. Yang, "Effects of Nano-CaCO3 content on the crystallization, mechanical properties, and cell structure of PP nanocomposites in microcellular injection molding". *Polymers.* Vol.10 no. 10, p 1160, 2018.

[16] L. Moyo, S. S. Ray, W. Sebati, and V. Ojijo, "The influence of filler surface modification on mechanical and material properties of layered double hydroxide-containing polypropylene composites," *J. Appl. Polym. Sci.*, vol. 134, no. 27, p. 45024, 2017.

[17] D. Y. Kim, G. H. Kim, D. Y. Lee, and K. H. Seo, "Effects of compatibility on foaming behavior of polypropylene/polyolefin elastomer blends prepared using a chemical blowing agent: ARTICLE," *J. Appl. Polym. Sci.*, vol. 134, no. 33, p. 45201, 2017.

[18] Y. Lin, Y. Liu, D. Zhang, and G. Wu, "Radiation resistance of polypropylene composites by incorporating reduced graphene oxide and antioxidant: A comparison study," *Compos. Sci. Technol.*, vol. 146, pp. 83–90, 2017.

[19] J. A. Mohandesi, A. Refahi, E. S. Meresht, S. Berenji, "Effect of temperature and particle weight fraction on mechanica and micromechanical properties of sand-polyethylene terephthalate composites: A laboratory and discrete element method study", *Composites,* vol. 42, pp. 1461-1467, 2011.

[20] Y. W. Leong,M. B. Abu Bakar,Z. A. Mohd. Ishak,A. Ariffin,B. Pukanszky, "Comparison of the mechanical properties and interfacial interactions between talc, kaolin, and calcium carbonate filled polypropylene composites", Journal of Applied Polymer Science, vol. 91, no. 5 , pp. 3315-3326, 2004.

[21] A.E. Sahin, T. Sinmazcelik, "Olivine particle reinforced polyphenylene sulfide matrix composites", Acta Physica Polonica A, Vol. 131, 481-483, 2017.

Bitlis Eren Üniversitesi Fen Bilimleri Dergisi
BİTLİS EREN UNIVERSITY JOURNAL OF SCIENCE
ISSN: 2147-3129/e-ISSN: 2147-3188
VOLUME: 12 NO: 1 PAGE: 57-65 YEAR: 2023
DOI:10.17798/bitlisfen.1190134

Deep Transfer Learning to Classify Mass and Calcification Pathologies from Screen Film Mammograms

Volkan Müjdat TİRYAKİ[1*]

[1]*School of Engineering, Department of Computer Engineering, C-107, Siirt University, Kezer Campus, 56100 Türkiye*
(ORCID: 0000-0003-1824-5260)

Keywords: Breast cancer, image classification, nodule, tumor, computer-aided diagnosis.

The number of breast cancer diagnoses is the largest among all cancers among women in the world. Breast cancer treatment is possible if it is diagnosed in the early stages. Mammography is a common imaging technique to detect breast cancer abnormalities. Breast cancer symptom screening is being performed by radiologists. In the last decade, deep learning was successfully applied to big image classification databases such as the ImageNet. In this study, the breast cancer pathology classification performances of the recent deep learning models were investigated by transfer learning and fine tuning. A total of 3,360 mammogram patches were used from the Digital Database for Screening Mammography (DDSM) and the Curated Breast Imaging Subset of DDSM (CBIS-DDSM) mammogram databases for deep learning model training, validating, and testing. Transfer learning and fine tuning were applied using Resnet50, Xception, NASNet, and EfficientNet-B7 network weights. The best classification performance was achieved by transfer learning from the Xception network. The computational costs of deep learning models were considered while selecting the best one. On the original CBIS-DDSM five-way test mammogram classification problem, the mean sensitivity, specificity, F1-score, and AUC were 0.7054, 0.9264, 0.7024, and 0.9317, respectively. The results show that the proposed models may be useful for the classification of breast cancer pathologies.

1. Introduction

Since the 1970s, researchers have been studying clinical decision support systems [1]–[3]. Breast cancer is the most frequently diagnosed cancer among women, and the incidence of the disease has been increasing in recent years [4]. If breast cancer is detected early, treatment is possible [5]. Mammography is obtained by exposing breasts to low-energy X-rays [6] in order to detect breast cancer abnormalities early [7].

The mammogram interpretation is a multi-step process that is still being performed by radiologists. Mammography screening is advised for women older than 50 years [8], [9]. In Türkiye, there were 11.15 M women at this age interval in 2021, which indicates the need for the number of breast cancer screenings per year [10]. An automated high-performance mammogram screening system could reduce the workload of radiologists and the number of unnecessary screenings and biopsies. The first computer-aided mammogram interpretation model was proposed by Ackerman and Gose in 1972 [11], wherein the researchers designed a feature extraction followed by a nearest neighbor breast lesion classification system. Automatic detection of a tumor tissue from mammography is related to texture analysis, and many different approaches have been investigated to date by new textural feature definitions and classifier models [12], such as the spherical wavelet transform [13] and geometric and textural feature extraction [14]. Computer-aided breast cancer research has also been conducted by other imaging modalities, such as microwave applications [15]. Despite these and other successful results in the literature, feature extraction–based machine learning methods can be time-consuming, particularly for medical image- or video-based

*Corresponding author: tiryakiv@siirt.edu.tr
Received: 17.10.2022, Accepted: 01.03.2023

analysis. Deep learning methods enable learning features from training data, and there are example studies in the literature related to stroke [16], carotid artery [17], [18], skin cancer [19], diabetes [20], Alzheimer's disease [21], and breast cancer [22]. Deep learning methods should be useful for the solution of problems related to other biomedical imaging modalities, so cross-disciplinary studies could possibly lead to new scientific advancements.

Regarding the applications of deep learning for breast cancer research, convolutional neural networks (CNN) were used for benign versus malignant breast mass classification [23]. In another study based on more than one million mammograms, the breast cancer screening performance of radiologists was shown to be improved when CNN-based diagnosis was used together with radiologists [24]. An end-to-end mammogram classifier based on a five-class mammogram patch classification like the one in the present study was investigated using Resnet50 and VGG16 [25]. Mass detection and classification have been performed by Momminet-V2 using multi-view mammograms [26]. The computational cost of deep learning model training is becoming a concern, and recently breast cancer mass pathology was classified by implementing pre-trained deep neural networks without transfer learning [27]. NASNet is a high performing CNN for image classification on the ImageNet [28], [29]. Recently, EfficientNets were proposed by considering the computational expense and the classification performance together [30]. Among EfficientNets, the EfficientNet-B7 is the best performing CNN model on the ImageNet.

In this study, transfer learning and fine tuning of recently proposed pre-trained deep neural networks, including Resnet50 [31], Xception [32], NASNetMobile [28], NASNetLarge [28], and EfficientNet-B7 [30] were investigated for the classification of normal, benign, and malignant masses, and benign and malignant calcification patches. These CNN models are among the best performing ones on ImageNet and the successful implementations of these networks for the breast cancer pathology classification problem are demonstrated in the present study. The Digital Database for Screening Mammography (DDSM) and the Curated Breast Imaging Subset of DDSM (CBIS-DDSM) datasets were used for deep learning model training [33]–[35]. This study is organized as follows: Section 2 includes materials and methods that describe the mammogram dataset, preprocessing, deep learning model training, and performance evaluation. Experimental results and discussion are presented in section 3, and conclusions and suggestions are given in section 4.

2. Material and Method

Significant amounts of data are necessary for deep learning model training. This study was conducted using publicly available datasets.

2.1. Dataset and preprocessing

The CBIS-DDSM and DDSM mammograms were selected as data sources since these are large and publicly available mammogram databases. The CBIS-DDSM database includes mammogram patches with the abnormality and pathology information in the form of mass versus calcification and benign versus malignant. The mammogram patches were resampled to 331×331 and saved as 8-bit gray level images. The normal tissue patches were randomly selected from the DDSM dataset craniocaudal (CC) views of mammogram regions which does not include any abnormalities [36], [37]. Breast cancer abnormalities have a great variety of shape, texture, and intensity, and two representative training patches from each class are given in Figure 1.

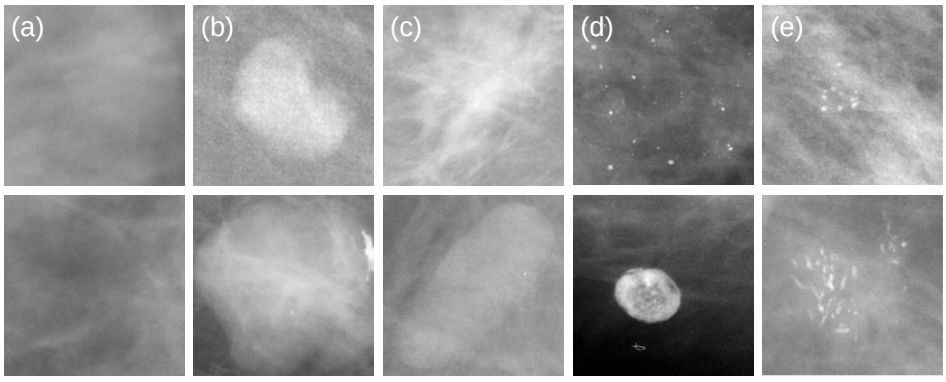

Figure 1. Two representative training patches belong to normal (a), benign mass (b), malignant mass (c), benign calcification (d), and malignant calcification (e).

Mammogram patches were classified into normal, benign mass, malignant mass, benign calcification, and malignant calcification. Patches that have a "benign without callback" annotation were considered "benign." Normal patches that do not include any breast cancer abnormalities were selected from the DDSM dataset because the CBIS-DDSM includes mammograms with abnormalities. Normal patches were extracted from the middle of the mammogram so that they do not include background pixels. Test mammograms defined in the CBIS-DDSM database were used as test data in the present study, and none of them were used for training or validating. The dataset was balanced by deleting excess files. Randomly selected 20% of the CBIS-DDSM training images were used as validation and rest of the mammograms were used for training. The percentages of the number of training, validation, and test patches were 65%, 16%, and 19%, respectively. The number of training, validation, and test patches is given in Table 1.

Table 1. The number of training, validating, and test patches in the dataset.

Folder	Normal	Benign mass	Malignant mass	Benign calcification	Malignant calcification	Total
Train	434	434	434	434	434	2170
Validation	109	109	109	109	109	545
Test	129	129	129	129	129	645
Total	672	672	672	672	672	3360

2.2. Hardware configuration

Deep learning models were trained on a workstation computer that has an NVIDIA RTX 3060 GPU, double Xeon E5-2630 2.6 GHz CPU, and a 16 GB RAM.

2.3. Deep transfer learning and fine tuning

Deep transfer learning classification models were implemented since they are known to reduce the training time, reduce the requirements for the amount of training data, and improve the performance [25], [38]. Data augmentation was applied to the patches by setting the width shift, height shift, zoom, and shear ranges to 0.2, rotation range to 90°, and enabling the vertical and horizontal random flips. The brightness range was not used since intensity is a feature that is used by radiologists for mass and calcification detection. Deep learning models were implemented by importing the weights of Resnet50, Xception, NASNetMobile, NASNetLarge, and EfficientNet-B7 [28] networks, which have 138 M, 23 M, 5 M, 88,9 M, and 66 M parameters, respectively. The models were named as backbone followed by TL (transfer learning). Adam optimizer was used [39]. Transfer learning and fine tuning were implemented by using the three-step approach described in Shen *et al.* [25]. First, all of the layers except the final layer were frozen, and the model was trained for three epochs with a 10^{-3} learning rate. Second, 33% of layers from the end were unfrozen and the model was trained for ten epochs with a 10^{-4} learning rate. Third, all layers were unfrozen and trained with a learning rate of 10^{-5} until one of the stopping criteria was met. Early stopping criteria were: (1) the maximum number of epochs was 150, and (2) the maximum number of consecutive epochs when the loss function did not decrease was ten. (3) The minimum learning rate was 10^{-8}. The transfer learning and fine tuning codes are accessible at https://github.com/tiryakiv/breast-cancer-pathology-classification.

2.4. Performance evaluation

Patch classification accuracy, sensitivity, specificity, and F-measure were defined as:

$$Accuracy = \frac{TP+TN}{TP+TN+FP+FN} \quad (1)$$

$$Sensitivity = \frac{TP}{TP+FN} \quad (2)$$

$$Specificity = \frac{TN}{TN+FP} \quad (3)$$

$$F-measure = \frac{2TP}{2TP+FP+FN} \quad (4)$$

where TP, TN, FP, and FN are abbreviations for true positive, true negative, false positive, and false negative, respectively. Sensitivity, specificity, and F-measure of each class were calculated. The area under the receiver operating curve (AUC) was analyzed, and a confusion matrix was constructed to evaluate the classification performance [40]. Accuracy, specificity, sensitivity, and F-measure show the classification performance, but they depend on the threshold level. Sensitivity shows the ratio of

correctly selected relevant items, and specificity shows the ratio of negatively selected elements to the true negative elements. AUC shows the overall performance of the binary classifier by considering all possible thresholds. In the present study, a one-versus-rest classifier was implemented for AUC calculations.

3. Results and Discussion

The classification results of normal, benign, and malignant masses, and benign and malignant calcification patches using ResNet50, Xception, NASNetMobile, NASNetLarge, and EfficientNet-B7 transfer learning methods on the validation data are shown in Table 2.

Table 2. The breast cancer pathology classification results on the validation data.

TL backbone	Accuracy	AUC	Train time
Resnet50	0.7321	0.9392	37 min
Xception	0.7193	**0.9407**	**29 min**
NASNetMobile	0.6807	0.9183	47 min
NASNetLarge	**0.7376**	0.9357	114 min
EfficientNet-B7	0.7156	**0.9407**	259 min

The Xception and EfficientNet-B7 TL models had the highest AUC, and the NASNetLarge TL model had the highest accuracy on the validation data. To compare the performances of all models, the confusion matrices on the validation data are given in Table 3.

Table 3. Breast cancer pathology classification confusion matrix on validation data. BC, MC, BM, MM, and N are abbreviations for benign calcification, malignant calcification, benign mass, malignant mass, and normal patches, respectively. TL: transfer learning. The highest *TP* for each class is given in bold.

Radiologist	Resnet50 TL predictions					Xception TL predictions					NASNetMobile TL predictions				
	BC	MC	BM	MM	N	BC	MC	BM	MM	N	BC	MC	BM	MM	N
BC	77	29	1	2	0	77	22	2	7	1	58	24	5	15	7
MC	14	74	0	21	0	17	68	6	18	0	4	65	10	28	2
BM	3	2	48	56	0	3	1	52	52	1	1	3	41	56	8
MM	2	4	7	96	0	3	3	13	90	0	1	1	8	**99**	0
N	0	1	2	2	104	2	0	1	1	105	0	0	0	1	**108**

Radiologist	NASNetLarge TL predictions					EfficientNet-B7 TL predictions				
	BC	MC	BM	MM	N	BC	MC	BM	MM	N
BC	**79**	22	2	4	2	65	39	1	3	1
MC	22	62	4	20	1	5	**85**	2	16	1
BM	2	0	**58**	46	3	0	2	48	56	3
MM	0	0	10	**99**	0	2	7	14	86	0
N	2	0	0	3	104	0	0	0	3	106

The confusion matrices in Table 3 showed that all models performed well in discriminating the normal patches. The highest misclassification rates were observed for the benign mass patches. *TP*s of the NASNet TL malignant mass were equal. EfficientNet-B7 TL model had the highest *TP* for malignant calcification patches. Based on overall accuracy and confusion matrices, the best breast pathology classification model was selected as NASNetLarge TL because it has the highest accuracy and the three *TP*s of the model were the highest among all of the models.

3.1. Test results

The performance of the NASNetLarge TL model trained by the breast cancer pathology patches was evaluated. The AUC and accuracy on the test data were 0.9404 and 0.7318 respectively. The performance difference between the validation and test data was close. To analyze the classification errors, the NASNetLarge TL model confusion matrix on the test data is given in Table 4.

Table 4. Breast cancer pathology classification confusion matrix on the test data

Radiologist	BC	76	33	8	10	2
	MC	35	84	0	9	1
	BM	6	2	88	29	4
	MM	4	3	26	95	1
	N	0	0	0	0	129
		BC	MC	BM	MM	N
		NASNetLarge TL predictions				

The confusion matrix in Table 4 showed that the malignant calcification patch misclassification probability as benign calcification was the highest. The misclassification probability of benign calcifications as malignant calcifications and benign masses as malignant masses was high. These results showed that the model has better discrimination for abnormality types than the pathology type. The patch classification performance of mass was better than calcification. The NASNetLarge TL model's sensitivity, specificity, and F-measure for each class are listed in Table 5.

The test results in Table 5 showed that the highest and lowest sensitivity were obtained on normal and benign calcification patches, respectively. Among the abnormalities, including patches, the highest specificity was obtained for malignant masses and the lowest specificity was obtained for benign calcification. The multi-class receiver operating characteristic (ROC) analysis of the NASNetLarge TL model is given in Figure 2.

Table 5. NASNetLarge TL model classification performance on the test patches. The best result for each metric is shown in bold.

Class	Sensitivity	Specificity	F-measure
Benign calcification	0.6281	0.8989	0.6080
Malign calcification	0.6885	0.9140	0.6693
Benign mass	0.7213	0.9216	0.7012
Malign mass	0.6643	0.9323	0.6985
Normal	**0.9416**	**1.0000**	**0.9699**

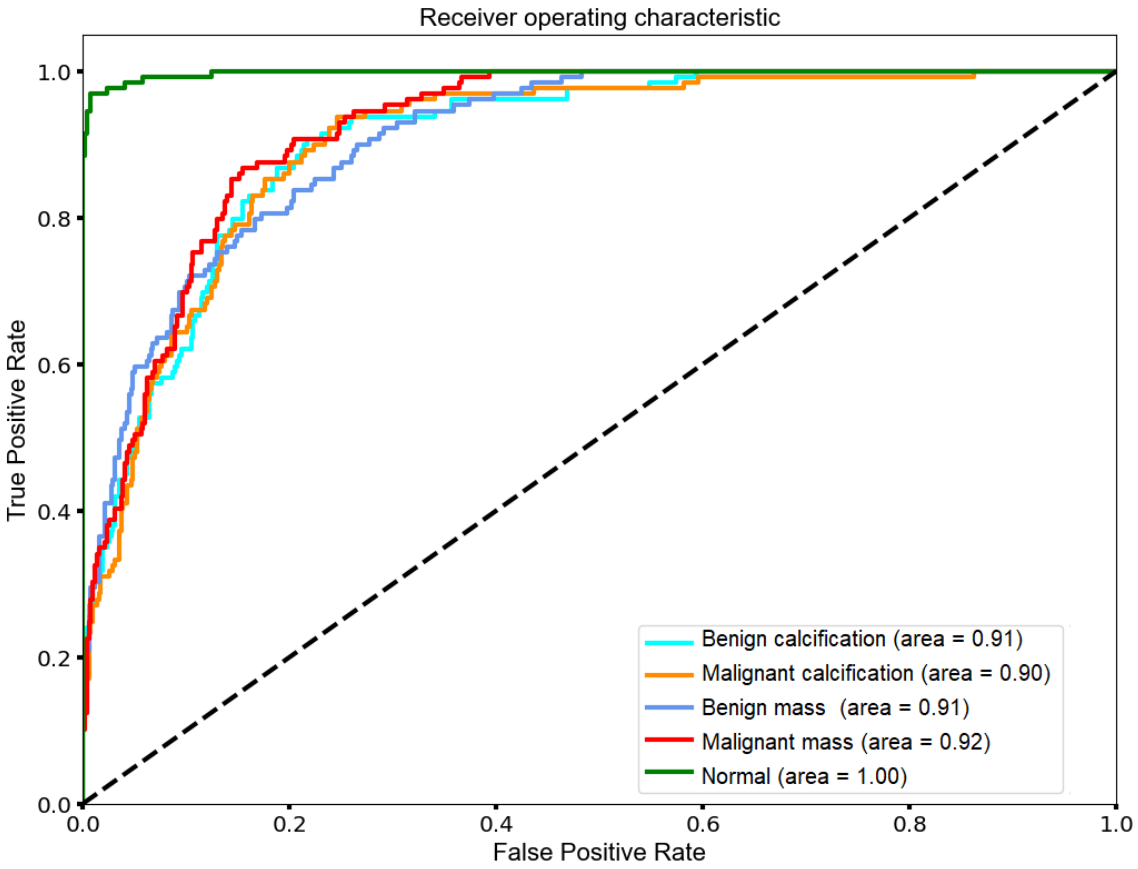

Figure 2. ROC analysis of a five-way breast cancer pathology classification. (One versus rest classifier)

Figure 2 showed that the mass abnormality classification performed better than the calcification abnormality classification. The performance of discriminating the malignant calcification patches was lower than benign calcification, on the other hand, the performance of discriminating the malignant mass was higher than benign mass. As expected, AUC of normal patches was better than the abnormality including patches. Computer-aided breast cancer diagnosis research involves a number of types of problems. Some studies in the literature focus on mass detection and classification [41], [42], and others focus on calcification detection and classification [43], [44]. A five-way classification of breast cancer abnormalities and the malignant behavior of tissues from mammograms were investigated in the present study. The closest work in the literature to the present one is Shen *et al.* [25], wherein the researchers used 2,478 CBIS-DDSM patches and achieved an accuracy of 0.99 on the test data when they applied the ResNet50 transfer learning method. The performance difference with the present study may be because of: 1) the difference in the number of patches (3,360 patches were used in the present study); 2) training, validating, and test data included DDSM normal mammograms in the present study; and 3) original CBIS-DDSM test images were used in the present study. The other study that is related to the present one is Hekal *et al.*, where the researchers investigated the four-way classification performance of benign calcification, malignant calcification, benign mass, and malignant mass [45]. They achieved an accuracy of 0.91 using AlexNet by training with 2800 CBIS-DDSM mammograms. The relatively higher accuracy than the present study can be explained by the lower number of classes (n=4) and the performance evaluation on the validation data. The five-way classification of breast cancer pathology patches similar to the present work was investigated by Chun-ming *et al.* [46]. They achieved an accuracy of 0.91 using the Deep Cooperation CNN model on the CBIS-DDSM dataset. Their model performance is higher than the present study, possibly because they used a smaller test dataset (%10) and their dataset was randomly distributed. In the present study, the classification performance of state-of-the-art transfer learning methods was demonstrated on the original CBIS-DDSM test dataset.

4. Conclusion and Suggestions

Transfer learning and fine tuning pre-trained deep neural networks have great potential for the classification of breast cancer abnormalities and pathologies. Pre-trained deep neural networks reduce the computational cost and yield high performance when they are used for different classification domains. In this study, successful transfer learning applications have been shown using the recent deep neural networks trained with the ImageNet. By applying transfer learning and fine tuning, the useful features learned from the ImageNet database were adopted for the current breast pathology classification problem. The best classification performance has been obtained by using the NASNetLarge network, which resulted in a 0.9404 AUC and 0.7318 accuracy. The NASNetLarge network can be used for the breast cancer pathology classification at the reported performance. The proposed model may be useful for detecting breast cancer abnormalities and classifying them as malignant versus benign.

The performance ranking of CNNs on the ImageNet was not the same for the breast cancer pathology classification models. This could be due to the contextual difference between the ImageNet images and the mammograms. The sensitivity of benign mass and benign calcification showed that further performance improvement can be investigated. Novel machine learning techniques and deep ensemble models will be investigated in the future to increase the system performance. The CBIS-DDSM and other databases have lesions that sometimes have mass and calcification abnormalities overlap. The classification of such tumors with double abnormalities will be investigated in the future.

Acknowledgments

The author thanks the Siirt University Scientific Research Projects Directorate for providing the NVIDIA GeForce RTX 3060 GPU under Grant No. 2021-SİÜMÜH-01. The author thanks the owners of the DDSM and CBIS-DDSM for publicly sharing the datasets for research.

Statement of Research and Publication Ethics

The study is complied with research and publication ethics.

References

[1] H. L. Bleich, "The computer as a consultant," *N. Engl. J. Med.*, vol. 284, no. 3, pp. 141–7, 1971.

[2] M. E. Cohen and D. Le Hudson, "A hybrid system for diagnosis involving biosignals," *Proc. 2005 IEEE Int. Conf. Comput. Intell. Meas. Syst. Appl. CIMSA 2005*, vol. 2005, no. July, pp. 312–315, 2005.

[3] I. Gökbay, S. Karaman, S. Yarman, and B. Yarman, "An intelligent decision support tool for early diagnosis of functional pituitary adenomas," *TWMS J. Appl. Eng. Math.*, vol. 5, no. 2, p. 169, 2015.

[4] V. Ozmen, "Breast Cancer in Turkey: Clinical and Histopathological Characteristics (Analysis of 13.240 Patients)," *J. Breast Heal.*, vol. 10, no. 2, pp. 98–105, 2014.

[5] S. W. Duffy *et al.*, "Mammography screening reduces rates of advanced and fatal breast cancers: Results in 549,091 women," *Cancer*, vol. 126, no. 13, pp. 2971–2979, 2020.

[6] P. Xi, C. Shu, and R. Goubran, "Abnormality Detection in Mammography using Deep Convolutional Neural Networks," in *2018 IEEE International Symposium on Medical Measurements and Applications, Proceedings*, 2018, pp. 1–6.

[7] J. Tang, R. M. Rangayyan, J. Xu, I. E. El Naqa, and Y. Yang, "Computer-aided detection and diagnosis of breast cancer with mammography: Recent advances," *IEEE Trans. Inf. Technol. Biomed.*, vol. 13, no. 2, pp. 236–251, 2009.

[8] "What Is Breast Cancer Screening?," *Center for disease control and prevention*, 2022. [Online]. Available: https://www.cdc.gov/cancer/breast/basic_info/screening.htm#:~:text=Breast Cancer Screening Recommendations&text=The USPSTF recommends that women,often to get a mammogram.

[9] L. Tabar *et al.*, "Efficacy of breast cancer screening by age. New results swedish two-county trial," *Cancer*, vol. 75, no. 10, pp. 2507–2517, 1995.

[10] TÜİK, "İstatistiklerle Kadın, 2021," *TÜİK veri portalı*, 2022. [Online]. Available: https://data.tuik.gov.tr/Bulten/Index?p=Istatistiklerle-Kadin-2021-45635. [Accessed: 06-Dec-2022].

[11] L. Ackerman and E. Gose, "Breast lesion classification by computer and xeroradiograph," *Cancer*, vol. 30, no. 4, pp. 1025–1035, 1972.

[12] Y. Kaya, "A new intelligent classifier for breast cancer diagnosis based on a rough set and extreme learning machine: Rs + elm," *Turkish J. Electr. Eng. Comput. Sci.*, vol. 21, no. SUPPL. 1, pp. 2079–2091, 2013.

[13] P. Görgel, A. Sertbas, and O. N. Uçan, "Computer-aided classification of breast masses in mammogram images based on spherical wavelet transform and support vector machines," *Expert Syst.*, vol. 32, no. 1, pp. 155–164, 2015.

[14] H. Singh, V. Sharma, and D. Singh, "Machine learning based computer aided diagnosis system for classification of breast masses in mammograms," *J. Phys. Conf. Ser.*, vol. 2267, no. 1, 2022.

[15] E. Onemli *et al.*, "Classification of rat mammary carcinoma with large scale in vivo microwave measurements," *Sci. Rep.*, vol. 12, no. 1, pp. 1–11, 2022.

[16] R. A. J. Alhatemi and S. Savaş, "Journal of Computer Science," *J. Comput. Sci.*, vol. IDAP-2022, pp. 192–201, 2022.

[17] S. Savaş, N. Topaloğlu, Ö. Kazcı, and P. N. Koşar, "Comparison of Deep Learning Models in Carotid Artery Intima-Media Thickness Ultrasound Images : CAIMTUSNet," *Bilişim Teknol. Derg.*, vol. 15, no. 1, pp. 1–12, 2022.

[18] S. Savaş, N. Topaloğlu, Ö. Kazcı, and P. N. Koşar, "Performance Comparison of Carotid Artery Intima Media Thickness Classification by Deep Learning Methods," in *International Congress on Human-Computer Interaction, Optimization and Robotic Applications*, 2019, pp. 125–131.

[19] D. K. A. Al-saedi and S. Savaş, "Journal of Computer Science," *J. Comput. Sci.*, vol. IDAP-2022, pp. 202–210, 2022.

[20] S. Buyrukoglu and A. Akbas, "Machine Learning based Early Prediction of Type 2 Diabetes : A New Hybrid Feature Selection Approach using Correlation Matrix with Heatmap and SFS," *Balk. J. Electr. Comput. Eng.*, vol. 10, no. 2, pp. 110–117, 2022.

[21] S. Buyrukoğlu, "Improvement of Machine Learning Models' Performances based on Ensemble Learning for the detection of Alzheimer Disease," in *2021 6th International Conference on Computer Science and Engineering (UBMK)*, 2021, pp. 102–106.

[22] A. Hamidinekoo, E. Denton, and R. Zwiggelaar, "Automated Mammogram Analysis with a Deep

Learning Pipeline," pp. 1–5, 2019.
[23] A. Jain and D. Levy, "Breast Mass Classification from Mammograms using Deep Convolutional Neural Networks," *arXiv Prepr. arXiv1612.00542*, 2016.
[24] N. Wu *et al.*, "Deep Neural Networks Improve Radiologists' Performance in Breast Cancer Screening," *IEEE Trans. Med. Imaging*, vol. 39, no. 4, pp. 1184–1194, 2020.
[25] L. Shen, L. R. Margoiles, J. H. Rothstein, E. Fluder, R. McBride, and W. Sieh, "Deep Learning to improve Breast cancer Detection on Screening Mammography," *Sci. Rep.*, vol. 9, no. 12495, pp. 1–12, 2019.
[26] Z. Yang *et al.*, "MommiNet-v2: Mammographic multi-view mass identification networks," *Med. Image Anal.*, vol. 73, p. 102204, 2021.
[27] E. Al-Mansour, M. Hussain, H. A. Aboalsamh, and Fazal-e-Amin, "An Efficient Method for Breast Mass Classification Using Pre-Trained Deep Convolutional Networks," *Mathematics*, vol. 10, no. 14, pp. 1–19, 2022.
[28] B. Zoph, V. Vasudevan, J. Shlens, and Q. V. Le, "Learning Transferable Architectures for Scalable Image Recognition," *Proc. IEEE Comput. Soc. Conf. Comput. Vis. Pattern Recognit.*, pp. 8697–8710, 2018.
[29] Jia Deng, Wei Dong, R. Socher, Li-Jia Li, Kai Li, and Li Fei-Fei, "ImageNet: A large-scale hierarchical image database," in *2009 IEEE Conference on Computer Vision and Pattern Recognition*, 2009, pp. 248–255.
[30] M. Tan and Q. V. Le, "EfficientNet: Rethinking model scaling for convolutional neural networks," *36th Int. Conf. Mach. Learn. ICML 2019*, vol. 2019-June, pp. 10691–10700, 2019.
[31] K. He, X. Zhang, S. Ren, and J. Sun, "Deep residual learning for image recognition," in *Proceedings of the IEEE Computer Society Conference on Computer Vision and Pattern Recognition*, 2016, vol. 2016-Decem, pp. 770–778.
[32] F. Chollet, "Xception: Deep learning with depthwise separable convolutions," *Proc. - 30th IEEE Conf. Comput. Vis. Pattern Recognition, CVPR 2017*, vol. 2017-January, pp. 1800–1807, 2017.
[33] R. S. Lee, F. Gimenez, A. Hoogi, and D. Rubin, "Curated Breast Imaging Subset of DDSM [Dataset]," 2016. [Online]. Available: https://wiki.cancerimagingarchive.net/display/Public/CBIS-DDSM#22516629cf2ec23796854d91bc86c4ae2e499baa.
[34] R. S. Lee, F. Gimenez, A. Hoogi, K. K. Miyake, M. Gorovoy, and D. L. Rubin, "A curated mammography data set for use in computer-aided detection and diagnosis research," *Sci. Data*, vol. 4, pp. 1–9, 2017.
[35] K. Clark *et al.*, "The Cancer Imaging Archive (TCIA): maintaining and operating a public information repository.," *J. Digit. Imaging*, vol. 26, no. 6, pp. 1045–1057, Dec. 2013.
[36] M. Heath *et al.*, "Current status of the Digital Database for Screening Mammography," in *Proceedings of the Fourth International Workshop on Digital Mammography*, 1998, pp. 457–460.
[37] M. Heath, K. Bowyer, D. Kopans, R. Moore, and W. P. Kegelmeyer, "The Digital Database for Screening Mammography," in *Proceedings of the Fifth International Workshop on Digital Mammography*, 2001, pp. 212–218.
[38] O. Russakovsky *et al.*, "ImageNet Large Scale Visual Recognition Challenge," *Int. J. Comput. Vis.*, vol. 115, no. 3, pp. 211–252, 2015.
[39] D. P. Kingma and J. L. Ba, "Adam: A method for stochastic optimization," *3rd Int. Conf. Learn. Represent. ICLR 2015 - Conf. Track Proc.*, pp. 1–15, 2015.
[40] F. Pedregosa *et al.*, "Scikit-learn: Machine Learning in Python," *J. Mach. Learn. Res.*, vol. 12, pp. 2825–2830, 2011.
[41] D. Abdelhafiz, J. Bi, R. Ammar, C. Yang, and S. Nabavi, "Convolutional neural network for automated mass segmentation in mammography," *BMC Bioinformatics*, vol. 21, no. Dl, pp. 1–16, 2020.
[42] Z. Assari, A. Mahloojifar, and N. Ahmadinejad, "Discrimination of benign and malignant solid breast masses using deep residual learning-based bimodal computer-aided diagnosis system," *Biomed. Signal Process. Control*, vol. 73, no. March 2021, p. 103453, 2022.
[43] R. Zamir *et al.*, "Segmenting microcalcifications in mammograms and its applications," *https://doi.org/10.1117/12.2580398*, vol. 11596, pp. 788–795, Feb. 2021.
[44] R. Hou *et al.*, "Anomaly Detection of Calcifications in Mammography Based on 11,000 Negative Cases," *IEEE Trans. Biomed. Eng.*, vol. 69, no. 5, pp. 1639–1650, 2022.

[45] A. A. Hekal, A. Elnakib, and H. E. Moustafa, "Automated early breast cancer detection and classification system," *Signal, Image Video Process.*, vol. 15, no. 7, pp. 1497–1505, 2021.

[46] T. Chun-ming, C. U. I. Xiao-mei, Y. U. Xiang, and Y. Fan, "Five Classifications of Mammography Images Based on Deep Cooperation Convolutional Neural Network," *Am. Sci. Res. J. Eng. Technol. Sci.*, vol. 57, no. 1, pp. 10–21, 2019.

Bitlis Eren Üniversitesi Fen Bilimleri Dergisi
BİTLİS EREN UNIVERSITY JOURNAL OF SCIENCE
ISSN: 2147-3129/e-ISSN: 2147-3188
VOLUME: 12 NO: 1 PAGE: 66-83 YEAR: 2023
DOI:10.17798/bitlisfen.1191373

Determination of resistance against the transmission of charged particles of Rhenium-Boron (Re-B) based alloys

Murat AYGÜN[1*]

[1]*Bitlis Eren University Faculty of Science and Literature Department of Physics*

(ORCID: 0000-0002-4276-3531)

Keywords: Stopping power, Electron, Heavy charged particle SRIM, ESTAR.

Abstract
In this study, the resistance of the Rhenium-Boron (Re-B) based alloys against the transmission of charged particles such as electrons, protons, alpha particles, carbon, and oxygen was investigated using the stopping power as the defining quantity. For this, the collision, radiative/nuclear, total stopping powers, and projected range of the charged particles in the Re40-B60, Re50-B50, Re58-B42, and Re60-B40 alloys were calculated using the ESTAR, and the Stopping and Range of Ions in Materials (SRIM) Monte Carlo code. It was found that the stopping powers of the heavy charged particles tended to decrease with increasing the rhenium concentration. These results suggest that the boron element is more suitable for heavy charged particle shielding materials compared to the rhenium element.

1. Introduction

Radiation is the emission or transfer of energy in the form of electromagnetic waves or particles and can be classified as ionizing and non-ionizing radiation. In this context, ionizing radiation can be evaluated in three categories: charged particles, photons and neutrons. Electrons (e), protons (p), alpha (α), and heavy ions (A>4) are considered as charged particles. The importance of radiation protection is increasing because the use of radiation emitting devices is very common in fields such as nuclear reactors, medicine, agriculture, and so on [1]. Developing radiation shielding materials and their usage is one method to reduce the radiation exposure risk [2]. Therefore, explaining the interaction of charged particles and matter will be important for radiation protection and a better understanding of radiation with various materials.

It is significant to determine the radiation shielding attitude of a material against charged particles such as electrons, protons, and alpha rays, and elements such as carbon and oxygen. In this context, the stopping power of the charged particles passing through the material is an important shielding parameter [3]. The stopping power is the rate of energy loss per unit path length in the target material [4], and has two cases, such as collisions and radiative/nuclear interactions. The total stopping power can be calculated as the sum of these two states.

Rhenium-based alloys are important materials evaluated in different fields of nuclear technology, such as nuclear fusion and atom probe tomography (APT) system components [5, 6]. For example, ^{186}Re has been applied to clinical radiotherapy applications by Mastren et al. [7]. Klueh et al. [8] have shown that the radiation shielding properties of an example stainless steel have increased with the addition of the Re. Korkut et al. [6] have developed novel high-temperature-resistant materials with different concentrations of Re and B (Re40-B60, Re50-B50, Re58-B42, and Re60-B40) in order to determine the neutron-shielding performances. However, it has been seen that the stopping powers and ranges for charged particles have not been determined for these new and important materials when we have searched the literature. Therefore, we think that eliminating this deficiency will be important.

* Corresponding author: maygun@beu.edu.tr
Received: 20.10.2022, Accepted: 23.02.2023

In this study, we calculate collision, radiative/nuclear and total stopping powers for charged particles such as electron (e), proton (H), alpha (He), carbon (C) and oxygen (O) for Re40-B60, Re50-B50, Re58-B42 and Re60-B40 alloys by using ESTAR provided by the National Institute of Standards and Technology (NIST) [9] and Stopping and Range of Ions in Materials (SRIM)-2013 [10] programs. In addition, we calculate ranges for all alloys and compare all the results with each other.

2. Material and Method

2.1. Stopping Power and Projected Range

The stopping power is the resistance of a material against the charged particles [11]. The stopping power can be evaluated as the sum of electronic (collisional) stopping power and nuclear stopping power. The electronic stopping power states the energy losses due to electronic interactions, while the nuclear stopping power expresses the energy losses based on the elastic collisions between the ion and the nuclei of atoms in the material. The stopping power depends on the magnitude of the radiation mass, charge, and kinetic energy as well as the effective atomic number and atomic density of the interacting medium [11]. In this context, the stopping power formula for heavy charged particles can be written as [12]

$$-\frac{dE}{dx} = 4\pi r_0^2 z^2 \frac{m_0 c^2}{\beta^2} NZ \left[ln\left(\frac{2m_0 c^2}{I}\beta^2\gamma^2\right) - \beta^2 \right] \quad (1)$$

and the stopping power formula for electrons can be given by

$$-\frac{dE}{dx} = 4\pi r_0^2 \frac{m_0 c^2}{\beta^2} NZ \left\{ ln\left(\frac{\beta\gamma\sqrt{\gamma-1}}{I} m_0 c^2\right) + \frac{1}{2\gamma^2}\left[\frac{(\gamma-1)^2}{8} + 1 - (\gamma^2 + 2\gamma - 1)\, ln\, 2\right]\right\} \quad (2)$$

where *dE/dx* is the charged particle stopping power, r_0 is the classical electron radius, *z* is the charge of the incident particle, m_0c^2 is the rest energy of the electron, β is the relative phase velocity of the particle, *N* is the particle density in the material through which the charged particle travels, *Z* is the atomic number of the material and *I* is mean excitation energy. If a compound or mixture of elements is concerned, $\langle I \rangle$ must be calculated according to Bethe theory as follows

$$\langle I \rangle = \exp\left\{ \frac{\left[\sum_j \left(\frac{Z_j}{A_j}\right) \ln I_j\right]}{\sum_j \left(\frac{w_j Z_j}{A_j}\right)} \right\} \quad (3)$$

where w_j, Z_j and A_j are the weight fraction, atomic number, and atomic weight of the *j*th element, respectively [13]. In this study, the collision, nuclear, and total stopping power parameters of the charged particles for Re40-B60, Re50-B50, Re58-B42 and Re60-B40 alloys are calculated. In this respect, the weight compositions and densities of the alloys are given in Table 1.

Table 1. Weight compositions and densities of the alloys [6]

Sample name	Rhenium (%)	Boron (%)	ρ (g/cm^3)
Re40-B60	40	60	9.81
Re50-B50	50	50	11.68
Re58-B42	58	42	13.17
Re60-B40	60	40	13.55

The projected range (R_P) is a significant parameter for determining nuclear radiation shielding and interactions with materials [14]. The R_P is assumed as the distance traveled by the particle within the medium previous to lose all of its energy [15]. The R_P of charged particles can be written as

$$R_P(E) = \int_0^E \frac{1}{\left(-\frac{dE}{dx}\right)} dE \quad (4)$$

where *E* is the charged particle energy (MeV) and *x* is distance of the charged particles travel through a material (in m).

2.2. Computer Programs

The Bethe formula is generally a good approximation for high-energy charged particles (>0.5 MeV) [16,17], although it is not very valid for low-energy

charged particles. On the other hand, the Bethe formula based on Barkas-Andersen [18] and Bloch [19] corrections can be more suitable for the low-energy regime [17].

The SRIM is a computer code containing the stopping and range ions in matter [10]. It can calculate electronic and nuclear stopping powers according to the ion type, its energy, and the target material type. Also, it uses the Köln Core and Bond (CAB) approach to estimate the stopping power in compounds [16]. There are versions such as SRIM-1998, SRIM-2003, SRIM-2006, SRIM-2008, and SRIM-2013 in the literature. In this work, the SRIM-2013 code, which is the latest version, is used to calculate the stopping power values and projected range versus particle energy.

The ESTAR is a computer code that can calculate collision, radiative, total stopping powers, and range of electrons for any element, compound, or mixture at any set of kinetic energies between 1 keV and 10 GeV. The ESTAR code needs to be entered the information such as the atomic composition, density, and excitation energy of the material. In the program, firstly, the analyzed material is determined, and then the desired or default energies are entered [9].

Results and Discussion

The total stopping power for electron interaction can be divided into two parts: collisional stopping power and radiative stopping power. The collision, radiative, and total stopping powers of the electrons for the Re40-B60, Re50-B50, Re58-B42, and Re60-B40 alloys at energies between 0.1 and 1000 MeV were calculated, and shown the variation with energy in Fig. 1. Additionally, to make a comparison, the collision, radiative, and total stopping powers for energies up to 15 MeV were given in Table 2. The total stopping powers of the electrons are among 1.334-71.40 MeV cm^2/g for Re40-B60, 1.298-84.21 MeV cm^2/g for Re50-B50, 1.269-94.47 MeV cm^2/g for Re58-B42 and 1.262–97.03 MeV cm^2/g for Re60-B40. For the electron, the total stopping powers generally decrease to the maximum of kinetic energy at 1.00 MeV, and then increase gradually as the energy increases. It was observed that the stopping powers of electrons decreased with the increase of the Re element and the decrease of the B element. As a result, we can say that the stopping powers of electrons for the B element are higher than those for the Re element.

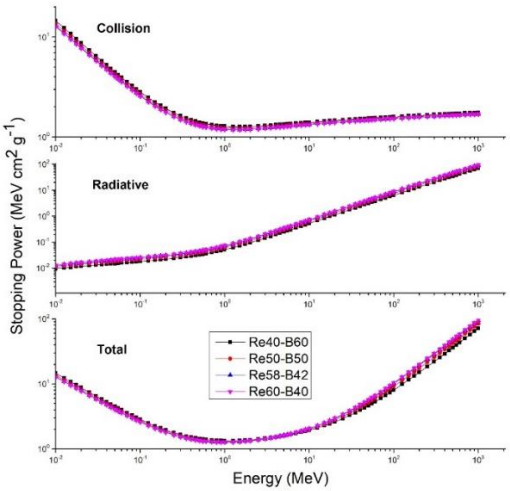

Figure 1. Variations of collision, radiative and total stopping powers of electron as a function of kinetic energy for Re40-B60, Re50-B50, Re58-B42, and Re60-B40 alloys

The collision, nuclear, and total stopping powers of the proton calculated for the alloys were given in Table 3, and were also displayed the variation with energy in Fig. 2. For the proton, it was seen that the total stopping powers decrease with increasing kinetic energy and have a maximum value at a kinetic energy of 0.1 MeV. The highest values of the total stopping powers of protons are at 0.1 MeV with value of 153.772 MeV cm^2/g, 138.356 MeV cm^2/g, 129.447 MeV cm^2/g and 127.545 MeV cm^2/g for Re40-B60, Re50-B50, Re58-B42 and Re60-B40, respectively. The smallest values of the total stopping powers of protons are at 1000 MeV, with values of 1.261 MeV cm^2/g, 1.246 MeV cm^2/g, 1.238 MeV cm^2/g and 1.236 MeV cm^2/g for Re40-B60, Re50-B50, Re58-B42 and Re60-B40, respectively. Also, the highest stopping power value (153.772 MeV $cm^2\ g^{-1}$) was found for the Re40-B60 alloy, and the smallest stopping power value (1.236 MeV $cm^2\ g^{-1}$) for the proton particle was recorded for the Re60-B40 alloy. Afterward, proton particle total stopping power for all the alloys are reduced progressively with increasing kinetic energy. It was realized that the total proton stopping powers decreased with the increase of the rhenium element and the decrease of the boron element. Thus, we can say that the proton stopping power of the B element is higher than the Re element.

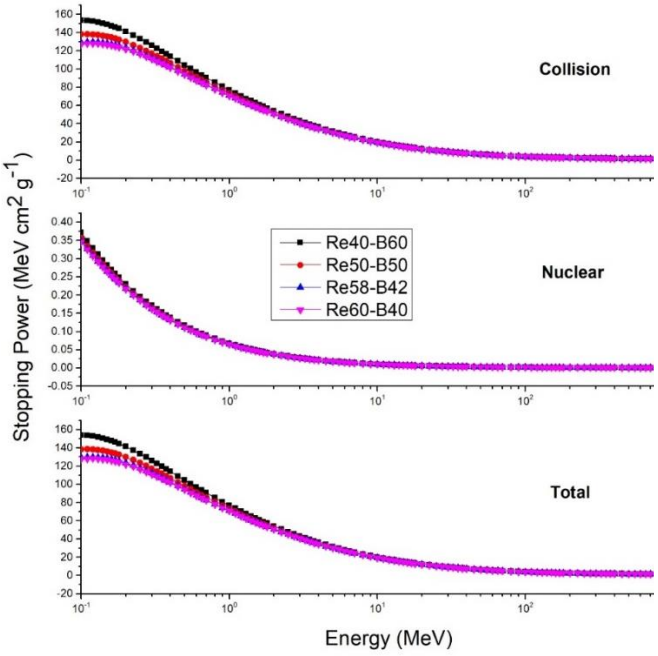

Figure 2. Variations of collision, nuclear and total stopping powers of proton as a function of kinetic energy for Re40-B60, Re50-B50, Re58-B42, and Re60-B40 alloys

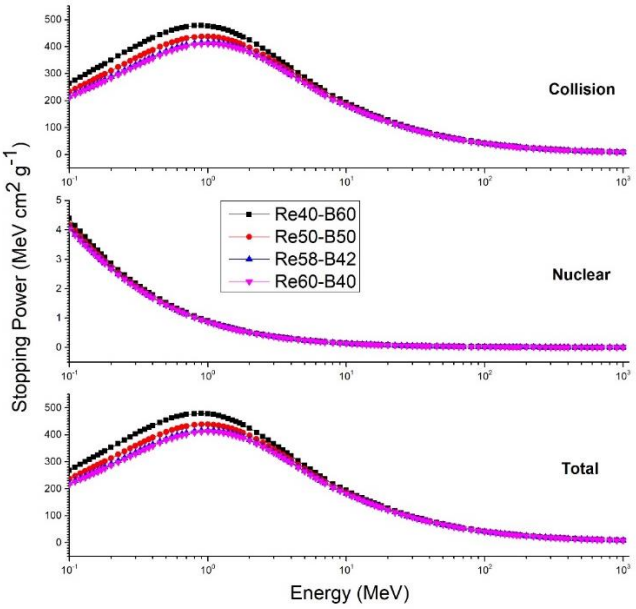

Figure 3. Variations of collision, nuclear and total stopping powers of alpha as a function of kinetic energy for Re40-B60, Re50-B50, Re58-B42, and Re60-B40 alloys

The collision, nuclear, and total stopping powers of the alpha particles calculated for the alloys were listed in Table 4 and were presented the variation with energy in Fig. 3. For the alpha particles, it was found that the total stopping powers increase with increasing kinetic energy and have a maximum value at the kinetic energies of 0.9-1.0 MeV. The total stopping power parameters of alpha are among 8.611-478.782 MeV cm^2/g for Re40-B60, 8.492-438.653 MeV cm^2/g for Re50-B50, 8.423- 416.365 MeV cm^2/g for Re58-B42 and 8.409- 411.662 MeV cm^2/g for Re60-B40. It was observed that the total alpha stopping powers decreased with the increase of the Re element and the decrease of the B element. As a result, we can state that the alpha stopping power of the B element is higher than the Re element.

The collision, nuclear and total stopping powers of the carbon for the alloys were calculated and given in Table 5, and were also shown the variation with energy in Fig. 4. For the carbon ions, it was found that the total stopping powers increase when the kinetic energy increases. The highest values of the total stopping powers of carbon ions are at 6.5 MeV with a value of 2245.294 MeV cm^2/g, at 7.0 MeV with a value of 2124.955 MeV cm^2/g, at 7.0 MeV with a value of 2055.901 MeV cm^2/g and at 7.0 MeV with a value of 2040.889 MeV cm^2/g for Re40-B60, Re50-B50, Re58-B42 and Re60-B40, respectively. The smallest values of the total stopping powers of carbon are at 1000 MeV with values of 155.257 MeV cm^2/g, 152.756 MeV cm^2/g, 151.355 MeV cm^2/g and 151.055 MeV cm^2/g for Re40-B60, Re50-B50, Re58-B42 and Re60-B40, respectively. It was noticed that the total carbon stopping powers decreased with the increase of the Re element and the decrease of the B element. Hence, we can remark that the carbon stopping power of the B element is higher than the Re element.

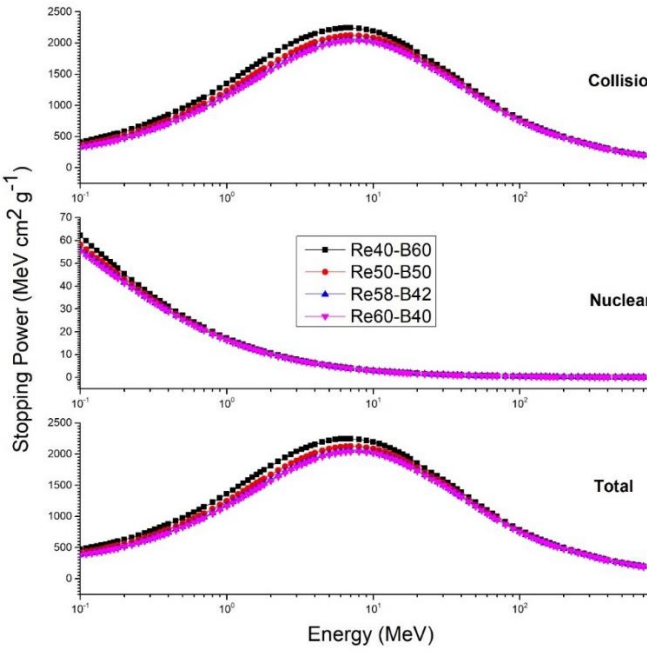

Figure 4. Variations of collision, nuclear and total stopping powers of carbon as a function of kinetic energy for Re40-B60, Re50-B50, Re58-B42, and Re60-B40 alloys

The collision, nuclear, and total stopping powers of the oxygen calculated for the alloys were given in Table 6 and were displayed the variation with energy in Fig. 5. For the oxygen ions, it was found that the total stopping powers increase with increasing kinetic energy and have a maximum value at kinetic energies of 10.0-11.0 MeV. The highest values of the total stopping powers of oxygen are at 10.0 MeV with a value of 3239.727 MeV cm^2/g, at 11.0 MeV with a value of 3074.097 MeV cm^2/g, at 11.0 MeV with a value of 2979.019 MeV cm^2/g and at 11.0 MeV with a value of 2959.003 MeV cm^2/g for Re40-B60, Re50-B50, Re58-B42 and Re60-B40, respectively. The smallest values of the total stopping powers of protons are at 1000 MeV with values of 345.530 MeV cm^2/g, 339.728 MeV cm^2/g, 336.427 MeV cm^2/g and 335.726 MeV cm^2/g for Re40-B60, Re50-B50, Re58-B42 and Re60-B40, respectively. It was observed that the total oxygen stopping power decreased with the increase of the Re element and the decrease of the B element. As a result, we can say that the oxygen stopping power of the B element is higher than the Re element.

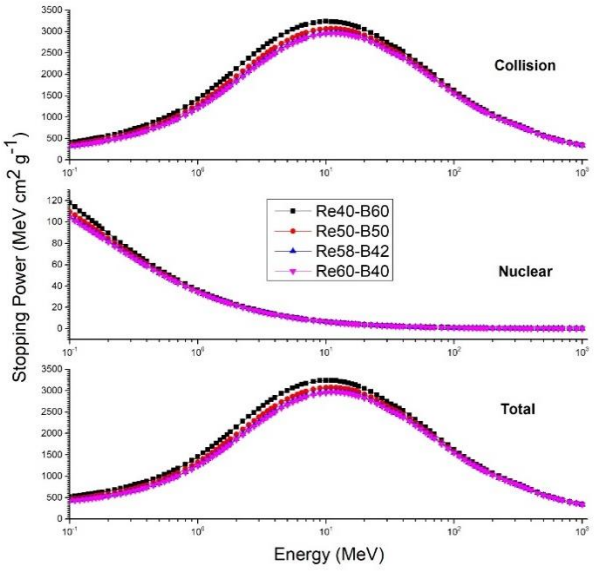

Figure 5. Variations of collision, nuclear and total stopping powers of oxygen as a function of kinetic energy for Re40-B60, Re50-B50, Re58-B42, and Re60-B40 alloys

Figure 6 shows the results of the projected range (R_P) of charged particles for Re40-B60, Re50-B50, Re58-B42, and Re60-B40 alloys. Obviously, the projected range value increases with the increase of the kinetic energy of the incident charged particles. Proton particles can move deeper than alpha, carbon, and oxygen particles because they have less mass than alpha, carbon, and oxygen particles. The charged particle ranges decrease with an increasing concentration of the Re element. Thus, the range of heavy charged particles changes in order of Re40-B60 > Re50-B50 > Re58-B42 > Re60-B40.

Table 2. Collision, radiative and total stopping powers (MeV cm^2 g^{-1}) for electrons

Energy (MeV)	Re40–B60			Re50–B50			Re58–B42			Re60–B40		
	$\left(\frac{dE}{dx}\right)_{Col.}$	$\left(\frac{dE}{dx}\right)_{Rad.}$	$\left(\frac{dE}{dx}\right)_{Total}$	$\left(\frac{dE}{dx}\right)_{Col.}$	$\left(\frac{dE}{dx}\right)_{Rad.}$	$\left(\frac{dE}{dx}\right)_{Total}$	$\left(\frac{dE}{dx}\right)_{Col.}$	$\left(\frac{dE}{dx}\right)_{Rad.}$	$\left(\frac{dE}{dx}\right)_{Total}$	$\left(\frac{dE}{dx}\right)_{Col.}$	$\left(\frac{dE}{dx}\right)_{Rad.}$	$\left(\frac{dE}{dx}\right)_{Total}$
0.100	2.829	0.018	2.847	2.696	0.022	2.718	2.591	0.025	2.616	2.565	0.025	2.591
0.125	2.474	0.019	2.494	2.361	0.023	2.384	2.271	0.026	2.298	2.248	0.027	2.276
0.150	2.234	0.020	2.254	2.133	0.024	2.158	2.053	0.028	2.082	2.034	0.029	2.063
0.175	2.061	0.021	2.082	1.969	0.025	1.995	1.897	0.029	1.926	1.879	0.030	1.909
0.200	1.931	0.022	1.953	1.846	0.027	1.873	1.779	0.030	1.810	1.762	0.031	1.794
0.250	1.749	0.023	1.773	1.674	0.029	1.703	1.614	0.033	1.647	1.599	0.034	1.634
0.300	1.629	0.025	1.655	1.560	0.031	1.592	1.506	0.035	1.542	1.493	0.036	1.529
0.350	1.546	0.027	1.573	1.482	0.033	1.515	1.431	0.038	1.469	1.418	0.039	1.457
0.400	1.485	0.029	1.514	1.424	0.035	1.460	1.376	0.040	1.417	1.364	0.041	1.406
0.450	1.440	0.030	1.471	1.381	0.037	1.419	1.335	0.042	1.378	1.324	0.044	1.368
0.500	1.405	0.032	1.438	1.349	0.039	1.388	1.304	0.045	1.350	1.293	0.046	1.340
0.550	1.378	0.034	1.412	1.323	0.041	1.365	1.280	0.047	1.328	1.269	0.049	1.319
0.600	1.356	0.036	1.392	1.303	0.044	1.347	1.261	0.050	1.311	1.250	0.051	1.302
0.700	1.325	0.040	1.365	1.274	0.048	1.322	1.234	0.055	1.289	1.224	0.057	1.281
0.800	1.305	0.044	1.349	1.255	0.053	1.308	1.216	0.060	1.277	1.206	0.062	1.269
0.900	1.291	0.048	1.339	1.243	0.058	1.301	1.205	0.066	1.271	1.195	0.068	1.264
1.000	1.282	0.052	1.334	1.235	0.063	1.298	1.197	0.071	1.269	1.188	0.074	1.262
1.250	1.272	0.062	1.334	1.226	0.075	1.302	1.190	0.086	1.276	1.181	0.088	1.270

1.500	1.270	0.073	1.344	1.226	0.088	1.314	1.191	0.101	1.292	1.182	0.104	1.286
1.750	1.273	0.084	1.358	1.229	0.102	1.332	1.195	0.116	1.311	1.187	0.119	1.306
2.000	1.278	0.096	1.375	1.235	0.116	1.351	1.201	0.132	1.333	1.193	0.135	1.329
2.500	1.290	0.120	1.411	1.248	0.144	1.393	1.215	0.164	1.379	1.207	0.169	1.376
3.000	1.303	0.145	1.448	1.261	0.174	1.435	1.228	0.197	1.426	1.220	0.203	1.424
3.500	1.315	0.170	1.485	1.273	0.204	1.478	1.241	0.231	1.473	1.233	0.238	1.472
4.000	1.326	0.196	1.522	1.285	0.235	1.520	1.253	0.266	1.519	1.245	0.274	1.519
4.500	1.336	0.222	1.558	1.295	0.266	1.561	1.264	0.301	1.565	1.256	0.310	1.566
5.000	1.345	0.248	1.594	1.305	0.298	1.603	1.274	0.337	1.611	1.266	0.347	1.613
5.500	1.354	0.275	1.629	1.313	0.330	1.644	1.283	0.373	1.656	1.275	0.384	1.659
6.000	1.361	0.303	1.664	1.321	0.362	1.684	1.291	0.410	1.701	1.283	0.422	1.705
7.000	1.375	0.358	1.734	1.336	0.428	1.764	1.305	0.484	1.790	1.298	0.498	1.797
8.000	1.387	0.415	1.802	1.348	0.495	1.844	1.318	0.560	1.879	1.311	0.576	1.887
9.000	1.398	0.472	1.870	1.359	0.563	1.923	1.329	0.637	1.967	1.322	0.655	1.978
10.00	1.407	0.530	1.937	1.369	0.632	2.001	1.339	0.714	2.054	1.332	0.735	2.068
12.50	1.427	0.677	2.105	1.389	0.808	2.197	1.361	0.912	2.273	1.354	0.938	2.292
15.00	1.443	0.828	2.271	1.406	0.986	2.392	1.377	1.114	2.491	1.371	1.145	2.516

Table 3. Collision, nuclear and total stopping powers (MeV cm^2 g^{-1}) for proton

Energy (MeV)	Re40–B60			Re50–B50			Re58–B42			Re60–B40		
	$\left(\frac{dE}{dx}\right)_{Col.}$	$\left(\frac{dE}{dx}\right)_{Nuc.}$	$\left(\frac{dE}{dx}\right)_{Total}$	$\left(\frac{dE}{dx}\right)_{Col.}$	$\left(\frac{dE}{dx}\right)_{Nuc.}$	$\left(\frac{dE}{dx}\right)_{Total}$	$\left(\frac{dE}{dx}\right)_{Col.}$	$\left(\frac{dE}{dx}\right)_{Nuc.}$	$\left(\frac{dE}{dx}\right)_{Total}$	$\left(\frac{dE}{dx}\right)_{Col.}$	$\left(\frac{dE}{dx}\right)_{Nuc.}$	$\left(\frac{dE}{dx}\right)_{Total}$
0.1	153.4	0.371	153.771	138.0	0.356	138.356	129.1	0.347	129.447	127.2	0.345	127.545
0.2	141.1	0.230	141.330	129.7	0.222	129.922	123.1	0.217	123.317	121.7	0.216	121.916
0.3	125.9	0.171	126.071	117.0	0.165	117.165	111.9	0.162	112.062	110.8	0.161	110.961
0.4	113.8	0.138	113.938	106.5	0.133	106.633	102.2	0.131	102.331	101.3	0.130	101.430
0.5	104.3	0.116	104.416	98.01	0.112	98.122	94.38	0.110	94.490	93.61	0.110	93.720
0.6	96.69	0.101	96.791	91.16	0.098	91.258	87.98	0.096	88.076	87.31	0.096	87.406
0.7	90.44	0.089	90.529	85.51	0.087	85.597	82.68	0.085	82.765	82.07	0.085	82.155
0.8	85.21	0.080	85.290	80.76	0.078	80.838	78.20	0.077	78.277	77.65	0.076	77.726
0.9	80.76	0.073	80.833	76.69	0.071	76.761	74.35	0.070	74.420	73.86	0.069	73.929
1.00	76.92	0.067	76.987	73.17	0.065	73.235	71.02	0.064	71.084	70.56	0.064	70.624
1.10	73.57	0.062	73.632	70.08	0.060	70.140	68.07	0.059	68.129	67.64	0.059	67.699
1.20	70.25	0.058	70.308	67.00	0.056	67.056	65.13	0.055	65.185	64.73	0.055	64.785
1.30	67.49	0.054	67.544	64.44	0.053	64.493	62.69	0.052	62.742	62.31	0.052	62.362
1.40	65.04	0.051	65.091	62.16	0.050	62.210	60.51	0.049	60.559	60.16	0.049	60.209
1.50	62.81	0.048	62.858	60.09	0.047	60.137	58.52	0.046	58.566	58.19	0.046	58.236
1.60	60.77	0.046	60.816	58.18	0.044	58.224	56.70	0.044	56.744	56.38	0.044	56.424
1.70	58.89	0.043	58.933	56.43	0.042	56.472	55.01	0.042	55.052	54.71	0.041	54.751
1.80	57.15	0.041	57.191	54.80	0.040	54.840	53.45	0.040	53.490	53.16	0.040	53.200

2.00	54.02	0.038	54.058	51.87	0.037	51.907	50.63	0.036	50.666	50.37	0.036	50.406
2.25	50.66	0.034	50.694	48.71	0.033	48.743	47.58	0.033	47.613	47.35	0.033	47.383
2.50	47.77	0.031	47.801	45.98	0.031	46.011	44.96	0.030	44.990	44.74	0.030	44.770
2.75	45.25	0.029	45.279	43.60	0.028	43.628	42.66	0.028	42.688	42.46	0.028	42.488
3.00	43.03	0.027	43.057	41.51	0.026	41.536	40.63	0.026	40.656	40.44	0.026	40.466
3.25	41.06	0.025	41.085	39.64	0.025	39.665	38.82	0.024	38.844	38.65	0.024	38.674
3.50	39.29	0.024	39.314	37.96	0.023	37.983	37.20	0.023	37.223	37.03	0.023	37.053
3.75	37.69	0.022	37.712	36.45	0.022	36.472	35.73	0.021	35.751	35.57	0.021	35.591
4.00	36.25	0.021	36.271	35.07	0.021	35.091	34.39	0.020	34.410	34.25	0.020	34.270
4.50	33.71	0.019	33.729	32.66	0.019	32.679	32.05	0.018	32.068	31.92	0.018	31.938
5.00	31.57	0.017	31.587	30.61	0.017	30.627	30.05	0.017	30.067	29.94	0.017	29.957
6.00	28.11	0.015	28.125	27.30	0.014	27.314	26.83	0.014	26.844	26.73	0.014	26.744
7.00	25.43	0.013	25.443	24.73	0.013	24.743	24.33	0.012	24.342	24.24	0.012	24.252
8.00	23.29	0.011	23.301	22.67	0.011	22.681	22.31	0.011	22.321	22.24	0.011	22.251
9.00	21.52	0.010	21.530	20.97	0.010	20.980	20.65	0.010	20.660	20.58	0.010	20.590
10.00	20.04	0.009	20.049	19.54	0.009	19.549	19.25	0.009	19.259	19.19	0.009	19.199
11.00	18.78	0.009	18.789	18.32	0.008	18.328	18.06	0.008	18.068	18.01	0.008	18.018
12.00	17.69	0.008	17.698	17.27	0.008	17.278	17.03	0.008	17.038	16.98	0.008	16.988
13.00	16.74	0.007	16.747	16.35	0.007	16.357	16.12	0.007	16.127	16.08	0.007	16.087
14.00	15.90	0.007	15.907	15.53	0.007	15.537	15.32	0.007	15.327	15.28	0.007	15.287
15.00	15.15	0.006	15.156	14.81	0.006	14.816	14.61	0.006	14.616	14.57	0.006	14.576

Table 4. Collision, nuclear and total stopping powers (MeV cm^2 g^{-1}) for alpha

Energy (MeV)	Re40–B60			Re50–B50			Re58–B42			Re60–B40		
	$\left(\frac{dE}{dx}\right)_{Col.}$	$\left(\frac{dE}{dx}\right)_{Nuc.}$	$\left(\frac{dE}{dx}\right)_{Total}$	$\left(\frac{dE}{dx}\right)_{Col.}$	$\left(\frac{dE}{dx}\right)_{Nuc.}$	$\left(\frac{dE}{dx}\right)_{Total}$	$\left(\frac{dE}{dx}\right)_{Col.}$	$\left(\frac{dE}{dx}\right)_{Nuc.}$	$\left(\frac{dE}{dx}\right)_{Total}$	$\left(\frac{dE}{dx}\right)_{Col.}$	$\left(\frac{dE}{dx}\right)_{Nuc.}$	$\left(\frac{dE}{dx}\right)_{Total}$
0.1	263.9	4.395	268.295	233.4	4.180	237.580	215.9	4.056	219.956	212.2	4.030	216.230
0.2	349.8	2.864	352.664	310.8	2.749	313.549	288.3	2.683	290.983	283.5	2.669	286.169
0.3	400.1	2.182	402.282	357.1	2.103	359.203	332.3	2.057	334.357	327.1	2.048	329.148
0.4	432.5	1.785	434.285	388.0	1.724	389.724	362.4	1.689	364.089	357.0	1.681	358.681
0.5	453.3	1.521	454.821	408.7	1.471	410.171	383.1	1.443	384.543	377.6	1.437	379.037
0.6	466.2	1.331	467.531	422.3	1.289	423.589	397.1	1.265	398.365	391.7	1.260	392.960
0.7	473.6	1.187	474.787	430.8	1.151	431.951	406.2	1.130	407.330	400.9	1.125	402.025
0.8	477.1	1.074	478.174	435.6	1.042	436.642	411.7	1.023	412.723	406.7	1.019	407.719
0.9	477.8	0.982	478.782	437.7	0.953	438.653	414.6	0.936	415.536	409.7	0.933	410.633
1.00	476.4	0.906	477.306	437.7	0.880	438.580	415.5	0.865	416.365	410.8	0.862	411.662
1.10	473.5	0.842	474.342	436.3	0.818	437.118	414.9	0.804	415.704	410.3	0.801	411.101
1.20	469.6	0.787	470.387	433.7	0.765	434.465	413.1	0.752	413.852	408.7	0.750	409.450
1.30	464.9	0.739	465.639	430.3	0.719	431.019	410.5	0.707	411.207	406.2	0.705	406.905
1.40	459.6	0.698	460.298	426.3	0.679	426.979	407.2	0.668	407.868	403.1	0.666	403.766
1.50	453.9	0.661	454.561	421.9	0.643	422.543	403.4	0.633	404.033	399.5	0.631	400.131
1.60	448.0	0.628	448.628	417.1	0.611	417.711	399.3	0.602	399.902	395.5	0.600	396.100
1.70	441.9	0.599	442.499	412.1	0.583	412.683	394.9	0.574	395.474	391.2	0.572	391.772
1.80	435.7	0.572	436.272	406.9	0.557	407.457	390.3	0.549	390.849	386.8	0.547	387.347

2.00	423.4	0.526	423.926	396.4	0.513	396.913	380.9	0.505	381.405	377.6	0.503	378.103
2.25	408.1	0.479	408.579	383.2	0.467	383.667	368.9	0.460	369.360	365.8	0.458	366.258
2.50	393.5	0.440	393.940	370.4	0.429	370.829	357.0	0.423	357.423	354.2	0.421	354.621
2.75	379.6	0.407	380.007	358.0	0.397	358.397	345.6	0.391	345.991	342.9	0.390	343.290
3.00	366.4	0.379	366.779	346.2	0.370	346.570	334.6	0.365	334.965	332.1	0.364	332.464
3.25	354.1	0.355	354.455	335.1	0.347	335.447	324.2	0.342	324.542	321.9	0.341	322.241
3.50	342.5	0.335	342.835	324.6	0.327	324.927	314.3	0.322	314.622	312.1	0.321	312.421
3.75	331.6	0.316	331.916	314.7	0.309	315.009	304.9	0.304	305.204	302.9	0.303	303.203
4.00	321.4	0.300	321.700	305.4	0.293	305.693	296.1	0.289	296.389	294.2	0.288	294.488
4.50	302.8	0.272	303.072	288.3	0.266	288.566	279.9	0.262	280.162	278.1	0.261	278.361
5.00	286.4	0.249	286.649	273.1	0.243	273.343	265.4	0.240	265.640	263.8	0.240	264.040
6.00	258.6	0.214	258.814	247.2	0.209	247.409	240.7	0.206	240.906	239.3	0.206	239.506
7.00	236.1	0.188	236.288	226.2	0.184	226.384	220.5	0.182	220.682	219.3	0.181	219.481
8.00	217.5	0.168	217.668	208.8	0.164	208.964	203.7	0.162	203.862	202.7	0.162	202.862
9.00	205.3	0.152	205.452	197.4	0.149	197.549	192.8	0.147	192.947	191.9	0.147	192.047
10.00	193.5	0.139	193.639	186.3	0.136	186.436	182.2	0.134	182.334	181.3	0.134	181.434
11.00	183.2	0.128	183.328	176.6	0.126	176.726	172.8	0.124	172.924	172.0	0.124	172.124
12.00	174.1	0.119	174.219	168.0	0.117	168.117	164.5	0.115	164.615	163.7	0.115	163.815
13.00	166.0	0.111	166.111	160.3	0.109	160.409	157.0	0.108	157.108	156.4	0.107	156.507
14.00	158.8	0.104	158.904	153.5	0.102	153.602	150.4	0.101	150.501	149.7	0.101	149.801
15.00	152.3	0.098	152.398	147.3	0.096	147.396	144.4	0.095	144.495	143.8	0.095	143.895

Table 5. Collision, nuclear and total stopping powers (MeV cm^2 g^{-1}) for carbon

Energy (MeV)	Re40–B60			Re50–B50			Re58–B42			Re60–B40		
	$\left(\frac{dE}{dx}\right)_{Col.}$	$\left(\frac{dE}{dx}\right)_{Nuc.}$	$\left(\frac{dE}{dx}\right)_{Total}$	$\left(\frac{dE}{dx}\right)_{Col.}$	$\left(\frac{dE}{dx}\right)_{Nuc.}$	$\left(\frac{dE}{dx}\right)_{Total}$	$\left(\frac{dE}{dx}\right)_{Col.}$	$\left(\frac{dE}{dx}\right)_{Nuc.}$	$\left(\frac{dE}{dx}\right)_{Total}$	$\left(\frac{dE}{dx}\right)_{Col.}$	$\left(\frac{dE}{dx}\right)_{Nuc.}$	$\left(\frac{dE}{dx}\right)_{Total}$
0.1	410.9	62.16	473.060	359.9	58.10	418.000	330.5	55.77	386.270	324.3	55.28	379.580
0.2	583.1	45.40	628.500	517.9	43.09	560.990	480.4	41.75	522.150	472.4	41.47	513.870
0.3	725.1	36.63	761.730	650.9	34.99	685.890	608.1	34.05	642.150	599.1	33.85	632.950
0.4	845.5	31.06	876.560	763.6	29.79	793.390	716.5	29.05	745.550	706.5	28.90	735.400
0.5	949.9	27.15	977.050	861.2	26.10	887.300	810.1	25.50	835.600	799.2	25.37	824.570
0.6	1043	24.23	1067.230	948.0	23.34	971.340	893.2	22.82	916.020	881.6	22.71	904.310
0.7	1128	21.95	1149.950	1027	21.17	1048.170	968.8	20.72	989.520	956.4	20.63	977.030
0.8	1206	20.10	1226.100	1100	19.42	1119.420	1038	19.02	1057.020	1025	18.94	1043.940
0.9	1278	18.58	1296.580	1167	17.97	1184.970	1103	17.61	1120.610	1089	17.53	1106.530
1.00	1345	17.30	1362.300	1229	16.74	1245.740	1162	16.42	1178.420	1148	16.35	1164.350
1.10	1407	16.21	1423.210	1287	15.69	1302.690	1218	15.40	1233.400	1203	15.33	1218.330
1.20	1464	15.26	1479.260	1341	14.79	1355.790	1269	14.51	1283.510	1254	14.45	1268.450
1.30	1518	14.43	1532.430	1391	13.99	1404.990	1318	13.73	1331.730	1302	13.68	1315.680
1.40	1567	13.70	1580.700	1437	13.28	1450.280	1363	13.04	1376.040	1347	12.99	1359.990
1.50	1613	13.04	1626.040	1481	12.65	1493.650	1405	12.43	1417.430	1389	12.38	1401.380
1.60	1656	12.45	1668.450	1522	12.09	1534.090	1444	11.87	1455.870	1428	11.83	1439.830
1.70	1696	11.92	1707.920	1560	11.57	1571.570	1481	11.37	1492.370	1465	11.33	1476.330
1.80	1733	11.44	1744.440	1595	11.11	1606.110	1516	10.92	1526.920	1499	10.88	1509.880

2.00	1800	10.59	1810.590	1660	10.29	1670.290	1579	10.12	1589.120	1562	10.08	1572.080
2.25	1872	9.710	1881.710	1730	9.442	1739.442	1648	9.288	1657.288	1631	9.255	1640.255
2.50	1933	8.978	1941.978	1790	8.735	1798.735	1708	8.596	1716.596	1690	8.566	1698.566
2.75	1985	8.359	1993.359	1842	8.137	1850.137	1759	8.009	1767.009	1741	7.982	1748.982
3.00	2029	7.828	2036.828	1886	7.623	1893.623	1803	7.505	1810.505	1786	7.479	1793.479
3.25	2067	7.366	2074.366	1924	7.176	1931.176	1842	7.066	1849.066	1825	7.043	1832.043
3.50	2099	6.961	2105.961	1957	6.783	1963.783	1876	6.681	1882.681	1858	6.659	1864.659
3.75	2126	6.602	2132.602	1986	6.435	1992.435	1905	6.339	1911.339	1888	6.319	1894.319
4.00	2149	6.282	2155.282	2010	6.125	2016.125	1930	6.034	1936.034	1913	6.015	1919.015
4.50	2185	5.734	2190.734	2049	5.593	2054.593	1971	5.512	1976.512	1954	5.494	1959.494
5.00	2210	5.281	2215.281	2077	5.153	2082.153	2001	5.080	2006.080	1985	5.064	1990.064
6.00	2237	4.575	2241.575	2110	4.467	2114.467	2037	4.405	2041.405	2022	4.392	2026.392
7.00	2241	4.048	2245.048	2121	3.955	2124.955	2052	3.901	2055.901	2037	3.889	2040.889
8.00	2232	3.638	2235.638	2117	3.555	2120.555	2051	3.508	2054.508	2037	3.498	2040.498
9.00	2214	3.309	2217.309	2104	3.235	2107.235	2041	3.192	2044.192	2028	3.183	2031.183
10.00	2190	3.038	2193.038	2084	2.971	2086.971	2024	2.933	2026.933	2011	2.925	2013.925
11.00	2161	2.812	2163.812	2060	2.751	2062.751	2001	2.715	2003.715	1989	2.708	1991.708
12.00	2129	2.619	2131.619	2032	2.563	2034.563	1976	2.530	1978.530	1964	2.523	1966.523
13.00	2096	2.453	2098.453	2002	2.401	2004.401	1948	2.371	1950.371	1936	2.364	1938.364
14.00	2062	2.308	2064.308	1971	2.259	1973.259	1919	2.231	1921.231	1908	2.225	1910.225
15.00	2027	2.181	2029.181	1939	2.135	1941.135	1888	2.109	1890.109	1878	2.103	1880.103

Table 6. Collision, nuclear and total stopping powers (MeV cm^2 g^{-1}) for oxygen

Energy (MeV)	Re40–B60			Re50–B50			Re58–B42			Re60–B40		
	$\left(\frac{dE}{dx}\right)_{Col.}$	$\left(\frac{dE}{dx}\right)_{Nuc.}$	$\left(\frac{dE}{dx}\right)_{Total}$	$\left(\frac{dE}{dx}\right)_{Col.}$	$\left(\frac{dE}{dx}\right)_{Nuc.}$	$\left(\frac{dE}{dx}\right)_{Total}$	$\left(\frac{dE}{dx}\right)_{Col.}$	$\left(\frac{dE}{dx}\right)_{Nuc.}$	$\left(\frac{dE}{dx}\right)_{Total}$	$\left(\frac{dE}{dx}\right)_{Col.}$	$\left(\frac{dE}{dx}\right)_{Nuc.}$	$\left(\frac{dE}{dx}\right)_{Total}$
0.1	401.2	117.9	519.100	350.8	109.6	460.4	321.8	104.9	426.700	315.7	103.9	419.600
0.2	565.3	89.48	654.780	498.4	84.62	583.02	459.9	81.83	541.730	451.8	81.24	533.040
0.3	697.9	73.68	771.580	621.8	70.20	692	578.0	68.19	646.190	568.7	67.77	636.470
0.4	818.9	63.31	882.210	735.0	60.57	795.57	686.8	59.00	745.800	676.6	58.67	735.270
0.5	931.6	55.86	987.460	840.4	53.61	894.01	787.9	52.31	840.210	776.7	52.03	828.730
0.6	1038	50.21	1088.210	939.4	48.28	987.68	882.7	47.17	929.870	870.6	46.94	917.540
0.7	1139	45.74	1184.740	1033	44.06	1077.06	972.6	43.09	1015.690	959.7	42.88	1002.580
0.8	1236	42.10	1278.100	1123	40.61	1163.61	1059	39.75	1098.750	1045	39.56	1084.560
0.9	1330	39.07	1369.070	1210	37.73	1247.73	1141	36.95	1177.950	1126	36.79	1162.790
1.00	1419	36.51	1455.510	1293	35.28	1328.28	1220	34.58	1254.580	1205	34.43	1239.430
1.10	1506	34.30	1540.300	1373	33.17	1406.17	1297	32.53	1329.530	1280	32.39	1312.390
1.20	1588	32.38	1620.380	1450	31.34	1481.34	1370	30.74	1400.740	1353	30.61	1383.610
1.30	1667	30.68	1697.680	1523	29.72	1552.72	1440	29.16	1469.160	1422	29.04	1451.040
1.40	1743	29.18	1772.180	1593	28.28	1621.28	1507	27.76	1534.760	1489	27.65	1516.650
1.50	1815	27.84	1842.840	1661	26.99	1687.99	1571	26.50	1597.500	1553	26.39	1579.390
1.60	1884	26.63	1910.630	1725	25.83	1750.83	1633	25.36	1658.360	1614	25.27	1639.270
1.70	1949	25.53	1974.530	1786	24.77	1810.77	1692	24.33	1716.330	1672	24.24	1696.240
1.80	2012	24.53	2036.530	1844	23.81	1867.81	1748	23.40	1771.400	1727	23.31	1750.310

2.00	2127	22.77	2149.770	1953	22.12	1975.12	1853	21.74	1874.740	1831	21.66	1852.660
2.25	2257	20.94	2277.940	2075	20.35	2095.35	1971	20.01	1991.010	1948	19.94	1967.940
2.50	2371	19.41	2390.410	2183	18.87	2201.87	2076	18.57	2094.570	2053	18.50	2071.500
2.75	2471	18.11	2489.110	2280	17.62	2297.62	2170	17.34	2187.340	2146	17.28	2163.280
3.00	2560	16.99	2576.990	2365	16.54	2381.54	2253	16.28	2269.280	2230	16.22	2246.220
3.25	2638	16.01	2654.010	2442	15.59	2457.59	2328	15.35	2343.350	2304	15.30	2319.300
3.50	2708	15.15	2723.150	2510	14.76	2524.76	2395	14.54	2409.540	2371	14.49	2385.490
3.75	2770	14.39	2784.390	2570	14.02	2584.02	2456	13.81	2469.810	2431	13.77	2444.770
4.00	2824	13.71	2837.710	2625	13.36	2638.36	2510	13.16	2523.160	2486	13.12	2499.120
4.50	2917	12.54	2929.540	2718	12.23	2730.23	2603	12.05	2615.050	2579	12.01	2591.010
5.00	2990	11.57	3001.570	2792	11.29	2803.29	2679	11.13	2690.130	2655	11.09	2666.090
6.00	3095	10.05	3105.050	2902	9.816	2911.816	2791	9.679	2800.679	2768	9.650	2777.650
7.00	3161	8.917	3169.917	2974	8.710	2982.71	2867	8.591	2875.591	2844	8.566	2852.566
8.00	3201	8.029	3209.029	3020	7.847	3027.847	2916	7.742	2923.742	2894	7.719	2901.719
9.00	3223	7.315	3230.315	3048	7.151	3055.151	2947	7.057	2954.057	2926	7.037	2933.037
10.00	3233	6.727	3239.727	3063	6.578	3069.578	2965	6.493	2971.493	2944	6.475	2950.475
11.00	3232	6.233	3238.233	3068	6.097	3074.097	2973	6.019	2979.019	2953	6.003	2959.003
12.00	3225	5.813	3230.813	3065	5.687	3070.687	2973	5.615	2978.615	2953	5.600	2958.600
13.00	3212	5.449	3217.449	3056	5.333	3061.333	2967	5.266	2972.266	2948	5.252	2953.252
14.00	3195	5.132	3200.132	3043	5.024	3048.024	2956	4.961	2960.961	2938	4.948	2942.948
15.00	3175	4.853	3179.853	3027	4.751	3031.751	2942	4.692	2946.692	2924	4.680	2928.680

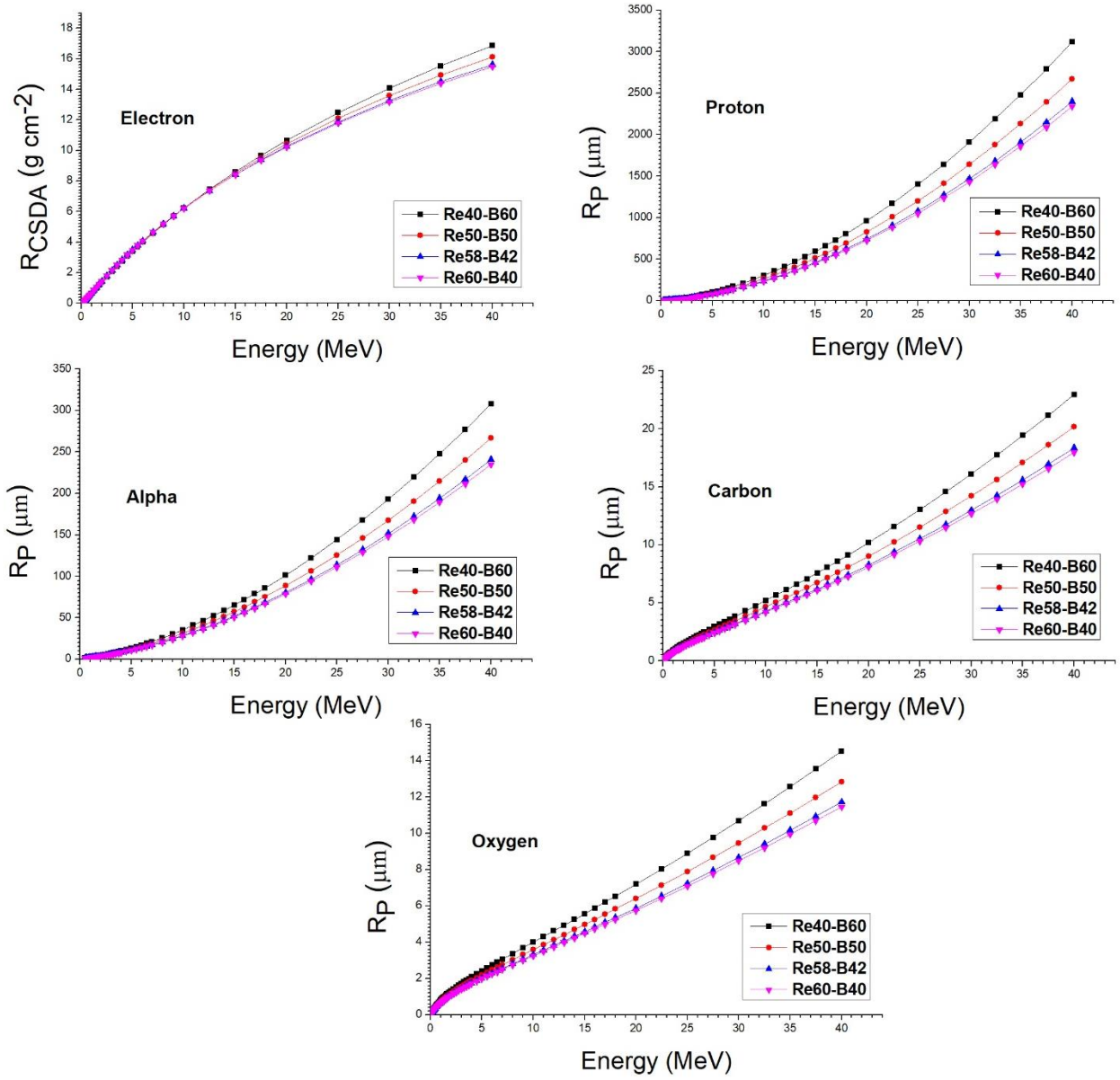

Figure 6. Variation of range (R) as a function of kinetic energy in Re40-B60, Re50-B50, Re58-B42, and Re60-B40 alloys shown for electron, proton, alpha, carbon and oxygen.

4. Conclusion and Suggestions

In the present research, we calculated collision, nuclear, and total stopping powers for charged particles such as electron, proton, alpha, carbon, and oxygen for Re60-B40, Re58-B42, Re50-B50, and Re40-B60 alloys by using the ESTAR and SRIM-2013 programs. We compared all the results with each other. The total stopping powers of charged particles (protons, alpha particles, heavy carbon, and oxygen ions) are minimum for the Re60-B40 alloy and maximum for the Re40-B60 alloy. Additionally, we noticed that the total stopping power decreased with the increase of the Re element and the decrease of the B element. Hence, we can deduce that the heavily charged particles have stopping powers in the following order: Re40-B60 > Re50-B50 > Re58-B42 > Re60-B40. Also, we can say that the charged particle ranges decrease with an increasing concentration of the Re element, and change in the order of Re40-B60 > Re50-B50 > Re58-B42 > Re60-B40.

Statement of Research and Publication Ethics

The study is complied with research and publication ethics

References

[1] Z. Aygun, N. Yarbasi and M. Aygun, "Spectroscopic and radiation shielding features of Nemrut, Pasinler, Sarıkamıs and Ikizdere obsidians in Turkey: Experimental and theoretical study," *Ceramics International*, vol. 47, pp. 34207-34217, 2021.

[2] Z. Aygun and M. Aygun, "A theoretical evaluation on radiation shielding features of Van-Ercis and Rize-Ikizdere (Türkiye) obsidians by using Phy-X/PSD code," *Sigma Journal of Engineering and Natural Sciences*, vol. 40, pp. 845–854, 2022.

[3] H. Osman and H. Gümüş, "Stopping power and CSDA range calculations of electrons and positrons over the 20 eV–1 GeV energy range in some water equivalent polymer gel dosimeters," *Applied Radiation and Isotopes*, vol. 179, pp. 110024, 2022.

[4] H. H. Andersen and P. Sigmund, "Stopping of heavy ions: a topical issue," *Nuclear Instruments and Methods in Physics Research Section B: Beam Interactions with Materials and Atoms*, vol. 195, pp. 1-2, 2002.

[5] A. Xu, D. E. J. Armstrong, C. Beck, M. P. Moody, G. D. W. Smith, P. A. J. Bagot and S. G. Roberts, "Ion irradiation induced clustering in W-Re-Ta, W-Re and W-Ta alloys: an atom probe tomography and nano indentation study," *Acta Materialia*, vol. 124, pp. 71-78, 2017.

[6] T. Korkut, H. Korkut, B. Aygün, Ö. Bayram, and A. Karabulut, "Investigation of high-temperature-resistant rhenium–boron neutron shields by experimental studies and Monte Carlo simulations," *Nuclear Science and Techniques*, Vol. 29:102, pp. 2-5, 2018.

[7] T. Mastren, V. Radchenko, H. T. Bach, E. R. Balkin, E. R. Birnbaum, M. Brugh, J. W. Engle, M. D. Gott, J. Guthrie, H. M. Hennkens, K. D. John, A. R. Ketring, M. Kuchuk, J. R. Maassen, C. M. Naranjo, F. M.

Nortier, T. E. Phelps, S. S. Jurisson, D. S. Wilbur and M. E. Fassbender, “Bulk production and evaluation of high specific activity 186gRe for cancer therapy using enriched 186WO3 targets in a proton beam,” *Nuclear Medicine and Biology*, vol. 49, pp. 24-29, 2017.

[8] R. L. Klueh, D. J. Alexander and M. A. Sokolov, “Effect of rhenium and osmium on mechanical properties of a 9Cr-2W-0.25V-0.07Ta-0.1C steel,” *Journal of Nuclear Materials*, vol. 279, pp. 91–99, 2000.

[9] National Institute of Standards and Technology. [Online]. Available: https://physics.nist.gov/PhysRefData/Star/Text/ESTAR.html [Accessed: Oct. 17, 2022].

[10] J. F. Ziegler, "SRIM-the stopping and range of ions in matter," [Online]. Available: http://www.srim.org (2009) [Accessed: Oct. 17, 2022].

[11] J. S. Alzahrani, A. V. Lebedev, S. A. Avanesov, A. Hammoud, Z. A. Alrowaili, Z. M. M. Mahmoud, I. O. Olarinoye, C. Sriwunkum and M. S. Al-Buriahi, Synthesis, “Optical properties and radiation shielding performance of TeO2-Na2O-BaO-WO3 glass system,” *Optik*, vol. 261, pp. 1-14, 2022.

[12] M. F. L’Annunziata, “Nuclear radiation, its interaction with matter and radioisotope decay,” *Handbook of Radioactivity Analysis*, 1-122, 2003.

[13] S. M. Seltzer and M. J. Berger, “Evaluation of the collision stopping power of elements and compounds for electrons and positrons,” *The International Journal of Applied Radiation and Isotopes*, vol. 33, pp. 1189–1218, 1982.

[14] W. Chaiphaksa, S. Yonphan, N. Chanthima, J. Kaewkhao and N. W. Sanwaranatee, “Computational approach of alpha and proton interaction of gadolinium bismuth borate glass system using SRIM programi,” *Materials Today: Proceedings*, vol. 65, pp. 2416-2420, 2022.

[15] O. I. Sallam, A. M. Madbouly, N. L. Moussa and A. Abdel-Galil, “Impact of radiation on CoO-doped borate glass: lead-free radiation shielding,” *Applied Physics A*, vol. 128, pp. 1-16, 2022.

[16] International Atomic Energy Agency (Nuclear Data Services), “Electronic stopping power of matter for ions,”. [Online]. Available: https://www-nds.iaea.org/stopping/ [Accessed: Oct. 17, 2022].

[17] S. R. Díaz, “Stopping power spectra of 4He ions in Zn, Cd and Pb-based semiconductors: A theoretical study for Rutherford Backscattering Spectroscopy analysis of metal chalcogenide thin films thickness,” *Solid State Communications*, vol. 341, pp. 114580, 2022.

[18] P. Sigmund and A. Schinner, “Notes on barkas-andersen effect,” *The European Physical Journal D*, vol. 68, pp. 318-325, 2014.

[19] L. E. Porter, “The barkas-effect correction to bethe–bloch stopping power,” *Advances in Quantum Chemistry*, vol. 46, pp. 91-119, 2004.

Bitlis Eren Üniversitesi Fen Bilimleri Dergisi
BİTLİS EREN UNIVERSITY JOURNAL OF SCIENCE
ISSN: 2147-3129/e-ISSN: 2147-3188
VOLUME: 12 NO: 1 PAGE: 84-92 YEAR: 2023
DOI:10.17798/bitlisfen.1191507

Mathematical modeling of CO_2 corrosion with NORSOK M 506

Begum SIRINOGLU DOGAN[1*], Ayla ALTINTEN[2]

[1] *Department of Chemical Engineering, Graduate School of Natural and Applied Sciences, Gazi University, 06500 Ankara, Turkey.*
[2] *Department of Chemical Engineering, Faculty of Engineering, Gazi University, 06570 Ankara, Turkey*
(ORCID:0000-0001-5779-8322) (ORCID:0000-0002-2048-8811)

Keywords: CO_2 corrosion, NORSOK M 506, Oil and gas industry, corrosion, corrosion modeling.

Abstract

The consequences of corrosion are catastrophic. Also costs to the global economy reached "$2.5 trillion, or world GDP's 3.4%". Despite the magnitude of the corrosion cost, it can be concluded that scientific studies on corrosion prevention are quite limited, except for high-risk sectors such as aviation and the fuel oil industry. It is important to fight against corrosion to ensure the safe operation of oil-carrying pipelines under the sea, and to prevent accidents and environmental damage. As a result of developing industry conditions and increasing needs, modeling corrosion is a very effective method for the prevention of corrosion. Industry, research companies, and universities have developed many corrosion rates and prediction models. One of them is the NORSOK M 506 model. In this study, the NORSOK M 506 CO_2 corrosion prediction model and the experimental results conducted by Nešić, Solvi and Enerhaug in 1995 were compared in terms of CO_2 corrosion rate. The results showed that the mathematical corrosion model calculated nearly six times higher than the experimental studies.

1. Introduction

The use of large-diameter, thin-walled pipes in pipeline transportation to meet the rapidly growing demand for oil and gas resources has also increased the risk of high pressure operations. However, undersea oil transportation poses a serious threat of corrosion due to the difficult operating conditions. The Pipeline and Hazardous Materials Safety Administration (PHMSA) of the United States Department of Transportation (USDOT) stated 18% of major accidents in the United States of America (USA) between 1988 and 2008 were due to corrosion of the equipment [1]. Accidents such as Flixborough, (the UK, 1974), Berre l'Etang (France, 1988), Kallo (Belgium, 2005) and Gironde (France, 2007) highlight the potential for serious consequences of serious accidents [2]. Aside from the fact that approximately 40% of the pipelines around the world have reached the end of their design life, when corrosion in the pipelines considered, it would be fair to say that it is possible to have a major accident in the oil industry at any time. The number of incidents may increase in pipelines that have reached the end of their design life, as internal corrosion poses an increasing threat over time [3]. The corrosion cost worldwide is $2.5 trillion, which corresponds to 3.4% of the world's GDP [4]. Considering that Italy ranks eighth among the ten most developed countries in the world with a gross product of $2.5 trillion, the importance of cost reduction can be better understood [5]. The National Society of Corrosion Engineers (NACE) published a research report titled International Measures of Prevention, Application, and Economics of Corrosion Technologies (IMPACT). The report concluded that studies on corrosion prevention will reduce the cost by between 15% and 35% [4]. This is a valuable ratio when dealing with an inevitable phenomenon like corrosion.

When fighting against corrosion there are several methods such as safety in design in the

* Corresponding author: altinten@gazi.edu.tr
Received: 19.10.2022, Accepted: 28.02.2023

industry, choosing the right material, strengthening the material, changing the ambient conditions (inhibitor addition, reducing the temperature and speed), cathodic and anodic protection, coating, modeling of corrosion damage, development of environmentally friendly economical corrosion protective materials like chromium despite its toxic, carcinogenic health effect [6] and coatings. Modeling operation conditions and accelerated corrosion tests in the laboratory environment may help to predict estimation of the remaining time to the major repair or replacement of equipment/material.

As a result of developing industry conditions and increasing needs, modeling prevention of corrosion. Despite the magnitude of corrosion is a very effective method for the corrosion cost, it can be concluded that scientific studies on corrosion prevention are quite limited, except for high-risk sectors such as aviation and the fuel oil industry. *European Union (EU) Major Accident Reporting System (eMARS)* database stated that 20 percent of the 137 major refinery incidents, that occurred since 1984 have been caused by corrosion [7]. When the accidents caused by corrosion in the oil industry are considered, as seen in Figure 1, pipelines take the first place in the equipment list covering the most frequent accidents [8].

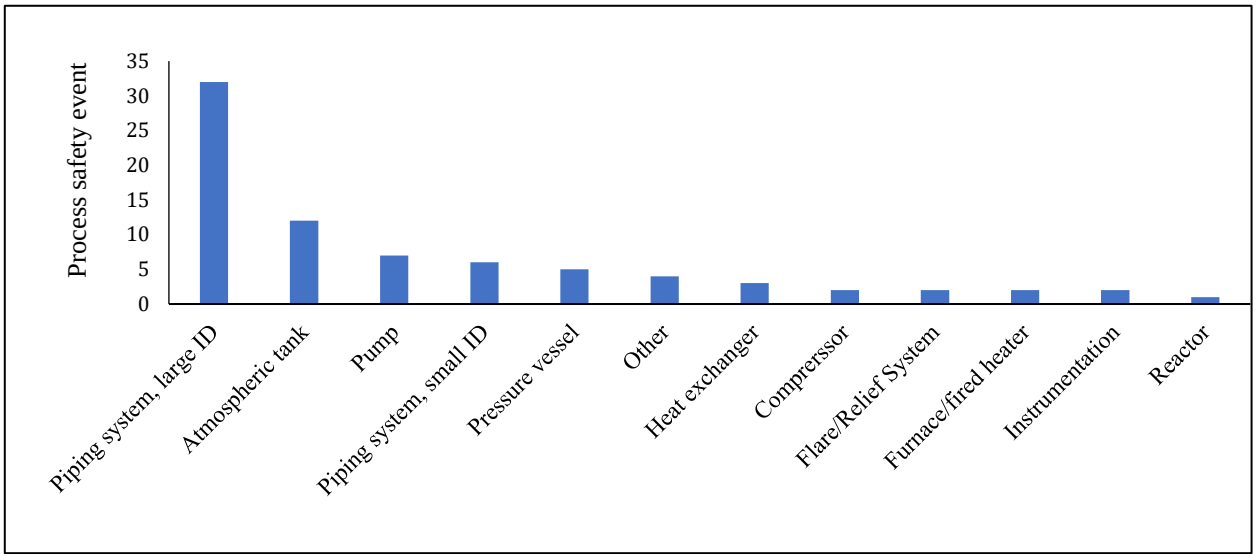

Figure 1. The number of process safety events (Tier 1) by equipment, redrawn from reference, redrawn.

Corrosion occurs both inside and outside of oil subsea pipelines, although the most intense corrosion occurs outside of the pipe, internal corrosion has gained importance since it is related to the design life. Internal corrosion involves high risk due to the nature of the transported materials, the presence of water, and dissolved gases such as CO_2 and H_2S. Crude oil is not corrosive, but they cause corrosion when electrolytes such as water are present in the environment [9]. The most common types of corrosion are organic acid, H2S, The use of large-diameter, thin-walled pipes in pipeline transportation to meet the rapidly growing demand for oil and gas resources has also increased the risk of high pressure operations. However, undersea oil transportation poses a serious threat of corrosion due to the difficult operating conditions. The Pipeline and Hazardous Materials Safety Administration (PHMSA) of the United States Department of Transportation (USDOT) stated 18% of major accidents in the United States of America (USA) between 1988 and 2008 were due to corrosion of the equipment [1]. Accidents such as Flixborough, (the UK, 1974), Berre l'Etang (France, 1988), Kallo (Belgium, 2005) and Gironde (France, 2007) highlight the potential for serious consequences of serious accidents [2].

Aside from the fact that approximately 40% of the pipelines around the world have reached the end of their design life, when corrosion in the pipelines considered, it would be fair to say that it is possible to have a major accident in the oil industry at any time. The O_2-induced corrosion, and sweet

corrosion (CO_2 corrosion) [10], [11]. As a result of developing industry conditions and increasing needs, modeling of corrosion damage emerges as a very effective method in the prevention of corrosion. To obtain a more accurate estimation rate for CO_2 [11]. Despite all these developments, corrosion rate prediction still exists as a problem to be solved for industries with high operational risk.

Although many papers studied NORSOK M506, the exact difference between experiment and mathematical modeling is still unknown. In this study, corrosion rate calculation was performed with the NORSOK M 506 model developed for modeling CO_2 corrosion and compared with the data collected with Nešić, Solvi and Enerhaug's (1995) experimental study [12]. With this approach, it is aimed to determine the difference between the experimental and mathematical corrosion rate estimation for high operational risk processes.

2. Material and Method

2.1. Nešić, Solvi and Enerhaug's experiment

In this study, the data from the experimental study [12] conducted by Nešić, Solvi and Enerhaug in 1995 were used. The corrosion rate was monitored using corrosion polarization resistance (LPR), potentio-dynamic scavenging and electrochemical impedance techniques. The research was intended to see how flow affected carbon dioxide corrosion in the lack of protective surface films. It has been trying to come up with solutions to the problems associated with the transportation of the oil and gas industry. Nešić et al., 1995 studied temperature, pH, and velocity effect on corrosion, a wide range of parameters ranging from laminar flow to highly turbulent flow were studied in test sections consisting of rotating cylinders and pipes: Temperature T=20-80°C, pH=4.0-6.0, partial pressure of CO_2 P_{CO_2} =1 bar (100 kPa) and partial pressure of H_2S P_{H_2S}=0 bar, velocity v=0-13 m/s, [NaCl]=1%, [HAc]=0 ppm, [Fe^{+2}]<1 ppm. The experiments are repeated several times, replicated and derived from LPR measurements confirmed by weight loss measurements. The test dataset used in theoretical calculation from the experiment was shown in Table 1 [12].

Table 1. Test dataset used in theoretical calculation from Nešić et al. 1995.

Parameter	Value
Test solution	Ionized water, CO_2 gas weighted 1% NaCl
Temperature (°C)	20, 50, 80
pH	4, 5, 6
CO_2 partial pressure (bar)	1
Flow rate (m/s)	2-12

2.2 NORSOK CO_2 corrosion model

The Norwegian petroleum industry created the standard NORSOK M 506 model to calculate the corrosion rate caused by CO_2 in hydrocarbon production and processing systems. The CO_2 corrosion rate at a place with temperature T is calculated using the NORSOK M 506 model. To make an ideal and safe design in multi-phase turbulent flow in subsea oil pipelines, the effects of operating parameters on pressure gradient, water cut and flow model should be investigated. In most experimental approaches, studies that can fully address these issues are limited. The model was created from the data obtained during the calibrating of the De Waard model [12], [13]. It allows the corrosion rate to be determined at temperatures between 5-150°C. The model revealed that the corrosion rate along the pipeline always decreases.

The model results were validated and verified by the experimental data. The model is made up of three empirical equations that calculate the corrosion rate in mm/year depending on the temperature range. Equation (1) is as the following [14].

$$CR_T = K_T \times f_{CO_2}^{0.62} \times \left(\frac{\tau}{19}\right)^{0.146+0.0324\ log(f_{CO_2})} \mathrm{x} f(pH)_T \quad (1)$$

CR_T, rate of corrosion in mm/year; K_T, the equilibrium constant at temperature T; f_{CO_2}, fugacity in bar; τ, shear stress Pa, pH-dependent function $f(pH)_T$ at temperature. K_T is a linear variable and changes depending on the temperature, presented in Table 2, T is the temperature in Celsius [14].

Table 2. Variation of K_T with temperature.

T (°C)	K_T	T (°C)	K_T
5	0.42	80	9.949
15	1.59	90	6.250
20	4.762	120	7.770
40	8.927	150	5.203
60	10.695		

The fugacity of CO_2 decreases with increasing temperature. Since pressure drops throughout the pipeline and due to high dependence on the system pressure (P), the fugacity diminishes with distance while the partial pressure (P_{CO2}) is assumed to be constant. The fugacity f_{CO2} in the NORSOK model, is calculated by following equations (2) and (3) [14].

$$f_{CO_2} = a \times P_{CO_2} \quad (2)$$

$$P_{CO_2} = CO_2\% \times P \quad (3)$$

In equations (2) and (3), f_{CO_2} is CO_2 fugacity, a fugacity constant, and P_{CO2} CO_2 partial pressure In equation (4) and (5) T_k is the temperature in Kelvin. The fugacity constant varies according to the pressure value [14]:

$$a = 10^{P(0.0031-1.4/T_k)} \text{ P}\leq 250 \text{ bar (25 000 000 Pa)} \quad (4)$$

$$a = 10^{250(0.0031-1.4/T_k)} \text{ P}>250 \text{ bar (25 000 000 Pa)} \quad (5)$$

pH is critical for corrosion calculation. In NORSOK M 506 corrosion model, variables in Table 3 are used to calculate pH effect ($f(pH)_T$) between temperature of 5-80°C [14]. For higher temperatures (90, 120, and 150°C) pH function is divided into three different pH ranges as shown in Table 4 [14].

Table 3. Equations for pH effect $f(pH)_T$ calculation.

T / pH	$3.5 \leq pH < 4.6$	$4.6 \leq pH < 6.5$
5	$f(pH) = 2.0676 - (0.2309 \times pH)$	$f(pH) = 4.342 - (1.051 \times pH)(0.0708 \times pH^2)$
15	$f(pH) = 2.0676 - (0.2309 \times pH)$	$f(pH) = 4.986 - (1.191 \times pH) + 0.0708 \times pH^2)$
20	$f(pH) = 2.0676 - (0.2309 \times pH)$	$f(pH) = 5.1885 - (1.2353 \times pH) + (0.0708 \times pH^2)$
40	$f(pH) = 2.0676 - (0.2309 \times pH)$	$f(pH) = 5.1885 - (1.2353 \times pH) + (0.0708 \times pH^2)$
60	f(pH) = 1.836 − (0.1818 × pH)	$f(pH) = 15.444 - (6.1291 \times pH) + (0.8204 \times pH^2) - (0.0371 \times pH^3)$
80	$f(pH) = 2.6727 - (0.3636 \times pH)$	$f(pH) = 331.68 \times e^{(-1.2618 \times pH)}$

Table 4. pH effect function for higher temperature.

T	pH	$f(pH)$
90	3.5 ≤ pH < 4.57	$f(pH) = 3.1355 - (0.4673 \times pH)$
90	4.57 ≤ pH ≤ 5.62	$f(pH) = 21254 \times e^{(-2.1811 \times pH)}$
90	5.62≤ pH ≤ 6.5	$f(pH) = 0.4014 - (0.0538 \times pH)$
120	3.5≤ pH < 4.3	$f(pH) = 1.5375 - (0.125 \times pH)$
120	4.3 ≤ pH < 5	$f(pH) = 5.9757 - (1.157 \times pH)$
120	5 ≤ pH ≤ 6.5	$f(pH) = 0.546125 - (0.071225 \times pH)$
150	3.5 ≤ pH < 3.8	$f(pH) = 1$
150	3.8 ≤ pH < 5	$f(pH) = 17.634 - (7.0945 \times pH) + (0.715 \times pH^2)$
150	5 ≤ pH ≤ 6.5	$f(pH) = 0.037$

The model calculates the mean shear stress (τ) on the walls of straight pipe sections at medium to high superficial velocities of either the liquid or gas velocities. This shear stress is used to calculate the corrosion rate in the pipe. If there are any obstacles or other geometrical changes in the flow, the shear stress will be higher than what is calculated by the computer program. Additionally, different flow regimes and obstacles may generate shear stress fluctuations where the shear stress peaks may be considerably higher than the average shear stress.

If the shear stress is high, this may cause mesa attacks, with corrosion rates significantly higher than what is estimated by the model [14].

$$\tau = 0.5 \times \rho_m \times f \times U_m^2 \quad (6)$$

In equations (6), f is friction factor, ρ_m mixture density (kg/m^3) U_m mixture velocity (m/s) [14]. In this study only one phase used, so no need to calculate mixture properties.

3. Results and Discussion

The data obtained from the experimental study was based on static conditions and also the shear stress was found by theoretical calculation in equation (6) by making some assumptions. In the mathematical modeling, the experimental conditions presented in Table 5 were taken into account.

Table 5. Test parameters in used NORSOK M 506 module.

Case	P_H	T (°C)	P_{CO_2} (bar)	V (m/s)
Case 1-8	4	20	1	2, 3, 4, 5, 6, 7, 10, 12
Case 9-16	5	20	1	2, 3, 4, 5, 6, 7, 10, 12
Case 17-24	6	20	1	2, 3, 4, 5, 6, 7, 10, 12
Case 25-32	4	50	1	2, 3, 4, 5, 6, 7, 10, 12
Case 33-40	4	80	1	2, 3, 4, 5, 6, 7, 10, 12

As a result of the theoretically calculated CO_2 corrosion rate, it is determined that 5.08 mm thinning would occur per year under these conditions. In the experiment, it is determined that corrosion rate would be 1.33 mm. However, NORSOK M 506 predicted four times higher for this case. Then the same calculations were repeated on 40 cases. The effects of flow rate, pH, and temperature on corrosion rate are explored in this section.

3.1 Effect of pH and flow rate

As mentioned earlier, in the experimental study all 40 cases were carried out with the assumption of the stable velocity. Then shear stresses were calculated according to this assumption. In this paper, the calculated shear stress values were used also for the mathematical modeling of CO_2 corrosion with NORSOK M 506 for comparison. To show flow rate and pH effects on corrosion rate, the researchers made measurements at different pH values. In Figure 2 the experimental study was compared with the mathematical model. The experimental results were shown in the dotted lines and the theoretical results were in the solid lines (Figure 2).

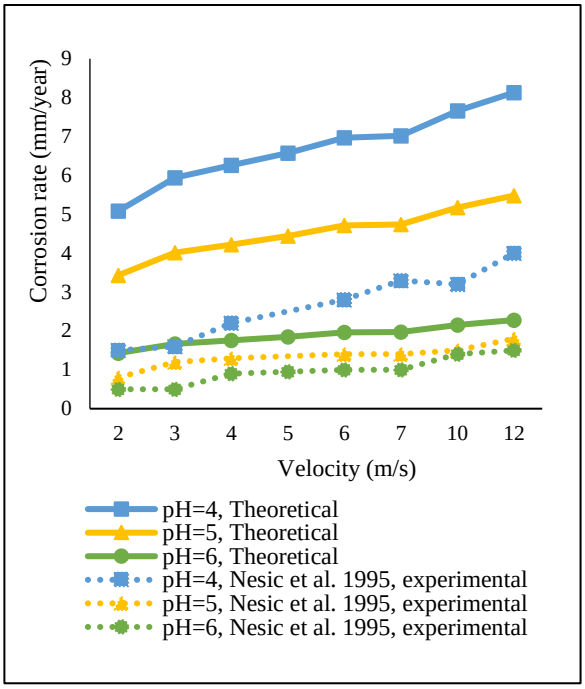

Figure 2. The effect of flow rate on corrosion rate at different pH values, comparison of values calculated with NORSOK, and experimental data from Nešić et al., 1995.
T=20 °C, P_{CO_2} = 1 bar, P_{total} =1 bar, pH=4.0-6.0, v=2-12 m/s.

As shown in Figure 2, the flow rate effect was greater in the mathematical model compared to the experiment. The same tendency was detected in the theoretical results also, the corrosion rate increased as the flow rate increased. This was more apparent at higher velocities, corrosion rate increased rapidly after flow rate v=7-12 m/s. However, this was the case when the solution pH was low. At higher pH values, the corrosion rate acceleration tendency was lower. The corrosion rate increased as the pH value decreased, but this increase was not rapid at high pH.

At high velocity conditions a more significant decrease is determined with increasing pH. In the mathematical model, as in the experiment, the fastest increase was observed at pH 4. While corrosion progresses rapidly to the metal surface during low pH, the corrosion rate decreases at moderate pH due to the partially protective feature of the protective film. At higher pH values, most minerals are insoluble and calcium carbonates build up on the surface and form a protective film, decreasing the corrosion rate [9], [13].

The theoretical results obtained with NORSOK M 506 were compared with the experimental results at v=2 and 4 m/s velocities for the effect of pH and velocity values at different temperatures (20 and

50°C). The results are given in Figure 3. There is no experimental data for pH=5 and 6 at temperatures 50 and 80°C. For this reason, at 50°C only theoretical results obtained from the NORSOK model were used in Figure 3. As expected, the values calculated with the NORSOK M 506 turned out to be higher when compared to the experimental data, the difference turns to be lower at high pH values, and temperature effects also decreased. As seen in Figure 3, the higher the pH value, the more consistent the experimental results of the NORSOK M 506 model. As expected the values calculated with the NORSOK M 506 turned out to be higher when compared to the experimental data, the difference turns to be lower at high pH values, and temperature effects also decreased. As seen in Figure 3, the higher the pH value, the more consistent the experimental results of the NORSOK M 506 model are.

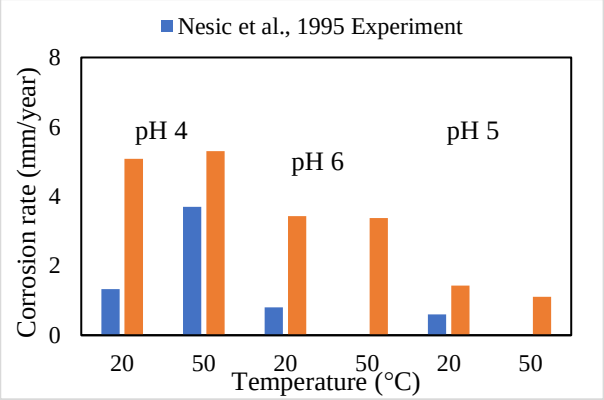

Figure 3. The variation of corrosion rate with pH at different temperatures, comparison of theoretical and experimental results from Nešić et al. 1995.
T =20, 50°C, P_{CO2} =1 bar, P_{total} =1 bar, pH=4.0-6.0, v=2, 4 m/s.

3.2 Effect of temperature

Since all physicochemical processes related to corrosion accelerate with temperature, the rate of corrosion increases with temperature [9], [13]. The rate of corrosion, increased as the temperature increased. Results are shown in Figure 4. The dots in solid lines are shown theoretical calculation, and the dots in dotted lines are shown experimental results.

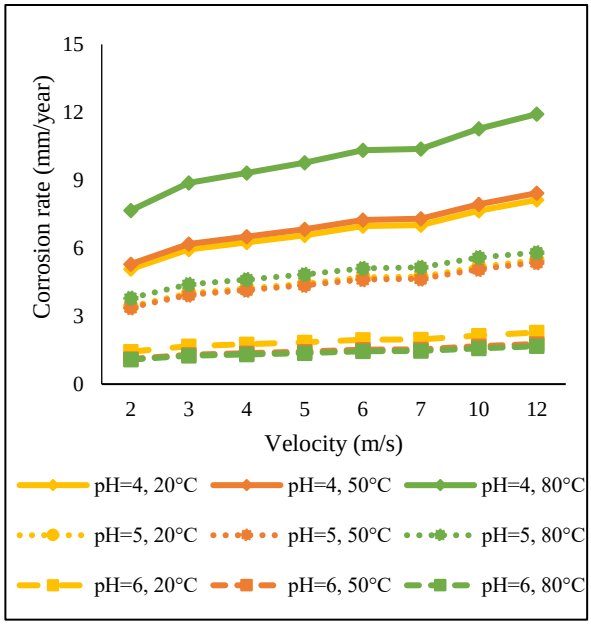

Figure 4. The effect of flow rate on corrosion rate, calculated by NORSOK, at different pH and temperature values.
T =20-80°C, P_{CO_2} = 1 bar, P_{total}=1 bar, pH=4.0-6.0, v=2-12 m/s.

As it is seen in Figure 4, the increase in corrosion rate is remarkable at high temperatures and low pH values in the mathematical model. In these conditions the effect of flow rate is more sensitive. At higher pH values, the effect of the flow rate decreased regardless of temperature. When corrosion rate is considered, although the effect of temperature was evident, the effect of pH is more dominant. After a 10 m/s flow rate, for a temperature of 20 and 80°C, pH 4, the increase in the corrosion rate is remarkable, but at pH 5 the difference between 20 and 80°C exceeding a flow rate of 10 m/s, was almost six-fold. Note that at high pH 6, the corrosion rate did not change much with temperature, while the effect of temperature increased as the pH decreased, however, the increase in the corrosion rate after 50°C was remarkable. Comparison with the model and the experimental study is shown in Figure 5. The effect of temperature was compared only at pH 4 because of a lack of experimental data. The dots in solid lines showed theoretical calculations, and the dots in dotted lines showed experimental results.

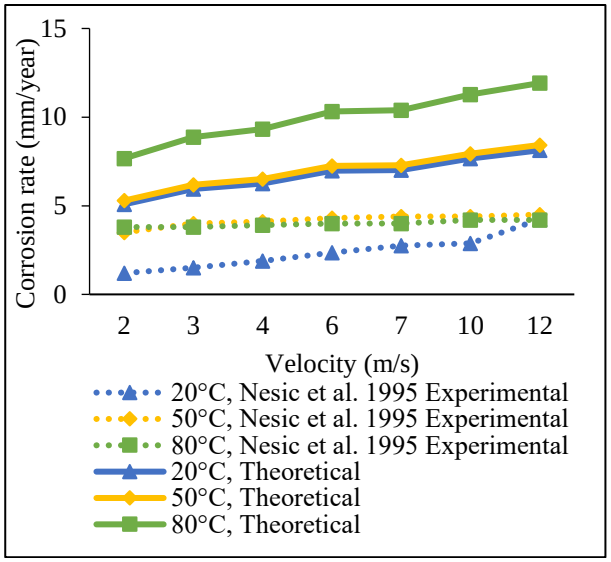

Figure 5. Comparison of theoretical results from NORSOK and experimental results from Nešić et al. 1995 about temperature effect on the rate of corrosion at various velocities.
T=20, 50, 80°C, P_{CO_2}=1 bar, P_{total}=1 bar, pH=4.0, v=2-12 m/s.

As seen in Figure 5, contrary to a sharp increase in corrosion rate at low temperatures in experimental study corrosion rate and flow rate increase with increasing temperature in the numerical model. And also the effect of the flow decreases at high temperatures in experimental study. In the NORSOK numerical model, the increase in corrosion rate with temperature has a higher acceleration after 50°C. For the determination of the difference between mathematical modeling and experimental study on CO_2 corrosion, a comparison was made using the cases given in Figure 6. T = 20°C, P_{CO2}=1 bar, P_{total} =1 bar, pH= 6.0, v=2-12 m/s.

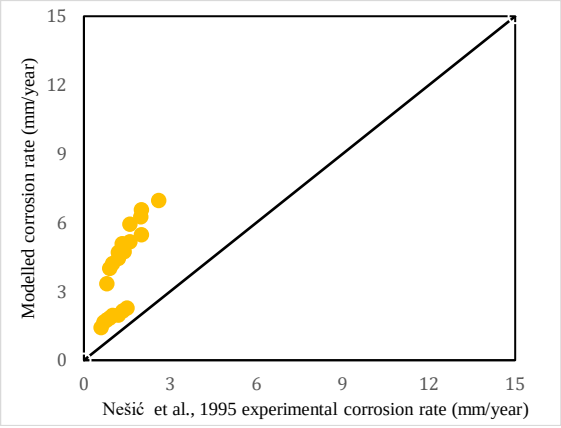

Figure 6. Comparison of the modeled corrosion rates by NORSOK with that obtained from Nešić et al., 1995 experimental study.

Although NORSOK M 506 shows a more conservative approach, except for extreme values the model has a moderately fit. At the extreme values of pH and temperature, there was a variance, however, it is acceptable because of the measurement errors in the experiment. As a result, the theoretical model has an acceptable correspondence reached and the differences are determined also more datasets could be produced in different conditions in comparison to the experimental study.

4. Conclusion and Suggestions

In this paper, the rate of CO_2 corrosion calculation was performed with the NORSOK M 506 model and the results are compared with the data collected with Nešić, Solvi and Enerhaug's (1995) experimental study and led to the following conclusions:

1. The flow rate effect was greater in the mathematical model compared to the experiment, and the corrosion rate increased as the flow rate increased. This was more apparent at higher velocities. Corrosion rate increased rapidly after flow rate v=7-12 m/s. However, this is the case when the solution pH is low. At higher pH, the corrosion rate acceleration tendency was lower.
2. At high velocity, a more significant decrease is determined with increasing pH. The fastest increase is observed at pH 4. While corrosion progresses rapidly to the metal surface during low pH, the corrosion rate decreases at moderate pH due to the partially protective feature of the protective film.
3. Experimental results at v=2 and 4 m/s velocities for the effect of pH and velocity values at different temperatures (20 and 50°C) are compared. As expected, the values calculated with the NORSOK M 506 turned out to be higher when compared to the experimental data. The higher the pH value, the more consistent the experimental results of the NORSOK M 506 model are.
4. At higher pH values, the effect of the flow rate decreased regardless of temperature. When corrosion rate is considered, although the effect of temperature was evident, the effect of pH is more dominant. After a 10 m/s flow rate, for a temperature of 20 and 80°C, pH 4, the increase in corrosion rate is remarkable, but at pH 5 the difference between 20 and 80°C exceeding a flow rate of 10 m/s, was almost six-fold.

In general, the level of corrosion rate increased with temperature and decreased with pH. Heating speeds up all the physicochemical processes causing corrosion and a lower pH indicates a higher concentration of corrosive H^+ ions. In extremes, like the lowest and highest temperature/pH combination, there is a certain variance. The NORSOK model is not tailored to suit a specific data set, but rather calibrated to optimum performance across a wide variety of operating parameters. Eliminating discrepancies is rather challenging. The researchers found that even tiny amounts of contamination steaming from contents are harmful and can lead to erroneous measurements. It was observed that there were contaminating metals on the sample surface at the experiment. It was discovered that the most serious contamination came from the rubber hose connecting the pumps to the lines, which is an active agent for corrosion inhibition. The performance of the NORSOK M 506 was therefore reasonable and in most cases acceptable and calculates nearly six times higher than experimental studies.

Contributions of the Authors

In the study carried out, Author 1 in the formation of the idea, design, and literature review, compilation, and interpretation of the results; Author 2 contributed to the evaluation, presentation, and analysis of the results obtained, in the titles of spelling and checking the article in terms of content.

Conflict of Interest Statement

There is no conflict of interest between the authors.

Statement of Research and Publication Ethics

There is no need for an ethics committee approval in the prepared article

References

[1] Pipeline and Hazardous Materials Safety Administration, Office of Pipeline Safety, "*Pipeline Integrity Management* in High Consequence Areas (*Gas Transmission Pipelines*)" Pipeline and Hazardous Materials Safety Administration, PHMSA Integrity Management Program. Under Delivery Order, DTRS56-02-D-70036. [Online]. Available: https://www.phmsa.dot.gov. [Accessed: Apr. 20, 2018].

[2] Analysis, Research, and Information on Accidents, Accident report number 5611, 163, 30934, 32675. Analysis, Research, and Information on Accidents ARIA database. [Online]. Available: https://www.aria.developpement-durable.gouv.fr. [Accessed: Apr. 20, 2018].

[3] C.R.F. Azevedo, "Failure Analysis of the crude oil pipeline." Engineering Failure Analysis., vol.14, 2007, pp. 978–994.

[4] National Association of *Corrosion* Engineers, "International Measures of Prevention, Application, and Economics of Corrosion Technologies (IMPACT)", the National Association of *Corrosion* Engineers NACE. [Online]. Available: http://impact.nace.org/documents. [Accessed: Apr. 22, 2018].

[5] *International Monetary Fund*, "World Economic Outlook Database", *International Monetary Fund*, *World Economic Outlook* IMF WEO. [Online]. Available: https://www.imf.org/en/Publications. [Accessed: Apr. 12, 2022].

[6] A. Kara, E. Demirbel, "Kinetic, Isotherm and Thermodynamic Analysis on Adsorption of Cr(VI) Ions from Aqueous Solutions by Synthesis and Characterization of Magnetic-Poly(divinylbenzene-vinylimidazole) Microbeads. Journal of Water Air Soil Pollution, vol. 223, pp. 2387–2403, 2012.

[7] JRC - MAHB, "Corrosion-Related Accidents in Petroleum Refineries: Lessons Learned from Accidents in EU and OECD Countries" The *JRC's* Major Accident Hazards Bureau. Luxembourg European Commission Public Office, 2013, pp. 2-3.

[8] Environmental Science for European Refining, "European downstream oil industry safety performance Statistical summary of reported incidents – 2018" Environmental Science for European Refining, CONCAWE Prepared for the Concawe Safety Management Group by C. Banner (Science Executive, Safety Management Group, Concawe) C. Davidson (Anything Hosted Ltd.). [Online]. Available: https://www.concawe.eu. [Accessed: May. 10, 2022].

[9] H. H. Uglig, Uhlig's Corrosion Handbook. 3rd ed., review R.W. Revie, New York, Wiley, 2001.
[10] M.B. Kermani, D. Harrop, “The Impact of Corrosion on Oil and Gas Industry.” SPE Production Facilities, vol.11, pp 186–190, 1996.
[11] S. Nesić, J. Postlethwaite, and M. Vrhovac, “CO_2 Corrosion of Carbon Steel - from Mechanistic to Empirical Modelling”, Journal of Corrosion Reviews, vol. 15, pp. 211-240, 1997.
[12] S. Nešić, G.T. Solvi, and J. Enerhaug, "Comparison of the Rotating Cylinder and Pipe Flow Tests for Flow-Sensitive Carbon Dioxide Corrosion" Journal of Corrosion, vol.51 (10), pp.773–786, 1995.
[13] S. Nešić, A. Kahyarian, and Y. S. Choi, "Implementation of a Comprehensive Mechanistic Prediction Model of Mild Steel Corrosion in Multiphase Oil and Gas Pipelines.” Journal of Corrosion, vol.75 (3), pp. 274-291, December 2018.
[14] NORSOK (2005). CO_2 Corrosion Rate Calculation Model. 2nd revision.

Bitlis Eren Üniversitesi Fen Bilimleri Dergisi
BİTLİS EREN UNIVERSITY JOURNAL OF SCIENCE
ISSN: 2147-3129/e-ISSN: 2147-3188
VOLUME: 12 NO: 1 PAGE: 93-96 YEAR: 2023
DOI:10.17798/bitlisfen.1192052

Automorphisms with Lie Ideals and (η,ξ)-derivations

Evrim GÜVEN*

Kocaeli University, Faculty of Arts and Science, Department of Mathematics, KOCAELİ, (ORCID: 0000-0001-5256-4447)

Keywords: Prime Ring, Lie Ideal, Derivation, Automorphism.

Abstract
In this study, prime ring S, which has been accepted to have charS≠2 characteristic, has been supposed also to have automorphism of η, ξ, κ, ε, λ and μ. It was aimed to examine the derivatives and automorphisms that provide certain identities on the Lie ideals of prime rings.

1. Introduction

Let S be a ring, η, ξ, κ, ε, λ and μ are mappings of S, and Z(S) denotes the center of S. By a prime ring, we mean a ring S in which for every x,y∈S, xSy=(0) implies x=0 or y=0. The operation of xy-yx, represented by the [x, y] commutator, and the operation of xy+yx, represented by the (x, y) commutator, has been selected from the elements of S. Morever [x, y]η,ξ=xη(y)-ξ(y)x and (x, y])η,ξ=xη(y)+ξ(y)x for x,y∈S. For subsets M, N of S, let [M, N]η,ξ ={[x, y]η,ξ |x∈M and y∈N}.

The set K that satisfies the [S, K]⊂K property is called a Lie ideal of S. Here, the set K is an additive subset of the ring S.

If $S = \left\{ \begin{pmatrix} x & y \\ z & t \end{pmatrix} \middle| x,y,z,t \in \mathbb{Z} \right\}$ and $K = \left\{ \begin{pmatrix} x & y \\ z & x \end{pmatrix} \middle| x,y,z \in \mathbb{Z} \right\}$ then K is a Lie ideal of S.

For all x,y∈S when both conditions F(x+y)=F(x)+F(y) and F(xy)=F(x)y+xF(y) is satisfied, F mapping is called as a derivation of S. For all x,y∈S, when the condition of d(xy)=d(x)η (y)+ ξ(x)d(y), d mapping is called as a (η,ξ)-derivation of S.

Over the years, the commutativity of the rings has been investigated under certain derivative conditions. Various generalizations have been made in examining the commutativity of a ring under these conditions.On the other hand, these conditions, which are considered as d ordinary derivations, are examined in α - derivation, (σ,τ)-derivation.

On the other hand, the commutativity of the ring was investigated by taking its ideal and (or) Lie ideal instead of the R ring in these conditions. In 1970, I. N. Herstein verified the R ring is commutative if the condition [d(S), d(S)]⊆ Z(S) is met, where S is a prime ring and its characteristic is different from the value of 2. d is a derivative of the S ring and is nonzero [5]. In the same work, I.N. Herstein also proved that the S ring is commutative if the d(S) condition is satisfied. Later, J. Bergen et al. proved that K⊂Z(S) when d(K)⊂Z(S) and K is the Lie ideal of S that has a value other than 2 and S is a ring that is prime [6].

In this study, prime ring S, which has been accepted to have charS≠2 characteristic, has been supposed also to have automorphism of η, ξ, κ, ε, λ and μ. Z(S) will denote the centre of an associative ring and Cη,ξ={c∈S|cη(r)=ξ(r)c, ∀ r∈S}. The equations frequently used in this study have been given below:

[xy,z]η,ξ=x[y,z]η,ξ-[x,ξ(z)]y=x[y,η(z)]+[x, z]η,ξy

[x,yz]η,ξ=ξ(y)[x, z]η,ξ+[x, y]η,ξη(z)

(xy,z)η,ξ=x(y,z)η,ξ-[x,ξ(z)]y=x[y,η(z)]+(x, z)η,ξy

(x,yz)η,ξ=ξ(y)(x, z)η,ξ+[x, y]η,ξη(z)=ξ(y)[x, z]η,ξ+(x, y)η,ξη(z)

* Corresponding author:evrim@kocaeli.edu.tr
Received: 21.10.2022, Accepted: 27.02.2023

2. Preliminary

Lemma 1 [1] If the condition $[[J, a]_{\eta,\xi}, b]_{\kappa,\varepsilon}=0$ is provided for the nonzero J ideal of the S ring, then $[\xi(a), \varepsilon(b)]$ becomes zero.

Lemma 2 [1] If the condition $[[a, J]_{\eta,\xi},b]_{\kappa,\varepsilon}=0$ is provided for the nonzero J ideal of the S ring, then $[a, \xi^{-1}\varepsilon(b)]_{\eta,\xi}$ becomes zero or $b\in Z(S)$.

Lemma 3 [2] If the condition $d(K)\subset C_{\kappa,\varepsilon}(S)$ is provided for the nonzero Lie ideal K of the S ring and d is a nonzero (η, ξ)-derivation of S, then $K\subset Z(S)$.

Lemma 4 [2] If the condition $d(K)\subset C_{\kappa,\varepsilon}(S)$ is provided for the nonzero Lie ideal K of the S ring then $a\in C_{\kappa,\varepsilon}(S)$ or $K\subset Z(S)$.

Lemma 5 [2] Let $d:S\rightarrow S$ be a nonzero (η, ξ)-derivation and $a\in S$. If J is an ideal of S that is nonzero such that $[d(J), a]_{\kappa,\varepsilon}\subset C_{\kappa,\varepsilon}$ (S) then $a\in Z(S)$ or $\{d\xi^{-1}\varepsilon(a)=0$ and $d\eta^{-1}\kappa(a)=0\}$.

Lemma 6 [2] If the condition $[a, d(J)]_{\kappa,\varepsilon}\subset C_{\lambda,\mu}(S)$ is provided for the nonzero ideal J of the S ring and d is a nonzero (η, ξ)-derivation of S and also $d\eta=\eta d$, $d\xi=\xi d$ then $a\in C_{\kappa,\varepsilon}(S)$ or S is commutative.

3. Automorphisms with Lie İdeals

Let $T:S\rightarrow S$ be a nonzero automorphism and $d:S\rightarrow S$ a nonzero (η, ξ)-derivation. Let K be a nonzero Lie ideal of S. In this note, some results on automorphisms and Lie ideals of prime rings have been proven as seen below.

Lemma 7 Let T be an automorphism of S and $a, b\in S$.
(i) $a\in C_{\kappa T,\varepsilon T}(S)$ if and only if $a\in C_{\kappa,\varepsilon}(S)$,
(ii) $T(a)\in C_{\kappa,\varepsilon}(S) \Leftrightarrow a\in C_{T^{-1}\kappa,\ T^{-1}\varepsilon}(S)$,
(iii) $[T(a),b]_{\kappa,\varepsilon}\in C_{\lambda,\mu}(S) \Leftrightarrow [a, b]_{T^{-1}\kappa,T^{-1}\varepsilon}\in C_{T^{-1}\lambda,T^{-1}\mu}(S)$,
(iv) If $C_{\lambda,\mu}(S)=0$ then $C_{T\lambda,T\mu}(S)=0$,
(v) $(T(a), b)_{\kappa,\varepsilon}\in C_{\lambda,\mu}(S) \Leftrightarrow (a, b)_{T^{-1}\kappa,T^{-1}\varepsilon}\in C_{T^{-1}\lambda,T^{-1}\mu}(S)$.

Proof
(i) $a\in C_{\kappa T,\varepsilon T}(S)\Leftrightarrow a\kappa T(r)-\varepsilon T(r)a=0,\forall r\in S\Leftrightarrow [a, T(S)]_{\kappa,\varepsilon}=0 \Leftrightarrow [a, S]_{\kappa,\varepsilon}=0 \Leftrightarrow a\in C_{\kappa,\varepsilon}(S)$.
(ii) $T(a)\in C_{\kappa,\varepsilon}(S \Leftrightarrow T(a)\kappa(r)-\varepsilon(r)T(a)=0,\forall r\in S$
$\Leftrightarrow T(aT^{-1}\kappa(r)-T^{-1}\varepsilon(r)a)=0 ,\forall r\in S$
$\Leftrightarrow aT^{-1}\kappa(r)-T^{-1}\varepsilon(r)a=0,\forall r\in S$
$\Leftrightarrow a\in C_{T^{-1}\kappa,T^{-1}\varepsilon}(S)$
(iii) $T(a)\kappa(b)- \varepsilon(b)T(a)\in C_{\lambda,\mu}(S)$
$\Leftrightarrow T(aT^{-1}\kappa(b)-T^{-1}\varepsilon(b)a)\in C_{\lambda,\mu}(S)$
$\Leftrightarrow (aT^{-1}\kappa(b)-T^{-1}\varepsilon(b)a)\in C_{T^{-1}\lambda,T^{-1}\mu}(S)$ by (ii)
$\Leftrightarrow [a, b]_{T^{-1}\kappa,\ T^{-1}\varepsilon}\in C_{T^{-1}\lambda,\ T^{-1}\mu}(S)$.
(iv) Let $C_{\lambda,\mu}(S)=0$. Then for any $a\in C_{T\lambda T,\mu}(S)$, $aT\lambda(r)-T\mu(r)a=0,\forall r\in S$
$\Rightarrow T^{-1}(a)\lambda(r)-\mu(r)T^{-1}(a)=0,\forall r\in S$
$\Rightarrow [T^{-1}(a), S]_{\lambda,\mu}=0 \Rightarrow T^{-1}(a)\in C_{\lambda,\mu}(S)=0$
$\Rightarrow T^{-1}(a)=0$
$\Rightarrow a=0$
$\Rightarrow C_{T\lambda,T\mu}(S)=0$.
On the other hand let $C_{T\lambda T,\mu}(S)=0$. Then we get $b\in C_{\lambda,\mu}(S)$
$\Rightarrow b\lambda(r)-\mu(r)b=0,\forall r\in S$
$\Rightarrow T(b)T\lambda(r)-T\mu(r)T(b))=0,\forall r\in S$
$\Rightarrow T(b)\in C_{T\lambda,T\mu}(S)=0$
$\Rightarrow T(b)=0$
$\Rightarrow b=0$
$\Rightarrow C_{\lambda,\mu}(S)=0$
(v) $(T(a), b)_{\kappa,\varepsilon}\in C_{\lambda,\mu}(S)$
$\Leftrightarrow T(a)\kappa(b)+\varepsilon(b)T(a)\in C_{\lambda,\mu}(S)$
$\Leftrightarrow T(aT^{-1}\kappa(b)+T^{-1}\varepsilon(b)a)\in C_{\lambda,\mu}(S)$
$\Leftrightarrow (aT^{-1}\kappa(b)+T^{-1}\varepsilon(b)a)\in C_{T^{-1}\lambda,T^{-1}\mu}(S)$ by (ii)
$\Leftrightarrow (a, b)_{T^{-1}\kappa,T^{-1}\varepsilon}\in C_{T^{-1}\lambda,T^{-1}\mu}(S)$.

Lemma 8 Let $T:S\rightarrow S$ be a ring automorphism and a, b, $c\in S$. The equations that have been given below are true.
(i) $T[a, b]_{\kappa,\varepsilon}=[T(a), b]_{T\kappa,T\varepsilon,}$
(ii) $T(C_{\kappa,\varepsilon}(S))=C_{T\kappa,T\varepsilon}(S)$,
(iii) $[a, T(b)]_{\kappa,\varepsilon}=[a, b]_{\kappa T,\varepsilon T,}$
(iv) $(a, T(b))_{\kappa,\varepsilon}=(a, b)_{\kappa T,\varepsilon T,}$
(v) $(T(a), b)_{\kappa,\varepsilon}=T(a, b)_{T^{-1}\kappa,T^{-1}\varepsilon.}$

Proof
(i) $T[a, b]_{\kappa,\varepsilon}=T(a\kappa(b)-\varepsilon(b)a)=T(a)T\kappa(b)-T\varepsilon(b)T(a)=[T(a), b]_{T\kappa,T\varepsilon.}$
(ii) $x\in T(C_{\kappa,\varepsilon}(S))$
$\Rightarrow x=T(a), a\in C_{\kappa,\varepsilon}(S)$
$\Rightarrow T^{-1}(x)=a, a\in C_{\kappa,\varepsilon}(S)$
$\Rightarrow T^{-1}(x)\in C_{\kappa,\varepsilon}(S)$
If we use (iii), $x\in C_{T\kappa,T\varepsilon}(S)$. On the other hand if $y\in C_{T\kappa,T\varepsilon}(S)$ then $yT\kappa(r)-T\varepsilon(r)y=0,\forall r\in S$. Since T is an automorphism then we get $T^{-1}(y)\kappa(r)-\varepsilon(r)T^{-1}(y)=0,\forall r\in S$. That is $T^{-1}(y)\in C_{\kappa,\varepsilon}(S)$. This implies that $y\in T(C_{\kappa,\varepsilon}(S))$.
(iii) $[a, T(b)]_{\kappa,\varepsilon}=a\kappa T(b)- \varepsilon T(b)a=[a, b]_{\kappa T,\varepsilon T}$
(iv) $(a, T(b))_{\kappa,\varepsilon}=a\kappa T(b)+\varepsilon T(b)a=(a, b)_{\kappa T,\varepsilon T}$
(v) $(T(a), b)_{\kappa,\varepsilon}=T(a)\kappa(b)+\varepsilon(b)T(a)=T(aT^{-1}\kappa(b)+T^{-1}\varepsilon(b)a)=T(a, b)_{T^{-1}\kappa,T^{-1}\varepsilon}$

Theorem 1 Let T be an automorphism of a ring S. Let K be a Lie ideal of S.
(i) If $T(K)\subset C_{\kappa,\varepsilon}(S)$ then $K\subset Z(S)$.
(ii) If $[T(K), a]_{\kappa,\varepsilon}\subset C_{\lambda,\mu}(S)$ then $a\in Z(S)$ or $K\subset Z(S)$.
(iii) If $[a, T(K)]_{\kappa,\varepsilon}\subset C_{\lambda,\mu}(S)$ then $a\in C_{\kappa,\varepsilon}(S)$ or $K\subset Z(S)$.
(iv) If $(T(K), a)_{\kappa,\varepsilon}=0$ then $a\in Z(S)$ or $K\subset Z(S)$.
(v) If $(a, T(K))_{\kappa,\varepsilon}=0$ then $a\in Z(S)$ or $K\subset Z(S)$.

Proof
(i) Let $T(K)\subset C_{\kappa,\varepsilon}(S)$.Then $K\subset C_{\lambda,\mu}(S)$ is obtained by Lemma 7 (ii), where $\lambda=T^{-1}\kappa$ and $\mu=T^{-1}\varepsilon$. That is $[K, S]_{\lambda,\mu}=0$.Here $T^{-1}\kappa$ and $T^{-1}\varepsilon$ are automorphisms of S and $[[S, K], S]_{\lambda,\mu}=0$. If we use Lemma 1 then we obtain that $[K, \varepsilon(S)]=0$ and so $K\subset Z(S)$.
(ii) Let K is a Lie ideal of R and $[T(K), a]_{\kappa,\varepsilon}\subset C_{\lambda,\mu}(S)$. Then we have $[K, a]_{T^{-1}\kappa,\ T^{-1}\varepsilon}\subset C_{T^{-1}\lambda,T^{-1}\mu}(S)$ by Lemma 7 (iii). This gives that $[[S, K], a]_{\phi,\theta}\subset C_{\lambda,\mu}(S)$, where $\phi=T^{-1}\kappa$ and $\theta=T^{-1}\varepsilon$ and so $[d(S), a]_{\phi,\theta}\subset C_{\lambda,\mu}(S)$ where $d(r)=[v, r]$, $\forall r\in S$ is a derivation. If we use Lemma 5 then we obtain that $a\in Z(R)$ or $d\phi^{-1}\mu(a)=0$. That is $a\in Z(S)$ or $[v, \phi^{-1}\mu(a)]=0$. Considering same argument for all $v\in K$ we get

$a\in Z(S)$ or $[K,\phi^{-1}\mu(a)]=0$.

If $[K, \phi^{-1}\mu(a)]=0$ then $a\in Z(S)$ or $K\subset Z(S)$ by [1].
(iii) If $[a,T(K)]_{\kappa,\varepsilon}\subset C_{\lambda,\mu}(S)$ then we have $[a, K]_{\kappa,\varepsilon}\subset C_{\lambda T,\mu T}(S)$ by Lemma 8 (iii). This means that $a\in C_{\kappa,\varepsilon}(S)$ or $K\subset Z(S)$ by Lemma 4.
(iv) Let $(T(K), a)_{\kappa,\varepsilon}=0$. Then we have $(K, a)_{T^{-1}\kappa,T^{-1}\varepsilon}=0$ by Lemma 8 (v). This means that $a\in Z(S)$ or $K\subset Z(S)$ by Corollary 2.
(v) $(a,T(K))_{\kappa,\varepsilon}=0$ implies that $(a, K)_{\kappa T,\varepsilon T}=0$ by Lemma 8 (iv). Considering Corollary 2 we obtain that $a\in C_{\kappa T,\varepsilon T}(S)$ or $K\subset Z(S)$. If $a\in C_{\kappa T,\varepsilon T}(S)$ then $[a, K]_{\kappa T,\varepsilon T}=0$ and so $a\in C_{\kappa,\varepsilon}(S)$ or $K\subset Z(S)$ by Lemma 4.

Corollary 1 Let $T:S\to S$ be a nonzero automorphism and K, L nonzero Lie ideals of S.
(i) If $[T(K), K]_{\kappa,\varepsilon}\subset C_{\lambda,\mu}(S)$ then $K\subset Z(S)$.
(ii) If $[K, T(K)]_{\kappa,\varepsilon}\subset C_{\lambda,\mu}(S)$ then $K\subset C_{\kappa,\varepsilon}(S)$ or $K\subset Z(S)$.
(iii) If $[K, L]_{\kappa,\varepsilon}\subset C_{\lambda,\mu}(S)$ then $K\subset Z(S)$ or $L\subset Z(S)$.

Proof
(i) Let $[T(K), K]_{\kappa,\varepsilon}\subset C_{\lambda,\mu}(S)$. Then we have $T(K)\subset C_{\kappa,\varepsilon}$ or $K\subset Z(S)$ by Lemma 4. If $T(K)\subset C_{\kappa,\varepsilon}(S)$ then $K\subset Z(S)$ by Theorem 1 (i).
(ii) $[K, T(K)]_{\kappa,\varepsilon}\subset C_{\lambda,\mu}(S)\Rightarrow K\subset C_{\kappa,\varepsilon}(S)$ or $K\subset Z(S)$ by Theorem 1(iii). If $K\subset C_{\kappa,\varepsilon}(S)$ then $[[S, K], S]_{\kappa,\varepsilon}=0$. This implies that $[K, \xi^{-1}\varepsilon(S)]=0$ by Lemma 1. That is $K\subset Z(S)$.
(iii) If we use Lemma 4 then we have $K\subset C_{\kappa,\varepsilon}(S)$ or $L\subset Z(S)$. Considering in the proof of the (ii) we get $K\subset Z(S)$ or $L\subset Z(S)$.

Theorem 2 Let K be a nonzero Lie ideal of S. Let $T:S\to S$ be a nonzero automorphism and $d:S\to S$ a nonzero (η, ξ)-derivation.
(i) If $[T(K), d(K)]_{\kappa,\varepsilon}\subset C_{\lambda,\mu}(S)$ then $K\subset Z(S)$.
(ii) If $[d(K), T(K)]_{\kappa,\varepsilon}\subset C_{\lambda,\mu}(S)$ then $K\subset Z(S)$.
(iii) If $(T(K), d(K))_{\kappa,\varepsilon}=0$ then $K\subset Z(S)$.
(iv) If $(d(K), T(K))_{\kappa,\varepsilon}=0$ then $K\subset Z(S)$.

Proof
(i) Let $[T(K), d(K)]_{\kappa,\varepsilon}\subset C_{\lambda,\mu}(S)$. Then we have $d(K)\subset Z(S)$ or $K\subset Z(S)$ by Theorem 1 (ii). Considering [4] we obtain that, $K\subset Z(S)$ finally.
(ii) Let $[d(K), T(K)]_{\kappa,\varepsilon}\subset C_{\lambda,\mu}(S)$. Using Theorem 1 (iii), we clearly see $K\subset Z(S)$.
(iii) Let $(T(K), d(K))_{\kappa,\varepsilon}=0$. In this case, we get $d(K)\subset Z(S)$ or $K\subset Z(S)$ by Theorem 1 (ii). Considering [4] we obtain that, $K\subset Z(S)$.
(iv) Suppose that $(d(K), T(K))_{\kappa,\varepsilon}=0$. Then we have $K\subset Z(S)$ by Theorem 1(ii).

4. Conclusion and Suggestions

In this paper, in the section named "Automorphisms with Lie İdeals", algebraic identities, including derivations on the prime ring, discuss, and we obtain derivations information.

We also examine algebraic identities involving derivations on the Lie ideal of the prime ring. We prove that the Lie ideal, which satisfies the identities discussed in the section, is obtained in the center of the prime ring.

In future studies, the hypotheses in this study can examine using homoderivations or semiderivations of the prime ring.

Acknowledgment

The author is thankful to the referee for his/her valuable suggestions.

Statement of Research and Publication Ethics

The study is complied with research and publication ethics

References

[1] E. Güven, K. Kaya and M. Soytürk, "Some Results on (σ,τ)-Lie Ideals", *Math. J. Okayama Univ*., 49, pp. 59-64, 2007.

[2] E. Güven, "Lie Ideals in Prime Rings with (σ,τ)−Derivation", *Int.journal of Algebra*, pp. 857-862, 2009.

[3] N. Aydın and K. Kaya, "Some Generalization in Prime Rings with (σ, τ)−Derivations", *Doğa-Tr.J.of Mathematics, 16* , pp. 169-176, 1992.

[4] H. Kandamar and K. Kaya, "Lie Ideals and (σ,τ)−Derivation in Prime Rings", *Hacettepe Bull.Nat. Sci. Eng*,.Vol. 21, pp. 29-33, 1992.

[5] I. N. Herstein, "On the Lie Structure of an Assosiative Rings", *Journal of Algebra*, 14, pp. 561-571, 1970.

[6] J. Bergen, I. N. Herstein and J. W. Kerr, "Lie Ideals and Derivation of Prime Rings", *Journal of Algebra*, 71, pp. 259-267, 1981.

[7] E. C. Posner, "Derivations in prime rings", *Proc. Amer. Math. Soc.*, 8, pp. 1093–1100, 1957.

[8] J. H. Mayne, "Centralizing automorphisms of prime rings", *Canad. Math. Bull.*, 19, 1976, no. 1, pp. 113–115, 1976.

[9] A. Rezi and M. Allam, "Techniques in array processing by means of transformations, " in *Control and Dynamic Systems*, Vol. 69, Multidemsional Systems, C. T. Leondes, Ed. San Diego: Academic Press, 1995, pp. 133-180.

[10] O. B. R. Strimpel, "Computer graphics," in *McGraw-Hill Encyclopedia of Science and Technology*, 8th ed., Vol. 4. New York: McGraw-Hill, 1997, pp. 279-283.

[11] W.-K. Chen, *Linear Networks and Systems*. Belmont, CA: Wadsworth, 1993, pp. 123-135.

[12] J. Vukman, "Identities wıth derivations and automorphisms on semiprime rings", *IJMMS*, 2005, pp. 1031-1038.

Bitlis Eren Üniversitesi Fen Bilimleri Dergisi
BİTLİS EREN UNIVERSITY JOURNAL OF SCIENCE
ISSN: 2147-3129/e-ISSN: 2147-3188
VOLUME: 12 NO: 1 PAGE: 97-103 YEAR: 2023
DOI:10.17798/bitlisfen.1195035

Effect of UV Aging on the Physical Properties of Polypropylene/Zinc Borate Polymer Composites

Elif ULUTAŞ[1*], Münir TAŞDEMİR[1]

1Marmara University, Technology Faculty,
Department of Metallurgical and Materials Engineering, İSTANBUL
(ORCID: 0000-0001-7753-8878) (ORCID: 0000-0001-8635-7251)

Keywords: Polypropylene, polymer composites, zinc borate, physical properties, UV aging.

Abstract

Plastics, which have a wide range in terms of production methods, have replaced traditional materials because their chemical and physical properties can be changed in the desired direction. The structural changes that occur when functional filler additives are used during production cause improvements in many physical properties of the new plastic. Using boron and boron compounds as additives positively affects the mechanical, thermal, electrical, optical, and physical properties of polymer composites. As it is known, plastics, which are flammable by nature, have a low oxygen index and therefore pose a danger to human life and the environment due to the threat of fire. In this study, the effects of zinc borate, which has flame-retardant properties, on the physical and morphological properties of polypropylene were investigated. In addition, the effects of aging were investigated by UV aging at 70°C for 15 and 30 days on the polymer composites produced in the study. PP/ZnB polymer composites with different concentrations (5, 10, 15, and 20%) were produced in a twin screw extruder to provide a more homogeneous mixture. Test samples of polymer composites, which were granulated with the help of a grinder, were successfully molded in the injection machine. Limit oxygen index (LOI) to examine the flaming behavior of the samples, heat deflection temperature (HDT), Vicat softening point, melt flow index (MFI) test to examine the thermal behavior, moisture content, and density test to examine the physical properties of the samples were performed. The microstructure examination of polymer composites was made with a scanning electron microscope (SEM).

1. Introduction

Polymers have a wide usage area in daily life and industry due to their easy processing, low cost, high corrosion resistance, lightweight, and many other advantages [1]. Despite these positive features, when used in the industry, they often do not give the desired feature and do not meet expectations. In such cases, fillers and additives of various sizes are added to alleviate the limitations in their mechanical and physical properties and to expand the application area [2]. Nowadays, inorganic particle reinforcement of organic polymers has become an area of great interest to improve the properties of polymers [3], [4], [5].

Although it has many application areas around the world, polypropylene is easily flammable due to its chemical composition, namely the C, H, and O elements it contains [6], [7]. However, they pose a serious threat to both the human body and the environment due to dripping and burning [8].

Polymers such as polypropylene emit toxic gases and smoke during their combustion, which causes a serious problem for the production and use of polymers. It is also known that aromatic polymers are less flammable than aliphatic polymers. Flame retardants are added during polymerization or processing to improve the burning behavior of polymers. Due to their low cost and ease of use,

* Corresponding author: elif.ulutas@marmara.edu.tr
Received: 26.10.2022 , Accepted: 03.02.2023

additive-type flame retardants are preferred more in industrial applications [9], [10], [11], [12], [13]. Especially zinc borate is among the boron components in the studies carried out for flame prevention and flame retardant in polymers. Zinc borate, which has smoke and afterglow suppressant properties, is used for both halogenated and non-halogenated polymers since they have a flame-retardant mechanism [14], [15], [16]. It is used to improve fire performance in paints, cables, fabrics, carpets, interior parts of automobiles and airplanes, textiles, paper, and polymeric materials [17], [18], [19], [20]. As a flame retardant and smoke suppressant, zinc borate is widely used in the plastics and electrical industries. Feng et al. [8] study investigated the flame retardancy effect of zinc borate on polypropylene composites. When 1% zinc borate was added to polymer composites, the LOI value increased from 27.1 to 30.7%, and in this case, zinc borate had a positive effect on the flame retardant properties and combustion performance of the composites. Similarly, Qin et al. [20] added zinc borate to the blend obtained by melting LLDPE/EVA mixtures and investigated the flammability and thermal stability behavior of the new mixture. Zinc borate, used as a flame retardant, increased the LOI value of the composites and also improved the UL-94 rating.

In this research article, the effect of zinc borate, which is used as a flame retardant in polymers, on the mechanical, thermal, and morphological properties of polypropylene was investigated. In addition, the effect of UV aging on polymer composites was investigated at 70°C for 0, 15, and 30-day periods. For the production of polymer composites containing zinc borate in different ratios, the melt mixing method in the extruder and the injection forming technique for the production of test samples were successfully applied. LOI was used to examine the flaming behavior of the samples; MFI, HDT, and Vicat softening point tests were used to examine the thermal behavior; and density, moisture content, and density tests were performed to examine the physical behavior of the samples. In addition, the microstructure examination of polymer composites was made with SEM. Then, the properties of the UV applied samples and the untreated samples were compared.

2. Material and Method

The values of PP (Moplen EP 3307) used in the study and supplied by Lyondell Basell are given as density 0.900 g/cm^3, MFI value 15 g/10 min (230°C, 2.16 kg), and thermal distortion temperature (0.45 MPa, unannealed) 95°C. Zinc borate ($ZnHBO_3$), containing B_2O_3 45.0-48.0% and ZnO 37.5-39.0% in its structure, was supplied by Jinan ShiChao Chemical Co., Ltd. (China) and had a specific gravity of 2.72 g/cm^3, particle diameter ≤ 5.0μ.

Table 1. Composition of the PP/ZnB polymer composites formulations.

Groups	Polypropylene (wt%)	ZnB (wt%)
1	100	-
2	95	5
3	90	10
4	85	15
5	80	20

Before polymer composite production, polypropylene, and zinc borate were dried in a vacuum oven at 105°C for 24 hours. Initial mixing of the solid compositions was done in an LB-5601 liquid-solid mixer (The Patterson-Kelley Co., Inc. USA) for 20 minutes. The mixture, which was prepared according to the ratios in Table 1, was mixed at a temperature of 180-220°C at a pressure of 15 bar and a rotation speed of 20 rpm using a Mikrosan brand twin screw extruder (Mikrosan Instrument Inc. Türkiye). As a result of this process of obtaining a homogeneous mixture, PP/ZnB polymer composites were produced. To remove the water from the structure of the composites exposed to water during cooling in extrusion, the drying process was carried out again in the vacuum oven. Then, the injection molding technique was successfully applied between 180-220°C temperatures, 90-100 bar pressure and 20 rpm speed. Moisture, HDT, Vicat softening point, density, MFI and LOI tests were performed on the produced test samples. SEM was used to examine the microstructure of polymer composites. The Devotrans brand test device was used to examine the thermal properties of polymers and for HDT and Vicat softening point tests performed by ISO 75 and ISO 307 standards, respectively. Density determination according to the ISO 2781 standard was made by taking the average of three samples. The MFI test, which allows commenting on the fluidity of the materials, was performed on the Zwick 4100 brand test device by the ISO 1133 standard. Moisture content testing of all mixtures was performed with Kern DBS 60-3 equipment according to the ASTM D6980 standard. LOI testing of all blends was performed with Devotrans LOI equipment according to the ISO 4589 standard. In the Devotrans brand preheated UV test cabinet was used for the UV aging

process, the light distance was set to 50mm and Osram 300W ultra-vitalux lamp type was used.

Figure 1. UV aging of PP/ZnB polymer composites

The fractured surfaces of the PP/ZnB polymer composites were coated to a thickness of 20Å gold-palladium mixture to avoid electrical charging by Polaron SC7640 (high-resolution spray coater) (UK). Microstructure investigation of polymer composites was carried out with a FEI Sirion XL30 FEG brand (Netherlands) SEM device at 20kV acceleration voltage.

3. Results and Discussion

The relationship between the LOI and the percentage of zinc borate in polypropylene polymer composites is shown in Figure 2-A. The inclusion of ZnB in the PP matrix increases the LOI value of the composites. For example, the LOI of the four different samples (5, 10, 15, and 20% wt ZnB, without UV) are measured as 21, 23, 24.3 and 25% respectively. The LOI of pure PP is 17%. In comparison with the LOI of pure PP, the LOI increases by 47% for the composites with a 20% wt ZnB concentration. Similar results are found in the other groups. On the other hand, UV holding time affects the LOI as well. For example, the LOI of PP/ZnB (80/20, without UV), PP/ZnB (80/20, 15 days UV), and PP/ZnB (80/20, 30 days UV), polymer composites are 25, 25.7 and 27% respectively. As the UV holding time increases, the LOI of the composites increases. The relationship between the HDT and the percentage of zinc borate in polypropylene polymer composites is shown in Figure 2-B. The inclusion of ZnB in the PP matrix increases HDT of the composite. For example, the HDT of the four different samples (5, 10, 15 and 20% wt ZnB, without UV) are measured as 101, 103, 105 and 108ºC respectively. The HDT of pure PP is 96ºC. In comparison with the HDT of pure PP, the HDT increases by 13% for the composites with a 20% wt ZnB concentration. Similar results are found in the other groups. On the other hand, UV holding time affects the HDT as well. For example, the HDT of PP/ZnB (80/20, without UV), PP/ZnB (80/20, 15 days UV), and PP/ZnB (80/20, 30 days UV), polymer composites are 108, 124 and 125ºC respectively. As the UV holding time increases, the HDT of the composites also increases. Ersoy and Tasdemir [21] investigated the effects of 5, 10, 15 and 20% zinc borate on the properties of HDPE. According to the results of the HDT test applied to the composites obtained by using a twin screw extruder it was observed that the addition of zinc borate decreased this value.

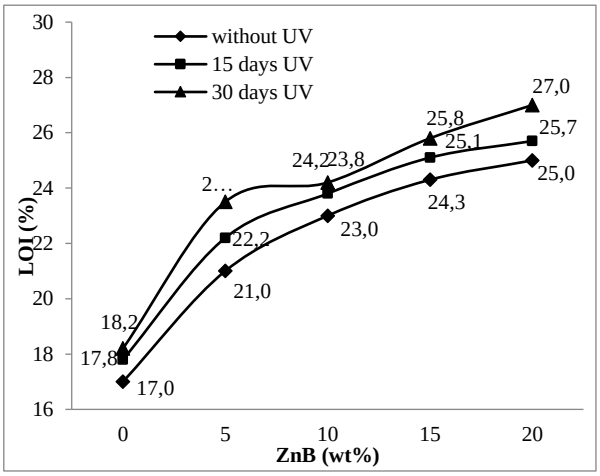

A

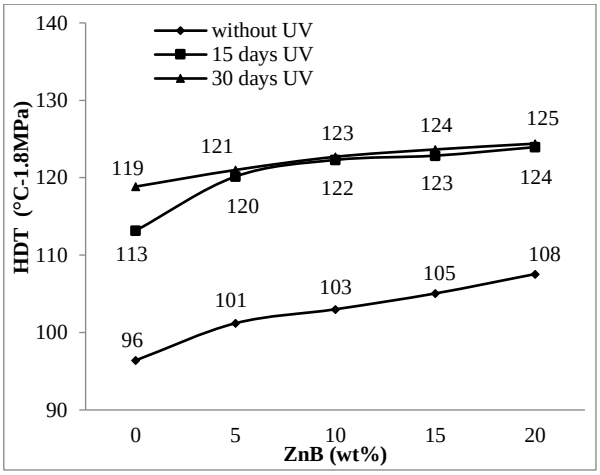

B

Figure 2. LOI and HDT values of the PP/ZnB polymer composites.

The relationship between the Vicat softening point and the percentage of zinc borate in polypropylene polymer composites is shown in Figure 3-A. With the inclusion of ZnB in the PP matrix, the Vicat softening point of the composite is found to be increasing. For example, the Vicat softening points of the four different samples (5, 10, 15 and 20% wt ZnB, without UV) are measured as 139, 140, 141 and 141ºC respectively. The Vicat softening point of pure PP is 138ºC. In comparison

with the Vicat softening point of pure PP, the Vicat softening point increases by 2% for the composites with a 20% wt ZnB concentration. Similar results are found in the other groups. On the other hand, the UV holding time affects the Vicat softening point as well. For example, the Vicat softening point of PP/ZnB (80/20, without UV), PP/ZnB (80/20, 15 days UV), and PP/ZnB (80/20, 30 days UV), polymer composites are 141, 145 and 154ºC respectively. The Vicat softening point of the composites increases by about 9% when the UV holding time is increased. Yerlesen and Tasdemir [22] investigated some properties of the composites obtained by adding zinc borate and zinc oxide at different rates to HDPE. The HDT and Vicat softening point tests have obtained similar results in their study. Depending on the increase in zinc oxide or zinc borate ratio, the HDT and Vicat softening point values of the composites increased.

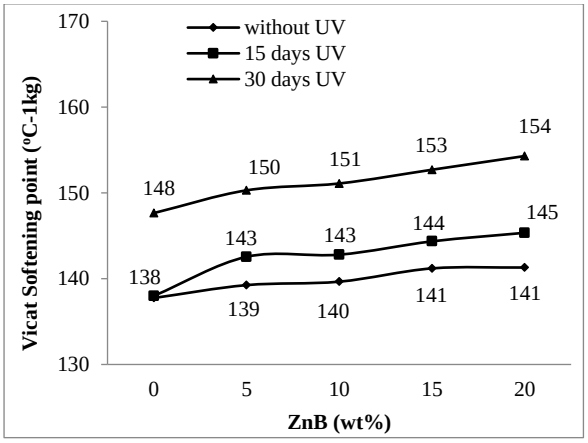

Figure 3. Vicat softening point and moisture content values of the PP/ZnB polymer composites.

The relationship between the moisture content and the percentage of zinc borate in polypropylene polymer composites is shown in Figure 3-B. With the inclusion of ZnB in the PP matrix, the moisture content of the composite is found to be increasing. For example, the moisture contents of the four different samples (5, 10, 15 and 20% wt ZnB, without UV) are measured as 0.96, 1.1, 1.1 and 1.1% respectively. The moisture content of pure PP is 0.95%. In comparison with the moisture content of pure PP, the moisture content increases by 16% for the composites with a 20% wt ZnB concentration. Similar results are found in the other groups. On the other hand, the UV holding time affects the moisture content as well. For example, the moisture contents of PP/ZnB (80/20, without UV), PP/ZnB (80/20, 15 days UV), and PP/ZnB (80/20, 30 days UV), polymer composites are 1.1, 0.77, and 0.75% respectively. As the UV holding time increases, the moisture content of the composites decreases by about 32%.

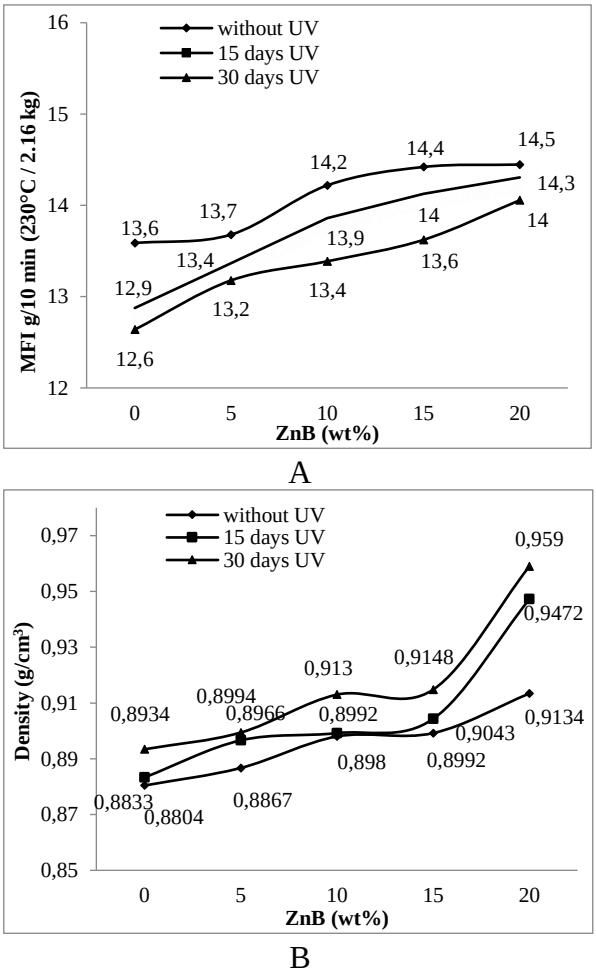

Figure 4. MFI and density values of the PP/ZnB polymer composites.

The relationship between the MFI and the percentage of zinc borate in polypropylene polymer composites is shown in Figure 4. With the inclusion of ZnB in the PP matrix, the MFI of the composite is found to be increasing. For example, the MFI of the four different samples (5, 10, 15 and 20% wt ZnB,

without UV) are measured as 13.7, 14.2, 14.4 and 14.5 (g/10 min) respectively. The MFI of pure PP is 13.6 (g/10 min). In comparison with the MFI of pure PP, the MFI increases by 7% for the composites with a 20% wt ZnB concentration. Similar results are found in the other groups. On the other hand, the UV holding time affects the MFI as well. For example, the MFI of PP/ZnB (80/20, without UV), PP/ZnB (80/20, 15 days UV), and PP/ZnB (80/20, 30 days UV), polymer composites are 14.5, 14.3 and 14 (g/10 min) respectively. When the UV holding time increases the MFI of the composites decreases. Guldas et al. [23] investigated the MFI values of the materials by adding different ratios of zinc borate to the powdered PP material. In the tests performed, it was determined that the MFI value increased due to the increase in temperature and pressure, while the MFI value decreased with the addition of zinc borate. The relationship between the density and the percentage of zinc borate in polypropylene polymer composites is shown in the Figure 4-B. With the inclusion of ZnB in the PP matrix, the density of the composite is found to be increasing. For example, the densities of the four different samples (5, 10, 15 and 20% wt ZnB, without UV) are measured as 0.8867, 0.8980, 0.8992 and 0.9134 g/cm^3 respectively. The density of pure PP is 0.8804 g/cm^3. In comparison with the density of pure PP, the density increases by 4% for the composites with a 20% wt ZnB concentration. Similar results are found in the other groups. On the other hand, the UV holding time affects the density as well. For example, the densities of PP/ZnB (80/20, without UV), PP/ZnB (80/20, 15 days UV), and PP/ZnB (80/20, 30 days UV), polymer composites are 0.9134, 0.9472 and 0.9590 g/cm^3 respectively. When the UV holding time increases, the density of the composites increases. The visuals of the microstructure analysis performed to examine the dispersion of the reinforcement/filling phase in the matrix, given in Figure 6, clearly show the contrast and boundaries between pp and zinc borate. Micrographs show that the zinc borate particles are homogeneously dispersed in the polymer matrix.

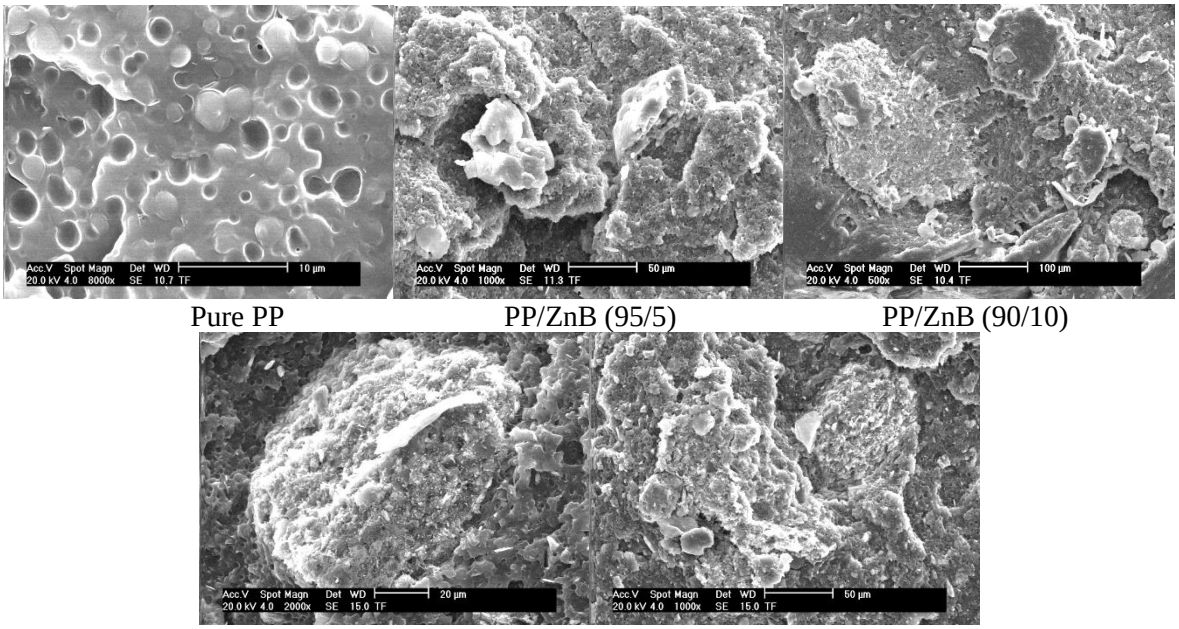

Figure 5. SEM photographs of PP/ZnB polymer composites.

4. Conclusion and Suggestions

The effects of zinc borate and UV holding time on some properties, such as LOI, HDT, Vicat softening point, moisture content, MFI, density, and morphology of PP/ZnB composites, were investigated. Zinc borate and UV holding time have marginal effects on some physical properties such as HDT, and moisture content of the composites. The following results were obtained: The inclusion of ZnB into the PP matrix has a positive effect on the LOI values of the composites. The LOI values of the composite obtained by adding 20% ZnB to pure PP increased by 47%. At the same time, the increase in UV holding time has a similar effect on LOI. With the inclusion of ZnB in the PP matrix, the LOI of the composite is found to be increasing. By adding 20% by weight of ZnB to pure PP, HDT and Vicat

softening point values increase by 13% and 2%, respectively. Similarly, the increase in UV holding time also increases the HDT and Vicat softening points of composites. The inclusion of ZnB in the PP matrix causes an increase in the moisture content and MFI value. The inclusion of 20% ZnB in the polymer matrix increases the MFI of the composite by 7%. In addition, moisture test results show that composites containing 20% ZnB have 16% more moisture absorption capacity compared to pure PP. On the other hand, the UV holding time increases the moisture content, and the MFI of the composites decreases. The micrographs indicate that the zinc borate particulates are homogeneously dispersed on the fractured surfaces of the PP matrix.

References

[1] Guo Y, Ruan K, Shi X, Yang X, Gu J, "Factors affecting thermal conductivities of the polymers and polymer composites: A review," *Composites Science and Technology*, vol. 193, pp. 108134, 2020.

[2] Fu S, Sun Z, Huang P, Li Y, Hu N, "Some basic aspects of polymer nanocomposites: A critical review," *Nano Materials Science*, vol. 1, pp. 2-30, 2019.

[3] Mamunya YP, Davydenko VV, Pissis P, Lebedev EV, "Electrical and thermal conductivity of polymers filled with metal powders," *European Polymer Journal*, vol. 38, no. 9, pp. 1887-1897, 2002.

[4] Mamunya YP, Zois H, Apekis L, Lebedev E V, "Influence of pressure on the electrical conductivity of metal powders used as fillers in polymer composites," *Powder Technology*, vol. 140, no. 1-2, pp. 49-55, 2004.

[5] Zhu K, Schmauder S, "Prediction of the failure properties of short fiber reinforced composites with metal and polymer matrix," *Computational Materials Science*, vol. 28, no. 3-4, pp. 743-748, 2003.

[6] Fontaine G, Bourbigot S, Duquesne S, "Neutralized flame retardant phosphorus agent: Facile synthesis, reaction to fire in PP and synergy with zinc borate," *Polymer Degradation and Stability*, vol. 93, pp. 68-76, 2008.

[7] Younis AA, "Evaluation flammability, mechanical and electrical properties of polypropylene after using zinc borates and montmorillonite," *Journal of Thermoplastic Composite Materials*, vol. 35, no. 2, pp. 1-15, 2019.

[8] Feng C, Zhanga Y, Liang D, Liua S, Chi Z, Xua J, "Influence of zinc borate on the flame retardancy and thermal stability of intumescent flame retardant polypropylene composites," *Journal of Analytical and Applied Pyrolysis*, vol. 115, pp. 224-232, 2015.

[9] Baltaci B, Çakal GO, Bayram G, Eroglu I, Özkar S, "Surfactant modified zinc borate synthesis and its effect on the properties of PET," *Powder Technology*, vol. 244, pp. 38-44, 2013.

[10] Shi X, Xiao Y, Yuan L, Sun J, "Hydrothermal synthesis and characterization of 2D and 3D $4ZnO{\cdot}B_2O_3{\cdot}H_2O$ nano/microstructures with different morphologies," *Powder Technology*, vol. 189, pp. 462-465, 2009.

[11] Ahmad Ramazani SA, Rahimi A, Frounchi M, Radman S, "Investigation of flame retardancy and physical–mechanical properties of zinc borate and aluminum hydroxide propylene composites," *Materials and Design*, vol. 29, pp. 1051-1056, 2008.

[12] Jiang M, Zhang Y, Yu Y,2 Zhang Q, Huang B, Chen Z, Chen T, Jiang J, "Flame retardancy of unsaturated polyester composites with modified ammonium polyphosphate, montmorillonite, and zinc borate," *Journal of Applied Polymer Science*, vol. 136, no. 11, 2019, doi: 47180.

[13] Wang Y, Zhang S, Wu1 X, Lu C, Cai Y, Ma L, Shi G, Yang L, "Effect of montmorillonite on the flame-resistant and mechanical properties of intumescent flame-retardant poly(butylene succinate) composites," *Journal of Thermal Analysis and Calorimetry*, vol. 128, no. 3, pp. 1417-1427, 2017.

[14] Li S, Long B, Wang Z, Tian Y, Zheng Y, Zhang Q, "Synthesis of hydrophobic zinc borate nanoflakes and its effect on flame retardant properties of polyethylene," *Journal of Solid State Chemistry*, vol. 183, pp. 957-962, 2010.

[15] Cui Y, Liu X, Tian Y, Ding N, Wang Z, "Controllable synthesis of three kinds of zinc borates and flame retardant properties in polyurethane foam," *Colloids and Surfaces A: Physicochemical and Engineering Aspects*, vol. 214, pp. 274-280, 2012.

[16] Makhlouf G, Hassan M, Nour M, Abdel-Monem YK, Abdelkhalik A, "Evaluation of fire performance of linear low-density polyethylene containing novel intumescent flame retardant," *Journal of Thermal Analysis and Calorimetry*, vol. 130, pp. 1031-1041, 2017.

[17] Ozkaraca AC, "Flame retardancy effects of zinc borate and nanoclay in abs, and boron compounds in PET," *Middle East Technical University. The Graduate School Of Natural And Applied Sciences*. The degree of master, 2011.

[18] Bölek H, "Production and characterization of zinc borate-polymer nano composites," *Marmara University Institute For Graduate Studies In Pure And Applied Sciences.* The degree of master, 2011.

[19] Ureyen ME, Kaynak E, "Effect of zinc borate on flammability of pet woven fabrics," *Advances in Polymer Technology*, 2019, doi: 7150736.

[20] Qin J, Liu N, Wang N, Li L, He W, Guo J, Chen X, Zhang K, Yu J, "Synergistic effect of modified expanded graphite and zinc borate on the flammability, thermal stability and crystallization behavior of lldpe/eva composites with $Mg(OH)_2$/$Al(OH)_3$," *Polymer Composites*, vol. 40, no. S1, pp. 687-694, 2019.

[21] Ersoy S, Tasdemir M, "Zinc oxide (ZnO), magnesium hydroxide [$Mg(OH)_2$] and calcium carbonate ($CaCO_3$) filled HDPE polymer composites: Mechanical, thermal and morphological properties," *Marmara University Journal of the Graduate School of Natural and Applied Sciences*, vol. 24, no. 4, pp. 93-104, 2012.

[22] Yerlesen U, Tasdemir M, "Effect of zinc oxide and zinc borate on mechanical properties of high density polyethylene," *Romanian Journal Of Materials*, vol. 45, no. 4, pp. 364-369, 2015.

[23] Guldas A, Cankaya A, Gullu A, Guru A, "Determinat on of rheological properties of zinc borate reinforced polypropylene," *Journal of the Faculty of Engineering and Architecture of Gazi University*, vol. 29, no. 2, pp. 227-234, 2014.

Bitlis Eren Üniversitesi Fen Bilimleri Dergisi
BİTLİS EREN UNIVERSITY JOURNAL OF SCIENCE
ISSN: 2147-3129/e-ISSN: 2147-3188
VOLUME: 12 NO: 1 PAGE: 104-114 YEAR: 2023
DOI:10.17798/bitlisfen.1195607

Snow Avalanche Risk Assessment using GIS-Based AHP for Bitlis Province

M. Cihan AYDIN[1], Elif S. BİRİNCİOĞLU[1], Ali Emre ULU[1*], Aydın BÜYÜKSARAÇ[2]

[1]*Bitlis Eren University, Department of Civil Engineering, Bitlis, Türkiye*
[2]*Çan Vocational School, Çanakkale Onsekiz Mart University, Çanakkale, Türkiye*

(ORCID: 0000-0002-5477-1033) (ORCID: 0000-0002-4317-9392) (ORCID: 0000-0001-7499-3891) (ORCID: 0000-0002-4279-4158)

Keywords: Snow Avalanche, AHP, GIS, Risk Assessment, Bitlis Province.

Abstract

Bitlis province, located in the Eastern Anatolia of Turkey, is the region with the highest snowfall in the country. Due to its highland and steep structure, the region is at high avalanche risk. The assessment of snow avalanche risks is critical in modern disaster management. In this study, the avalanche risks were assessed using the analytical hierarchy process (AHP), which is an effective multiple criteria decision-making method. The avalanche risk was considered to depend on many factors, such as temperature, slope, elevation, aspect, land use, soil, lithology, precipitation, distance to the fault and population. The outputs obtained from the method were mapped in the GIS environment, and thus the avalanche risks of the region were determined. According to the results, especially the highland and steep southern parts and the two volcanic mountain foothills in the region were evaluated as high risk. The study results were validated by comparing past avalanche events and some previous research.

1. Introduction

Avalanche events are generally seen in rough, mountainous, and steeply sloping lands where there is no vegetation. Avalanches occur as a result of the snow mass accumulating in layers on the valley slopes sliding down the slope rapidly as a result of a first movement that starts with the effect of internal or external forces [1]. Physical factors such as topographic structure, earthquakes, vegetation features, gravity, the amount of snow mass, and human factors are effective in avalanche formation [2]. The main reason for avalanche formation is that the weak layer under the snow cover loses its ability to carry the load arising from the cover.

Pre-disaster risk assessments play an important role in minimizing disaster damage. For this reason, many methods have been presented in the literature for the hazard and risk assessment of natural disasters such as avalanches. Natural disaster risks depend on many factors, such as the meteorological, environmental, topographical, and human characteristics of the region. Therefore, multiple decision-making methods are often used to assess avalanche-like risks. One of these methods is the Analytical Hierarchy Process (AHP). Gret-Regamey and Straub [3] used a combined procedure of a Bayesian network with GIS for avalanche risk assessment in their study area (Davos, Switzerland), performing explicit modelling of all relevant parameters. Nefeslioglu et al. [4] used a modified analytical hierarchy process to assess avalanche hazards. They concluded that this method is a powerful tool for decision support problems, especially in complex situations. Kumar et al. [5] performed an avalanche susceptibility study for Nubra Valley using AHP with a multi-criteria decision method based GIS environment. The most important factors affecting the avalanche were considered to be slope, elevation, aspect, curvature, terrain roughness, and ground cover. Varol [6] reported that meteorological, environmental,

*Corresponding author: aeulu@beu.edu.tr
Received: 27.10.2022, Accepted: 12.12.2022

topographical, and human factors should be taken into account in order to better evaluate and predict the snow avalanche, which is one of the hydrogeological disasters. Their effort is on the susceptibility maps of avalanche potential in the Uzungol in northeastern Turkey using some methods such as the Frequency Ratio (Fr), Analytical Hierarchy Process (AHP), and Fuzzy-AHP (FAHP). In the study, five criteria, namely slope, aspect, elevation, curvature, and vegetation, were applied to the model. Naseryu and Kalkan [7] performed an avalanche risk assessment using GIS based AHP for Van province, neighboring Bitlis in Turkey. In their study, they considered some basic parameters for avalanches, i.e., elevation, slope, aspect, curvature, and land cover. Elmastaş and Özcanli [8] determined the avalanche disaster areas of Bitlis using the GIS environment, and then analyzed the avalanche risk depending on only slope criterion. Göksu and Leventeli [9] obtained an avalanche sensitivity map of Bitlis province by combining elevation, gradient, aspect, curvature and land use maps with the help of GIS technique, and controlled their results by remote sensing method. However, in these last two studies, no multiple decision-making method was applied. Another study on the study area was conducted by Selçuk [10]. This study pointed out that most avalanche fatalities in Turkey have occurred in Bitlis Province, and within the scope of this study, the sensitivity and accuracy analysis for the avalanche hazard in Bitlis province was evaluated by using geographic information system (GIS) based multi-criteria decision analysis (MCDA). Five decision criteria, such as elevation, slope, aspect, vegetation density, and land use, were taken into account in the study, but some other important criteria affecting avalanche events, such as seismicity, lithology, population, precipitation/snowfall, temperature, and soil, were not considered. Flood [11], landslide [12], and rockfall [13] risk analyses were also performed for the same region using a GIS-based AHP.

As the brief literature review above indicates, multi-criteria decision making methods are a very powerful tool for assessing natural disaster risks such as avalanches when combined with GIS techniques. A few studies have been conducted on the avalanche risk assessment of the province of Bitlis, which is at high avalanche risk. In these previous studies, it was seen that either the number of criteria was not sufficient or any multiple decision-making technique was not applied. Many of these studies also failed to account for risk factors such as population. In this study, avalanche risk assessment for Bitlis province, which is the place with the highest snowfall in Turkey, was carried out using a GIS-based AHP method with a large data set.

2. Material and Method

2.1. Study Area

The region most exposed to avalanche events in Turkey is the Eastern Anatolia Region due to its barren and mountainous terrain with heavy snowfall [14]. As seen in Fig. 1, the maximum snow depth in Turkey is concentrated in the province of Bitlis, which is our study area. Also in Fig. 2, the second place where avalanches are most common in this region is Bitlis after Bingöl. The average elevation of Bitlis province, considered the application area in this study, is 1500 m above sea level, and its area is 6707 km^2. The area, which has a volcanic structure, is also located in a seismically active region. In terms of climate characteristics, Bitlis and its surroundings are a transition between the harsh continental climate of Eastern Anatolia and the Mediterranean climate. The region's location at the crossroads of hot and flat Southeastern Anatolia and cold and mountainous Eastern Anatolia provides a microclimatic feature. The humid air originating from Lake Van, which is the largest soda lake in the world at 1650 m elevation in the east, is another important factor in the heavy snowfall in the region. In the region, between 1959 and 2020, the lowest temperature in the region was -24.1 °C in January, and the highest temperature was 34.3 °C in July. The annual average temperature is given as 9.0 ^oC. The maximum snow depth between these years was measured as 250 cm. The total precipitation falling on the area is 1047 mm on average. The total precipitation falling on the area is 1047 mm on average [15]. About 50% of this precipitation is in the form of snowfall in winter and partly in spring and autumn. Fig. 3 depicts monthly snow covered days (a) and monthly average snow depths (b) observed at two measurement stations over many years. According to these graphs, the region is covered with snow for 6 months of the year and the snow thickness reaches 250 cm on average in January, February and March. These climatic factors are the main reasons for the frequent avalanche events in the region. In addition, the mountainous and steep topography and tectonic structure of the region are other important factors that increase the avalanche risk.

In the province of Bitlis, 265 avalanche events were reported between 1950 and 2019. Bitlis province is the region with the highest amount of snowfall in Turkey. Terzi [16] showed that Bitlis is the first in Turkey with a 50-year period ground snow load of 4.6 kN/m^2 (Fig. 4). Aydin and Isık [17] explained the reason for this as a micro-climatic feature display in which climate transitions occur in

the region, and they reported 11.87 kN/m^2 the ground snow loads with the 50-year return period depending on the meteorological measurements and their statistical analyses. Based on these results, they warned that the current standards and codes do not reflect the actual snow loads. According to Elmastaş and Özcanli [8,] approximately 50% of Bitlis province is at risk of avalanche. Ekinci et al. [18] assessed the natural disaster diversity of Bitlis Province using Fine-Kinney method. They found that the settlements, especially in the rugged southern parts of the area (Hizan, Mutki and Tatvan towns together with Bitlis center) are at high risk. According to Göksu and Leventeli [9], Bitlis is the province where avalanche disasters occur the most in Turkey. The numbers of avalanche events that occurred in the study area between 1960 and 2020 are given in Fig. 5.

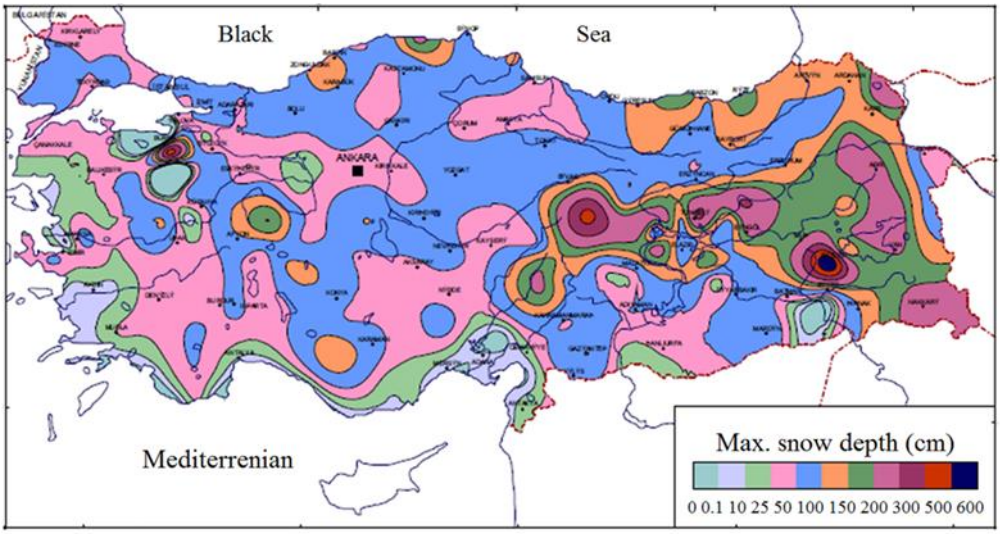

Figure 1. Map of maximum snow depth in Turkey [19]

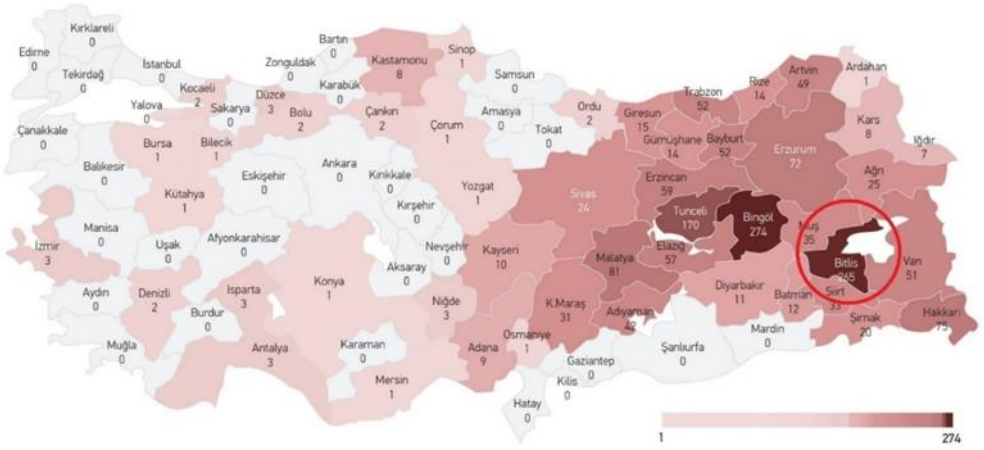

Figure 2. Location of application area and avalanche events in Turkey between 1950 and 2019 [20]

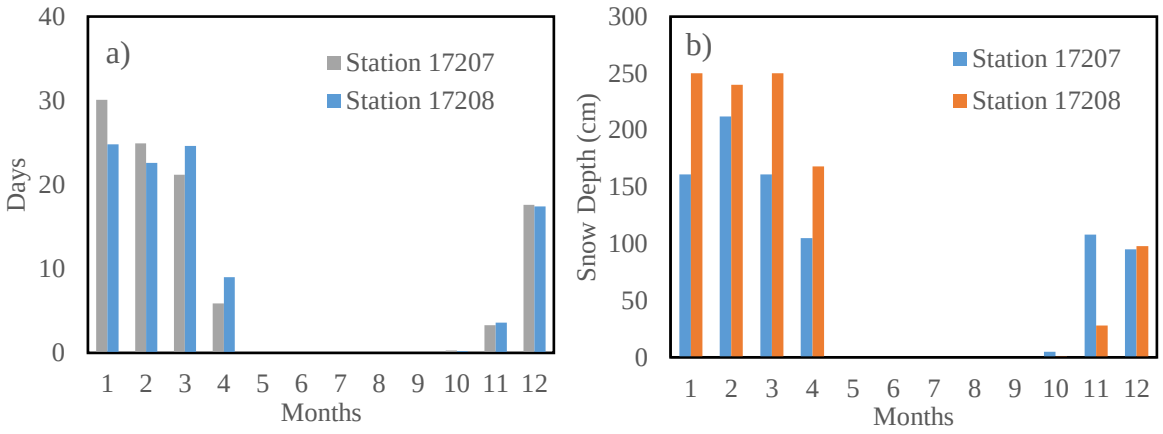

Figure 3. For long years; a) monthly number of days with snow cover, b) monthly depth of snow cover (cm)

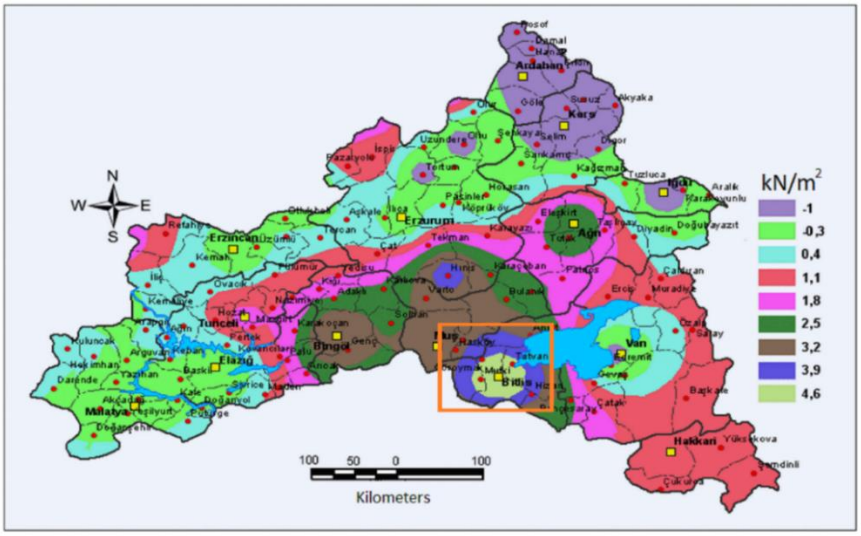

Figure 4. Normalized ground snow loads with the 50-year return period in the Eastern Anatolia region in Turkey [16]

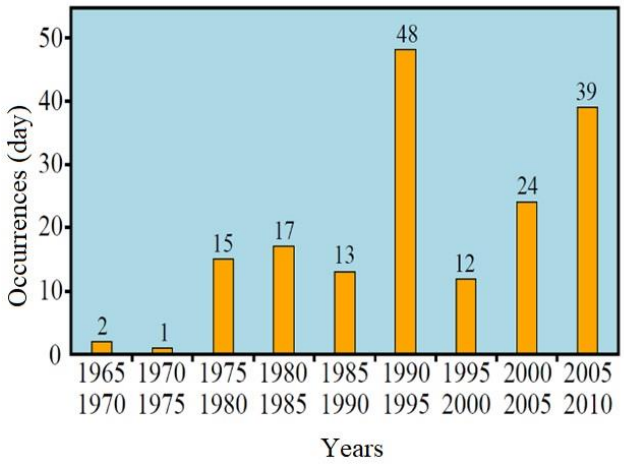

Figure 5. Annual avalanche event numbers between 1965 and 2010 [18]

2.2. Methodology

The Analytical Hierarchy Process (AHP) introduced by Saaty [21] is the most widely used method among Multi-Criteria Decision Making Methods (MCDM). In AHP, the hierarchical structure and comparison matrix are explained as the first step, and then the

comparison matrix is transformed into a priority vector and the fit ratio is determined according to random index values [22]. Fig. 6 shows a schematic of the three-level hierarchical structure used for a MCDM problem, with the high-level decision goal representing the lower-level criteria and, if any, the lower-level alternatives [23]. Here, decision options are at the lowest level. AHP can be used with many criteria according to their common characteristics, so the number of criteria and the correct definition of each criterion are important for the consistency of pairwise comparison. After the hierarchical structure is established, the importance levels of the criteria are discussed with the decision makers, the importance density of the criteria is scored between 1 and 9, and the bilateral relations between the criteria are determined [23].

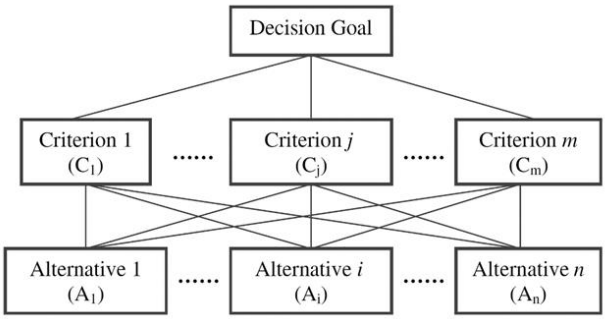

Figure 6. Network of three-level hierarchical structure for MCDM problem [23]

After the normalized matrix is obtained, the average of each row of the matrix gives the weight vector. The product of the weight vector and the comparison matrix gives the following matrix of priorities.

$$[AW_i] = [A][W_i] \quad (1)$$

The maximum eigenvalue (λ_{max}) is obtained by the following equation:

$$\lambda_{max} = \frac{1}{n}\sum_{i=1}^{n}\frac{AW_i}{W_i} \quad (2)$$

where, n is criteria number, *A* is the pairwise comparison matrix, and *W* is the weight vector. Saaty [21] called this method for determining the weight vector as the fundamental right eigenvector method (EM). It was suggested in the literature that the pairwise comparison matrix A should have an acceptable consistency controlled by the consistency ratio (CR) [23]:

$$CI = \frac{(\lambda_{max} - n)}{(n-1)} \quad (3)$$

$$CR = \frac{CI}{RI} \quad (4)$$

In which, the *CI* is the consistency index, *RI* is the random inconsistency index taken from Table 1.

Table 1. *RI* values according to numbers of criteria (n = 1 – 15) [24]

n	1	2	3	4	5	6	7	8	9	10	11	12	13	14	15
RI	0.00	0.00	0.58	0.90	1.12	1.24	1.32	1.41	1.45	1.49	1.51	1.48	1.56	1.57	1.59

When *CR* < 0.10, the comparison matrix has reached acceptable consistency, otherwise, the decision-making process must be repeated until consistency is achieved. *CR* = 0.00 means that the consistency reaches the best value [24], [25].

3. Results and Discussion

3.1. Snow Avalanche Risk Assessment

Generally, risk is evaluated as the product of hazards and vulnerabilities. The factors (criteria) that may have the potential for any damage, harm, or adverse health effects on property and people are described as hazards. The vulnerability, on the other hand, is the susceptibility to damage or harm to a property or people. In other words, while the hazard refers to the factors that affect the event, the vulnerability refers to the factors that are affected by the event. In this study, precipitation, temperature, slope, elevation, aspect, soil, lithology, and fault were considered as hazard factor, while land use and population as vulnerability, as seen in the flow chart of GIS-based AHP in Fig. 7. According to the AHP results, the final risk score is calculated as follows [26], [27] and then visualized using GIS.

$$R = \sum_{i=1}^{n} w_i \times c_i \quad (5)$$

where, w_i and c_i represent the weights and the overall criteria respectively. The dataset of the criteria in Fig. 7 were obtained from open sources of the relevant institutions [15], [28]-[36].

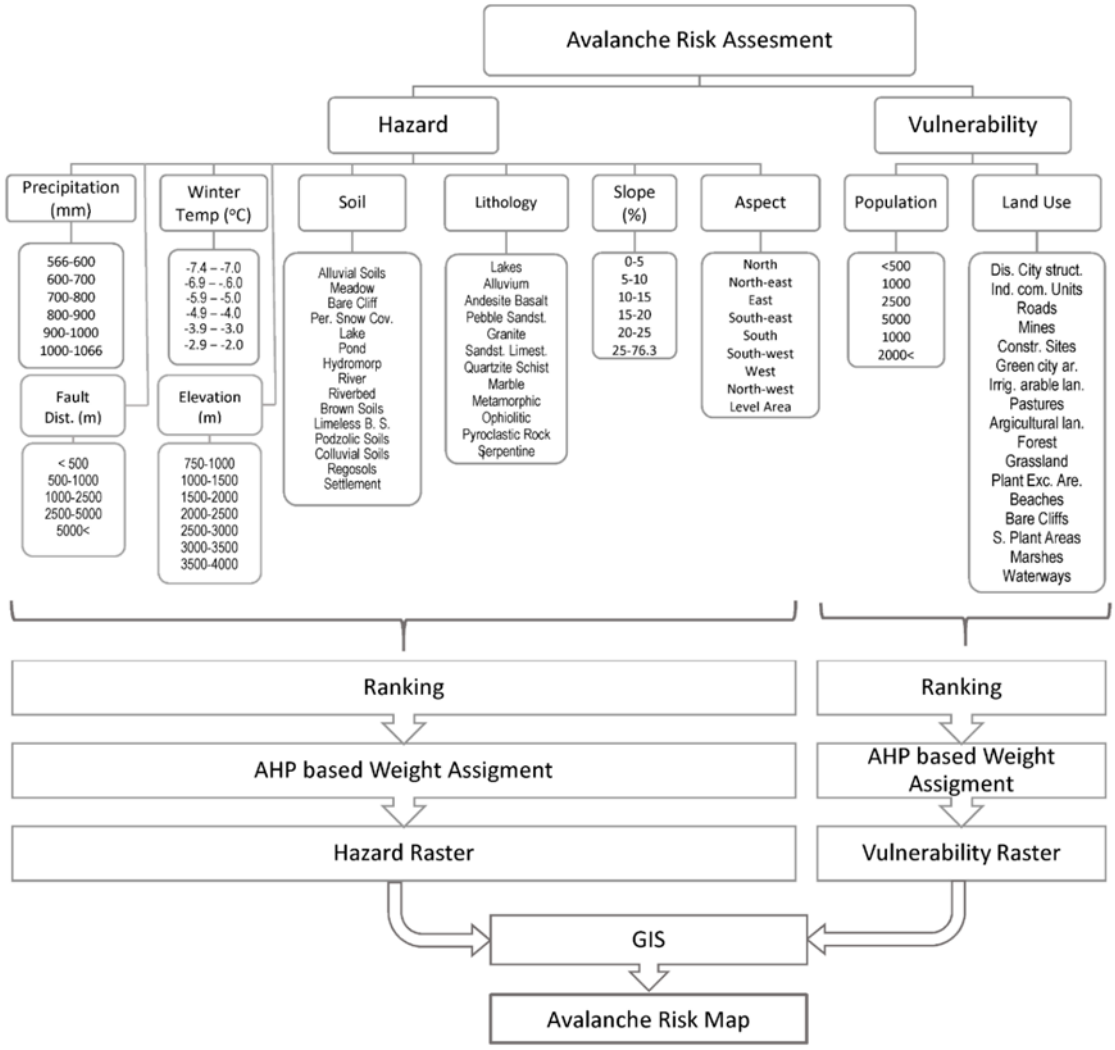

Figure 7. Flow-chart of the GIS-based AHP for risk assessment of snow avalanche

Table 2. Derivation of the weight vector based on the normalization matrix

Matrix A	Tem.	Slope	Eleva.	Aspect	L. use	Soil	Lit.	Prec.	Fault.	Pop.	W_i (%)
Temperature	0.302	0.476	0.367	0.311	0.255	0.208	0.200	0.178	0.157	0.127	25.8
Slope	0.101	0.159	0.245	0.233	0.191	0.208	0.200	0.178	0.157	0.127	18.0
Elevation	0.101	0.079	0.122	0.233	0.191	0.139	0.150	0.133	0.131	0.127	14.1
Aspect	0.076	0.053	0.041	0.078	0.191	0.139	0.150	0.133	0.131	0.109	11.0
Land use	0.076	0.053	0.041	0.026	0.064	0.139	0.100	0.133	0.131	0.109	8.7
Soil	0.101	0.053	0.061	0.039	0.032	0.069	0.100	0.089	0.105	0.109	7.6
Lithology	0.076	0.040	0.041	0.026	0.032	0.035	0.050	0.089	0.079	0.091	5.6
Precipitation	0.076	0.040	0.041	0.026	0.021	0.035	0.025	0.044	0.079	0.091	4.8
Fault distance	0.050	0.026	0.025	0.016	0.013	0.017	0.017	0.015	0.026	0.091	3.0
Population	0.043	0.023	0.018	0.013	0.011	0.012	0.010	0.009	0.005	0.018	1.6

In order to obtain the normalization matrix in Table 2, firstly, each criterion is scored and a pairwise comparison matrix is created based on expert opinion. Then, the score of each criterion is divided by the sum of its own column and the elements of the normalization matrix are calculated. The average of each row of the normalization matrix gives the weight of the relevant criterion. According to the relations given in the methodology section, the parameters of AHP were calculated as λ_{max} = 10.992, RI = 1.49 from Table 1, CI = 0.110 and CR = 0.07. The consistency ratio CR = 7% < 10% which indicates the consistency of the comparison matrix. As a result, the weights of the criteria were estimated as %25.8 of the temperature, 18% of the slope, 14.1% of the elevation, 11% of the aspect, %8.7 of the land use, %7.6 of the soil, 5.6% of the lithology, 4.8 of the precipitation, 3.0 of the fault distance, and 1.6% of the population, as seen in Table 2.

3.2. Spatial Analysis

The hazard and vulnerability maps effective for avalanches were presented in Fig. 8. The raster maps in this figure were obtained by transferring the scores of each criterion used in AHP to the GIS environment. One of the criteria that can affect the avalanche is temperature. Since snow accumulations are greater in cold areas, local cold areas in the north of the temperature map in Fig. 9 were scored high, and warm areas in the south were scored low. The volcanic Mount Süphan in the north appears to be the coldest part due to its high elevation and the colder climate of the north. However, although the southern parts are warmer, due to the mountainous and rugged nature of these parts, many snowfalls occur, and in this case, the effect of the slope comes to the fore. As can be seen on the slope map, the mountainous and rugged southern parts are more critical in terms of avalanche risk. High-altitude areas are riskier areas in terms of avalanches as both the slope and snowfall increase. Therefore, higher regions on the elevation map are scored higher. Due to the temperature differences during the day, the risk is higher on the southern faces. For this reason, the southern surfaces are rated with a higher hazard score in the aspect map. Avalanche susceptibility is high in land use, particularly on high and steep slopes prone to avalanches. Additionally, while the hazard score is low in flat alluvial lands on the soil map, rough soil structures with hard and steep structures are considered as riskier places. Although the entire region has high snowfall, the central and southern regions where precipitation is concentrated are under higher avalanche risk, as can be seen from the precipitation map. On the other hand, since active fault zones can trigger avalanches, the hazard score of the regions close to the faults is considered high in the fault map. Another factor vulnerable to avalanche risk is population. The high-population residential areas are more vulnerable to avalanche risk than other areas, as seen in the population map in Fig. 8.

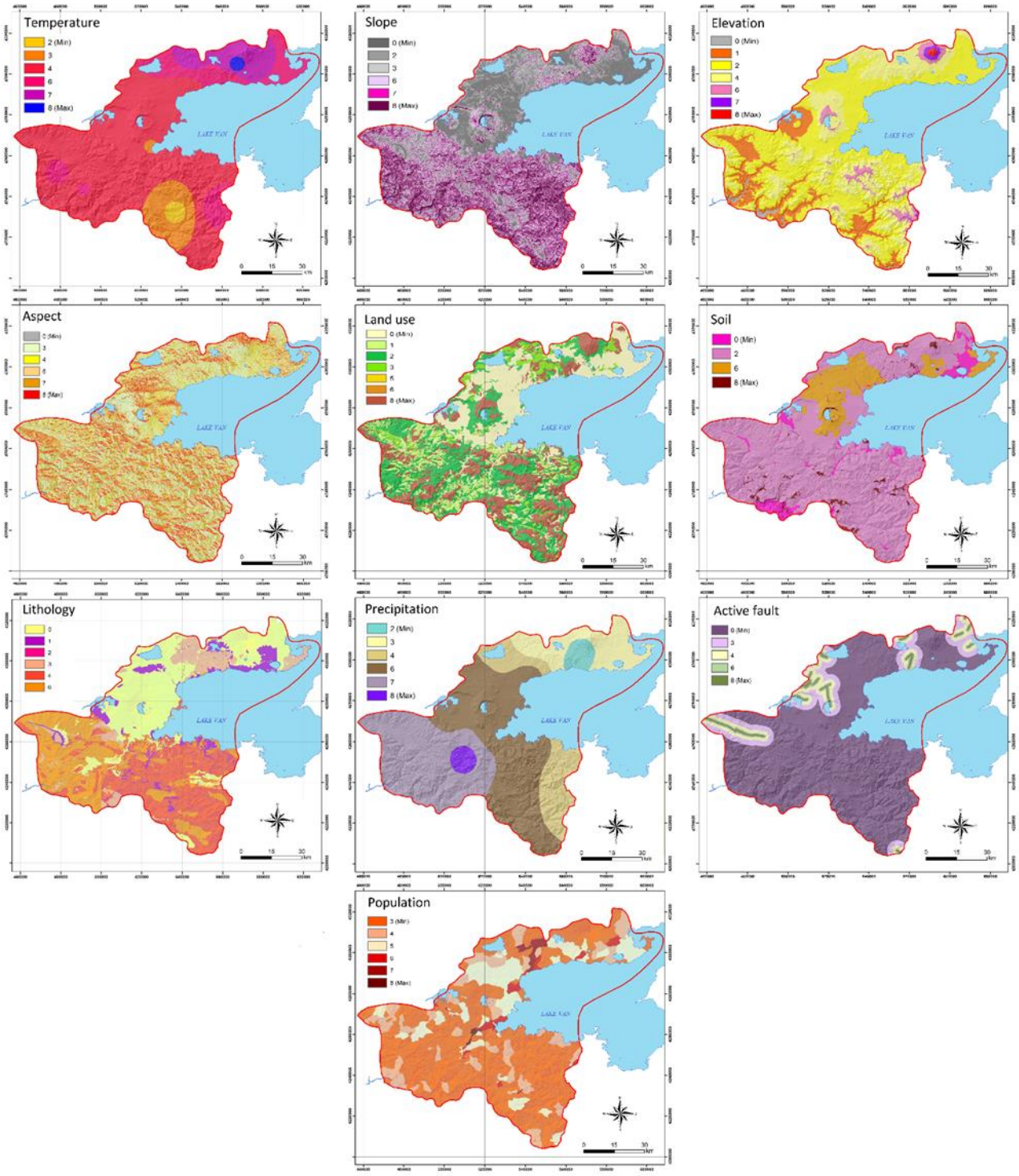

Figure 8. Raster maps of the criteria effective on avalanche risk

The maps in Fig. 8 were processed in the GIS environment in proportion to their weights gained from AHP, and the resulting risk map for snow avalanches is presented in Fig. 9. As can be seen in this risk map, especially the highland and steep southern regions were determined to be high risk, and the relatively flat middle regions were determined to be low risk. It is seen that the regions with the highest avalanche risk are the foothills of Suphan Mountain in the north and the highlands in the east of Hizan district in the south. The foothills of the Nemrut Crater Lake, which are rising in the middle flat region, are also under high avalanche risk. In order to verify the risk map, avalanche events observed in the past few years and the avalanche sensitivity map obtained by Göksu and Leventeli [9] are given in Figs. 10a and

Fig. 10b respectively. Accordingly, it was observed that the avalanche events that occurred in the past generally overlap with the medium and high-risk regions of the risk map obtained in this study. In addition, the obtained map is also compatible with the avalanche vulnerability map presented by Göksu and Leventeli [9], which was only obtained by overlaying some of the land criteria with the GIS. The study results also match significantly with the risk-hazard map of the region presented by Selçuk [10]. The results indicate the verification of the risk map in this study.

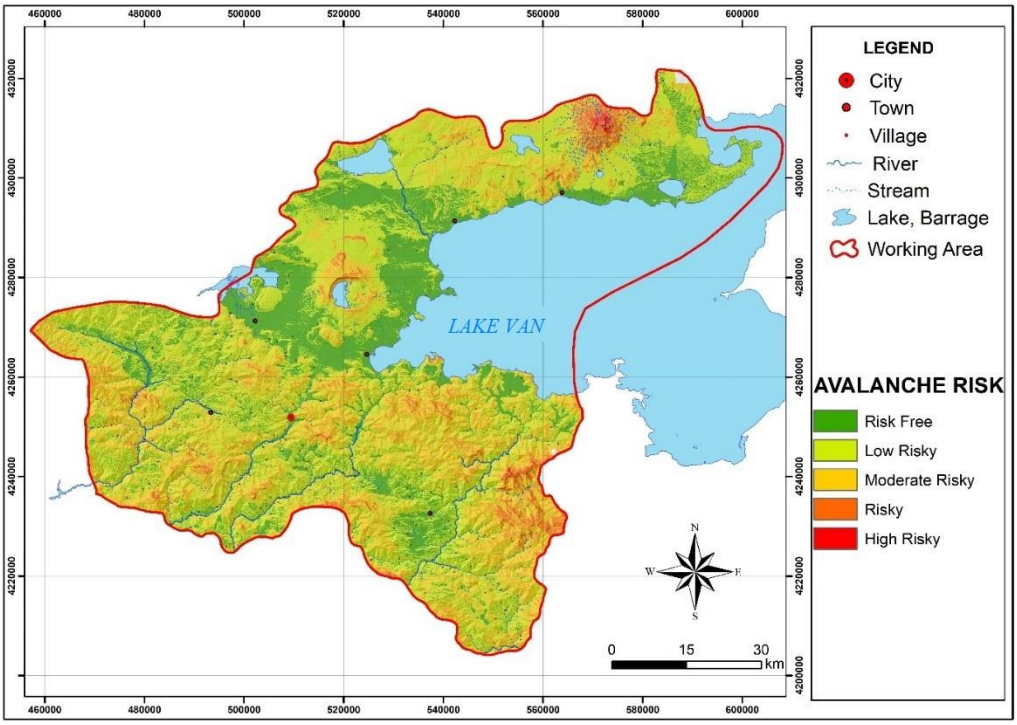

Figure 9. Final risk map of the snow avalanche

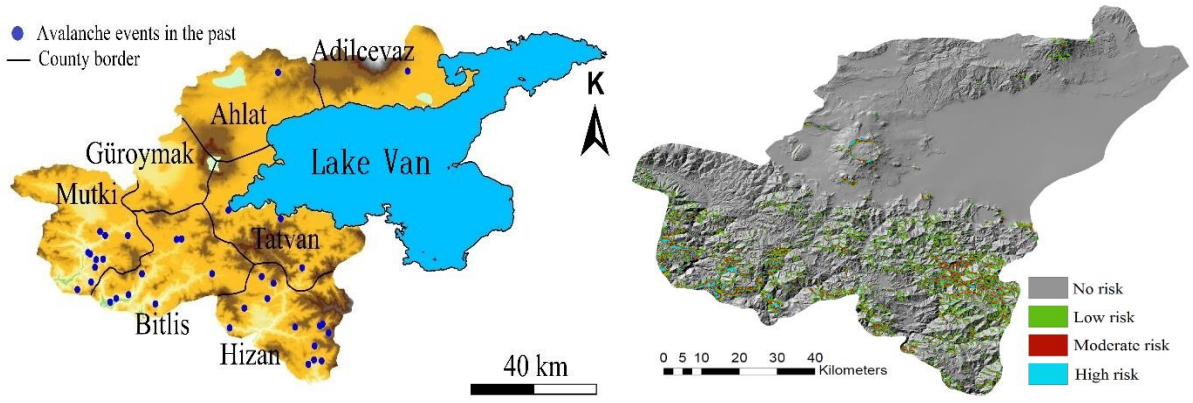

Figure 10. a) Locations of avalanche events in Bitlis between 1965 and 2010 [18], b) The avalanche sensitivity map of the Bitlis [37]

4. Conclusions

In this study, avalanche risks in the province of Bitlis, which is the region with the highest snowfall in Turkey, were assessed using a GIS-based AHP. The avalanche risk of the study area was mapped based on the weights of temperature, slope, elevation, aspect, land use, soil, lithology, precipitation, distance to a fault, and population criteria. According to the results of the study, the highland and steep southern regions of the study area were obtained as high-risk areas, and the relatively flat middle regions were determined as

low-risk areas. The highest-risk regions are the foothills of Süphan Mountain in the north and the highlands in the east of Hizan district in the south. The foothills of the Nemrut Crater Lake are also under high avalanche risk. The obtained risk map is in agreement with the avalanche events of the past and with a previous avalanche susceptibility map in the literature.

The findings obtained from the study will make important contributions to effective disaster management against avalanche events in the study area. Thus, it will be possible to prevent important losses of life and property that may occur in the region. An innovative interactive risk assessment of the region can be performed by combining the risk maps obtained from this study with the risk maps obtained for other disaster types. These risk maps are expected to make significant contributions to institutions and academics operating in this field today and in the future.

Contributions of the authors

M.C.A.: Risk assessment and writing the manuscript, E.S.B.: Rastering and spatial analysis, A.E.U.: Risk assessment and editing, A.B.: Spatial analysis.

Conflict of Interest Statement

There is no conflict of interest between the authors.

Statement of Research and Publication Ethics

The study is complied with research and publication ethics.

References

[1] I. Gurer, H. Tuncel, "Türkiye'de çığ sorunu ve bugünkü durumu," in A.Ü. Türkiye Coğrafyası Araştırma ve Uygulama Merkezi 2. Sempozyumu bildirileri. 1994.

[2] C. Sahin, "Türkiye afetler coğrafyası," Gazi Üniv. Yayın no: 172. Ankara, 1991.

[3] A. Gret-Regamey and D. Straub, "Spatially explicit avalanche risk assessment linking Bayesian networks to a GIS," Nat. Hazards Earth Syst. Sci., 6, 911–926, 2006.

[4] H.A. Nefeslioglu, E.A. Sezer, C. Gokceoglu, and Z. Ayasd, "A modified analytical hierarchy process (M-AHP) approach for decision support systems in natural hazard assessments," Computers &Geosciences, 59: 1–8, 2013. http://dx.doi.org/10.1016/j.cageo.2013.05.010

[5] S. Kumar, P.K. Srivastava, and Snehmani, "GIS-based MCDA–AHP modelling for avalanche susceptibility mapping of Nubra valley region, Indian Himalaya," Geocarto International, 32(11): 1254–1267, 2017 https://doi.org/10.1080/10106049.2016.1206626

[6] N. Varol, "Avalanche susceptibility mapping with the use of frequency ratio, fuzzy and classical analytical hierarchy process for Uzungol area, Turkey," Cold Regions Science and Technology, 2022, 194: 103439. https://doi.org/10.1016/j.coldregions.2021.103439

[7] S. Nasery and K. Kalkan, "Snow avalanche risk mapping using GIS-based multi-criteria decision analysis: the case of Van, Turkey," Arabian Journal of Geosciences, 2021, 14: 782. https://doi.org/10.1007/s12517-021-07112-4

[8] N. Elmastas and M. Ozcanli, "Avalanche disaster areas and avalanche risk analysis in the provence of Bitlis," VI. National Geography Symposium, 3-5 November 2010. TUCAUM, Ankara, Turkey, 2011.

[9] A. E. Göksu and Y. Leventeli, "Determination of the avalanche hazard zones using geographic information systems: a case study from Bitlis province," 9th International Symposium on eastern Mediterranean Geology, 07 – 11 May 2018, Antalya/Turkey, 2018.

[10] L. Selçuk, "An avalanche hazard model for Bitlis Province, Turkey, using GIS based multicriteria decision analysis," Turkish J Earth Sci, 2013, 22: 523-535. doi:10.3906/yer-1201-10

[11] M. C. Aydin, E. S. Birincioglu, "Flood risk analysis using GIS-based analytical hierarchy process: a case study of Bitlis Province," Applied Water Science, 2022, 12:122, 1 – 10. https://doi.org/10.1007/s13201-022-01655-x.

[12] M. C. Aydın, E. S. Birincioğlu and A. Büyüksaraç, "Landslide Susceptibility Mapping in Bitlis Province using GIS-based AHP method," Turkish Journal of Remote Sensing and GIS, 2022, 3 (2), 160-171.

[13] M. C. Aydın, E. S. Birincioğlu and A. Büyüksaraç, "Risk Assessment of Rockfall using GIS-Based Analytical Hierarchy Process: A Case Study of Bitlis Province," Bitlis Eren University Journal of Science and Technology, 2020, 12 (1), 43-50.

[14] E. Işık, M. H. Özlük, "Natural disasters analysis of Bitlis province and suggestions", in 3rd International Science Technology and Engineering Conference (ISTE-C 2012), December, Dubai, Unites Arab Emirates.
[15] MGM, "Precipitation Data, Climate-Data," Turkish State Meteorological Service, 2021, https://www.mgm.gov.tr/, Access date 16.12.2021.
[16] C. Terzi, "Production of Ground Snow Load Map and Determination of Roof Snow Loads in Eastern Anatolia Region," PhD Thesis, KTU Institute of Science, 2011.
[17] M. C. Aydin, and E. Işik, "Evaluation of Ground Snow Loads in the Micro-climate Regions," Russian Meteorology and Hydrology, 2015, 40(11): 741–748.
[18] R. Ekinci, A. Buyuksarac, Y. L. Ekinci, and E. Isik, "Natural Disaster Diversity Assessment of Bitlis Province," Journal of Natural Hazards and Environment, 6(1): 1-11, 2020, DOI: 10.21324/dacd.535189
[19] DMI, "Kar Örtülü Günler Sayısı, Karlı Günler Sayısı, Maksimum Kar Kalınlıkları Haritaları," Devlet Meteoroloji İşleri Genel Müdürlüğü, Zirai Meteoroloji ve İklim Rasatları Daire Başkanlığı, Ankara, 2000
[20] AFAD, "Overview of 2019 and natural event statistics within the scope of disaster management" (in Turkish), T.R. Ministry of Interior, Disaster and Emergency Management, 2019. Presidency, www.afad.gov.tr. Access Date: 26.01.2022.
[21] T. L. Saaty, "The analytic hierarchy process," New York: McGraw-Hill, New York, 1980, pp 20–25.
[22] G. Can, "Using geographical information systems and analytical hierarchy method for site selection for wind turbine plants: The case of Çanakkale province," Master Thesis, Graduate School of Natural and Applied Science, Çanakkale Onsekiz Mart University, Turkey, 2019.
[23] Y. Wang, J. Liu, and T. Elhag, "An Integrated AHP-DEA Methodology for Bridge Risk Assessment," Computers & Industrial Engineering, 54(3): 513-525, 2008.
[24] T. L. Saaty, "How to make a decision: The analytic hierarchy process," European Journal of Operational Research, 48(1): 9–26, 1990.
[25] N. Subramanian and R. Ramanathan, "A review of applications of Analytic Hierarchy Process in operations management," Int. J Production Economics, 2012, 138: 215-241.
[26] S. Hajkowicz and K. Collins, "A review of multiple criteria analysis for water resource planning and management," Water Resour Manag. 2007, 21:1553–1566. https://doi.org/10.1007/s11269-006-9112-5
[27] O. Ekmekcioglu, K. Koc, and M. Ozger, "District based flood risk assessment in Istanbul using fuzzy analytical hierarchy process," Stochastic Environmental Research and Risk Assessment 2021, 35:617–637. https://doi.org/10.1007/s00477-020-01924-8
[28] AFAD, "Turkey earthquake maps," 2021. https://tdth.afad.gov.tr/, Access date: 23.01.2021.
[29] HGM, "Republic of Turkiye Ministry of National Defense General Directorate of Mapping. Turkish administrative borders data," 2021. https://www.harita.gov.tr/ Access date: 16.12.2021.
[30] USGS, "Earth Data and Digital Elevation Model (DEM) for Bitlis province," United States Geological Survey (USGS), 2021. https://www.usgs.gov/ Access date: 16.12.2021.
[31] TAD, "Agricultural Land Evaluation Portal (TAD Portal)," Republic of Turkey Ministry of Agriculture and Forestry General Directorate of Agricultural Reform. 2021. https://www.tarimorman.gov.tr/ Access date: 16.12.2021.
[32] Copernicus, "Data of land use from Copernicus land Monitoring Service," 2021, https://land.copernicus.eu/ Access date: 16.12.2021.
[33] MTA, "Data of geological structure from GeoScience Mab Viewer and Drawing Editor," General Directorate of Mineral Research and Expolaration of Türkiye, 2021, http://yerbilimleri.mta.gov.tr/anasayfa.aspx, Access date: 16.12.2021.
[34] TUIK, "Population data from Data Portal for Statistical," Turkish Statistical Institute, 2021, https://data.tuik.gov.tr/ Access date: 16.12.2021.
[35] Climate-Data, https://tr.climate-data.org/ , Access date: 16.12.2021.
[36] Geofabrik, "Maps and Data," https://www.geofabrik.de/data/, Access date: 16.12.2021.
[37] A. E. Göksu, "Avalanche Susceptibility Analysis Report (in Turkish)," Disaster and Emergency Management Presidency (AFAD), Bitlis, Turkey, 2017.

Bitlis Eren Üniversitesi Fen Bilimleri Dergisi
BİTLİS EREN UNIVERSITY JOURNAL OF SCIENCE
ISSN: 2147-3129/e-ISSN: 2147-3188
VOLUME: 12 NO: 1 PAGE: 115-125 YEAR: 2023
DOI:10.17798/bitlisfen.1198854

Physical and mechanical properties of pozzolanic materials blended cement mortars before and after the freeze-thaw cycles

Berivan FİLİZ[1] Zehra Funda AKBULUT[2*], Soner GÜLER[3]

[1]*Department of Environmental Engineering, University of Van Yuzuncu Yıl, 65080, Van, Turkey*
[2*]Department of Mining Engineering, University of Van Yuzuncu Yıl, 65080, Van,Turkey
[3]*Department of Civil Engineering, University of Van Yuzuncu Yıl, 65080, Van, Turkey*
(ORCID: 0000-0001-8462-570X) (ORCID: 0000-0003-3055-3450) (ORCID: 0000-0002-9470-8557)

Keywords: Freeze thaw resistance, Industrial wastes, Mortars, Physical and mechanical properties

Abstract

Today, the production of Portland cement (PC) causes a significant release of carbon dioxide (CO2) gas into the atmosphere. The CO2 gases released into the atmosphere create environmental pollution worldwide and prevent current and future generations from living in a cleaner environment. To minimize the harmful effect of the PC on the environment, it is used in concrete mixtrues by displacing it in specific proportions with different industrial wastes. Using industrial wastes such as fly ash (FA), silica fume (SF), and marble powder (MP) in concrete mixtures by replacing cement in specific proportions is vital in terms of sustainability. The primary purpose of this study is to examine the effects of FA, SF, and MP comparatively replaced with cement at the rates of 10%, 20%, and 30% on the flowability, mass loss (ML), and residual compressive strength (RCS) of mortars before and after freeze-thaw (F-T) cycles. According to the results, the effects of FA, SF, and MP on mortars' fresh and hardened properties vary considerably. However, using FA, SF, and MP instead of cement significantly improves the matrix's weak cement/aggregate interface transition zones (ITZ) by showing the filler effect. They contribute considerably to reducing mass losses and increasing the RCS capacities of mortars. Compared to room conditions, the reduction in RCS capacities of the control mortar was 21.32% after 200 F-T cycles, while the decrease in RCS capacities of FA-, SD-, and MP-added mortars was between 7.86% and 19.85%. While the mass loss of the control sample after the 200 F-T cycle is 1.23%, the mass loss of mortars with FA, SF, and MP additives is lower and varies between 0.44% and 1.02%.

1. Introduction

The use of ready-mixed concrete in developing countries such as China, India, and Turkey is increasing daily due to the rapid augmentation in industrialization and infrastructure investments. In addition, the construction of new residences to meet the housing needs of the rapidly growing population in these countries quickly raises the demand for ready-mixed concrete. This situation leads to a significant increase in the use of Portland cement (PC), one of the main components of ready-mixed concrete [1]-[4]. The clinker production stage causes considerable carbon dioxide (CO_2) emissions in PC production processes. During the production of 1 ton of PC, approximately 0.85-1 ton of CO2 is released into the atmosphere [5]. As it is known, CO_2 is called greenhouse gas, and these gases cause significant air pollution and global warming. Therefore, in recent years, studies on using some industrial wastes in concrete mixes instead of PC have gained momentum in terms of sustainability. [6], [7]. Some of the most commonly used industrial waste supplementary cementitious materials in concrete mixtures that can be replaced with PC are fly ash (FA), silica fume (SF), and marble powder (MP). FA is a waste product resulting from the combustion of ground coal at 1100-1600 ^{o}C in thermal power plants. Approximately 50

*Corresponding author: fundaakbulut@yyu.edu.tr
Received: 03.11.2022, Accepted: 28.02.2023

million tons of lignite coal are used annually in thermal power plants in Turkey. As a result, each year, 12 million tons of waste FA are released into the environment [8]. SF is a gray-colored waste powder obtained from the reduction of high-purity quartzite with silicon or ferrosilicon alloy with coke in electric arc furnaces. As a result of production at Antalya Ferrochrome facilities in Turkey, around 500-1000 tons of waste SF material are produced annually [9]. MP is formed either during the production of block marble in quarries or during the processing of blocks by cutting them in the factory so that the marble can be used, or during the production of slab marble. Turkey is among the wealthiest countries in the world in terms of marble, with a total of 5.2 billion m^3 (13.9 billion tons) of marble reserves, which has approximately 40% of the world's resources [10]. In Turkey, 40-60% of the 7 million tons of marble produced annually, which can be expressed as a million tons, is dumped on the roadsides or around the production facilities [11]. Concrete is exposed to many physical and chemical effects depending on the time during its service life, and therefore its strength and durability properties are significantly reduced. One of the most important physical effects that negatively affect the strength and durability properties of concrete is the freeze-thaw (F-T) effect. As is known, when water freezes, it expands in volume. When the water in the pores and capillary spaces freezes, it expands and exerts stresses on the walls of these gaps and pores, resulting in micro cracks. As a result of the volumetric expansion and freezing of water after repeated F-T effects, deterioration, fragmentation, and ruptures occur in the concrete microstructure. As a result, the service life of concrete is shortened, maintenance costs increase, and it becomes uneconomical [12], [13]. One of the most effective ways to improve the strength and durability properties of concrete exposed to F-T cycles is to use FA, SF, and MP in concrete mixtures by replacing PC in specific proportions. The benefits of FA, SF, and MP such as strengthening the bonding at the aggregate interface of the cement matrix (paste), creating a denser structure with a higher composition by filling the voids in the concrete microstructure, preventing the formation of sweating and plastic shrinkage, and strengthening the concrete internal system against harmful chemicals by reducing permeability. Furthermore, due to the higher specific surface area of SF compared to cement, it accelerates the setting of concrete, creates an additional reaction surface for hydration, creates additional calcium-silicate-hydrate (C-S-H) gels due to its high pozzolanic activity, and fills gel voids and capillary voids. Thus, some researchers have strongly recommended using FA, SF, and MP to improve the strength and durability properties of concrete against F-T cycles [14]-[25].

2. Material and Method

CEM I 42.5 R type ordinary Portland cement (OPC) [26], CEN standard sand as fine aggregate [27], F-class FA, SF, MP, and superplasticizer were used in cement mortar mixtures. F-class FA was obtained from İskenderun Sugözü Thermal Power Plant. SF was supplied from Etibank Ferrochrome facilities in Antalya province. Marble slurry was obtained from the waste storage area of a marble factory in Van province and was used in cement mortar after drying in an oven for 24 hours at 105 oC. The chemical properties of OPC, FA, SF, and MP are given in Table 1. The physical properties of OPC, FA, SF, and MP are given in Table 2.

Table 1. Chemical properties of OPC, FA, SF, and MP materials

Composition (%)	OPC	FA	SF	MP
SiO_2	18.83	61.10	92.18	0.50
Al_2O_3	5.17	24.20	0.73	0.25
Fe_2O_3	3.47	8.22	0.66	0.21
CaO	64.4	1.97	0.40	55.30
MgO	3.76	2.42	0.27	0.12
TiO_2	0.04	1.27	0.11	0.04
K_2O	0.71	0.42	0.82	0.01
Na_2O	0.46	0.11	0.17	0.24
Loss on ignition	1.25	2.48	2.26	43.26

Table 2. The physical properties of OPC, FA, SF, and MP

Physical properties	OPC	FA	SF	MP
Specific gravity	3.17	2.24	2.20	2.70
Blaine fineness (cm^2/g)	3984	2872	200000	3412

Polycarboxylate ether-based Master Glenium SKY 3675 superplasticizer (SP) with a density of 1.03-1.07 kg/m3 and a pH value of 5-7 at 20 °C was used in the experiments. An automatic programmable cement mixer produced FA-, SF-, and MP-blended cement mortars. In the experimental study, 10 mortar mixtures were prepared, including 1 control and 9 SF, FA, and MP-added mixtures. Amounts of 500 g

cement, 225 g water, and 1350 g standard sand were used in the control mortar [28]. The samples' ML, RCS, and RFS values were obtained by averaging the measurements made at room temperature and at the ends of 50, 100, and 150 F-T cycles. The samples' ML, RCS, and RFS values were obtained using 150 samples, 3 samples from each mixture. Samples of the same ages were tested and compared to determine the samples' reductions in RCS capacity. RFS values of all samples were carried out under 3-point loading on prismatic samples with dimensions of 40 x 40 x 160 mm. The residual compressive strength (RCS) test was carried out at 28 days on the unbroken side surfaces of the specimens with dimensions of 40 x 40 x 160 mm, divided into two parts. Therefore, six compressive strength values were obtained for the three specimens [27]. FA, SF, and MP were used by replacing 10, 20, and 30% of the cement weight, respectively. The amount of SP was used in different proportions for all mixtures to obtain appropriate workability values by considering the material properties of FA, SF, and MP. In the mixing phase of FA-, SF-, and MP-blended cement mortars, cement, waste materials, and distilled water were first added into the cement mixer and mixed for approximately 30 s at low speed. Throughout the next 30 s, standard sand was automatically poured into the mixer, and the mixer continued to mix at high speed for another 30 s. The mixer was stopped after 1 minute and 30 s, and the mortars adhering to the wall of the container were stripped. After fresh cement mortar experiments, control and FA-, SF-, and MP-blended cement mortars were filled into prismatic molds with 40 mm x 40 mm x 160 mm dimensions for hardened cement mortar tests. A shaking table set the cement mortar well in the molds. First, the mortar was filled to half the mold and compacted using 60 shaking processes. Afterward, 60 shakes were used to fill the entire mortar mold. The samples filled in the molds were kept under ambient conditions for 24 hours. After that, the molds were removed, and all the specimens were water-cured at 20 ^{o}C for 28 days. The samples removed from the curing pool were kept in an oven at 105 °C for 48 hours until they reached a constant weight. First, the weights and the compressive and flexural strengths of the samples taken out of the oven (3 samples from each mixture) were determined at ambient conditions. The other samples were left in a plastic bucket filled with water and exposed to 50, 100, and 200 freeze-thaw cycles in the freeze-thaw test cabinet. After each freeze-thaw cycle, the samples were dried in an oven for 48 hours, and their weights, compressive and flexural strengths were measured again. The mix-design of the control and blended cement mortars are given in Table 3.

Table 3. Mix designs of control and blended cement mortars

Mix cod	Mixes	C (g)	S (g)	Su (%)	W (g)	SP (%)	w/b
P0	Control	500	1350	0	225	0.6	0.45
P1	FA-10	450	1350	10	225	0.6	0.45
P2	FA-20	400	1350	20	225	0.5	0.45
P3	FA-30	350	1350	30	225	0.4	0.45
P4	SF-10	450	1350	10	225	0.8	0.45
P5	SF-20	400	1350	20	225	0.9	0.45
P6	SF-30	350	1350	30	225	1.0	0.45
P7	MP-10	450	1350	10	225	0.7	0.45
P8	MP-20	400	1350	20	225	0.8	0.45
P9	MP-30	350	1350	30	225	0.9	0.45

Notation: C: Cement, Su: Supplement, S: Sand, W: Water

Firstly, the fresh properties of control and blended cement mortars were determined [29]. For this purpose, a flow table test was used to determine the fresh cement mortars' spreading diameters. The spreading diameters of the mortars were obtained by averaging two measurements perpendicular to each other on the spreading table. After the properties of fresh mortar were determined, the specimens with dimensions of 40 x 40 x 160 mm after 28 days of curing were subjected to 50, 100, and 200 F-T cycles. A freely programmable freeze-thaw test cabin was used in freeze-thaw tests of cement mortars. Specimens in the freeze-thaw test cabin were subjected to freezing for 12 hours at -20 ℃ and thawing for 12 hours at 20 ℃ in accordance with the ASTM C 666 standard [30]. Two procedures are given to evaluate the resistance of concrete against the freeze-thaw effect in accordance with the ASTM C666 standard. Both of these methods employ rapid freeze-thaw cycles. In procedure A, freezing and thawing are carried out in the water. In procedure B, freezing is carried out in the air, and thawing is carried out in the water. Procedure A was followed in this study. The mass loss and compressive strength of the control and cement blended mortars were carried out at room temperature and after 50, 100, and 200 F-T cycles. Three specimens were tested, and their average values were used to determine the physical and mechanical properties of control and FA-, SF-, and MP-blended cement mortars under room conditions and after each round of F-T cycles. The loading rates of flexural strength and compressive strength tests were 50 N/s and 2400 N/s, respectively. The Field Emission Scanning Electron Microscope (FESEM) analyses were performed only for the control and FA-20, SF-20, and MP-20 samples to observe the changes in the microstructural properties

of the selected cement mortars at room temperature and after 50, 100, and 200 F-T cycles. To capture images with FESEM analysis, microscopic samples were taken from the specimens and subjected to SEM analysis using the Zeiss Sigma 300 FESEM brand device. FESEM analyses were carried out on the pieces with 1 x 1000 magnification. The schematic view of the testing stages is given in Figure 1.

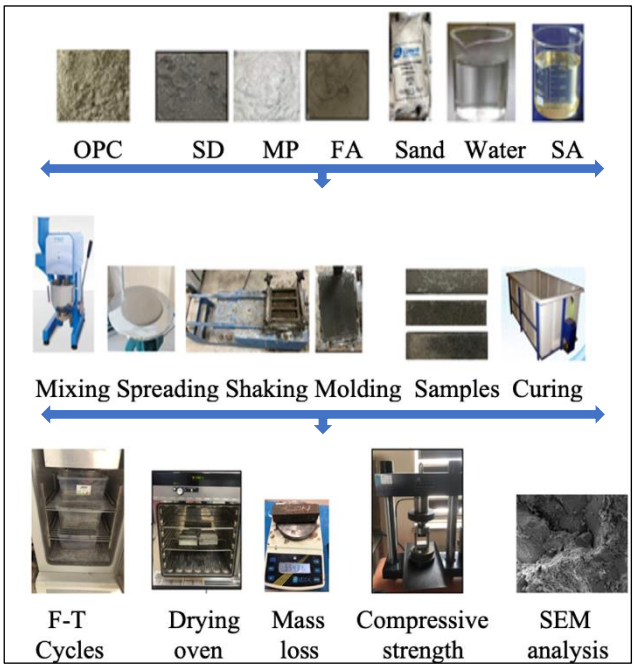

Figure 1.The schematic view of the testing stages

3. Results and Discussion

3.1. Flow Table

The flow table test was used to determine the workability of fresh cement mortars, and the spreading diameters of all the cement mortars were measured. The spreading diameters of fresh cement mortars are given in Table 4. Primarily, many trial mixes were prepared to ensure that the mixtures had similar workability properties. For the control and FA-, SF-, and MP-blended cement mortars to have nearly the same workability properties and thus have close spreading diameters, SP ratios were changed, provided that the water/cement (w/c) ratio was kept constant at 0.5. Therefore, while the SP was used as 0.6% of the control mortar's cement weight, it increased to 1.0% of the cement weight in the SF-30 mixture. Furthermore, the positive contribution of FA to the workability of cement mortar due to its spherical grain structure led to SP being used at a lower rate (0.4, 0.5, and 0.6%) in the FA-blended cement mortars. In addition, it was considered that the angular grain structure of MP would damage the workability of cement mortars, so the ratio of SP in MP-blended cement mortars (0.7, 0.8, and 0.9%) is a little higher than in control mortars. As seen from Table 2, while the spreading diameter of the control cement mortar was 175 mm, the spreading diameters of FA-, SF-, and MP-blended cement mortars vary between 180-191 mm, 168-174 mm, and 178-183 mm, respectively. It can also be said from these results that SF highly negatively affects the workability properties of concrete. The main reason is that fresh concrete has a higher viscosity with the addition of a large amount of SF, which decreases the workability of concrete. This situation has been stated by some researchers [31], [32]. However, the researchers could not agree on an optimum value for the cement-displaced SF ratio. Khedr and Abou-Zeid [33] stated that the workability properties of concrete decrease linearly when the SF content replacing cement increases from 0 to 25%. However, Zhang and Li [34] emphasized that the workability decreased significantly when the ratio of SF displaced by cement increased from 6% to 9%. Still, the decrease in workability was smaller when more than 9% SF was used.

Table 4. Spreading diameters of fresh cement mortars

Mix cod	Mixes	Diameter (mm)
P0	Control	175
P1	FA-10	180
P2	FA-20	187
P3	FA-30	191
P4	SF-10	174
P5	SF-20	170
P6	SF-30	168
P7	MP-10	178
P8	MP-20	183
P9	MP-30	182

3.2. Mass Loss

The mass loss (ML) results after F-T cycles are given in Table 5 and Figure 2. It was found that all samples had minimal mass losses after F-T cycles (lower than 1.5%). The pressure stresses applied by the water in the cavities of the concrete elements with a hollow structure due to the temperature drop below zero may cause the concrete to crumble, break up, and throw pieces. Such a result is due to the increased volume of water due to freezing. Some of the most effective ways to make concrete resistant to F-T cycles are reducing cement dosage, reducing shrinkage and heat of hydration, keeping the water/cement ratio low, and

using air-entraining admixtures [35]-[37]. Since using air-entraining admixtures may cause a significant decrease in the mechanical properties of the concrete, it is recommended to be used under certain limits. In cases where no additives are used, one of the most effective ways to reduce cement dosage is to replace waste materials with a pozzolanic character, such as FA, SF, and MP replaced, with cement. Using these pozzolanic materials reduces the shrinkage and hydration rate, and as a result, it can limit the development of cracks on the outer and inner surfaces of the concrete. In this study, it is seen that the mass losses of all samples increase in direct proportion to the increase in the number of F-T cycles. The ML values of the P0 control sample after the 50, 100, and 200 F-T cycles were 0.48%, 0.88%, and 1.23%, respectively. When we look at the ML values of the P1 and P9 samples after 200 F-T cycles, it is seen that they vary between 0.44% and 1.02%.

Figure 1 shows that the P1-P9 samples have lower ML values than the P0 control sample after all F-T cycles, except for the P6 sample's mass loss after 50 F-T cycles. The most important reason is that FA, SF, and MP replaced with cement strengthen weak ITZ regions in the matrix and reduce the damage to the sample's internal structure after F-T cycles. This is to preserve the integrity of the samples better, minimizing the development of cracks in their internal structures. Furthermore, it can be said that P4-P6 specimens with SF-blended cement mortars have slightly lower ML values compared to FA- and MP-blended cement mortars. This is because SF showed higher pozzolanic activity, formed new C-S-H gels, and had a better filler effect in the microstructure of mortars [38-39]. As a result, the samples could maintain their integrity better. Ince et al. [25] showed that the mortar substituted with 20% SF instead of cement lost less mass than the control concrete after freezing and thawing. In addition, the increase in the number of F-T cycles caused the hydraulic pressure in the cement matrix and increased the formation of microcracks.

3.2. Residual Compressive Strength

The residual compressive strengths (RCS) of control and FA-, SF-, and MP-blended cement mortars are given in Table 6 and Figure 3. As seen in Figure 3, as the number of F-T cycles increased, the RCS of the samples decreased more. Compared to room conditions, the decrease in compressive strength of P0 control cement mortar after 200 F-T cycles was 21.32%. At the same time, the reduction in compressive strength of FA-, SD-, and MP-blended P1-P9 cement mortars was measured between 7.86 and 19.35%. Furthermore, the decrease in compressive strength of all P1-P9 mortars after 200 F-T cycles is lower than that of the P0 control mortar. In addition, while the proportion of MP substituted for cement increased from 10% to 30%, the compressive strength decreased proportionally for P7-P9 MP-blended cement mortars. At the same time, a linear trend could not be obtained for FA- and SF-blended cement mortars. Also, SF-blended cement mortars have higher compressive strengths after 200 F-T cycles than FA- and MP-blended cement mortars. Due to its high fineness and pozzolanic properties, silica fume fills the voids in the mortar much better than MP and FA additives and supports final strength development. In addition, the fact that the pozzolanic activity of silica fume is much higher than that of MP and FA additives has played a very influential role in gaining the strength of the cement mortar. Accordingly, it shows higher pozzolanic activity and forms C-S-H bonds with greater strength.

Furthermore, SF fills the gaps in the cement mortar better than FA and MP due to having a fineness modulus approximately 100 times higher than ordinary Portland cement fineness. As a result, SF minimizes the F-T effects in the cement microstructure and causes the specimens to gain more RCS. The contribution of SF obtained as a result of this study to the RCS of control cement mortar is highly consistent with the results of some studies [4], [14], [15], [18]. In addition, due to the high fineness of SD, it increases the density of mortar and concrete, allowing the capillary spaces between cement and aggregate to be filled with more hydration products [40]. Although FA-blended cement mortars do not reach the values of SF-blended cement mortars, they have a higher RCS against FT cycles than MP samples, thanks to the pozzolanic activity that does not exist in MP. Undoubtedly, it should be remembered that the contribution of FA after 28 days is more limited as it is faster to chemically react with water and form new C-S-H bonds at later ages. If the measurements were made later, it is evident that the microstructures of the FA-blended cement mortars would be more robust, and their RCS would be higher. The contribution of MP to the compressive strength of mortar after F-T cycles is due only to the pore-filling features. However, this contribution is effective up to 10%, decreasing at 20% and 30% replacement rates. This is because using MP at higher speeds has a dilution effect, limiting the impact of cement in forming C-S-H bonds. Substitution with more than 10% MP was also emphasized to reduce the binder content and cause dilution [41]. Ince et al. [25] also noted that the compressive strength loss of the cement and 20% SF-replaced mortar samples was

19%, while the compressive strength loss of the control mortar was 26% after 336 F-T cycles.

Table 5. Mass loss of control and blended cement mortars

Mix code	Mixes	50 F-T (%)	SD	100 F-T (%)	SD	200 F-T (%)	SD
P0	Control	0.48	0.02	0.88	0.03	1.23	0.03
P1	FA-10	0.37	0.04	0.61	0.03	0.75	0.04
P2	FA-20	0.18	0.04	0.56	0.02	0.54	0.02
P3	FA-30	0.41	0.03	0.68	0.02	0.89	0.02
P4	SF-10	0.19	0.03	0.47	0.03	0.64	0.02
P5	SF-20	0.14	0.02	0.36	0.02	0.44	0.04
P6	SF-30	0.23	0.02	0.51	0.04	0.72	0.04
P7	MP-10	0.35	0.02	0.72	0.04	0.87	0.03
P8	MP-20	0.47	0.04	0.65	0.03	0.81	0.02
P9	MP-30	0.51	0.03	0.81	0.04	1.02	0.02

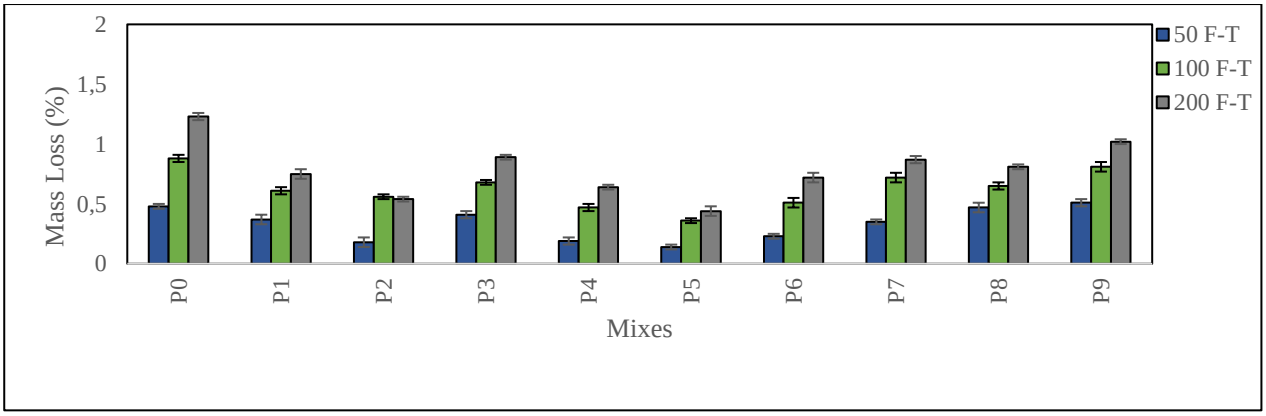

Figure 2. Variation of mass loss of control and FA, SF and MP blended cement mortar specimens

Table 6. Residual compressive strength (RCS) of control and blended cement mortars

Mix code		Residual Compressive Strength 0 F-T (MPa)	SD	50 F-T (MPa)	SD	100 F-T (MPa)	SD	200 F-T (MPa)	SD
P0	Control	49.15	1.63	46.27	1.66	42.49	2.41	38.67	2.54
P1	FA-10	50.65	2.23	50.32	2.00	47.08	2.05	43.76	2.16
P2	FA-20	48.82	2.15	48.21	1.41	45.69	0.63	42.89	1.70
P3	FA-30	50.28	2.03	48.91	0.68	44.12	1.53	42.11	2.69
P4	SF-10	63.26	2.34	62.87	1.69	59.63	2.18	56.38	2.87
P5	SF-20	68.14	1.82	67.76	2.55	64.98	1.57	62.36	2.51
P6	SF-30	75.91	2.33	73.95	0.98	72.11	3.31	69.94	1.61
P7	MP-10	49.51	2.62	48.79	2.42	45.87	1.90	42.34	2.94
P8	MP-20	45.43	1.90	44.17	2.19	41.21	2.88	37.76	2.42
P9	MP-30	48.52	1.66	46.52	2.76	41.87	2.67	39.13	1.66

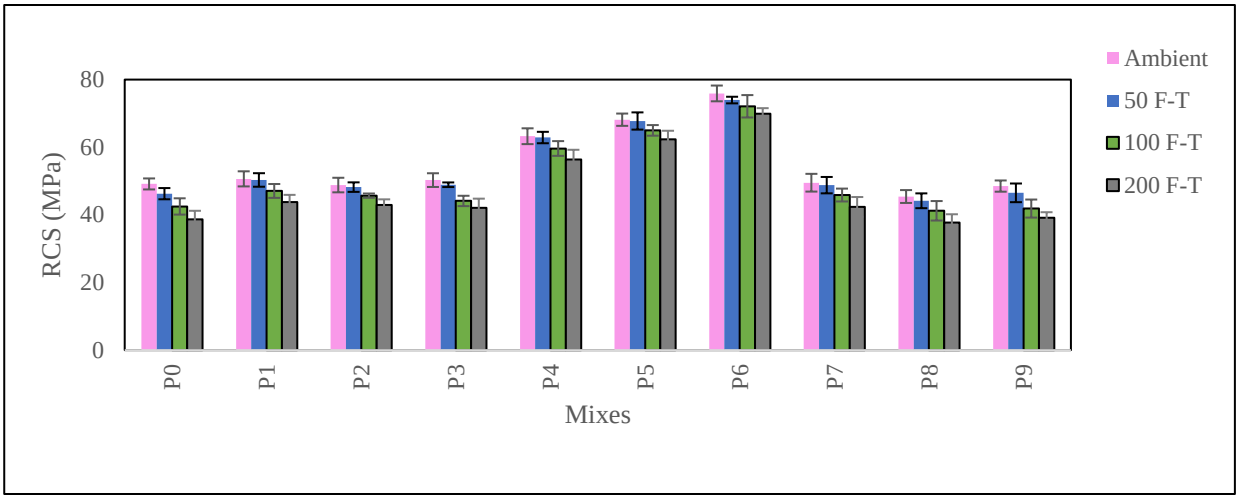

Figure 3. Variation of residual compressive strength of control and FA, SF and MP blended cement mortar specimens

3.2. FESEM Analysis

The FESEM images of control and FA-20, SF-20, and MP-20 blended cement mortars under room conditions, and after 50, 100, and 200 F-T cycles are shown in Figure 4. As seen in Figure 4, however, while control, FA-, SF-, and MP-blended cement mortars have a more robust microstructure under room conditions, it is seen that micro-cracks turn into larger macro cracks as a result of integrity deterioration in the microstructures after increasing F-T cycles. It is also seen that these cracks become more pronounced after 100 and 200 F-T cycles compared to 50 F-T processes. In addition, the control mortar appears to have larger and deeper cracks after 100 and 200 F-T cycles compared to FA, SF, and MP mortars. Although FA mortars have a more robust microstructure due to their high pozzolanic activity, it is not as much as SF mortars compared to MP mortars. In addition, it is observed that SF-blended cement mortars retain their integrity better than FA- and MP-blended cement mortars and have thinner and more minor cracks.

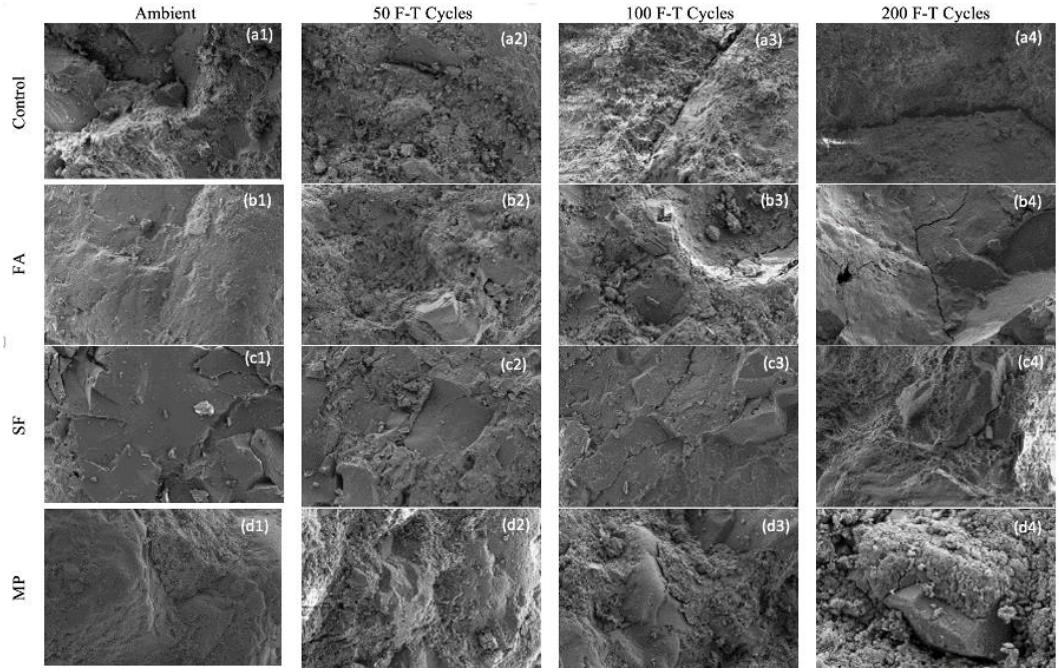

Figure 4. FESEM images of control and FA, SF and MP blended cement mortar specimens

One of the most important reasons is that SF has a high fineness modulus, so it fills the gaps between cement grains better and ensures that the mixtures have a better interfacial transition zone (ITZ) and impermeable microstructure [25], [42], [43], [44]. Another reason is that SF has high pozzolanic activity due to its high percentage of Si particles. Ca(OH)2 hydrated products are known to form as a result of the reaction of cement with water. Ca(OH)2 is a water-soluble phase that does not contribute to the strength and is responsible for the hollow structure of concrete. Thus, a minimum of $Ca(OH)_2$ is preferred in cement mortar. $Ca(OH)_2$ chemically reacts with SF, which has a very high amount of silicon (Si) in its chemical composition. Therefore, the new C-S-H bonds formed due to the chemical reaction of Si particles with $Ca(OH)_2$ enabled SF mortars to better protect their microstructure resistance after increasing F-T cycles and maintain higher residual compressive strength [45], [46].

4. Conclusion and Suggestions

This study examines the effects of fly ash (FA), silica fume (SF), and marble powder (MP), which are used at 10%, 20%, and 30% substitution for cement, on cement mortar's fresh and hardened properties after freeze-thaw (F-T) cycles. In addition, FESEM analyses at ambient conditions and after F-T processes were performed to investigate changes in the microstructures of samples. As a result of this study, the following conclusions were obtained.

•As the number of F-T cycles increases, there is a considerable decrease in the physical and mechanical properties of the samples. This decrease was more evident, especially after 200 F-T cycles.

•Adding FA and MP to the comparative mixtures to the P0 control mixture increased the workability of the mixes and, therefore, the spreading diameters. In contrast, the spreading diameters of the SF-added combinations decreased. Therefore, to obtain good workability in SF additive mixtures, the SP additive ratio should be slightly higher than in other varieties.

•ML values of FA, SF, and MP added to P1-P9 samples after F-T cycles were higher than the P0 control sample. The most important reason for this is that with the strengthening of the ITZ regions of FA, SF, and MP, the integrity of the sample is less lost after F-T cycles, and the cracks formed in the internal structures due to this are limited.

•SF-blended cement mortars (P3-P6) are much more effective than FA- and MP-blended cement mortars in improving control mortars' physical and mechanical properties against F-T cycles due to their high fineness modulus and high pozzolanic activity. FA, SF, and MP significantly improve the microstructure of the cement matrix and contribute considerably to the strength and durability properties of the concrete against the F-T cycles.

Acknowledgment

This study is supported by the Department of Scientific Research Projects of the University of Van Yüzüncü Yıl, Van, Turkey, with the project ID 8936.

Contributions of the authors

The contributions of each author to the article should be indicated.

Conflict of Interest Statement

There is no conflict of interest between the authors.

Statement of Research and Publication Ethics

The study is complied with research and publication ethics.

References

[1] D. Hatungimana, C. Taşköprü, M. Ichedef, M. M. Saç, and Ş. Yazıcı, "Compressive strength, water absorption, water sorptivity and surface radon exhalation rate of silica fume and fly ash based mortar," *Journal of Building Engineering,* vol. 23, pp. 369-376, 2019.

[2] M.M. Hossain, M.R. Karim, M. Hasan, M.K. Hossain, and M.F.M. Zain, "Durability of mortar and concrete made up of pozzolans as a partial replacement of cement: A review," *Construction and Building Material,* vol. 116, pp. 128-140, 2016.

[3] Y. Liu, Y. Zhuge, W. Duan, G. Huang, and Y. Yao, "Modification of microstructure and physical properties of cement-based mortar made with limestone and alum sludge," *Journal of Building Engineering,* vol. 58, pp.105000, 2022.

[4] J. Wang, B. Ma, H. Tan, C. Du, Z. Chu, Z. Luo, and P., Wang, "Hydration and mechanical properties of cement-marble powder system incorporating triisopropanolamine", *Construction and Building Materials,* vol. 266, pp.121068, 2021.

[5] M. Criado, I. Sobrados, I., J.M. Bastidas, and J. Sanz, "Corrosion behaviour of coated steel rebars in carbonated and chloride-contaminated alkali-activated fly ash mortar," *Progress in Organic Coatings*, vol. 99, pp. 11-22, 2016.

[6] F.N. Stafford, A.C. Dias, L. Arroja, J.A. Labrincha, and D.Hotza, "Life cycle assessment of the production of Portland cement: a Southern Europe case study," *Journal of Cleaner Production,* vol. 126, pp. 159-165, 2016.

[7] N. Singh, A.R. Varsha, A. R. Sai, and M. Sufyan-Ud-Din, "Strength, electrical resistivity and sulfate attack resistance of blended mortars produced with agriculture waste ashes," *Case Studies in Construction Materials*, vol. 16, pp. e00944, 2022.

[8] İ. Demir, "Uçucu külün hafif yapı malzemesi üretiminde kullanılması," Yapı Teknolojileri Elektronik Dergisi, vol 1(1), pp. 21-24, 2015.

[9] H. Eker, A. Bascetin, "Influence of silica fume on mechanical property of cemented paste backfill," *Construction and Building Materials*, vol. 317, pp.126089, 2022.

[10] M. E. Altinay, "Bucak ilçesi mermer sektörünün mevcut durum analizi (Master's thesis, Sosyal Bilimler Enstitüsü)". 2019.

[11] Q. Iqbal, M. A. Musarat, N. Ullah, W. S. Alaloul, M. B. A. Rabbani, W. Al Madhoun, and S. Iqbal "Marble Dust Effect on the Air Quality: An Environmental Assessment Approach," *Sustainability*, vol.14(7), pp. 3831, 2022.

[12] R. Wang, Z. Hu, Y. Li, K. Wang, H. Zhang, "Review on the deterioration and approaches to enhance the durability of concrete in the freeze–thaw environment," *Construction and Building Materials*, vol. 321, pp.126371, 2022.

[13] C. Chen, R. Zhang, L. Zhou, and Y. Wang, "Influence of Waste Tire Particles on Freeze–Thaw Resistance and Impermeability Performance of Waste Tires/Sand-Based Autoclaved Aerated," *Concrete Composites. Buildings*, vol. 12(1), pp. 33, 2022.

[14] T. Gonen, S. Yazicioglu, and B. Demirel, "The influence of freezing-thawing cycles on the capillary water absorption and porosity of concrete with mineral admixture," *KSCE Journal of Civil Engineering*, vol.19(3), pp. 667-671, 2015.

[15] Karakurt, C., and Bayazıt, Y. "Freeze-thaw resistance of normal and high strength concretes produced with fly ash and silica fume," Advances in Materials Science and Engineering, vol. 2015, pp. 1-8, 2015.

[16] M. Gruszczyński, and M. Lenart, "Durability of mortars modified with the addition of amorphous aluminum silicate and silica fume," *Theoretical and Applied Fracture Mechanics*, vol. 107, pp. 102526, 2020.

[17] A. Mardani-Aghabaglou, G.İ. Sezer, and K. Ramyar, "Comparison of fly ash, silica fume and metakaolin from mechanical properties and durability performance of mortar mixtures view point," *Construction and Building Materials*, vol. 70, pp.17-25, 2020.

[18] C. S. Shon, A. Abdigaliyev, S. Bagitova, C.W. Chung, D. Kim, "Determination of air-void system and modified frost resistance number for freeze-thaw resistance evaluation of ternary blended concrete made of ordinary Portland cement/silica fume/class F fly ash," *Cold Regions Science and Technology*, vol. 155, pp. 127-136, 2018.

[19] A.Benli, K. Turk, and C. Kina, C. "Influence of silica fume and class F fly ash on mechanical and rheological properties and freeze-thaw durability of self-compacting mortars," *Journal of Cold Regions Engineering*, vol. 32(3), p. 04018009, 2018.

[20] P.A. Shirule, A. Rahman and R.D. Gupta, "Partial replacement of cement with marble dust powder," Int J Adv Eng Res Stud. vol. 1, pp.175–177, 2012.

[21] O. Gencel, C. Ozel, F. Koksal, E. Erdogmus, G. Martínez-Barrera, and W .Brostow, "Properties of concrete paving blocks made with waste marble," *Journal of Cleaner Production*, vol. 2(1), pp. 62-70, 2012.

[22] Y. Xi, E. Anastasiou, A. Karozou, and S. Silvestri, "Fresh and hardened properties of cement mortars using marble sludge fines and cement sludge fines," *Construction and Building Materials*, vol. 220, pp.142-148, 2019.

[23] J. Wang, B. Ma, H.Tan, C. Du, Z. Chu, Z. Luo, and P. Wang,"Hydration and mechanical properties of cement-marble powder system incorporating triisopropanolamine," *Construction and Building Materials,* vol. 266, no. 121068, p. 121068, 2021.

[24] K. Vardhan, S. Goyal, R. Siddique, and M. Singh, "Mechanical properties and microstructural analysis of cement mortar incorporating marble powder as partial replacement of cement. *Construction and Building Materials*," vol. 96, pp. 615–621,2015.

[25] Ince, C., Hamza, A., Derogar, S and Ball, R.J. "Utilisation of waste marble dust for improved durability and cost efficiency of pozzolanic concrete," *Journal of Cleaner Production,* vol. 270, no. 122213, p. 122213, 2020.

[26] Turkish Standards Institute, "Cement-Part 1: General Cements- Composition, Properties, and Suitability Criteria, "TS EN 197-1," Turkey, 2012.

[27] Turkish Standards Institute, Cement Test Methods - Part 1: Determination of Strength, "TS EN 196-1," Turkey, 2016.

[28] Turkish Standards Institute, "Mixing for concrete-specifications for sampling, testing and assessing the suitability of water, including water recovered from processes in the concrete industry, as mixing water for concrete," TS EN 1008, Turkey, 2003.

[29] Turkish Standards Institute, "Methods of Test for Mortar for Masonory-Part 3: Determination of Consistence of Fresh Mortar (by flow table)," "TS EN 1015-3/A2", Turkey, 2007.

[30] ASTM C666/C666M-15, Standard test method for resistance of concrete two rapid freezing and thawing," ASTM International, West Conshohocken, PA, 2015.

[31] G. Adil, J T. Kevern, D. Mann, "Influence of silica fume on mechanical and durability of pervious concrete," *Construction and Building Materials,* vol. 247, pp. 11845, 2020.

[32] D. D. L. Chung, "Improving cement-based materials by using silica fume," Journal of Materials Science. vol. 37 no. 4, pp. 673-682, 2002.

[33] A. S. Kheder, and N.M. Abou- Zeid, "Characteristics of Silica-Fume Concrete," *Journal of Materials in Civil Engineering,* vol. 6(3), 1994.

[34] P. Zhang, and Q. Li, "Effect of silica fume on the durability of concrete composites containing fly ash,"*Science and Engineering of Composite Materials,* vol. 20(1), pp. 57–65, 2013.

[35] L. E. Tunstall, M. T. Ley, and G. W. Scherer, "Air entraining admixtures: Mechanisms, evaluations, and interactions," *Cement and Concrete Research,* vol. 150, pp.106557, 2021.

[36] C. Foy, M. Pigeon, and N. Banthia, "Freeze-thaw durability and deicer salt scaling resistance of a 0, 25 water-cement ratio concrete," *Cement and Concrete Research,* vol. 18(4), pp. 604-614, 1988.

[37] H. Yazıcı, "The effect of silica fume and high-volume Class C fly ash on mechanical properties, chloride penetration and freeze–thaw resistance of self-compacting concrete," *Construction and building Materials,* vol. 22(4), pp. 456-462, 2008.

[38] B. Zhang, H. Tan, W. Shen, G. Xu, B. Ma, and X. Ji, "Nano-silica and silica fume modified cement mortar used as Surface Protection Material to enhance the impermeability," *Cement and Concrete Composites,* vol. 92, pp. 7-17, 2018.

[39] A. Sadrmomtazi, A. Fasihi, F. Balalaei, and A. K. Haghi, "Investigation of mechanical and physical properties of mortars containing silica fume and nano-SiO2," *In Proceedings of the third international conference on concrete and development,* Tehran, Iran (pp. 27-29), 2009.

[40] M. A. Sanjuán, C. Argiz, J. C. Gálvez, and A. Moragues, "Effect of silica fume fineness on the improvement of Portland cement strength performance," *Construction and Building Materials,* vol. 96, pp. 55-64, 2015.

[41] K. Yamanel, U. Durak, S. İlkentapar, İ. İ. Atabey, O. Karahan, and C. Duran, "Influence of waste marble powder as a replacement on the properties of mortar," Journal of Construction, vol.18 (2), pp. 290-300, 2019.

[42] S. Aparna, D. Sathyan and K. B. Anand, "Microstructural and rate of water absorption study on fly-ash incorporated cement mortar," *Materials Today: Proceedings,* vol. 5(11), pp. 23692-23701, 2018.

[43] F. Collins, J.G. and Sanjayan, "Effects of ultra-fine materials on workability and strength of concrete containing alkali-activated slag as the binder," *Cement Concrete and Research,* vol. 29(3), pp. 459-462, 1999.

[44] R. Choudhary, R. Gupta, R. Nagar, "Impact on fresh, mechanical, and microstructural properties of high strength self-compacting concrete by marble cutting slurry waste, fly ash, and silica fume," *Construction and Building Materials*, vol. 239, pp.117888, 2020.

[45] M. J. Munir, S.M.S., Kazmi, and Y. F. Wu, "Efficiency of waste marble powder in controlling alkali–silica reaction of concrete: A Sustainable Approach," *Construction and. Building Materials*, vol.154, pp. 590-599, 2017.

[46] P. Duan, Z. Shui, W. Chen, and C. Shen, "Effects of metakaolin, silica fume and slag on pore structure, interfacial transition zone and compressive strength of concrete," *Construction and Building Materials*, vol. 44, pp. 1–6, 2013.

Bitlis Eren Üniversitesi Fen Bilimleri Dergisi
BİTLİS EREN UNIVERSITY JOURNAL OF SCIENCE
ISSN: 2147-3129/e-ISSN: 2147-3188
VOLUME: 12 NO: 1 PAGE: 126-139 YEAR: 2023
DOI:10.17798/bitlisfen.1200742

An Investigation of Hydrological Drought Characteristics in Kızılırmak Basin, Türkiye: Impacts and Trends

Ibrahim Halil DEGER[1*], Mehmet Ishak YUCE[2], Musa ESIT[3]

[1]*Hasan Kalyoncu University, Civil Engineering Department, Gaziantep, Türkiye*
[2]*Gaziantep University, Civil Engineering Department, Gaziantep, Türkiye*
[3]*Adıyaman University, Civil Enginering Department, Adıyaman, Türkiye*
(ORCID: 0000-0001-6360-3923) (ORCID: 0000-0002-6267-9528) (ORCID: 0000-0003-4509-7283)

Keywords: Hydrological Drought, ITA, SDI, Kızılırmak Basin, Trend Analysis

Abstract

Drought is a natural disaster generally defined as precipitations significantly below the precipitation recorded in actual times. Many researchers classified drought as meteorological, hydrological, agricultural, and socio-economic. Hydrological drought occurs when deficiencies in the surface and ground waters occur due to the long-term lack of precipitation. In this study, a hydrological drought analysis has been performed for Kızılırmak Basin which is the second biggest basin in Türkiye, using the Streamflow Drought Index (SDI) and Innovative Trend Analysis (ITA) for the time scales of 1, 3, 6, 9, 12-month. Monthly mean streamflow records for 7 stations are obtained from the General Directorate of State Hydraulic Works (known as DSI. Drought severity and duration, which are two important drought characteristics, have been calculated for each time scale with their occurrence terms. Results show that Mild Drought and Wet (SDI≥0) have the highest percentage of occurrences. Using Run Theory, the longest lasted and highest drought has been noted in the SDI-12-time scale of E15A017 station with 149.72 and 103 months as severity and duration, respectively. From the highest severity and longest lasted droughts, it is seen that starting with 2000-year, the basin is exposed to the highest occurrence of droughts. The results of the ITA analysis show that in most of the SDI series of any time scale, a trend is existent and these trends are mostly decreasing trends. Therefore, these results have shown that the basin needs to be kept from the potential effects of droughts with an effective water resources management plan..

1. Introduction

A drought, a natural disaster, has been defined by many researchers and organizations from different viewpoints Mishra and Singh [1] have specified droughts as environmental disasters. In the Intergovernmental Panel on Climate Change report (IPCC,2022) drought has been noted as one of the migration's most common climatic drivers [2]. United Nations Office for Disaster Risk Reduction [3] has defined droughts as recurrent events which affect large areas around the world each year. Vicente Serrano et al. [4] have defined drought as one of the biggest natural hazards that impact sectors and systems that have big impacts on agriculture, water resources, and natural ecosystems. Eşit and Yüce [5] have specified that drought is the destruction that has important environmental and economic influences and that it may form in any part of the world and in any climate, independent from forests and deserts.

Although there are many classifications for drought, it has been classified into four classes by [1], [6]. These classifications are meteorological drought, hydrological drought, agricultural drought, and socio-economic drought. Hydrological drought is associated with a term when surface and subsurface

*Corresponding author:ibrahim.deger@hku.edu.tr
Received: 07.11.2022, Accepted: 01.02.2023

water is insufficient for specified water uses [1],[7], [8], [9].

There are many methods to characterize the drought, and in addition to this, using indices is common [10], [11]. Considering the published literature, indexes such as the Palmer Hydrological Drought Severity Index (PHDI), Standardized Streamflow Index (SSFI), Standardized Reservoir Supply Index (SRSI), Standardized Water-level Index (SWI), Streamflow Drought Index (SDI), Surface Water Supply Index (SWSI) are used to analyze hydrological drought [12]. SDI, which has been used to analyze hydrological drought in this study, has been found formerly by [13]. This index whose application manner requires only monthly mean streamflow records as data is similar to the Standardized Precipitation Index (SPI) [9], [14], [15].

Drought is characterized by its duration and severity [16]. Drought duration has been described by Dracup et al. [17] as the time period between the start and end of a drought, while drought severity has been defined by Wilhite [18] as the level of precipitation deficit or the level of influences as a result of the deficit.

Analyzing droughts by trend methods such as Mann-Kendall, Sperman's Rho, and Innovative Trend Analysis have taken a great deal of attraction to scientists [19]–[23]. The innovative trend analysis (ITA) method which has been proposed by Şen [24] is a method that has been used in many studies because it is simple and efficient [25], [26].

According to the literature, there have been lots of studies in which SDI is used to analyze hydrologic droughts in Türkiye. Kale [27] has made a hydrological drought analysis for Akarçay closed basin in Türkiye by benefiting from SDI and four river gauging stations whose data range from 1966 to 2011 years for the periods of 3, 6, 9, and 12 months. In order to check the trend presence in the time series Mann-Kendall test has been utilized. In the relevant study, the author has found out that SDI values in k=1, 2, 3, and 4 reference periods mostly belong to the mild drought and wet categories. Gümüş et al. [28] have made a hydrological drought assessment for Murat River-Palu in the Euphrates Basin utilizing SDI for 1, 3, 6, and 12-month time scales based on dry, wet, and normal classes. In the relevant study, the normal class has been found to have the highest percentages in all time scales. Ozkaya and Zerberg [29] have made drought analyses for 47 stations of the upper Tigris Basin Türkiye using a data set ranging from 1972 to 2011 data period by using SDI for the time scales of 3, 6, and 12 months. In their study, it has been noted that nearly all stations have at least one severe drought during the study period and based on SDI-3 (October-December) analysis, all stations experienced droughts between 1999-2011. Katiopoğlu et al. [21] investigated trend analysis of hydrological droughts using SDI, Mann-Kendall, Innovative Trend Analysis, and Thiel Shen Approach. Authors have used DrinC (Drought Indices Calculator) for SDI calculation and stated that a lot of mild droughts have been observed while the number of extreme droughts is less. They also stated that out of 2 stations decreasing trends were recorded in both dry and wet terms accepting the 0 value as a threshold in the assessment. Altin et al.[30] have made a study about determining drought intensity by hydrological drought analysis in Seyhan and Ceyhan Rivers, Türkiye. They employed the analysis using the Streamflow Drought Index (SDI) and 43-year period data, which ranges from 1972 to 2014 in 4 stations, from 1973 to 2015 in 2 stations, and from 1969 to 2011 in 2 stations for 3, 6, 9, and 12-month overlapping periods. The authors stated that hydrological drought analysis shows that drought years are more predominant after 2000-2001. Kumanlioglu [7] has made a study for the characterization of meteorological and hydrological droughts for Gediz Basin and again with this study using SRI (Standardized Runoff Index) for hydrological drought analysis and SPI and SPEI (standardized precipitation and evaporation index) for meteorological drought analysis, it has been stated that mild drought class has been mostly detected drought category in the 12-month time scale for Acisu, Selendi, Deliinis, and Demirci sub-basins Simsek [31] performed a hydrological drought study on 3, 6, and 12-month time scales for Mediterranean Basins of Türkiye using SDI and streamflow data from 29 gauging stations. In the relevant study, the author has used the Mann-Kendall test for trend detection, Sen's slope method for slope values and the Inverse Distance Weighting (IDW) method for the spatial distribution of droughts. Then the author found out that mild drought type is the most recurring drought type and an important increase in drought severity has been detected in recent years. However, a few drought studies have been done for Kızılırmak Basin. For example, Arslan et al. [32] performed a meteorological drought analysis for the time scales of 1, 3, 6, 9, 12, and 60 months using SPI. Authors have specified that a 60-month time scale has been used as the first in their study on drought analysis of Kızılırmak Basin based on SPI. They have found out that notable increases have been noted in the duration of the last droughts on 12 and 60-month time scales. Akturk et al. [33] have made a meteorological drought assessment using SPI for the time scales of 1, 3, 6, 12, and 24 months and the spatial distribution of droughts

has been done by IDW. The authors have found out that 31 of 58 years are drought years, while 28 of them are mild droughts. Also, they reported that the spatial distribution of historical droughts has shown that the basin was under extreme drought influences during 1973-2013.

In this study, the aim is to make a hydrological drought analysis for the Kızılırmak Basin using SDI for the time scales of 1, 3, 6, 9, and 12 months. For this purpose, 7 stations in the basin have been selected and monthly mean streamflow records have been taken from the General Directorate of State Hydraulic Works (known as DSI). Two important drought characteristics which are drought duration with their maximum ones have been calculated with their occurrence terms. The ITA method has been used to detect possible drought in two cases (SDI<0 and SDI≥0) for all time scales. The results of this study are expected to be beneficial for local authorities in water resource planning management plans, and drought action plans.

2. Material and Method

2.1. Materials

Kızılırmak Basin, which is situated at 32.80°–38.35° East longitudes and 35°–41.75° North latitudes [33], has 82. 221 km^2 area (almost 10.49% of Türkiye) is the second biggest basin in Türkiye (Figure 1). The basin covers all or parts of Ankara, Çankırı, Yozgat, Çorum, Kırıkkale, Kırşehir, Nevşehir, Kayseri, Sivas, Samsun, Sinop, Kastamonu, Aksaray, Niğde, Tokat, Erzincan, Amasya and Konya provinces of Türkiye. Because the basin covers a wide area, there are various types of climates in the basin [34]. While the semi-arid climate type prevails in the interior regions, the humid and semi-humid climate types are dominant in the coastal parts of the Kızılırmak Basin facing the Black Sea and therefore the climate conditions of settlements change according to their geographical position [34]. The Kızılırmak River which is the longest river in Türkiye has a length of 1263 km and spills its water into the Black Sea.

In this study, streamflow data from 7 gauging stations which are in Kızılırmak Basin and have been taken from the (DSI) were used to perform hydrological drought analysis. The details of these stations have been given in Table 1, and their locations have been shown in Figure 1

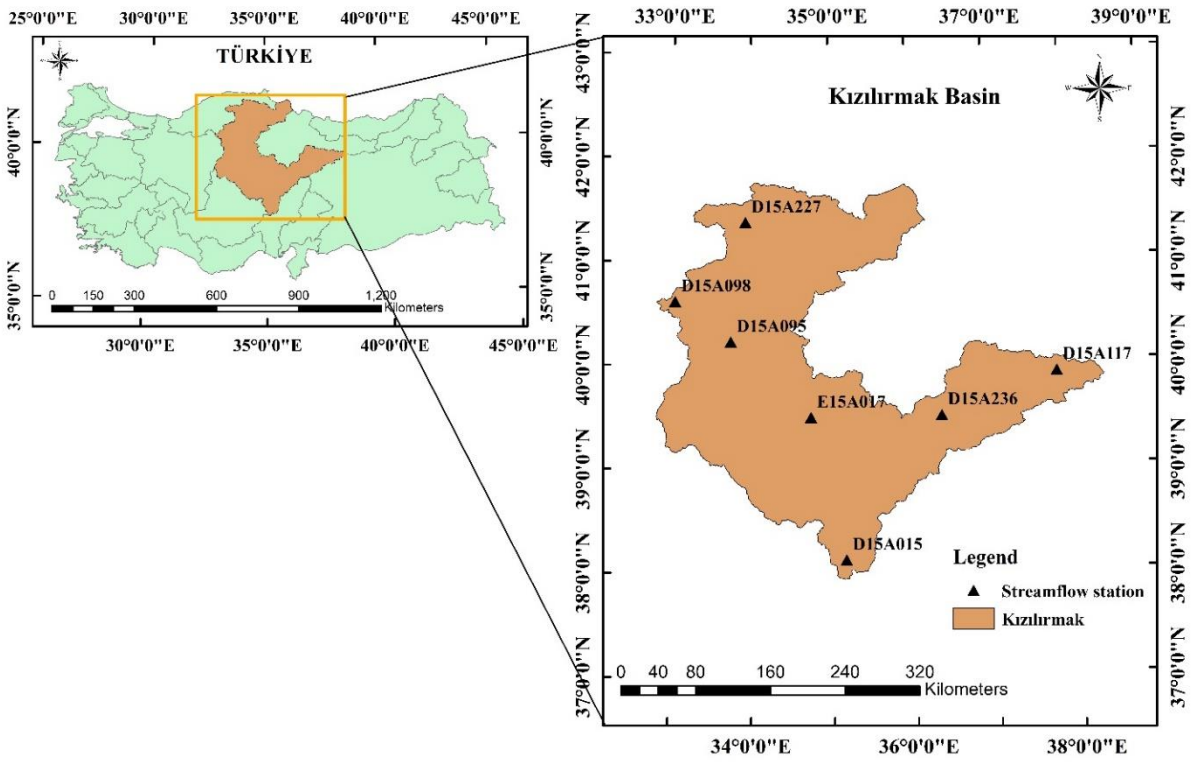

Figure 1. Kızılırmak Basin and Streamflow Gauging stations

Table 1. Data Stations

Station Name	Station Number	Latitude (N)	Longitude (E)	Height (m)	Data Range
Dündarli Suyu Hacibeyli	D15A015	38°7'51"	35°9'58"	1215	1961-2014
Taretözü D. Yeşilyazi	D15A095	40°13'54"	33°44'37"	684	1988-2013
Söğütözü Deresi Yuva	D15A098	40°37'3"	33°2'21"	1296	1995-2019
Kızılırmak Ahmethaci	D15A117	39°54'23"	37°49'33"	1361	1971-2019
Karadere Ç. Deliler	D15A227	41°22'52"	33°55'36"	710	1999-2019
Akcakişla D. Bozkurt	D15A236	39°30'34"	36°22'23"	1210	1988-2019
Karanlik D. Şefaatli	E15A017	39°30'11"	34°44'42"	895	1953-2019

.

2.2 Method

2.2.1. Streamflow Drought Index (SDI)

Streamflow drought is an index that has been proposed by Nalbantis and Tsakiris [13] in order to perform hydrological drought analysis. The calculation process is similar to that of the Standard Precipitation Index (SPI) but monthly average streamflow records are used to calculate this index, instead of precipitation data [35]. To calculate the index, the total streamflow is denoted by $X_{i,j}^{k}$ in a given month j and year i depending on the time scale k (1, 3, 6, 9, 12 months) and it can be computed from given equations [36], [37].

$$X_{i,j}^{k} = \sum_{l=13-k+j}^{12} V_{i-1,l} + \sum_{l=1}^{j} V_{i,l} \quad if\ j < k \qquad (1)$$

$$X_{i,j}^{k} = \sum_{l=j-k+1}^{j} V_{i,l} \quad if\ j \geq k \qquad (2)$$

Where $V_{i-1,\,l,}$ and $V_{i,l}$ represent streamflow volumes in the years of *i-1* and *i*, respectively. Based on the given information by Nalbantis and Tsakiris [13] because streamflow records can have skewed probability distribution, the Gamma distribution can be used. Therefore, before the computation of SDI, Gama distribution has been used by following steps.

The probability distribution function of Gamma distribution *g(x)* is determined by [38].

$$g(x) = \frac{1}{\beta^{a}\Gamma(a)} x^{a-1} e^{-\frac{x}{\beta}} \qquad (3)$$

Where *Γ(a)* is the gamma function and it is computed by [39].

$$\Gamma(a) = \int_{0}^{\infty} y^{a-1} e^{-y}\, dy \qquad (4)$$

For maximum likelihood method estimation, the parameters of Gamma distribution which are shape (α), and scale (β) can be calculated by [38] as follows:

$$a = \frac{1}{4A}\left(1 + \sqrt{1 + \frac{4A}{3}}\right) \qquad (5)$$

$$\beta = \frac{\bar{x}}{a} \qquad (6)$$

And where A is determined by [16], [38]

$$A = \ln(\bar{x}) - \frac{\sum \ln(x)}{n} \qquad (7)$$

n is the number of streamflow records instead of rainfall records and $\bar{x}$ is the mean of x. Then cumulative distribution function is computed by [38].

$$H(x) = q + (1 - q)G(x) \qquad (8)$$

Where q denotes the probability of zero and *G(x)* is the cumulative distribution for the selected month and time scale. If m is accepted as showing the number of zeros, then *q* can be calculated from *q=m/n* [38]. Then, *H(x)* is converted to the standard normal variable Z which has 0 mean and

1 as variance and represents the SDI value. Then via Table 2 [37] SDI values in a month and desired time scale are associated with a drought class based on its value

Table 2. Drought classification [37]

SDI Value	Category
SDI ≥2.00	Extremely Wet
1.50≤ SDI <2.00	Severely Wet
1.00≤ SDI <1.50	Moderately Wet
0≤ SDI <1.00	Mildly Wet
-1≤ SDI <0.00	Mild Drought
-1.50≤ SDI <-1.00	Moderate Drought
-2.00≤ SDI <-1.50	Severe Drought
SDI ≤-2.00	Extreme Drought

2.2.2. Estimation of Drought Severity and Drought Duration

Drought severity and drought duration are two important drought characteristics in drought analysis, and they can be easily determined by Yevjevich's Run Theory [40] and are calculated SDI values of any time scale. Using definitions in the literature, drought duration (D) describes a period which is between the beginning and end of drought while severity (S) is a cumulative summation of SDI values below the critical level with the unit of the month [17], [37] as it is demonstrated in Figure 2

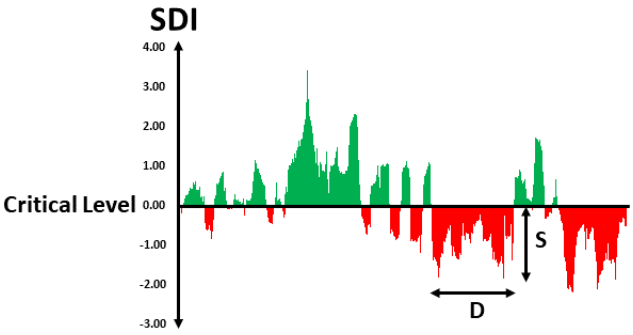

Figure 2. Drought severity (S) and duration(D)

2.2.3. Innovative Trend Analysis (ITA)

Innovative Trend Analysis (ITA) was proposed by Şen in 2012 [24], and it is a method that, unlike the most common methods, avoids a set of assumptions such as the independent structure of the time series, normality of the distribution, and data length. Based on the manner of application of the method, firstly, the data is divided into two equal parts, as both parts are in ascending order, and secondly, as it is shown in Figure 3, a 1:1 line (45^o), that shows no trend line between increasing decreasing trends, is created [19], [24], [25], [41],[42]. As it can be seen from Figure 3, any point on 1:1 line indicates no trend case, while the points above the 1:1 line show an increasing trend, and the points below the line represent a decreasing trend. In this study, ITA has been applied to determine the SDI series (1, 3, 6, 9, 12), and trends of each series have been evaluated by two classifications which are SDI<0 and SDI≥0

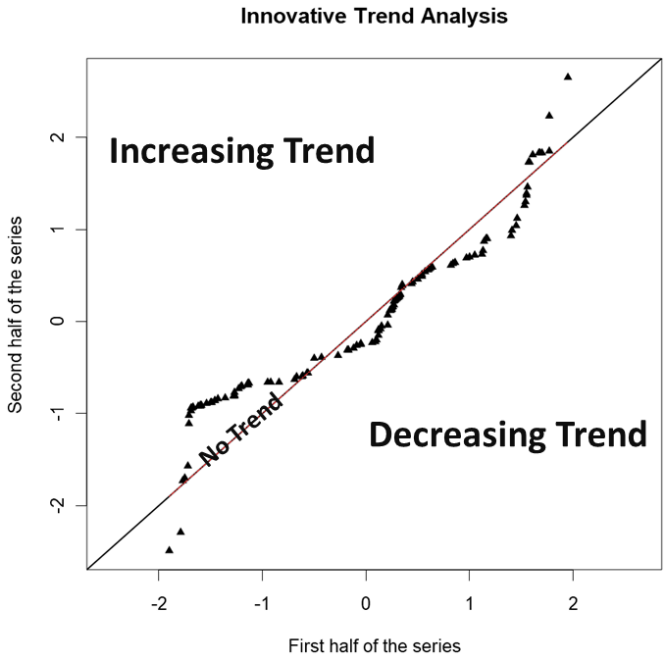

Figure. 3 ITA Template by Şen [24]

Results and Discussion

3.1. Results

In this study, using SDI, Yevjevich's Run Theory, and ITA, a hydrological drought analysis has been performed for the Kızılırmak Basin of Türkiye for the time scales of 1, 3, 6, 9, and 12 months. Calculated SDI values have been classified according to Table 1 and statistical analysis based on the percentage of occurrences has been given in Table 3. In all time scales of all stations, minimum and maximum percentages of occurrences of drought and Wet (SDI≥0) classes have been investigated, and Table 4 has been obtained. In both tables, the Wet categories given in Table 1 have been combined as "Wet" which includes SDI≥0. The following conclusions have been drawn from the findings.

- In all time scales for all stations, as can be seen from Table 3, the Mild Drought and Wet (SDI≥0) categories have the highest percentage of occurrences.

- Because Mild Drought and Wet (SDI≥0) classes have the highest percentage of occurrences, Table 4 includes the stations with the lowest and highest values of these categories among all stations. From Table 4 in all time scales, the E15A017 station, which is situated in almost the middle of the basin gives minimum values in the Mild Drought class, while the D15A236 station gives minimum values in the Wet class except at SDI-1. However, it is not possible to construct a similar relationship for maximum values.

- From Tables 3 and 4, Moderate Drought has higher minimum and maximum percentages than Severe and Extreme drought classes while Severe Drought has higher minimum and maximum percentages than Extreme Drought in all time scales.

To make the assessment simpler and more understandable if all drought categories in Table 1 are considered as "dry" (SDI<0) and all Wet categories are combined as "Wet" (SDI≥0), in SDI-1 5 stations, in SDI-3 3 stations, in SDI-6 3 stations, in SDI-9 3 stations, in SDI-12 2 stations dry percentages are higher than wet percentages.

Using obtained SDI values in all time scales and Yevjevich's Run Theory, drought severity, and drought duration have been calculated. Among these calculations, the droughts that have the highest severity and the longest-lasting have been analyzed to search the term in which the basin may have been affected and are given in Table 5. Figure 4 depicts the time series in which the most severe and/or longest-lasting events occurred. The following conclusions have been drawn from the findings.

- Among all time scales and all stations, both the longest and the highest droughts have been obtained in the SDI-12 time scale at the E15A017 station with 149.72 and 103 months as severity and duration respectively. But it is important to note that the same station also produces the same duration, but a slightly smaller severity on the SDI-9 time scale.

- From Table 5, it is clearly seen that in any time scale, it is possible that the highest values may not occur at the same time and same station. Unlike the time scales of SDI-6, SDI-9, and SDI-12, in SDI-1 and SDI-3, the highest values belong to different stations and time intervals.

Although there are drought events that have been detected before the 2000s, the basin has been exposed to the highest-valued droughts, which started in 2000

Table 3. Percentage occurrences of drought and wet categories based on SDI values

	SDI TIME SCALE				
SN	SDI-1	SDI-3	SDI-6	SDI-9	SDI-12
D15A015	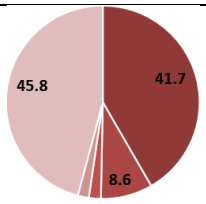	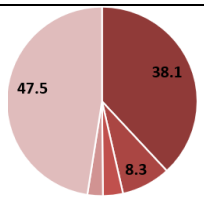	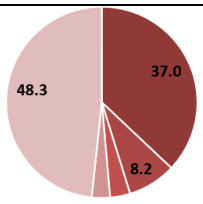	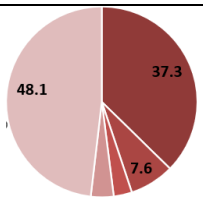	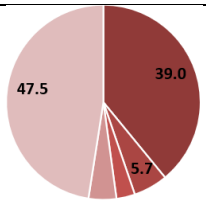
D15A095	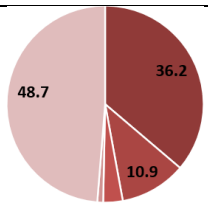	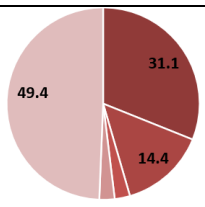	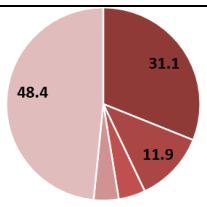	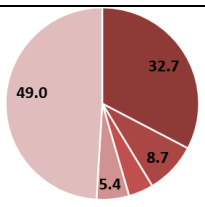	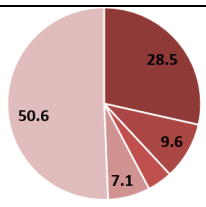

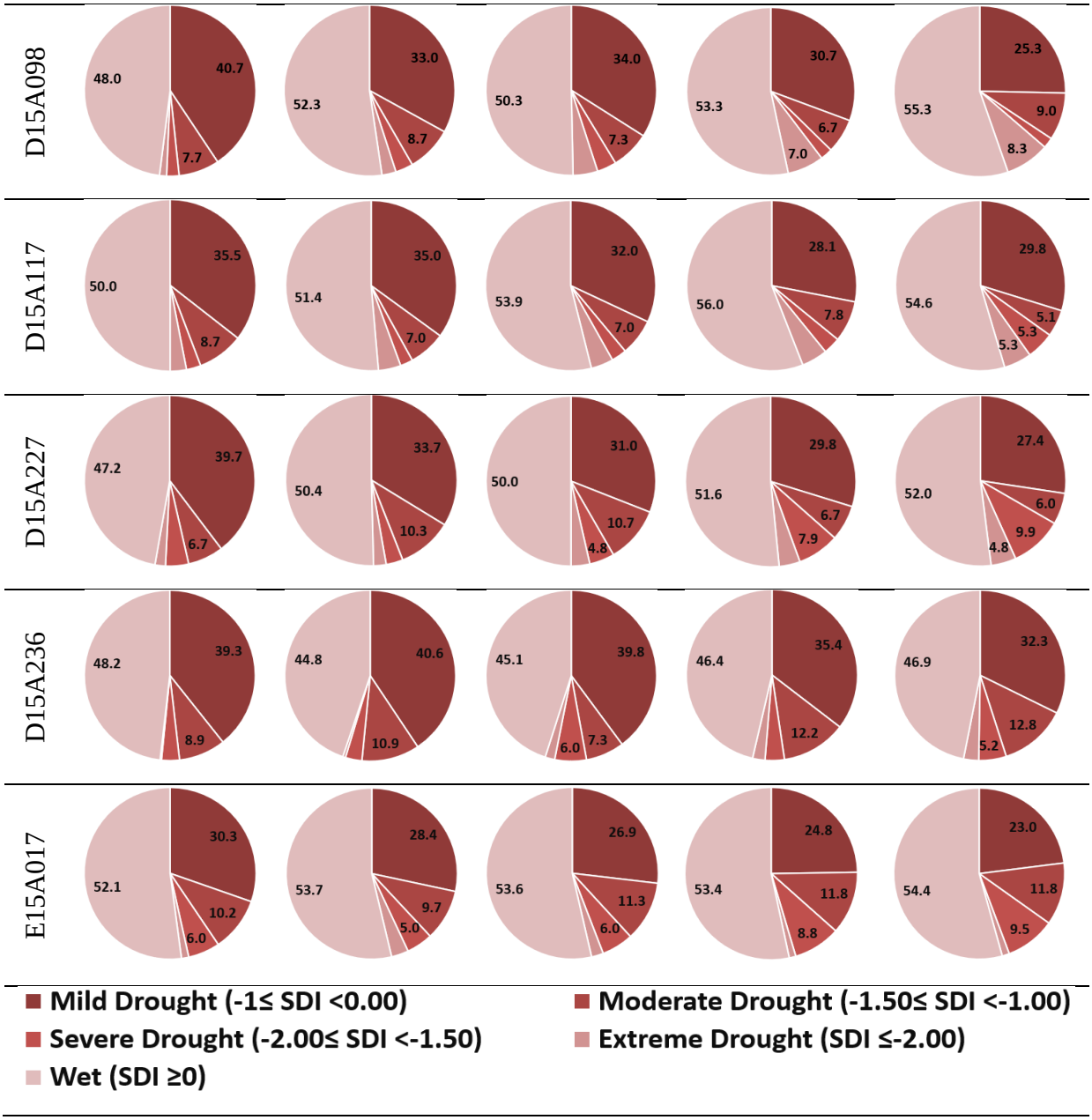

Table 4. Statistics of SDI Classes

Minimum Percentages (%)					
	SDI-1	SDI-3	SDI-6	SDI-9	SDI-12
Mild Drought	30.35	28.36	26.87	24.75	23.01
Moderate Drought	6.75	6.97	6.97	6.67	5.10
Severe Drought	2.01	2.38	2.89	2.33	2.00
Extreme Drought	0.26	0.52	1.82	1.24	1.37
Wet (SDI≥0)	45.83	44.79	45.05	46.35	46.88
Stations of Minimum Percentages					
	SDI-1	SDI-3	SDI-6	SDI-9	SDI-12
Mild Drought	E15A017	E15A017	E15A017	E15A017	E15A017
Wet (SDI≥0)	D15A015	D15A236	D15A236	D15A236	D15A236
Maximum Percentages (%)					

	SDI-1	SDI-3	SDI-6	SDI-9	SDI-12
Mild Drought	41.67	40.63	39.84	37.35	39.04
Moderate Drought	10.90	14.42	11.86	12.24	12.76
Severe Drought	5.97	4.98	5.99	8.83	9.92
Extreme Drought	3.06	4.25	4.67	7.00	8.33
Wet (SDI≥0)	52.11	53.73	53.91	55.95	55.33
Stations of Maximum Percentages					
	SDI-1	SDI-3	SDI-6	SDI-9	SDI-12
Mild Drought	D15A015	D15A236	D15A236	D15A015	D15A016
Wet (SDI≥0)	EA15017	EA15017	D15A117	D15A117	D15A098

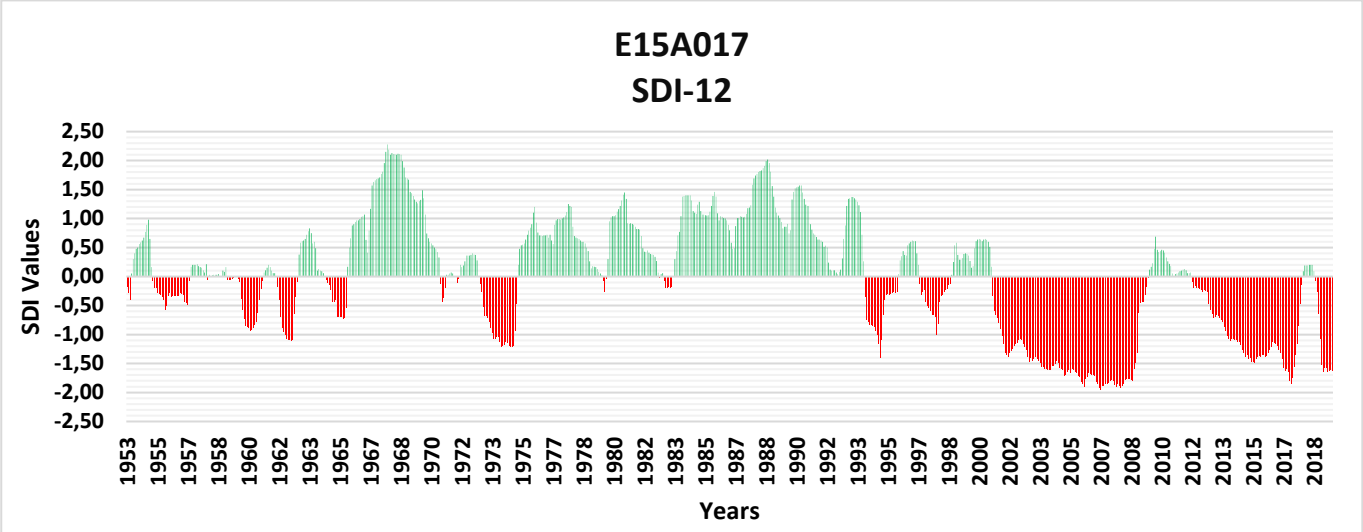

Figure. 4 The time Series of the Longest Lasted and Highest Drought

Table 5. Drought Severity and Duration Statistics

The Longest Lasted Droughts				
Time Scale	Date	Station	Severity	Duration (Months)
1	2016(3)-2019(7)	D15A236	30.48	41
3	2004(5)-2008(9)	D15A236	39.7	53
6	2001(3)-2009(7)	E15A017	127.7	101
9	2001(3)-2009(9)	E15A017	143.34	103
12	2001(5)-2009(11)	E15A017	149.72	103
The Highest Droughts				
Time Scale	Date	Station	Severity	Duration (Months)
1	2007(7)-2010(5)	D15A095	37.32	35

3	2007(9)-2010(9)	D15A095	45.57	37
6	2001(3)-2009(7)	E15A017	127.7	101
9	2001(3)-2009(9)	E15A017	143.34	103
12	2001(5)-2009(11)	E15A017	149.72	103

ITA methodology has been applied to the SDI time series separately in order to control SDI values, and obtained trend graphs have been given in Figure 5. In all analyses of both classes (SDI<0 and SDI≥0) trends with decreasing behavior have been presented as "↓" while increasing trend and no trend cases have been presented as "↑" and "0" respectively. The trend results have been given in Table 6. The following results have been obtained.

- Looking at Figure 5 and Table 6, it can be said that in most of the cases of all-time scales, a trend is present. Among 70 analyses (5*7*2=70), 78.57% of analyses have a decreasing trend, while percentages of increasing and no trend cases are 12.85% and 8.57% respectively.

- According to Table 6, D15A015, D15A098, and D15A236 stations have shown monotonic decreasing trends in both cases (SDI<0 and SDI≥0) of all time scales. E15A017 station also has decreasing trends in both cases of 3,6,9,12-month time scales. D15A117 have shown decreasing trends in both cases of 6, 9, 12- month time scales.

- D15A095 is the station where no trend case was mostly detected (5 times and 4 of them are in case of SDI≥0) while no trend case was detected only once in E15A017.

- An increasing trend of the case has been detected in D15A227 station most (7 times, and 5 of them are in SDI<0 cases). Also, in D15A117, increasing trends have been detected twice and both of them are in SDI≥0.

Again, from Table 6, a fixed trend behavior has not been detected for either SDI<0 or SDI≥0 considering all time scales of stations

Table 6. ITA trend results

		Stations						
Time Scale	SDI Class	D15A015	D15A095	D15A098	D15A117	D15A227	D15A236	E15A017
1	SDI<0	↓	0	↓	↓	↑	↓	↓
	SDI≥0	↓	0	↓	↑	↑	↓	0
3	SDI<0	↓	↓	↓	↓	↑	↓	↓
	SDI≥0	↓	↓	↓	↑	↑	↓	↓
6	SDI<0	↓	↓	↓	↓	↑	↓	↓
	SDI≥0	↓	0	↓	↓	↓	↓	↓
9	SDI<0	↓	↓	↓	↓	↑	↓	↓
	SDI≥0	↓	0	↓	↓	↓	↓	↓
12	SDI<0	↓	↓	↓	↓	↑	↓	↓
	SDI≥0	↓	0	↓	↓	↓	↓	↓

3.2. Discussion

Based on the literature review, several drought analyses have been done for different basins in Türkiye and worldwide. However, a few drought studies have been done for hydrological drought analysis in Kızılırmak Basin. The mild drought type was found to be the most common among all drought categories in this study. When it is compared to studies made for Kızılırmak Basin similar results have been detected. For example,

Arslan et al. [32] discovered that the occurrence of mild drought terms is the highest among all drought categories across all time scales studied using SPI. As another example, in a meteorological drought analysis of Kızılırmak Basin by SPI, Akturk et al. [33] have obtained that 31 years of 58 years have been affected by droughts while 28 years of this 31 years belong to mild drought. When it comes to other basins, Simsek [31] has stated that Mild drought is the recurrent type of drought in the Mediterranean Basins. Katipoğlu et al. [21] have found that in Yeşilırmak Basin which is neighbour to Kızılırmak Basin, there are lots of mild droughts in the basin between 1970-2011 water years. The same drought years as in this study have been noted in many drought analyses [7], [21], [29], [31], and [33]. Because a high number of decreasing trends have been detected with ITA in this study, researchers of [21], [26], [42] have found decreasing trends using ITA methodology as well. Even Simsek [31] has found decreasing trends for Mediterranean Basins by Mann-Kendall test. Therefore, the trend results of these studies verify the trend results of this study.

4. Conclusion and Suggestions

In this study, using the monthly mean streamflow records of 7 gauging stations that have been taken from the General Directorate of State Hydraulic Works (DSI), SDI, and ITA, a hydrological drought analysis has been performed for the time scales of 1, 3, 6, 9, and 12-month for Kızılırmak Basin of Türkiye. According to the results of the study, the conclusions are as follows:

- Mild drought and Wet (SDI≥0) have the highest percentage of occurrences in all time scales at all stations. To make the assessment simpler, when all drought categories are combined as “dry” (SDI<0) and all Wet categories are combined as “Wet” (SDI≥0) except at SDI-1, the Wet category is higher than dry ones at least 4 stations.
- Based on analysis of drought classes, it has been concluded that among Moderate, Severe, and Extreme drought classes, Moderate Drought has the highest minimum and maximum percentages while Severe Drought has higher minimum and maximum percentages than Extreme Drought in all time scales.
- Using Run Theory, the longest lasted and highest drought has been noted in the SDI-12 time scale of E15A017 station with 149.72 and 103 months as severity and duration respectively.
- Considering the determined maximum values of drought severity and duration, the basin is exposed to the longest-lasting and highest droughts starting with the year 2000 and later.
- ITA results show that most of the SDI series in any time scale has a trend, and decreasing trends dominate the analysis with 78.57%, while 3 stations, which are D15A015, D15A098, and D15A236, have completely decreasing trends.

As a result of the study's findings, it is clear that effective precautions must be taken to protect water resources and water-related sectors from the potential effects of drought. This is clearly possible by making effective water resources management plans and updating current analysis continuously. The results of this study are expected to be beneficial for local authorities

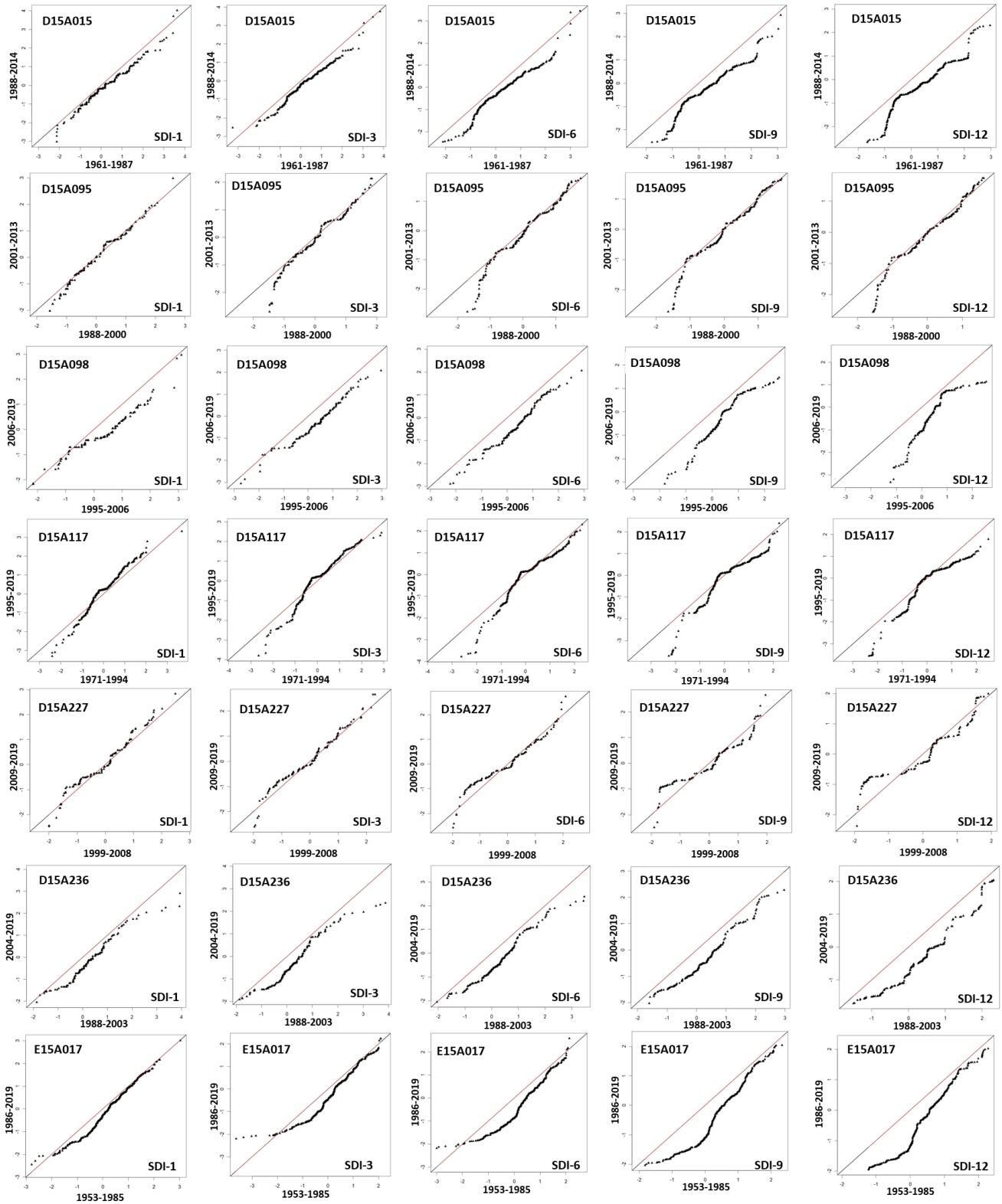

Figure. 5 ITA graphical results

Acknowledgment

The authors are thankful to the General Directorate of State Hydraulic Works (DSI) for providing the data which has been used in this study.

Contributions of the authors

The authors of this study have worked together in all steps of the study and contributed to the study equally.

Conflict of Interest Statement

There is no conflict of interest between the authors.

Statement of Research and Publication Ethics

The study is complied with research and publication ethics.

References

[1] A. K. Mishra ve V. P. Singh, "A review of drought concepts", *Journal of Hydrology*, vol. 391, no.1, pp. 202-216, September 2010, doi: 10.1016/j.jhydrol.2010.07.012.

[2] IPCC, "Climate Change 2022: Impacts, Adaptation and Vulnerability. Contribution of Working Group II to the Sixth Assessment Report of the Intergovernmental Panel on Climate Change [H.-O. Pörtner, D.C. Roberts, M. Tignor, E.S. Poloczanska, K. Mintenbeck, A. Alegría, M. Craig, S. Langsdorf, S. Löschke, V. Möller, A. Okem, B. Rama (eds.)] Cambridge University Press. Cambridge University Press, Cambridge, UK and New York, NY, USA, 3056 pp., doi:10.1017/9781009325844."

[3] Erian, W., Pulwarty, R., Vogt, J.V., AbuZeid, K., Bert, F., Bruntrup, M., El-Askary, H., de Estrada, M., Gaupp, F., Grundy, M., Hadwen, T., Hagenlocher, M., Kairu, G., Lamhauge, N., Li, W., Mahon, R., Maia, R., Martins, E.S.P.R., Meza, I., de los Milagos Skansi, M. et al. (2021). *GAR Special Report* on Drought 2021. United Nations Office for Disaster Risk Reduction (UNDRR). [Online]. Available: http://collections.unu.edu/view/UNU:8334 [Accessed: Sept.29,2022]

[4] S. M. Vicente-Serrano, J. I. López-Moreno, S. Beguería, J. Lorenzo-Lacruz, C. Azorin-Molina, ve E. Morán-Tejeda, "Accurate Computation of a Streamflow Drought Index", *Journal of Hydrologic Engineering*, vol. 17, no. 2, pp. 318-332, February 2012, doi: 10.1061/(ASCE)HE.1943-5584.0000433.

[5] M. Eşit ve M. Yüce, "Kopula Yöntemi ile Osmaniye Bölgesinin İki Değişkenli Kuraklık Frekans Analizi", *Academic Platform - Journal of Engineering and Science*, vol. 9, no: 3, Art. no. 3, September 2021, doi: 10.21541/apjes.728959.

[6] D. A. Wilhite ve M. H. Glantz, "Understanding: the Drought Phenomenon: The Role of Definitions", *Water International*, vol. 10, no. 3, pp. 111-120, January 1985, doi: 10.1080/02508068508686328.

[7] A. A. Kumanlioglu, "Characterizing meteorological and hydrological droughts: A case study of the Gediz River Basin, Turkey", *Meteorological Applications*, vol. 27, no: 1, s. e1857, 2020, doi: 10.1002/met.1857.

[8] V. Gümüş, "Akım Kuraklık İndeksi İle Asi Havzasının Hidrolojik Kuraklık Analizi", *Gazi University Journal of Science Part C: Design and Technology*, vol. 5, no: 1, Art. no: 1, March 2017.

[9] S. Yaltı ve H. Aksu, "Drought Analysis of Iğdır Turkey", *Turkish Journal of Agriculture - Food Science and Technology*, vol. 7, no: 12, Art. no: 12, December 2019, doi: 10.24925/turjaf.v7i12.2227-2232.3004.

[10] G. Tsakiris *vd.*, "Drought characterization. Drought management guidelines technical annex, 58, 85-102.", 2007.

[11] A. Zargar, R. Sadiq, B. Naser, ve F. I. Khan, "A review of drought indices", *Environ. Rev.*, vol. 19, no NA, pp. 333-349, Ara. 2011, doi: 10.1139/a11-013.

[12] M. D. Svoboda ve B. A. Fuchs, "Handbook of Drought Indicators and Indices*", *Drought and Water Crises*, CRC Press, 2017.

[13] I. Nalbantis ve G. Tsakiris, "Assessment of Hydrological Drought Revisited", *Water Resour Manage*, vol. 23, no. 5, pp. 881-897, March 2009, doi: 10.1007/s11269-008-9305-1.

[14] Y. Avsaroglu ve V. Gumus, "Assessment of hydrological drought return periods with bivariate copulas in the Tigris river basin, Turkey", *Meteorol Atmos Phys*, vol. 134, no: 6, pp. 95, December 2022, doi: 10.1007/s00703-022-00933-2.

[15] E. Turhan, S. Değerli, ve E. N. Çatal, "Long-Term Hydrological Drought Analysis in Agricultural Irrigation Area: The Case of Dörtyol-Erzin Plain, Turkey", *CTNS*, pp. 501-512, July 2022, doi: 10.47068/ctns.2022.v11i21.054.

[16] M. Eşit ve M. İ. Yüce, "Çok Değişkenli Kuraklık Frekans Analizi ve Risk Değerlendirmesi: Kahramanmaraş Örneği", *Doğal Afetler ve Çevre Dergisi*, vol. 8, no.2, Art. pp 2, July. 2022, doi: 10.21324/dacd.1066958.

[17] J. A. Dracup, K. S. Lee, ve E. G. Paulson Jr., "On the definition of droughts", *Water Resources Research*, vol. 16, no. 2, pp. 297-302, 1980, doi: 10.1029/WR016i002p00297.

[18] D. A. Wilhite, "Wilhite, D. A. (2004) Drought as a natural hazard, in international perspectives on natural disasters; occurrence, mitigation, and consequences, edited by JP Stollman, J. Lidson and LM Dechano. pp.147-162.", 2004.

[19] A. Elouissi, B. Benzater, I. Dabanli, M. Habi, A. Harizia, ve A. Hamimed, "Drought investigation and trend assessment in Macta watershed (Algeria) by SPI and ITA methodology", *Arab J Geosci*, vol. 14, no. 14, pp. 1329, July 2021, doi: 10.1007/s12517-021-07670-7.

[20] M. I. Yuce ve M. Esit, "Drought monitoring in Ceyhan Basin, Turkey", *Journal of Applied Water Engineering and Research*, vol. 9, no. 4, pp. 293-314, October. 2021, doi: 10.1080/23249676.2021.1932616.

[21] O. M. Katipoğlu, S. N. Yeşilyurt, ve H. Y. Dalkiliç, "Yeşilırmak havzasındaki hidrolojik kuraklıkların Mann-Kendall ve Yenilikçi Şen yöntemi ile trend analizi", *Gümüşhane Üniversitesi Fen Bilimleri Dergisi*, vol. 12, no. 2, Art. no. 2, April 2022, doi: 10.17714/gumusfenbil.1026893.

[22] P. Bhunia, P. Das, ve R. Maiti, "Meteorological Drought Study Through SPI in Three Drought Prone Districts of West Bengal, India", *Earth Syst Environ*, vol. 4, no: 1, pp. 43-55, March 2020, doi: 10.1007/s41748-019-00137-6.

[23] A. Danandeh Mehr ve B. Vaheddoost, "Identification of the trends associated with the SPI and SPEI indices across Ankara, Turkey", *Theor Appl Climatol*, vol. 139, no. 3, pp. 1531-1542, February 2020, doi: 10.1007/s00704-019-03071-9.

[24] Z. Şen, "Innovative Trend Analysis Methodology", *Journal of Hydrologic Engineering*, vol. 17, no. 9, pp. 1042-1046, September 2012, doi: 10.1061/(ASCE)HE.1943-5584.0000556.

[25] M. S. Ashraf, I. Ahmad, N. M. Khan, F. Zhang, A. Bilal, ve J. Guo, "Streamflow Variations in Monthly, Seasonal, Annual and Extreme Values Using Mann-Kendall, Spearmen's Rho and Innovative Trend Analysis", *Water Resour Manage*, vol. 35, no: 1, pp. 243-261, January 2021, doi: 10.1007/s11269-020-02723-0.

[26] V. Gumus, Y. Avsaroglu, ve O. Simsek, "Streamflow trends in the Tigris river basin using Mann−Kendall and innovative trend analysis methods", *J Earth Syst Sci*, vol. 131, no. 1, pp. 34, January. 2022, doi: 10.1007/s12040-021-01770-4.

[27] M. M. Kale, "Akarçay Kapalı Havzası için Hidrolojik Kuraklık Analizi", *Coğrafya Dergisi*, no. 42, Art. no. 42, July 2021.

[28] V. Gümüş, M. S. Yildiz, ve O. Şimşek, "Hidrolojik Kuraklık Değerlendirmesi: Murat Nehri-Palu Örneği", *Harran Üniversitesi Mühendislik Dergisi*, vol. 3, no. 3, Art. no. 3, December 2018.

[29] A. Ozkaya ve Y. Zerberg, "A 40-Year Analysis of the Hydrological Drought Index for the Tigris Basin, Turkey", *Water*, vol. 11, no. 4, Art. no. 4, April 2019, doi: 10.3390/w11040657.

[30] T. B. Altın, F. Sarış, ve B. N. Altın, "Determination of drought intensity in Seyhan and Ceyhan River Basins, Turkey, by hydrological drought analysis", *Theor Appl Climatol*, vol. 139, no. 1, pp. 95-107, January 2020, doi: 10.1007/s00704-019-02957-y.

[31] O. Simsek, "Hydrological drought analysis of Mediterranean basins, Turkey", *Arab J Geosci*, vol. 14, no. 20, pp. 2136, October 2021, doi: 10.1007/s12517-021-08501-5.

[32] O. Arslan, A. BiLgiL, ve O. Veske, "Standart Yağış İndisi Yöntemi İle Kızılırmak Havzası'nın Meteorolojik Kuraklık Analizi", *Ömer Halisdemir Üniversitesi Mühendislik Bilimleri Dergisi*, vol. 5, no. 2, pp. 188-194, July 2016, doi: 10.28948/ngumuh.295572.

[33] G. Akturk, U. Zeybekoglu, ve O. Yildiz, "Assessment of meteorological drought analysis in the Kizilirmak River Basin, Turkey", *Arab J Geosci*, vol. 15, no. 9, pp. 850, April 2022, doi: 10.1007/s12517-022-10119-0.

[34] Tarım ve Orman Bakanlığı, "Kızılırmak Havzası Taşkın Yonetim Plani Yönetici Özeti". T.C. Tarım ve Orman Bakanlığı, 2019. [Online].

Available: https://www.tarimorman.gov.tr/SYGM/Sayfalar/Detay.aspx?SayfaId=53 [Accessed: Oct. 3,2022]

[35] A. Malik, A. Kumar, S. Q. Salih, ve Z. M. Yaseen, "Hydrological Drought Investigation Using Streamflow Drought Index", içinde *Intelligent Data Analytics for Decision-Support Systems in Hazard Mitigation: Theory and Practice of Hazard Mitigation*, R. C. Deo, P. Samui, O. Kisi, ve Z. M. Yaseen, Ed. Singapore: Springer, 2021, pp. 63-88. doi: 10.1007/978-981-15-5772-9_4.

[36] A. A. Paulo, L. S. Pereira, ve P. G. Matias, "Analysis of Local and Regional Droughts in Southern Portugal using the Theory of Runs and the Standardised Precipitation Index", *Tools for Drought Mitigation in Mediterranean Regions*, G. Rossi, A. Cancelliere, L. S. Pereira, T. Oweis, M. Shatanawi, ve A. Zairi, Ed. Dordrecht: Springer Netherlands, 2003, pp. 55-78. doi: 10.1007/978-94-010-0129-8_4.

[37] X. Hong, S. Guo, Y. Zhou, ve L. Xiong, "Uncertainties in assessing hydrological drought using streamflow drought index for the upper Yangtze River basin", *Stoch Environ Res Risk Assess*, vol. 29, no. 4, pp. 1235-1247, May 2015, doi: 10.1007/s00477-014-0949-5.

[38] H. C. S. Thom, "Some methods of climatological analysis, World Meteorological Organization (WMO), Technical Note No. 81 (WMO - No. 199.TP.I03), Geneva, Switzerland, 69ss.", 1966.

[39] D. C. Edwards, "Characteristics of 20th Century drought in the United States at multiple time scales. Air Force Inst of Tech Wright-Patterson Afb Oh.", 1997.

[40] V. Yevjevich, "An objective approach to definitions and investigations of continental hydrologic droughts", *Journal of Hydrology*, vol. 7, no. 3, pp. 353, March 1967, doi: 10.1016/0022-1694(69)90110-3.

[41] S. Berhail, M. Tourki, I. Merrouche, ve H. Bendekiche, "Geo-statistical assessment of meteorological drought in the context of climate change: case of the Macta basin (Northwest of Algeria)", *Model. Earth Syst. Environ.*, vol. 8, no. 1, pp. 81-101, March 2022, doi: 10.1007/s40808-020-01055-7.

[42] U. Serencam, "Innovative trend analysis of total annual rainfall and temperature variability case study: Yesilirmak region, Turkey", *Arab J Geosci*, vol. 12, no. 23, pp. 704, November 2019, doi: 10.1007/s12517-019-4903-1.

Bitlis Eren Üniversitesi Fen Bilimleri Dergisi
BİTLİS EREN UNIVERSITY JOURNAL OF SCIENCE
ISSN: 2147-3129/e-ISSN: 2147-3188
VOLUME: 12 NO: 1 PAGE: 140-145 YEAR: 2023
DOI:10.17798/bitlisfen.1205458

Commercial Lighting Design in Human-Centered Lighting Concept

Şakir PARLAKYILDIZ[1*]

[1]*Bitlis Eren University, Technical Sciences Vocational School, 13100, Bitlis*
(ORCID: 0000-0003-0885-023X)

Keywords: Lighting, Luminance, Circadian, Human-Centered Lighting.

Abstract

In this study, the lighting design of a building in the Organized Industrial Zone, which was converted from a warehouse to a commercial kitchen, was designed according to the Human-Centered Lighting concept. Point lighting calculations were made for commercial kitchen environments with artificial lighting. In order to reduce the negative effects of lighting on human health, lighting that will not disrupt the circadian rhythm should be provided. By using direct lighting, without changing the architectural design, it has been tried to provide optimum lighting suitable for human biology with low-cost artificial lighting arrangements. According to WELL standards, an average of at least 500 lux conditions should be provided in the relevant work area on counters and other food preparation or production areas in Commercial Kitchen Lighting. This area, which was designed as a warehouse for this purpose, was designed as a commercial kitchen in terms of lighting. As a result of the design, a lighting design was made in accordance with the WELL standards according to the Human-Centered Lighting concept. In this way, the visual comfort of the working personnel is improved and optimum circadian effects are provided.

1. Introduction

Each place has different lighting needs according to its usage characteristics and intensity. Lighting designs; Direct use of elements such as geographical features, architectural design, general concept, intended use. Lighting design is one of the major costs of the overall architecture and the entire space. Because artificial lighting sources have direct effects on the people using the space. Just as the architecture of the buildings is planned according to their intended use, the lighting design is planned according to their useful life and purpose. It reveals different placements in lighting designs, even in the smallest units of the houses, in presentations used in different shapes and purposes such as kitchen, living room, bedroom. As soon as the sun begins to illuminate the earth, the main determinant of the day cycle is daylight. Daylight determines when to wake up and when to sleep. Daylight has a direct effect on people both physically and psychologically. For this reason, the basic element in building designs from the past to the present is daylight. Facade direction and window width in buildings are shaped accordingly. Daylight is also decisive in terms of its effects on health and energy savings. A controlled building that can make maximum use of daylight provides a healthy and energy-efficient use. However, nowadays, the usage density criterion has become a priority rather than the use of daylight in designs. That's why there are offices, hospitals, and even homes that don't get any light. Developed as a solution to this situation, Human Centric Lighting brings the light intensity and color temperature of daylight to indoor spaces. Thus, it supports the correct balancing of people's biological rhythms even in an area completely independent of the outside world [1-4].

Human Centric Lighting (HCL) enables people to increase their living comfort by supporting them with the right artificial light with features closest to daylight. Acting as a simulation of the sun indoors, HCL primarily aims to provide a healthy light. Light is very important for the circadian rhythm, which determines people's daily hormonal patterns. The

*Corresponding author: sparlakyildiz@beu.edu.tr
Received: 15.11.2022, Accepted: 07.03.2023

biological effects of light conditions can be listed as the sleep-wake cycle, heart rate-blood pressure, body temperature, hormone release, metabolic activities, and concentration-motivation.

In traditional lighting designs that do not have the dynamism of natural daylight, the light has a constant color temperature. Whereas, daylight has a blue wavelength in the morning and a yellow wavelength in the afternoon. This difference in daylight affects the intensity of activities and mobility during the day. Artificial lighting that does not adapt to daylight can lead to disruptions and imbalances in the circadian rhythm. Circadian rhythm disorder manifests itself as fatigue, lack of motivation, anxiety, and sleep disorder in humans.

HCL supports the circadian rhythm at the right time, with the ideal color temperature and light intensity. It can be adjusted with wireless automation systems, making it possible to be specially designed for spaces or personal needs. Thus, a suitable cycle can be created for people working at different working hours [5-8].

2. Human – Centric Lighting Concept

Human Centric Lighting, at the right time, with the right artificial light support, artificial light; It is a lighting concept that aims to increase the comfort of life by regulating its visual, biological, and psychological effects. The Human-Centered Lighting concept is aimed at using the effects of light sources in the most efficient way. Natural sunlight, which is our source of life; changes dynamically in color temperature, and quantity. However, due to today's conditions, artificial light sources are used mostly in indoor places where we spend our time. These artificial light sources usually have a fixed color temperature and color intensity. This situation adversely affects human health.

HCL, at the right time, with the right artificial light support; is a lighting concept that aims to increase the comfort of life by regulating its visual, biological, and psychological effects. the human-Centered Lighting concept, it is aimed to use the effects of light sources in the most efficient way. Natural sunlight, which is our source of life; changes dynamically in color temperature, and quantity. However, due to today's conditions, artificial light sources are used mostly in indoor places where we spend our time. These artificial light sources usually have a fixed color temperature and color intensity. This situation adversely affects human health. The Human Centric Lighting concept allows artificial light to change dynamically like natural daylight [9-12]. With this concept, the spread, intensity, and color temperature of the light provided by artificial light sources can be managed. Thus, when designing lighting systems, the visual, biological, and psychological effects of light on people are taken into account. In cases where the health-related effects of light are not taken into account, disruptions in the sleep-wake cycle, low efficiency, performance, and concentration, and some imbalances in mood may occur. The Human Centric Lighting concept aims to increase efficiency by providing the right light intensity and color temperature in order to prevent such negative effects [11-15].

The use of artificial light, especially in corporate buildings, brings with it intense energy consumption. In such cases, energy efficiency is ensured in the long term thanks to the Human Centric Lighting concept. In addition, it enables the creation of healthy and high-productivity spaces by providing positive effects on people. The HCL concept, which includes holistic lighting and space planning, appropriate installation, and correct application processes, is dynamic and functional from start to finish. As the difference between artificial lights and sunlight increases, it becomes difficult to adapt and the Circadian Rhythm is disturbed. The light spectrum of good lighting should be similar to the spectrum distribution in daylight.

The appropriate Lighting also directly affects the perception, aesthetics, comfort, psychology, and performance of people. While all these elements are negatively affected in a place that is not properly illuminated, it is possible to increase efficiency by creating a direct positive effect on people, thanks to the Human-Centered Lighting concept. The concept of Human-Centered Lighting, which can be applied to all living and working areas, has critical importance especially for offices that are used heavily and for places such as hospitals, which have great importance for health. In accordance with the principle of Human Centric Lighting, it is aimed to provide the highest benefit in terms of efficiency and health by calculating the psychological and biological effects of light on people. With this concept, not only energy is managed efficiently; but At the same time, by increasing the contribution and creativity of the employees, much more benefits than expected can be created. In visual lighting design, the goal is to support visual acuity level by setting a threshold for adequate light levels and by asking for lighting to be balanced indoors. According to the WELL standards, an average of at least 500 lux lighting should be provided on counters and other food preparation or production areas in Commercial Kitchen Lighting.

According to the Circadian Lighting Design criteria specified in the WELL standards, the purpose of Human Centric Lighting is to support circadian health by setting a minimum threshold for daytime light intensity [9-11, 16-19]. Light is one of the main drivers of the circadian system, which begins in the brain, regulating physiological rhythms throughout the tissues-organs of the body, influencing hormone levels and the sleep-wake cycle. The method should be given in detail and clearly in terms of the reproducibility of the study. According to the Human Centric Lighting concept, Equivalent Melanopic Lux is measured in the vertical plane at eye level with respect to the human body. According to the Human Centric Lighting concept, the aim of visual lighting design is to set a threshold for sufficient light level and to support balanced visual acuity. According to WELL standards, an average of at least 500 lux lighting should be provided on counters and other food preparation or production areas in Commercial Kitchen Lighting [9-11].

2.1. Lighting Criteria

The lighting quality should always provide adequate visual performance for the task involved. Average illuminance level, uniform distribution, glare control, and color rendering are the quality parameters taken into account in providing visual comfort. Inadequate lighting makes documents or computer screens difficult to see due to inappropriate lighting levels, glare, and unwanted shadows. Insufficient lighting prevents the correct perception of the environment, objects, and colors. Artificial lighting systems can be useful in environments where daylight is not sufficiently utilized. By controlling the light intensity, optimum illumination can be made according to the hours [20-26].

The human-oriented lighting concept is measured as the vertical lighting level. Horizontal lighting requirements in the working plane are a familiar concept. However, there is no planar conversion method between vertical lighting and horizontal lighting. Since the amount of light in the vertical plane is a combination of direct light from a luminaire, light reflected from walls, light reflected from ceilings, and light from windows, this method, which depends entirely on how the light is transmitted to the space, is called the Equivalent Melanopic Lux value. For Circadian Lighting Design, the criterion of providing any limit value condition of U_o value is not taken into consideration [9-11, 27-30].

2.2. Illuminance Level

The illuminance level, which is the ratio of the incident luminous flux per unit time to the surface area, is defined as equal to the luminous flux of the surface divided by the area of that surface. Its symbol is 'E' and its unit is lx. However, the unit used in America is a foot candle'. Mathematically, E (Illuminance Level) is called the ratio of Luminous Flux to Area. While the intensity of light falling on a given surface area does not change, the illuminance level in that area does not change. The 'Illumination quality' changes. However, although the light intensity remains the same, the illumination level depends on the change in distance. In general, when referring to the measured and recommended illuminance levels, the values reaching the horizontal operating plane are referred to. However, the levels read on different surfaces depend on the location of the source and the measuring instrument. They differ in the same environment. For example, if the illuminance level meter is towards light sources, from horizontal (close to the line of sight)) high values will be read [20-26].

3. Results and Discussion

In Commercial Kitchen Lighting, an average of at least 500 lux conditions have been tried to be achieved in counters and other food preparation or production areas. For this purpose, an area designed as a warehouse is designed as a commercial kitchen in terms of lighting. The warehouse, which has been transformed in terms of lighting, is seen in Figure 1.

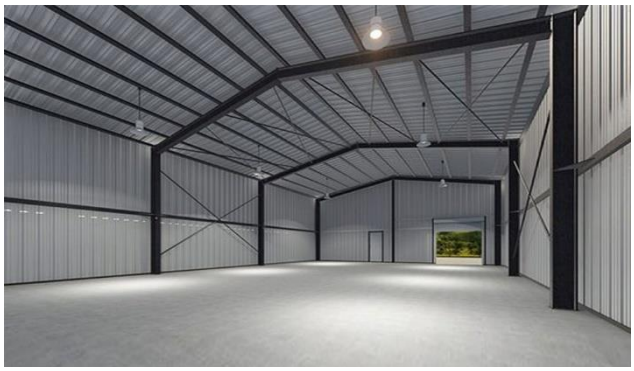

Figure 1. The warehouse transformed in terms of lighting.

The ceiling height of the lamps is 7 m. for this reason, the distance between the surface to be illuminated and the lamp is included in the calculation as 7 m. According to the Human Centered Lighting concept, an average of 500 lux lighting should be provided in the $E_{average}$. The luminaires to be used in area lighting

have been selected considering the level of illumination, the brightness level of the area and walls, lighting homogeneity, and economy. Calculations were determined according to the point illuminance method.

The lighting system for area-surface parameters is in a double-row suspension arrangement. The top view of the area for which the Point Lighting Calculation is made is shown in Figure 2.

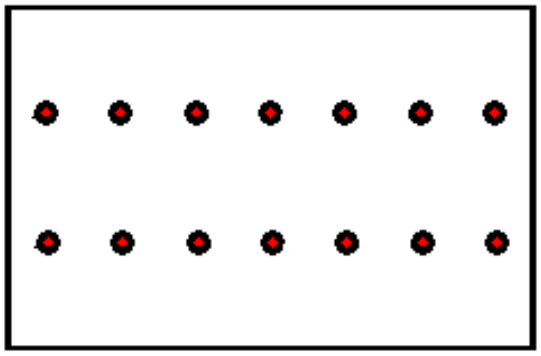

Figure 2. The top view of the area for which the Point Lighting Calculation is made.

As the lighting parameters, features such as the distance between lamps, lamp height, lamp distance to the surface, IP protection class, pollution rate, cleaning time, and maintenance factor were selected as the lighting parameters. For the luminaire parameters, variables such as the angle of the luminaire relative to the surface, the luminaire's power, its lifetime, and luminous flux were taken into account in the calculation. LED luminaires with a luminous flux value of 55000 lumens were used in the commercial kitchen environment. Luminaire angles were chosen as 0, floor reflectivity 0.10, and maintenance factor 0.93 (for less polluted environments cleaned annually). An enclosed area with insufficient natural lighting is chosen. The working area is 12 m wide and 90 m long. The area between the two luminaires where the point lighting calculation is made is divided into 90 points. The average illuminance level ($E_{average}$) was calculated for each rectangular area by dividing the 12 m * 11 m area into 90 equal parts of 1.10 m * 1.333 m dimensions. $E_{average}$ should provide 500 lux and above.

Table 1. Lighting parameters

Height of luminaire from ground (m)	7
Distance between luminaires (m)	11
Armature Angle (degree)	0°
Type of the Lamp	LED
Lighting Arrangement	Double row
Lamp luminous (flux)	55000
Area Length (m)	90
Area Width(m)	12
Ground reflectance factor	0.10
Maintenance Factor (once a year)	0.93
Height of luminaire from ground (m)	7

In Table 1, for the daytime, direct lighting scenario, the condition of having an $E_{average}$ value of 500 lux and above for 90 points in the selected area has been checked. Circadian Lighting Design was successfully completed with direct lighting during the day. Because while the current level of light is insufficient, it is understood that the amount of light that human biology will need is provided in this environment by increasing the amount of light. The illuminance values of 90 points calculated for direct lighting are shown in Table 2.

Table 2. Illuminance values for 90 points calculated for direct lighting.

	E_{min}=100 Lux		E_{max}=631.96 Lux		$E_{avarage}$=500.96 Lux					
m/m	0.550	1.650	2.750	3.850	4.950	6.050	7.150	8.250	9.350	10.450
0.667	328.808	326.709	351.947	366.130	363.079	363.109	366.222	352.103	326.931	329.099
2.000	426.705	428.186	453.276	488.577	510.843	510.872	488.659	453.415	428.387	426.967
3.333	504.162	502.317	520.878	581.300	627.982	628.006	581.372	521.000	502.488	504.390
4.667	573.610	573.158	586.788	627.863	631.934	631.956	627.929	586.901	573.319	573.823
6.000	622.362	586.300	583.452	613.171	586.355	586.378	613.238	583.565	586.462	622.576
7.333	573.610	573.158	586.788	627.863	631.934	631.956	627.929	586.901	573.319	573.823
8.667	504.162	502.314	520.878	581.300	627.982	628.006	581.372	521.000	502.488	504.390
10.000	426.705	428.189	453.276	488.577	510.843	510.871	488.659	453.415	428.387	426.967
11.333	328.808	326.709	351.947	366.130	363.079	363.109	366.222	352.103	326.931	329.099

4. Conclusion and Suggestions

Indoor lighting should be used to support circadian rhythm in a variety of application areas, such as schools, offices, hospitals, prisons, and other businesses operating in confined spaces where area lighting is provided. In the new generation of human-centered architectural design, lighting systems must not only meet the visual needs but also support the biological (eg sleep-wake order) and psychological (eg mood, mental fatigue, stress) needs of the individuals. In human-oriented lighting solutions, lighting systems that offer optimized light settings according to the time of day, weather (cloudy or sunny), and the body's metabolism status (sleepy or stressed) should be used.

As a result, it is necessary to make maximum use of daylight for the physical and biological needs of human beings and for a sustainable environment. In addition to the use of daylight, making artificial light suitable for human nature positively affects health. Commercial Kitchen Lighting has an average of at least 500 lux in counters and other food preparation or production areas. Special lighting should be made by the lighting designer according to the needs and standards of each project. Human-Oriented According to the lighting concept, architectural lighting design was made in accordance with the criteria of WELL standards. In this respect, the lighting design is successful because the $E_{average}$ value was calculated as 500.96 lux in this study.

Statement of Research and Publication Ethics

The study is complied with research and publication ethics

References

[1] R. M. Figueiro, M. Bullough, J. and A. Bierman, "*A model of phototransduction by the human circadian system*", Brain Research Rev, vol. 50(2), pp. 213-228, 2005.

[2] M. S. Rea, M. G. Figueiro, A. Bierman and R. Hamner, "*Modelling the spectral sensitivity of the human circadian system*", Lighting Research & Technology, vol. 44(4), pp. 86-96, 2012.

[3] Z. Ok Davarcı, M. Sahin, M. Akar, "*Luminance measurement and estimation methods in road*", Light & Engineering, Vol. 30,6, 2022.

[4] M. S. Cengiz, "*Lighting master plan application in living areas*", Light & Engineering, Vol. 30, 6, pp. 124-132, 2022.

[5] M.S. Cengiz, "*Human Centered Architectural Illumination Design in Prisons*", Light & Engineering, Vol. 30, 2, pp. 46–54, 2022

[6] P. R. Boyce, Human factors in lighting Third Edition, 2014. ISBN 9780429104763.

[7] P. R. Boyce, Light, lighting and human health, Lighting Research & Technology. First Published April 28, 2021.

[8] M. S. Cengiz, "*Use of Daylight in Houses and Villas from Modern Architectural Buildings*", European Journal of Science and Technology-Avrupa Bilim ve Teknoloji *Dergisi*, Vol. 38,4, pp. 247-258, 2022.

[9] International WELL Building Instute-Circadian Lighting Design Q4-2020, Melanopic Light Intensity for Work Areas 2020 version. https://standard.wellcertified.com/light/circadian-lighting-design

[10] International WELL Building Instute-Circadian Lighting Design, Light, Light Features- Q4-2020 version, 2020. https://standard.wellcertified.com/light

[11] Ö. Memiş, and N. Ekren, "*İnsan Odaklı Aydınlatma*", International. Per. Recent Tech. in Applied Engineering., 1:30-35, 2019.

[12] S. B. Efe, and D. Varhan, "*Interior Lighting of a Historical Building by Using LED Luminaires a Case Study of Fatih Paşa Mosque, Light and Engineering"*, 28(4), pp. 77–83, 2020.

[13] S.B. Efe, "*UPFC Based Real-Time Optimization of Power Systems for Dynamic Voltage Regulation*", Computer Modeling in Engineering & Sciences. Vol. 116, pp. 391-406, 2018.

[14] M. S. Cengiz, "*Effects of Luminaire Angle and Illumination Topology on Illumination Parameters in Road Lighting*", Light & Engineering, 28(4), pp. 47–55, 2020.

[15] M. S. Cengiz, "*Role of Functional Illumınation Urban Beautification: Qatar-Doha Road Illumınation Case*", Light & Engineering, Vol. 30,3, pp. 34-42, 2022.

[16] R. I., Stolyarevskaya, "*Revıew of The Features of Using Mini-Spectroradiometers with CCD-Arrays in Applied Photometry*", Light & Engineering, Vol. 29, # 1, pp. 21–29, 2021.

[17] J. B. Aizenberg, and V. P. Budak, "*The Science of Light Engineering, Fields of Application and Theoretical Foundations*", *Light & Engineering*, Vol. 26, # 3, pp, 4-6, 2018

[18] M. S. Cengiz, and Ç. Cengiz, "*Numerical Analysis of Tunnel LED Lighting Maintenance Factor*", IIUM Engineering Journal. Vol. 19(2), pp.154-163, 2018.

[19] Cengiz, M.S. Effects of Luminaire Angle on Illumination Performance in Tunnel Lighting, *Balkan Journal of Electrical & Computer Engineering*, Vol. 7(3), pp. 250–256, 2019.

[20] CIE 140:2000 - Road Lighting Calculations. CIE140, International Commission on Illumination, *Road Lighting Calculations,* Vienna-Austria, 33 (2000).

[21] CIE 140:2019 Road Lighting Calculations. CIE 140, International Commission on Illumination, *2nd Edition* ISBN:978-3-902842-56-5, 2019.

[22] A. Ivashin Eugene, B. B. Khlevnoy, S.Shirokov Stanislav, and V. Tishchenko Eugene, "*Development of New Photometric Standards Based on High Power LEDs*", Light & Engineering, Vol. 26,1, pp. 58–62, 2018.

[23] M. Ferencikova and S. Darula, "*Availabity of Dayligting in School Operating Time*", Light & Engineering, V25, #2, pp. 71–78, 2017.

[24] M. S. Cengiz, "*The Relationship between Maintenance Factor and Lighting Level in Tunnel Lighting*", Light & Engineering, vol. 27(3), pp. 75–88, 2019.

[25] M. S. Cengiz, "*The Interaction of Daylight with Design and Place in Religious Buildings According to Modern Architecture*", European Journal of Science and Technology-Avrupa Bilim ve Teknoloji Dergisi, Vol. 35, #4, pp. 195-202, 2022.

[26] Y. Sayan, Y. Kim J., and H. Wu H. "*Residual Stress Measurement of a Single-step Sintered Planar Anode Supported SC-SOFC Using Fluorescence Spectroscopy*", *Bitlis Eren Üniversitesi Fen Bilimleri Dergisi*, vol. 11,3, pp. 902-910, 2022.

[27] Y. Sayan, Venkatesan V,Guk E, Wu H, Kim J-S., "*Single-step fabrication of ananode supported planar single-chamber solid oxidefuel cell*", Internaional Journal Appl. Ceram. Technol. pp. 1–13, 2018.

[28] A. A. Tikhomirov, S. A. Ushakova, S A, and V. N. Shikhov, "*Features Choice of Light Sources for BioTechnical Life Support Systems for Space Applications*", Light & Engineering, Vol. 26,4, pp. 117–121, 2018.

[29] V. P. Budak, M. D. Kovyrkova, D. N. Makarov, S. Yu. Minaeva and A. A. Skornyakova, "*Light Design – Development of Creativity of Light Engineering Students*", Svetotekhnika, # 1, pp. 80–83, 2019.

[30] V. N. Kuzmin and S. E: Nikolaev, "*Methods and Devices for Quick Evaluation of Optical Radiation Energy Efficiency under Photoculture Conditions*", Light & Engineering, Vol. 24,4, pp. 99–104, 2016.

Bitlis Eren Üniversitesi Fen Bilimleri Dergisi
BİTLİS EREN UNIVERSITY JOURNAL OF SCIENCE
ISSN: 2147-3129/e-ISSN: 2147-3188
VOLUME: 12 NO: 1 PAGE: 146-150 YEAR: 2023
DOI:10.17798/bitlisfen.1205608

Synthesis of N-Mannich bases from 5-((4-methylpiperazin-1-yl)methyl)-1,3,4-oxadiazole-2-thiol

Yıldız UYGUN CEBECİ*

Chemistry Department, Faculty of Science, Kırklareli University, Kırklareli, Turkey

(ORCID: 0000-0001-7949-0329)

Keywords: Mannich base, synthesis, 1,3,4-oxadiazole

Abstract Methyl (4-methylpiperazin-1-yl)acetate (**2**) were synthesized by the condensation of compound (**1**) with ethyl bromoacetate in basic media. The synthesis of acid hydrazide derivatives (**3**) was brought about as a result of the reaction between compound (**2**) aand hydrazine hydrate. In the presence of basic conditions, the reaction of 2-(4-methylpiperazin-1-yl)acetohydrazide (**3**) with carbon disulfide resulted in the formation of 5-((4-methylpiperazin-1-yl)methyl)-1,3,4-oxadiazole-2-thiol (**4**). The reactions of (**4**) with different primary and secondary amines in the presence of formaldehyde ledato the formation of the corresponding Mannich bases (**5a-f**).

1. Introduction

In the synthesis of a broad range of bioactive components, the Mannich reaction is an essential stage in the process of synthesis. In the development of secondary and tertiary amine derivatives [1–3], it is an extremely important step in the process. The *N*-Mannich bases that are synthesized from NH-heterocycles and other compounds that are structurally linked to them have the potential to display a diverse range of pharmacological activities. Antimicrobial treatment is one example of these behaviors [4–6], antifungal [7], anti-HIV [8], antitubercular [9], neuroprotection [10], and anticancer activity. In a recent publication [11], the amazing biological activity associated with N-substituted isoindolin-1,3 diones was investigated.

These diones are members of an important group of compounds. It has been demonstrated that they are efficient against a number of different types of fungi [12], as well as inflammation and pain [13], convulsions [14], and bacteria [15], in addition to being antioxidants and hemolysers. N-Mannich bases of isoindolin-1,3-dione (phthalimide) and Mannich bases containing a phthalimide moiety have been discovered to be highly effective antibacterial, anthelmintic, and insecticidal agents [16,17]. These compounds are significant from a synthetic as biologically active compound.

Therefore, the use of the 5-((4-methylpiperazin-1-yl)methyl)-1,3,4-oxadiazole-2-thiol 4 in the N-Mannich process is going to be the primary focus of this investigation. The general schematic representation of the synthesis of N-Mannich Bases from 5-((4-methylpiperazin-1-yl)methyl)-1,3,4-oxa diazole-2-thiol **(4)** is given in the fig 1.

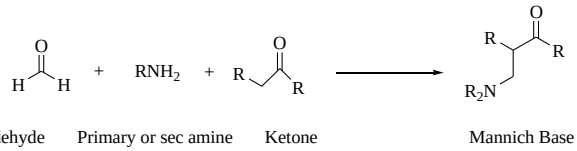

Fig. 1- The general schematic representation of Mannich reaction

2. Experimental Section

2.1. Chemistry

All of the chemicals were obtained from Fluka Chemie AG Buchs, which is located in Buchs, Switzerland, and utilized in its original form. The

*Corresponding author: yildizuygun41@hotmail.com
Received: 16.11.2022, Accepted: 09.03.2023

melting points of the synthetic compounds were determined using a Büchi B-540 melting point instrument and open capillaries. The results have not been adjusted for accuracy. A technique known as thin-layer chromatography (TLC) was performed on silica gel 60 F254 aluminum sheets in order to monitor the reactions. To locate the peaks, ultraviolet light was employed in conjunction with a mobile phase that was composed of ethyl acetate and ethyl ether in a ratio of 1:1. When recording FT-IR spectra, a spectrometer from at he 1600 series of Perkin Elmer's FTIR was used. ^{1}H NMR and ^{13}C NMR spectra were registered in DMSO-*d6* on a BRUKER AVENE II 400 MHz NMR Spectrometer (400.13 MHz for ^{1}H and 100.62 MHz for ^{13}C) or Varian-Mercury 200 MHz NMR Spectrometer (200 MHz for ^{1}H and 50 MHz for ^{13}C). Chemical shifts are given in ppm with respect to Me_4Si as an internal standard.

2.1.1 Ethyl 2-(4-methylpiperazin-1-yl)acetate (2)

To a solution of compound 1 (10 mmol) in tetrahydrofuran, triethylamine (20 mmol) was added, and after stirring for a period at room temperature, ethyl bromoacetate (10 mmol) was added dropwise; the mixture was then stirred for 24 hours at room temperature. Then, the solution was evaporated until it was completely dry, and the resulting white solid was filtered out.

Yield: % 89, m.p: 85-87°C. FT IR (υ_{max}, cm^{-1}): 1734 (C=O). ^{1}H NMR (DMSO-d_6, δ ppm): 1.17-1.20 (3H, m, CH_3), 1.99 (2H, s, CH_2), 2.14 (2H, s, CH_2), 2.30 (2H, s, CH_2), 3.17 (2H, s, CH_2), 3,40 (2H, d, *J*= 4,0 Hz, CH_2), 4,08 (3H, t, *J*= 16,0 Hz, CH_3). ^{13}C NMR (DMSO-d_6, δ ppm): 14.57 (CH_3), 46.17 (CH_3), 53.24 (CH_2), 55.06 (CH_2), 58.98 (CH_2), 60.20 (CH_2), 63.93 (CH_2), 170.36 (C=O). EI MS *m/z* (%): 173.25 ($[M+1]^+$, 100), 195.40 ($[M+Na]^+$, 70).

2.1.2. 2-(4-methylpiperazin-1-yl)acetohydrazide (3)

Compound 2 (10 mmol) was dissolved in ethanol, and then hydrazine hydrate (25 mmol) was added to the mixture, which was then refluxed for 15 hours. After a night in the fridge, the white solid was filtered off, and the crude product was crystallized in ethanol/water (2:1).

Yield: % 85, m.p: 134-136 ^{0}C. FT IR (υ_{max}, cm^{-1}): 1734 (C=O). ^{1}H NMR (DMSO-d_6, δ ppm): 2. 14 (3H, s, CH_3), 2.30 (2H, s, CH_2), 2.40 (4H, s, $2CH_2$), 2.88 (4H, s, $2CH_2$), 3.75 (2H, brs, NH_2), 8.84 (1H, s, NH). ^{13}C NMR (DMSO-d_6, δ ppm): 46.20 (CH_3), 53.21 ($2CH_2$), 55.01 ($2CH_2$), 60.37 (CH_2), 168.69 (C=O). EI MS *m/z* (%): 173.89 ($[M+1]^+$, 100), 195.75 ($[M+Na]^+$, 75).

2.1.3. 5-((4-methylpiperazin-1-yl)methyl)-1,3,4-oxadiazole-2-thiol (4)

The mixture of compound 3 (10 mmol) and carbon disulfide (20 mmol) in absolute ethanol was refluxed in the presence of dried potassium hydroxide (10 mmol) for 14 h. Then, the resulting solution was cooled to room temperature and acidified with acetic acid. The precipitate formed was filtered off, washed with water, and recrystallized from ethyl acetate:petroleum ether (1:3) Yield 72 %. M.p: 210–212^{0}C. FT IR (υ_{max}, cm^{-1}): 2755 (SH), 1596 (C=N), 1172 (C=S). ^{1}H NMR (DMSO-d_6, δ ppm): 2.44 (3H, s, CH_3), 2.65 (2H, s, CH_2), 2.88 (2H, s, CH_2), 3.10 (2H, s, CH_2), 3.48 (2H, s, CH_2), 3.78 (2H, s, CH_2) 13.95 (1H, s, SH). ^{13}C NMR (DMSO-d_6, δ ppm): 15.20 (CH_3), 50.51 (CH_2), 52.10 (CH_2), 53.69 (CH_2), 54.12 (CH_2), 55.12 (CH_2), 166.20 (C), 185.36 (C=S). EI MS *m/z* (%): 215.63 ($[M+1]^+$, 100), 189.52 (75), 110.23 (51).

2.2. General Method for the Synthesis of Compounds 5a-f

Following adding appropriate amine (10 mmol) to a solution of the corresponding compound 4 (10 mmol) in dimethyl formamide, the mixture was stirred for 24 hours at room temperature in the presence of formaldehyde (30 mmol). To obtain the required chemical, the solid precipitate was first filtered out, then washed with water, and finally recrystallized from a mixture of 1:1 dimethyl sulfoxide and water.

2.2.1 5-((4-methylpiperazin-1-yl)methyl)-3-(morpholinomethyl)-1,3,4-oxadiazole-2(3H)-thione (5a)

Yield 80 %. M.p: 198-200^{0}C. FT IR (υ_{max}, cm^{-1}): 1585 (C=N). ^{1}H NMR (DMSO-d_6, δ ppm): 2.28 (3H, s, CH_3), 2.43 (2H, s, CH_2), 2.45 (2H, s, CH_2), 2.49 (2H, s, CH_2), 2.60 (2H, s, CH_2), 2.78 (t, *J*=4.45, 4H, CH_2-N-CH_2), 3.58 (t, *J*=4.40, 4H, CH_2-O-CH_2), 5.16 (s, 2H, N-CH_2-N).

^{13}C NMR (DMSO-d_6, δ ppm): 46.05 (CH_3), 49.24 (CH_2), 52.85 (CH_2), 53.47 ($2CH_2$), 54.48 ($2CH_2$), 64.86 ($2CH_2$), 66.82 ($2CH_2$), 156.80 (C), 183.84 (C=S). EI MS *m/z* (%): 313.85 ($[M+1]^+$, 100), 247.52 (85), 178.12 (71), 113.65 (53).

2.2.2. 5-((4-methylpiperazin-1-yl)methyl)-3-(thiomorpholinomethyl)-1,3,4-oxadiazole-2(3H)-thione (5b)

Yield 82 %. M.p: 202-204^{0}C. FT IR (υ_{max}, cm^{-1}): 1578 (C=N). ^{1}H NMR (DMSO-d_6, δ ppm): 2.30 (3H, s, CH_3), 2.45 (2H, s, CH_2), 2.47 (2H, s, CH_2), 2.52 (2H, s, CH_2), 2.63 (2H, s, CH_2), 2.67 (2H, s, CH_2) 2.70 (2H, s, CH_2), 3.73 (2H, s, CH_2), 3.81 (2H, s, CH_2), 4.22 (2H, s, CH_2), 5.10 (2H, s, CH_2). ^{13}C NMR (DMSO-d_6, δ ppm): 46.10 (CH_3), 49.57 (CH_2), 52.78 (CH_2), 53.41 ($2CH_2$), 54.40 ($2CH_2$), 64.78 ($2CH_2$), 66.80 ($2CH_2$), 156.85 (C), 183.90 (C=S). EI MS *m/z* (%): 330.52 ([M+1]$^+$, 100), 279.02 (85), 245.36 (70), 198.52 (54).

2.2.3. 3,5-bis((4-methylpiperazin-1-yl)methyl)-1,3,4-oxadiazole-2(3H)-thione (5c)

Yield 84 %. M.p: 189-191^{0}C. FT IR (υ_{max}, cm^{-1}): 1598 (C=N). ^{1}H NMR (DMSO-d_6, δ ppm): 2.27 (3H, s, CH_3), 2.28 (3H, s, CH_3), 2.40 (4H, s, $2CH_2$), 2.42 (2H, s, CH_2), 2.50 (2H, s, CH_2), 2.58 (2H, s, CH_2), 2.60 (2H, s, CH_2) 2.61 (2H, s, CH_2), 3.82 (2H, s, CH_2), 4.23 (2H, s, CH_2), 5.07 (2H, s, CH_2).^{13}C NMR (DMSO-d_6, δ ppm): 30.12 (CH_3), 32.89 (CH_3), 48.37 (CH_2), 51.70 (CH_2), 53.92 ($2CH_2$), 54.49 ($2CH_2$), 64.65 ($2CH_2$), 66.89 ($2CH_2$), 156.12 (C), 183.88 (C=S). EI MS *m/z* (%): 327.90 ([M+1]$^+$, 100), 270.19 (73), 190.52 (59), 171.30 (48).

2.2.4. 3-((furan-2-ylmethylamino)methyl)-5-((4-methylpiperazin-1-yl)methyl)-1,3,4-oxadiazole-2(3H)-thione (5d)

Yield 86 %. M.p: 178-180^{0}C. FT IR (υ_{max}, cm^{-1}): 3215 (NH), 1581 (C=N). ^{1}H NMR (DMSO-d_6, δ ppm): 2.39 (3H, s, CH_3), 2.39 (2H, s, CH_2), 2.44 (2H, s, CH_2), 2.59 (2H, s, CH_2), 2.61 (2H, s, CH_2), 2.67 (2H, s, CH_2) 2.75 (2H, s, CH_2), 4.22 (2H, s, CH_2), 4.63 (2H, s, CH_2), 5.14 (1H, s, NH). 6.19 (1H, s, furf), 6.24 (1H, s, furf), 7.28 (1H, s, furf). ^{13}C NMR (DMSO-d_6, δ ppm): 32.12 (CH_3), 47.71 (CH_2), 56.63 ($2CH_2$), 63.79 ($2CH_2$), 65.97 ($2CH_2$), 119.52 (CH), 120.12 (CH), 122.67 (CH), 155.29 ©, 157.12 ©, 181.20 (C=S). EI MS *m/z* (%): 324.63 ([M+1]$^+$, 100), 198.30 (77), 170.12 (51), 152.39 (43).

2.2.5. 1-ethyl-6-fluoro-7-(4-((5-((4-methyl piperazin-1-yl)methyl)-2-thioxo-1,3,4-oxadiazol-3(2H)-yl)methyl)piperazin-1-yl)-4-oxo-1,4-dihydroquinoline-3-carboxylic acid (5e)

Yield 91 %. M.p: 232-235 ^{0}C. FT IR (υ_{max}, cm^{-1}): 3385 (OH), 1593 (C=N), 1723 (C=O), 1741 (C=O). ^{1}H NMR (DMSO-d_6, δ ppm): 1.20 (3H, s, CH_3), 1.47 (3H, s, CH_3), 2.43 (2H, s, CH_2), 2.49 (2H, s, CH_2), 2.63 (2H, s, CH_2), 2.80 (2H, s, CH_2), 2.87 (2H, s, CH_2) 3.56 (2H, s, CH_2), 3.62 (2H, s, CH_2), 3.90 (2H, s, CH_2), 4.09 (2H, s, CH_2), 4.73 (2H, s, CH_2), 5.31 (2H, s, CH_2), 6.34 (1H, s, arH), 7.49 (1H, s, arH), 8.08 (1H, s, arH), 12.14 (1H, s, OH).^{13}C NMR (DMSO-d_6, δ ppm): 19.20 (CH_3), 24.52 (CH_3), 48.23 (CH_2), 54.89 ($2CH_2$), 61.70 ($2CH_2$), 63.49 ($2CH_2$), 65.55 (CH_2), 66.10 (CH_2), 67.35 (CH_2), 68.43 (CH_2), arC: [114.12 (CH), 116.98 (CH), 126.58 (C), 127.37 (C), 128.30 (C)] 131.89 (C), 136.89 (C), 148.73 (quinolone CH), 175.12 (C=O), 176.52 (C=O), 181.20 (C=S). EI MS *m/z* (%): 546.52 ([M+1]$^+$, 100), 198.12 (78), 170.36 (55).

2.2.6. 1-cyclopropyl-6-fluoro-7-(4-((5-((4-methyl piperazin-1-yl)methyl)-2-thioxo-1,3,4-oxa diazol-3(2H)-yl)methyl)piperazin-1-yl)-4-oxo-1,4-di hydroquinoline-3-carboxylic acid (5f)

Yield 93 %. M.p: 237-239 ^{0}C. FT IR (υ_{max}, cm^{-1}): 3324 (OH), 1593 (C=N), 1713 (C=O), 1739 (C=O). ^{1}H NMR (DMSO-d_6, δ ppm): 1.41 (3H, s, CH_3), 2.38 (2H, s, CH_2), 2.45 (2H, s, CH_2), 2.57 (2H, s, CH_2), 2.79 (2H, s, CH_2), 2.96 (2H, s, CH_2), 3.57 (2H, s, CH_2), 3.69 (2H, s, CH_2), 3.83 (2H, s, CH_2), 4.12 (2H, s, CH_2), 4.64 (2H, s, CH_2), 5.26 (2H, s, CH_2), 5.70 (2H, s, CH_2), 6.98 (1H, s, arH), 7.10 (1H, s, arH), 8.20 (1H, s, CH), 9.21 (1H, s, CH), 15.03 (1H, s, OH). ^{13}C NMR (DMSO-d_6, δ ppm): 17.13 (CH_3), 40.23 (CH_2), 51.89 ($2CH_2$), 57.96 ($2CH_2$), 61.10 ($2CH_2$), 63.79 (CH_2), 64.07 (CH_2), 65.10 (CH_2), 66.53 (CH_2), 67.27 (CH_2), 107.12 (CH), arC: [112.03 (CH), 113.79 (CH), 124.79 (C), 126.81 (C), 129.41 (C), 145.12 (C)] 134.10 (C), 137.90 (C), 148.12 (quinolone CH), 177.23 (C=O), 179.15 (C=O), 181.66 (C=S). EI MS *m/z* (%): 558.10 ([M+1]$^+$, 100), 340.12 (76), 210.12 (63), 198.13 (40).

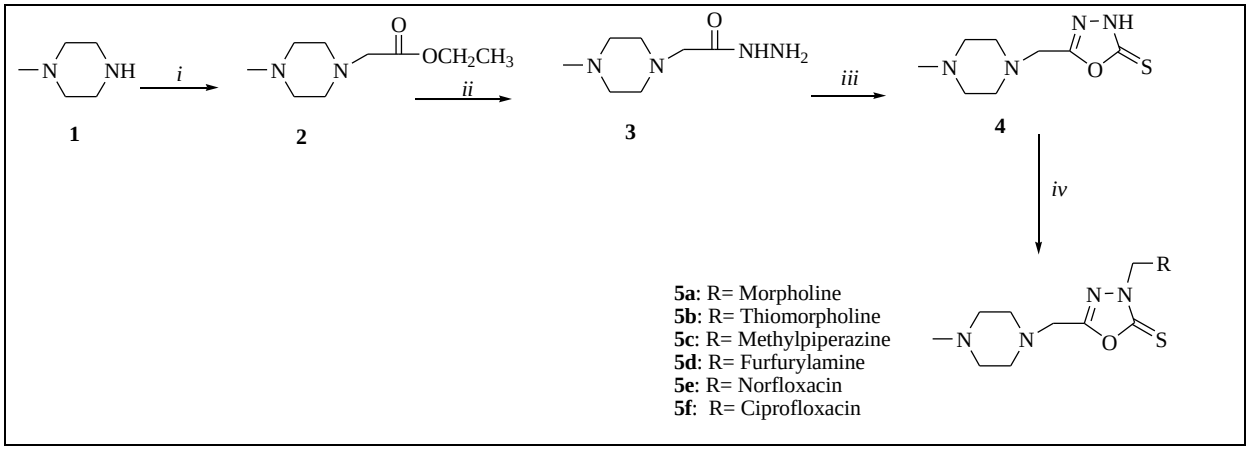

Scheme 1: *i*. $BrCH_2COOEt$, EtOH; *ii*. NH_2NH_2, EtOH; *iii*: CS_2, KOH, EtOH, *iv*: dimethyl formamide, seconder amine, room temperature, 24 h.

3. Results and Discussion

During the research process, we made an attempt to synthesize various new 1,3,4-oxadiazoles mannich derivates. The structure of the target products was determined by using data from ^{1}H NMR, ^{13}C NMR, FT IR, and EI-MS. The synthetic procedures that were applied in order to obtain the compounds of interest are presented in Scheme 1.

By using a wide variety of amines in the synthesis process, research were able to successfully produce a variety of N-Mannich bases of 1,3,4-oxadiazole 4, with yields ranging anywhere from 80% to 93%. Compound (**2**) IR spectra showed pronounced absorption at 1734 cm^{-1} (C=O), while its ^{1}H-NMR spectra displayed five singlets (-CH_2) between 1.99 and 3.39 ppm. Compound (**3**) ^{1}H NMR spectra didn't have any signals that belonged to the -OCH_2CH_3 group, hence this can be concluded. Instead, new signals were created from the hydrazide structure, and these signals indicated between 3.75 ppm (–$NHNH_2$) and 8.84 ppm (–$NHNH_2$) when integrating for two proton and one proton, respectively (controlled by changing with D_2O). As seen in our previous studies, nh-nh2 peaks are observed in these intervals [18]. The infrared spectra of acid hydrazides (**3**) showed the occurrence of a novel peak at 1734 cm^{-1}, which was determined by their chemical composition. Compound (**4**) was made as a result of the treatment of compound (**3**) with carbon disulfide in basic media. Because of this treatment, the hydrazide side chain was converted into the 1,3,4-thiadiazole ring, which led to the synthesis of compound (**4**). The fact that 1,3,4-oxadiazoles can exist in their mercapto-thioxo tautomeric forms [19-21] is common knowledge. The infrared spectra of compound (**4**) revealed two stretching bands as a result of this tautomerism. Another of these bands, seen at 2755 cm^{-1}, corresponds to the –SH group, and the other band, recorded at 1172 cm^{-1}, reflects the presence of the -C=S group. As seen in the literature studies, the -SH peak is observed in these intervals [22]. When these bands were seen, they were found to be stretching in directions that were diametrically opposed to one another. In addition, the outcomes of the NMR, mass, and elemental tests performed on compound (**4**) were satisfactory. Compounds (**5a-f**) were produced by carrying out the Mannich reaction on compound (**4**) with a number of different amines in the presence of a solution of formaldehyde. During the process of creating compounds (**5a-f**), this reaction was one of the steps that was carried out. In the ^{1}H NMR and ^{13}C NMR spectra of compounds, additional signals coming from amine moieties were observed at the attended chemical ranges. These signals were observed at the molecular ranges that were being addressed to. The spectra of the molecules revealed the presence of these signals. There is no evidence that shows the presence of the NH band on the ^{1}H NMR or FT-IR spectra of any of the products (**5a-f**). On the other hand, in the spectra of the molecules' ^{1}H NMR and ^{13}C NMR, additional signals that came from amine moieties were found at the concerned chemical ranges. These signals were observed at the chemical ranges that were under investigation. This suggests that the NH band is absent from the spectrum. Recordings of mass spectrum data showed that these molecules displayed information that was in line with their structures.

3. Conclusion

In this study, methyl piperazine was first converted to an ester derivative and then to a hydrazide derivative. Then the hydrazide compound was converted to the

oxadiazole derivative compound. By reacting the 1,3,4-oxadiazole derivative compound with different amines, some Mannich derivative compounds were formed. For the characterization of all synthesized compounds, melting point determination, Infread spectrum, ^{1}H-NMR spectrum and ^{13}C-NMR measurements were made. As a result of all the characterization studies, the structures of the synthesized compounds were confirmed.

Statement of Research and Publication Ethics

The study is complied with research and publication ethics

References

[1] S. G. Subramaniapillai, *J Chem Sci* 2013, *125*, 467.
[2] G. Roman, *Eur J Med Chem* 2015, *89*, 743.
[3] J. R. Dimmock, P. Kumar, *Curr Med Chem* 1997, *4*, 1.
[4] A. V. Bogdanov, A. M. Vazykhova, N. R. Khasiyatullina, D. B. Krivolapov, A. B. Dobrynin, A. D. Voloshina, V. F. Mironov, V. F., *Chem Heterocycl Comp* 2016, *52*, 25.
[5] S. George, R. Chkraborty, M. Parameswaran, A. Rajan, T. K. Ravi, *J Heterocycl Chem* 2015, *52*, 211.
[6] H. Guo, *Eur J Med Chem* 2019, *164*, 678.
[7] S. Shen, X. Sun, Y. Liu, B. Chen, R. Jin, H. Ma, *J Heterocycl Chem* 2015, *52*, 1296.
[8] T. R. Bal, B. Anand, P. Yogeeswari, D. Sriram, *Bioorg Med Chem Lett* 2005, *15*, 4451.
[9] T. Aboul-Fadl, F. A. S. Bin-Jubair, *Int J Res Pharm. Sci* 2010, *1*,113.
[10] Chen, G.; Ning,Y.; Zhao, W.; Zhang,Y.; Zhang, Y.; Hao,X.; Wang, Y.; Mu, S. *Lett Drug Des Discov* 2016, *13*, 395.
[11] Kushwaha,N.; Kaushik, D. *J Applied Pharm Sci* 2016, *6*, 159.
[12] L. Pan, X. Li, C. Gong, H. Jin, *Qin. B. Microbial Pathogenesis* 2016, *95*, 186.
[13] A. M. Alanazi, A. S. El-Azab, I. A. Al-Suwaidan, K. H. ElTahir, Y. A. Asiri, N. I. Abdel-Aziz, A. Abdel-Aziz, *Eur J Med Chem* 2015, *92*, 115.
[14] S. Arti Kumar, D. Pathak, *Int J Pharm Tech Res* 2011, *3*, 2104.
[15] P. S. Nayab, M. Irfan, M. Abid, M. Pulaganti, C. Nagaraju, S. K. Chitta, *Luminescence* 2017, *32*, 298.
[16] R. Bamnela, S. P. Shrivastava, *Indian J Chem* 2014, *53B*, 1128.
[17] D. Sachan, J. P. Singh, D. Sachan, S. Gangwar, *Amer J Pharm Tech Res* 2012, *2*, 491.
[18] Y., Uygun Cebeci, Ş., Ceylan, N., Demirbaş, S., Alpay Karaoğlu, Microwave-assisted Synthesis of Novel Mannich Base and Conazole Derivatives Containing Biologically Active Pharmacological Groups, Letters in Drug Design & Discovery, 2021, 18, 1-15.
[19] H., Bayrak, A., Demirbas, N., Demirbas, S., Alpay-Karaoglu, Synthesis of some new 1,2,4-triazoles, their Mannich and Schiff bases and evaluation of their antimicrobial activities. Eur. J.Med. Chem. 2009, 44, 1057–1066.
[20] A., Demirbas, S., Ceylan, N., Demirbas, Synthesis of some new five membered heterocycles, a facile synthesis of oxazolidinones. J. Heterocycl. Chem. 2007, 44, 1271–1280.
[21] N., Demirbaş, R., Uğurluoğlu, Synthesis of novel 4-alkylidene- and 4-alkylamino-5-oxo-4,5- dihydro-[1,2,4]triazole derivatives and investigation of their antitumor activities. Turk. J. Chem. 2004, 28, 559–571.
[22] H., Bayrak, A., Demirbas, S., Alpay Karaoğlu, N., Demirbaş, Synthesis of some new 1,2,4-triazoles, their Mannich and Schiff bases and evaluation of their antimicrobial activities, European Journal of Medicinal Chemistry 44 (2009) 1057-1066

Bitlis Eren Üniversitesi Fen Bilimleri Dergisi
BİTLİS EREN UNIVERSITY JOURNAL OF SCIENCE
ISSN: 2147-3129/e-ISSN: 2147-3188
VOLUME: 12 NO: 1 PAGE: 151-157 YEAR: 2023
DOI:10.17798/bitlisfen.1217727

Examining The Effect of Different Networks on Foreign Object Debris Detection

Duygu KAYA*

Firat University, Faculty of Engineering, Electrical-Electronics Engineering, Elazığ/ Turkey
dgur@firat.edu.tr
(ORCID: 0000-0002-6453-631X)

Keywords: Foreign Object Debris, Deep Learning, Pre-trained networks.

Abstract

Foreign Object Debris (FOD) at airports poses a risk to aircraft and passenger safety. FOD can seriously harm aircraft engines and injure personnel. Accurate and careful FOD detection is of great importance for a safe flight. According to the FAA's report, FOD types are aircraft fasteners such as nut, safety; aircraft parts such as fuel blast, landing gear parts, rubber parts; construction materials such as wooden pieces, stones; plastic materials, natural plant and animal parts. For this purpose, in this study, the effect of different networks and optimizer on object detection and accuracy analysis were examined by using a data set of possible materials at the airport. AlexNet, Resnet18 and Squeezenet networks were used. Application is applied two stages. The first one, 3000 data were divided into two parts, 70% to 30%, training and test data, and the results were obtained. The second one, 3000 data were used for training, except for the training data, 440 data were used for validation. Also, for each application, both SGDM and ADAM optimizer are used. The best result is obtained from ADAM optimizer with Resnet18, accuracy rate is %99,56.

1. Introduction

FOD is defined as a living or inanimate object that is not in a suitable location that can damage employees, equipment or aircraft within the airport [1]. Objects such as tools left on the runway, fragments from the ground, animal remains, and pebbles carried by the wind, plastic, metal and tin components threaten flight safety and may even cause fatal accidents. Since FOD is critical safety hazard and effect the economic hazard, FOD recognition system is useful for reducing its damages. Aviation organizations around the world have detailed various FOD detection technologies in order to prevent debris hazard on runways, maintain clean and safe aircraft maneuvering areas, and prevent FOD damage to aircraft [2]. Some countries have a FOD detection system. FODRAD, the first and only FOD detection radar developed in Turkey, was established at Antalya Airport in 2018. FODRAD is a mm-wave radar system that is designed to meet the recommendation criteria of Federal Aviation Administration (FAA) AC150/5220-24 and performs 24/7 surveillance [3]. Considering this application, some studies have been carried out in the literature. Han et al. [4] created a FOD dataset at runways of Shanghai Hongqiao International Airport and campus of their research institute and created a FOD recognition system based on both Transfer Learning and D-CNN. In [5], the authors used the Yolo3 algorithm for FOD detection. They used deep residual network to extract features from the data and multi-scale feature fusion for small-scale FOD detection. In [6], a dataset named FOD-A was created. They used machine learning models for object detection. In [7] for initial dataset unmanned aerial system (UAS) and portable cameras are used to collect the data at the airport. Later these FOD video were split into frames and using You Only Look Once algorithm efficiency detection was done. In [8], YOLOv4 which is one of the YOLO model, is used with transfer learning and obtained fast results for FOD detection. In [9], the authors present a spatial

* Corresponding author: dgur@firat.edu.tr
Received: 12.12.2022, Accepted: 23.02.2023

transformer network (STN), region recommendation network (RPN) and convolutional neural network (CNN)-based method for detecting FOD. In [10], DenseNet and Faster R-CNN are used for small scale FOD detection. In [11], the authors proposed to collect images with drones and detect any FODs with an artificial intelligence-based specific trained algorithm. In [12], the authors propose a new random forest-based FOD detection framework that uses representative PVF to accurately segment FOD regions and effectively suppress background interference in airport images. In [13], to classify FOD images, an ensemble learning algorithm, namely KNN, Adaboost, and Random Forest Tree, is used. As feature extraction methods, Linear Discriminant Analysis (LDA) and Gray-level co-occurrence matrix(GLCM) are used.

FOD is materials that can harm the airport, airport personnel and aircraft. Taking measures to detect and remove these materials with a smart system before it is too late will provide security and contribute to the prevention of serious economic losses. In the literature, efficient results have been obtained with the Yolo algorithm for deep learning-based object recognition. In this study, the pros and cons of different optimization algorithms are examined and a performance comparison is made between the selected ADAM and SGDM algorithms. Also, AlexNet, Resnet18 and Squeezenet pre-trained networks are used and the success rate of the current method is compared with the literature.

2. Material and Method

2.1. Dataset

Created by the researchers using the runway and its surroundings, the dataset has three labels: metal, concrete, and plastic [4], [14]. The dataset consists of a total of 3440 images, of which 3000 are training and 440 tests. In the training set, each class has 1000 images, and in the validation set, concrete has 100, metal 105, and plastic 235 images. In this study, two applications are applied. The first one, 70% of the 3000 data was used for training and 30% for testing. The second one, 3000 data used for training and test, except for this data, 440 data were used for validation and performance analysis was examined. Some images of the dataset are available in Figure 1. The numbers of the FOD dataset are given in Table 1. Also, bar graph of data distribution is in Figure 2.

Figure 1. Samples of dataset

Table 1. Dataset distribution

Dataset	Training	Validation
Concrete	1000	100
Metal	1000	105
Plastic	1000	235
Total	**3000**	**440**

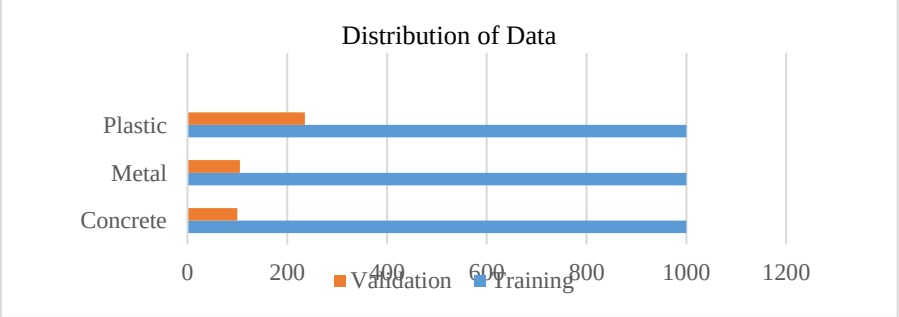

Figure 2. Bar graph of data distribution

2.2 Methods

Machine learning has long been a very popular field for detecting and evaluating any situation [15]-[17]. Machine learning requires feature extraction from raw data with a feature extraction method. However, with the use of deep learning approach recently, this feature extraction process is done with its own layers without the need for a separate feature extraction method has made this area the center of attention. Deep learning has the advantage of learning information by creating deep architectures. Also, with deep learning, the model automatically provides fast learning [18].

In this study, the features of the FOD dataset with different networks, such as AlexNet, Resnet18 and Squeezenet, were extracted and the classification results were compared. For each application, SGDM and ADAM (Adaptive Moment Estimation) optimizers are used. The block diagram of the study is given in Figure 3.

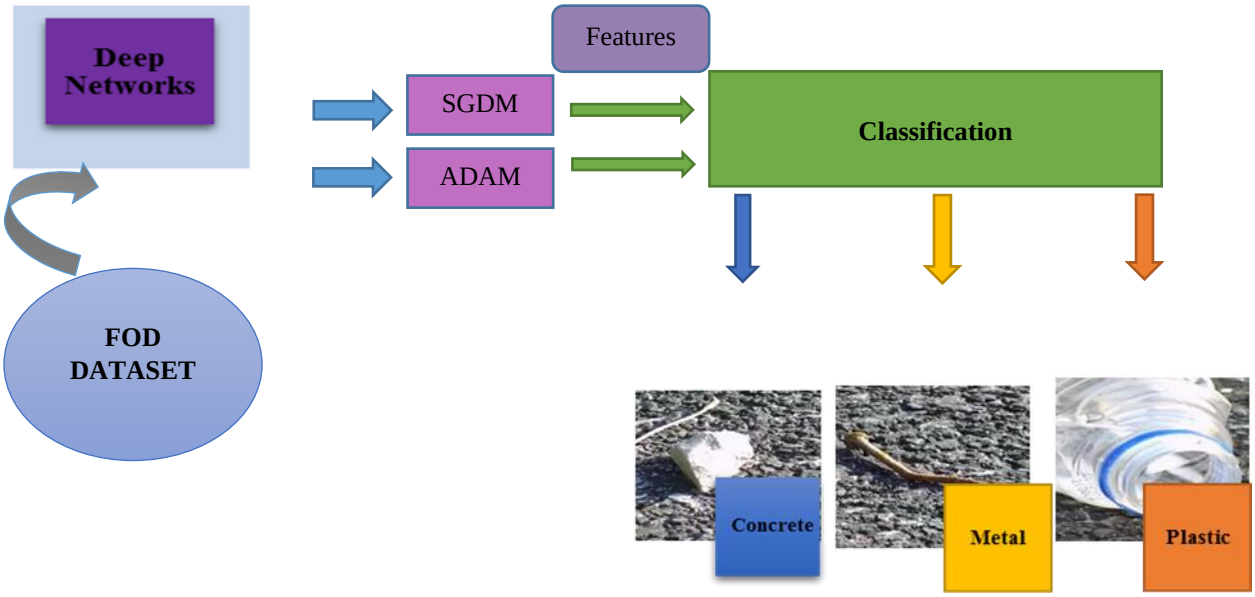

Figure 3. The block diagram of the used method

2.2.1. Pre-Trained Networks

The architectures used in the deep network are shown in Figure 4. AlexNet model proposed by Alex Krishevskyi et al. [19] is an important step in the field of deep learning [20], showing high performance in object recognition and image classification, which includes 1000 class labels. In this architecture, a total of seven layers are used, 5 of which are convolutional and two are fully connected, named FC6 and FC7. The first of the convolutional layers uses 11 * 11, the second 5 * 5, and the rest use 3 * 3 filters. ReLU activation function and maximum pooling are used in the architecture. ResNet-18 is a convolutional neural network that is 18 layers deep. The pre-trained network can classify images into 1000 object categories. As a result, the network has learned rich feature representations for a wide range of images. The network has an image input size of 224-by-224 [21]. The feature vector is obtained from the fully connected layer called “fc1000” in the ResNet network. SqueezeNet is an architecture was developed by Iandola et al [22] and that is 18 layers deep. The network has an image input size of 227-by-227. This architecture aims to achieve fast and efficient accuracy rates with the architecture they create with few parameters [22].

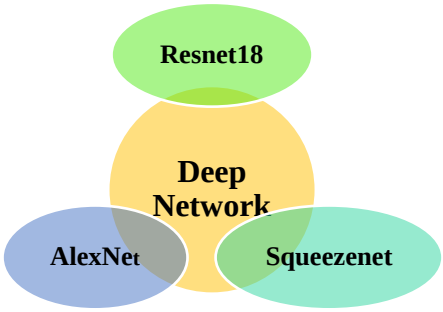

Figure 4. The used deep networks

2.2.2. Optimization Algorithms

Optimization is used to min the difference between the output generated by the network and the actual value. SGD (Stochastic gradient descent), Momentum, Adagrad, RMSProp, Adadelta and ADAM algorithms are frequently used in Machine Learning. In SGD, the gradient weights of the randomly received training data are updated instead of the gradients in the whole data. Draws a zigzag path to the global minimum point. In case using SGD alone, the initial cost value may oscillate to the smallest point at different derivative values calculated at each step. This will take time to reach the minimum value. Therefore, by using SGD together with momentum, oscillations will decrease and these oscillations will be large horizontally and small vertically. Thus, it will be possible to reach a quick result [23].

Adagrad makes frequent updates for infrequent parameters and smaller updates for frequent parameters. Here, each parameter has its own learning rate, and according to the characteristics of the algorithm, this learning rate gradually decreases and stops learning at some point in time. Adadelta uses momentum summary of square difference between existing weights and updated weights. RMSprop squares momentum gradients and prevents rapid decline. the learning rates of each of the parameters. That is, it combines the positive aspects of RmsProb and momentum. [24]

The ADAM algorithm is known as adaptive estimation. ADAM's algorithm, unlike Adadelta, stores learning rate and momentum changes in memory; that is, it combines the positive aspects of RMSprop and momentum. It also performs better than SGD in terms of speed [25].

3. Results and Discussion

The application was made in two stages and the results are given in tables. In the first application, 70% of the 3000 data was reserved for training and 30% for testing. The program was run as it is and the results were obtained. In the other application, 3000 data were used for training-testing at a rate of 70% to 30%, and 440 data was used for validation.

As seen in Tables 2 and Table 3 some parameter values are given. The mini-batch size means how many data the model will process simultaneously. While the model is being trained, the data is included in the training in parts. In deep learning, the first piece is trained, the performance of the model is tested, and the weights are updated according to the performance. Then the model is retrained with the new training set and the weights are updated again. Each of these training steps is called “epoch”. Before training the data, shuffling is done with Shuffle. Here, data shuffling is done in each epoch. Optimization methods are used to solve the optimum value in solving nonlinear problems.‘initial learn’ represents the learning rate. The ‘Validation Frequency’ value is the number of iterations between evaluations of validation metrics.

In this work, Verbose, max epoch, Mini Batch size, validation frequency, initial learn are 50,10,64,50,0.001, respectively. Shuffle is done every epoch.

For application 1, only 3000 data used both training and test. Also Table 2 presents experimental results for this application. As seen in Table 2, the best result is obtained with ‘ADAM’ optimizer for Resnet18. But, the other results are close to each other. Figure 5 shows accuracy comparisons both optimizers for application 1.

For application 2, 3000 data were used for training-testing at a rate of 70% to 30%, and 440 data was used for validation. As seen in Table 3, the best result is obtained with ‘ADAM’ optimizer.

Table 2. Experimental Results for Application 1

Models	Max Epoch	MiniBatch Size	Shuffle	Algorithm	Initial Learn	Validation Frequency	Accuracy Rate
AlexNET	10	64	Everyepoch	SGDM	0.0001	50	% 97.22
Resnet18	10	64	Everyepoch	SGDM	0.0001	50	% 98.22
Squeezenet	10	64	Everyepoch	SGDM	0.0001	50	% 97.56
AlexNET	10	64	Everyepoch	ADAM	0.0001	50	% 98.44
Resnet18	10	64	Everyepoch	ADAM	0.0001	50	% 99.56
Squeezenet	10	64	Everyepoch	ADAM	0.0001	50	% 98.89

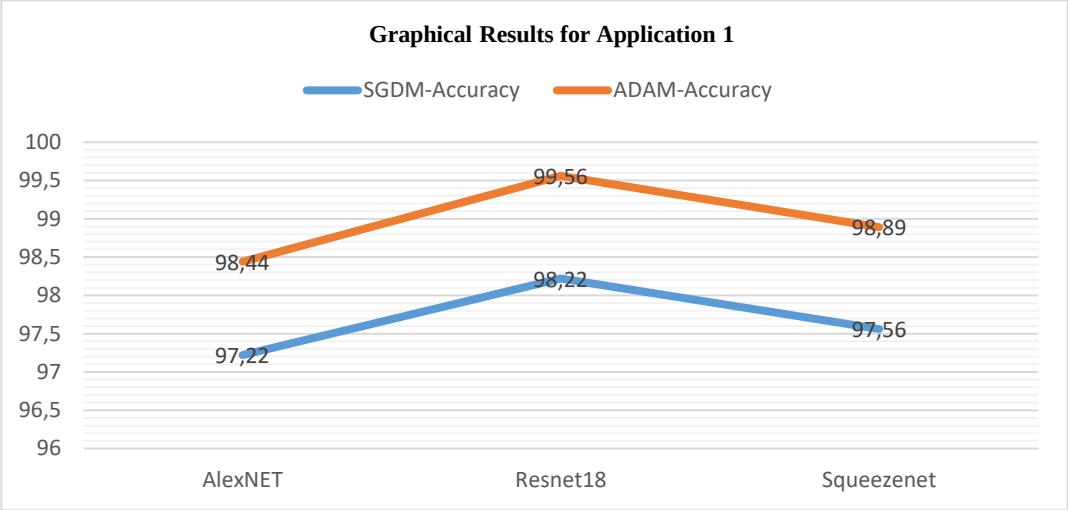

Figure 5. Graphical Comparison for Application 1

In second application, the performance is low due to the fact that the validation data source. Therefore, the obtained results were lower than the first application. But, the best result is obtained with ADAM optimizer.

Table 3. Experimental Results for Application 2

Models	Max Epoch	MiniBatch Size	Shuffle	Algorithm	Initial Learn	Validation Frequency	Accuracy Rate
AlexNET	10	64	Everyepoch	SGDM	0.0001	50	% 75.91
Resnet18	10	64	Everyepoch	SGDM	0.0001	50	% 71.36
Squeezenet	10	64	Everyepoch	SGDM	0.0001	50	% 75.91
AlexNET	10	64	Everyepoch	ADAM	0.0001	50	% 79.32
Resnet18	10	64	Everyepoch	ADAM	0.0001	50	% 71.36
Squeezenet	10	64	Everyepoch	ADAM	0.0001	50	% 73.86

Table 4 presents literature comparisons of different FOD datasets in terms of method and success parameters, such as accuracy, precision, recall, True Positive(TP), False Negative(FN), Average Precision (AP). As seen in Table 4, artificial intelligence-based methods have yielded important results.

Table 4. Literature Comparisons

Author	Dataset	Method	Performance
[4]	create a FOD dataset consisting of images from the runways of Shanghai Hongqiao International Airport and the campus of research institute.	deep convolutional neural network (D-CNN) model.	Accuracy=%78
[5]	established a picture dataset for airport runways	YOLOv3	mAP=%92.2 Recall=0.931 FPS=32
[6]	FOD-A dataset created	SSD	SSD loss=0.651
[8]	collected using a drone on the runways of an air force range.	YOLOv4-csp	AP=%92.13 TP=2099 FN=210 Precision=0.83 Recall=0.91
[9]	sampled by a vehicular imaging system in Tianjin Binhai International Airport	CNN (RPN + FOD Detector)	mAP=98.41%
		CNN(STN+FODclassification+fine-tune)	Recall=97.67%
[10]	collected on the airport runway by a HIKVISION camera	Faster R-CNN with DenseNet	Accuracy=%95.6
[11]	Collected by Drone at an airport runway.	the online general model and the local compact model.	Precision % / Recall % / mAP %

	Precision %		Recall %		mAP %	
	G	C	G	C	G	C
Multi	77	96.3	72.7	5.6	77.5	40.7
Single	85.7	88.8	90.5	37.2	94	55.4

[12]	collected by research group at Shahe Airport in Beijing, China.	random forest-based FOD detection framework that uses representative PVF	Precision=%94.88 Recall=%95.43 mAP= %93.47

4. Conclusion and Suggestions

Apart from preventing damage to the airport, airport personnel and aircraft, FOD shortens the delay time of the aircraft, and with a more advanced application, it can make an effective detection even in adverse weather conditions day and night. In this paper, to detect foreign object debris detection with different networks and optimizers are compared with two stages. In the first stage of this study, the data reserved for training in the data set were separated as training and test at certain rates and results were obtained. In the second step, an external dataset is used for validation. One of the important advantages of deep learning is that it has gradient descent based optimization algorithms that minimize the error. SGD, Momentum, Adagarad, RMSprop, Adadelta and Adam algorithms are the most well-known optimization algorithms. Some weights are updated with the frequently used SGD.

Since momentum gradients are used to reduce the excess oscillation that occurs while searching for the optimum point in SGD, a controlled descent takes place and the oscillation decreases. In terms of the smoothness of the data used in the first application, the success of the first application was higher, and it was seen that Adam optimizer was also an efficient algorithm.

Statement of Research and Publication Ethics

The study is complied with research and publication ethics.

References

[1] International Civil Aviation Organization (ICAO) Annex 14 Recommendation.

[2] S. A.Yahyaai, A. A. Khan, M. A.Siyabi, A.Mehmood, T. Hussain, "LiDAR Based Remote Sensing System for Foreign Object Debris Detection (FODD *)", Journal of Space Technology*, 2020, Vol. 10(1) 13-18.

[3] https://www.faa.gov/documentLibrary/media/Advisory_Circular/AC_150_5220-24.pdf (accessed in 13.03.2023)

[4] H. Xu, Z. Han, S. Feng, H. Zhou and Y. Fang, "Foreign object debris material recognition based on convolutional neural networks", *EURASIP Journal on Image and Video Processing*, 2018:21, https://doi.org/10.1186/s13640-018-0261-2

[5] P. Li, H. Li, "Research on FOD Detection for Airport Runway based on YOLOv3", *Proceedings of the 39th Chinese Control Conference*, July 27-29, 2020, Shenyang, China

[6] T. Munyer, Pei-Chi Huang, C. Huang, X. Zhong, "FOD-A: A Dataset for Foreign Object Debris in Airports", *https://arxiv.org/abs/2110.03072*

[7] T.J.E. Munyer, C. Huang, D. Brinkman, X. Zhong, "Integrative Use of Computer Vision and Unmanned Aircraft Technologies in Public Inspection: Foreign Object Debris Image Collection", *Proc Int Conf Digit Gov Res.* 2021 Jun;2021:437-443. doi: 10.1145/3463677.3463743. Epub 2021 Jun 9. PMID: 35098266; PMCID: PMC8796661.

[8] M. Noroozi, A. Shah, "Towards optimal foreign object debris detection in an airport environment", *Expert Systems with Applications*, 2023, Vol.213, Part A, 118829, Issn 0957-4174, https://doi.org/10.1016/j.eswa.2022.118829.

[9] X. Cao, P. Wang, C. Meng, X Bai, G. Gong, M Liu, J Qi, "Region Based CNN for Foreign Object Debris Detection on Airfield Pavement", *Sensors* 2018, 18, 737. https://doi.org/10.3390/s18030737.

[10] Y. Liu, Y. Li, J. Liu, X. Peng, Y. Zhou and Y. L. Murphey, "FOD Detection using DenseNet with Focal Loss of Object Samples for Airport Runway," *2018 IEEE Symposium Series on Computational Intelligence (SSCI), Bangalore, India, 2018, pp. 547-554, doi: 10.1109/SSCI.2018.8628648.*

[11] A. Parker, F. Gonzalez and P. Trotter, "Live Detection of Foreign Object Debris on Runways Detection using Drones and AI", *2022 IEEE Aerospace Conference (AERO), Big Sky, MT, USA, 2022, pp. 1-13, doi: 10.1109/AERO53065.2022.9843697.*

[12] Y. Jing., H. Zheng, C. Lin, W. Zheng, K. Dong, and X. Li. "Foreign Object Debris Detection for Optical Imaging Sensors Based on Random Forest", *Sensors* 22, no. 7: 2463. https://doi.org/10.3390/s22072463.

[13] D. R Shaker and A.R Abbas, "Foreign Object Debris Material Recognition based on Ensemble Learning Algorithm" *J. Phys.: Conf. Ser. 2022, 2322 012091 DOI 10.1088/1742-6596/2322/1/012091*

[14] https://drive.google.com/file/d/1UTxZQUipkX6_rC9AoCaweeeeOPrOG1_B (accessed in 13.03.2023)

[15] A. Addapa, P. Ramaswamy & K. Mungara, "Object Detection/Recognition Using Machine Learning Techniques in AWS", 2020, *The International journal of analytical and experimental modal analysis*, ISSN NO:0886-9367.

[16] A. T. Ali, H. S. Abdullah & M.N. Fadhil, "Voice recognition system using machine learning techniques" *Materials Today: 2021 Proceedings*. ISSN 2214-7853, https://doi.org/10.1016/j.matpr.2021.04.075

[17] M.M. Ahsan, S.A. Luna, Z. Siddique, "Machine-Learning-Based Disease Diagnosis: A Comprehensive Review", *Healthcare (Basel)*, 2022 Mar 15;10(3):541. doi: 10.3390/healthcare10030541. PMID: 35327018; PMCID: PMC8950225.

[18] M. Coşkun, Ö. Yıldırım., A. Uçar, Y. Demir. "An Overview of Popular Deep Learning Methods". *European Journal of Technique (EJT)* 7, 2017: 165-176

[19] A. Krizhevsky, I. Sutskever & G. E. Hinton, "Imagenet classification with deep convolutional neural networks". *Advances in neural information processing systems*, 25, 2012.

[20] Md. Z. Alom, T. M. Taha, C. Yakopcic, S. Westberg, P. Sidike, M. S. Nasrin, B. C V. Esesn, A A S. Awwal & V. K. Asari, "The history began from alexnet: A comprehensive survey on deep learning approaches",2018, *arXiv preprint arXiv:1803.01164.*

[21] https://www.mathworks.com/help/deeplearning/ref/resnet18.html. (accessed in 18.01.2023)

[22] F.N. Iandola, S. Han, M.W. Moskewicz, K. Ashraf, W.J. Dally, K. Keutzer, "SqueezeNet: AlexNet-level accuracy with 50x fewer parameters and< 0.5 MB model size", *3th International Conference on Learning Representations. Toulon: ICLR*, 2016, pp.1-13, 2016

[23] F. Kurt "Evrişimli Sinir Ağlarında Hiper Parametrelerin Etkisinin İncelenmesi," *Yüksek Lisans Tezi, Hacettepe Üniversitesi, Eğitim Bilimleri Enstitüsü*, Ankara, 2018.

[24] E. Seyyarer, F. Ayata, T. Uçkan, & A. Karci, "Derin Öğrenmede Kullanılan Optimizasyon Algoritmalarının Uygulanması ve Kıyaslanması" *Computer Science*, 2020, 5 (2), 90-98.

[25] https://medium.com/deep-learning-turkiye/derin-ogrenme-uygulamalarinda-en-sik-kullanilan-hiper-parametreler-ece8e9125c4 (accessed in 14.03.2023).

Bitlis Eren Üniversitesi Fen Bilimleri Dergisi
BİTLİS EREN UNIVERSITY JOURNAL OF SCIENCE
ISSN: 2147-3129/e-ISSN: 2147-3188
VOLUME: 12 NO: 1 PAGE: 158-165 YEAR: 2023
DOI:10.17798/bitlisfen.1219638

Development of Oleuropein Incorporated Chitosan Films for Antioxidant Active Food Packaging Applications

Ayça AYDOĞDU EMİR[1*], Fatmagül KAYA[1]

[1] *Çanakkale Onsekiz Mart University, Faculty of Canakkale Applied Sciences, Department of Food Technology, Canakkale, Turkey.)*

(ORCID: 0000-0003-3877-9200) (ORCID: 0000-0003-4810-9585)

Keywords: oleuropein, chitosan, water vapor permeability, antioxidant activity, opacity.

Abstract

Oleuropein is the major phenolic component of olive leaf extract. In the present study, oleuropein was incorporated into chitosan films, and the physical properties and antioxidant activity of the films were determined. The chitosan-to-oleuropein ratio was arranged as 1:1, 1:0.5, 2:1, and 2:0.5. Physical properties including moisture content, density, solubility, water vapor permeability, color, and opacity were measured. The results showed that the addition of oleuropein improved the water vapor barrier and decreased the solubility of chitosan films. The oleuropein-added films had the same density and moisture content as chitosan films. Oleuropein incorporation resulted in higher opacity and b* values, whereas a* and L* values decreased. Chitosan films with oleuropein showed strong antioxidant activity. Films at chitosan/oleuropein ratio as 1:1 could be good candidate for active packaging material due to exhibiting good water vapor barrier, opacity, and antioxidant property.

1. Introduction

Olive leaves are a significant waste from olive oil production, and they can be considered a cheap and rich source of phenolic compounds. In general, olive leaves contain about 30 phenolic compounds, which are phenolic acids (gallic acid, coumaric acid, ferulic acid, syringic acid, caffeic acid, vanillic acid), phenolic alcohols (tyrosol, hydroxytyrosol), flavonoids (luteolin, apigenin, quercetin, cyanidin), secoiridoids (oleuropein, verbascoside, ligroside) and lignans [1]. Oleuropein is a heterosidic ester of β-glucosylatedelenolic acid and hydroxytyrosol. C25H32O13 is the molecular formula of oleuropein, and its molecular weight is 540.51 g mol-1 [2]. Oleuropein is mainly present in olive tree leaves and olives. It is also present in small amounts in olive oil and is responsible for the bitter taste of olives and olive oil [3].. The studies demonstrated significant health benefits, including the prevention of coronary heart disease, neurodegenerative diseases, and cancer [4]. Oleuropein has shown strong antimicrobial properties in several studies. Sudjana et al. stated that oleuropein, as the main component of leaf extract, showed antimicrobial activity against Helicobacter pylori, Campylobacter jejuni, and Staphylococcus aureus [5]. In a similar study, oleuropein was found to have inhibitory effect especially on Gram(+) bacteria [6].

In recent years, due to health and environmental concerns about the use of petrochemical-based plastics, biopolymer-based packages have received great attention for replacing plastic food packaging. Carbohydrate polymers such as starch, pectin, cellulose derivatives, and chitosan could be good alternatives for biopolymer-based packaging materials [7]. Among them, chitosan, a cationic polysaccharide consisting of β -1,4-linked D-glucosamine and N-acetyl-d-glucosamine, has been shown to be a potential packaging material due to being nontoxic, biodegradable, biocompatible and also having antimicrobial properties [8]. Showing

*Corresponding author: ayca.aydogdu@comu.edu.tr
Received: 15.12.2022, Accepted: 23.02.2023

antimicrobial properties makes chitosan as film matrix for active food packaging design to minimize food deterioration and extend the shelf life of foods. To enhance the antimicrobial activity of chitosan films, extracts of phenolic compounds such as grape seed extract [9], onion skin extracts [10], and rich cactus pear extract [11], have been commonly used. Moreover, essential oils like tea tree oil [12], lemon, thyme, and cinnamon oils [13], and basil oil [13], were used to increase the antimicrobial activity of chitosan films to be used as active packaging materials. On the contrary, the antioxidant activity of chitosan films is almost negligible, so it is needed to fortify the antioxidant activity of chitosan films to minimize oxidation of food during storage. Although synthetic antioxidants (butylated hydroxyanisole (BHA), butylated hydroxytoluene (BHT), tert-butyl hydroquinone (TBHQ) etc.) show high stability and low cost, due to safety and health concerns, consumers do not prefer packages having synthetic antioxidants [14]. Therefore, natural antioxidants have received great attention as a way to replace synthetic ones. The incorporation of phenolic compounds, in particular, has been found to be effective in providing strong antioxidant activity for chitosan films. In the study of Kadam et al., pine needle extract was incorporated into chitosan films, and a significant increase in the antioxidant activity of chitosan films was observed [15]. In a similar study, blueberry and blackberry pomace extracts were used as active agents, and phenolic compounds incorporated into chitosan films showed strong antioxidant activity [16].

The main aim of this study is to produce oleuropein incorporated chitosan films to be used as biodegradable active packaging materials. The effects of different oleuropein and chitosan concentrations on the physical (density, moisture content, water solubility, water vapor permeability, opacity, and color) and antioxidant properties of chitosan-based films were evaluated.

2. Material and Method

2.1. Materials

Chitosan was bought from Sigma-Aldrich Chemie Gmbh (Darmstadt, Germany), and oleuropein powder was provided by Kale Naturel Ltd. Şti. Glycerol (≥%99), 2,2-Diphenyl-1-picrylhydrazyl, Folin-Ciocalteau reagent, sodium carbonate) were purchased from Sigma-Aldrich Chemie Gmbh (Darmstadt, Germany).

2.1. Methods

2.2.1 Film preparation

To prepare chitosan solutions (1% and 2% (w/v)), 1 g and 2 g of chitosan were dissolved in 100 ml of acetic acid solution (1% v/v). Glycerol was added to the prepared solutions by arranging chitosan: glycerol ratio 2:1 (w/w). The solutions were stirred for 2 hours with a magnetic stirrer. %5 and %2.5 (w/v) oleuropein were dissolved in ethanol/water (80/20) solution and the slurry was centrifuged at 3500 rpm for 10 minutes to remove unsoluble parts. To obtain a chitosan/oleuropein ratio as 1:1, 1:0.5, 2:1, 2:0.5, oleuropein was added to chitosan solutions. 15 ml of solutions were cast over petri plates for 48 h at 25°C. Before physical analyses, the films were stored in a desiccator at 52% and 20°C for conditioning. The oleuropein incorporated chitosan films were named as Ch1Ole1, Ch1Ole0.5, Ch2Ole1, Ch2Ole0.5. 1% and 2% chitosan films were prepared and labelled as Ch1 and Ch2, respectively.

2.2.2 Thickness of films

The film thickness was measured using a digital micrometer (Dial thickness gauge No. 7301, Mitutoyo Co. Ltd., Tokyo, Japan). Six random readings from three films were taken.

2.2.3. Density, moisture content and solubility of films

The initial weight of films being at 2 cm × 2 cm was recorded (W_1). Until the samples reached a constant weight (W_2), the films were dried in an oven at 105 °C. The density was calculated from Eqn. [1];

$$\boldsymbol{Density} = \frac{\boldsymbol{W_2}}{\boldsymbol{Area \times Thickness}} \quad (1)$$

Moisture content (%, wet basis) was found from the Eqn. [2];

$$Moisture\ content\ (\%) = \frac{W_1 - W_2}{W_1} \times 100 \quad (2)$$

The dried films (W_2) were put in 30 ml of distilled water at room temperature and waited for 24 h. Then, the undissolved parts were dried in an oven set at 105°C for 24 h, and the weight of the dried undissolved parts was recorded (W_3). Solubility was calculated by Eqn. [3];

$$Solubility\ (\%) = \frac{W_2 - W_3}{W_2} \times 100 \quad (3)$$

2.2.4. Color of films

The film color was determined using a Chroma Meter CR400 colorimeter (Konica Minolta, Inc., Japan). L*(lightness), a*(redness- greenness), b* (yellowness-blueness) were used to characterize the color of films, and the total color difference ΔE was calculated using the following Eqn. [4];

$$\Delta E = \sqrt{(L_0{}^* - L^*)^2 + (a_0{}^* - a^*)^2 + (b_0{}^* - b^*)^2} \quad (4)$$

where $L_0{}^*$, $a_0{}^*$ and $b_0{}^*$ are the color measurements of $BaSO_4$ plate.

2.2.5. Opacity of films

The film opacity was measured at 600 nm using a UV–visible spectrophotometer (UV-1800, Shimadzu, Kyoto, Japan). Opacity values were determined according to the method of Aydogdu et al. with Eqn. [5]; [17];

$$Opacity = \frac{A_{600}}{x} \quad (5)$$

where A_{600} is the absorbance at 600 nm and x is the thickness value of films (mm). Greater opacity values indicate lower transparency of the films. Three pieces were taken from each film for measurement; three replicates were measured for each formulation.

2.2.6. Water vapor permeability of films (WVP)

WVP of films was determined with the modified version of ASTM E-96 described by Aydogdu et al. [17].The custom-built test cups were used in this experiment. To provide the films with 100% RH, 30 mL of distilled water was used to fill the cups. The cups were placed in a desiccator at 40% RH using silica gel. The cups were weighed at 3 h intervals. The water vapor transmission rate (WVTR) was calculated from the slopes of weight loss data vs. time. Then the WVP values were calculated by using Eqn. [6];

$$WVP = \frac{WVTR \times \Delta x}{S \times (R_1 - R_2)} \quad (6)$$

where x is the thickness of the films (m), S is the saturated water vapor pressure (Pa) at measured temperature, R_1 and R_2 are the relative humidity inside the cups and desiccator, relatively. The measurements were performed in duplicate.

2.2.7. DPPH radical-scavenging activity

The modified method described by Aydogdu et al. [18] was applied to determine the DPPH radical-scavenging activity. Pieces of films (0.1 g) and 10 ml of ethanol/water (80/20) were mixed. 3.9 mL $DPPH^{\cdot}$ radical solution was added to 100 µl sample solutions in the dark at room temperature. After 1 hour, the absorbance of mixtures was measured at 517 nm by a spectrophotometer (UV 1800, Shimadzu, Columbia, USA). The antioxidant activity (%AA) of the films was defined by Eqn. [7] ;

$$\text{DPPH scavenging activity (AA)}(\%) = \frac{A_{control} - A_{film}}{A_{control}} \times 100 \quad (7)$$

where $A_{control}$ and A_{film} are the absorbance values of the DPPH solution without and with the presence of the sample solutions.

2.2.8. Total phenolic content (TPC) of films

The TPC of films was determined by the modified Folin–Ciocalteau method [19]. To extract phenolic compounds from the film, about 0.1-0.2 g of the film was put in 10 ml of ethanol water mixture (4:1 v/v). According to absorbance values, samples were diluted, and 1 ml of sample and 2.5 ml of 0.2 N Folin-Ciocalteau reagent were mixed. Then, the mixture was kept in dark for 5 min. 2 ml of a 75 g/L sodium carbonate solution were added to the mixture. 1 hour in dark at room temperature was waited. The absorbance values of mixtures at 760 nm were measured by a spectrophotometer (UV 1800, Shimadzu, Columbia, USA), and TPC was determined by Eqn. [8] ;

$$\text{TPC}\left(\text{mg}\frac{\text{GAE}}{\text{g}}\text{film}\right) = \frac{C \times V \times D}{W_S} \quad (8)$$

where C is the concentration corresponding to the measured absorbance value from the calibration curve

(mg/L), V is the volume of the solution (L), D is the dilution rate, and Ws is the weight of the film (g).

2.2.9 Statistical analysis

Data were analyzed by MINITAB (version 16, State College, PA, USA). An analysis of variance (ANOVA) was applied, and Tukey's Multiple Comparison Test was used for the identification of the significance of differences among values ($p \leq 0.05$).

3. Results and Discussion

3.1 Moisture Content, Thickness, Density and Solubility

Table 1 represents the thickness, solubility, moisture content, and density of films. The thickness values were within the range of 0.036-0.042 mm, and no significant difference between the films was observed ($p > 0.05$). While the density of oleuropein incorporated chitosan films lay within the range of 1.21-1.34 g/cm3, the density values of chitosan films (1% and 2%) were 0.55 and 0.62 g/cm3. Although there is no significant difference in the density of films with varying amounts of oleuropein, the addition of oleuropein increased the density of chitosan films significantly. The moisture content of both chitosan and oleuropein incorporated chitosan films was in the range of about 16%-19% which is similar to phenolic acid incorporated chitosan films [8],[10]. The chitosan films containing oleuropein showed a considerable reduction ($p \leq 0.05$) in water solubility as compared to the control chitosan films. The interaction between oleuropein and chitosan chains reduced the interaction of water with the chitosan. A similar trend was found by Rambabu et al. [20], which showed the addition of mango leaf extract decreased the solubility of chitosan from 27% to 17% (wb).

3.2 WVP

The WVP value of films is an indication of moisture transfer between food and environment, so it is a critical parameter that affects the shelf lives of foods. WVP values of films are shown in Table 1. The addition of oleuropein resulted in films with a lower WVP, which was desirable to minimize moisture transfer. The reason could be related to filling of the gaps existing in the matrix with the help of oleuropein [20]. This is consistent with the density results, and the incorporation of oleuropein into the chitosan film caused denser films (Table 1). Moreover, oleuropein as a phenolic compound interact with reactive groups of chitosan by hydrogen or covalent bonding and these interactions could decrease the amount of available hydrogen groups to obtain hydrophilic bonding with water [21]. Therefore, the affinity of chitosan films towards the water could be reduced by oleuropein addition. Similar reducing effects of phenolic compounds on WVP values of films were observed in several studies, such as propolis [22], blueberries [16], tea extract [8], etc.

3.3 Color and Opacity

The color parameters (L*, a*, b*, and ΔE*) of films were represented in Table 2. It is obviously seen that oleuropein addition decreased L* values of chitosan films which is an evidence of obtaining darker films. Oleuropein incorporation resulted in lower a* and higher b* values. a* value represents greenness (-) and redness (+) and b value represent yellowness (+) and blueness (-). The color of oleuropein as olive leaf extract is greenish yellow, so chitosan films including oleuropein showed a* values in the range of -3.13 and -4.12. Moreover, as the oleuropein amount increased, the b* values of chitosan films increased significantly ($p \leq 0.05$). Although chitosan films were almost colorless, a significant ΔE* increase was observed by adding oleuropein into chitosan films. ΔE* values of Ch_Ole films were in the range of 23.39- 34.99. If ΔE* value is greater than 5, the color change of films can be detected by observers [23] so the color change of oleuropein incorporated chitosan films was easily visible.

The transparency of films affects customer acceptance, so it is a crucial property of packaging material. Although transparent packaging makes it possible to see the product directly, it is not appropriate for the packaging of photo-sensitive foods. The opacity values of films are shown in Table 2. Chitosan films having 1.15 and 1.52 A mm−1 opacity were almost transparent. When oleuropein added to films, the opacity values reached up to 5.8 A mm−1. The addition of oleuropein resulted in light scattering and yielded in higher opacity. Similar studies demonstrated that phenolic acid addition increased opacity values for green tea extract [21], pomegranate peel extract [24], black soybean seed coat extract [25], apple peel polyphenols [26] etc.

Table 1. Thickness, moisture content, solubility, density and water vapor permeability (WVP) values of chitosan and oleuropein incorporated chitosan films

Films	Thickness(mm)	Moisture Content (%)	Solubility (%)	Density (g/cm^3)	WVP x 10^{10} ($g\ m^{-1}\ s^{-1}\ Pa^{-1}$)
Ch1Ole1	0.042±0.002^a	16.38±0.36^a	27.43±2.33^b	1.34±0.13^a	1.401±0.012^b
Ch1Ole0.5	0.036±0.001^a	17.05±0.06^a	26.64±0.19^b	1.21±0.12^a	1.394±0.013^b
Ch2Ole1	0.038±0.004^a	18.92±0.56^a	29.13±1.74^b	1.22±0.11^a	1.423±0.024^b
Ch2Ole0.5	0.036±0.001^a	18.43±0.74^a	28.33±1.77^b	1.30±0.11^a	1.442±0.036^b
Ch1	0.040±0.003^a	18.32±0.20^a	32.87±3.31^a	0.55±0.02^b	2.729±0.048^a
Ch2	0.040±0.002^a	17.55±0.38^a	32.33±2.41^a	0.62±0.02^b	2.616±0.016^a

Different letter superscripts in the same line indicate a statistically significant difference ($p \leq 0.05$). ± indicates standard error.

Table 2. Color parameters and opacity values of chitosan and oleuropein incorporated chitosan films

Films	L*	a*	b*	ΔE*	Opacity (A mm^{-1})
Ch1Ole1	82.29±1.48^b	-4.12±0.55^b	34.52±1.70^a	34.99±3.41^a	4.36±0.25^a
Ch1Ole0.5	83.24±1.48^b	-3.13±0.22^b	27.17±1.63^b	24.84±2.54^b	5.00±0.69^a
Ch2Ole1	81.94±0.64^b	-3.72±0.16^b	31.05±2.08^a	32.03±2.09^a	5.46±0.55^a
Ch2Ole0.5	84.07±1.38^b	-3.41±0.28^b	23.79±1.20^b	23.39±2.04^b	5.80±0.25^a
Ch1	91.82±0.22^a	-0.65±0.03^a	1.15±0.23^c	6.00±0.57^c	1.15±0.11^b
Ch2	91.89±0.42^a	-0.54±0.10^a	0.56±0.11^c	5.57±0.18^c	1.52±0.12^b

Different letter superscripts in the same line indicate a statistically significant difference ($p \leq 0.05$). ± indicates standard error

3.4 TPC and Antioxidant Activity

Table 3 shows the total phenolic content and antioxidant activity of films. As shown in Table 3, oleuropein incorporation significantly increased the total phenolic content of chitosan films, as expected. Ch1Ole1 films showed the highest total phenolic content (35.10±1.44 mg GAE/g film) with a chitosan to oleuropein ratio of 1:1 w/w. Oleuropein is one of the dominant phenolic acids in olive leaves and fruits [27]. Phenolic compounds are potential antioxidants, so oleuropein added chitosan films showed antioxidant activity between 67.21 %- 98.25. In fact, chitosan films showed meager antioxidant activity with about 17-18%. [20] stated that chitosan polysaccharide chain enhanced antioxidant activity. However, these values are not enough to suggest films as an active packaging material. Oleuropein, as an antioxidant source, enhanced the antioxidant activity of chitosan films. Antioxidant activity of films was directly correlated to their total phenolic contents. Therefore, due to having the highest total phenolic content, Ch1Ole1 films showed the strongest antioxidant activity at nearly 100%. Thus, Ch1Ole1 films could be a good option for the antioxidant food package.

Table 3. TPC and DPPH activity of chitosan and oleuropein incorporated chitosan films

Films	TPC (mg GAE/g film)	DPPH activity (%)
Ch1Ole1	35.10±1.44^a	98.25±1.50^a
Ch1Ole0.5	26.02±1.31^b	84.72±3.46^b
Ch2Ole1	17.84±0.95^c	83.66±1.81^b
Ch2Ole0.5	12.60±1.43^d	67.21±2.74^c
Ch1	1.90±0.07^e	18.45±2.20^d
Ch2	2.45±0.16^e	17.85±0.38^d

Different letter superscripts in the same line indicate a statistically significant difference ($p \leq 0.05$). ± indicates standard error.

4. Conclusion

Oleuropein is one of the major phenolic compounds in olives and olive leaves. With the addition of oleuropein, the thickness and moisture content of films were not affected, but water solubility and water vapor permeability decreased significantly, suggesting that the water barrier property of the film was improved. Oleuropein incorporation reduced the lightness and increased the greenness and blueness of the chitosan films. Besides, more opaque films were obtained by increasing oleuropein content. The total phenolic content of chitosan films increased as the

amount of oleuropein increased, representing significant antioxidant activity up to nearly 100% when combined with the chitosan films. Conclusively, enhanced water vapor permeability, water solubility, opacity, and strong antioxidant activity indicate that chitosan films containing oleuropein can be a promising alternative to biodegradable active packaging materials for shelf-life extension of foods.

Acknowledgment

This research was supported by the Scientific and Technological Research Council of Turkey (TÜBİTAK) [2209A- Research Project Support Program for Undergraduate Students].

Contributions of the authors

Ayca Aydogdu Emir: conceptualization, supervision, methodology, investigation, writing—original draft; Fatmagül Kaya: methodology, investigation, writing—original draft, visualization.

Conflict of Interest Statement

There is no conflict of interest between the authors.

Statement of Research and Publication Ethics

The study is complied with research and publication ethics.

References

[1] H. B. Malayoğlu and B. Aktaş, "Zeytin Yağı İşleme Yan Ürünlerinden Zeytin Yaprağı ile Zeytin Karasuyunun Antimikrobiyal ve Antioksidan Etkileri," *Hayvansal Üretim*, vol. 52, no. 1, pp. 49–58, 2011.

[2] S. Şahin and M. Bilgin, "Olive tree (Olea europaea L.) leaf as a waste by-product of table olive and olive oil industry: a review," *J. Sci. Food Agric.*, vol. 98, no. 4, pp. 1271–1279, 2018, doi: 10.1002/jsfa.8619.

[3] I. Mourtzinos, F. Salta, K. Yannakopoulou, A. Chiou, and V. T. Karathanos, "Encapsulation of olive leaf extract in β-cyclodextrin," *J. Agric. Food Chem.*, vol. 55, no. 20, pp. 8088–8094, 2007, doi: 10.1021/jf0709698.

[4] R. González-Ortega, M. Faieta, C. D. Di Mattia, L. Valbonetti, and P. Pittia, "Microencapsulation of olive leaf extract by freeze-drying: Effect of carrier composition on process efficiency and technological properties of the powders," *J. Food Eng.*, vol. 285, 2020, doi: 10.1016/j.jfoodeng.2020.110089.

[5] A. N. Sudjana *et al.*, "Antimicrobial activity of commercial Olea europaea (olive) leaf extract," *Int. J. Antimicrob. Agents*, vol. 33, no. 5, pp. 461–463, May 2009, doi: 10.1016/j.ijantimicag.2008.10.026.

[6] A. T. Serra *et al.*, "In vitro evaluation of olive- and grape-based natural extracts as potential preservatives for food," *Innov. Food Sci. Emerg. Technol.*, vol. 9, no. 3, pp. 311–319, 2008, doi: 10.1016/j.ifset.2007.07.011.

[7] L. Sun, J. Sun, L. Chen, P. Niu, X. Yang, and Y. Guo, "Preparation and characterization of chitosan film incorporated with thinned young apple polyphenols as an active packaging material,"

Carbohydr. Polym., vol. 163, pp. 81–91, 2017, doi: 10.1016/j.carbpol.2017.01.016.

[8] Y. Peng, Y. Wu, and Y. Li, "Development of tea extracts and chitosan composite films for active packaging materials," *Int. J. Biol. Macromol.*, vol. 59, pp. 282–289, 2013, doi: 10.1016/j.ijbiomac.2013.04.019.

[9] A. Mojaddar, L. Amene, and N. Mehran, "Chitosan coating incorporated with grape seed extract and Origanum vulgare essential oil : an active packaging for turkey meat preservation," *J. Food Meas. Charact.*, vol. 15, no. 3, pp. 2790–2804, 2021, doi: 10.1007/s11694-021-00867-0.

[10] C. Wang *et al.*, "Preparation and characterization of chitosan-based antioxidant composite films containing onion skin ethanolic extracts," *J. Food Meas. Charact.*, vol. 16, no. 1, pp. 598–609, 2022, doi: 10.1007/s11694-021-01187-z.

[11] X. Yao, H. Hu, Y. Qin, and J. Liu, "Development of antioxidant, antimicrobial and ammonia-sensitive films based on quaternary ammonium chitosan, polyvinyl alcohol and betalains-rich cactus pears (Opuntia ficus-indica) extract," *Food Hydrocoll.*, vol. 106, no. March, 2020, doi: 10.1016/j.foodhyd.2020.105896.

[12] L. Sánchez-gonzález, C. González-martínez, A. Chiralt, and M. Cháfer, "Physical and antimicrobial properties of chitosan – tea tree essential oil composite films," *J. Food Eng.*, vol. 98, no. 4, pp. 443–452, 2010, doi: 10.1016/j.jfoodeng.2010.01.026.

[13] Y. Peng and Y. Li, "Combined effects of two kinds of essential oils on physical, mechanical and structural properties of chitosan films," *Food Hydrocoll.*, vol. 36, pp. 287–293, 2014, doi: 10.1016/j.foodhyd.2013.10.013.

[14] S. C. Lourenço, M. Mold, and V. D. Alves, "Antioxidants of Natural Plant Origins : From Sources to Food Industry Applications," *Molecules*, vol. 24, no. 22, p. 4132, 2019.

[15] A. A. Kadam, S. Singh, and K. K. Gaikwad, "Chitosan based antioxidant films incorporated with pine needles (Cedrus deodara) extract for active food packaging applications," *Food Control*, vol. 124, no. June 2020, p. 107877, 2021, doi: 10.1016/j.foodcont.2021.107877.

[16] M. Kurek, I. Elez, M. Tran, M. Šč, V. Dragovi, and K. Gali, "Development and evaluation of a novel antioxidant and pH indicator film based on chitosan and food waste sources of antioxidants," *Food Hydrocoll.*, vol. 84, pp. 238–246, 2018, doi: 10.1016/j.foodhyd.2018.05.050.

[17] A. Aydogdu, E. Kirtil, G. Sumnu, M. H. Oztop, and Y. Aydogdu, "Utilization of lentil flour as a biopolymer source for the development of edible films," *J. Appl. Polym. Sci.*, vol. 135, no. 23, p. 46356, Jun. 2018, doi: 10.1002/app.46356.

[18] A. Aydogdu, E. Yildiz, Y. Aydogdu, G. Sumnu, S. Sahin, and Z. Ayhan, "Enhancing oxidative stability of walnuts by using gallic acid loaded lentil flour based electrospun nanofibers as active packaging material," *Food Hydrocoll.*, vol. 95, no. April, pp. 245–255, 2019, doi: 10.1016/j.foodhyd.2019.04.020.

[19] H. Wang, L. Hao, P. Wang, M. Chen, S. Jiang, and S. Jiang, "Release kinetics and antibacterial activity of curcumin loaded zein fibers," *Food Hydrocoll.*, vol. 63, pp. 437–446, Feb. 2017, doi: 10.1016/J.FOODHYD.2016.09.028.

[20] K. Rambabu, G. Bharath, F. Banat, P. Loke, and H. Hernández, "Mango leaf extract incorporated chitosan antioxidant fi lm for active food packaging," *Int. J. Biol. Macromol.*, vol. 126, pp. 1234–1243, 2019, doi: 10.1016/j.ijbiomac.2018.12.196.

[21] U. Siripatrawan and B. R. Harte, "Physical properties and antioxidant activity of an active film from chitosan incorporated with green tea extract," *Food Hydrocoll.*, vol. 24, no. 8, pp. 770–775, 2010, doi: 10.1016/j.foodhyd.2010.04.003.

[22] U. Siripatrawan and W. Vitchayakitti, "Improving functional properties of chitosan films as active food packaging by incorporating with propolis," *Food Hydrocoll.*, vol. 61, pp. 695–702, 2016, doi: 10.1016/j.foodhyd.2016.06.001.

[23] C. K. da Silva, D. J. da S. Mastrantonio, J. A. V. Costa, and M. G. de Morais, "Innovative pH sensors developed from ultrafine fibers containing açaí (Euterpe oleracea) extract," *Food Chem.*, vol. 294, pp. 397–404, Oct. 2019, doi: 10.1016/J.FOODCHEM.2019.05.059.

[24] G. Yuan, H. Lv, B. Yang, X. Chen, and H. Sun, "Physical Properties, Antioxidant and Antimicrobial Activity of Chitosan Films Containing Carvacrol and Pomegranate Peel Extract," *Molecules*, vol. 20, pp. 11034–11045, 2015, doi: 10.3390/molecules200611034.

[25] X. Wang, H. Yong, L. Gao, L. Li, M. Jin, and J. Liu, "Preparation and characterization of antioxidant

and pH-sensitive films based on chitosan and black soybean seed coat extract," *Food Hydrocoll.*, vol. 89, no. October 2018, pp. 56–66, 2019, doi: 10.1016/j.foodhyd.2018.10.019.

[26] A. Riaz *et al.*, "Preparation and characterization of chitosan-based antimicrobial active food packaging film incorporated with apple peel polyphenols," *Int. J. Biol. Macromol.*, vol. 114, pp. 547–555, 2018, doi: 10.1016/j.ijbiomac.2018.03.126.

[27] J. Thielmann, S. Kohnen, and C. Hauser, "Antimicrobial activity of Olea europaea Linné extracts and their applicability as natural food preservative agents," *Int. J. Food Microbiol.*, vol. 251, pp. 48–66, 2017, doi: 10.1016/j.ijfoodmicro.2017.03.019.

Bitlis Eren Üniversitesi Fen Bilimleri Dergisi
BİTLİS EREN UNIVERSITY JOURNAL OF SCIENCE
ISSN: 2147-3129/e-ISSN: 2147-3188
VOLUME: 12 NO: 1 PAGE: 166-179 YEAR: 2023
DOI:10.17798/bitlisfen.1220301

Computational Prediction of Interactions Between SARS-CoV-2 and Human Protein Pairs by PSSM-Based Images

Zeynep Banu ÖZGER[1*], Zeynep ÇAKABAY[1]

[1] *Kahramanmaraş Sutcu Imam University, 46040, Kahramanmaras, Türkiye*

(ORCID:0000-0003-2614-3803) (ORCID: 0000-0001-7059-2337)

Keywords: Feature Projection, Pathogen-Host Protein Interaction, Siamese Neural Network, SARS-CoV-2

Abstract

Identifying protein-protein interactions is essential to predict the behavior of the virus and to design antiviral drugs against an infection. Like other viruses, SARS-CoV-2 virus must interact with a host cell in order to survive. Such interaction results in an infection in the host organism. Knowing which human protein interacts with the SARS-CoV-2 protein is an essential step in preventing viral infection. In silico approaches provide a reference for in vitro validation to protein-protein interaction studies by finding interacting protein pair candidates. The representation of proteins is one of the key steps for protein interaction network prediction. In this study, we proposed an image representation of proteins based on position-specific scoring matrices (PSSM). PSSMs are matrices that are obtained from multiple sequence alignments. In each of its cells, there is information about the probability of the occurrence of amino acids or nucleotides. PSSM matrices were handled as gray-scale images and called PSSM images. The main motivation of the study is to investigate whether these PSSM images are a suitable protein representation method. To determine adequate image size, conversion to grayscale images was performed at different sizes. SARS-CoV-2-human protein interaction network prediction based on image classification with siamese neural network and Resnet50 was performed on PSSM image datasets of different sizes. The accuracy results obtained with 200x200 size images and siamese neural network as 0.915, and with 400x400 size images and Resnet50 as 0.922 showed that PSSM images can be used for protein representation.

1. Introduction

Proteins are polymers formed by the polymerization of amino acids. Each protein has its own features due to its amino acid sequences. These sequences also determine the function of the protein [1]. Many biological events in our body occur as a result of the binding/dissociation of proteins with each other. Understanding protein-protein interactions has a critical role in drug and peptide design. Additionally, understanding the root causes of protein interactions is a big step towards controlling events at the molecular level. The proteins interact via their surface domains as shown in Figure 1. In order for it to interact, the two protein interfaces must be compatible with each other, both shapely and chemically [2].

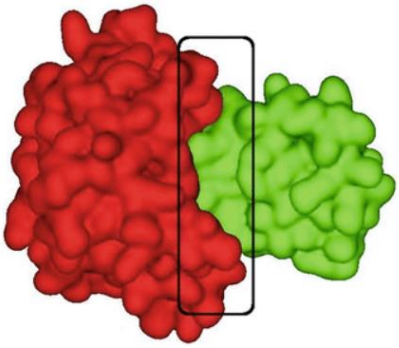

Figure 1. Protein protein interaction [8].

Detection of protein interactions is performed by in vitro, in vivo or in silico methods [3]. Interaction detection by in vitro methods is done with

*Corresponding author: zeynepozger@ksu.edu.tr

Received: 16.12.2022, Accepted: 26.02.2023

microorganisms, cells or biological molecules other than living organisms [4]. In vivo methods are performed on living organisms or cells, as are clinical studies in animals. It is usually applied after in vitro tests [5]. Both have time, place, and cost constraints as they must be performed in a clinical setting. In silico studies are studies performed with computers or simulations [6]. It provides an advantage in terms of reducing the need for clinical research. Considering the existence of a large number of proteins in the body, it is a costly process to investigate whether they interact with each other in the clinical setting. Instead, by identifying proteins with high interaction potential, clinical validation of only these proteins saves time [7]. In this context, different approaches are applied. Studies on the classification of medical documents [9] make it easier to reach the studies presented in a certain field. Protein primary structures [10-12], association rule mining [13], protein domain profiles [14], gene ontology [15, 16], 3D structures of proteins [17], domain-domain motif interactions [18], domain and sequence signature [19], network topology [20], phylogenetic trees [21], text mining [22] are common methods for identifying protein-protein interactions (PPI).

Virus genomes require a host cell to replicate themselves. The way of entry into the host cell is through protein interactions. That is, a protein of the virus and a protein of the host cell must interact with each other [23]. Coronaviruses are infections in which animal viruses such as bat and mink acquires the ability to infect humans [24]. In drug development for coronavirus outbreaks, targeting proteins involved in host-pathogen interactions is important to prevent the spread of epidemics [25]. Like other viruses, SARS-CoV-2 must interact with host cell proteins to reach the host cell and replicate its genome.

Although the SARS-CoV-2 epidemic seems to be under control, it continues to exist in the world. However, the presence of epidemic diseases such as MERS and SARS-CoV seen in the past is an indication that there may be various epidemics belonging to the coronavirus family in the future. Genome data from past coronavirus outbreaks has been pioneering in treatment studies developed for the SARS-CoV-2 virus. Therefore, it is important to determine the entry routes of the SARS-CoV-2 virus into the host cell, so that the world does not fall into a bottleneck, as in SARS-CoV-2, in future coronavirus outbreaks. In order to develop preventive and therapeutic drugs, researchers continue their studies to understand the interactions of SARS-CoV-2 and human proteins. So, there are a limited number of in silico studies presented in the literature. Lanchantin et al. [26], proposed a transfer learning method for predicting SARS-CoV-2-human protein interactions. The work is based on the idea that polypeptide sequences that occur between interacting proteins can be conserved in different organisms. Authors used transfer learning to learn these short protein motifs. Because known interaction data for SARS-CoV-2 is limited, the model was trained with pathogen-host interaction data of other viruses [27]. The success of the proposed method was also applied to predict the interaction of different viruses, and the obtained AUROC (area under receiver operating characteristics curve) value for SARS-CoV-2 has been reported as 0.753.

According to Du et al. [27], SARS-CoV-2 can infect humans as well as some mammals such as cats, dogs, and tigers. These infected animals can infect the virus humans. In the study, a 2-level multi-level perceptron network (MLP) with 2 levels was used to build a protein-protein interaction network. The MLP network was trained with 7 human coronaviruses and 17 hosts. In conclusion, the authors found 19 possible interactions between human and SARS-CoV-2 proteins. The SARS-CoV-2 virus belongs to beta coronavirus family. This coronavirus family has 5 subtypes: sarbecovirus, embecovirus, merbecovirus, hibecovirus and nobecovirus [28]. Since SARS-CoV and SARS-CoV-2 viruses belong to the sarbecovirus type, Khorsand et al. [29], focused on these types of viruses. The authors used a three-layer neural network in their study. The first layer contains the proteins of alpha influenza viruses similar to SARS-CoV-2 viruses. The second layer includes the known alpha influenza virus-human protein interactions. And the third one contains the known SARS-CoV-2-human protein interactions. Of the 87894 sarbevirus-human interactions found, 7201 were reported to be SARS-CoV-2-human protein-protein interactions. Khan and Khan [25] investigated protein-protein interactions for MERS, SARS-CoV, and SARS-CoV-2 and they identified common host targets with bioinformatics tools for these outbreaks. The known interactions are obtained from BioGrid [30] database. Dey et al. [31], determined SARS-CoV-2-human protein-protein interactions using machine learning techniques with sequence-based data. The algorithms were trained on 332 interactions discovered by Gordon et al. [32] using affinity purification mass spectrometry method. In the study, three sequence-based features (amino acid composition, conjoint triad, pseudo amino acid composition) were obtained from protein amino acid sequences. The decisions of SVM and random forest learners were combined with the ensemble majority voting technique. The best prediction score obtained was reported as 72.33% accuracy rate. In addition, the authors presented a gene ontology term analysis of

predicted 1326 human proteins interactions. Pirolli et al. [33] aimed to find the binding receptors between the spike protein of SARS-CoV-2 and the human angiotensin converting enzyme (ACE2) protein. They focused their research on the ACE2 protein because the spike protein uses ACE2 to enter the host cell. In their study, the authors predicted binding receptors with a convolutional neural network-based quantitative structure activity relationship (QSAR) model. Lee [34] proposed a virus type-independent PPI estimation method. The authors obtained 80,775 virus-human PPI from the STRING database. They represented the PPI network of known interactions with a bipartite graph. Using the nodes in the graph, they obtained fractional compositions of 20 amino acids. Then, they extracted features from these composition profiles with 72 different distance/similarity measurements. They made predictions with models trained with random forest and XGBoost. The XGBoost model achieved the best performance with an accuracy value of 68%. SARS-CoV-2-human protein interaction prediction with the trained models was performed with an accuracy of 58%. In the study presented at [35], Bell et al. presented a pipeline they call PEPPI. PEPPI is a virus type-independent consensus model and includes structure similarity, conjoint-triad-based neural network, sequence similarity, and functional association data. The modules are combined with the naive Bayesian consensus classifier. The authors tested their model also on SARS-CoV-2-human protein interactions. The pipeline correctly predicted 94 out of 128 interactions.

A protein-protein interaction detection problem with computational methods can be handled as a binary or multi-label classification problem. The training data consists of host proteins interacting and non-interacting with a pathogen protein. There may be more than one known protein for a virus species. In the binary classification approach, it is not necessary to know which protein of the virus a host protein interacts with. That is, if a host protein interacts with any protein of the virus, its label will be 1, otherwise it will be 0. In the multi-class classification approach, however, it is necessary to know which protein of the virus interacts with the host protein. The label of each different protein of the virus is different. In the dataset, each host protein is labeled with the label of the virus protein that interacts with or does not interact with that protein of the virus.

The binary classification approach does not need to know which protein of the virus an interaction is with. It is sufficient for the virus to know that any protein interacts with a host protein. This approach is advantageous given the difficulty of obtaining validated interaction data in a lab setting. However, the trained model can only tell whether it interacts with the virus of interest for a given host protein. To train a model with a multi-class approach the model needs data with sufficient interactions for each protein of the virus. However, such a model tells not only that the given host protein interacts with the virus protein but with which protein of the virus it interacts with.

In protein-protein interaction network studies, position specific scoring matrices are generally used for inferences such as the biological information they contain and some properties of amino acids. Within the scope of this study, it is being investigated whether PSSM matrices can be used as images to realize a protein-protein interaction prediction problem for SARS-CoV-2. For this purpose, the known interacting protein pairs were converted into gray-scale images of different sizes. Based on the lack of studies on protein interaction network prediction by in silico analysis for SARS-CoV-2, a method has been proposed to identify possible proteins that could be targeted in treatment development for SARS-CoV-2. The problem was handled both as a multi-class problem using siamese neural network and a binary-class problem using Resnet50.

There are numerous approaches to extract features from proteins for protein interaction network prediction. These approaches are generally geared towards exploiting protein primary and secondary sequences and the physicochemical properties of proteins. The contribution of this study is to show that proteins can be converted into image data with PSSM matrices, and protein interaction network prediction can be made with siamese neural networks trained with positive and negative interactions.

2. Material and Method

2.1. Dataset Description

Classification algorithms need samples in each class in the dataset for training. The positive class samples are taken from the study by Gordon et al. [32]. In the dataset, there are 332 interactions between 27 SARS-CoV-2 proteins and 332 human proteins. The dataset consists of 2 columns. The first column contains the primary amino acid sequence of a SARS-CoV-2 protein and the second column contains the primary amino acid sequence of the human protein determined to interact with this SARS-CoV-2 protein. The

Table 1. Numbers of human proteins interacted with SARS-CoV-2 proteins

SARS-CoV-2 Protein	#interacting human protein	SARS-CoV-2 Protein	#interacting human protein	SARS-CoV-2 Protein	#interacting human protein
Envelope	6	**Nsp7**	32	**Orf3a**	8
Membran	30	**Nsp8**	24	**Orf3b**	1
Nucleocapside	15	**Nsp9**	16	**Orf6**	3
Spike	2	**Nsp10**	5	**Orf7a**	2
Nsp1	6	**Nsp11**	1	**Orf8**	47
Nsp2	7	**Nsp12**	20	**Orf9b**	11
Nsp4	8	**Nsp13**	40	**Orf9c**	26
Nsp5	3	**Nsp14**	3	**Orf10**	9
Nsp6	4	**Nsp15**	3		

shortest of these sequences consists of 13 amino acids and the longest consists of 5596 amino acids. Since there is more than one human protein determined to interact with a SARS-CoV-2 protein, information on how many human proteins each SARS-CoV-2 protein interacts with is given in Table 1.

In the learning phase, algorithms need both interactive and non-interactive examples. However, experiments to identify interacting protein pairs are not focused on finding non-interacting proteins. Therefore there is no gold standard for saying that a protein is non-interacting with a specific virus [36]. Different approaches such as random sampling [37], subcellular localization [38], and sequence similarity [23] techniques were used in studies to determine negative proteins. In our study, we used the sequence similarity [12] approach. The basic idea underlying this method is that the sequence similarity of host proteins interacting with a virus protein can be high. In bioinformatics, the most similar regions of different gene or protein sequences can be detected by sequence alignment methods. Thus, information such as the functions of these genes or proteins and which organism they belong to can be determined to a large extent. Substitution matrices are used to calculate the similarity scores of proteins. Substitution matrices are matrices consisting of the biological significance or randomness scores of the occurrences of the standard 20 amino acids. Blosum62 [39] was used as the substitution matrix in this process performed in the R environment.

5873 human proteins not found in the positive dataset were obtained from Uniprot [40]. These are candidate negative proteins. The sequence similarity matrix was constructed with 332 positive proteins and candidate negative proteins. The sequence identity matrix contains similarity ratios of the proteins. Rows represent the positive human proteins and columns represent candidate negative proteins. Therefore, the size of this matrix was 332x5873. Each cell includes the similarity ratio of the corresponding positive protein and the candidate negative protein.

As seen in Table 1, the number of human proteins that interact with each SARS-CoV-2 protein varies. The negative dataset was created by considering the protein counts in the positive dataset. For example, the dataset includes 6 human proteins identified to interact with the envelope protein of SARS-CoV-2 (Table 1). Of the candidate negative proteins, 6 proteins with the lowest sequence similarity to these 6 human proteins were identified. These were added to the negative dataset and labeled as human proteins non-interacting proteins with the envelope protein. This process was repeated for all SARS-CoV-2 proteins. Thus, as many non-interacting proteins were added to the dataset as the number of interacting proteins for each SARS-CoV-2 protein. As the total number of interacting proteins was 332, the number of non-interacting proteins added to the dataset was also 332.

2.2. Position Specific Scoring Matrices (PSSM)

Proteins are polypeptides formed by the covalent bonding of amino acids to each other in a certain type, in a certain number and in a certain sequence [41]. There are 20 amino acids. When amino acids come together in a different order, different proteins are formed. PSSM matrices contain the probability of occurrence of each amino acid and nucleotide at each position [42]. For proteins, the row number of the PSSM matrix is equal to the amino acid number, i.e. 20. The number of columns of the matrix is equal to the length of the protein sequence. The value of each cell is the probability that the corresponding amino acid is in the corresponding position. These probabilities are derived from multiple sequence alignment [43] scores. In bioinformatics, PSSM matrices can be used for a variety of tasks such as

predicting the attributes of a protein [44]. Building a PSSM matrix is given in Figure 2.

Protein sequences were downloaded from Uniprot in Fasta format. PSSM matrices of positive, negative and SARS-CoV-2 proteins were constructed separately using Blosum62 substitution matrix in R environment with "protr" [45] package.

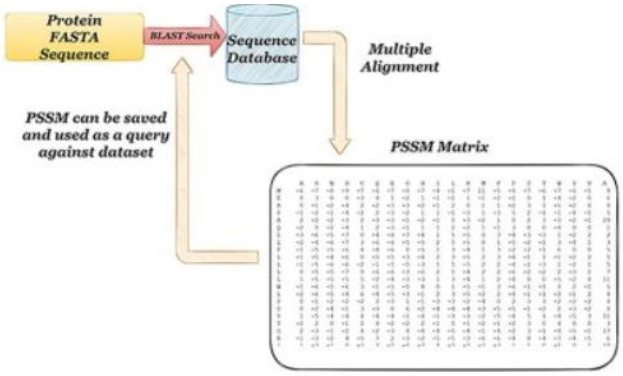

Figure 2. Building a PSSM matrix [44].

2.3. Convolutional Neural Networks (CNN)

The convolutional neural network is a deep learning architecture that is generally used for image processing. CNN uses different processes to capture features in images. Then, using these features, a CNN network classifies the images. A CNN network basically consists of a convolutional layer, a pooling layer, and a fully connected layer. Images are matrices of pixels. The purpose of the convolution layer is to try to capture certain features in the image with a filter smaller than the original image size. The pooling layer aims to reduce dimensionality [46]. In this way, computational complexity is reduced and unnecessary features are eliminated. The fully connected layer transforms the pixel matrix which passes through the convolutional and pooling layers several times into a flat vector. After these processes, images can be classified using traditional neural networks [47]. The general architecture of CNN is given in Figure 3.

2.4. Residual Neural Networks (RNN)

Resnet is an enhanced version of CNNs [49]. When deep networks begin to converge, the problem of degradation arises [50]. Resnet was developed to

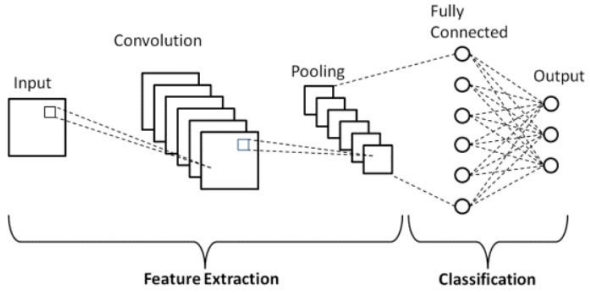

Figure 3. General architecture of CNN [48].

solve this degradation problem of CNN. In Resnet, there are shortcuts between layers. Resnet includes residual blocks to reduce training errors. The scheme of residual blocks are given in Figure 4. These shortcut links allow one or more layers to be skipped. Thus, now blocks and inputs can propagate faster over the remaining connections between layers. In this way, the degradation problem is prevented as the network deepens [49]. Resnet also uses bottleneck blocks to make training faster. The general network architecture of Resnet is given in Figure 5.

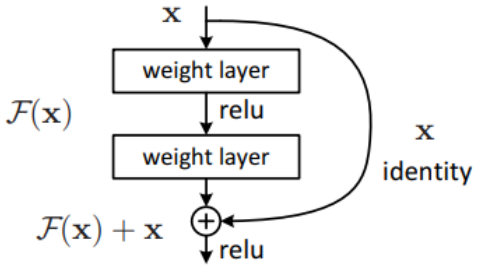

Figure 4. Residual blocks of Resnet [48].

Resnet50 [49] is a pre-trained 50-layer network. The authors in [49] trained the network with the ImageNet dataset. ImageNet [51] is a reference dataset created for use in object recognition research. Thus, researchers working on object recognition can perform transfer learning by applying fine-tuning on previously learned parameters according to their own datasets. In this study, we used the Resnet50 architecture for the protein interaction network prediction problems. We converted the protein sequences to PSSM images and trained the network with this images. Since protein interaction network detection is not an object recognition problem, we did not use pre-trained parameters.

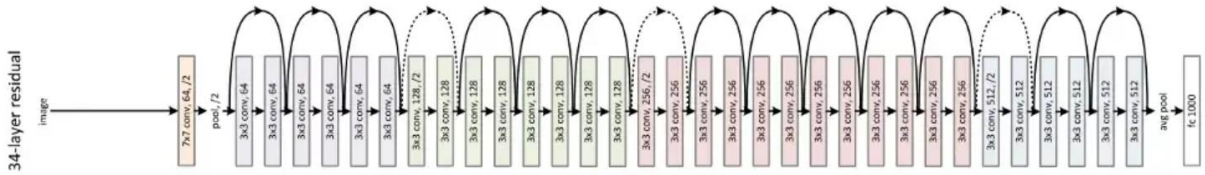

Figure 5. General architecture of Resnet [49].

2.5. Siamese Neural Networks (SNN)

The siamese network does similarity learning using two identical network architectures. Two entries are given to the network. Siamese network contains two separate neural networks. Subnets share parameters. These shared parameters allow to distinguish between two entries that are the same or different. The first subnet encodes the first input, and the second subnet encodes the second input. The Siamese network decides that these inputs belong to the same or different things, based on the difference between the two encoding outputs [52]. The general architecture of the Siamese network is given in Figure 6.

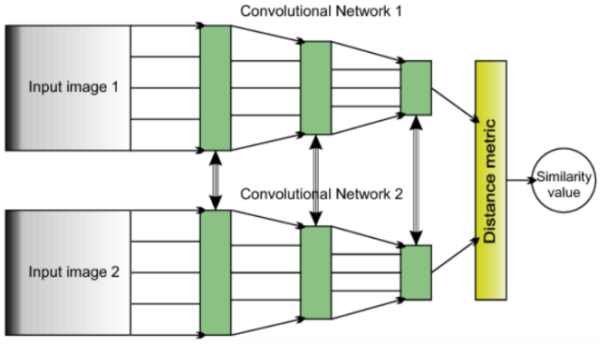

Figure 6. General architecture of SNN [53].

SNNs are powerful networks, especially for learning complex relationships between two images [54]. We trained SNN with interacting and non-interacting protein pairs. For interacting protein pairs, the first input is the PSSM image of positive protein and the second is the PSSM image of SARS-CoV-2 protein. For non-interacting protein pairs, the first input is the PSSM image of negative protein and the second is the PSSM image of SARS-CoV-2 protein. Convolutional layers learn the filters and are responsible for finding common patterns between proteins. Because the two subnets share parameters, the network is expected to find similar properties for interacting proteins. SNN takes a pair of images as input and gives the probability of similarity of these two images as output. In our problem, the image pairs supplied to the network are PSSM images of SARS-CoV-2 and human proteins with and without interaction. The output of the network is the probability whether a pair of PSSM images given to it are interactive. According to the similarity value, it is important to determine the threshold value correctly in order to decide whether the proteins are interacting or not. According to the results obtained from the positive and negative samples during the training phase, it was decided experimentally that the value of 0.5 was an appropriate threshold value (Eq. 1).

$$x_i = \begin{cases} non-interacting, if\ similarity < 0.5 \\ interacting, if\ similarity \geq 0.5 \end{cases} \quad (1)$$

2.6. General Framework of the Proposed Method

In this study, it was investigated whether the use of PSSM matrices as images is suitable for the protein-protein interaction problem. The general framework for converting PSSM matrices to images is given in Figure 7. Protein sequences of human and SARS-CoV-2 proteins were obtained from Uniprot database. Uniprot [40] is a public and universal database. It contains detailed information about proteins such as protein sequences and functions. PSSM matrices were obtained using the Blosum62 substitution matrix. The size of the PSSM matrix is 20xL. 20 indicates the unique amino acid number and L indicates the length of the protein. All matrices were converted to grayscale images of different sizes (20x20, 50x50, 100x100, 200x200, 400x400). The prediction phase was applied separately for each image scale.

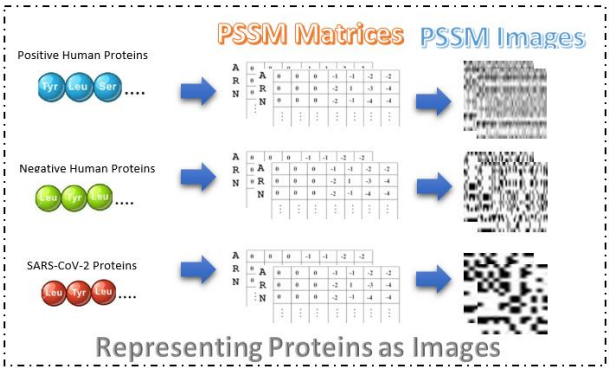

Figure 7. Encoding proteins as Images.

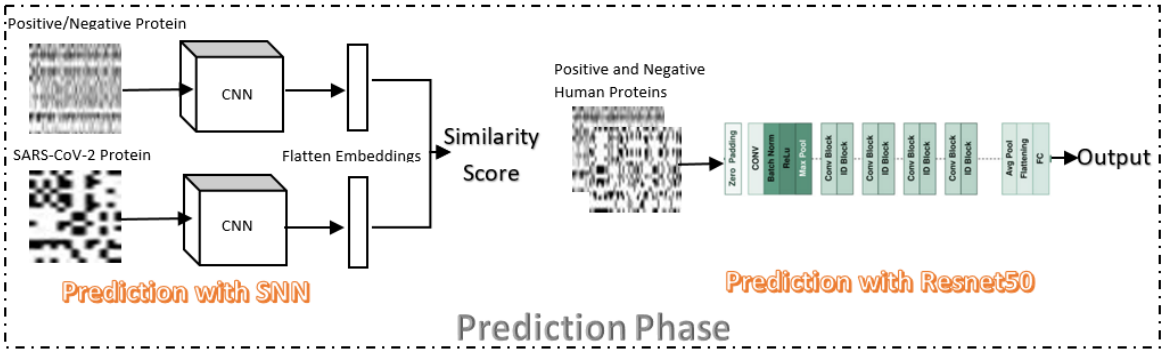

Figure 8. Framework of interaction prediction process.

Table 2. Parameters of networks

Network	#Layers	Batch size	Epochs	Act. func.	Loss func.
SNN	2 2D conv layers, a flatten layer, a dense layer.	16	20	Relu	Contrasive loss
Resnet50	48 conv layers, a max pool layer, an average pool layer.	32	20	Relu	Binary-crossentropy

The prediction phase of the proposed method is given in Figure 8. In the prediction phase, two image classification algorithms were applied and the results were compared. The dataset is divided into train and test sets as 70% and 30% respectively. An SNN network is trained with pairs of images that are related and unrelated to each other. This trained model predicts whether a new pair of images to be given are related to each other. In our problem, "associated" means that a virus and host protein pair are interacting. Therefore, in the training phase, we gave the PSSM images of interacting and non-interacting protein pairs to the SNN. There are 332 interacting protein pairs and 332 non-interacting protein pairs in the dataset. After the network was trained, the SNN learned the common features between these interacting protein pairs. Also, the network learned common features between non-interacting protein pairs. The architecture of Resnet50 is different from SNN. Resnet50 was trained with PSSM images of positive and negative proteins. In the dataset, there are 332 positive proteins and 332 negative proteins. After the network was trained, Resnet50 learned the features of positive and negative proteins.

SNN algorithm was applied as suggested in Chicco [42] using Python environment and Keras library. Resnet50 was implemented using the Matlab environment and Deep Learning Toolbox. Parameters of networks are given in Table 2.

2.7. Evaluation Metrics

To decide whether PSSM matrices are suitable data for detecting interacting proteins, we compared the performances of the algorithms and the performances of PSSM matrices of different sizes according to accuracy, positive predictive value (PPV), negative predictive value (NPV), sensitivity, and F-measure scores. All of these metrics are used to evaluate the classification performance of an algorithm and calculated from the confusion matrix [55]. Confusion matrix diagram is given in Table 3. Accuracy [56] is the ratio of the number of correctly predicted interacting and non-interacting proteins to the total number of samples. Accuracy is a metric that is widely used to measure the success of a model but does not appear to be sufficient on its own. PPV [57], also known as precision, shows how many of the proteins that the model predicts as interacting are actually interacting. NPV [57] shows how many of the proteins that the model predicts as non-interacting are actually non-interacting. Sensitivity [57], also known as recall, measures how many of the proteins known to interact are correctly predicted. F-Measure [58] is calculated by taking the harmonic average of precision and recall values. It is especially important for unevenly distributed datasets. Because it measures not only the error costs of false negatives or false positives but all error costs as well. The mathematical expressions of all these metrics are given in equations 2-6. In the equations, TP, FP, TN, and FN represent true positives, false positives, true negatives, and false negatives, respectively.

Table 3. Confusion matrix

		Prediction Results	
Actual Results		Positive (PP)	Negative (NP)
	Positive (P)	True Positive (TP)	False Negative (FN)
	Negative (N)	False Positive (FP)	True Negative (TN)

$$Accuracy = \frac{TP+TN}{TP+TN+FP+FN} \quad (2)$$

$$PPV/Precision = \frac{TP}{TP+FP} \quad (3)$$

$$NPV = \frac{TN}{TN+FN} \quad (4)$$

$$Sensitivity/Recall = \frac{TP}{TP+FN} \quad (5)$$

$$F - Measure = \frac{2*Precision*Recall}{Precision+Recall} \quad (6)$$

3. Results and Discussion

We investigated whether we could predict the protein-protein interaction network for SARS-CoV-2 from PSSM matrices, which are considered as images within the scope of the study. For this purpose PSSM matrices were converted to grayscale images to train the networks. To decide, which size is appropriate, conversion was done in different sizes. We converted PSSM matrices of positive, negative, and SARS-CoV-2 proteins into 20x20, 50x50, 100x100, 200x200, and 400x400 images, separately. It is clear that big-size images can contain more features but at the same time, big-size images require more computation time.

To compare the performances of binary and multi-class classification approaches, a model for both approaches was applied. The interaction data were labeled as binary classes (positive proteins labeled as 1 and negative proteins labeled as 0) and trained with Resnet50. The output of the network is information whether the relevant human protein interacts with any SARS-CoV-2 protein. SNN behaves like a multi-class classifier by its nature. Because the network receives a pair of images. In our problem, given to the network is PSSM images of SARS-CoV-2 and human proteins. The network output returns information about whether these 2 proteins interacted with each other. This output also acts as a multi-class classifier, as it can tell which SARS-CoV-2 protein interacts with the relevant human protein. In other words, since the inputs given in SNNs determine the classes, there is no need to define multiple classes. In our solution, one of them is a specific protein of a virus and the other one is a host protein. If the output of the network is close to 1, it means that these two proteins are interacting and it also tells which protein of the virus is in interacting.
The data set was randomly divided into train and test sets. The test set ratio was determined as 30%. It was ensured that there were equal numbers of positive and negative samples in the test set. As seen in Table 1, the number of human proteins with which SARS-CoV-2 proteins interact in the data set varies. To avoid the results from being specific to a particular training-test set, we repeated the dividing train-test sets process 5 times and took into account the average results. In order to determine whether the PSSM matrices, which are considered as images, are suitable for detecting interacting protein pairs, image classification was performed with SNN and Resnet50 and their performances were compared. In addition, the performances of different-sized images were also compared to decide on the appropriate image size.

The Table 4 includes a comparison of the average accuracy, PPV, and NPV results of the test phase according to learners and size of PSSM images. Standard deviation values are also given in the Table 4 to examine how the results vary according to different test sets. According to the results, both algorithms can detect virus-host protein interactions with PSSM matrices for SARS-CoV-2. While SNN got the best accuracy results with 200x200 PSSM images, Resnet50 got the best results with 400x400 PSSM images. Although promising results are obtained with PSSM images smaller than 200x200, it can be seen from the results that images of 200x200 and 400x400 sizes contain more distinctive features. PPV is an important metric because it contains information about how many of the proteins that the algorithm finds interactive are actually interactive. NPV on the other hand gives the accuracy rate of proteins labeled as non-interacting. Studies for protein-protein interaction network detection focus on finding interacted proteins rather than non-interacting proteins. One of the advantages of an in silico analysis is to reduce candidate solutions that need to be validated by in vitro or in vivo analyses. For all these reasons, a high PPV value is preferred. SNN achieved better results for big images (200x200 and 400x400) however Resnet50 achieved better results for small images. The standard deviation values calculated according to the results of the test set are generally low. This shows that the algorithms do not obtain very different results compared to the different test sets,

Table 4. Average results for test process

Image Size	SNN			Resnet50		
	Acc	PPV	NPV	Acc	PPV	NPV
20x20	0.805±0.097	0.821±0.122	0.802±0.11	0.844±0.02	0.866±0.044	0.834±0.055
50x50	0.885±0.093	0.867±0.103	0.907±0.08	0.877±0.054	0.874±0.05	0.909±0.112
100x100	0.891±0.054	0.892±0.083	0.896±0.042	0.910±0.024	**0.896±0.026**	0.933±0.069
200x200	**0.915±0.084**	0.893±0.112	**0.957±0.055**	0.840±0.136	0.879±0.111	0.895±0.183
400x400	0.903±0.059	**0.937±0.075**	0.888±0.087	**0.922±0.02**	**0.896±0.024**	**0.960±0.063**

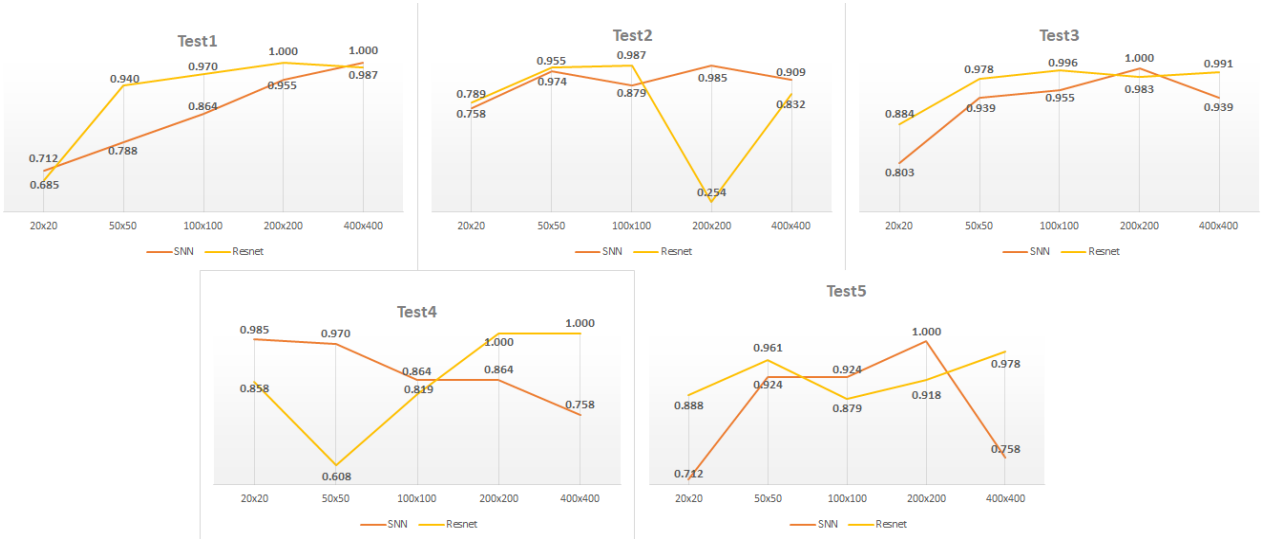

Figure 9. Sensitivity charts according to different test sets

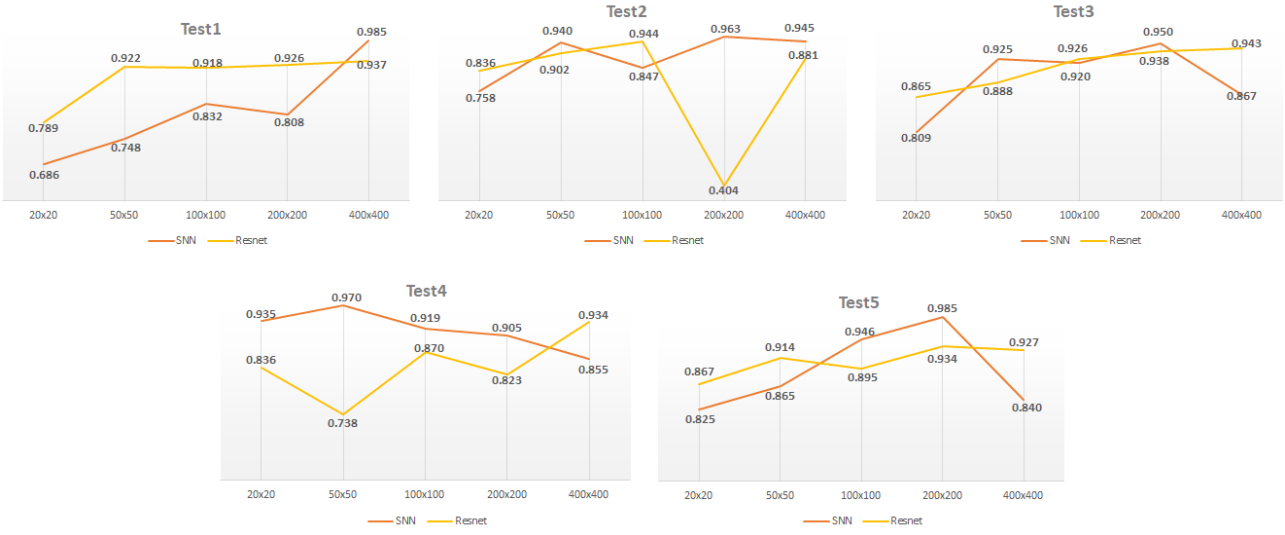

Figure 10. F-Measure charts according to different test sets

that is, the results obtained are not dependent on a specific test set.

The sensitivity and F-measure results obtained from the test sets are given in Figure 9 and Figure 10 respectively. In the charts, the metrics are compared according to the results from each test set. It has been observed that increasing the size does not always increase success for the same PSSM images in a test set. In some test sets like Test 1 and Test 3, the sensitivity value is 1 and the F-Measure value is very close to 1 for 200x200 and 400x400 image sizes. The dataset contains many human proteins that have been confirmed to interact for one SARS-CoV-2 protein, while there are very few human proteins for some SARS-CoV-2 proteins. Because test sets were generated with randomly selected samples, interactions for some SARS-CoV-2 proteins are represented adequately and for others are underrepresented. This situation caused the algorithms not to learn some interaction features well. It is also seen that the algorithms can not obtain results to close each other in the same test set and the same PSSM image size. This is an indication that algorithms learn different features from the same dataset. Resnet's results were more affected by the size of the images, while SNN's results were less dependent on data size.

As mentioned earlier, there are very few in silico studies in the literature to predict protein-protein interaction for SARS-CoV-2. In terms of giving an idea, in Table 5, we compared the results of these studies. Lanchantin et al. [26] used transfer learning, Du et al. [27] used multi-layer perceptron and Dey et al. [31] proposed machine learning algorithms. In the datasets used by Lanchantin et al. [26] and Du et al. [27], there are protein interactions for different viruses as well as SARS-CoV-2. Dey et al. [31], on the other hand, predicted protein interaction network with the dataset used in this study. The machine learning algorithms were trained with sequence-based features extracted from SARS-CoV-2 and human proteins in the dataset. Lee [34] performed a virus type-independent PPI estimation method. They extracted features based on text mining and network similarity from a dataset of interactions of different virus strains with human proteins. They trained the feature dataset with random forest and XGBoost, and performed SARS-CoV-2-human protein interaction prediction with the obtained model. SARS-CoV-2-human interactions were obtained from the IntAct database. The accuracy value of the model developed by the authors for SARS-CoV-2 data was given as 57%. Bell et al. [35] predicted the SARS-CoV-2-human protein interaction network with their pipeline named PEPPI. Estimates were made for 128 interactions obtained from the PSICQUIC27 database. These interactions are between SARS-CoV and/or SARS-CoV-2 and human proteins. The proposed method correctly predicted 94 out of 128 interactions. It can be seen from the results that more successful predictions were obtained with the proposed method.

Table 5. Comparison with recent studies

	F-Measure	Accuracy
Lanchantin et al. [26]	0.114	-
Du et al. [27]	0.867	-
Dey et al. [31]	-	0.723
Lee [34]	-	0.571
Bell et al. [35]		0.734
Proposed Method	**0.880**	**0.922**

The main motivation of this study was the question of whether a model for protein interaction network prediction can be developed with PSSM images. The results obtained show that PSSM images are suitable data for this purpose. The strength of the SNN network is that it can tell which protein of a virus a host protein is interacting with. In other words, the network learns the common features of the virus protein and the host protein with which it interacts. Its high success in predicting positive interactions is another strength of the network. The weakness of the network was its inability to show high performance in learning both negative and positive interactions. As can be seen from Table 4, while it learned only negative interactions well for 200x200 images, it learned positive interactions better for 400x400 images

In cases where experimental data are scarce, a binary classifier developed with a strong network such as Resnet50 can identify whether a host protein interacts with a virus. The weakness of the model developed with Resnet50 is that it cannot tell which virus protein the interaction is with. If the training data can be increased, this deficiency can be eliminated by handling the problem with a multi-class classification approach. However, it will take time to increase the data as the training data are obtained with in-vitro and in-vivo analyzes.

4. Conclusion and Suggestions

The emergence of SARS-CoV-2 virus after SARs-CoV and MERS viruses and causing a pandemic reveals the importance of developing rapid treatment for viral diseases, but it is an indication that similar epidemics may be repeated in the future. In order to understand the behavior of pathogenic viruses that need a host cell to copy their genome, it is necessary to know which protein in the host cell interacts with it. Protein-protein interactions are the main way proteins perform their functions. Therefore, analyzing the protein-protein interactions between the host and pathogenic viruses is useful for understanding the mechanisms of viral infections. In this way, effective antiviral drugs against drug resistance can be designed. Laboratory experiments are needed to definitively identify interacting protein pairs. However, in silico studies can shed light on in vivo analyzes.

Here, an in silico-based prediction of SARS-CoV-2-human protein interaction was performed. Most in silico approaches benefit learning algorithms, and appropriate representations of protein pairs must be obtained in order to make a prediction with learning algorithms. We proposed using PSSM matrices of proteins. The PSSM matrices were converted to grayscale images and SNN and Resnet algorithms were trained with these images. The dataset used for training consists of experimentally confirmed SARS-CoV-2-human protein pairs with which they interact. Because the size of PSSM matrices depends on the length of the protein, different proteins have different sizes of PSSM matrices. A standard scaling was used during the conversion of PSSM matrices to images to obtain images of the same size for all proteins. We converted PSSM matrices into 20x20, 50x50, 100x100, 200x200 and 400x400 size images to decide what size is sufficient to perform a successful protein-protein interaction process. The networks were individually trained with groups of this image size. The randomly selected 30% of the data set was used as the test set. The dataset was divided into train-test sets 5 times with the same procedure. For each training set, models were trained separately and tested with corresponding test set. The average results of the test performances of the models were taken into account in the comparisons. SNN achieved the best average performance with 200x200 PSSM images with an accuracy of 0.915, while Resnet50 achieved the best average performance with 400x400 PSSM images with an accuracy of 0.922. These results showed that protein-protein interaction network prediction can be performed successfully with images obtained from PSSM matrices. The 2 identical subnets contained in the SNN can successfully learn the common properties of interacting and non-interacting human-virus protein pairs. Since PSSM matrices include biological information and some amino acid features, they are used to obtain this information about protein pairs in protein-protein interaction problems. We converted PSSM matrices to images. Obtained results demonstrate that PSSM image approach is useful for predicting interacting protein pairs. It is hoped that the proposed method will provide reference for in vivo studies by applying to protein pairs with unknown interaction status.

Acknowledgment
This work is supported by Turkish Scientific and Technical Research Council-TÜBİTAK with the project number 122E114.

Contributions of the authors
Zeynep Banu Özger: Conceptualization, Writing – original draft, Methodology, Validation, Software, Visualization, Writing – review & editing. Zeynep Çakabay: Validation, Software, Visualization.

Conflict of Interest Statement

The authors declare no conflict of interest

Statement of Research and Publication Ethics
The study is complied with research and publication ethics

References

[1] P. Koehl, "Protein structure similarities". *Current opinion in structural biology*, 11(3), 348-353, 2001. doi: 10.1016/S0959-440X(00)00214-1.

[2] D. P. Ryan, and J. M. Matthews, "Protein–protein interactions in human disease". *Current Opinion in Structural Biology*, 15(4), 441-446, 2005. doi: 10.1016/j.sbi.2005.06.001

[3] V. Altuntaş, and M. Gök, "Protein–protein etkileşimi tespit yöntemleri, veri tabanları ve veri güvenilirliği". *Avrupa Bilim ve Teknoloji Dergisi*, (19), 722-733, 2020. doi: doi.org/10.31590/ejosat.724390.

[4] J. Piehler, "New methodologies for measuring protein interactions in vivo and in vitro". *Current Opinion in Structural Biology*, 15(1), 4-14, 2005. doi: 10.1016/j.sbi.2005.01.008.

[5] S. Xing, N. Wallmeroth, K. W. Berendzen, and C. Grefen, "Techniques for the analysis of protein-protein interactions in vivo". *Plant Physiology*, 171(2), 727-758,2016. doi: 10.1104/pp.16.00470.

[6] S. Vivona, J. L. Gardy, S. Ramachandran, F. S. Brinkman, G. P. S. Raghava, D. R. Flower, and F. Filippini, "Computer-aided biotechnology: from immuno-informatics to reverse vaccinology". *Trends in Biotechnology*, 26(4), 190-200, 2008. doi: 10.1016/j.tibtech.2007.12.006.

[7] S. J. Y. Macalino, S. Basith, N. A. B. Clavio, H. Chang, S. Kang, and S. Choi, "Evolution of in silico strategies for protein-protein interaction drug discovery". *Molecules*, 23(8), 1963, 2018. doi: 10.3390/molecules23081963.

[8] P. Kangueane, and C. Nilofer. "Principles of Protein-Protein Interaction," in *Protein-Protein and Domain-Domain Interactions*. Springer, Singapore, 2018. doi:10.1007/978-981-10-7347-2_8.

[9] B. Parlak, and A. K. Uysal. "On classification of abstracts obtained from medical journals". *Journal of Information Science*, 2020, 46(5), 648-663.

[10] L. Dey, and A. Mukhopadhyay, "A classification-based approach to prediction of dengue virus and human protein-protein interactions using amino acid composition and conjoint triad features," in *2019 IEEE Region 10 Symposium (TENSYMP)*, 2019, June, pp. 373-378, IEEE.

[11] Y. Ma, T. He, Y. Tan, and X. Jiang, "Seq-bel: Sequence-based ensemble learning for predicting virus-human protein-protein interaction". *IEEE/ACM Transactions on Computational Biology and Bioinformatics*, 19(3), 1322-1333,2020. doi: 10.1109/TCBB.2020.3008157.

[12] X. Yang, S. Yang, Q. Li, S. Wuchty, and Z. Zhang, "Prediction of human-virus protein-protein interactions through a sequence embedding-based machine learning method". *Computational and Structural Biotechnology Journal*, Vol.18, pp. 153-161, 2020. doi: 10.1016/j.csbj.2019.12.005

[13] A. Mukhopadhyay, U. Maulik, and S. Bandyopadhyay, "A novel biclustering approach to association rule mining for predicting HIV-1–human protein interactions". *PLoS One*, 7(4), e32289, 2012. doi: 10.1371/journal.pone.0032289.

[14] S. K. Ng, Z. Zhang, and S. H. Tan, "Integrative approach for computationally inferring protein domain interactions". *Bioinformatics*, 19(8), 923-929, 2003. doi: 10.1093/bioinformatics/btg118.

[15] N. Zhang, M. Jiang, T. Huang, and Y. D. Cai, "Identification of Influenza A/H7N9 virus infection-related human genes based on shortest paths in a virus-human protein interaction network". *BioMed Research International*, 2014, 2014. doi: 10.1155/2014/239462.

[16] S. Bandyopadhyay, and K. Mallick, "A new feature vector based on gene ontology terms for protein-protein interaction prediction". *IEEE/ACM Transactions on Computational Biology and Bioinformatics*, 14(4), 762-770, 2016. doi: 10.1109/TCBB.2016.2555304.

[17] H. Ge, Z. Liu, G. M. Church, and M. Vidal, "Correlation between transcriptome and interactome mapping data from Saccharomyces cerevisiae". *Nature Genetics*, 29(4), 482-486, 2001. doi: doi.org/10.1038/ng776.

[18] A. Zhang, L. He, and Y. Wang, "Prediction of GCRV virus-host protein interactome based on structural motif-domain interactions". *BMC Bioinformatics*, 18(1), 1-13, 2017. doi: 10.1186/s12859-017-1500-8.

[19] M. D. Dyer, T. M. Murali, and B. W. Sobral, "Computational prediction of host-pathogen protein–protein interactions". *Bioinformatics*, 23(13), i159-i166, 2007. doi: 10.1016/j.patter.2021.100242.

[20] A. Birlutiu, F. d'Alché-Buc, and T. Heskes, "A bayesian framework for combining protein and network topology information for predicting protein-protein interactions". *IEEE/ACM Transactions on Computational Biology and Bioinformatics*, 12(3), 538-550, 2014. doi: 10.1109/TCBB.2014.2359441.

[21] S. Erten, X. Li, G. Bebek, J. Li, and M. Koyutürk, "Phylogenetic analysis of modularity in protein interaction networks". *BMC Bioinformatics*, 10(1), 1-14, 2009. doi: 10.1186/1471-2105-10-333.

[22] N. Papanikolaou, G. A. Pavlopoulos, T. Theodosiou, and I. Iliopoulos, "Protein–protein interaction predictions using text mining methods". *Methods*, 74, 47-53, 2015. doi: 10.1016/j.ymeth.2014.10.026.

[23] B. Khorsand, A. Savadi, J. Zahiri, and M. Naghibzadeh, "Alpha influenza virus infiltration prediction using virus-human protein-protein interaction network". *Mathematical Biosciences and Engineering*, 17(4), 3109-3129, 2020. doi: 10.3934/mbe.2020176.

[24] P. Zhou, X. L. Yang, X. G. Wang, B. Hu, L. Zhang, W. Zhang, ... and Z. L. Shi, "A pneumonia outbreak associated with a new coronavirus of probable bat origin". *Nature*, 579(7798), 270-273, 2020. doi: 10.1038/s41586-020-2012-7

[25] A. A. Khan, and Z. Khan, "Comparative host–pathogen protein–protein interaction analysis of recent coronavirus outbreaks and important host targets identification". *Briefings in Bioinformatics*, 22(2), 1206-1214, 2021. doi: 10.1093/bib/bbaa207.

[26] J. Lanchantin, A. Sekhon, C. Miller, and Y. Qi, "Transfer learning with motiftrans-formers for predicting protein-protein interactions between a novel virus and humans". B*ioRxiv*, 36, i659-i667, 2020. doi: 10.1101/2020.12.14.422772.

[27] H. Du, F. Chen, H. Liu, and P. Hong, "Network-based virus-host interaction prediction with application to SARS-CoV-2". *Patterns*, 2(5), 100242, 2021. doi: 10.1016/j.patter.2021.100242.

[28] S. Su, G. Wong, W. Shi, J. Liu, A. C. Lai, J. Zhou, ... and G. F. Gao, "Epidemiology, genetic recombination, and pathogenesis of coronaviruses". *Trends in Microbiology*, 24(6), 490-502, 2016. doi: 10.1016/j.tim.2016.03.003.

[29] B. Khorsand, A. Savadi and M. Naghibzadeh, "SARS-CoV-2-human protein-protein interaction network". *Informatics in Medicine Unlocked*, 20, 100413, 2020. doi: 10.1016/j.imu.2020.100413.

[30] R. Oughtred, C. Stark, B. J. Breitkreutz, J. Rust, L. Boucher, C. Chang, ... and M. Tyers, "The BioGRID interaction database: 2019 update". *Nucleic Acids Research*, 47(D1), D529-D541, 2019. doi: 10.1093/nar/gky1079.

[31] L. Dey, S. Chakraborty and A. Mukhopadhyay, "Machine learning techniques for sequence-based prediction of viral–host interactions between SARS-CoV-2 and human proteins". *Biomedical Journal*, 43(5), 438-450, 2020. doi: 10.1016/j.bj.2020.08.003.

[32] D. E. Gordon, G. M. Jang, M. Bouhaddou, J. Xu, K. Obernier, K. M. White ... and N. J. Krogan, "A SARS-CoV-2 protein interaction map reveals targets for drug repurposing". *Nature*, 583(7816), 459-468, 2020. doi: 10.1038/s41586-020-2286-9.

[33] D. Pirolli, B. Righino, and M. C. De Rosa. "Targeting SARS-CoV-2 Spike Protein/ACE2 Protein-Protein Interactions: a Computational Study". *Molecular Informatics*, 2021, 40(6), 2060080.

[34] H. J. Lee. "An interactome landscape of SARS-CoV-2 virus-human protein-protein interactions by protein sequence-based multi-label classifiers". *BioRxiv*, 2021.

[35] E. W. Bell, J. H. Schwartz, P. L. Freddolino, and Y. Zhang. "PEPPI: Whole-proteome protein-protein interaction prediction through structure and sequence similarity, functional association, and machine learning". *Journal of Molecular Biology*, 2022, 167530.

[36] G. Launay, N. Ceres, and J. Martin. "Non-interacting proteins may resemble interacting proteins: prevalence and implications". *Scientific reports*, 2017, 7(1), 1-12.

[37] R. K. Barman, S. Saha, and S. Das. "Prediction of interactions between viral and host proteins using supervised machine learning methods". *PloS One*, 2014, 9(11), e112034.

[38] T. Sun, B. Zhou, L. Lai and J. Pei. "Sequence-based prediction of protein protein interaction using a deep-learning algorithm". *BMC Bioinformatics*, 2017, 18(1), 1-8.

[39] S.R. Eddy. "Where did the BLOSUM62 alignment score matrix come from?" *Nature Biotechnology*, 2004, 22(8), 1035-1036.

[40] UniProt Consortium. "UniProt: a hub for protein information". *Nucleic Acids Research*, 2015, 43(D1), D204-D212.

[41] J. D. Bernal. "Structure of proteins". *Nature*, 1939, 143(3625), 663-667.

[42] J. C. Jeong, X. Lin, and X. W. Chen. "On position-specific scoring matrix for protein function prediction". *IEEE/ACM Transactions on Computational Biology and Bioinformatics*, 2010, 8(2), 308-315.

[43] R.C. Edgar, and S. Batzoglou. "Multiple sequence alignment". *Current Opinion in Structural Biology*, 2006, 16(3), 368-373.

[44] A. Mohammadi, J. Zahiri, S. Mohammadi, M. Khodarahmi, and S. S. Arab, "PSSMCOOL: a comprehensive R package for generating evolutionary-based descriptors of protein sequences from PSSM profiles". *Biology Methods and Protocols*, 7(1), bpac008, 2022. doi: 10.1093/biomethods/bpac008

[45] N. Xiao, D. S. Cao, M. F. Zhu, and Q. S. Xu, "protr/ProtrWeb: R package and web server for generating various numerical representation schemes of protein sequences". *Bioinformatics*, 31(11), 1857-1859, 2015.

[46] S. Albawi, T. A. Mohammed and S. Al-Zawi. "Understanding of a convolutional neural network", in *2017 International Conference on Engineering and Technology (ICET)*, 2017, pp. 1-6, IEEE.

[47] J. Wu, "Introduction to convolutional neural networks". *National Key Lab for Novel Software Technology*. Nanjing University. China, 5(23), 495, 2017.

[48] S. Balaji, S. (2020, Aug 29). "Binary Image classifier CNN using TensorFlow", *medium.com*. Aug. 29, 2020. [Online]. Available: https://medium.com/techiepedia/binary-image-classifier-cnn-using-tensorflow-a3f5d6746697. [Accessed: 15/11/2022].

[49] K. He, X. Zhang, S. Ren and J. Sun, "Deep residual learning for image recognition", in *Proceedings of the IEEE Conference on Computer Vision and Pattern Recognition*, 2016, IEEE, pp. 770-778.

[50] P. Roy, S. Ghosh, S. Bhattacharya and U. Pal. "Effects of degradations on deep neural network architectures". A*rXiv*, abs/1807.10108, 2018

[51] J. Deng, W. Dong, R. Socher, L. J. Li, K. Li, and L. Fei-Fei. "Imagenet: A large-scale hierarchical image database", in *2009 IEEE Conference on Computer Vision and Pattern Recognition*, June, 2009, pp. 248-255, IEEE.

[52] D. Chicco, "Siamese Neural Networks: An Overview", in: *Cartwright, H. (eds) Artificial Neural Networks. Methods in Molecular Biology*, vol 2190. Humana, New York, NY, 2021. doi:10.1007/978-1-0716-0826-5_3.

[53] L. Hudec, and W. Bencsova, "Texture similarity evaluation via siamese convolutional neural network", in *2018 25th International Conference on Systems, Signals and Image Processing (IWSSIP)*, June, 2018, pp. 1-5, IEEE.

[54] M. D. Li, K. Chang, B. Bearce, C. Y. Chang, A. J. Huang, J. P. Campbell, ... and J. Kalpathy-Cramer. "Siamese neural networks for continuous disease severity evaluation and change detection in medical imaging". *NPJ Digital Medicine*, 2020, 3(1), 1-9.

[55] J. Liang. "Confusion matrix". *POGIL Activity Clearinghouse*, 2022, 3(4).

[56] S. V. Stehman. "Selecting and interpreting measures of thematic classification accuracy". *Remote sensing of Environment*, 1997, 62(1), 77-89.

[57] H. B. Wong and G. H. Lim. "Measures of diagnostic accuracy: sensitivity, specificity, PPV and NPV", in *Proceedings of Singapore Healthcare*, 2011, 20(4), 316-318.

[58] D. M. Powers. "Evaluation: from precision, recall and F-measure to ROC, informedness, markedness and correlation". *ArXiv preprint arXiv:2010.16061*, 2020.

Bitlis Eren Üniversitesi Fen Bilimleri Dergisi
BİTLİS EREN UNIVERSITY JOURNAL OF SCIENCE
ISSN: 2147-3129/e-ISSN: 2147-3188
VOLUME: 12 NO: 1 PAGE: 180-191 YEAR: 2023
DOI:10.17798/bitlisfen.1220772

Computational Thermal Analysis of Divergent and Convergent Flow Channels for Cooling Plates in PEM Fuel Cells

Mahmut Caner ACAR[1*]

[1] *Nigde Omer Halisdemir University, Engineering Faculty, Mechanical Engineering Department, Nigde, Türkiye*

(ORCID:0000-0002-6206-5374)

Keywords: CFD, Fluid flow, Heat transfer, Cooling, PEM fuel cell.

Abstract

During the operation of polymer electrolyte membrane fuel cells excess heat is generated as a result of electrochemical reactions. This heat raises the temperature of the polymer electrolyte membrane fuel cells, which can damage the membrane. Homogeneity of the temperature through the fuel cell is important in terms of stability and performance. Thermal management is therefore essential and is provided by the cooling channels formed on the bipolar plates or cooling plates. In this paper, a three-dimensional computational analysis of the cooling plate with divergent and convergent flow field designs is carried out. In this context, heat transfer and fluid flow performances of these two different flow fields are considered in terms of temperature uniformity, maximum temperature and pressure drop. Numerical results demonstrated that the more uniform temperature distribution along the fuel cell could be achieved with divergent flow field design. Furthermore, when a divergent design is used, the maximum surface temperature of the cooling plate and the pressure drop between the inlet and outlet of the channel are reduced.

1. Introduction

Due to the depletion of fossil fuels caused by its over consumption and increased dependence on energy, studies have been focused on new energy sources. In addition, the use of conventional fossil fuels as energy sources causes environmental pollution and climate changes. For those reasons, attentions on new energy sources have been increased. Hydrogen is seen as one of most popular environmentally friendly energy sources, especially when used in fuel cell applications. Among the fuel cell types, the PEM fuel cells have superior advantages such as higher power density, lower operating temperature, silent operation and rapid start up [1], [2]. Thus, these fuel cells can be preferred in many fields such as automobile industries, military applications and stationary power systems [3].

The schematic of a PEM fuel cell components and its cooling channel are shown in Figure 1. The hydrogen and air/oxygen enter the cell from anode and cathode sides, respectively. While the hydrogen oxidation reactions take place in anode side, Equation (1), oxygen reduction reactions take place in the cathode side, Equation (2). Only water and heat are produced as by product during these electrochemical reactions, Equation (3).

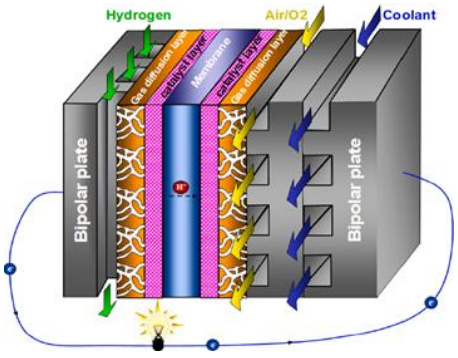

Figure 1. PEM fuel cell components and cooling channel [4].

*Corresponding author: mahmutcaneracar@ohu.edu.tr
Received: 18.12.2022, Accepted: 03.03.2023

Anode reaction: $H_2 \rightarrow 2H^+ + 2e^-$ (1)

Cathode reaction: $\frac{1}{2}O_2 + 2H^+ + 2e^- \rightarrow H_2O$ (2)

Total reaction: $H_2 + \frac{1}{2}O_2 \rightarrow H_2O$ (3)

In addition to water, heat is also generated as a result of electrochemical reactions. This excess heat causes the cell temperature to rise excessively over time and damages the membrane. Therefore, it needs to be removed from the cell by a proper cooling method. Usually, the cooling plates are made of either graphite or metallic materials. The most commonly used metallic materials are stainless steel, aluminum, titanium and its alloys [5]–[8]. The flow channels are machined when graphite is used as cooling plate. However, in addition to machining, stamping, hydroforming or roll forming methods are also utilized in the case of metallic plates [9]–[12]. The cooling fluids are circulated through the flow fields formed on cooling plates. There are many types of flow field designs considered in the literature [2], [13]–[15]. The most practical designs are serpentine, parallel and parallel-serpentine [16]. Using different flow field designs has some advantages and disadvantages. For example, some of them are superior in terms of heat removal performance, however, they may lead to higher pressure drops, resulting in higher pumping power [17], [18]. Thus, both the thermal and hydraulic performances of the cooling plates should be evaluated together.

Many flow channel types, including both conventional parallel, serpentine, parallel-serpentine and some other special designs, have been studied by researchers in the literature [19]–[23]. The effects of different flow field designs on thermal performance for a graphite cooling plate with an area of 18×18 cm^2 were computationally investigated by Baek et al. [17]. In this context, two conventional serpentine designs (Model A and Model B), two multi pass serpentine designs (Model C and Model D), one parallel design (Model E) and one spiral design (Model F) were considered. According to their results, the Model C and Model D showed better thermal performance than the Model A and Model B. The Model E exhibited the smallest pressure drop, while the worst temperature distribution was obtained with this design. Ravishankar et al. [24] performed a detailed numerical analysis on flow field types for one conventional serpentine and one conventional spiral design and four novel designs, including distributed serpentine, divided serpentine, distributed spiral and divided spiral. The cooling plate was made of aluminum. The highest and lowest pressure drop values were obtained with divided spiral (many turn regions) and conventional serpentine designs, respectively. The distributed serpentine design presented the best temperature uniformity with 25% progress over the serpentine type. Rahgoshay et al. [25] simulated a PEM fuel cell with two traditional serpentine parallel flow field designs. They also compared the results obtained from the cooling plates with an isothermal model (constant temperature). The results showed that the value of maximum temperature was almost the same for serpentine and parallel design. However, about 24% improvement was observed in temperature uniformity when serpentine design was considered as flow field. They also indicated that the cooling flow fields should be considered during the numerical analysis of a PEM fuel cell to obtain more accurate temperature distribution inside the fuel cell. In another study, Ghasemi et al. [26] conducted a simulation study for a PEM fuel cell with conventional serpentine type reactant flow field. The simulations were carried out for six different cooling channel designs: one traditional parallel, one traditional serpentine, one traditional spiral, and three different novel designs. Even if a largest pressure drop was obtained with traditional spiral flow field design, the lowest temperature difference of 3.38 K and lowest temperature uniformity index (U_T) of 0.58 K were also achieved with this channel type.

According to the open literature, there are many studies on flow field design of cooling plates in PEM fuel cells. Mostly, spiral, serpentine, parallel and parallel-serpentine flow fields were evaluated in those researches. In this paper, unconventional divergent and convergent flow field designs are investigated. For this purpose, a cooling plate made of graphite with a 10×10 cm^2 area is used in the computational fluid dynamic (CFD) analysis. The CFD studies were carried out with Ansys-Fluent commercial program. The heat removal and fluid flow performances of divergent and convergent flow fields were compared in terms of temperature uniformity, maximum temperature and fluid pressure drop.

2. Material and Method

In order to build a fuel cell stack and produce the required output power, many fuel cell units are typically serially connected. A coolant circulates through the channels of cooling plates and absorbs the heat produced to prevent the fuel cell from overheating. Figure 2a shows the geometry of cooling plates with the divergent and convergent flow fields used in this study. The cooling plate thickness

is 2 mm and it has 32 flow channels for both designs. The dimension of the channel is seen in Figure 2b. The channel width increases and decreases with an angle of 0.57 degrees from inlet to outlet for divergent and convergent flow fields, respectively. The divergent flow field design has an inlet width of 1 mm and an outlet width of 2 mm. In the case of convergent design, the inlet width is 2 mm, and the outlet width is 1 mm. The channel deep for both flow fields is 1 mm.

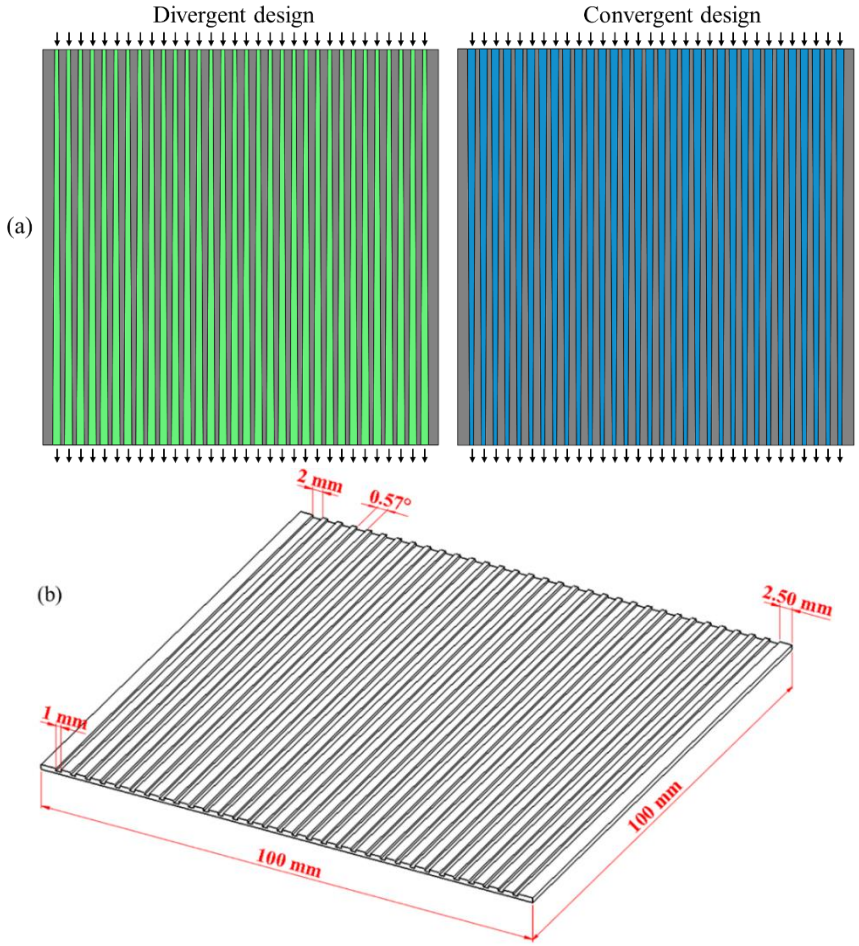

Figure 2. (a) Divergent and convergent flow fields, (b) dimension of the channel.

2.2. Governing equations

A comprehensive simulation of fluid flow and heat transfer within the cooling plates was performed using the commercial CFD program Ansys-Fluent. The finite volume discretization technique is used in this software to solve the mass conservation, momentum and energy equations. The governing equations for the Newtonian, laminar, steady state and incompressible fluid flow across the cooling plate are as follows:

$$\frac{\partial u_j}{\partial x_j} = 0 \tag{4}$$

$$\boldsymbol{\rho}\left(\boldsymbol{u_j}\frac{\boldsymbol{\partial u_i}}{\boldsymbol{\partial x_j}}\right) = \frac{\boldsymbol{\partial p}}{\boldsymbol{\partial x_i}} + \frac{\boldsymbol{\partial}}{\boldsymbol{\partial x_j}}\left(\boldsymbol{\mu}\frac{\boldsymbol{\partial u_i}}{\boldsymbol{\partial x_j}}\right) \tag{5}$$

$$\boldsymbol{\rho c_p}\left(\boldsymbol{u_j}\frac{\boldsymbol{\partial T}}{\boldsymbol{\partial x_j}}\right) = \frac{\boldsymbol{\partial}}{\boldsymbol{\partial x_j}}\left(\boldsymbol{k}\frac{\boldsymbol{\partial T}}{\boldsymbol{\partial x_j}}\right) \tag{6}$$

where $\boldsymbol{u}$ is the velocity, $\boldsymbol{p}$ is the pressure and $\boldsymbol{T}$ is the temperature. In addition, $\boldsymbol{k}, \boldsymbol{\rho}, \boldsymbol{c_p}$ and $\boldsymbol{\mu}$ are the thermal conductivity, density, specific heat capacity and dynamic viscosity, respectively.

The energy equation for the solid regions is described with Equation (7).

$$\frac{\boldsymbol{\partial}}{\boldsymbol{\partial x_j}}\left(\boldsymbol{k}\frac{\boldsymbol{\partial T}}{\boldsymbol{\partial x_j}}\right) = \mathbf{0} \tag{7}$$

2.3. Operating and boundary conditions

In the simulation process, water is selected as coolant and graphite is used as cooling plate

material. Table 1 shows the thermo-physical properties of graphite. Since the thermo-physical properties of water vary with temperature, the polynomial functions represented by Eqs. (8)-(10) were applied to the program [27]. However, because the change in C_p at the temperatures considered was so small (less than 1%), this property was kept constant during the simulations at 4179 J/kg K. The coolant enters the channel at a constant temperature of 40 ˚C. Four different mass flow rates (ṁ) of 8.0×10^{-4} kg/s, 1.6×10^{-3} kg/s, 2.4×10^{-3} kg/s and 3.2×10^{-3} kg/s are considered during the numerical analysis. The value used for the surface heat flux (q″) is 5000 W/m^2 which is typical for PEMFCs under normal operating conditions [17]. Also, Equation (11) can be used to determine the generated heat flux for each cell during the PEM fuel cell operation. The operating parameters for the simulation are seen in Table 1.

$$\mu = 0.258\times10^{-10}T^4 - 0.358\times10^{-7}T^3 + 0.186\times10^{-4}T^2 - 0.432\times10^{-2}T + 0.378 \quad (8)$$

$$k = 0.754\times10^{-9}T^4 - 0.988\times10^{-6}T^3 + 0.474\times10^{-3}T^2 - 0.974\times10^{-1}T + 7.745 \quad (9)$$

$$\rho = -0.180\times10^{-6}T^4 + 0.248\times10^{-3}T^3 - 0.131T^2 + 30.824T - 1690.497 \quad (10)$$

$$\boldsymbol{Q_i} = (\mathbf{1.23} - \boldsymbol{V_i})\boldsymbol{i} \quad (11)$$

where 1.23 is the value of open circuit voltage, $\boldsymbol{V_i}$ is the working voltage of the PEM fuel cell and $\boldsymbol{i}$ is the electrical current density.

Table 1. Thermo-physical properties of graphite and operating conditions.

Parameters	Values	Units
Cooling plate properties		
Density	2250	kg/m^3
Specific heat capacity	690	J/kg K
Thermal conductivity	24	W/m K
Operating conditions		
Coolant inlet temperature	40	˚C
Coolant mass flow rate	8.0×10^{-4}, 1.6×10^{-3}, 2.4×10^{-3} 3.2×10^{-3}	kg/s
Heat flux	5000	W/m^2

Figure 3 depicts the cooling plate's half domain together with symmetry boundary condition, heat flux boundary condition, solid and coolant regions. The heat flux is implemented on the bottom surface of the cooling plate. To reduce the computational time, cooling plate's half domain is considered and therefore, symmetrical boundary condition is applied in the CFD analysis. A constant mass flow rate boundary condition and a constant pressure condition are applied at the channel inlets and outlets, respectively.

2.4. Numerical procedure and model validation

A 3D finite volume technique is used to numerically solve the governing equations within the computational domain. The pressure and velocity fields are linked using the well-known Coupled algorithm. The least squares cell-based gradient is considered for the spatial discretization. The second order upwind scheme is used for the momentum and energy equations, whereas the second order method is chosen for pressure. The computations are considered to have converged when the residuals of the continuity, momentum and energy equations fall below 1×10^{-4}, 1×10^{-7} and 1×10^{-9}, respectively.

To prove the accuracy of the numerical results, a grid dependence analysis is also conducted. For this purpose, the outputs of five different grid structures with element numbers of 364,958, 839,020, 1,453,500, 1,986,264 and 2,545,272 are compared with each other. The grid dependence test of the divergent and convergent flow fields based on the coolant outlet temperature is shown in Figure 4a. As can be seen from the

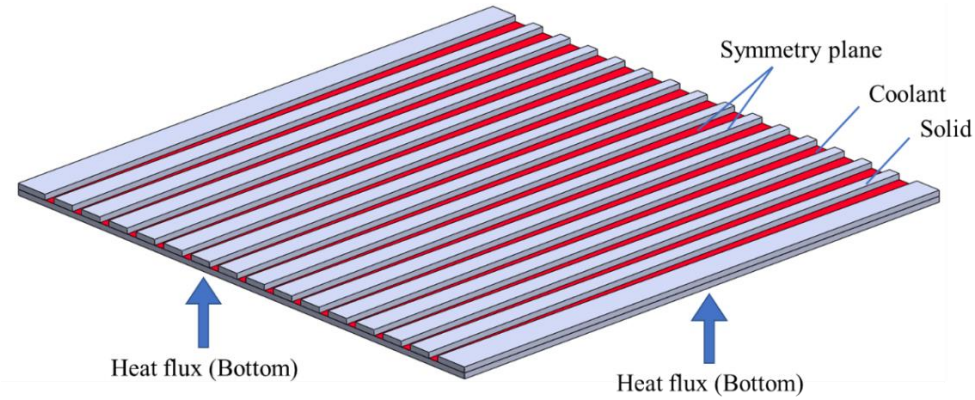

Figure 3. Boundary conditions for the cooling plate half domain.

figure, the variation in outlet temperature is very small after element number of 1,986,264 for both divergent and convergent channels. Similarly, a small change is obtained in pressure drop between the inlet and outlet of the channel when the element number exceeds the same value (Figure 4b). Therefore, a grid structure with 1,986,264 elements is chosen in the simulation analysis.

To verify the numerical results obtained from the CFD analysis, an experimental study done by Raghuraman et al. was considered [28]. For this purpose, simulation results obtained for the coolant temperature at the channel outlet and pressure drop between the inlet and outlet of the channel were compared with the experiment as depicted in Figure 5. Figure 5a shows that the simulation results and experimental data agree well for whole Reynolds number values ranging from 50 to 350, with a maximum deviation of 5.3%. Figure 5b displays that the values of pressure drop computed numerically for the complete Reynolds number are quite close to those measured experimentally.

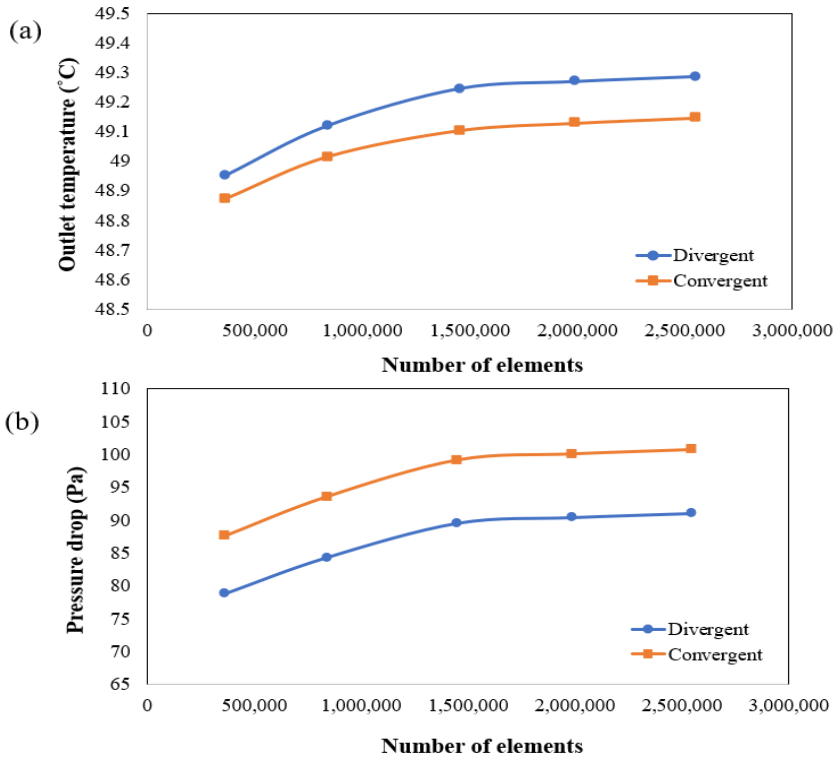

Figure 4. Grid dependence test for (a) coolant outlet temperature, (b) pressure drop.

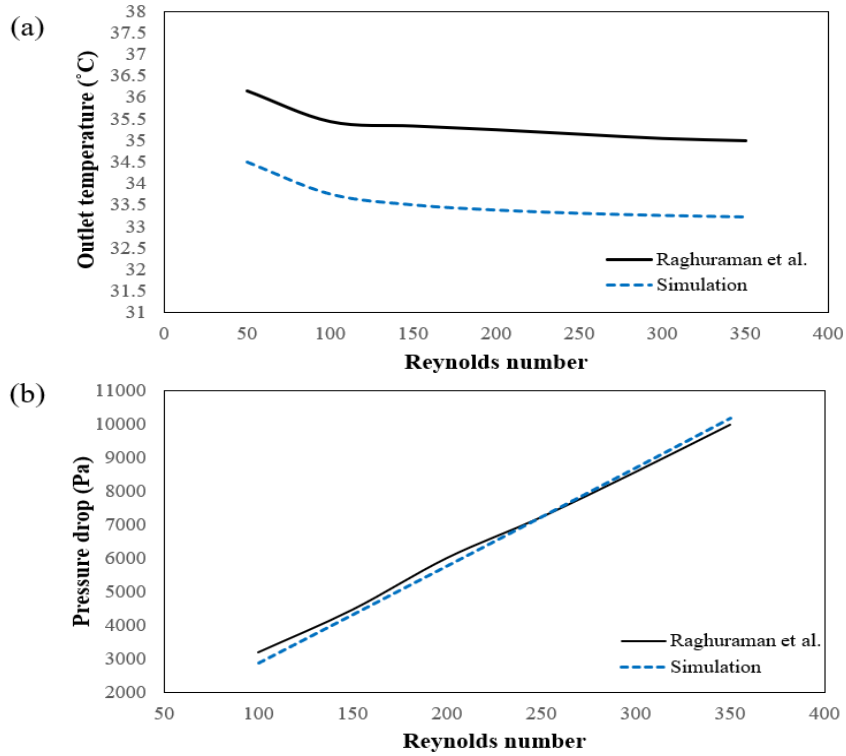

Figure 5. Model validation study for (a) outlet temperature, (b) pressure drop.

3. Results and Discussion

For various mass flow rates of 8.0×10^{-4} kg/s, 1.6×10^{-3} kg/s, 2.4×10^{-3} kg/s and 3.2×10^{-3} kg/s, the thermal and fluid flow performances of the cooling plate with divergent and convergent flow fields are investigated in terms of temperature uniformity, maximum temperature and pressure drop. Throughout the simulation, the coolant inlet temperature and heat flux imposed from the bottom surface of the cooling plate are kept constant at 40 ˚C and 5000 W/m^2, respectively.

It is critical for the stability and performance of the PEM fuel cells to maintain as uniform a temperature as possible. There is a criterion known as the index of uniform temperature (IUT) [29] for analyzing the temperature homogeneity at a surface area. The IUT has been utilized in thermal applications where temperature distribution is essential. The difference between the surface temperature and the average surface temperature at the heat transfer surface can be measured quantitatively using the IUT. In other words, IUT equals zero when the temperature distribution is entirely uniform. The IUT is calculated by the following equation:

$$IUT = \frac{\int_A |T - T_{avg}| dA}{\int_A dA} \quad \text{and} \quad T_{avg} = \frac{\int_A T dA}{\int_A dA} \tag{12}$$

where T is the surface temperature, T_{avg} is the average surface temperature and A is the surface area. Equation (12) is only applicable on the heat flux boundary conditions [30].

Table 2 shows the simulation results of maximum and minimum surface temperatures (T_{max} and T_{min}), temperature difference (ΔT) between T_{max} and T_{min}, IUT and pressure drop (ΔP) at an inlet temperature (T_{in}) of 40 ˚C, a heat flux of 5000 W/m^2 and a mass flow rate of 1.6×10^{-3} kg/s. T_{max} and ΔT are lower in the divergent channels by 0.35 ˚C and 0.63 ˚C, respectively. In addition, smaller IUT is obtained for divergent flow fields, which can be considered as an improvement in temperature distribution along the heat flux surface. As a result, using a divergent channel instead of a convergent one improves temperature uniformity by 11.77%. The divergent channel also reduces the pressure drop by 7.93%, indicating that less pumping power is required. The % Improvement is determined by Equation (13) as follows:

Table 2. Simulation results for divergent and convergent flow fields.

Parameters	Divergent channel	Convergent channel	% Improvement
T_{max} (˚C)	53.89	54.24	-
T_{min} (˚C)	41.54	41.27	-
ΔT (˚C)	12.34	12.97	-
IUT (˚C)	2.02	2.29	11.79
ΔP (Pa)	83.01	90.17	7.94

$$\%Improvement = \frac{|x_c - x_d|}{x_c} \times 100 \quad (13)$$

where x_c and x_d are the calculated values obtained from convergent and divergent flow field designs, respectively.

For convergent and divergent flow fields, the distribution of temperature at the bottom surface of cooling plate is seen in Figure 6. Here, mass flow rate, coolant inlet temperature and heat flux are 1.6×10^{-3} kg/s, 40 ˚C and 5000 W/m^2, respectively. The coolant temperature rises from the inlet to the outlet of the channels due to the continuous absorption of reaction heat by the coolant. Highest surface temperature of 54.3 ˚C and 53.9 ˚C are obtained in case of convergent and divergent flow fields, respectively. Furthermore, when a convergent channel is used, higher temperature zones are observed at the end corner regions. Figure 7 represents the change in temperature distribution at the cooling plate's symmetry plane under the same operating conditions as in Figure 6. Similarly, while temperatures are lower near the inlet region, they are higher closer to the channel outlet. In the case of convergent channel design, the highest temperature is obtained.

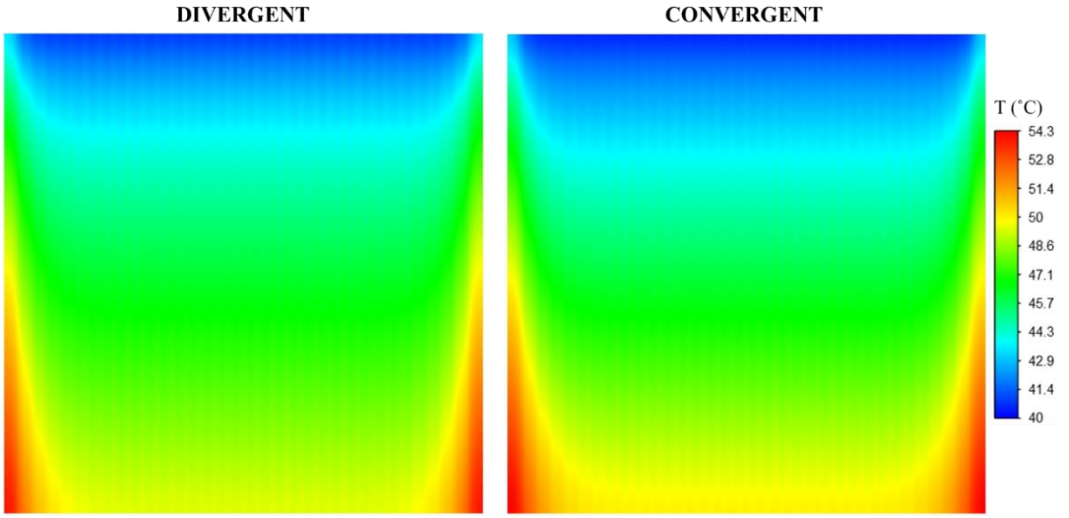

Figure 6. Distribution of temperature at the bottom surface.

Figure 8 depicts the pressure drop distribution between the inlet and outlet of the cooling channels with an inlet coolant temperature of 40 ˚C, a mass flow rate of 1.6×10^{-3} kg/s, and a heat flux of 5000 W/m^2. As illustrated in the figure, the pressure drops along the coolant channels are greater in the convergent design, indicating higher pumping power.

Figure 9 shows the changes in IUT as a function of coolant mass flow rate at a constant inlet temperature and heat flux. Because increasing mass flow rate causes a decrease in cooling plate surface temperature, the IUT declines with coolant flow rate. Lower IUT values are observed for divergent flow design at all coolant flow rates. At high mass flow rates, the %Improvement takes greater values. Since the lowest IUTs are obtained in the case of divergent channels, it can be said that a more uniform temperature distribution can be achieved with this design.

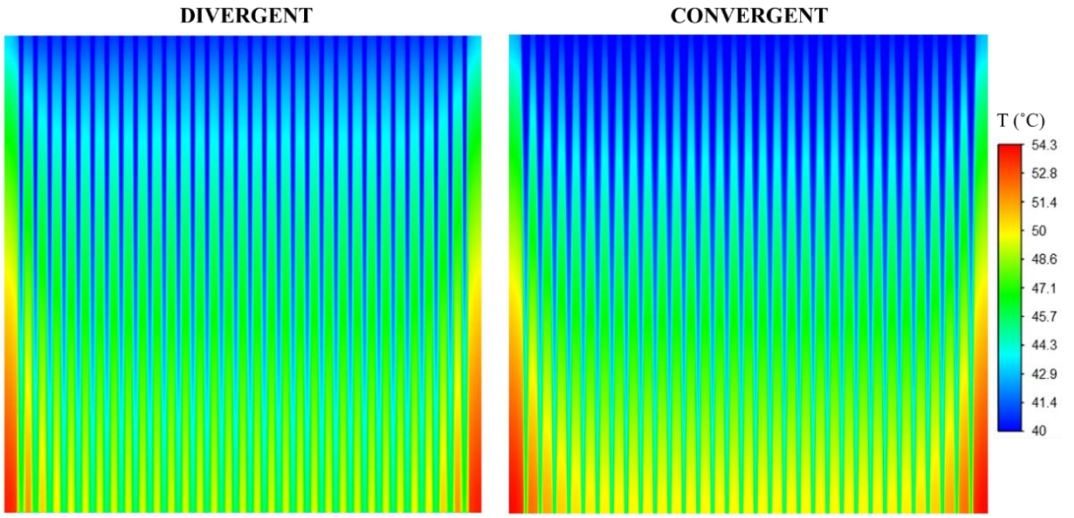

Figure 7. Distribution of temperature at the symmetry surface.

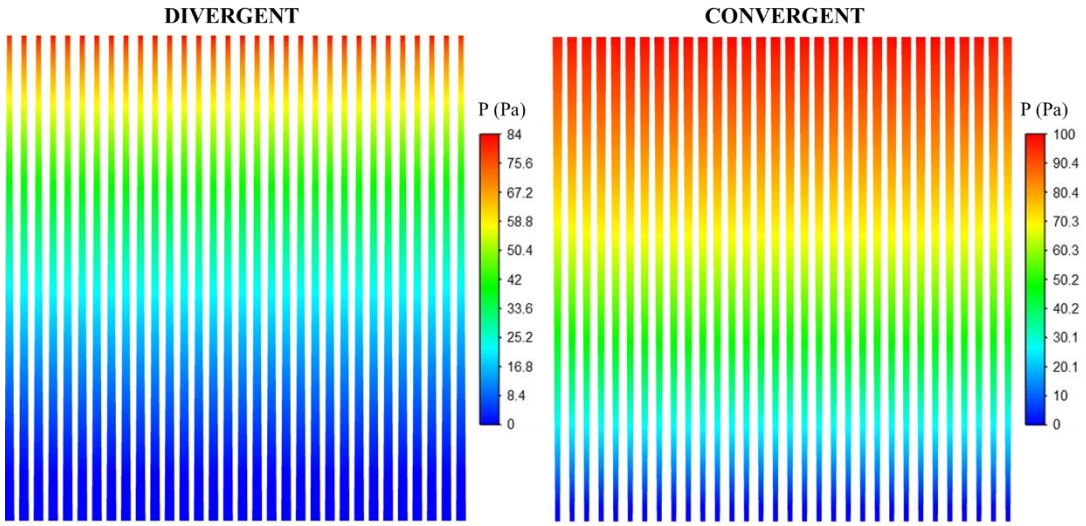

Figure 8. Distribution of pressure drop along the cooling channels.

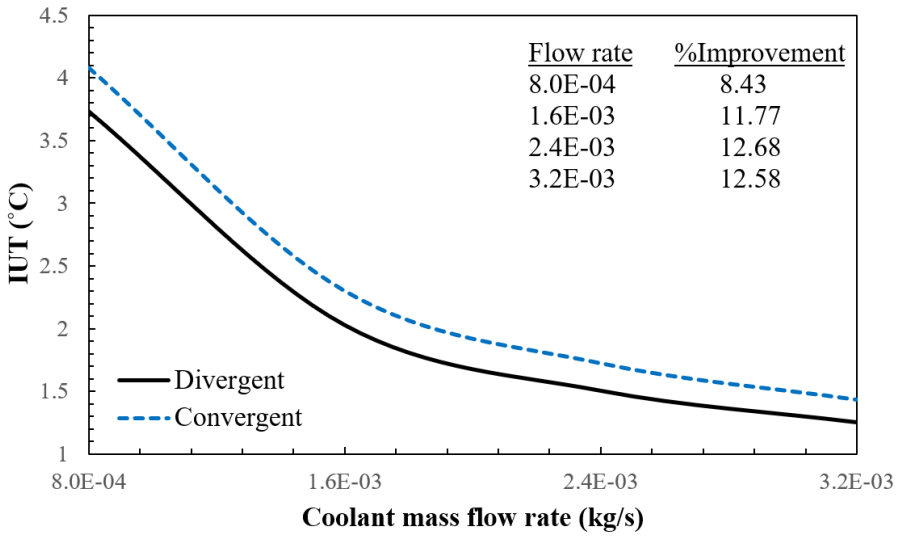

Figure 9. Variation of IUT with mass flow rate (T_{in} = 40 °C, q″ = 5000 W/m^2).

Figure 10 displays the variation in average temperature at the cooling plate's bottom surface for two channel designs. The average surface temperature decreases as the coolant mass flow rate increases. At low flow rates, the difference in average surface temperature between divergent and convergent channels is quite small; however, it gets greater values at higher mass flow rates.

Maintaining the cooling plate's maximum surface temperature at a specific level is crucial for ensuring the thermal stability of the cell. In fact, it is the most crucial factor in avoiding thermal damage. The maximum temperature of two channel designs along the cooling plate bottom surface is presented in Figure 11. As expected, the mass flow rate has a negative effect on the maximum surface temperature, and it can cause a decrease in this parameter for both channel designs. The maximum surface temperature difference between divergent and convergent channels decreases very slowly with mass flow rate. It is 0.33 ˚C at the mass flow rate of 8.0×10^{-4} kg/s and 0.23 ˚C at the mass flow rate of 3.2×10^{-3} kg/s.

The temperature difference results between maximum and minimum bottom surface temperature are plotted in Figure 12. Again, based on the coolant mass flow rate, a decreasing trend in temperature difference can be seen. According to the graph, the divergent design has lower temperature differences at whole mass flow rate ranges, which may result in an improvement in IUT.

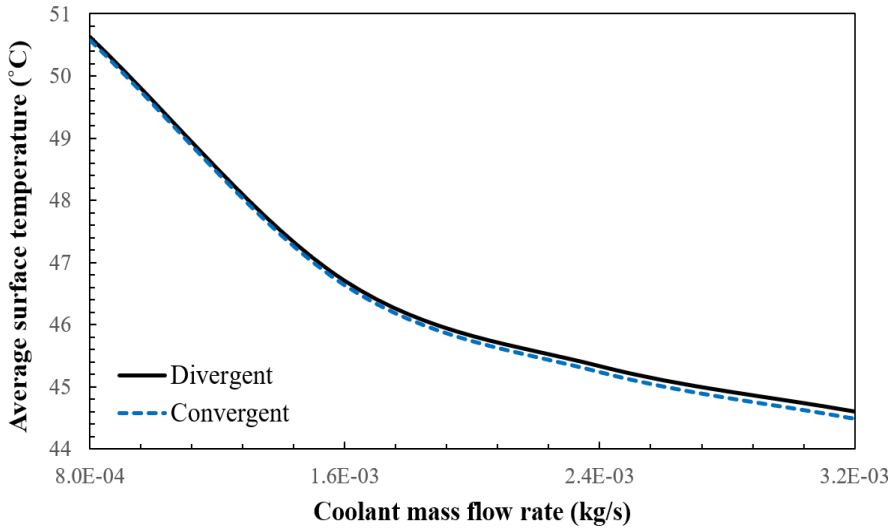

Figure 10. Variation of average temperature with mass flow rate (T_{in} = 40 ˚C, q″ = 5000 W/m^2).

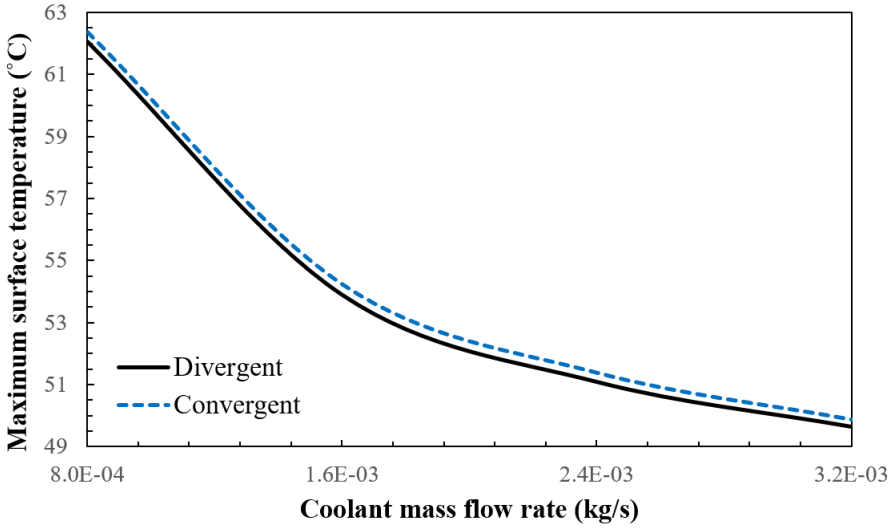

Figure 11. Variation of maximum temperature with mass flow rate (T_{in} = 40 ˚C, q″ = 5000 W/m^2).

Figure 13 depicts the simulated influence of coolant mass flow rate on pressure drop for two different designs. As it is seen in the figure, lower pressure drop values are obtained with divergent flow field, indicating low pumping power requirements. This is due to the higher velocity values of the coolant in the divergent channel. It is clearly shown in Figure 13 that the difference between two designs is small at low flow rates and becomes larger as the mass flow rate increases. When using a divergent flow field design instead of a convergent one, pressure drop would be reduced by 1.00%, 7.93%, 12.89%, and 17.04% at mass flow rates of 8.0×10^{-4} kg/s, 1.6×10^{-3} kg/s, 2.4×10^{-3} kg/s, and 3.2×10^{-3} kg/s, respectively.

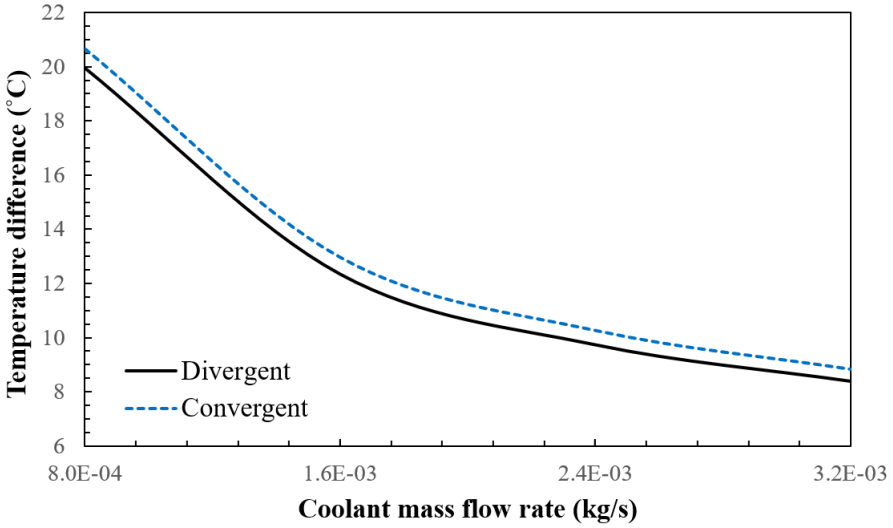

Figure 12. Variation of temperature difference with mass flow rate (T_{in} = 40 ˚C, q″ = 5000 W/m^2).

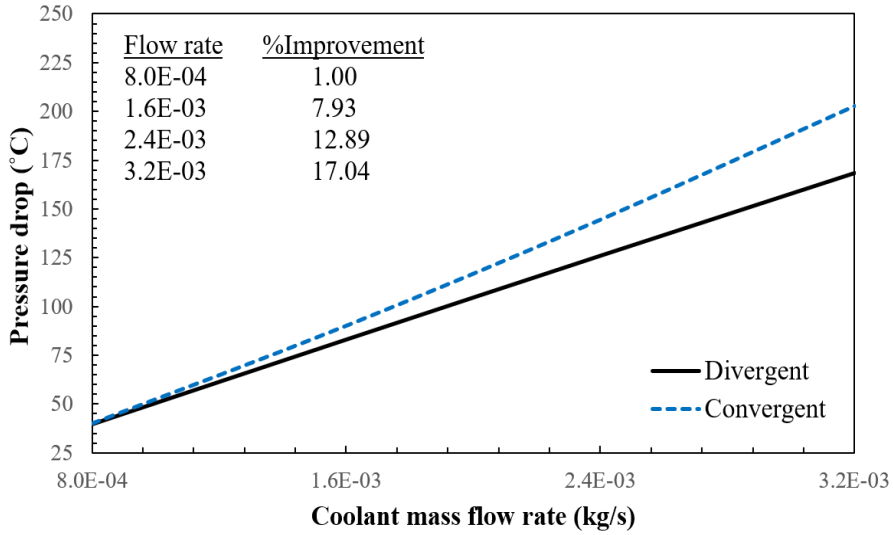

Figure 13. Variation of pressure drop with mass flow rate (T_{in} = 40 ˚C, q″ = 5000 W/m^2).

4. Conclusion and Suggestions

A numerical study was conducted for a graphite cooling plate with a 10×10 cm^2 area. In this context, the heat transfer and fluid flow performances of divergent and convergent flow field designs were investigated and compared. The cooling performance of these two designs were simulated according to the temperature uniformity, maximum temperature on bottom surface and pressure drop between inlet and outlet of the flow channels. While the coolant inlet temperature (40 ˚C) and heat flux (5000 W/m^2) were kept constant during the simulation, the coolant flow rates were varied from 8.0×10^{-4} kg/s to 3.2×10^{-3} kg/s.

Increasing coolant mass flow rates reduced IUT, maximum surface temperature, average surface

temperature and temperature difference between maximum and minimum surface temperatures. The pressure drop, on the other hand, increased as the flow rate increased. The uniformity of the temperature through the bottom surface of the cooling plate improved by 8.43%, 11.77%, 12.68% and 12.58% at the mass flow rates of 8.0×10^{-4}, 1.6×10^{-3}, 2.4×10^{-3} and 3.2×10^{-3}, respectively, when divergent design was considered instead of convergent design. Therefore, it can be concluded that the divergent flow field design provides a more uniform temperature across the cooling plate. Divergent design also resulted in lower maximum temperature values on the bottom surface of the cooling plate. In the case of divergent flow channel, the pressure drop was reduced by up to 17.04%.

In conclusion, it was discovered that the divergent flow field design was the more efficient design for sustaining more uniform temperature distribution across the cooling plate or fuel cell active area. In addition, because divergent channel design produced lower pressure drops, this design would require less pumping power. Overall, the findings of this paper will be useful for designing PEM fuel cell cooling systems as well as other applications where thermal management and fluid flow are important.

Statement of Research and Publication Ethics

The study is complied with research and publication ethics.

References

[1] E. Afshari and S. A. Jazayeri, "Effects of the cell thermal behavior and water phase change on a proton exchange membrane fuel cell performance," *Energy Convers. Manag.*, vol. 51, no. 4, pp. 655–662, 2010, doi: 10.1016/j.enconman.2009.11.004.

[2] S. A. Atyabi and E. Afshari, "A numerical multiphase CFD simulation for PEMFC with parallel sinusoidal flow fields," *J. Therm. Anal. Calorim.*, vol. 135, no. 3, pp. 1823–1833, 2019, doi: 10.1007/s10973-018-7270-3.

[3] Y. Wang, K. S. Chen, J. Mishler, S. C. Cho, and X. C. Adroher, "A review of polymer electrolyte membrane fuel cells: Technology, applications, and needs on fundamental research," *Appl. Energy*, vol. 88, no. 4, pp. 981–1007, 2011, doi: 10.1016/j.apenergy.2010.09.030.

[4] Y. Wang, "Modeling of two-phase transport in the diffusion media of polymer electrolyte fuel cells," *J. Power Sources*, vol. 185, no. 1, pp. 261–271, 2008, doi: 10.1016/j.jpowsour.2008.07.007.

[5] H. Pourrahmani *et al.*, "A Review on the Long-Term Performance of Proton Exchange Membrane Fuel Cells: From Degradation Modeling to the Effects of Bipolar Plates, Sealings, and Contaminants," *Energies*, vol. 15, no. 14, 2022, doi: 10.3390/en15145081.

[6] Y. Song *et al.*, "Review on current research of materials, fabrication and application for bipolar plate in proton exchange membrane fuel cell," *Int. J. Hydrogen Energy*, vol. 45, no. 54, pp. 29832–29847, 2020, doi: 10.1016/j.ijhydene.2019.07.231.

[7] R. A. Antunes, M. C. L. Oliveira, G. Ett, and V. Ett, "Corrosion of metal bipolar plates for PEM fuel cells: A review," *Int. J. Hydrogen Energy*, vol. 35, no. 8, pp. 3632–3647, 2010, doi: 10.1016/j.ijhydene.2010.01.059.

[8] K. Xiong, W. Wu, S. Wang, and L. Zhang, "Modeling, design, materials and fabrication of bipolar plates for proton exchange membrane fuel cell: A review," *Appl. Energy*, vol. 301, no. June, 2021, doi: 10.1016/j.apenergy.2021.117443.

[9] Y. Leng, P. Ming, D. Yang, and C. Zhang, "Stainless steel bipolar plates for proton exchange membrane fuel cells: Materials, flow channel design and forming processes," *J. Power Sources*, vol. 451, no. October 2019, p. 227783, 2020, doi: 10.1016/j.jpowsour.2020.227783.

[10] S. Porstmann, T. Wannemacher, and W. G. Drossel, "A comprehensive comparison of state-of-the-art manufacturing methods for fuel cell bipolar plates including anticipated future industry trends," *J. Manuf. Process.*, vol. 60, no. October, pp. 366–383, 2020, doi: 10.1016/j.jmapro.2020.10.041.

[11] M. M. Barzegari and F. A. Khatir, "Study of thickness distribution and dimensional accuracy of stamped metallic bipolar plates," *Int. J. Hydrogen Energy*, vol. 44, no. 59, pp. 31360–31371, 2019, doi: 10.1016/j.ijhydene.2019.09.225.

[12] H. Talebi-Ghadikolaee, M. Elyasi, and M. J. Mirnia, "Investigation of failure during rubber pad forming of metallic bipolar plates," *Thin-Walled Struct.*, vol. 150, no. February, p. 106671, 2020, doi: 10.1016/j.tws.2020.106671.

[13] E. Alizadeh, S. M. Rahgoshay, M. Rahimi-Esbo, M. Khorshidian, and S. H. M. Saadat, "A novel cooling

flow field design for polymer electrolyte membrane fuel cell stack," *Int. J. Hydrogen Energy*, vol. 41, no. 20, pp. 8525–8532, 2016, doi: 10.1016/j.ijhydene.2016.03.187.

[14] X. Chen *et al.*, "Numerical study of a MIMO-shaped cooling plate in PEMFC stack for heat transfer enhancement," *Energy Reports*, vol. 7, pp. 5804–5814, 2021, doi: 10.1016/j.egyr.2021.09.010.

[15] M. Saeedan, M. Ziaei-Rad, and E. Afshari, "Numerical thermal analysis of nanofluid flow through the cooling channels of a polymer electrolyte membrane fuel cell filled with metal foam," *Int. J. Energy Res.*, vol. 44, no. 7, pp. 5730–5748, 2020, doi: 10.1002/er.5332.

[16] S. Asghari, H. Akhgar, and B. F. Imani, "Design of thermal management subsystem for a 5 kW polymer electrolyte membrane fuel cell system," *J. Power Sources*, vol. 196, no. 6, pp. 3141–3148, 2011, doi: 10.1016/j.jpowsour.2010.11.077.

[17] S. M. Baek, S. H. Yu, J. H. Nam, and C. J. Kim, "A numerical study on uniform cooling of large-scale PEMFCs with different coolant flow field designs," *Appl. Therm. Eng.*, vol. 31, no. 8–9, pp. 1427–1434, 2011, doi: 10.1016/j.applthermaleng.2011.01.009.

[18] S. A. Atyabi, E. Afshari, E. Zohravi, and C. M. Udemu, "Three-dimensional simulation of different flow fields of proton exchange membrane fuel cell using a multi-phase coupled model with cooling channel," *Energy*, vol. 234, p. 121247, 2021, doi: 10.1016/j.energy.2021.121247.

[19] S. Li and B. Sundén, "Numerical study on thermal performance of non-uniform flow channel designs for cooling plates of PEM fuel cells," *Numer. Heat Transf. Part A Appl.*, vol. 74, no. 1, pp. 917–930, 2018, doi: 10.1080/10407782.2018.1486642.

[20] M. Seyhan, Y. E. Akansu, M. Murat, Y. Korkmaz, and S. O. Akansu, "Performance prediction of PEM fuel cell with wavy serpentine flow channel by using artificial neural network," *Int. J. Hydrogen Energy*, vol. 42, no. 40, pp. 25619–25629, 2017, doi: 10.1016/j.ijhydene.2017.04.001.

[21] B. Timurkutluk and M. Z. Chowdhury, "Numerical Investigation of Convergent and Divergent Parallel Flow Fields for PEMFCs," *Fuel Cells*, vol. 18, no. 4, pp. 441–448, 2018, doi: 10.1002/fuce.201800029.

[22] M. Z. Chowdhury and B. Timurkutluk, "Transport phenomena of convergent and divergent serpentine flow fields for PEMFC," *Energy*, vol. 161, pp. 104–117, 2018, doi: 10.1016/j.energy.2018.07.143.

[23] S. A. Ghadhban, W. H. Alawee, and H. A. Dhahad, "Study effects of bio-inspired flow filed design on Polymer Electrolyte Membrane fuel cell performance," *Case Stud. Therm. Eng.*, vol. 24, no. May 2020, p. 100841, 2021, doi: 10.1016/j.csite.2021.100841.

[24] S. Ravishankar and K. Arul Prakash, "Numerical studies on thermal performance of novel cooling plate designs in polymer electrolyte membrane fuel cell stacks," *Appl. Therm. Eng.*, vol. 66, no. 1–2, pp. 239–251, 2014, doi: 10.1016/j.applthermaleng.2014.01.068.

[25] S. M. Rahgoshay, A. A. Ranjbar, A. Ramiar, and E. Alizadeh, "Thermal investigation of a PEM fuel cell with cooling flow field," *Energy*, vol. 134, pp. 61–73, 2017, doi: 10.1016/j.energy.2017.05.151.

[26] M. Ghasemi, A. Ramiar, A. A. Ranjbar, and S. M. Rahgoshay, "A numerical study on thermal analysis and cooling flow fields effect on PEMFC performance," *Int. J. Hydrogen Energy*, vol. 42, no. 38, pp. 24319–24337, 2017, doi: 10.1016/j.ijhydene.2017.08.036.

[27] M. C. Acar, "Channel to rib width ratio effect on thermal performance of cooling plate in polymer electrolyte membrane fuel cell," *Fuel Cells*, vol. 22, no. 5, pp. 154–168, 2022, doi: 10.1002/fuce.202200082.

[28] D. R. S. Raghuraman, R. Thundil Karuppa Raj, P. K. Nagarajan, and B. V. A. Rao, "Influence of aspect ratio on the thermal performance of rectangular shaped micro channel heat sink using CFD code," *Alexandria Eng. J.*, vol. 56, no. 1, pp. 43–54, 2017, doi: 10.1016/j.aej.2016.08.033.

[29] F. C. Chen, Z. Gao, R. O. Loutfy, and M. Hecht, "Analysis of Optimal Heat Transfer in a PEM Fuel Cell Cooling Plate," *Fuel Cells*, vol. 3, no. 4, pp. 181–188, 2003, doi: 10.1002/fuce.200330112.

[30] E. Afshari, M. Ziaei-Rad, and M. M. Dehkordi, "Numerical investigation on a novel zigzag-shaped flow channel design for cooling plates of PEM fuel cells," *J. Energy Inst.*, vol. 90, no. 5, pp. 752–763, 2017, doi: 10.1016/j.joei.2016.07.002.

Bitlis Eren Üniversitesi Fen Bilimleri Dergisi
BİTLİS EREN UNIVERSITY JOURNAL OF SCIENCE
ISSN: 2147-3129/e-ISSN: 2147-3188
VOLUME: 12 NO: 1 PAGE: 192-198 YEAR: 2023
DOI:10.17798/bitlisfen.1220957

A Nested Square Shaped Metasurface-Based Broadband Linear Polarization Converter for Ku-Band Applications

Yunus KAYA[1*]

[1]*Bayburt University, Department of Electricity and Energy, Bayburt 69000, Turkey*
(ORCID: 0000-0002-2380-5915)

Keywords: Ku-band, Metasurface, Broadband, Linear polarization converter.

Abstract
This paper presents a wideband, thin, low-cost, and easy to fabricate linear polarization (LP) converter design utilizing metasurface (MS) for Ku-band (12-18 GHz) applications (also in the 18-19 GHz part of the K-band (18-27 GHz)). The design has a topology on a 1.6 mm thick FR-4 dielectric material with copper MS on the front and an entirely copper slab on the back. The presented design shows a polarization conversion ratio (PCR) of beyond 90% within the 12-19 GHz frequency band and also over 99% in the 12.5-13.1 and 16.32-17.64 GHz frequency ranges. To further give insight into the physical structure of the suggested MS-based polarization converter (PC), both the u – v axes are analyzed, and the existing surface behaviors at resonance frequencies are investigated. We compare the performance outputs with other Ku-band PCs, and the efficiencies of the suggested strategy over current MS-based LP converters are emphasized.

1. Introduction

The polarization condition for an electromagnetic (EM) wave expresses the aspect of the swing of the electric field part at a constant point in the free space, taking time into account. The polarization converter (PC) has the competency to alter the EM wave direction. Manipulation of the polarization status of the EM wave has received great attention because of its popular application areas, such as communication and remote perception [1]. PCs among the polarization manipulation equipment have proven the importance of EM wave PC from the microwave frequency region to the THz frequency region with several applications such as radar cross field degradation in invisibility technology [2], [3] and antenna design [4], [5]. Traditionally, polarization conversion is achieved by the effect of birefringence in crystals found in nature [6]. The weak anisotropies, bulkiness, large power losses, and angle-dependent polarization responses of these crystals limit their practical use. In order to eliminate these disadvantages, metasurface (MS) structures have recently been used in diverse applications. Examples of such applications are excellent lenses [7], an invisibility cloak [8], a superior absorber [9], and a PC [10]. So far, PCs relying on MS structures have been utilized in the microwave [10], infrared [11], and visible regimes [12], [13] due to their flexible and easy profile.

In general, PCs may be developed to perform in transmission [14] and/or reflection status [15]. PCs with the transmission mode necessitate multi-layer mechanisms, making their fabrication a very difficult task and a time-consuming component [16]. Meanwhile, PCs with reflective mode may be seen in a single-layer with metallic material-dielectric substrate material-metallic material setting [17]. Particularly, the manageable design style of reflective mode PCs [13], [17]-[22] on a single-layer moving in a linear manner has obtained significant interest. Another attractive property of a reflective PC design is the extension of the bandwidth to be appropriate in practice.

In this study, a single-layer, thin, low-cost, and MS-based broadband reflective linear polarization (LP) converter is designed specifically for Ku-band studies. The suggested converter includes an MS structure designed on the front side of a dielectric substrate material (FR-4) and a ground

*Corresponding author: ykaya@bayburt.edu.tr
Received: 19.12.2022, Accepted: 03.03.2023

plane with metallic termination on the back surface. The efficiency of the suggested idea was tested through a set of simulations in comparison to Ku-band PCs using crescent-shaped MS [19], double crescent-shaped MS [20], fishbone-shaped MS [21], and two-corner-cut square patch MS [22]. The suggested converter ensures an LP conversion with a polarization conversion ratio (PCR) bigger than 90% all over the Ku-band (microwave band of frequencies from 12 to 18 GHz), as well as in the 18-19 GHz part of the K-band (microwave band of frequencies from 18 to 27 GHz). Therefore, this design can be simply implemented for Ku-band microwave applications.

2. Material and Method

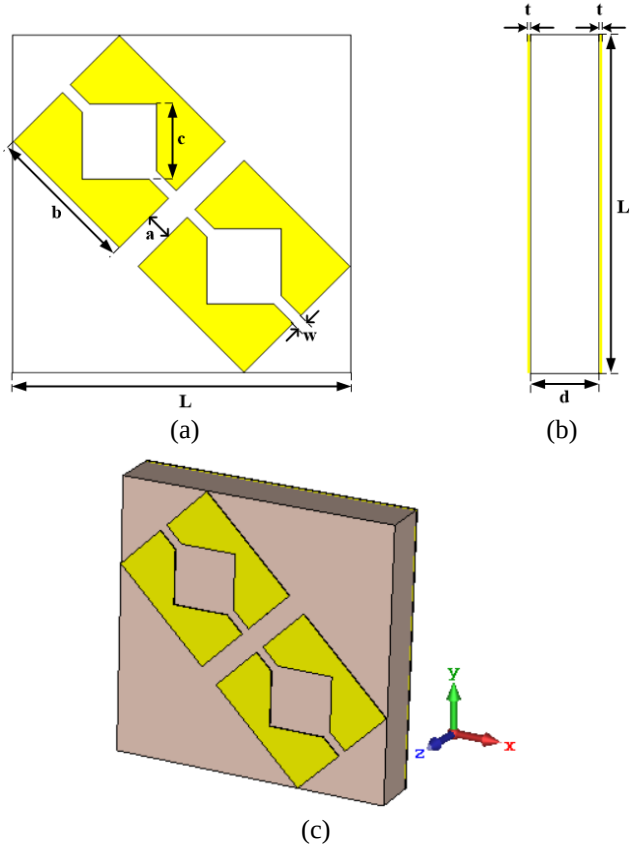

Figure 1. The suggested LP converter with (a) front view, (b) left side view, and (c) coordinate system layout with three-dimensional representation.

The suggested LP converter is designed on a substrate material with an MS on the front side and an all-metal termination on the back surface. Copper (with its electrical conductivity $\sigma = 5.8\times10^7$ S/m) was selected for MS and metal finishing, respectively, located on the front and back surfaces of the substrate. The substrate in the middle part is FR-4 dielectric material (the relative dielectric constant (ε_r) is 4.3 and the loss tangent (tanδ) is 0.025), which is easily available on the market. The thickness of the copper is t = 0.035 mm and the thickness of FR-4 material is d = 1.6 mm. The shape of the MS consists of two symmetrical nested squares (additionally, the nested square shape consists of one filled and the other empty square), with the distance between the two symmetrical shapes a = 0.7 mm, and the other dimensions in Figure 1 are L = 9 mm, b = 4 mm, c = 2 mm, and w = 0.3 mm.

To clarify the basis of the process of the suggested PC, it is necessary to conduct some EM analysis. It is assumed that the EM wave propagates to the MS-based PC in the +z-direction with the y-polarized electric field intensity (E_y) and the harmonic dependence $e^{j\omega t}$ in time (ω: angular frequency), the incident wave (E_i) in the phasor space is defined as follows.

$$\overrightarrow{E_i} = a_y E_y e^{-jkz} \tag{1}$$

Here k is the wave number. For LP conversion, the EM wave with an electric field component in the y-direction will be reflected in the same direction (y-direction – co-polarization) or in the direction normal to the incident plane (x-direction – cross-polarization) after hitting the MS. In this scenario, the reflected wave (E_r) is given as follows.

$$\overrightarrow{E_r} = \left(a_x E_{rx} + a_y E_{ry}\right) e^{jkz} \tag{2}$$

Here, E_{rx} and E_{ry} are the components of the electric field intensity of the reflected wave in the x- and y-directions, respectively. Likewise, E_{ix} and E_{iy} are the components of the electric field intensity of the incident wave in the x- and y-directions, respectively; the co-reflection coefficient – R_{yy} and the cross-reflection coefficient – R_{xy} for the wave polarized in the electric field intensity y-direction are denoted as follows.

$$R_{yy} = \frac{E_{ry}}{E_{iy}} \text{ and } R_{xy} = \frac{E_{rx}}{E_{iy}} \tag{3}$$

With the usage of R_{yy} and R_{xy} coefficients in Equation (3), the PCR value of the LP for the y-polarized incident wave may be obtained as follows [18]-[22].

$$PCR = \frac{\left|R_{xy}\right|^2}{\left|R_{xy}\right|^2 + \left|R_{yy}\right|^2} \tag{4}$$

Here |*| denotes the magnitude of "*". In addition, to deeply understand the physical operation of the LP concept for the suggested design, the y-polarized incident wave was separated in the u – v axes, which is shown in Figure 2.

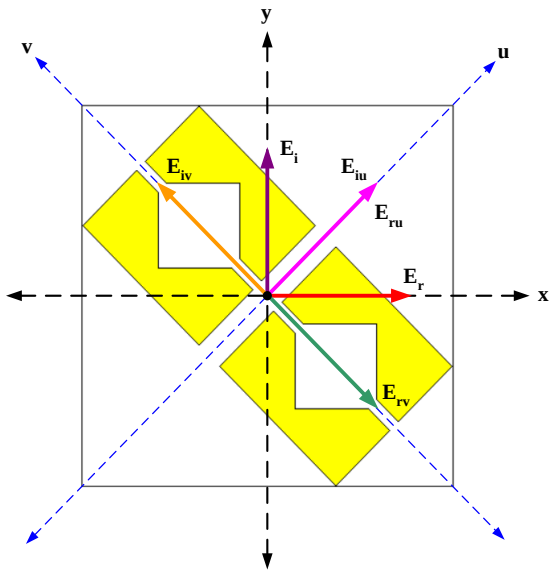

Figure 2. Decomposition of incident (E_i) and reflected wave (E_r) into u- (E_{iu} and E_{ru}) and v-axes (E_{iv} and E_{rv}) for the suggested design.

In Figure 2, E_{iu} and E_{iv} represent the electric field intensity parts of the incident wave in the u- and v-directions, respectively, and similarly, E_{ru} and E_{rv} represent the electric field intensity components in the u- and v-directions of the reflected wave, respectively. Accordingly, the incident and reflected wave (E_i and E_r, respectively) may be stated by decomposing into the u- and v-axes [18], [20]:

$$\overrightarrow{E_i} = a_u E_{iu} e^{j\varphi_{iu}} + a_v E_{iv} e^{j\varphi_{iv}} \quad (5)$$

$$\overrightarrow{E_r} = a_u r_{uu} E_{ru} e^{j\varphi_{ru}} + a_v r_{vv} E_{rv} e^{j\varphi_{rv}} \quad (6)$$

In Equations (5) and (6), φ_{iu} and φ_{iv} denote the phases of the incident wave in the u- and v-directions, respectively, and similarly, φ_{ru} and φ_{rv}, the phases of the reflected wave in the u- and v-directions, respectively. Additionally, here r_{uu} and r_{vv} are reflection coefficients in the u- and v-directions, respectively, and are expressed as follows.

$$r_{uu} = \frac{E_{ru}}{E_{iu}} \text{ and } r_{vv} = \frac{E_{rv}}{E_{iv}} \quad (7)$$

For the LP conversion, according to Figure 2, the components in the +u- and +v-directions must be reflected in the +u- and –v-directions with the same amplitude. So, $|r_{uu}|$ and $|r_{vv}|$ must be equal to 1. In addition, $\varphi_{uu} = 0^o$ must be since the incident wave in the +u-direction is reflected in the +u-direction. Similarly, φ_{vv} must be equal to -180^o in order for the incident wave in the +v-direction to be reflected in the –v-direction. Therefore, the reflection coefficients in the u- and v-directions for the x-polarized reflection of the y-polarized wave, that is, for the LP conversion, $|r_{uu}| \cong |r_{vv}| \cong 1$ and phase difference $\Delta\varphi = |\varphi_{uu} - \varphi_{vv}| = 180^o$ must be.

3. Results and Discussion

3.1. Simulation Results

The suggested MS-based LP converter, whose geometry is given in Figure 1, was created in the CST Microwave Studio program as shown in Figure 1(c). The simulations were conducted in the frequency domain, in the 7-21 GHz frequency range, and by choosing the tetrahedral mesh type. Accordingly, the co- and cross-reflection coefficients for the suggested PC design are presented in Figures 3(a) and 3(b) in terms of dB and amplitude, respectively. As seen in Figure 3(a), MS resonates at 12.776 and 17.016 GHz, and the R_{xy} is around –1.1 dB while the R_{yy} is below –11 dB in the 12-19 GHz frequency band. From Figure 3(b), it is noted that the $|R_{yy}|$ and $|R_{xy}|$ given as amplitudes are below 0.28 and above 0.87, respectively, within the specified frequency range. Figure 3(d) shows the PCR data obtained using Equation (4). As seen in Figure 3(d), PCR is over 90% in the 12-19 GHz frequency band. Additionally, the PCR value is over 99% in the frequency ranges of 12.5-13.1 and 16.32-17.64 GHz.

The reflection coefficients ($|r_{uu}|$ and $|r_{vv}|$) and phases (φ_{uu}, φ_{vv}, and $\Delta\varphi$) in the u – v directions of the suggested design are given in Figures 4(a) and 4(b), respectively. It can be noted from Figure 4(a) that LP is achieved (12-19 GHz frequency range) and at other frequencies, the $|r_{uu}|$ and $|r_{vv}|$ in the u – v axes are roughly equal to 1. In addition, from Figure 4(b), which shows the phase differences in the u- and v-directions, it is noted that the phase difference in the u – v directions is roughly 180^o ($\Delta\varphi = |\varphi_{uu} - \varphi_{vv}| = 180^o$) in the frequency range of 12-19 GHz.

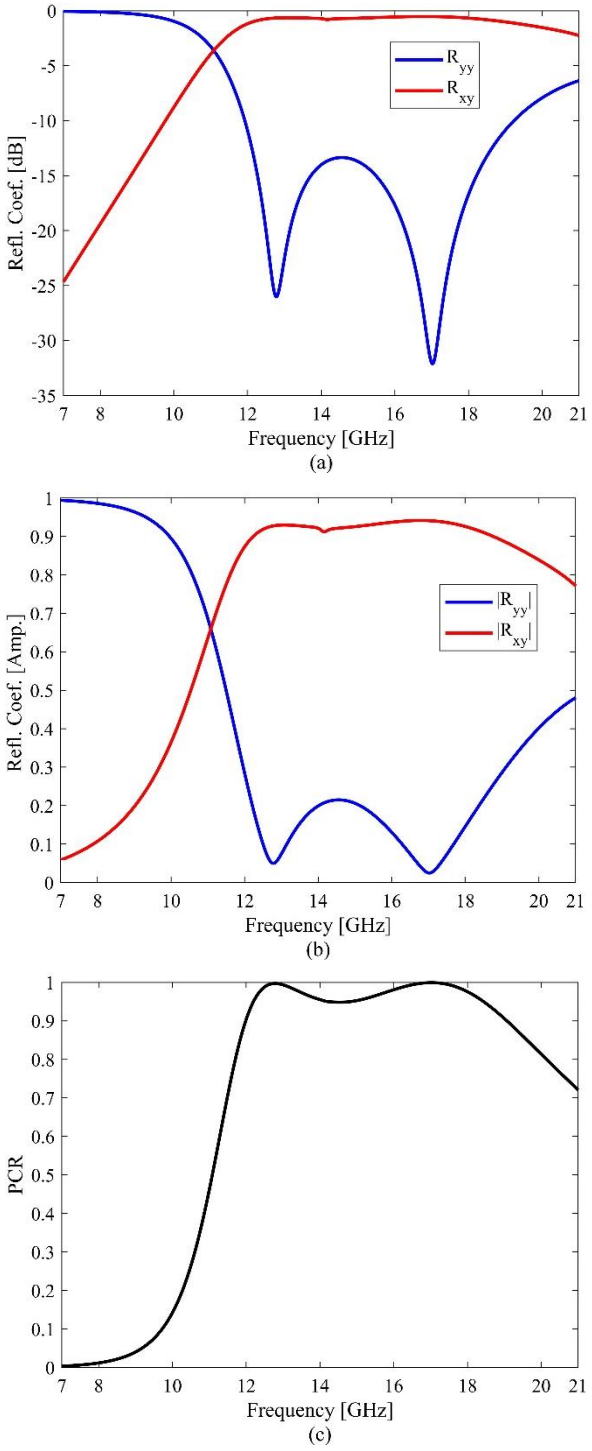

Figure 3. In the 7-21 GHz frequency range of the suggested PC; (a) reflection coefficient in dB (R_{yy} and R_{xy}), (b) reflection coefficient in amplitude ($|R_{yy}|$ and $|R_{xy}|$), and (c) PCR value.

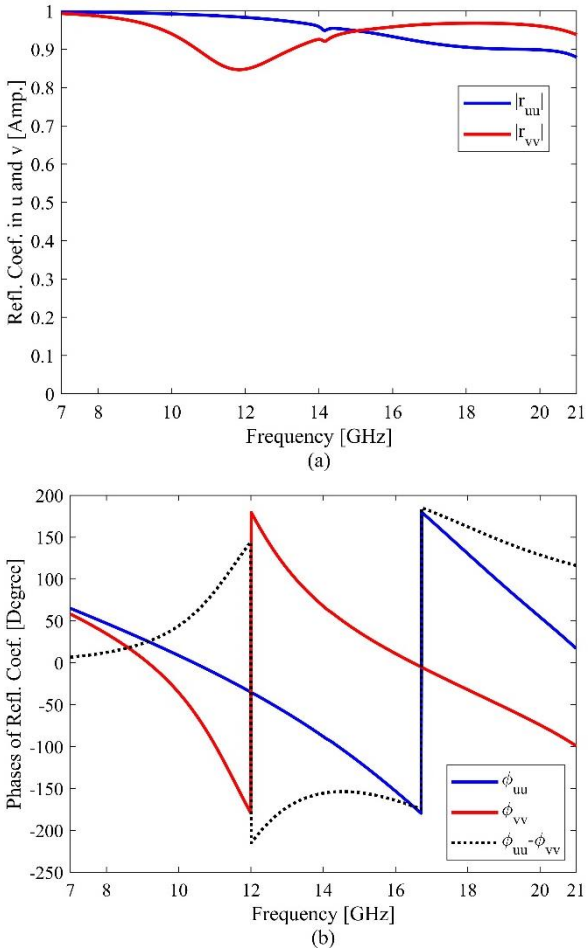

Figure 4. (a) Reflection coefficients ($|r_{uu}|$ and $|r_{vv}|$) and (b) phases (φ_{uu}, φ_{vv}, and $\Delta\varphi$) in the u – v directions of the suggested PC.

When the EM wave is sent to the MS-based PC, electrical and magnetic polarizations occur on the structure. This polarization causes the generation of electric and magnetic currents. In this context, surface current behaviors on metal parts (MS and metal termination) were investigated at resonance frequencies to know the physical mechanism of the suggested PC and to further examine its performance and effectiveness. Accordingly, Figures 5(a)- 5(d) show the surface currents in MS and metal termination at resonance frequencies, namely 12.776 and 17.016 GHz. When Figure 5(a) and Figure 5(c) are examined together, it is seen that the surface currents at 12.776 GHz are anti-parallel, and when Figures 5(b) and 5(d) are examined together, the surface currents at 17.016 GHz are also anti-parallel. This shows that the suggested MS-based LP converter design has a magnetic resonance at both resonance frequencies, namely 12.776 GHz and 17.016 GHz (on the contrary, the parallelism of the currents would indicate electrical resonance at the mentioned frequency).

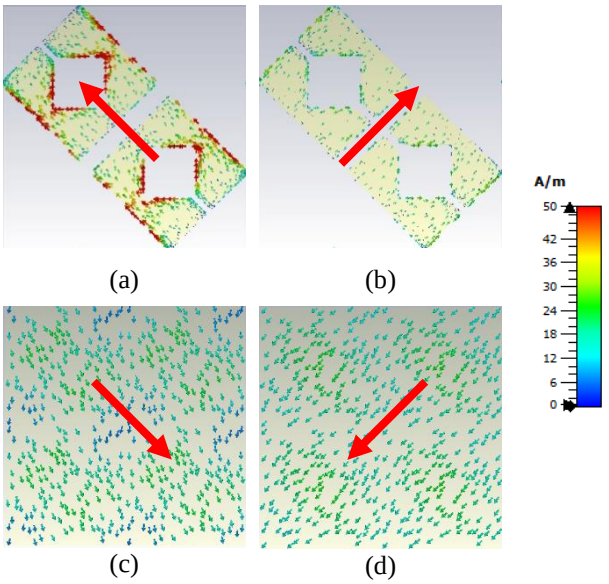

Figure 5. Distributions of surface currents for (a), (b) MS and (c), (d) metal termination for resonance frequencies of 12.776 and 17.016 GHz, respectively.

3.2. Discussion

The suggested PC's conversion performance was compared with other reference Ku-band LP converters [19]-[22] in terms of conversion bandwidth, substrate type, and substrate thickness, as shown in Table 1. The suggested design provides LP conversion with a wider bandgap than [19] and [20] in terms of conversion bandwidth. In fact, the suggested design provides LP conversion in the entire Ku-band (a microwave band of frequencies from 12 to 18 GHz) as well as in the 18-19 GHz part of the K-band (a microwave band of frequencies from 18 to 27 GHz). When the studies made according to the thickness in terms of wavelength are examined, the suggested design is 36% less thick than [22]. In terms of substrate thickness, the suggested design is thinner than both [21] and [22]. Therefore, the suggested design can be used for applications requiring thinner material. In addition, FR-4 dielectric was used as the substrate material in the suggested design, and it is both cheaper and more available than the F4-B substrate material used in [20] and [22]. This reduces the manufacturing complexity of our design. Therefore, the suggested design can be produced effectively at a lower cost than [20] and [22]. Looking at the PCR efficiency, all reference LP converters in Table 1 have a PCR value of 90%. In addition, while the MS-based LP converter we recommend has more than a 90% PCR value in the 12-19 GHz frequency range, it has a PCR value of over 99% in the 12.5-13.1 and 16.32-17.64 GHz frequency ranges.

Table 1. Comparison of the suggested PC with reference Ku-band LP converters [19]-[22]

Study	Conversion Bandwidth [GHz]	Substrate Thickness	Substrate Type	PCR Efficiency
[19]	12-18	1.6 mm (0.064λ)	FR-4	90%
[20]	11.9-18.05	1.5 mm (0.059λ)	F4-B	90%
[21]	9.24-17.64	2 mm (0.061λ)	FR-4	90%
[22]	10-18.4	3 mm (0.100λ)	F4-B	90%
Suggested Design	12-19	1.6 mm (0.064λ)	FR-4	90%

4. Conclusion

In this study, an LP converter operating in the 12-19 GHz frequency range for microwave Ku-band applications was suggested and validated by using the CST Microwave Studio program. The suggested PC provides over 90% PCR in the 12-19 GHz frequency range, as well as over 99% in the 12.5-13.1 and 16.32-17.64 GHz frequency ranges. In the suggested design, an easily accessible 1.6 mm thick FR-4 dielectric material is used as the substrate. For this reason, the suggested design can also be used in cases where very thin applications are required, with a thickness of 0.064λ. The suggested design is a single structure. This reduces the production's complexity.

Statement of Research and Publication Ethics

The study is complied with research and publication ethics.

References

[1] N. K. Grady, J. E. Heyes, D. R. Chowdhury, Y. Zeng, M. T. Reiten, A. K. Azad, A. J. Taylor, D. A. R. Dalvit, and H. T. Chen, "Terahertz metamaterials for linear polarization conversion and anomalous refraction," *Science*, vol. 340, no. 6138, pp. 1304-1307, Jun. 2013.

[2] Y. T. Jia, Y. Liu, Y. J. Guo, K. Li, and S. X. Gong, "Broadband polarization rotation reflective surfaces and their applications to RCS reduction," *IEEE Transactions on Antennas and Propagation*, vol. 64, no. 1, pp. 179-188, Jan. 2016.

[3] P. Su, Y. J. Zhao, S. L. Jia, W. W. Shi, and H. L. Wang, "An ultra-wideband and polarization-independent metasurface for RCS reduction," *Scientific Reports*, vol. 6, art. no. 20387, Feb. 2016.

[4] C. F. Yang, X. W. Zhu, P. F. Liu, W. Hong, H. L. Feng, and Y. H. Shi, "A circularly polarized horn antenna based on an FSS polarization converter," *IEEE Antennas and Wireless Propagation Letters*, vol. 19, no. 2, pp. 277-281, Feb. 2020.

[5] Q. Zheng, C. J. Guo, G. A. E. Vandenbosch, and J. Ding, "Low-profile circularly polarized array with gain enhancement and RCS reduction using polarization conversion EBG structures," *IEEE Transactions on Antennas and Propagation*, vol. 68, no. 3, pp. 2440-2445, Mar. 2020.

[6] A. J. Danner, T. Tyc, and U. Leonhardt, "Controlling birefringence in dielectrics," *Nature Photonics*, vol. 5, no. 6, pp. 357-359, Jun. 2011.

[7] J. B. Pendry, "Negative refraction makes a perfect lens," *Physical Review Letters*, vol. 85, no. 18, pp. 3966-3969, Oct. 2000.

[8] D. C. Liang, J. Q. Gu, J. G. Han, Y. M. Yang, S. Zhang, and W. L. Zhang, "Robust large dimension terahertz cloaking," *Advanced Materials*, vol. 24, no. 7, pp. 916-921, Feb. 2012.

[9] N. I. Landy, S. Sajuyigbe, J. J. Mock, D. R. Smith, and W. J. Padilla, "Perfect metamaterial absorber," *Physical Review Letters*, vol. 100, no. 20, art. no. 207402, May 2008.

[10] H. L. Zhu, S. W. Cheung, K. L. Chung, and T. I. Yuk, "Linear-to-circular polarization conversion using metasurface," *IEEE Transactions on Antennas and Propagation*, vol. 61, no. 9, pp. 4615-4623, Sep. 2013.

[11] Z. J. Zhang, J. Luo, M. W. Song, and H. L. Yu, "Large-area, broadband and high-efficiency near-infrared linear polarization manipulating metasurface fabricated by orthogonal interference lithography," *Applied Physics Letters*, vol. 107, no. 24, art. no. 241904, Dec. 2015.

[12] Q. T. Li, F. L. Dong, B. Wang, F. Y. Gan, J. J. Chen, Z. W. Song, L. X. Xu, W. G. Chu, Y. F. Xiao, Q. H. Gong, and Y. Li, "Polarization-independent and high-efficiency dielectric metasurfaces for visible light," *Optics Express*, vol. 24, no. 15, pp. 16309-16319, Jul. 2016.

[13] Z. H. Fang, H. Chen, D. An, C. R. Luo, and X. P. Zhao, "Manipulation of visible-light polarization with dendritic cell-cluster metasurfaces," *Scientific Reports*, vol. 8, art. no. 9696, Jun. 2018.

[14] F. Costa and M. Borgese, "Systematic design of transmission-type polarization converters comprising multilayered anisotropic metasurfaces," *Physical Review Applied*, vol. 14, no. 3, art. no. 034049, Sep. 2020.

[15] B. M. Zhang, C. H. Zhu, R. Zhang, X. F. Yang, Y. Wang, and X.M. Liu, "Dual-band wide-angle reflective circular polarization converter with orthogonal polarization modes," *Sensors*, vol. 22, no. 24, art. no. 9728, Dec. 2022.

[16] S. M. A. M. H. Abadi and N. Behdad, "Wideband linear-to-circular polarization converters based on miniaturized-element frequency selective surfaces," *IEEE Transactions on Antennas and Propagation*, vol. 64, no. 2, pp. 525-534, Feb. 2016.

[17] X. F. Yang, T. Qi, Y. H. Zeng, X. M. Liu, G. Lu, and Q. Cai, "Broadband reflective polarization rotator built on single substrate," *Electronics*, vol. 10, no. 8, art. no. 916, Apr. 2021.

[18] X. Gao, X. Han, W. P. Cao, H. O. Li, H. F. Ma, and T. J. Cui, "Ultra-wideband and high-efficiency linear polarization converter based on double V-shaped metasurface," *IEEE Transactions on Antennas and Propagation*, vol. 63, no. 8, pp. 3522-3530, Aug. 2015.

[19] T. Q. H. Nguyen, T. K. T. Nguyen, T. Q. M. Nguyen, T. N. Cao, H. L. Phan, N. M. Luong, D. T. Le, X. K. Bui, C. L. Truong, and D. L. Vu, "Simple design of a wideband and wide-angle reflective linear polarization converter based on crescent-shaped metamaterial for Ku-band applications," *Optics Communications*, vol. 486, art. no. 126773, May 2021.

[20] X. K. Yang, Z. Ding, and Z. P. Zhang, "Broadband linear polarization conversion across complete Ku band based on ultrathin metasurface," *AEU International Journal of Electronics and Communications*, vol. 138, art. no. 153884, Aug. 2021.

[21] Q. Zheng, C. J. Guo, H. X. Li, and J. Ding, "Broadband radar cross-section reduction using polarization conversion metasurface," *International Journal of Microwave and Wireless Technologies*, vol. 10, no. 2, pp. 197-206, Mar. 2018.

[22] B. Q. Lin, X. Y. Da, J. L. Wu, W. Li, Y. W. Fang, and Z. H. Zhu, "Ultra-wideband and high-efficiency cross polarization converter based on anisotropic metasurface," *Microwave and Optical Technology Letters*, vol. 58, no. 10, pp. 2402-2405, Oct. 2016.

Bitlis Eren Üniversitesi Fen Bilimleri Dergisi
BİTLİS EREN UNIVERSITY JOURNAL OF SCIENCE
ISSN: 2147-3129/e-ISSN: 2147-3188
VOLUME: 12 NO: 1 PAGE: 199-206 YEAR: 2023
DOI:10.17798/bitlisfen.1222870

Application of the Taguchi and ANOVA Methods to Optimize Ventilation Parameters for Infection Risk Based on the Wells-Riley Model

Bahadir Erman YUCE[1*]

[1]*Bitlis Eren University, Mechanical Engineering Department, Bitlis, Turkiye*

(ORCID:0000-0002-2432-964X)

Keywords: Wells Riley, Optimization, Infection Risk, Covid-19.

Abstract

The coronavirus pandemic has caused many deaths and affected societies with social and economic problems as a consequence of its effects. Many different measures were taken to stop or reduce the spread of the virus, like wearing a face mask and reorganizing school activities, transportation, and meetings. As an alternative to these measures, ventilation is a critical engineering solution that can help reduce the infection risk in the indoor environment. In this study, the Taguchi method was used to investigate the effects of ventilation parameters t (volume, inlet velocity), and quanta emission rates on the Wells-Riley method-based infection risk probability. The orthogonal array was used to create the experimental design. Then, each parameter was analyzed according to the performance criterion (infection risk probability) using signal-to-noise (S/N) ratios, and the order of importance of the parameters was calculated. The contribution ratio of each parameter to infection risk was calculated with both the Taguchi method and the ANOVA method, and these results confirmed each other. Consequently, these data were used to identify worst-case and best-case scenarios to minimize the risk of infection in the indoor environment.

1. Introduction

The COVID-19 pandemic showed the importance of infection control measures, especially in indoor environments. The transmission of the SARS-CoV-2 virus, which causes COVID-19, can occur through respiratory droplets or close contact with infected individuals [1]. Many measures were taken by the governments around the world to prevent the spread during the pandemic process. Regulations were made for organizations in closed environments, masks became mandatory in many areas, and most closed areas were rearranged depending on social distance.

The Wells-Riley method is a method that quantifies the probability of infection risk and has been widely used to estimate the risk of infection transmission in indoor environments, as it considers a variety of factors that can influence the risk of infection, such as the room volume, ventilation rate, breathing rate, quanta emission rate, and exposure time. Many epidemic modeling studies have used the Wells-Riley equation as part of their mathematical model [2]. Some researchers modified the Wells-Riley equation, developed dose-response models, and used additional numerical modeling techniques to provide more comprehensive risk assessments [3]–[5]. The number of studies using the Wells-Riley method has increased with the Covid-19 pandemic, and many researchers used this method with the computational Fluid Dynamics (HAD) method [6]–[8].

However, this method has some limitations because it does not consider the effect of other variables that may affect the transmission of infection, such as the level of personal protective equipment (PPE), gender or physiological differences, etc. Many researchers have proposed ways to improve this model. In addition, the effect of

*Corresponding author: beyuce@beu.edu.tr
Received: 22.12.2022, Accepted: 01.03.2023

each parameter used in the Wells-Riley model on infection risk probability is not clear. This is essential because it defines the strategies for decreasing infection risk in indoor environments.

To address these limitations and the challenges posed by the COVID-19 pandemic, a novel approach, the Taguchi optimization method, was used in this study to optimize the infection risk calculated using the Wells-Riley method. The Taguchi method involves the systematic variation of multiple parameters in a controlled experiment by means of a orthogonal array and the use of statistical analysis to determine the optimal combination of these parameters that results in the desired outcome, which in this case is minimized infection risk [9]. The contribution ratio of each parameter is also calculated with the Taguchi method, and these results were confirmed with another statistical method, ANOVA.

In this study, the levels of room volume, inlet velocity, and quanta emission rate values that will minimize the possibility of infection risk in the room were investigated. Each parameter was considered in a large range. The order of importance of the parameters and, accordingly, the best- and worst-case scenarios were obtained.

2. Material and Method

In this study, the effects of room volume, inlet velocity, and quanta emission rate on the risk of infection in the room were investigated using the Wells-Riley method. Parameters and their values are given in Table 1. All parameters were investigated over a large range. Inlet velocity values have a critical effect on infection risk; because of this reason a large range is also examined for this parameter. The quanta emission rates were determined as 3.1 (resting, oral breathing), 21 (heavy activity, oral breathing), and 42 quanta/h (light activity, talking) [10]. Room volume was also considered in the analysis, and its values were defined as 18, 42, and 60 m^3.

Table 1. Investigated parameters

	Parameters	Levels 1	2	3
A	Volume (m^3)	18	42	60
B	Velocity (m/s)	1	2	3
C	Quanta emission rate (quanta/h)	3.1	21	42

2.1 Wells-Riley Method

The Wells-Riley method is used to model the risk of indoor airborne transmission of infectious diseases such as tuberculosis and Covid-19 and is based on quanta. Quanta was proposed as a hypothetical unit of infection dose in Wells' work [11]. Quanta is defined as the number of airborne infectious particles required to infect a person. [3]. In other words, it can be defined as the droplet nuclei in the air that can cause infection in 63% of the people in the environment [10]. The Wells-Riley equation was defined as [12]:

$$P = 1 - e^{-n} \tag{1}$$

In Equation 1, P is the probability of infection risk and n is the inhaled quanta. The quanta calculation can be done according to Equation 2:

$$n = C_{avg} Q_b D \tag{2}$$

In Equation 2, C_{avg} (quanta/m^3) represents the time-averaged quanta concentration, Q_b the volumetric breathing rate of an occupant, and D (h) occupancy time.

$$\frac{dC}{dt} = \frac{E}{V} - \lambda C \tag{3}$$

In Equation 3, E (quanta/h) is the quanta emission rate (quanta/h), V (m^3) is the volume of the room, λ (1/h) is the first-order loss rate coefficient for quanta/h. λ is sum of deposition onto surfaces λ_{dep} (1/h), ventilation (ACH) λ_V (1/h), virus decay k (1/h) ($\lambda = \lambda_{dep} + \lambda_V + k$). The surface deposition loss rate was considered to be 0.3 1/h [13], [14] and virus decay was considered averaged value of 0.32 1/h [15], [16] according to literature [10].

It is assumed that the quanta concentration is 0 at the initial state, and then after the equation (3) is solved, the average quanta concentration can be calculated as below:

$$C(t) = \frac{E}{\lambda V}\left(1 - e^{-\lambda D}\right) \tag{4}$$

In Equation 4, t (h) is the time.

$$C_{avg} = \int_0^D C(t)dt \; \frac{E}{\lambda V}\left[1 - \frac{1}{\lambda D}\left(1 - e^{-\lambda D}\right)\right] \tag{5}$$

2.2 Taguchi Method

Taguchi method, which was developed by Taguchi [9], was successfully applied to many disciplines [17]–[21]. Taguchi method uses signal/noise ratios (S/N) to obtain the importance order of parameters, contribution ratios, and best- and worst-case scenarios [22].

Yuce et al. [23] discussed the solution steps and advantages of the Taguchi method in detail. Details on the methodology can be accessed from the related study. Three parameters (volume, inlet velocity, and quanta emission rate) and 3 different values of each parameter were examined in this study. As a result of this, the L9 (33) orthogonal array was used. Since the objective function is infection risk in this study, the 'smaller the better' approach was used according to the assumption that the smallest value is the best, as shown in Equation 6:

$$S/_N = -10log\left(\frac{1}{n}\sum_{i=1}^{n} Y_i^2\right) \quad (6)$$

In the Taguchi method, the factors determining the order of importance are obtained by the delta values. Delta values are calculated by the difference between the maximum and minimum S/N ratios for each parameter. The parameter with the largest delta value represents the most effective parameter [23].

Table 2 shows the L9 (33) orthogonal array created for this study. Nine different scenarios were determined for this design. Infection risk calculations were made for each scenario. Then, using equation 6, S/N ratios were calculated.

Table 2. Taguchi L9 (33) orthogonal array and calculated infection risk and S/N values

No.	Volume (m^3)	Velocity (m/s)	Quanta emission rate (quanta/h)	Infection Risk (%)	S/N
1	18	1	3.1	4.35	27.33
2	18	2	21.0	14.27	16.89
3	18	3	42.0	18.68	14.56
4	42	1	21.0	24.73	12.15
5	42	2	42.0	25.83	11.77
6	42	3	3.1	1.48	36.48
7	60	1	42.0	42.02	7.54
8	60	2	3.1	2.13	33.56
9	60	3	21.0	9.50	20.45

2.3 Analysis of Variance (ANOVA)

ANOVA is a commonly employed statistical method that helps understand the impact of each variable on the experimental outcome. The procedure for ANOVA includes the following steps [23]:

The total sum of squares (SS_T) can be calculated as [24]:

$$SS_T = \sum_{i=1}^{N} (Y_i - \bar{Y})^2 \quad (7)$$

In equation 7, N represents the number of cases in the orthogonal array and Y_i represents the result for the i_{th} case,

$$\bar{Y} = \frac{1}{N}\sum_{i=1}^{N} Y_i \quad (8)$$

The overall sum of the squared deviations, SS_T, is made up of both the sum of the squared error, SS_e, and the sum of the squared deviations due to each process parameter, SS_P, hence SS_P is defined as [24]:

$$SS_P = \sum_{j=1}^{t} \frac{(SY_j)^2}{t} - \frac{1}{N}\left[\sum_{i=1}^{N} Y_i\right]^2 \quad (9)$$

In equation 9, P represents a specific parameter, j is the level of that parameter, t indicates the number of times each level of the parameter is repeated, SY_j represents the sum of the experimental results for the parameter P at level j, and SS_e represents the sum of squares from the error parameters, as shown below [24]:

$$SS_e = SS_T - SS_A - SS_B - SS_C - SS_D - SS_E \quad (10)$$

The overall degree of freedom, D_T, is equal to N-1, and the degree of freedom for each evaluated

parameter, D_P, is also equal to N-1. The variance of the tested parameter, V_P, is calculated as $\llbracket SS_P/D_P$. The F-value for each design parameter can be determined by dividing the variance of that parameter by the variance of the error, $F_P = V_P/V_e$. The percentage contribution, ρ, is calculated as [24]:

$$\rho_P = \frac{SS_P}{SS_T} \tag{11}$$

3. Results and Discussion

Infection risk and, accordingly, S/N ratio values for nine different conditions were obtained, and they are shown in Table 2. These S/N ratio values were used to calculate the average S/N ratio values for each level of each parameter. Average S/N ratio values are shown in Table 3. Delta values were also obtained according to the average values.

In Figure 1, the variation of the S/N ratios depending on the levels of the examined parameters is shown. Among the examined parameters according to the order of importance in Table 3 and the S/N ratio values in Figure 3, the most effective parameter on the infection risk probability is the quanta emission rate.

Figure 1 shows that the possibility of infection risk is significantly reduced by a low quanta emission rate (3.1 quanta/h). The inlet velocity is the second important parameter, and as the amount of fresh air given to the environment increases, the risk of infection decreases. The lowest probability of infection risk according to inlet velocity is at 3 m/s. The parameter that has the least effect on the risk of infection is the room volume, and the risk of infection decreases as the volume increases.

Delta values were calculated for each parameter as Volume$_{0.92}$<Inlet velocity$_{8.16}$<quanta emission rate$_{21.17}$. Contribution ratios of each parameter on infection risk probability were obtained with the delta values. The volume, inlet velocity, and quanta emission rate have contribution ratios on infection risk as 3.04, 26.98, and 69.98% respectively.

According to Figure 1, the parameter levels corresponding to the minimum infection risk are 60 m^3 for the volume, 2 m/s for the inlet velocity, and 3.1 quanta/h for the breathing rate. The best case is not within the orthogonal array shown in Table 2. The infection risk probability was calculated as 1.46% when the infection risk was calculated in the Wells-Riley equation according to these values and this result is lower than all the values in the orthogonal array. The closest value to this is 1.48% in the 6th scenario. Scenario 6 has the same values as the best-case scenario except for volume, and the reduction in infection risk was also small, as the room volume had a low impact on infection risk.

Figure 1 shows that the infection risk probability is the highest, and for the worst-case scenario, the volume is 18 m^3, the inlet volume is 1 m/s, and the quanta emission rate is 42 quanta/h. The worst case is not included in the scenarios within the orthogonal array as it is in the best case. The infection risk probability was calculated in the Wells-Riley equation according to these values as 45.23% and this result is higher than all the values in the orthogonal array. The closest situation to this scenario is seen in scenario 7 and the infection risk value is 42.02%. As similar to best case, the parameter that is different in this scenario is the volume value, and due to the small effect value of the volume, the difference between it and the highest value seen in scenario 7 is low.

Table 3. The order of importance of parameters according to mean S/N ratios

Level	Volume (m^3)	Velocity (m/s)	Quanta emission rate (quanta/h)
1	19.6	15.67	32.45
2	20.13	20.74	16.49
3	20.51	23.83	11.29
Delta	0.92	8.16	21.17
Rank	3	2	1
Contribution (%)	3.04	26.98	69.98

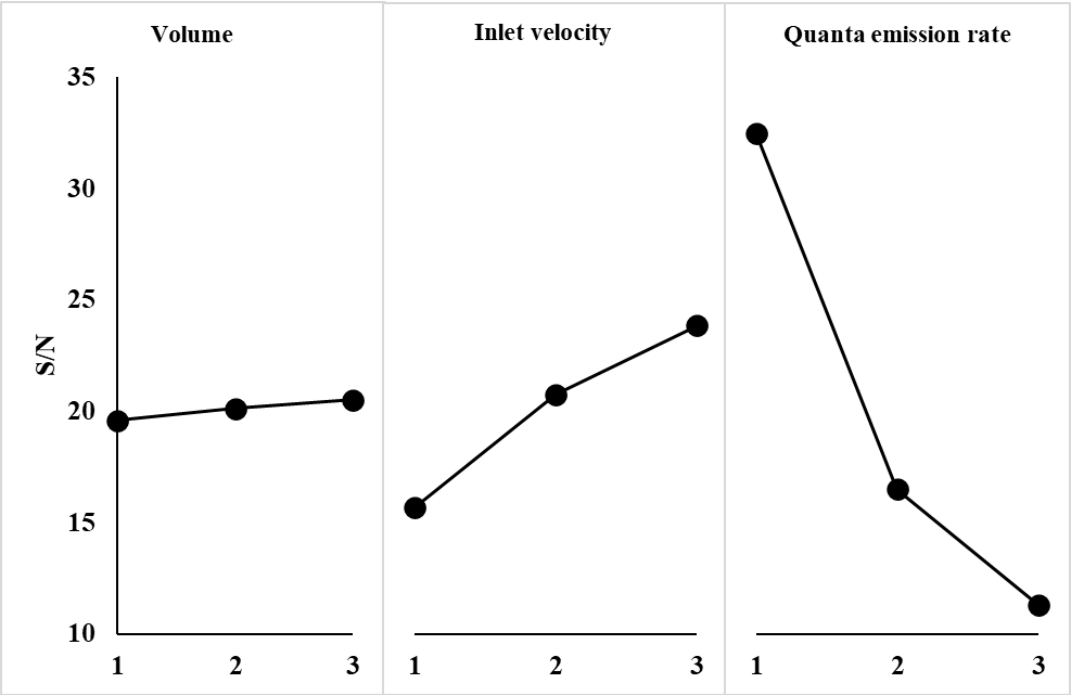

Figure 1. Variation of S/N ratios according to volume, inlet velocity, and quanta emission rate

ANOVA results are shown in Table 4. The results of the contribution ratios for each parameter are similar to those of the Taguchi analysis. The main difference between these statistical methods is based on the contribution ratio of the supply velocity, which corresponds to a 6% difference. Results of two methods are compared with each other in Figure 2.

Table 4. ANOVA results and contribution ratios of parameters on infection risk

Parameters	DOF	SS	MS	F-Value	Contribution ratio
Volume (m^3)	2	0.005	0.003	0.94	3.74%
Velocity (m/s)	2	0.030	0.015	5.2	20.76%
Quanta emission rate (quanta/h)	2	0.103	0.052	17.92	71.51%
Error	2	0.006	0.003		3.99%
Total	8	0.144			100.00%

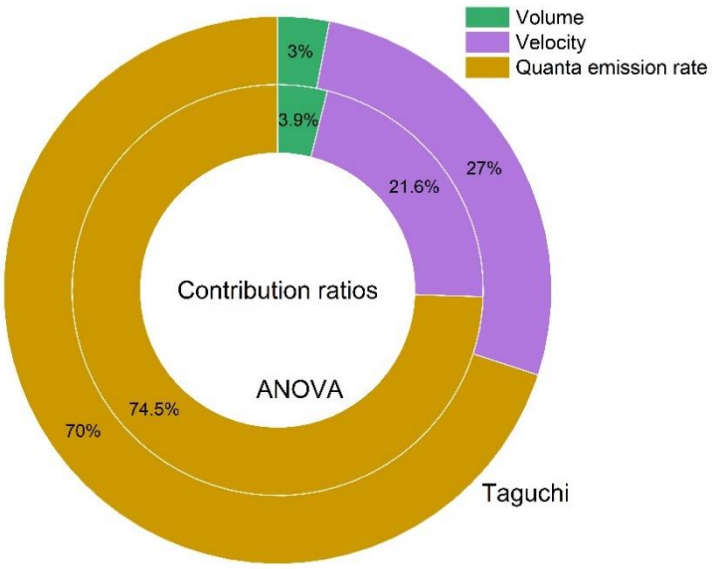

Figure 2. Comparison of contribution ratios of parameters obtained from Taguchi and ANOVA analysis.

3. Conclusion and Suggestions

In the study, the effects of different room volumes, inlet velocity, and the quanta emission rate on the infection risk probability calculated with the Wells-Riley equation were investigated by the Taguchi method. In the study, the best and worst-case scenarios were obtained, and the risk of infection was 1.46% in the best case and 45.23% in the worst case.

Among the parameters examined, the most effective parameter was found to be the quanta emission rate with an effect of 69.98%. Since this value changes depending on the person's activity (talking coughing, sneezing, etc.), it is possible to interpret that solutions such as the use of face masks will be effective in reducing the infection risk probability. The second important parameter is the inlet velocity. Ventilation is an important engineering solution that can reduce the risk of infection with its 27% contribution ratio. These values were also confirmed with ANOVA analysis with small differences. According to ANOVA analysis, the effect of the quanta emission rate is 71.51%, supply velocity is 20.76% and volume is 3.74% on infection risk.

It was seen that the room volume was the least effective parameter on the probability of infection risk and decreased the risk of infection (3%) with increasing values. This contribution rate is pretty low compared to others and this effect will be even smaller in real life, given that the room volume is a constant parameter and does not vary over a wide range of buildings. This situation can be interpreted as a positive output in the struggle against epidemics and allows to focus on other parameters that can be changed dynamically instead of fixed parameters such as room volume in buildings and can benefit the solution of the infection risk problem. In addition, these results carry studies that have volumetric differences on different room or space types, further than being a case study.

The limitations of this study rely on the limitations of the Wells-Riley method. Uniformity, the steady-state approach, neglecting gender and physiological differences are the main weaknesses of the model. This study can be improved in the future by coupling the CFD method and improving the equation with the help of the literature.

Statement of Research and Publication Ethics

The study is complied with research and publication ethics.

References

[1] W. H. Organization, "Coronavirus disease (COVID-19) advice for the public: Mythbusters," 2022. https://www.who.int/emergencies/diseases/novel-coronavirus-2019/advice-for-public/myth-busters (accessed Dec. 21, 2022).

[2] J. Burkett, "Defining Viruses And Droplet Release: Virus Transmission Modes and Mitigation Strategies, Part 1," *ASHRAE J.*, vol. 63, no. 3, pp. 24–29, 2021.

[3] G. N. Sze To and C. Y. H. H. Chao, "Review and comparison between the Wells-Riley and dose-response approaches to risk assessment of infectious respiratory diseases.," *Indoor Air*, vol. 20, no. 1, pp. 2–16, Feb. 2010, doi: 10.1111/j.1600-0668.2009.00621.x.

[4] M. Z. Bazant and J. W. M. Bush, "A guideline to limit indoor airborne transmission of COVID-19," *Proc. Natl. Acad. Sci.*, vol. 118, no. 17, Apr. 2021, doi: 10.1073/pnas.2018995118.

[5] W. W. Nazaroff, M. Nicas, and S. L. Miller, "Framework for Evaluating Measures to Control Nosocomial Tuberculosis Transmission," *Indoor Air*, vol. 8, no. 4, pp. 205–218, Dec. 1998, doi: 10.1111/j.1600-0668.1998.00002.x.

[6] Z. Liu *et al.*, "Potential infection risk assessment of improper bioaerosol experiment operation in one BSL-3 laboratory based on the improved Wells-Riley method," *Build. Environ.*, vol. 201, p. 107974, Aug. 2021, doi: 10.1016/j.buildenv.2021.107974.

[7] Y. Yan, X. Li, Y. Shang, and J. Tu, "Evaluation of airborne disease infection risks in an airliner cabin using the Lagrangian-based Wells-Riley approach," *Build. Environ.*, vol. 121, pp. 79–92, Aug. 2017, doi: 10.1016/j.buildenv.2017.05.013.

[8] Z. Wang, E. R. Galea, A. Grandison, J. Ewer, and F. Jia, "A coupled Computational Fluid Dynamics and Wells-Riley model to predict COVID-19 infection probability for passengers on long-distance trains," *Saf. Sci.*, vol. 147, p. 105572, Mar. 2022, doi: 10.1016/j.ssci.2021.105572.

[9] G. Taguchi, *Introduction to Quality Engineering*. Tokyo: Asian Productivity Organization, 1990.

[10] REHVA, "REHVA COVID-19 guidance document, How to Operate HVAC and Other Building Service Systems to Prevent the Spread of the Coronavirus (SARS-CoV-2) Disease (COVID-19) in Workplaces," *Fed. Eur. Heating, Vent. Air Cond. Assoc.*, 2020.

[11] W. F. Wells, *Airborne Contagion and Air Hygiene. An Ecological Study of Droplet Infections*. Cambridge, MA: Cambridge University Press, 1955.

[12] E. C. Riley, G. Murphy, and R. L. Riley, "Airborne spread of measles in a suburban elementary school," *Am. J. Epidemiol.*, vol. 107, no. 5, 1978, doi: 10.1093/oxfordjournals.aje.a112560.

[13] T. L. Thatcher, A. C. K. Lai, R. Moreno-Jackson, R. G. Sextro, and W. W. Nazaroff, "Effects of room furnishings and air speed on particle deposition rates indoors," *Atmos. Environ.*, vol. 36, no. 11, pp. 1811–1819, Apr. 2002, doi: 10.1016/S1352-2310(02)00157-7.

[14] E. Diapouli, A. Chaloulakou, and P. Koutrakis, "Estimating the concentration of indoor particles of outdoor origin: A review," *J. Air Waste Manage. Assoc.*, vol. 63, no. 10, pp. 1113–1129, Oct. 2013, doi: 10.1080/10962247.2013.791649.

[15] A. C. Fears *et al.*, "Comparative dynamic aerosol efficiencies of three emergent coronaviruses and the unusual persistence of SARS-CoV-2 in aerosol suspensions.," *medRxiv Prepr. Serv. Heal. Sci.*, Apr. 2020, doi: 10.1101/2020.04.13.20063784.

[16] N. van Doremalen *et al.*, "Aerosol and Surface Stability of SARS-CoV-2 as Compared with SARS-CoV-1," *N. Engl. J. Med.*, vol. 382, no. 16, pp. 1564–1567, Apr. 2020, doi: 10.1056/NEJMc2004973.

[17] N. Arslanoglu and A. Yigit, "Experimental investigation of radiation effect on human thermal comfort by Taguchi method," *Appl. Therm. Eng.*, vol. 92, pp. 18–23, Jan. 2016, doi: 10.1016/j.applthermaleng.2015.09.070.

[18] C.-W. Chang and C.-P. Kuo, "Evaluation of surface roughness in laser-assisted machining of aluminum oxide ceramics with Taguchi method," *Int. J. Mach. Tools Manuf.*, vol. 47, no. 1, pp. 141–147, 2007, doi: 10.1016/j.ijmachtools.2006.02.009.

[19] A. M. Pinar, O. Uluer, and V. Kırmaci, "Optimization of counter flow Ranque–Hilsch vortex tube performance using Taguchi method," *Int. J. Refrig.*, vol. 32, no. 6, pp. 1487–1494, Sep. 2009, doi: 10.1016/j.ijrefrig.2009.02.018.

[20] S. Özel, E. Vural, and M. Binici, "Optimization of the effect of thermal barrier coating (TBC) on diesel engine performance by Taguchi method," *Fuel*, vol. 263, p. 116537, Mar. 2020, doi:

10.1016/j.fuel.2019.116537.

[21] M. Tutar, H. Aydin, C. Yuce, N. Yavuz, and A. Bayram, "The optimisation of process parameters for friction stir spot-welded AA3003-H12 aluminium alloy using a Taguchi orthogonal array," *Mater. Des.*, vol. 63, pp. 789–797, Nov. 2014, doi: 10.1016/j.matdes.2014.07.003.

[22] N. Arslanoglu and A. Yigit, "Investigation of efficient parameters on optimum insulation thickness based on theoretical-Taguchi combined method," *Environ. Prog. Sustain. Energy*, vol. 36, no. 6, pp. 1824–1831, Nov. 2017, doi: 10.1002/ep.12628.

[23] B. E. Yuce, P. V. Nielsen, and P. Wargocki, "The use of Taguchi, ANOVA, and GRA methods to optimize CFD analyses of ventilation performance in buildings," *Build. Environ.*, vol. 225, p. 109587, Nov. 2022, doi: 10.1016/j.buildenv.2022.109587.

[24] C. Vidal, V. Infante, P. Peças, and P. Vilaça, "Application of Taguchi Method in the Optimization of Friction Stir Welding Parameters of an Aeronautic Aluminium Alloy," *Int. J. Adv. Mater. Manuf. Charact.*, vol. 3, no. 1, pp. 21–26, Mar. 2013, doi: 10.11127/ijammc.2013.02.005.

Bitlis Eren Üniversitesi Fen Bilimleri Dergisi
BİTLİS EREN UNIVERSITY JOURNAL OF SCIENCE
ISSN: 2147-3129/e-ISSN: 2147-3188
VOLUME: 12 NO: 1 PAGE: 207-214 YEAR: 2023
DOI:10.17798/bitlisfen.1223614

Determination of the effectiveness of carbons obtained from the co-carbonization of duckweed and waste coffee on crystal violet removal

Mikail Olam[1*]

[1]Mechanical Engineering Department, Firat University, Elazig, Turkey

(ORCID:0000-0002-4153-1612)

Keywords: duckweed, waste coffee, carbonization, adsorption, crystal violet..

Abstract

With the development of industry, the rate of industrial dyes in municipal wastewater is increasing day by day. The use of environmentally friendly, economical and highly efficient adsorbents for their removal has recently gained importance. In this study, crystal violet (CV) in wastewater was removed by carbonizing waste coffee (wC) and duckweed (DW) formed on the surface of municipal wastewater treatment plant pools. DW and wC samples were carbonized together and separately at N_2 of 100 mL/min and 800 °C in a tubular reactor for 90 minutes. Adsorption experimental studies were performed at adsorbent amount of 0.5 g, 6 pH, temperature of 30 °C, initial concentration of 50-100 mg/L and contact time of 60 min. SEM and FTIR analyzes were performed for the characterization of the adsorbents. In XRD analysis, wC and carbonized wC (cwC) were amorphous, and co-carbonized wC and DW (cDW/wC) was semi-crystalline. The most effective adsorbent for CV dye removal from wastewater is DW/wC. Its adsorption capacity was 8.29 mg/L, and its CV removal was 83%.

1. Introduction

Activated carbons, which have a high surface area, can be produced from many sources such as biomass and waste plastics [1], [2]. They are used as separation/purification of gases and liquids, removal of toxic substances, catalyst/catalyst support, supercapacitor and electrode [3]-[6]. Generally, activated carbon is obtained from biomass/wastes in an inert gas (N_2, etc.) environment at a temperature of 400-1000 °C in a process time of 30-90 minutes [7]-[10]. Subsequently, the resulting carbons can increase the physical/chemical activation process surface areas and surface activity [11]. After the carbonization process of a biomass, many micro, meso and macro pores are formed in its structures [12], [13]. If physical or chemical activation is not performed before/after the carbonization process, micropores will not form significantly [14], [15]. In this study, activated carbons were produced from duckweed (DW) which is grown on the surfaces of biological treatmen[1]t ponds in municipal wastewater treatment plants and disposed as a waste, and waste coffee (wC) resulting from the use of filter coffee. DW and wC were carbonized both together and separately, and their effectiveness on the removal of crystal violet (CV) in wastewater was investigated. Chemical formula of CV is $C_{25}H_{30}N_3Cl$, its molecular weight is 407.98 g mol^{-1}.

Duckweed (DW) is a fast-growing biomass in ponds and stagnant freshwater sources of municipal wastewater biological treatment plants [16], [17]. Due to the potential of this biomass source, there are many studies on biofuel production and activated carbon. It contains approximately 47% carbon (C) , 47% oxygen (O), 6% hydrogen (H) and 1% other ingredient [18], [19]. Coffee, one of the most consumed beverages, its cone contains 55% C, 7% H, 35% O, 3% N+S [20], [21]. Activated carbon was produced from these carbon-rich wastes.

The efficacy of the produced activated carbons was determined by removing crystal violet (CV), a cationic dye used in the paint industry [22].

[1]Corresponding author: mikailolam@gmail.com

Received: 23.12.2022, Accepted: 23.02.2023

The cationic dyes are more harmful than anionic dyes as they easily interact with cell membrane surfaces and can be concentrated in the cytoplasm inside the cell [23], [24]. In addition, CV is widely used in applications such as medicinal solutions, animal feeds [25]. However, as a result of these applications, its discharge into the seas and lakes through municipal wastewater is considered a biological life-threatening substance, as it is a strong carcinogen and allows tumor growth [26], [27]. Therefore, the removal of CV from wastewater is very important in terms of environment and biological life.

2. Material and Method

DWs, which are genus lemne minor, were obtained from the municipal wastewater treatment plant in Malatya, Turkey. wCs were collected and used as a result of the use of Nestle brand filter coffee. DWs and wCs were ground to 0.1-0.25 mm after drying at room temperature (25 °C, 1 atm). In ultimate analysis of wC, it contains 48% C, 6% H, 0.3% N and 45.7% O. The O was calculated from difference. The samples were carbonized in N_2 (100 mL/min) medium for 90 min at 800 °C in a tubular reactor. The resulting products were used in experimental studies on subjects in an airtight glass tube. In experimental studies, crystal violet (Carlo Erba, C.I.: 42555, Cas No: 548-62-9, purity: 99%) was used as absorbate. CV solution was prepared by dissolving 1000 mg/L in distilled water and used in adsorption experiments.

The amount of CV adsorbed (adsorption capacity, qe) and the removal percentage of CV (Removal %) were calculated by applying the Eqs. (1) and (2), respectively.

$$q_e = \frac{Co-Ce}{m} \text{ x } V \qquad (1)$$

$$Removal\ (\%) = \frac{Co-Ce}{Co} \text{ x } 100 \qquad (2)$$

Where, qe is the amount of CV adsorbed per gram of activated carbon (mg/g). Ce is the concentration (mg/L) of non-adsorbed CV in solution. Co is the initial concentration of CV (mg/L). m is the amount of activated carbon (g). V is the volume (L) of the CV solution.

3. Results and Discussion

3.1. Characterization of adsorbent

Activated carbons obtained from carbonization of wC, DW and the DW/wC were analyzed by SEM (LEO-EVO 40) for natural, pre-adsorption and post-adsorption characterization. Adsorption experiments were analyzed in Thermo Electron Corporation Evolution 500 UV device at maximum CV wavelength (λ_{max}=590 nm). Quantitative determinations of DW before and after carbonization were made with FTIR (PerkinElmer Spectrum One) device with 128 scans, 2 cm^{-1} resolution and 4000-650 cm^{-1} spectrum range. SEM analyzes of DW before and after carbonization are given in Figure 1. SEM analyzes of wC before and after carbonization are given in Figure 2. SEM analyzes of DW and wC after co-carbonization and after adsorption are given in Figure 3. As seen in Figure 1a, there were no porous structures in the surface morphology of DW before carbonization, while porous structures were observed after carbonization (Figure 1b). Similarly, as seen in Figure 2a, it was observed that wC did not have porous structures before carbonization, but these pores were formed after carbonization (Figure 2b). As seen in Figure 3a, porous structures were formed in the surface morphology of DW and wC after carbonization together. These pores were more than DW (Fig. 1b) and wC (Fig. 2b). Similarly, Li et al. showed that more microporous, mesoporous and macroporous structures were formed after coal and poplar bark biomass co-carbonization treatment than alone [28]. As seen in Figure 1-3, it can be said that mostly meso and macropores are formed after carbonization.

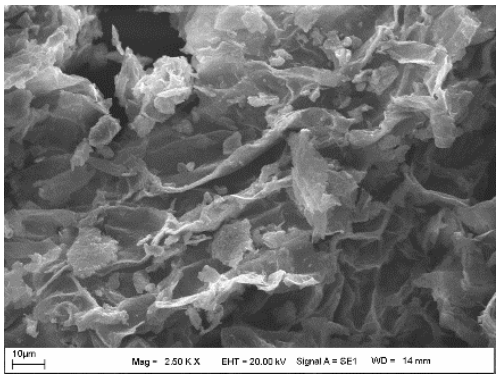

a) before carbonization

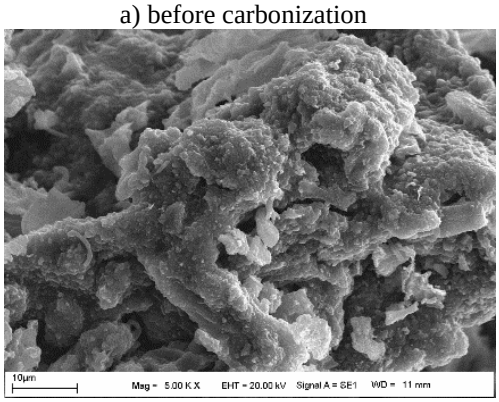

b) after carbonization

Figure 1: SEM image of DW

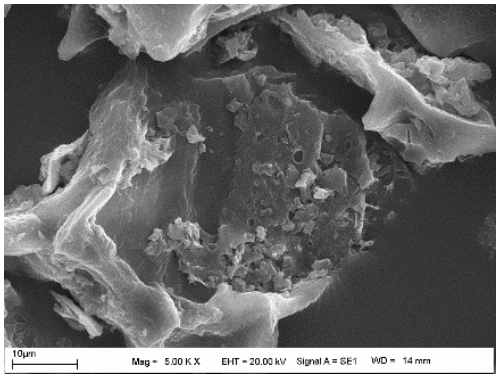

a) before carbonization

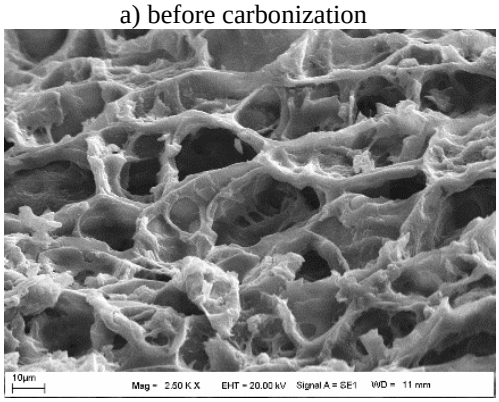

b) after carbonization

Figure 2: SEM image of wC

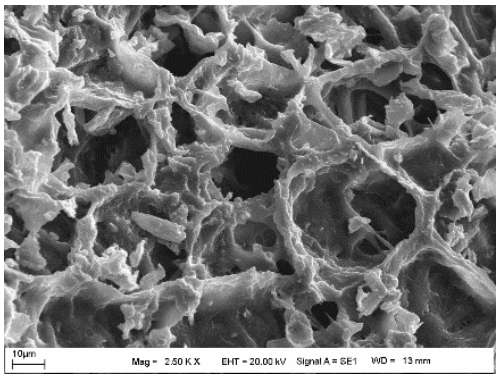

a) after carbonization

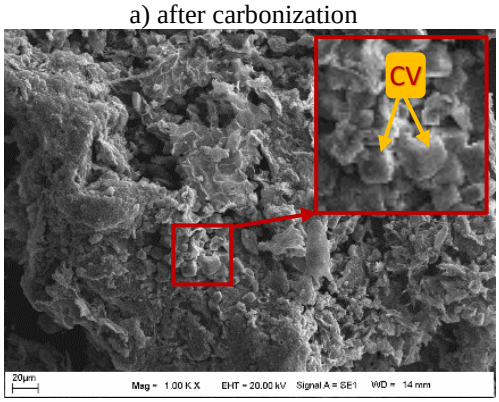

b) after adsorption

Figure 3: SEM image of the DW/wC

In the FTIR analysis of natural wC given in Figure 4, the main peaks occurred 3786 cm^{-1}, 3659 cm^{-1}, 2917 cm^{-1}, 2853 cm^{-1}, 1739 cm^{-1} and 1025 cm^{-1}. They related to O-H stretch at 3780 cm^{-1} and 3652 cm^{-1}, and C-H stretching at 2917 cm^{-1} and 2863 cm^{-1}, C-O-C stretching at 1025 cm^{-1}, and C-H deformation vibration at 1376 cm^{-1}, and C-OH band at 1151 cm^{-1} [29], [30]. The C-O-C stretch of wC at 1025 cm^{-1} indicate the presence of cellulosic and semi-cellulosic structures [31], [32]. The presence of 2917 cm^{-1} and 2853 cm^{-1} peaks indicates asymmetric and symmetrical stretching of the C-H bonds in the aliphatic chains of wC [33]. In other words, it shows the presence of methyl and methylene groups in wC [34]. The band of wC at 1739 cm^{-1} depends on the carbonyl (C=O) vibration associated with the ester group in triglycerides [35]. These bands almost all disappeared after carbonization (cwC). Briefly, no functional group was almost observed because of high carbon content of the cwC. Because the absence of bands caused by stretch and vibrations containing hydrogen (H) and oxygen (O) is an indication of high rates of carbonization, and this may result in the absence of FTIR spectrums [36]. When FTIR analysis was examined in DW and wC co-carbonization (cDW/wC), 3786 cm^{-1}, 3659 cm^{-1}, 2308 cm^{-1}, 1376 $cm^{-1}$and 1000 cm^{-1} peaks were dominant. The cDW/wC shows the presence of 3786

cm^{-1} and 3659 cm^{-1} O-H groups of the adsorbent, and peaks in the range of 1300-1000 cm^{-1} indicate the presence of C-O groups, and a peak of 1376 cm^{-1} indicates O-H bending vibrations [37], [38]. The peak at 2308 cm^{-1} represents the presence of ketone groups (C=O stretches) [39].

In the XRD analysis of wC, the formation of a 23° broad diffraction peak and the absence of any prominent diffraction peaks indicated that its structure was amorphous (Figure 5). It was observed that the structure of wC (cwC) did not change after carbonization. However, a broad diffraction peak occurred at 2θ =10°, indicative of the presence of graphene oxides formed in disordered microcrystalline structures [40]. In co-carbonization of DW and wC (cDW/wC), broad diffraction peaks and intensity decreased at 10° and 23° diffusion. However, they appeared peaks at 28°, 31°, 40°, 44° and 50°. In the XRD phase analysis of the cDW/wC, the diffraction peaks of KCl, CaS and Ca were indexed. These inorganic substances may have caused the formation of the crystal structure. As a result, it can be said that wC and the cwC are amorphous and the cDW/wC is semi-crystalline.

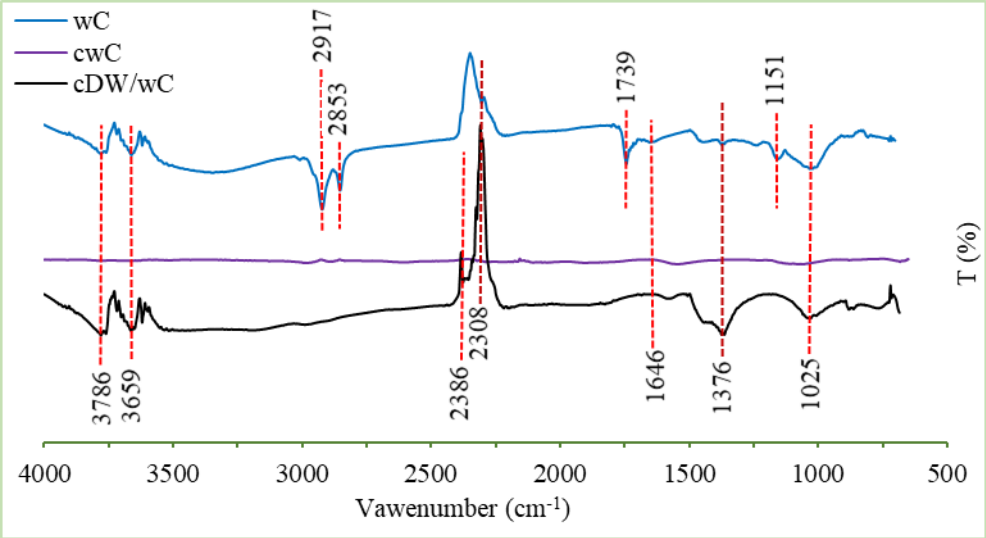

Figure 4: FTIR analysis; wC: waste coffee, cwC: carbonized waste coffee, cDW/wC: carbonized duckweed and waste coffee

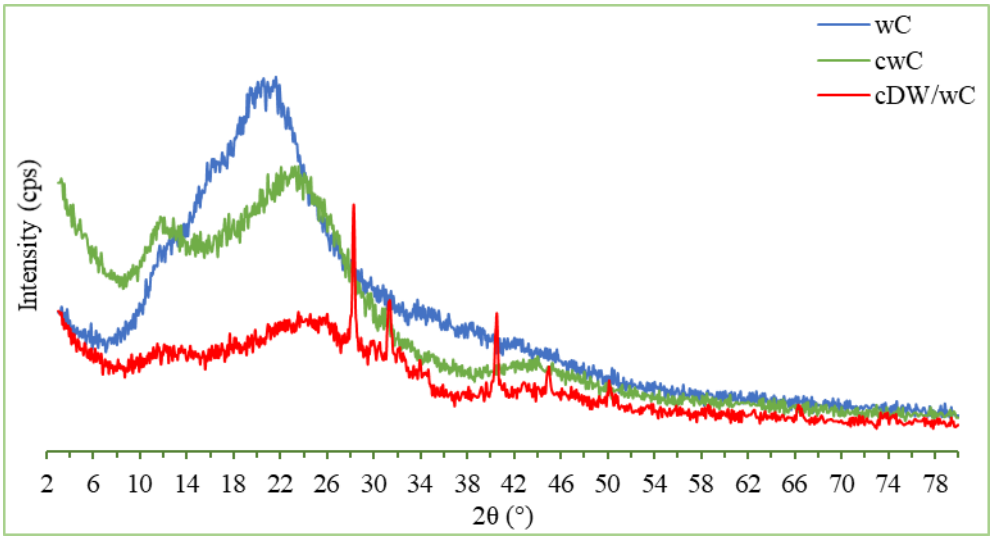

Figure 5: XRD analysis; wC: waste coffee, cwC: carbonized waste coffee, cDW/wC: carbonized duckweed and waste coffee

3.2. Adsorption capacity of adsorbent

The removal (%) values of crystal violet dye in wastewater of activated carbons produced from DW, wC and their mixtures are given in Table 1. Adsorption experimental studies were performed at adsorbent amount of 0.5 g, 6 pH, temperature of 30 °C, initial concentration of 50-100 mg/L and contact time of 60 min. As shown in the SEM analysis in Figure 3b of activated carbons obtained as a result of the co-carbonization of DW and wC, CV dye was observed to absorb. While 25% of CV was removed with wC activated carbons (wC50) at an initial concentration of 50 mg/L, it increased to 96% with DW activated carbons (DW50). However, when the CV concentration was increased from 50 mg/L to 100% mg/L, the CV removal decreased to 70% (DW100). It can be said that it is caused when the amount of adsorbent is not sufficient for removal with the increase of the CV concentration in the solution [41]. However, the removal of CV increased by 83% when the DW/wC adsorbent (DW/wC100) was used instead of DW activated carbons (DW100). It can be said that the DW/wC has better CV removal than DW and wC.

In Figure 6, the adsorption capacity of activated carbons obtained after carbonization of wC in 50mg/L CV solution is 2.52 mg/L (wC50). The DW was 9.62 mg/L (DW50). The adsorption capacity of DW in 100 mg/L CV solution was 7.03 mg/L (DW100). Activated carbons obtained as a result of co-carbonization of DW and wC were 8.29 mg/L (DW/wC100). It can be said that the adsorption capacity of DW is better than wC (Figure 6). This is thought to be due to the differences in the functional groups in the structures of DW and wC (Figure 4). However, in the carbonization process of CV with DW, the adsorption capacity was higher than that of DW. As a result, it was observed that all the obtained adsorbents were able to remove crystal violet (CV) dye from wastewater, and the best adsorbent was the DW/wC.

Table 1: Removal of CV

Sample name	initial concentration of CV (mg/L)	Removal (%)
wC50	50	25
DW50	50	96
DW100	100	70
DW/wC100	100	83

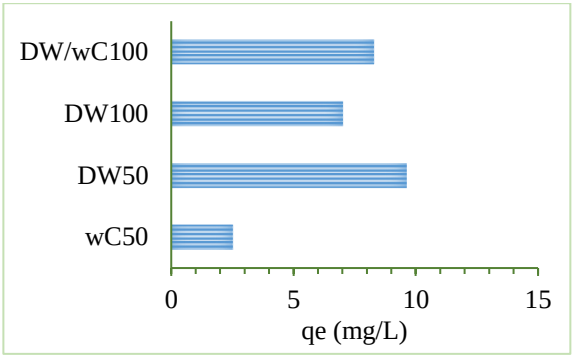

Figure 6: Adsorption capacity

4. Conclusion and Suggestions

This study investigated the effect of carbonized duckweed (DW), waste coffee (wC) and their blends on the removal of crystal violet (CV) in wastewater.

- In the FTIR analysis, the peaks of the functional groups of DW and wC changed after carbonization.
- According to SEM analyzes and adsorption studies, DW, wC and the DW/wC adsorbents removed CV dye.
- The highest adsorption capacity and CV removal were 8.29 mg/L and 83% in the co-carbonization of DW and wC, respectively.
- The lowest adsorption capacity and CV removal were 2.52 mg/L and 25% in carbonization of wC, respectively.
- According to XRD analysis, wC and the cwC are amorphous and the cDW/wC is semi-crystalline.

Adsorbents were found to be effective and inexpensive for CV dye removal in wastewater. For optimum conditions of DW/wC in CV removal, adsorption parameters need to be determined.

Conflict of Interest Statement

There is no conflict of interest between the authors.

Statement of Research and Publication Ethics

Research and publication ethics compiled within the study.

References

[1] K. Yang, J. Peng, C. Srinivasakannan, L. Zhang, H. Xia, and X. Duan, "Preparation of high surface area activated carbon from coconut shells using microwave heating," *Bioresour. Technol.*, vol. 101, no. 15, pp. 6163–6169, Aug. 2010, doi: 10.1016/J.BIORTECH.2010.03.001.

[2] M. Olam, "Production of Activated Carbon from Waste PET' Chars," *Int. J. Environ. Monit. Anal.*, vol. 10, no. 2, p. 39, 2022, doi: 10.11648/j.ijema.20221002.13.

[3] H. Oda and Y. Nakagawa, "Removal of ionic substances from dilute solution using activated carbon electrodes," *Carbon N. Y.*, vol. 41, no. 5, pp. 1037–1047, Jan. 2003, doi: 10.1016/S0008-6223(03)00013-7.

[4] A. Yuan and Q. Zhang, "A novel hybrid manganese dioxide/activated carbon supercapacitor using lithium hydroxide electrolyte," *Electrochem. commun.*, vol. 8, no. 7, pp. 1173–1178, Jul. 2006, doi: 10.1016/J.ELECOM.2006.05.018.

[5] A. M. Fuente, G. Pulgar, F. González, C. Pesquera, and C. Blanco, "Activated carbon supported Pt catalysts: effect of support texture and metal precursor on activity of acetone hydrogenation," *Appl. Catal. A Gen.*, vol. 208, no. 1–2, pp. 35–46, Feb. 2001, doi: 10.1016/S0926-860X(00)00699-2.

[6] S. H. Moon and J. W. Shim, "A novel process for CO2/CH4 gas separation on activated carbon fibers—electric swing adsorption," *J. Colloid Interface Sci.*, vol. 298, no. 2, pp. 523–528, Jun. 2006, doi: 10.1016/J.JCIS.2005.12.052.

[7] R. Baccar, M. Sarrà, J. Bouzid, M. Feki, and P. Blánquez, "Removal of pharmaceutical compounds by activated carbon prepared from agricultural by-product," *Chem. Eng. J.*, vol. 211–212, pp. 310–317, Nov. 2012, doi: 10.1016/J.CEJ.2012.09.099.

[8] O. Ioannidou and A. Zabaniotou, "Agricultural residues as precursors for activated carbon production—A review," *Renew. Sustain. Energy Rev.*, vol. 11, no. 9, pp. 1966–2005, Dec. 2007, doi: 10.1016/j.rser.2006.03.013.

[9] H. Haykiri-Acma, S. Yaman, and S. Kucukbayrak, "Gasification of biomass chars in steam–nitrogen mixture," *Energy Convers. Manag.*, vol. 47, no. 7–8, pp. 1004–1013, May 2006, doi: 10.1016/J.ENCONMAN.2005.06.003.

[10] M. Ahmedna, W. E. Marshall, and R. M. Rao, "Production of granular activated carbons from select agricultural by-products and evaluation of their physical, chemical and adsorption properties," *Bioresour. Technol.*, vol. 71, no. 2, pp. 113–123, Jan. 2000, doi: 10.1016/S0960-8524(99)00070-X.

[11] J. A. Maciá-Agulló, B. C. Moore, D. Cazorla-Amorós, and A. Linares-Solano, "Activation of coal tar pitch carbon fibres: Physical activation vs. chemical activation," *Carbon N. Y.*, vol. 42, no. 7, pp. 1367–1370, Jan. 2004, doi: 10.1016/J.CARBON.2004.01.013.

[12] A. Khamkeaw, T. Asavamongkolkul, T. Perngyai, B. Jongsomjit, and M. Phisalaphong, "Interconnected Micro, Meso, and Macro Porous Activated Carbon from Bacterial Nanocellulose for Superior Adsorption Properties and Effective Catalytic Performance," *Mol. 2020, Vol. 25, Page 4063*, vol. 25, no. 18, p. 4063, Sep. 2020, doi: 10.3390/MOLECULES25184063.

[13] Z. Hu and M. P. Srinivasan, "Mesoporous high-surface-area activated carbon," *Microporous Mesoporous Mater.*, vol. 43, no. 3, pp. 267–275, May 2001, doi: 10.1016/S1387-1811(00)00355-3.

[14] F. Caturla, M. Molina-Sabio, and F. Rodríguez-Reinoso, "Preparation of activated carbon by chemical activation with ZnCl2," *Carbon N. Y.*, vol. 29, no. 7, pp. 999–1007, Jan. 1991, doi: 10.1016/0008-6223(91)90179-M.

[15] P. Paraskeva, D. Kalderis, and E. Diamadopoulos, "Production of activated carbon from agricultural by-products," *J. Chem. Technol. Biotechnol.*, vol. 83, no. 5, pp. 581–592, May 2008, doi: 10.1002/JCTB.1847.

[16] J. Xu, H. Zhao, A. M. Stomp, and J. J. Cheng, "The production of duckweed as a source of biofuels," *Biofuels*, vol. 3, no. 5. Future Science LtdLondon, UK, pp. 589–601, Sep. 09, 2012. doi: 10.4155/bfs.12.31.

[17] J. Vymazal, "Constructed Wetlands, Surface Flow," in *Encyclopedia of Ecology*, Elsevier, 2008, pp. 765–776. doi: 10.1016/B978-008045405-4.00079-3.

[18] D. Yadav, L. Barbora, D. Bora, S. Mitra, L. Rangan, and P. Mahanta, "An assessment of duckweed as a potential lignocellulosic feedstock for biogas production," *Int. Biodeterior. Biodegradation*, vol. 119, pp. 253–259, Apr. 2017, doi: 10.1016/j.ibiod.2016.09.007.

[19] C. Wang and Q. Lin, "The investigation on combustion behavior of sewage sludge and duckweed blends," in *IOP Conference Series: Earth and Environmental Science*, Dec. 2020, vol. 605, no. 1, p. 012026. doi: 10.1088/1755-1315/605/1/012026.

[20] X. Li, V. Strezov, and T. Kan, "Energy recovery potential analysis of spent coffee grounds pyrolysis products," *J. Anal. Appl. Pyrolysis*, vol. 110, no. 1, pp. 79–87, Nov. 2014, doi: 10.1016/J.JAAP.2014.08.012.

[21] C. L. Mendoza Martinez *et al.*, "Characterization of residual biomasses from the coffee production chain and assessment the potential for energy purposes," *Biomass and Bioenergy*, vol. 120, pp. 68–76, Jan. 2019, doi: 10.1016/J.BIOMBIOE.2018.11.003.

[22] B. K. Nandi, A. Goswami, A. K. Das, B. Mondal, and M. K. Purkait, "Kinetic and equilibrium studies on the adsorption of crystal violet dye using Kaolin as an adsorbent," *Sep. Sci. Technol.*, vol. 43, no. 6, pp. 1382–1403, Jan. 2008, doi: 10.1080/01496390701885331.

[23] O. J. Hao, H. Kim, and P. C. Chiang, "Decolorization of wastewater," *Critical Reviews in Environmental Science and Technology*, vol. 30, no. 4. TAYLOR & FRANCIS, pp. 449–505, 2000. doi: 10.1080/10643380091184237.

[24] K. P. Singh, S. Gupta, A. K. Singh, and S. Sinha, "Optimizing adsorption of crystal violet dye from water by magnetic nanocomposite using response surface modeling approach," *J. Hazard. Mater.*, vol. 186, no. 2–3, pp. 1462–1473, Feb. 2011, doi: 10.1016/j.jhazmat.2010.12.032.

[25] E. ADAMS, "The antibacterial action of crystal violet*," *J. Pharm. Pharmacol.*, vol. 19, no. 12, pp. 821–826, Dec. 1967, doi: 10.1111/J.2042-7158.1967.TB09550.X.

[26] S. Gülcemal and B. Çetinkaya, "Palladium-EDTA and palladium-EdteH4 catalyzed Heck coupling reactions in pure water," *Turkish J. Chem.*, vol. 37, no. 5, pp. 840–847, Mar. 2013, doi: 10.3906/kim-1304-12.

[27] S. Mani and R. N. Bharagava, "Exposure to crystal violet, its toxic, genotoxic and carcinogenic effects on environment and its degradation and detoxification for environmental safety," *Rev. Environ. Contam. Toxicol.*, vol. 237, pp. 71–104, 2016, doi: 10.1007/978-3-319-23573-8_4.

[28] Y. Li, L. Lu, S. Lyu, H. Xu, X. Ren, and Y. A. Levendis, "Activated coke preparation by physical activation of coal and biomass co-carbonized chars," *J. Anal. Appl. Pyrolysis*, vol. 156, p. 105137, Jun. 2021, doi: 10.1016/J.JAAP.2021.105137.

[29] R. Osama, H. M. Awad, M. G. Ibrahim, and A. Tawfik, "Mechanistic and economic assessment of polyester wastewater treatment via baffled duckweed pond," *J. Water Process Eng.*, vol. 35, p. 101179, Jun. 2020, doi: 10.1016/J.JWPE.2020.101179.

[30] C. Valencia, C. Valencia, F. Zuluaga, M. Valencia, J. Mina, and C. Grande-Tovar, "Synthesis and Application of Scaffolds of Chitosan-Graphene Oxide by the Freeze-Drying Method for Tissue Regeneration," *Molecules*, vol. 23, no. 10, p. 2651, Oct. 2018, doi: 10.3390/molecules23102651.

[31] R. Gusain and S. Suthar, "Potential of aquatic weeds (Lemna gibba, Lemna minor, Pistia stratiotes and Eichhornia sp.) in biofuel production," *Process Saf. Environ. Prot.*, vol. 109, pp. 233–241, Jul. 2017, doi: 10.1016/J.PSEP.2017.03.030.

[32] J. Varshosaz, F. Hassanzadeh, H. Sadeghi Aliabadi, M. Nayebsadrian, M. Banitalebi, and M. Rostami, "Synthesis and characterization of folate-targeted dextran/retinoic acid micelles for doxorubicin delivery in acute leukemia," *Biomed Res. Int.*, vol. 2014, 2014, doi: 10.1155/2014/525684.

[33] D. Pujol *et al.*, "The chemical composition of exhausted coffee waste," *Ind. Crops Prod.*, vol. 50, pp. 423–429, Oct. 2013, doi: 10.1016/J.INDCROP.2013.07.056.

[34] A. P. Craig, A. S. Franca, and L. S. Oliveira, "Discrimination between defective and non-defective roasted coffees by diffuse reflectance infrared Fourier transform spectroscopy," *LWT*, vol. 47, no. 2, pp. 505–511, 2012, doi: 10.1016/J.LWT.2012.02.016.

[35] A. P. Craig, A. S. Franca, and L. S. Oliveira, "Evaluation of the potential of FTIR and chemometrics for separation between defective and non-defective coffees," *Food Chem.*, vol. 132, no. 3, pp. 1368–1374, Jun. 2012, doi: 10.1016/J.FOODCHEM.2011.11.121.

[36] Y. Chen, C. Zou, M. Mastalerz, S. Hu, C. Gasaway, and X. Tao, "Applications of Micro-Fourier Transform Infrared Spectroscopy (FTIR) in the Geological Sciences—A Review," *Int. J. Mol. Sci. 2015, Vol. 16, Pages 30223-30250*, vol. 16, no. 12, pp. 30223–30250, Dec. 2015, doi: 10.3390/IJMS161226227.

[37] A. N. A. El-Hendawy, "Variation in the FTIR spectra of a biomass under impregnation, carbonization and oxidation conditions," *J. Anal. Appl. Pyrolysis*, vol. 75, no. 2, pp. 159–166, Mar. 2006, doi: 10.1016/J.JAAP.2005.05.004.

[38] D. Mohan, A. Sarswat, V. K. Singh, M. Alexandre-Franco, and C. U. Pittman, "Development of magnetic activated carbon from almond shells for trinitrophenol removal from water," *Chem. Eng. J.*, vol. 172, no. 2–3, pp. 1111–1125, Aug. 2011, doi: 10.1016/J.CEJ.2011.06.054.

[39] H. ShamsiJazeyi and T. Kaghazchi, "Investigation of nitric acid treatment of activated carbon for enhanced aqueous mercury removal," *J. Ind. Eng. Chem.*, vol. 16, no. 5, pp. 852–858, Sep. 2010, doi: 10.1016/j.jiec.2010.03.012.

[40] Q. T. Ain, S. H. Haq, A. Alshammari, M. A. Al-Mutlaq, and M. N. Anjum, "The systemic effect of PEG-nGO-induced oxidative stress in vivo in a rodent model," *Beilstein J. Nanotechnol.*, vol. 10, pp. 901–911, Apr. 2019, doi: 10.3762/BJNANO.10.91.

[41] R. Goswami and A. Kumar Dey, "Synthesis and application of treated activated carbon for cationic dye removal from modelled aqueous solution," *Arab. J. Chem.*, vol. 15, no. 11, p. 104290, Nov. 2022, doi: 10.1016/J.ARABJC.2022.104290.

Bitlis Eren Üniversitesi Fen Bilimleri Dergisi
BİTLİS EREN UNIVERSITY JOURNAL OF SCIENCE
ISSN: 2147-3129/e-ISSN: 2147-3188
VOLUME: 12 NO: 1 PAGE: 215-225 YEAR: 2023
DOI:10.17798/bitlisfen.1225312

An Image Compression Method Based on Subspace and Downsampling

Serkan KESER[1*]

[1]*Kirsehir Ahi Evran University, Department of Electrical and Electronics Engineering, Kirsehir 40100, Turkey*

(ORCID: 0000-0001-8435-0507)

Keywords: Image compression, Downsampling, Transform coefficient matrix, KLT

Abstract

This study proposes a new Karhunen-Loeve transform-based algorithm with acceptable computational complexity for lossy image compression. The proposed study includes a simple algorithm using downsampling and KLT. This algorithm is based on an autocorrelation matrix found by clustering the highly correlated image rows obtained by applying downsampling to an image. The KLT is applied to the blocks of the downsampled image using the eigenvector matrix of the autocorrelation matrix, and the transform coefficient matrix is obtained. One of the important features of the proposed method (PM) is sufficient for a test image to have one transform matrix with low dimensional. The PM was compared with JPEG, BPG, and JPEG2000 compression methods for the Peak signal-to-noise ratio- Human Visual System (PSNR-HVS) and the Structural Similarity Index Measure (SSIM) metrics. The mean PSNR-HVS values of the PM, JPEG, JPEG2000, and BPG were 37.44, 37.16, 37.45, and 39.14, respectively, and their mean SSIM values were 0.95, 0.93, 0.952, and 0.962, respectively. It has been observed that the PM generally gives better results than other methods for images containing low-frequency components at high compression ratios. As a result, PM can be used to compress images, especially those containing low-frequency components.

1. Introduction

Transform encoding is often used to code an image. The purpose of transform coding is to represent the image with fewer data without degrading the quality of the image too much. [1]. Furthermore, transform coding-based image compression applications require low calculation costs. Transform coding is a popular approach to signal compression by compacting the signal's energy to fewer coefficients, enabling the signal's representation with as few bits as possible [2-4]. Various transforms have been applied to signal and image compression, including classical transforms like Discrete Fourier Transform (DFT), Walsh-Hadamard Transform (WHT), Discrete Cosine Transform (DCT), Wavelet Transform (WT), and Karhunen Loeve Transform (KLT). Some of these studies are used in the health areas [5-7]. Thus, large-scale data can be compressed and converted into smaller-sized data in these areas, and faster analysis can be performed. A wavelet-based algorithm is proposed for satellite image compression in [8]. Digital image compression using the Walsh Hadamard transform is performed in [9]. An image compression algorithm for the predictor of JPEG-LS has been used in [10]. In another paper [11], the author explains the JPEG2000 working structure comprehensively with examples, and the authors analyze wavelet transform and give a detailed introduction to Wavelet Toolbox software [12].

Usually, transform coding-based compression methods are preferred for lossy compression cases. DCT- and Wavelet Transform-based methods are widely used for image compression. DCT is the most popular transform in JPEG-based methods [13,14], and WT also became

* Corresponding author:skeser@ahievran@edu.tr
Received: 27.12.2022, Accepted: 02.03.2023

popular with JPEG2000 [15-17]. The Better Portable Graphics (BPG) is a state-of-the-art image compression format for coding digital images, and it is a new image format. Its main advantages are high compression rate, compression much more than JPEG for similar quality, and a subset of the High-Efficiency Video Coding (HEVC) open video compression standard [18-20]. The HEVC standard is a newly designed video compressor [21]. It has also been developed in a new format, such as AV1, that performs effective video compression [22]. When the image compression methods, including downsampling and upsampling in the literature, are examined, it is seen that downsampling is performed on the encoder side and upsampling on the decoder side. These studies have shown that images can be compressed using image coding standards (JPEG, JPEG2000) at low bit rates [23-29].

Bruckstein et al. [23] show how downsampling an image at low bit rates is applied, and the overall PSNR performance using the JPEG standard is improved. In [24], the authors first filtered the image with an all-phase DCT filter and then compressed it using JPEG. Another similar method is designed as an interpolation-dependent image downsampling method [25]. In another study, researchers have presented an image coding method based on random downsampling and compressive sensing image recovery method [26]. In [27], a novel perceptual image coding scheme is proposed via adaptive block-based super-resolution directed downsampling. However, the algorithms mentioned above are only applied to low-bit-rate image compression since their performance would degrade with the increasing coding bit rate [27]. In [28], an adaptive downsampling method is developed to solve this problem. This method is developed to be compared with standard compression methods at all bit rates, unlike these studies in [25] and [26]. The same idea improves video compression performance at low bit rates [29]. If the signal is well-correlated, most of the signal's energy can be compressed into a few transform coefficients by applying KLT. Although KLT (or PCA) is the most efficient orthogonal transform in energy compression and decorrelation, it was not used for real compression applications due to its signal-dependent nature [30]. However, with the increasing computational power of communication systems and computers, signal-specific methods (such as KLT-based compression algorithms) can be applied for real image compression applications using intelligent techniques [30-34].

In [30], their method first spectrally decorrelates the image using Vector Quantization and Principal Component Analysis (PCA) and then applies the JPEG2000 algorithm to the Principal Components (PCs) exploiting spatial correlations for compression. A method proposed for image compression with PCA blocks of images is trained using a Generalized Hebbian Algorithm (GHA), and then eigenvectors are estimated [31]. Another study selected Eigen images with maximum energy for face image compression with PCA [32]. PCA and Wavelet Difference Reduction (WDR) coding-based techniques have been proposed in another method, which combines PCA and Wavelet Difference Reduction (WDR)-based approaches to achieve a high compression ratio while maintaining the perceptual quality of the image [33]. This study obtained better results than JPEG2000 at high compression rates with the WDR and PCA methods. Another paper proposes an adaptive image transformation (AIT) approach for a group of image blocks that derives transformation kernels from KLT [34]. This study emphasizes that the obtained results are better than JPEG, especially at low compression ratios. In addition, a lossy image compression architecture utilizes the advantages of a convolutional autoencoder (CAE) to achieve a high coding efficiency [35]. In this paper, to generate a more energy-compact representation, they use the principal components analysis (PCA) to rotate the feature maps produced by the CAE and then apply the quantization and entropy coder to generate the codes.

This study developed a new KLT-based image lossy compression algorithm with a good compression performance and reasonable computational complexity. In addition, one other difference between the proposed study and the studies above is that PCA and JPEG2000, WDR, CAE, and AIT are used as hybrids in those studies. Unlike the studies mentioned above, the PM presents a simple algorithm that includes only the downsampling of images and the application of KLT. One of the biggest problems of KLT-based image compression is sending the calculated transform matrix to the decoder side. If the size of this matrix is big, then more computations and bits need to be sent. In this study, an 8x8-dimensional transform matrix is used for a test image; thus, the computational complexity and the number of bits sent have been significantly reduced. First, the image ($N \times N$) is used for two subsampling in the horizontal and vertical directions, and four sub-images ($N / 2 \times N / 2$) are obtained to increase the correlation between the rows of a test image. The rows of these four sub-images are combined, and a new image of $2N \times N/2$ size is obtained. Then, the KLT is applied to all image blocks using eigenvectors of the autocorrelation matrix

obtained from this new image's blocks. Transform (KL) coefficients are obtained using eigenvectors corresponding to the largest M eigenvalues. Next, an algorithm based on Huffman coding [36] has been applied to transform coefficient blocks. This algorithm is applied to the differences among consecutive column coefficients. Thus, if the similarity of the successive transform coefficients increases, higher compression ratios can be achieved using the proposed algorithm. In addition, the proposed algorithms can be used for the image's sizes of N×P or P×N. This paper used the PSNR-HVS and SSIM methods to find better the image quality perceived by humans [37, 38]. In experimental studies, it has been seen that better results can be obtained by using the proposed simple compression algorithm, especially for images containing low-frequency components and highly compressed images. The study is organized as follows. First, the proposed KLT-based method is introduced in section 2. In this section, the encoder, difference matrices, Huffman coding method, decoder, and the complexity of the proposed algorithm are explained, respectively. Then, experimental results and discussions are given in Section 3, and the conclusion is given in section 4.

2. Material and Method

2.1. Materials

Forty test images have been used for the experimental research of this study. The test images are grayscale with a resolution of 8 bits ranging from sizes 256×256, 300×300, 512×512, and 640×640. The images with different structures from different databases were used to see the performance of the proposed method. While some of these images are commonly used in the literature as Barbara, Cameraman, Boat, and Baboon, others consist of the Brodatz texture [41], Salzburg Texture Image Database (Stex-512) [42], and Caltech-101 image databases [43].

2.2. Methods

If the signal is well-correlated, most of the signal's energy can be compressed into a few transform coefficients by applying KLT. Firstly, KLT is applied to all image blocks using eigenvectors of the autocorrelation matrix obtained from the blocks of the new image of 2N×N/2 size. In this way, a transform matrix of only 8×8 is sent to the decoder side for a test picture. In the study, Huffman coding has been applied to the difference matrix of the transform coefficient. In experimental studies, the proposed method's PSNR-HVS and SSIM values have been compared to JPEG, JPEG2000, and BFG.

2.2.1. The Proposed Subspace Method

An 8×8-dimensional eigenvector matrix has been used in the study. M-dimensional transform coefficients are obtained using the eigenvectors corresponding to the largest M eigenvalues (M<8). Next, the difference matrix ($\boldsymbol{C_{diff}}$) is found by taking the successive differences of the transform coefficient vectors to make more compression. The proposed compression method contains the following essential parts:

(i) The difference matrices are found on the encoder side using preprocessing the image and applying KLT to the blocks. Then, obtained transform matrices are coded by using Huffman coding. Finally, the bits of the difference matrices, the eigenvector matrix (**Φ**), and the obtained average block vectors (**V**) by using DCT are sent to the decoder side.

(ii) The bits of these matrices are obtained to reconstruct the test image on the receiving side. First, all blocks are reconstructed using the generated eigenvector matrices and transform coefficients. Next, these blocks are combined, and an image of size 2N×N/2 is performed. Finally, the image (2N×N/2) is upsampled to obtain a reconstructed image of size N×N.

2.2.2. Preprocessing of the Test Images

On the encoder side, the size (N×N) of the original image is converted to a 2N×N/2-dimensional image by downsampling. Then, the image is divided into 8×N/2-dimensional blocks, and an autocorrelation matrix is found using all of them. Firstly, the image is downsampled using the mathematical expressions below, and sub-images are obtained

$$\boldsymbol{I_s} = \boldsymbol{I}(k_a, k_b) \; a=1,2 \text{ and } b=1,2, \qquad (1)$$

where $\boldsymbol{I}$ is shown test images, k_1 ($k_1 = 1,3,5,\dots,N-1$) and k_2 ($k_2 = 2,4,6,\dots,N$) represent the pixel indices of the rows and columns of images, and $\mathbf{I}_s$ represents the sub-images. Four sub-images are found as follows,

$$\boldsymbol{I_1} = \boldsymbol{I}(k_a, k_b), \qquad a=1 \text{ and } b=1,$$

$$\boldsymbol{I_2} = \boldsymbol{I}(k_a, k_b)\,, \quad \text{a=1 and b=2,}$$
$$\boldsymbol{I_3} = \boldsymbol{I}(k_a, k_b)\,, \quad \text{a=2 and b=1,}$$
$$\boldsymbol{I_4} = \boldsymbol{I}(k_a, k_b)\,, \quad \text{a=2 and b=2,}$$

i-th row of each sub-image is concatenated, and a 2N×N/2 -dimensional matrix is obtained. The 2N×N/2-dimensional image is shown in Figure 1 below.

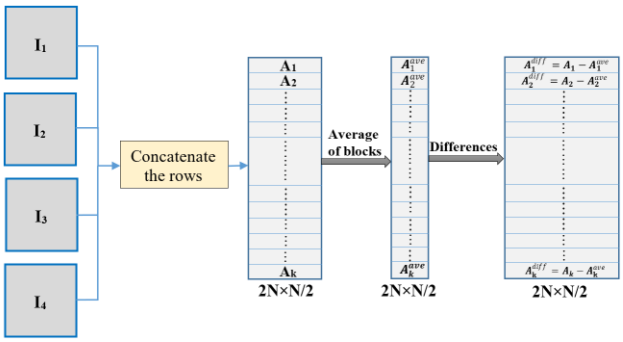

Figure 1. Obtaining a new image of size 2NxN/2 by downsampling

$$\boldsymbol{A_k} = \boldsymbol{A}(i,j), \tag{2}$$

where $\boldsymbol{A_k} \in \boldsymbol{R}^{\mathbf{8}\times\frac{N}{2}}$, *i*=1,2,…,8, *j*=1,2,…, *N*/2, *k*=1,2,…, *N*/4, indices *i* and *j* are the row and column of **A**, respectively. The total number of matrices of size *8×N/2* is *N/4*, and an average vector of 8×1 length is obtained as follows for each block ($\boldsymbol{A_k}$).

$$\boldsymbol{A_k^{ave}} = \frac{1}{\left(\frac{N}{2}\right)} \sum_{m=1}^{\frac{N}{2}} \boldsymbol{A_k}(m), \tag{3}$$

where $\boldsymbol{A_k^{ave}} \in \boldsymbol{R}^{\mathbf{8\times 1}}$, *k*=1,2,…, N/4, and *m* is the column index of $\boldsymbol{A_k}$. Then, the *k-th* mean vector ($\boldsymbol{A_k^{ave}}$) is subtracted from the *m-th* column of $\mathbf{A_k}$, and the *k-th* difference matrix $\boldsymbol{A_k^{diff}}$ is found as follows,

$$\boldsymbol{A_k^{diff}} = \boldsymbol{A_k}(m) - \boldsymbol{A_k^{ave}}, \tag{4}$$

where $\boldsymbol{A_k^{diff}} \in \mathbf{R}^{8\times\frac{N}{2}}$ and *m*=1,2,…,N/2. The autocorrelation matrices are formed by using these matrices ($\mathbf{A}^{\text{diff}}$). The autocorrelation matrix for the difference blocks is obtained as follows,

$$\mathbf{U} = \sum_{r=1}^{k} (\boldsymbol{A_r^{diff}})(\boldsymbol{A_r^{diff}})^T, \tag{5}$$

where $\mathbf{U} \in \mathbf{R}^{\mathbf{8\times 8}}$. Eigenvectors are calculated for the autocorrelation matrix ($\boldsymbol{U}$). When the eigenvalues of the autocorrelation matrix are sorted in descending order $\{\lambda_1 > \lambda_2 > \ldots > \lambda_8\}$, an eigenvector matrix, Φ, is formed by stacking the eigenvectors corresponding to **U**'s largest M eigenvalues, as shown in Equation 2.

$$\boldsymbol{\Phi} = \{\phi_1, \phi_2, \ldots, \phi_M\}, \tag{6}$$

where ϕ's are 8-dimensional eigenvectors and $\boldsymbol{\Phi} \in \mathbf{R}^{\mathbf{8\times M}}$. KLT is applied to the blocks using eigenvector and autocorrelation matrices, and transform coefficients are obtained. The *k-th* coefficient matrix ($\mathbf{Y}_k$), which is the corresponding *k-th* block, can be written as

$$\mathbf{Y}_k = \boldsymbol{\Phi}^T \boldsymbol{A}_k^{diff}, \tag{7}$$

where $\mathbf{Y}_k \in \mathbf{R}^{\mathbf{M\times N/2}}$. Then, quantization is achieved by sample–wise dividing each column in the *k-th* transform matrix ($\mathbf{Y}_k$) with the corresponding column in the quantization vector (**q**), then rounding to the nearest integer value.

$$\mathbf{C_k^{(u,v)}} = round\left(\frac{\mathbf{Y_k^{(u,v)}}}{\boldsymbol{\alpha}.\mathbf{q^{(u,v)}}}\right) \tag{8}$$

where the quantization vector ($\boldsymbol{q}$) is weighted using a scalar quantization (quality) constant ($\boldsymbol{\alpha}$). This way, the compression ratio is controlled using the scalar coefficient (α) and the selected coefficient (M) size. All the transform matrices ($\mathbf{C_k}$) obtained in Equation 8. are combined, and the matrix **C** of size $M\times N^2/8$ is obtained.

2.2.3. Transform Difference Matrix (TDM)

Subsequently, for the columns of the combined transform matrix $\boldsymbol{C}$, ($\boldsymbol{C} \in \boldsymbol{R}^{\boldsymbol{M}\times\frac{\boldsymbol{N^2}}{\mathbf{8}}}$), the *t*-th column of the $\boldsymbol{C}$ is subtracted from its *(t+1)*-th column. Thus, only the difference values are compressed and sent. This process allows fewer bits to be assigned to the elements of consecutive columns. The pseudo-code of the algorithm is as follows.

Algorithm 1: Calculating the transform difference matrix

Input: Transform matrix ($\boldsymbol{C}$)
Output: Difference matrix ($\boldsymbol{C_{diff}}$)
for t=1 **to** $N^2/8$-1 **do**
Calculate *t*-th difference column,
$\boldsymbol{C_{diff}(t) = C(t) - C(t+1)}$
end
Equalize the first column of $\boldsymbol{C_{diff}}$ to the first column of $\boldsymbol{C}$,
$\boldsymbol{C_{diff}(1) = C(1)}$

Algorithms can be developed to assign a bit less for the difference matrix $\boldsymbol{C_{diff}}$ according to matrix **C,** and thus the image can be better compressed. In experimental studies, it is seen that column vectors are generally similar to each other, especially for consecutive similar columns. The most common ones are given in Figure 2 below.

$$\begin{bmatrix} 0 & 1 & -1 & 2 & -2 & 0 & 0 \\ 0 & 0 & 0 & 0 & 0 & 1 & -1 \\ 0 & 0 & 0 & 0 & 0 & 0 & 0 \\ 0 & 0 & 0 & 0 & 0 & 0 & 0 \end{bmatrix}$$

Figure 2. Some vectors commonly encountered in difference matrices

The algorithm developed focused on similar columns mentioned above.

2.2.4. Class Bits and Average DCT Coefficients

Many bits will be assigned to each vector element. However, similar columns can be clustered, and Huffman encoding can be applied depending on the possibilities generated by the column number of each cluster. When the obtained TDM was examined, most consecutive columns had similar values. These columns are combined, and Huffman coding is applied as a vector. The same columns of the TDM are stacked using vector quantization, and clusters are obtained. The clusters with the most number of columns are sorted in descending order, $C_s=\{\boldsymbol{C_1}, \boldsymbol{C_2}, \boldsymbol{C_3}, \dots, \boldsymbol{C_m}\}$, where m is the number of clusters and $\boldsymbol{C_s} \in \boldsymbol{R^{M\times(N^2/8)}}$. Class A is created by taking the ones corresponding to the first t $(\boldsymbol{C_1}, \boldsymbol{C_2}, \boldsymbol{C_t})$. The dictionary-A is obtained by applying Huffman coding according to the number of columns in the clusters of class A. Class B is performed with the remaining clusters $(\boldsymbol{C_{t+1}}, \boldsymbol{C_{t+2}}, \dots, \boldsymbol{C_m})$. The cluster's columns of class B are combined and create the vector **V**. Finally, the dictionary-B is obtained by applying Huffman coding to the vector **V** [36]. If the *l*-th column of the TDM of a test image belongs to class A, the bits are assigned according to dictionary-A. Otherwise, the bits are set to each element in the column using dictionary-B. An additional bit assignment is used for each column vector at the encoder side. This bit represents the class of columns. If the column belongs to class B, zero bit '0' is used; otherwise, one bit '1' is used. These bits are called 'class bits'. Besides, 1D Discrete cosine transform (DCT-II) is applied for each *k-th* average vector $(\boldsymbol{A_k^{ave}})$ in the study. The size of the DCT coefficient vector is eight. This vector is given for each mean vector as follows,

$$\boldsymbol{D_k}[s] = \text{Round}\left(\sum_{n=0}^{7} 2(\boldsymbol{A_k^{ave}}[n]) \cos\left(\frac{\pi}{16} s(2n+1)\right)\right), 0 \le s < 8 \quad (9)$$

The vector $(\boldsymbol{F}=\begin{bmatrix} D_1 \\ D_2 \\ \vdots \\ D_k \end{bmatrix})$ containing the DCT coefficients is obtained by combining all the DCT vectors.

where $\mathbf{F} \in \mathbf{R^{2N\times 1}}$. Huffman coding is applied for the **F** vector. Then the bits of the dictionary and DCT coefficients are sent to the receiving side. In Figure 3, the encoder parts of the proposed method are shown for a test image.

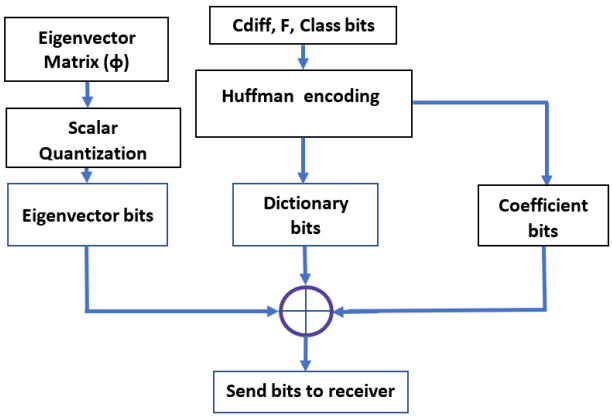

Figure 3. Block diagram of the encoder side

As can be seen from Figure 3, the transform difference matrix $\boldsymbol{(C_{diff})}$, **V,** and class bits are coded by Huffman coding. Thus, the dictionary and coefficient bits are obtained. The bits of eigenvectors, dictionaries, and coefficients are sent to the receiver side. In the encoder part, the bits of the eigenvectors' elements corresponding only to the largest *M* eigenvalues are sent to the decoder. Then, the 10-bit assignment is performed by scalar quantization for each element of the remaining eigenvectors. Eigenvectors corresponding to the largest M (M<8) eigenvalues of autocorrelation matrices are used in the study.

2.2.5. Reconstruction of the Test Images

On the decoder side, the received difference matrices, average vectors $(\widehat{\boldsymbol{A}}_k^{ave})$ dictionaries and the bits of the eigenvector matrix are decoded. Firstly, the difference matrix is obtained, then the consecutive

columns of the TDM are summed using the algorithm given below, and the transform matrix ($\boldsymbol{C}$) is found.

Algorithm 2: Calculating the transform matrix

Input: Transform matrix ($\boldsymbol{C}$)
Output: Difference matrix ($\boldsymbol{C_{diff}}$)
for t=1 **to** N/2-1 **do**
Calculate *t*-th column,
$C(t) = C_{diff}(t) + C_{diff}(t+1)$
end

The *k-th* DCT coefficients $(\widehat{\boldsymbol{D}}_k)$ are obtained by decoding the bits on the receiving side. Then, with inverse DCT, approximate *k-th* average vectors ($\widehat{\boldsymbol{A}}_k^{ave}$) are found. The *k-th* dequantized transform matrix for the image blocks becomes:

$$\widehat{\boldsymbol{Y}}_k = \boldsymbol{q}^{u,v}\boldsymbol{C}_{\boldsymbol{k}}^{\boldsymbol{u,v}},\ k=1,2,\ldots,N/4 \qquad (10)$$

where $\boldsymbol{C_k}, \widehat{\boldsymbol{Y}}_k \in \boldsymbol{R}^{\boldsymbol{M}\times\frac{\boldsymbol{N}}{\boldsymbol{2}}}$. Then, the blocks of the image are reconstructed using the eigenvector matrix. The *k-th* decompressed image block ($\widehat{\boldsymbol{I}}_{\boldsymbol{k}} \in \boldsymbol{R}^{\boldsymbol{8}\times\frac{\boldsymbol{N}}{\boldsymbol{2}}}$) is obtained by using the eigenvector matrix and dequantized transform matrix as follows,

$$\widehat{\boldsymbol{I}}_{\boldsymbol{k}} = \boldsymbol{\Phi}\widehat{\boldsymbol{Y}}_{\boldsymbol{k}} + \widehat{\boldsymbol{A}}_{\boldsymbol{k}}^{\boldsymbol{ave}}, \qquad (11)$$

these blocks are combined, and the reconstructed image ($\widehat{\boldsymbol{I}}$) of size *2N×N/2* is obtained. Then, four sub-images are performed from this image ($\widehat{\boldsymbol{I}}$). Each sub-mage is upsampled by 2, and the reconstructed image (*N×N*) is found. All of these processes are shown in Figure 4. DaC indicates Dictionary and Coefficient in Figure 4

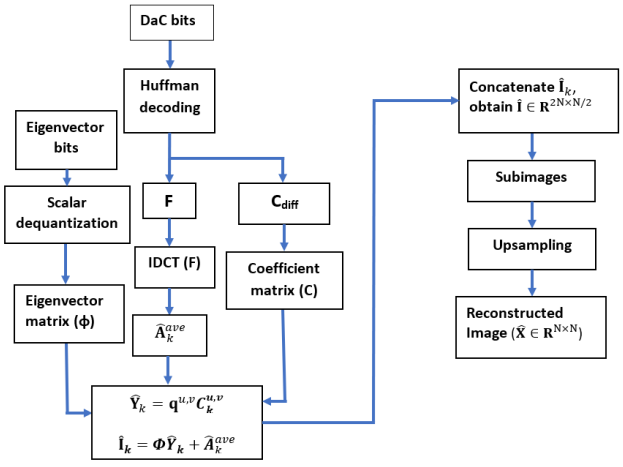

Figure 4. Block diagram of the decoder side

2.2.6. The Complexity of the Proposed Algorithm

Two critical factors in image coding are the algorithm's compression rate and execution complexity. For the proposed method's algorithm complexity, the sum of coding and decoding times per pixel of the image was measured in microseconds. It is known that JPEG has less computational cost than JPEG2000 [39]. Therefore, only the computational cost of the JPEG is compared with the proposed method in this study. Matlab codes in [40] were used for the algorithm of the JPEG standard. The proposed method (PM) was evaluated for three different compression rates (BPP) ranges. The average microseconds per pixel (ASPP) values for 40 test images are given in Table 1 below.

Table 1. The average ASPP values of PM and JPEG for three different compression ranges

BPP	PM (ASPP)	JPEG (ASPP)
(1-1.6)	29.7	10.8
(0.66-0.9)	10.2	10.6
(0.4-0.61)	5.7	10.5

As shown in Table 1, the PM has less ASPP than Jpeg, especially for BPP: (0.66-0.9). Especially at high compression rates (BPP: (0.4-0.61)), the ASPP of the PM is about half that of JPEG. However, when BPP: (1-1.6), the PM's ASPP value is approximately three times that of JPEG

3. Experimental Results and Discussion

The algorithm execution times have been obtained on a desktop PC with a 3 GHz (I5-7400) and 8 GB Ram under Windows 10. All images are individually compressed using PM, JPEG, JPEG2000, and BPG at different compression rates ranging from 0.4 bpp to 2 bpp. Some of the test images belonging to various databases are shown in Figure 5 below
The SSIM and PSNR-HVS values obtained for each image are given in Figure 6 below. Test image numbers and compression ratios of images are also shown in the columns to the right of Figure 6
Figures 6 (a) and 6 (b) show that the PSNR-HVS and SSIM values of BPG are higher than those of the PM, JPEG, and JPEG2000 for most test images. Besides, the PSNR-HVS and SSIM values of the PM are better than those of JPEG and JPEG2000 for some images. However, BPG has been the method that produces the best quality images in general for 40 test images. Images containing high-frequency components are generally low-compression images in figure 6. The proposed method for these images gave a lower performance, especially compared to JPEG2000 and

BPG. Nevertheless, the PM produced images of better or approximate quality compared to other methods for images containing low-frequency components. On the other hand, it is seen that PM gives lower PSNR-HVS values in some images with indices 6, 8, 25, 26, 27, and 35 than in other methods. When these images were examined, it was seen that they generally had high frequencies. Therefore, the average SSIM and PSNR-HVS values of four methods are given for these images in Table 2 below**.**

According to the results shown in Table 2, the BPG has the best scores in terms of average SSIM and PSNR-HVS values. Besides, the PM's SSIM and PSNR-HVS values are higher than JPEG. As a result of the study, the PM generates better scores than JPEG but worse than BPG and JPEG2000 in average SSIM and PSNR-HVS values. On the other hand, in some images, such as the test image in Figure 7, PM achieved much better results than other methods. When this image is examined, it can be seen that it has high and low frequency regions. This shows that PM can give good results in images with different frequencies. For example, a reconstructed test image found using the PM, JPEG, JPEG2000, and BPG is presented in Figure 7, respectively

Although the proposed method's average PSNR-HVS and SSIM values were lower than the BPG, its PSNR-HVS and SSIM values are significantly better than other methods for test images in Figure 7.

Some studies using PCA in the literature can compress images with better quality than JPEG2000 [30,33,35]. However, these studies used algorithms such as hybrid PCA+ JPEG2000 [30], PCA+Wavelet [33], and PCA+CAE [35]. Therefore, the computation time of these studies is longer than JPEG and JPEG2000. The proposed method, on the other hand, has less or close computation time compared to JPEG and JPEG2000, especially at high or medium compression ratios. Because it uses only a KLT-based simple compression algorithm. However, when the same images used in [33] and in this study were examined, it was seen that the study in [33] gave higher PSNR values than the PM.

3. Conclusion and Suggestions

This manuscript generates a new KLT-based method for performing lossy image compression. The main goal of this method is to provide a good compression performance at reasonable computational complexity. Unfortunately, KLT is a signal-dependent transform that disadvantages practical applications. However, this problem was overcome by using a transform (eigenvector) matrix, whose size is as small as possible. This study differs from other studies as it obtains highly correlated pixel blocks with downsampling to compress the image better. The study proposes a KLT-based image compression method applied to the merged blocks of sub-images found by downsampling. The differences among consecutive transform coefficient columns are compressed with this algorithm. It has been observed that the transform matrix used in this way gives satisfactory results. This study only uses an 8x8-dimensional transform matrix for a test image. First, the image is subsampled, and four sub-images are obtained. Next, the rows of these four sub-images are combined, and a new image of 2N×N/2 size is obtained. Then, the KLT is applied to all image blocks using eigenvectors of the autocorrelation matrix obtained from this new image's blocks. Next, transform coefficients are obtained using eigenvectors corresponding to the largest M eigenvalues. Next, Huffman coding is applied to the differences between consecutive column coefficients. In the study, test images are collected from different databases. Thus, the performance of the proposed method is examined for images with various frequency components. In the results found for the test images, the average PSNR-HVS and SSIM values of the proposed method were better than JPEG, very close to JPEG2000, and lower than BPG. The proposed method's mean PSNR-HVS and SSIM values were 37.44 and 0.950, respectively. The mean PSNR-HVS values for JPEG, JPEG2000, and BPG were 37.16, 37.45, and 39.14, respectively, and their mean SSIM values were 0.930, 0.952, and 0.962, respectively. It has been observed that the PM generally gives better results than those of the JPEG and JPEG2000 in images containing low-frequency components at high compression ratios. However, the compression performance of the PM was decreased in images containing high-frequency components at low compression ratios. The computation time of the PM is about two times less than JPEG at compression ratios between 0.4 and 0.6, and it was close to JPEG between 0.66 and 0.9. When these results are examined, it is seen that the PM gives better or close results compared to other methods, especially for images containing low-frequency components. Thus, PM can be used to compress such images

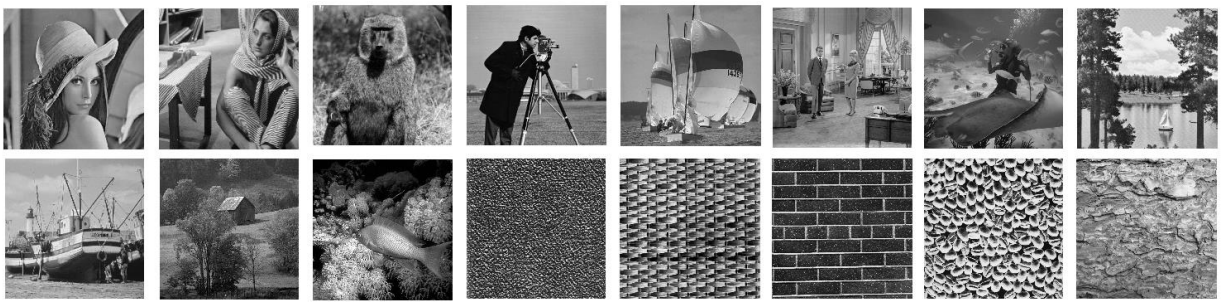

Figure 5. Some of the test images belonging to various databases

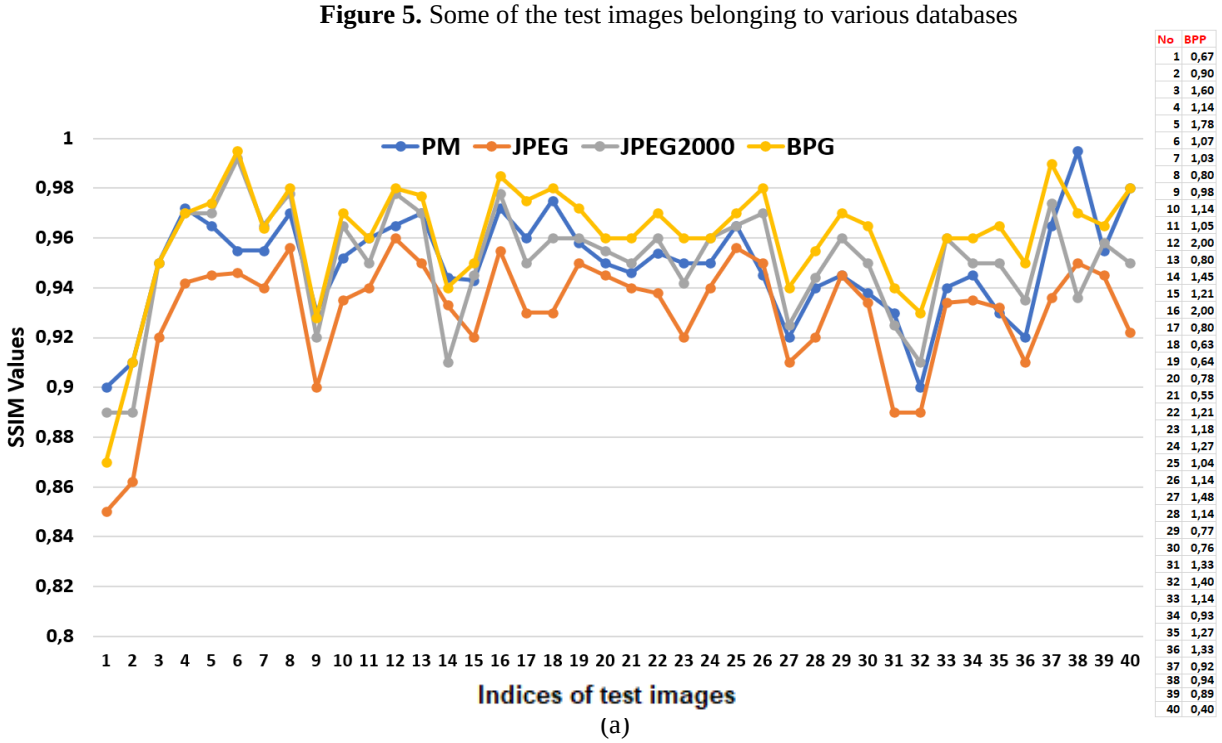

No	BPP
1	0,67
2	0,90
3	1,60
4	1,14
5	1,78
6	1,07
7	1,03
8	0,80
9	0,98
10	1,14
11	1,05
12	2,00
13	0,80
14	1,45
15	1,21
16	2,00
17	0,80
18	0,63
19	0,64
20	0,78
21	0,55
22	1,21
23	1,18
24	1,27
25	1,04
26	1,14
27	1,48
28	1,14
29	0,77
30	0,76
31	1,33
32	1,40
33	1,14
34	0,93
35	1,27
36	1,33
37	0,92
38	0,94
39	0,89
40	0,40

(a)

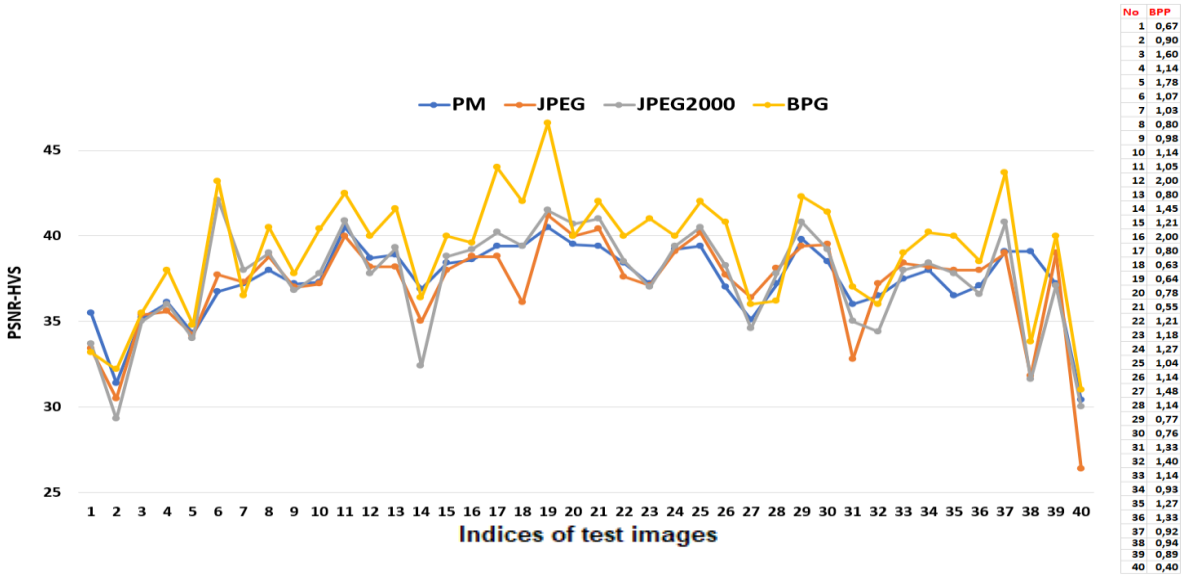

(b)

Figure 6. SSIM (a) and PSNR-HVS (b) values for PM, JPEG, JPEG2000, and BPG.

Table 2. The average SSIM and PSNR-HVS values of the methods

SSIM				PSNR-HVS			
PM	**JPEG**	**JPEG2K**	**BPG**	**PM**	**JPEG**	**JPEG2K**	**BPG**
0.950	0.930	0.952	0.962	37.44	37.16	37.45	39.14

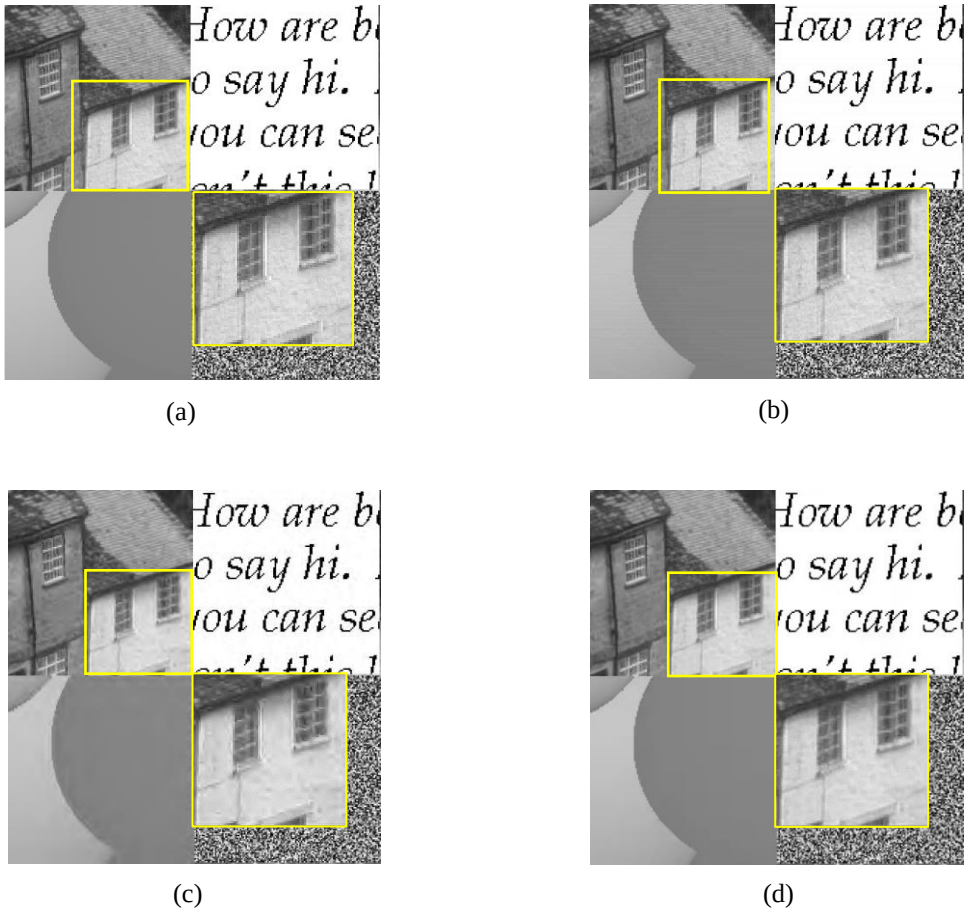

(a) (b) (c) (d)

Figure 7. The original image (a), PM (b) (SSIM: 0.99, PSNR:40, BPP: 0.94), JPEG2000 (c) (SSIM: 0.93, PSNR:29.2, BPP: 0.94), and BPG (d) (SSIM: 0.97, PSNR:33.8, BPP: 0.94)

Statement of Research and Publication Ethics

The study is complied with research and publication ethics

References

[1] Bhatt, A., Ashutosh, K. B., and Bhatt, K., "Image compression algorithms under JPEG with lapped orthogonal transform and discrete cosine transformation.", *International Journal of Engineering Research and Development, 7*(3): 6-10, 2013.

[2] Katharotiya, A., Patel, S., and Goyani, M., "Comparative Analysis between DCT & DWT Techniques of Image Compression.", *Journal of Information Engineering and Applications, 1*(2): 9-17, , 2011.

[3] Effros, M., and Chou, P. A., "Weighted universal transform coding: Universal image compression with the Karhunen-Loeve transform." In Proceedings., International Conference on Image Processing, Washington, USA, 61-64, 1995.

[4] Ahmed, N., Natarajan, T., and Rao, K. R., "Discrete cosine transform." *IEEE transactions on Computers*, 100(1): 90-93, 1974.

[5] Roy A.B., Dey D., Mohanty B. and Banerjee D., "Comparison of FFT, DCT, DWT, WHT compression techniques on electrocardiogram and photo plethysmography signals." *Special Issue of International Journal of Computer Applications* (Inte. Conf. on Computing, Communication and Sensor Network, CCSN'2012), 6-11, 2012.

[6] OH, T. H., and Besar, R., "Medical image compression using JPEG-2000 and JPEG: A comparison study". *Journal of Mechanics in Medicine and Biology*, 2(03n04), 313-328, 2002.

[7] Bharath, K. N., and Padmajadevi, G., "Hybrid compression using dwt-dct and huffman encoding techniques for biomedical image and video applications". *International Journal of Computer Science and Mobile Computing*, 2(5), 255-261, 2013.

[8] Muthukumaran, N., and Ravi, R., "The performances analysis of fast efficient lossless satellite image compression and decompression for wavelet based algorithm". *Wireless Personal Communications*, 81(2), 839-859, 2015.

[9] Ghrare, S.E., and Khobaiz, A.R. "Digital image compression using block truncation coding and Walsh Hadamard transform hybrid technique." *International Conference on Computer, Communications, and Control Technology* (I4CT), 477-480, 2014.

[10] Xie, Y., Jing, X., Sun, S., and Hong, L., "A fast and low complicated image compression algorithm for predictor of JPEG-LS.", *IEEE International Conference on Network Infrastructure and Digital Content*, Beijing, China, 353-356, 2009.

[11] Skodras, A., Christopoulos, C., Ebrahimi, T., "The JPEG 2000 still image compression standard.", *IEEE Signal processing magazine*, 18(5): 36-58, 2001.

[12] Sun, C., Li, Q., and Liu, J., "The study of Digital Image Compression based on wavelets", *International Conference on Audio, Language and Image Processing*, Shanghai, China, 312-316, 2010.

[13] M. A. Engin and B. Cavusoglu, "New Approach in Image Compression: 3D Spiral JPEG," in *IEEE Communications Letters*, vol. 15, no. 11, pp. 1234-1236, 2011.

[14] Ince, I. F., Bulut, F., Kilic, I., Yildirim, M. E., & Ince, O. F. "Low dynamic range discrete cosine transform (LDR-DCT) for high-performance JPEG image compression". *The Visual Computer*, *38*(5), 1845-1870, 2022.

[15] Shinde, A. A., and Kanjalkar, P., "The comparison of different transform based methods for ECG data compression.", *International Conference on Signal Processing, Communication, Computing and Networking Technologies*, 332-335, 2011.

[16] Telagarapu, P., Naveen, V. J., Prasanthi, A. L., and Santhi, G. V., "Image compression using DCT and wavelet transformations.", *International Journal of Signal Processing, Image Processing and Pattern Recognition*, 4(3): 61-74, 2011.

[17] Hartung, F., and Girod, B., "Watermarking of uncompressed and compressed video". *Signal processing*, 66(3): 283-301, 1998.

[18] Hofbauer, H., Rathgeb, C., Wagner, J., Uhl, A., and Busch, C., "Investigation of Better Portable Graphics Compression for Iris Biometric Recognition," *2015 International Conference of the Biometrics Special Interest Group (BIOSIG)*, Darmstadt, Germany, 1-4, 2015.

[19] F. Bellard. BPG Image format. http://http://bellard.org/bpg . Access date: 10.06.2019.

[20] YEE, David, et al. "Medical image compression based on region of interest using better portable graphics (BPG).", *IEEE international conference on systems, man, and cybernetics (SMC)*, Banff, AB, Canada, 216-221, 2017.

[21] Sullivan, G. J., Ohm, J. R., Han, W. J., and Wiegand, T., "Overview of the high efficiency video coding (HEVC) standard". *IEEE Transactions on circuits and systems for video technology*, 22(12):1649-1668, 2012.

[22] Chen, Y., Murherjee, D., Han, J., Grange, A., Xu, Y., Liu, Z., and Chiang, C. H., "An overview of core coding tools in the AV1 video codec". *In Picture Coding Symposium (PCS), IEEE*, 41-45, 2018.

[23] A. M. Bruckstein, M. Elad, and R. Kimmel, "Down-scaling for better transform compression," *IEEE Trans. Image Process*., 12(9): 1132–1144,2003.

[24] C. Y. Wang et al., "JPEG-based image coding algorithm at low bit rates with down-sampling and interpolation," in *4th Int. Conf. On Wireless Communications, Networking and Mobile Computing (WiCOM'08)*, pp. 1–5, IEEE, Dalian, 1-5, 2008.

[25] Y. B. Zhang et al., "Interpolation-dependent image downsampling,"*IEEE Trans. Image Process*. , 20(11): 3291–3296, 2011.

[26] R. Pournaghi, X. L. Wu, and X. M. Liu, "Low bit-rate image coding via local random down-sampling," in Picture Coding Symp. (PCS), *IEEE, San Jose, California*, 329–332, 2013.
[27] Chen, H., He, X., Ma, M., Qing, L., and Teng, Q., "Low bit rates image compression via adaptive block downsampling and super resolution". *Journal of Electronic Imaging*, 25(1): 013004, 2016.
[28] W. S. Lin and L. Dong, "Adaptive downsampling to improve image compression at low bit rates," *IEEE Trans. Image Process*, 15(9): 2513–2521, 2006.
[29] V. A. Nguyen, Y. P. Tan, and W. S. Lin, "Adaptive downsampling/upsampling for better video compression at low bit rate," in *IEEE Int. Symp. On Circuits and Systems*, 1624–1627, 2008.
[30] Báscones, D., González, C., and Mozos, D., "Hyperspectral image compression using vector quantization, PCA and JPEG2000". *Remote sensing*, 10(6), 907, 2018.
[31] Wang, C. W., and Jeng, J. H., "Image compression using PCA with clustering". *In 2012 International Symposium on Intelligent Signal Processing and Communications Systems IEEE*, 458-462, 2012.
[32] Liu, Y. R., and Kau, L. J., "Scalable face image compression based on Principal Component Analysis and arithmetic Coding". *In 2017 IEEE International Conference on Consumer Electronics-Taiwan (ICCE-TW), IEEE*, 265-266, 2017.
[33] Vaish, A., and Kumar, M., "WDR coding based image compression technique using PCA". *In 2015 International Conference on Signal Processing and Communication (ICSC), IEEE*,360-365, 2015.
[34] Rafael do Esprito Santo, "Principal Component Analysis applied to digital image compression", *Hospital Israelita Albert Einstein HIAE,* Sao Paulo (SP), Brazil, 2012.
[35] Cheng, Z., Sun, H., Takeuchi, M., and Katto, J., "Deep convolutional autoencoder-based lossy image compression". *In 2018 Picture Coding Symposium (PCS)*, pp. 253-257, IEEE, 2018.
[36] BULUT, F., "Huffman Algoritmasıyla Kayıpsız Hızlı Metin Sıkıştırma". *El-Cezeri Journal of Science and Engineering*, 3(2), 2016.
[37] Egiazarian, K., Astola, J., Ponomarenko, N., Lukin, V., Battisti, F., and Carli, M., "New full-reference quality metrics based on HVS." *In Proceedings of the Second International Workshop on Video Processing and Quality Metrics*, (4) , 2006.
[38] Hore, A., and Ziou, D., "Image quality metrics: PSNR vs. SSIM.", *20th international conference on pattern recognition*, Istanbul, Turkey, 2366-2369, 2010.
[39] Marcellin, M. W., Gormish, M. J., Bilgin, A., and Boliek, M. P. "An overview of JPEG-2000.", *In Proceedings DCC 2000. Data Compression Conference, Snowbird*, UT, USA, 523-541, 2000.
[40] Gonzalez, R. C. and Woods, R. E., *Digital Image Processing*, 3rd ed., Upper Saddle River, NJ, USA: Prentice-Hall,Inc., 2006.
[41] P. Brodatz, Textures: *A Photographic Album for Artists and Designers*. Dover Publications, 1966.
[42] STex, Salzburg texture image database (STex). Available online at <http://wavelab.at/sources/STex/>, 2009.
[43] Fei-fei, L., Fergus, R., and Perona, P., "One-shot learning of object categories". *IEEE Trans.* PAMI, 2006.

Bitlis Eren Üniversitesi Fen Bilimleri Dergisi
BİTLİS EREN UNIVERSITY JOURNAL OF SCIENCE
ISSN: 2147-3129/e-ISSN: 2147-3188
VOLUME: 12 NO: 1 PAGE: 226-241 YEAR: 2023
DOI:10.17798/bitlisfen.1225375

Fungus Classification Based on CNN Deep Learning Model

Serhat ORAL[1], İrfan ÖKTEN[2**], Uğur YÜZGEÇ[1]

[1]*Bilecik Şeyh Edebali University, Faculty of Engineering, Computer Engineering, Bilecik*
[2]*Bitlis Eren University, Tatvan Vocational School, Department of Computer Technologies, Bitlis*
(ORCID:0009-0005-2761-1295) (ORCID:0000-0001-9898-7859) (ORCID:0000-0002-5364-6265)

Keywords: Deep Learning, Convolutional Neural Networks, Flutter, Mushroom Classification, Image Classification.

Abstract
Artificial intelligence has been developing day by day and has started to take a more prominent place in human life. As computer technologies advance, research on artificial intelligence has also increased in this direction. One of the main goals of this research is to examine how real problems in human life can be solved using artificial intelligence-based deep learning, and to present a case study. Poisoning from the consumption of poisonous fungi is a common problem worldwide. To prevent these poisonings, a mobile application has been developed using Convolutional Neural Networks (CNNs) and transfer learning to detect the species of fungus. The application informs the user about the type of fungus, whether it is poisonous or non-toxic, and whether it is safe to eat. The aim of this study is to reduce poisoning events caused by incorrect fungus detection and to facilitate the identification of fungus species. The developed deep learning model is integrated into a mobile application developed by Flutter that is a mobile application development framework, which enable the detection of fungus species from images taken from the camera or selected from the gallery. CNNs and the EfficientNetV2 model, a transfer learning method, were used. By using these two methods together, the classification accuracy rate for 77 fungus species was obtained as 97%.

1. Introduction

Artificial intelligence is evolving day by day and occupying a larger and larger place in human life. As computer technologies develop and become more powerful, the number of researches and studies on artificial intelligence also increases in the same direction. Today, artificial intelligence, which continues to develop by dividing into many sub-branches, is widely used to solve problems in human life. It has gained a place in many fields, from routine tasks in daily life to tasks that are difficult for humans to learn and require time. One of the things that are taken into consideration while developing artificial intelligence technologies is the compatibility and usability with the devices used by people in daily life. The purpose here is computer, phone, tablet, wearable technology, etc., which are used very often in daily life to be actively introduced into human life and to benefit from more artificial intelligence. For this reason, studies on artificial intelligence for mobile devices outside of computers have increased significantly recently.

Fungi have been used for medicine and food by humans for centuries. While some of the hundreds of fungus species found in nature are poisonous, others are non-poisonous. However, some poisonous fungus species and non-poisonous fungus species can be very similar in appearance. Therefore, it is important to have a good knowledge of fungi and to have studied and used a variety of fungi in order to distinguish them. People who are not familiar with fungi may experience poisoning events when they try to eat fungi. To prevent poisoning events caused by fungi and to prevent the collection of the wrong fungus species, the idea of developing a mobile application that can detect the types of fungi has emerged. A Convolutional Neural Network (CNN) model has been utilized to solve the problem of distinguishing a large number of similar fungus

* Corresponding author: iokten@beu.edu.tr
Received: 28.01.2022, Accepted: 03.03.2023

species. This model aims to solve a difficult problem that would take people a long time to learn, using the power of artificial intelligence. The developed model uses a picture of the fungus to inform the user about the type of fungus, whether it is poisonous, and whether it is edible.

The application environment for the deep learning model developed in this study is a mobile device, which is very suitable for the problem being addressed. Since mobile devices are easily portable and are devices that most people are already familiar with using, the likelihood of experiencing difficulties while using the developed application is very low. Additionally, the highly developed camera systems in mobile phones make them ideal tools for solving image classification problems. For these reasons, the goal of this project is to provide a practical solution to the mentioned problem by combining deep learning and the power of mobile devices.

Much work has been done on the use of Convolutional Neural Networks (CNNs) and analysis of image data within the scope of Deep Learning. LeCun et al. discussed the subject of deep learning in general in their study [1]. By touching on the usage areas in the modern world, they explained the working logic of the foundation of deep learning and also explained the CNNs used for supervised learning and classification. There are several layers found in CNNs. These are: Convolutional Layer, Pooling Layer and Fully Connected Layer [2].

Transfer learning is a machine learning technique in which a model that has been trained on one task is re-purposed and fine-tuned for a different but related task. It involves using knowledge gained while solving one problem to solve a different, but related, problem. This can be done by transferring the weights and biases learned from one model to another model, or by using the pre-trained layers of a model as the starting point for a new model. There are different CNN models used for image classification and proven success according to the period in which they were developed. Some of these models are AlexNet, GoogLeNet, VGG-Net and ResNet [3]. Developing a deep learning model from scratch in a classification problem may not always be a logical approach. We can achieve high success and save time by training proven models with our own datasets. For all these reasons, the method called Transfer Learning was used in this study.

The proposed method in this study is original in the sense that it utilizes deep learning techniques, specifically Convolutional Neural Networks and transfer learning, to develop a mobile application that can accurately detect and classify different species of fungi from images taken from a camera or selected from a gallery. This approach is unique in its focus on solving a real-world problem, specifically the prevention of poisoning from the consumption of poisonous fungi, through the use of cutting-edge artificial intelligence techniques. The use of transfer learning with the EfficientNetV2 model is also noteworthy, as this method has been shown to improve the accuracy of deep learning models while requiring less training data, making it a promising approach for future research in this field. Overall, the proposed method represents a novel and innovative approach to solving a significant public health issue using advanced artificial intelligence techniques.

2. Material and Method

There are several methods for recognizing fungi, including traditional methods such as microscopy and taxonomic keys, as well as newer methods such as DNA sequencing and machine learning. Deep learning architectures such as convolutional neural networks (CNNs) can be trained to classify fungi based on their physical characteristics such as shape, size, and color. These algorithms can be used to build tools such as mobile applications or websites that can help users identify different fungi based on images or other data. Some studies on fungus classification in literature and deep learning are summarized in Table 1.

Table 1. Some studies on deep learning and on fungus classification.

Authors	Title of Study	Datasets	Experimental results	Year
Picek, L. et al.	Fungi Recognition: A Practical use Case	FGVCx Fungi Classification Kaggle	Accuracy rate : %79	2022 [4]
Picek, L. et al.	Automatic Fungi Recognition: Deep Learning Meets Mycology	Danish Fungi 2020 (DF20)	Accuracy rate : %79	2022 [5]

Krizhevsky, A. et al.	ImageNet Classification with Deep Convolutional Neural Networks	ImageNet LSVRC-2010 contest	top-5 test error rate of 15.3%	2012) [6]
He, K. et al.	Delving Deep into Rectifiers: Surpassing Human-Level Performance on ImageNet Classification	ImageNet LSVRC-2012 contest	top-5 test error rate of 4.94%	2015 [7]
Kamnitsas, K. et al.	Efficient multi-scale 3D CNN with fully connected CRF for accurate brain lesion segmentation	BRATS 2015 and ISLES 2015	Accuracy rate : %77	2017 [8]
Kayalı, N.Z. and İlhan Omurca, S.	Classification of Chinese Number Patterns with Convolutional Neural Networks (CNN)	MNIST dataset	Accuracy rate : %97	2021 [9]
Bozkurt, F. and Yağanoğlu, M.	Detection of COVID-19 from Lung X-Ray Images Using Deep Convolutional Neural Networks	Kaggle's COVID-19 radiography database	Accuracy rate : %97.17	2021 [10]
Ökten, İ. and Yüzgeç U.	Detection of Rice Crop Disease with Convolutional Neural Network	Kaggle's Rice Leaf İmages database	Accuracy rate : %97.57	2022 [11]

3. Material and Method

In this section, the deep learning type and methods to be used are mentioned. The usage areas, working logic and architecture of convolutional neural networks are explained. The environment in which deep learning studies will be carried out is introduced and the benefits it provides to the developers are explained. At the same time, important libraries to be used are also introduced.

3.1. Convolutional Neural Network (CNN)

One of the most popular models for classification from image data is the CNN model. The features of an image are extracted by passing the input image through multiple convolutional layers. The convolution layer is the basic building block of a CNN and is where most of the computation occurs. Typically, 3x3 filters are used to extract the features of the image. These filters scan all image pixels and perform convolution, as shown in Figure 1, resulting in a feature map [12]. After each convolution operation, the ReLU activation function is applied to the feature map.

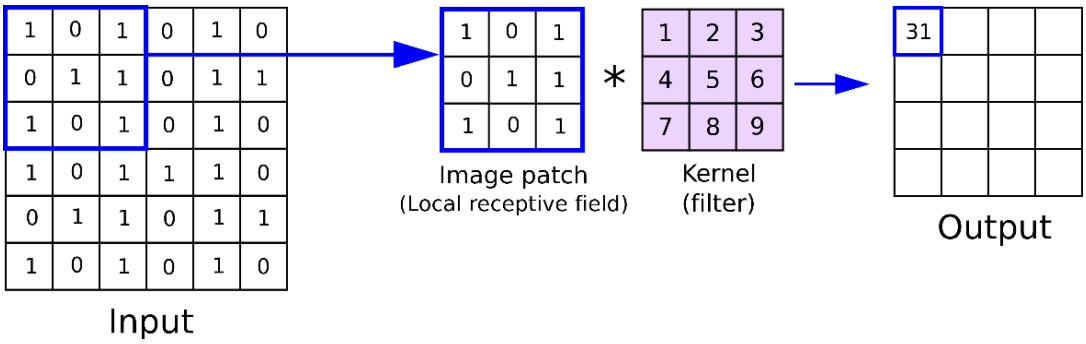

Figure 1. Illustration of the convolution operation [13].

Another layer in a CNN is the pooling layer. Pooling layers are used to further reduce the number of parameters and computational complexity of the model by gradually reducing the dimensionality of the representation. The largest pixel within the selected pooling size is transferred to the output. In the example shown in Figure 2, a 2x2 max-pooling process was applied by shifting it by 2 steps (pixels) [14]. This scales the feature map up to 25% while keeping the depth volume at its standard size [3].

A CNN model structure is shown as an example in Figure 3. Here, the input image undergoes a series of convolution and pooling operations, resulting in a final array through the fully connected

layer. The highest value in the sequence determines the class to which the image belongs.

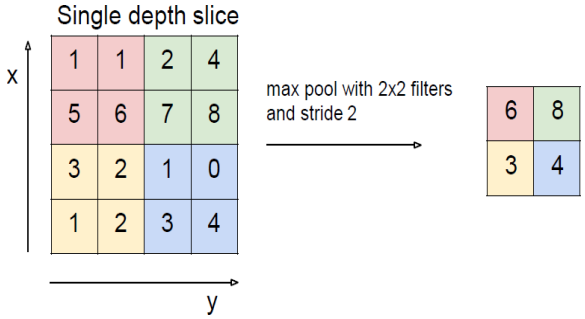

Figure 2. Max-pool operation [14].

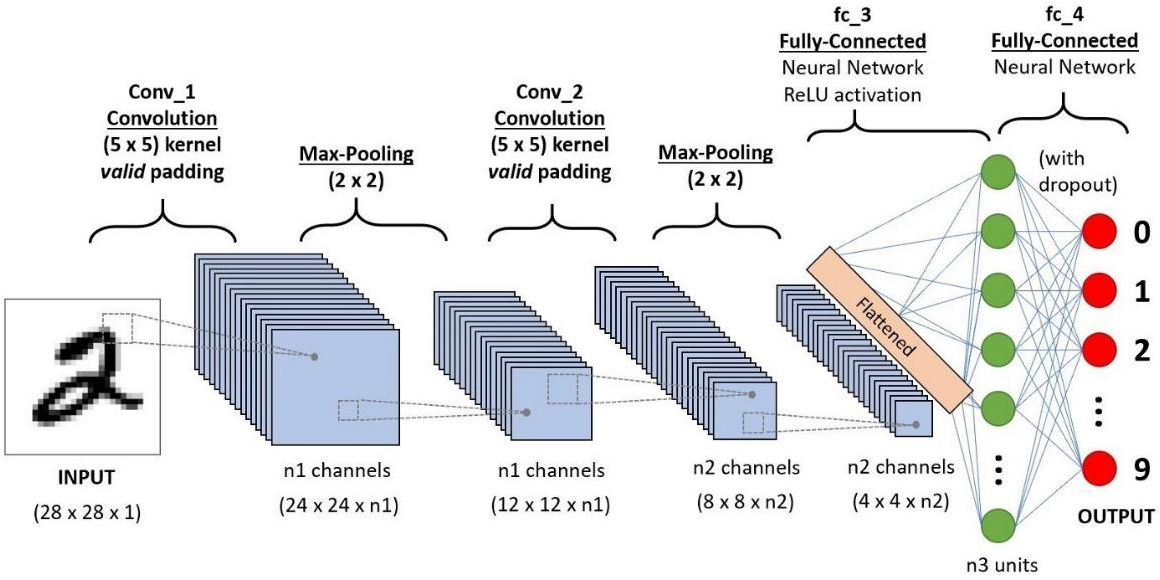

Figure 3. A sample CNN model structure [15].

3.2. Transfer Learning

Learning transfer is a machine learning technique in which a model that has been trained on one task is applied to a related, but different task. This can be useful when we have a smaller data set for the new task and don't have enough data to train a new model from scratch. It can also be useful when we need to train a model quickly, or when we want to use a pre-trained model as a starting point and then fine-tune it for a specific task [16]. There are two main approaches to learning transfer: feature extraction and fine-tuning.

Feature extraction involves using the pre-trained model as a fixed feature extractor, where the output of the pre-trained model's layers is taken as input for a new model. This new model is then trained on the new task using these extracted features. Fine-tuning involves unfreezing some of the layers of the pre-trained model and retraining them using the new data. This can be useful when the new task is similar enough to the original task that we can leverage the knowledge learned by the pre-trained model.

Image recognition has made significant advances in recent years due to the availability of large-scale datasets such as ImageNet, which contains over 1.2 million categorized natural images from over 1000 classes. Convolutional neural networks (CNNs) trained on these datasets have achieved successful results on various object detection and image segmentation tasks [17].

3.3. Feature Extraction

In multiclassification problems, the output layer of each model is specific to the dataset it is trained on. In other words, if the model is trained with a data set containing 50 classes, there must be 50 neurons in the output layer of the model. CNN models trained with ImageNet therefore have output layers with 1000 neurons. When we apply these pre-trained models to our own dataset and problem, we pull without the last

layers and add the appropriate output layer ourselves. The parts to be changed and preserved in the original model are basically shown in Figure 4.

In the feature extraction method, the weights are preserved by freezing the layers of the pre-trained model. Since training will not take place in these layers, the weights will not be updated. Here, the classification process is carried out by making use of the information learned from the previous training. Training takes place only in the last added layers.

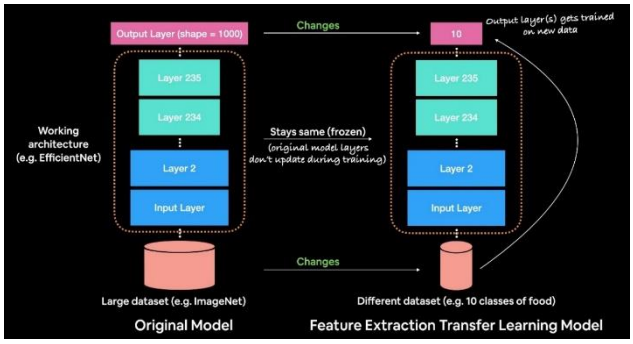

Figure 4. Application of feature extraction method to the model [18].

3.4. Fine-Tuning

Fine-tuning is a method of learning transfer in which all or part of the pre-trained model is unfrozen and retrained on the new data using a low learning rate. This is in contrast to feature extraction, where the pre-trained model is used as a fixed feature extractor and a new model is trained on the extracted features. Fine-tuning can lead to significant improvements by adapting the previously learned features to the new data. Figure 5 illustrates the difference between these two methods. It is often effective to use both feature extraction and fine-tuning together in learning transfer.

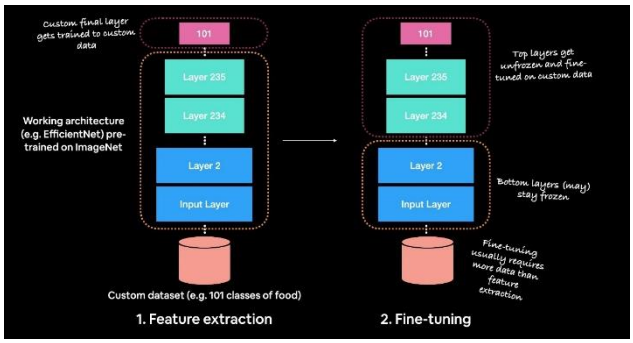

Figure 5. Feature extraction and fine-tuning [18].

3.5. EfficientNetV2B1 Model

The efficiency of deep learning in training is often related to the size of the model and the amount of training data. For instance, GPT-3, a very large model with a lot of training data, can achieve significant success in a few steps, but this requires weeks of training on thousands of GPUs, which can be complex and time-consuming. In contrast, techniques like learning transfer can be more efficient because they allow for the use of smaller models with fewer parameters, as long as the model is well-designed and effective at achieving successful results. EfficientNetV2 is a family of small size image classification models that provide good parameter efficiency and faster training as seen in Figure 6. It includes developed models in various sizes.

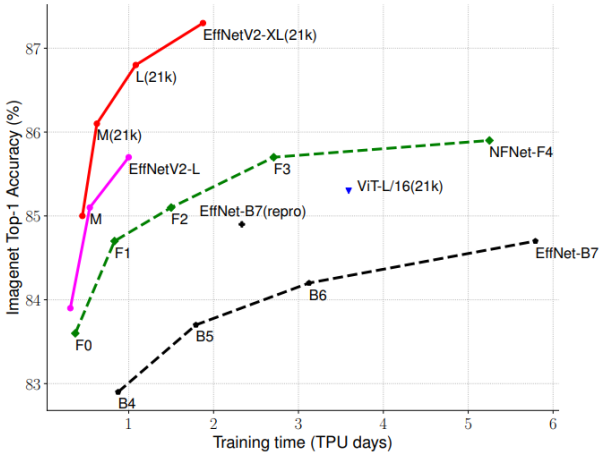

(a) Training efficiency.

	EfficientNet (2019)	ResNet-RS (2021)	DeiT/ViT (2021)	EfficientNetV2 (ours)
Top-1 Acc.	84.3%	84.0%	83.1%	83.9%
Parameters	43M	164M	86M	24M

(b) Parameter efficiency.

Figure 6. Training and parameter efficiency of EfficientNetV2 model [19].

The EfficientNetV2 is an improved version of the EfficientNet model, which has gained popularity due to its ability to balance accuracy and efficiency. The EfficientNetV2 model achieves state-of-the-art performance on image classification tasks, while requiring fewer parameters and achieving faster inference times compared to other popular deep learning models. The model is highly scalable and adaptable to different image sizes and resolutions, making it suitable for a wide range of applications. Its transfer learning capabilities and robustness to noise also make it an attractive option for developers working with limited training data or lower-quality

images. Overall, the EfficientNetV2 model is a valuable tool for computer vision applications and is likely to play an important role in the continued development of AI technologies. Compared to EfficientNet and newer runs, the EfficientNetV2 is up to 6.8x smaller while training up to 11x faster [19].

EfficientNetV2B1 is one of the smaller models in the EfficientNet family, with a moderate number of parameters and computational cost. It was designed for image classification tasks and has shown good performance on a variety of benchmarks. EfficientNetV2 models are an improvement over the original EfficientNet models, with better performance and fewer parameters. EfficientNetV2B1 is trained on the ImageNet dataset, which contains over 1 million labeled images from 1000 classes. It is a widely used benchmark for image classification tasks, and many CNN models are trained and evaluated on it. Therefore, EfficientNetV2B1 model was used in the fungus classification application to be developed.

3.6. Software Libraries

Within the scope of this study, the Python programming language was used to create the CNN model. Python is used in many areas and contains various libraries for different areas. It also supports developers and researchers with very powerful and useful libraries in the field of machine learning. In the fungus classification application, TensorFlow and Keras libraries supported by Google were used. Also, the Matplotlib and NumPy were used for data visualization and numerical computing.

3.7. Flutter

Flutter is an open source user interface development kit created by Google. It is used to develop applications for Android, iOS, Windows, Mac, Linux and the web [20]. It has a layered architecture that gives developers control over every pixel on the screen, using a set of built-in widgets.

Flutter is powered by Skia, a hardware-accelerated graphics library that is used in Chrome and Android, and it is designed to support fast, error-free graphics on both iOS and Android devices. The Flutter framework is built on the Dart platform, which provides support for 32-bit and 64-bit ARM machine code for iOS and Android, as well as JavaScript for the web and compiling to Intel x64 for desktop devices. Flutter is a good choice for developing deep learning models because of its fast performance and ability to create visually appealing apps.

4. Training and Test of the CNN Model

4.1. Data Set

In 2018, the "FGVCx Fungi Classification" competition was held on Kaggle [21] using data provided and sponsored by the Danish Swampe Atlas [22]. The Danish Fungus Atlas contains 8560 expert-approved fungus species and has been supported by over 4000 volunteers, resulting in over 1 million labeled data points. The FGVCx Fungi Dataset, created for the competition, includes 85578 images for training and 4182 images for verification of 1394 fungal species. There is also a set of test data consisting of 9758 images whose labels are not publicly available. For the purpose of this study, 77 fungus species from the competition's dataset were selected, resulting in a training dataset of 6733 fungus images, a validation dataset of 231 images, and a test dataset of 400 images.

The data set used to train the model should have a folder structure as shown in Figure 7. The FGVCx Fungi dataset does not come divided into training and validation sets, but rather is loaded as a whole. Information about which images should be used for training and which should be used for validation is provided in JSON format. A Python script was created to divide the data into training and validation sets based on this information.

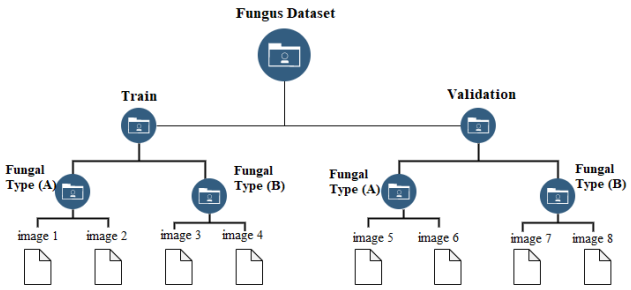

Figure 7. The desired folder structure of the data set.

4.2. Data Augmentation

The amount of data is crucial in deep learning. If a model has too many parameters relative to the number of training examples and has a complex structure, it may suffer from overfitting [23]. This means that while the model performs well on the training data, it may not perform as well on tests or in real-life classification. In other words, the model has memorized the few training examples it has seen and has difficulty generalizing to new examples. Data augmentation techniques, such as rotation, flip, and adding random noise, can help to improve the image

recognition accuracy [23,24]. These techniques involve modifying the training data in order to create additional, slightly different examples that can be used to train the model.

In this study, a data augmentation layer was implemented to augment the data during training. This layer was integrated into the model using the Keras functional API and will automatically apply data augmentation during the training phase. When using this model, it will not be necessary to manually perform data augmentation. The Keras library can be used to create a data augmentation layer, which can modify images during training according to the properties specified in the layer. Figure 8 shows some examples of the augmented images produced by the data augmentation layer.

Figure 8. Some images regenerated by the data augmentation layer.

4.3. Creating the Model

In this section, the pre-trained model was retrieved from the Keras functional API, modified with necessary additions, and trained. The model building process involved two stages: feature extraction and fine-tuning. At the end of each stage, the model's accuracy and loss were plotted in curve graphs.

4.3.1. Feature Extraction

EfficientNetV2B1, a model trained on the ImageNet1k dataset, will be used in this study. To utilize Transfer Learning, it is important to freeze the model by disabling the trainability of its layers. This helps to preserve the previously learned weights and avoids making any changes to them. In this case, the model was trained for 25 epochs.

To build the main model, the previously created data augmentation layer and input layer must be added. The Keras functional API offers a lot of flexibility and convenience for modifying the model by adding different layers as if adding a chain to different parts of the model. First, the input layer is included. Next, the data augmentation layer is added. Then, the EfficientNetV2B1 model, which forms the main part of the model, is added. A Global Average Pooling layer is then created and added to the end of the modified model. This layer is used to make the feature maps easier to interpret, rather than directly providing the feature maps to the fully connected layer. Finally, an output layer with 77 neurons is created to return 77 possibilities for an image, representing the 77 fungus species in the dataset. The "softmax" activation function is used in the output layer for multi-class classification, producing outputs between [0,1] indicating the probability that each input belongs to a class. The layers of the model are shown in Figure 9.

The image data used in the model was resized to 224x224x3 dimensions. The choice of optimization algorithm should take into account the characteristics of the problem and the dataset. In this case, the Adam optimization algorithm was used in the training process. After preparing the layers and parameters, the training process for the proposed model was initiated.

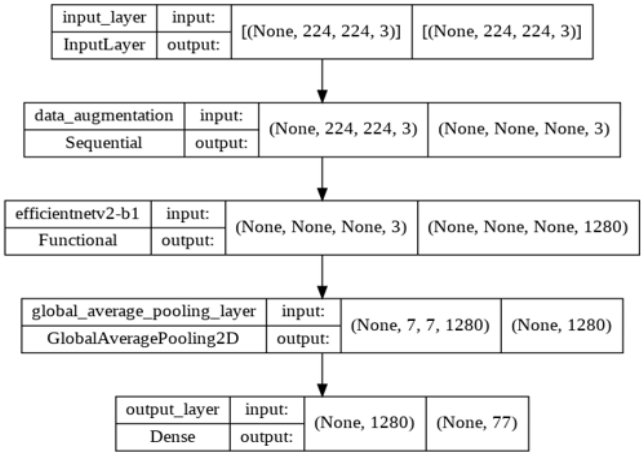

Figure 9. The structure of the proposed model.

Table 2 shows the first 5 and last 5 epoch values obtained in the initial training of the model. During training, the model was also validated using validation data at each epoch. Figure 10 plots the loss and accuracy values for feature extraction, which is the first training step. Both the table and the plotted curves can be used to make inferences about the model's performance.

Table 2. The results obtained in the first training of the model.

Epoch	Duration	Training loss	Traning accuracy	Loss of validation	Accuracy of validation
1/25	149s	2.8566	0.3575	2.0017	0.5281
2/25	96s	1.6368	0.6318	1.4246	0.6623
3/25	82s	1.2636	0.7079	1.1679	0.7446
4/25	79s	1.0594	0.7493	0.9908	0.7835
5/25	71s	0.9274	0.7760	0.8876	0.8139
...	...	...	...	...	...
21/25	45s	0.3353	0.9247	0.4228	0.8918
22/25	46s	0.3244	0.9266	0.4134	0.8961
23/25	43s	0.3150	0.9265	0.4084	0.9048
24/25	43s	0.2958	0.9335	0.3950	0.9004
25/25	44s	0.2794	0.9393	0.3814	0.9091

The model performed well in the first epoch, with a validation success rate of 0.5281 after one epoch of training. While this is a good value, it is expected that the loss would be quite high at the beginning of training. As training progressed, the model became more accurate and made fewer mistakes, as seen in the curves in Figure 10.

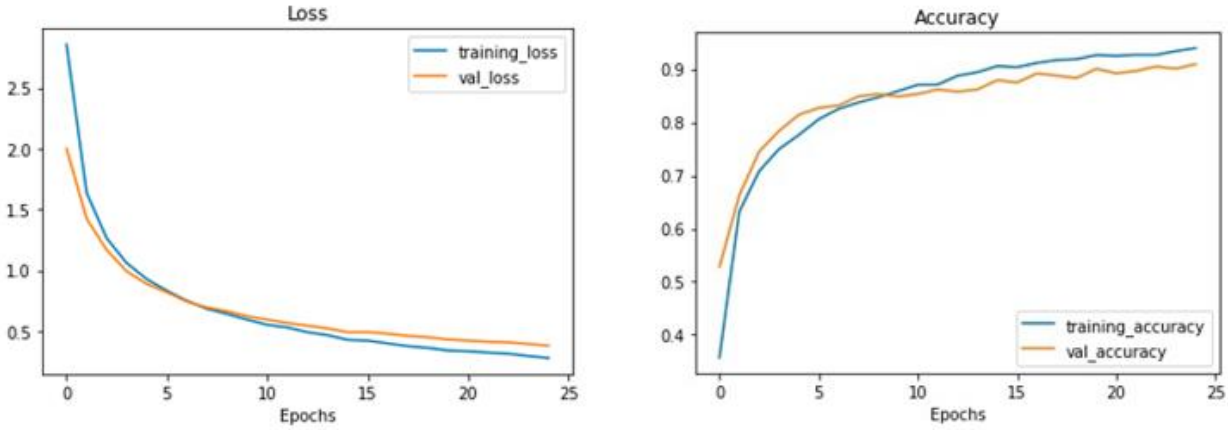

Figure 10. Loss and accuracy curves for 25 epochs.

The parts at the end of the curves remain stable and do not diverge from each other, indicating that the model is making consistent predictions in the validation tests compared to the predictions made during training. This suggests that there is no overfitting. If the last parts of the curves were widely separated and continued to diverge, it would indicate that the model is memorizing the data and further precautions would be necessary. Figure 10(b) shows some fluctuation at the last parts of the accuracy curves. Additionally, examining the last three epochs in the table reveals that saturation has begun to be reached for feature extraction, with the accuracy value increasing very slowly. The accuracy values for training and validation also appear to be starting to diverge towards the end, indicating that the training should be stopped at this point.

If the number of epochs is increased further, the model may start to overfit. It is important to pay attention to this and analyze the results of the training carefully. To reduce fluctuation in the curves and improve the model's performance, fine-tuning was applied to the model

4.3.2. Fine-Tuning

In this stage, the model was trained for 10 epochs by enabling the trainability feature for the last 15 layers of the model. This fine-tuning and updating is expected to improve the model's performance. To begin, all layers of the model are made trainable. Then, a loop is created and all layers except the last 15 are frozen again. This leaves only the last 15 layers as trainable. The training speed of the model is also reduced 100 times compared to normal. During the fine-tuning phase, training is performed at a much lower rate than usual. Finally, training continues from the last epoch value that the model reached in its previous training. The results of the model, which received a total of 35 epochs of training, are summarized in Table 3, and the curve graphs are shown in Figures 11 and 12.

Figure 11. Accuracy curves of the model after fine tuning.

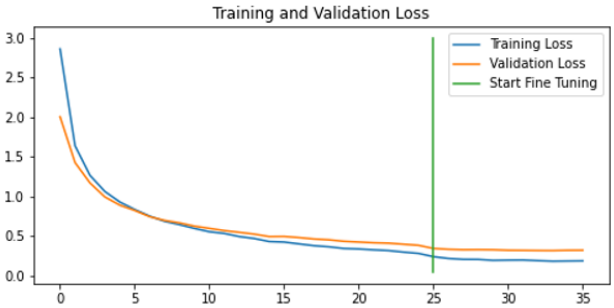

Figure 12. Loss curves of the model after fine tuning.

Table 3. Results obtained in the fine-tuning phase.

Epoch	Duration	Training loss	Training accuracy	Loss of validation	Accuracy of validation
25/35	62s	0.2384	0.9445	0.3420	0.9091
26/35	45s	0.2157	0.9459	0.3313	0.9134
27/35	45s	0.2046	0.9479	0.3263	0.9134
28/35	45s	0.2037	0.9459	0.3276	0.9177
29/35	44s	0.1920	0.9476	0.3257	0.9134
30/35	45s	0.1951	0.9465	0.3189	0.9264
31/35	45s	0.1963	0.9464	0.3174	0.9264
32/35	44s	0.1880	0.9491	0.3158	0.9264
33/35	43s	0.1812	0.9520	0.3150	0.9264
34/35	43s	0.1835	0.9528	0.3186	0.9221
35/35	42s	0.1851	0.9498	0.3194	0.9264

4.4. Testing the Model

When the developed model is evaluated using test data consisting of 400 images, it is found that the accuracy is 97% and the loss value is 0.1441. In addition to these values, various metrics are used to evaluate the performance of classification models. By calculating these values, various inferences can be made and a confusion matrix can be created. To evaluate the model performance, some metrics were utilized in this study. These are Accuracy, Loss-Categorical Cross-Entropy, Precision, Recall, and F1 Score. Accuracy is the most common metric used to evaluate classification models. It represents the percentage of correctly classified instances out of the total number of instances in the dataset. The Loss-Categorical Cross-Entropy is a loss function that measures the performance of a multi-class classification model by calculating the difference between the predicted probability distribution and the actual probability distribution of the target variable. Precision is a metric that measures the proportion of true positive predictions out of all the positive predictions made by the model. Recall is a metric that measures the proportion of true positive

predictions out of all the actual positive instances in the dataset. F1 score is the harmonic mean of precision and recall, and is a popular metric for evaluating classification models. It provides a balanced measure of precision and recall, and is particularly useful when the dataset is imbalanced. The formulas for calculating these metrics are summarized in Table 4, and the results of these metrics calculated for test of the proposed model are given in Table 5. PREC, REC, TN, TP, FN, and FP used in model evaluation metrics formulas are Precision, Recall, True Negative, True Positive, False Negative, and False Positive, respectively.

The success rate of the model was recorded and then the network was tested on real images. To do this, fungus images from different sources were uploaded to Google Colaboratory and provided as input to the trained network, and the classification results were obtained. The classification rates and images from the test results are shown in Figure 13. To demonstrate the performance of the model, the confusion matrix obtained using the samples of 77 fungal species is shown in Figure 14.

Table 4. Metrics and formulas used in model evaluation.

Metrics	Formula
Accuracy	$\frac{TP+TN}{TP+FP+Fn+TN}$
Loss-Categorical Cross-Entropy	$\sum_{i=0}^{outputsize} y_i * log\hat{y}_i$
Precision	$\frac{TP}{TP+FP}$
Recall	$\frac{TP}{TP+FN}$
F1 Score	$\frac{2*PREC*REC}{PREC+REC}$

Table 5. Evaluation results of the model.

Accuracy	0.9700
Loss	0.1441
Precision	0.9746
Recall	0.9696
F1 Score	0.9694

Figure 13. Classification results of test fungus images.

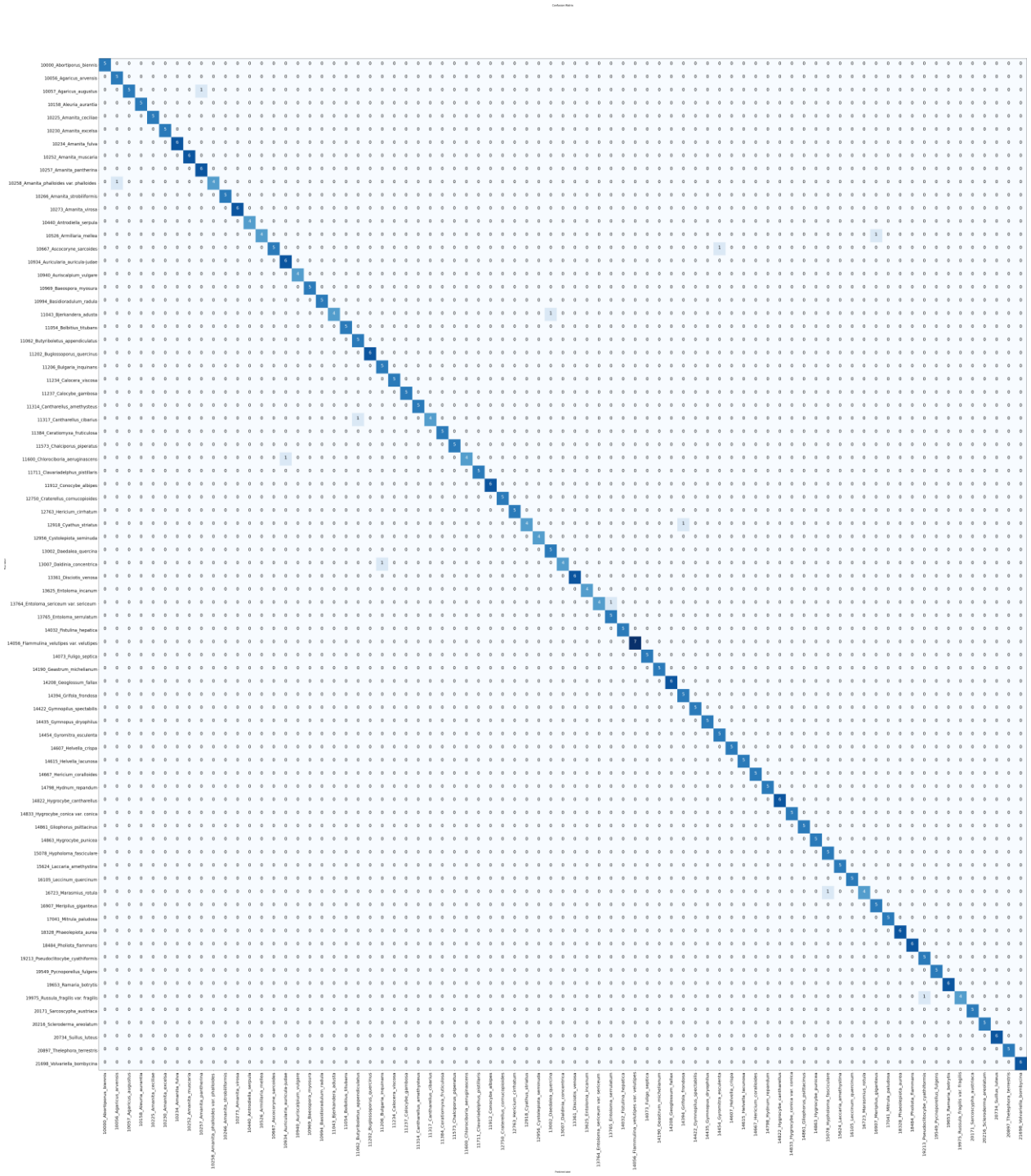

Figure 14. Confusion matrix of 77 fungal species used in the model.

5. Mobile Application Developed for Fungus Species Detection

After training the model for detecting fungus species, the trained model was saved. Since the model was developed in Colaboratory, the trained network is also saved here. However, the saved model cannot be used directly on mobile devices. Instead, the model was converted to the tflite format in the Colaboratory environment for use on mobile devices. A mobile application was then developed using the Dart programming language and the Flutter UI kit.

5.1. Application Homepage

When the application is first opened, the homepage shown in Figure 15 appears to the user.

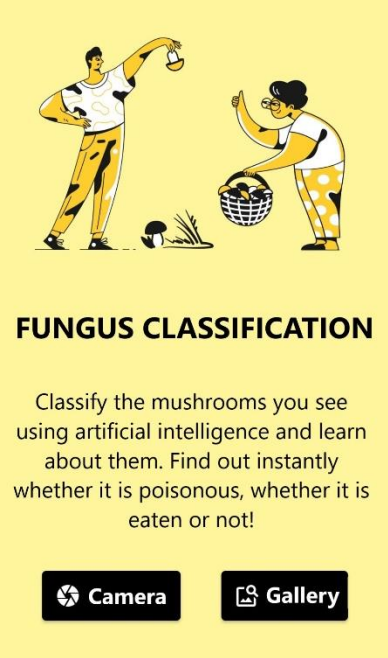

Figure 15. Application homepage.

The main purpose of this page is to allow the user to input fungus images for classification and display the results. The user has two options for importing fungus images: taking a photo with the camera or choosing an image from the gallery. Two buttons are provided on the homepage to perform these actions.

5.2. Results Page

In the result page shown in Figure 16, images from the main page are input to the model, which classifies the fungus species and returns the name of the species in the image. A dictionary structure was also created that contains information about the fungus species, such as whether they are poisonous, edible, and found in certain regions. By using the fungus name returned by the model, the corresponding information in the dictionary structure is retrieved and displayed to the user. Some symbols were also created and used to convey information about the condition of the fungus. These symbols and their meanings are shown in Figure 17. Separate dictionaries have been created for these symbols, and the information symbol for the relevant fungus is printed by checking these dictionaries.

Figure 16. Some screenshots of the fungus classification results.

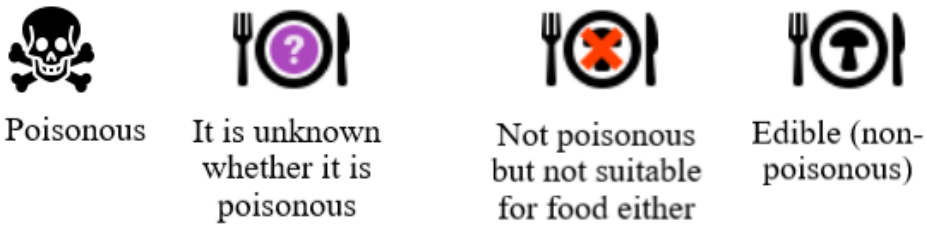

Figure 17. Warning symbols about fungus classification.

6. Conclusion and Future Works

In this study, we discuss the use of deep learning to solve an image classification problem. The main idea is to demonstrate that problems can be quickly and easily solved by following appropriate methods and steps with transfer learning. To this end, we chose the fungus species classification problem and developed a study to solve it, including discussions of convolutional neural networks and transfer learning.

Since the problem involves image classification, it is important that fungus images can be easily obtained. Therefore, the study was designed to be implemented in a mobile application. The model for classification was first prepared on Google Colaboratory, then converted to the "TensorFlow Lite" model and used in the mobile application.

The prepared model accurately classifies 77 fungus classes with high rates of success. When tested with 400 fungus images, the model achieved an accuracy of 0.97 and an average F1 score of 0.9694. One of the main challenges in fungus classification is that different fungus species can be very similar to each other, making it difficult for the human eye to distinguish them and requiring extensive knowledge and expertise. Deep learning models may also utilized to accurately classify fungus species that are very similar to each other. To minimize this, it is important to have a diverse and rich dataset for training. This should be considered if a larger number of fungus species classifications are to be performed, as the number of species increases, the similarity in appearance between the fungus species will increase and the problem will become more complex and difficult. In addition, paying attention to overfitting and allowing for longer training periods will also contribute to better learning success.

The mobile application developed to utilize the machine learning model has demonstrated successful performance. The application, which has a simple design, is optimized for fast and accurate classification of fungus species. Proper planning is crucial for the application's success, as issues such as data migration and page loading can significantly impact its performance. The application includes a dictionary of 77 fungus species, which allows users to access and view information about specific fungi by using the species name returned by the model through classification.

When using deep learning to solve a problem, it is important to first clearly define the problem and thoroughly analyze it. The complexity of the problem should be taken into account when selecting appropriate data for the model. In the field of deep learning, data plays a crucial role. If the data is not clean, accurate, and relevant to the problem at hand, it is likely that the model will not perform well. One of the major factors driving the rapid growth of this field is the availability of large, high-quality data sets. It is essential to carefully consider these two key steps in the process of using deep learning.

In the future, the work presented in this study could be expanded and refined to further improve the accuracy and efficiency of the model. One potential direction for future work is to increase the number of fungus species that the model can classify. This would require a larger and more diverse dataset for training, as well as more sophisticated techniques for handling the increased complexity of the classification problem. Another potential area for improvement is to optimize the mobile application's performance and

user experience, such as by implementing more advanced features or incorporating user feedback. Finally, the techniques and methods presented in this study could be applied to other image classification problems, opening up new opportunities for using deep learning to solve real-world problems.

Contributions of the authors

This study is a study prepared by Serhat ORAL and İrfan ÖKTEN under the consultancy of Prof Dr Uğur YÜZGEÇ. Serhat ORAL contributed to the finding of the data, the algorithm of the model and the preparation of the software, İrfan ÖKTEN contributed to the development of the software and the writing of the article in this study, and Uğur YÜZGEÇ contributed to the editing and consultancy of the article.

Conflict of Interest Statement

There is no conflict of interest between the authors.

Statement of Research and Publication Ethics

The study is complied with research and publication ethics

References

[1] Y. LeCun, Y. Bengio, and G. Hinton, "Deep learning," *Nature*, vol. 521, no. 7553, pp. 436–444, 2015.

[2] K. O'Shea and R. Nash, "An Introduction to Convolutional Neural Networks," *arXiv [cs.NE]*, 2015.

[3] F. Sultana, A. Sufian, and P. Dutta, "Advancements in image classification using convolutional Neural Network," *arXiv [cs.CV]*, 2019.

[4] L. Picek, M. Šulc, J. Matas, J. Heilmann-Clausen, T. S. Jeppesen, and E. Lind, "Automatic fungi recognition: Deep learning meets mycology," *Sensors (Basel)*, vol. 22, no. 2, p. 633, 2022.

[5] S. Sladojevic *et al.*, *Fungi Recognition: A Practical Use Case*. 2020.

[6] A. Krizhevsky, I. Sutskever, and G. E. Hinton, "ImageNet classification with deep convolutional neural networks," *Commun. ACM*, vol. 60, no. 6, pp. 84–90, 2017.

[7] K. He, X. Zhang, S. Ren, and J. Sun, "Delving deep into rectifiers: Surpassing human-level performance on ImageNet classification," in *2015 IEEE International Conference on Computer Vision (ICCV)*, 2015.

[8] K. Kamnitsas *et al.*, "Efficient multi-scale 3D CNN with fully connected CRF for accurate brain lesion segmentation," *Med. Image Anal.*, vol. 36, pp. 61–78, 2017.

[9] N. Z. Kayalı and S. Ve Ilhan Omurca, *Konvolüsyonel Sinir Ağları (CNN) ile Çin Sayı Örüntülerinin Sınıflandırması*. 2021.

[10] F. Bozkurt ve M. Yağanoğlu, "Derin Evrişimli Sinir Ağları Kullanarak Akciğer X-Ray Görüntülerinden COVID-19 Tespiti", *Veri Bilimi*, c. 4, sayı. 2, ss. 1-8, Ağu. 2021.

[11] İ. Ökten ve U. Yüzgeç, "Evrişimli Sinir Ağı ile Çeltik Bitkisi Hastalığının Tespiti", *Bitlis Eren Üniversitesi Fen Bilimleri Dergisi*, c. 11, sayı. 1, ss. 203-217, Mar. 2022, doi:10.17798/bitlisfen.1014393.

[12] "What are Convolutional Neural Networks?" *Ibm.com*. [Online]. Available: https://www.ibm.com/topics/convolutional-neural-networks. [Accessed: 27-Dec-2022].

[13] A. H. Reynolds, "Anh H. reynolds," *Anh H. Reynolds*. [Online]. Available: https://anhreynolds.com/blogs/cnn.html. [Accessed: 27-Dec-2022].

[14] A. Kızrak, "DERİNE DAHA DERİNE: Evrişimli Sinir Ağları - ayyüce kızrak, ph.D," *Medium*, 28-May-2018. [Online]. Available: https://ayyucekizrak.medium.com/deri%CC%87ne-daha-deri%CC%87ne-evri%C5%9Fimli-sinir-a%C4%9Flar%C4%B1-2813a2c8b2a9. [Accessed: 27-Dec-2022].

[15] S. Saha, "A comprehensive guide to convolutional neural networks — the ELI5 way," *Towards Data Science*, 15-Dec-2018. [Online]. Available: https://towardsdatascience.com/a-comprehensive-guide-to-convolutional-neural-networks-the-eli5-way-3bd2b1164a53. [Accessed: 27-Dec-2022].

[16] M. Hussain, J. J. Bird, and D. R. Faria, "A study on CNN transfer learning for image classification," in *Advances in Intelligent Systems and Computing*, Cham: Springer International Publishing, 2019, pp. 191–202.

[17] H.-C. Shin *et al.*, "Deep convolutional neural networks for computer-aided detection: CNN architectures, dataset characteristics and transfer learning," *IEEE Trans. Med. Imaging*, vol. 35, no. 5, pp. 1285–1298, 2016.

[18] S. Lee, "(TF2) Transfer Learning - Feature Extraction," *AAA (All About AI)*, 05-Mar-2022. [Online]. Available: https://seunghan96.github.io/dlf/TF2_4%EC%9E%A5/. [Accessed: 27-Dec-2022].

[19] M. Tan and Q. V. Le, "EfficientNetV2: Smaller models and faster training," *arXiv [cs.CV]*, 2021.

[20] Wikipedia contributors, "Flutter," *Wikipedia, The Free Encyclopedia*. [Online]. Available: https://tr.wikipedia.org/w/index.php?title=Flutter&oldid=27787028.

[21] "2018 FGCVx fungi classification challenge," *Kaggle.com*. [Online]. Available: https://www.kaggle.com/competitions/fungi-challenge-fgvc-2018/overview. [Accessed: 27-Dec-2022].

[22] "Danmarks officielle database for svampefund," *Danmarks SvampeatlasXXXXX*. [Online]. Available: https://svampe.databasen.org/en/. [Accessed: 27-Dec-2022].

[23] Z. Zhong, L. Zheng, G. Kang, S. Li, and Y. Yang, "Random Erasing Data Augmentation," *Proc. Conf. AAAI Artif. Intell.*, vol. 34, no. 07, pp. 13001–13008, 2020.

[24] W. Li, C. Chen, M. Zhang, H. Li, and Q. Du, "Data augmentation for hyperspectral image classification with deep CNN," *IEEE Geosci. Remote Sens. Lett.*, vol. 16, no. 4, pp. 593–597, 2019.

Bitlis Eren Üniversitesi Fen Bilimleri Dergisi
BİTLİS EREN UNIVERSITY JOURNAL OF SCIENCE
ISSN: 2147-3129/e-ISSN: 2147-3188
VOLUME: 12 NO: 1 PAGE: 242-246 YEAR: 2023
DOI:10.17798/bitlisfen.1231238

The Combined Use of SCD Probiotics and Tauroursodeoksikolik Asit (TUDCA) is More Effective in Controlling Anxiety-Like Behavior in Aged Rats

Taha CEYLANİ[1-2*], Hikmet Taner TEKER[3]

[1]*Department of Molecular Biology and Genetics, Muş Alparslan University, Muş, Turkey*
[2]*Department of Food Quality Control and Analysis, Muş Alparslan University, Muş, Turkey*
[3]*Department of Medical Biology and Genetics, Ankara Medipol University, Ankara, Turkey*
(ORCİD:0000-0002-3041-6010), (ORCİD:0000-0002-6621-3071)

Keywords: SCD Probiotics, TUDCA, Open Field, Elevated Plus Maze, Anxiety, Sprague-Dawley.

Abstract
In this study, the effects of TUDCA administration with a SCD probiotics for one week on locomotors activity and anxious behavior were investigated. Male Saprague-Dawley rats aged 24 months were used as the model organism. At the end of the application, open-field and elevated plus maze behavioral tests were performed on the rats. Although SCD probiotics were more effective on anxious behavior, the group in which they were administered together had a significantly greater effect on locomotor activity and anxious behavior. This study provides important evidence that combining SCD probiotics and TUDCA administration may be more beneficial to behavior.

1. Introduction

The gut microbiota (GM) and its metabolites play a role in modulating gastrointestinal functions by affecting intestinal permeability, motility, and sensitivity, mucosal immune function, and the release of neurotransmitters and gastrointestinal hormones from enteroendocrine and enterochromaffin cells [1]. Preclinical data also demonstrates that GM and its compounds influence a variety of behavioral and brain functions, including stress response, emotional reactions, pain modulation, eating behavior, and brain biochemistry [2]. The majority of probiotics are found in the human digestive tract, where they can aid the host by helping to keep the microbiota in balance [3]. Daily life often involves the ingestion of active bacteria preparations containing popular probiotics like Lactobacillus or Bifidobacterium [4]. A great deal of progress has been made in the study of probiotics in recent years, and a great many studies have shown that probiotics play a crucial role in preserving human health. In the case of Crohn's disease and other chronic inflammatory disorders, probiotics can be helpful in managing symptoms. In addition, probiotics may reduce the risk of developing cancer, obesity, and diabetes. There is growing proof that probiotics can help strengthen immune systems and keep people healthy [5]. With different strains of probiotics, a wide variety of effects of gut microbial modulation were reported on emotional behavior, social interactions, learning and memory, and ingestive behaviors [2].

The numerous microbial metabolites of dietary substrates, such as bile acids and short-chain fatty acids (SCFAs), constitute the primary basis for the regulatory activities of the gut microbiota. Bile acids are metabolic products of dietary substrates. Their function is crucial in metabolic processes and immune system modulation [6]. While the liver is responsible for synthesizing primary bile acids from cholesterol, several bacterial species in the intestines including Clostridium and Eubacterium are responsible for converting them into secondary bile acids [7]. Intestinal dysbiosis and inflammation are brought on by bile acid dysregulation or bile acid-activated receptor dysfunction [8]. Regulation of bile acid production and metabolism is a major function of the gut microbiota [9]. In humans, the microbiota in the intestines is the only source of ursodeoxycholic acid (UDCA), a secondary bile acid. The conjugation

*Corresponding author: t.ceylani@alparslan.edu.tr
Received: 08.01.2023, Accepted: 03.03.2023

of taurine with UDCA occurs in the liver via enterohepatic circulation [10]. TUDCA has been shown to resolve endoplasmic reticulum stress by functioning as a chemical chaperone [11]. This study also showed that TUDCA improved the gut microbiota in high-fat-fed mice, which in turn reduced the absorption and production of lipids in the small intestine [12]. TUDCA has been found to be neuroprotective in many animal models of neurological illness [13]. In this study, the effects of SCD Probiotics and TUDCA administered to aged rats for one week on anxious behavior and locomotor activity were evaluated.

2. Material and Method

2.1. Animal Studies

The male Sprague-Dawley rat (24-month old) species was used. Four groups were formed: the control group (n = 7) and the group that TUDCA administered group (n = 7) for 7 days; the group that was administered SCD probiotics (n = 7) for 7 days; and the group that TUDCA administered during the SCD probiotics supplementation (n = 7) for 7 days. The usual rat food was provided on an ad libitum basis to the animals. TUDCA was administered intravenously from the tail to each animal at 300 mg/kg [14]. The SCD probiotics supplement was given by oral gavage at a dose of 3 mL (1 x 108 CFU) per day [15]. SCD Probiotic Human Beverage contains *Bacillus subtilis, Bifidobacterium bifidum, Bifidobacterium lognum, Lactobacillus acidophillus, Lactobacillus bulgaricus, Lactobacillus casei, Lactobacillus fermentum, Lactobacillus plantarum, Lactococcus lactis, Saccharomyces cerevisiae*, and *Streptococcus thermophiles* species. One day after the end of the application, open field and elevated plus maze behavioral tests were applied to the rats in the experimental and control groups, respectively.

2.2. Behavioral Tests

2.2.1. Open field test (OF)

The open-field test evaluates the rats' locomotor activity as well as their anxiety levels. The test was done in a 60 x 60 x 50 centimeter square box made of untreated, black-painted wood. The animal was placed at the side wall's middle. Computer-aided video caught the animal's locomotion. The open field was divided into sixteen equal squares by virtual lines, twelve of which made up the arena's periphery zone, and four of which made up its core zone. The technology monitored 10 minute intervals of time and distance in each zone [16].

2.2.2. Elevated plus maze test (EPM)

The EPM test is used to assess the level of anxiety in mice and rats. It consists of a platform (10×10 cm) in the center, two open arms (50×10 cm) and two (50×10 cm) arms covered with plastic glass 30 cm high and consists of in the apparatus designed as a plus, open arms and closed arms face each other. The cross-shaped labyrinth consisting of four arms is at a height of 80 cm from the ground. For each experiment, only one rat is placed in the center of the cross maze and allowed to explore the maze for five minutes. At the end of the given time, the time spent by the mouse in the closed and opens arms and the numbers of crossing between arms are recorded with a computer-aided video system [16].

2.3. Statistics

The statistical analysis results were given as the mean ± value plus the standard error of the mean (SEM). One-Way Anova test was utilized to compare the behavior between the control (Cnt), Tudca (Tudca), SCD probiotics (Prb), and Tudca administration during the SCD probiotics supplementation (TdPrb) groups. The comparison was carried out using the GraphPad Prism 9 program (GraphPad Software, USA). The degrees of significance were denoted as * $p < 0.05$, ** $p < 0.01$, and *** $p < 0.001$.

3. Results and Discussion

The effects of aging are most evident on cognitive states and behavior. In particular, there is a significant decrease in learning and memory abilities [17]. This situation also triggers anxious behavior [18]. Today, many different approaches continue to be tested to reverse the effects of aging. As the importance of the role of GM in health and disease conditions was understood, probiotic bacteria that play a role in the regulation of gut microbiota moved to a more important position [19]. There are many different probiotic products available commercially today. TUDCA is another common product that is easily accessible commercially, owing to its regulatory role on intestinal microbiota. However, the positive effects of both probiotic use and TUDCA on cognitive states and behavior make them even more important [13,19]. In this study, the effects of co-administration of TUDCA and SCD probiotics human beverages containing 11 different probiotic bacteria

on locomotor activity and anxious behavior in aged rats were investigated. There was no significant difference between the groups in terms of time spent in motion in the periphery in the first 5 minutes of the open field test (p = 0,1629) (**Figure 1A**). However, the animals in the TdPrb group, in which the TUDCA and SCD probiotics were given together, appear to be willing to investigate the test apparatus further. Since the rats used in the study are 24 months old, which corresponds to 60–70 years of age for humans, the differences that are not significant are actually valuable [20]. Despite the fact that there was no statistically significant difference between the groups in terms of the central area studies in the first 5 minutes (p = 0.1096), it is seen that the rats in the Tudca group explored the central area more than the other groups (**Figure 1B)**. At the second 5 minutes, there was a significant difference between the groups in the periphery (p = 0.0497) and it is seen that the rats in the TdPrb group continued to explore the test apparatus more than the other groups (**Figure 1C)**. At the second 5 minutes, there was no significant difference between groups in their preference for the central area (p = 0.1476) (**Figure 1D)**.

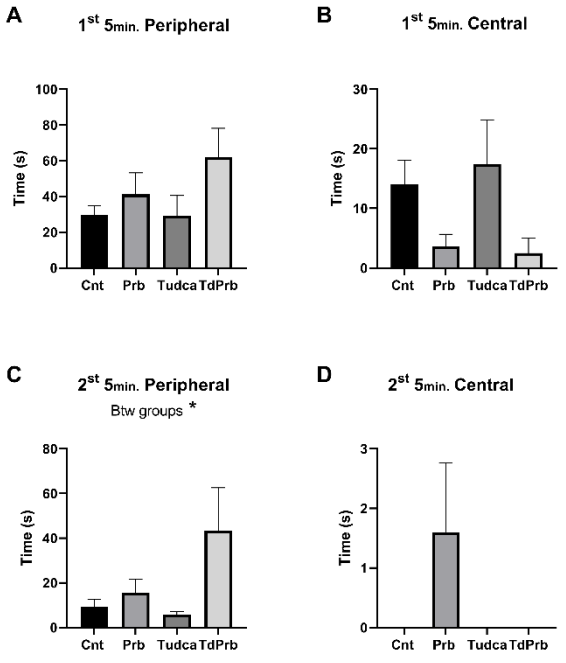

Figure 1. The mean distance moved in the periphery (A & C) and the center (B & D) of the OF during the 1st (upper row) and 2nd (lower row) 5-minute control periods (Cnt), Tudca (Tudca), SCD probiotics (Prb), and Tudca administration during the SCD probiotics supplementation (TdPrb) groups. Error bars represent SEM and asterisks indicate the statistical significance: *p < 0.05.

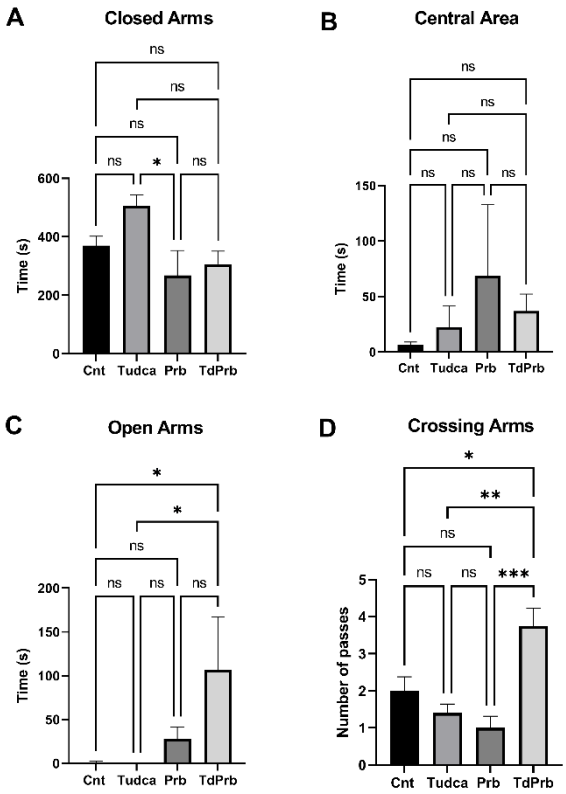

Figure 2. The mean time spent in the EPM's closed arms, open arms, and center zone and the number of passes between closed arms in control (Cnt), Tudca (Tudca), SCD probiotics (Prb), and Tudca administration during the SCD probiotics supplementation (TdPrb) groups. Error bars represent the standard error of the mean and asterisks indicate the significance level: *p < 0.05; **p < 0.01 and *** p < 0.001.

The number of passes between the arms shows the behavior of the animals to search the test apparatus [22]. According to the EPM results, there was a significant difference between the groups in preferring the closed arm (p= 0.0318). There was a significant difference between the Tudca and Prb groups in the comparison of the groups with each other (p = 0.0275) (**Figure 2A)**. This indicates that the SCD probiotics is more effective on anxious behavior than TUDCA. While there was no significant difference between the groups in their preference for the central area (p = 0.5310), it is seen that the Prb group spent more time in this area (**Figure 2B)**. However, there was a significant difference between the groups in their preference for open space (p = 0.0244). In addition, when comparing the groups with each other, it is seen that the TdPrb group, in which TUDCA and SCD probiotics were used together, investigated the open space significantly more than the Tudca (p = 0.0356) and control groups (p = 0.0249) (**Figure 2C)**. The most significant difference

between the groups was in terms of transition between arms ($p = 0.0009$). In the comparison of the groups with each other, it is seen that the rats in the TdPrb group exhibit significant test apparatus research behavior TdPrb vs. Cnt ($p = 0.0188$), TdPrb vs. Tudca ($p = 0.0032$), TdPrb vs. Prb ($p = 0.0007$) (**Figure 2D)**.

Although it is known that both probiotic use and TUDCA separately have positive effects on behavior, this study shows that using both together is more effective on both locomotor activity and anxious behavior. Even though it is not possible to say whether TUDCA or the probiotic used is more effective, the use of SCD probiotics seems to be more effective on anxious behavior. The probiotic content used with TUDCA also plays an important role in seeing this difference since the effects of probiotics depend on a variety of factors, including the probiotic species, its concentration, and duration, as well as the host's age and health state [23]. Species contained in SCD probiotics are known to have a positive effect on behavior. For example, *Bacillus subtilis,* one of the most well-known probiotic bacteria, produces l-tryptophan, and the increase in serotonin in the hypothalamus acts as an antidepressant that reduces anxious behavior [24]. In addition, numerous animal studies indicate that *Bifidobacterium longum* can significantly reduce anxious behavior [25]. *Lactobacillus plantarum* [26], *Lactobacillus casei* [27] and *Lactobacillus fermentum* [28] are also probiotic strains that have a strong effect on anxious behavior. On the other hand, since younger and smaller model organisms can investigate test apparatuses more actively, this allows for more reliable results in behavioral tests. Due to both their advanced age and large size, 24-month-old rats may not be very willing to use research test apparatus such as EPM. However, the significant differences occurring in as little as one week indicate the strong effect of both TUDCA and SCD probiotics bacteria on locomotors activity and anxiety-like behavior.

4. Conclusion and Suggestions

This study evaluated the effects of administering SCD probiotics supplement with TUDCA on anxious behavior and locomotors activity. The SCD probiotics was more effective on anxious behavior. When used together, they are more effective on both locomotors activity and anxious behavior.

Statement of Competing Interests
The authors have no competing interests

Research and Publication Ethics Statement
Research and publishing ethics were followed

Conflict of Interest Statement
There is no conflict of interest between the authors.

Statement of Research and Publication Ethics
This study was carried out with the approval of the Ethics Committee (approval number: 2022/03) from the Saki Yenilli Experimental Animal Production and Practice Laboratory.

References

[1] J. F. Cryan and T. G. Dinan, "Mind-altering microorganisms: the impact of the gut microbiota on brain and behaviour," *Nat. Rev. Neurosci*., vol. 13, no. 10, pp. 701–712, 2012.
[2] C. R. Martin and E. A. Mayer, "Gut-brain axis and behavior," Nestle Nutr. Inst. Workshop Ser., vol. 88, pp. 45–53, 2017.
[3] G. Stavrou and K. Kotzampassi, "Gut microbiome, surgical complications and probiotics," *Ann. Gastroenterol.*, vol. 30, no. 1, pp. 45–53, 2017.
[4] R. George Kerry, J. K. Patra, S. Gouda, Y. Park, H.-S. Shin, and G. Das, "Benefaction of probiotics for human health: A review," *J. Food Drug Anal.*, vol. 26, no. 3, pp. 927–939, 2018.
[5] K. M. Maslowski and C. R. Mackay, "Diet, gut microbiota and immune responses," *Nat. Immunol.*, vol. 12, no. 1, pp. 5–9, 2011.
[6] Z. Song et al., "Taxonomic profiling and populational patterns of bacterial bile salt hydrolase (BSH) genes based on worldwide human gut microbiome," *Microbiome*, vol. 7, no. 1, p. 9, 2019.
[7] P. Gérard, "Metabolism of cholesterol and bile acids by the gut Microbiota," *Pathogens*, vol. 3, no. 1, pp. 14–24, 2013.
[8] M. L. Chen, K. Takeda, and M. S. Sundrud, "Emerging roles of bile acids in mucosal immunity and inflammation," *Mucosal Immunol.*, vol. 12, no. 4, pp. 851–861, 2019.

[9] S. L. Long, C. G. M. Gahan, and S. A. Joyce, "Interactions between gut bacteria and bile in health and disease," *Mol. Aspects Med.*, vol. 56, pp. 54–65, 2017.
[10] J. A. Winston and C. M. Theriot, "Diversification of host bile acids by members of the gut microbiota," *Gut Microbes*, vol. 11, no. 2, pp. 158–171, 2020.
[11] E. A. Franzosa et al., "Gut microbiome structure and metabolic activity in inflammatory bowel disease," *Nat. Microbiol.*, vol. 4, no. 2, pp. 293–305, 2019.
[12] Q. Lu, Z. Jiang, Q. Wang, H. Hu, and G. Zhao, "The effect of Tauroursodeoxycholic acid (TUDCA) and gut microbiota on murine gallbladder stone formation," *Ann. Hepatol.*, vol. 23, no. 100289, p. 100289, 2021.
[13] X. Wu et al., "Protective effects of tauroursodeoxycholic acid on lipopolysaccharide-induced cognitive impairment and neurotoxicity in mice," *Int. Immunopharmacol.*, vol. 72, pp. 166–175, 2019.
[14] M. Song et al., "Tauroursodeoxycholic acid (TUDCA) improves intestinal barrier function associated with TGR5-MLCK pathway and the alteration of serum metabolites and gut bacteria in weaned piglets," *J. Anim. Sci. Biotechnol.*, vol. 13, no. 1, p. 73, 2022.
[15] X. Zheng, S. Wang, and W. Jia, "Calorie restriction and its impact on gut microbial composition and global metabolism," *Front. Med.*, vol. 12, no. 6, pp. 634–644, 2018.
[16] T. Ceylani, E. Jakubowska-Doğru, R. Gurbanov, H. T. Teker, and A. G. Gozen, "The effects of repeated antibiotic administration to juvenile BALB/c mice on the microbiota status and animal behavior at the adult age," *Heliyon*, vol. 4, no. 6, p. e00644, 2018.
[17] J. M. Castellano, "Blood-based therapies to combat aging," *Gerontology*, vol. 65, no. 1, pp. 84–89, 2019.
[18] E. D. Nolte, K. A. Nolte, and S. S. Yan, "Anxiety and task performance changes in an aging mouse model," *Biochem. Biophys. Res. Commun.*, vol. 514, no. 1, pp. 246–251, 2019.
[19] C.-S. Kim et al., "Probiotic supplementation improves cognitive function and mood with changes in gut Microbiota in community-dwelling older adults: A randomized, double-blind, placebo-controlled, multicenter trial," *J. Gerontol. A Biol. Sci. Med. Sci.*, vol. 76, no. 1, pp. 32–40, 2021.
[20] P. Sengupta, "The laboratory rat: Relating its age with human's," *Int. J. Prev. Med.*, vol. 4, no. 6, pp. 624–630, 2013.
[21] A. A. Walf and C. A. Frye, "The use of the elevated plus maze as an assay of anxiety-related behavior in rodents," *Nat. Protoc.*, vol. 2, no. 2, pp. 322–328, 2007.
[22] M. Komada, K. Takao, and T. Miyakawa, "Elevated plus maze for mice," J. Vis. Exp., no. 22, 2008.
[23] T. Eom, Y. S. Kim, C. H. Choi, M. J. Sadowsky, and T. Unno, "Current understanding of microbiota- and dietary-therapies for treating inflammatory bowel disease," *J. Microbiol.*, vol. 56, no. 3, pp. 189–198, 2018.
[24] Z. Chen et al., "Bacillus subtilis promotes the release of 5-HT to regulate intestinal peristalsis in STC mice via bile acid and its receptor TGR5 pathway," *Dig. Dis. Sci.*, vol. 67, no. 9, pp. 4410–4421, 2022.
[25] K. Leung and S. Thuret, "Gut Microbiota: A modulator of brain plasticity and cognitive function in ageing," *Healthcare (Basel)*, vol. 3, no. 4, pp. 898–916, 2015.
[26] Y.-W. Liu et al., "Psychotropic effects of Lactobacillus plantarum PS128 in early life-stressed and naïve adult mice," *Brain Res.*, vol. 1631, pp. 1–12, 2016.
[27] A. V. Rao et al., "A randomized, double-blind, placebo-controlled pilot study of a probiotic in emotional symptoms of chronic fatigue syndrome," Gut Pathog., vol. 1, no. 1, p. 6, 2009.
[28] T. Wang et al., "Lactobacillus fermentum NS9 restores the antibiotic induced physiological and psychological abnormalities in rats," *Benef. Microbes*, vol. 6, no. 5, pp. 707–717, 2015.

Bitlis Eren Üniversitesi Fen Bilimleri Dergisi
BİTLİS EREN UNIVERSITY JOURNAL OF SCIENCE
ISSN: 2147-3129/e-ISSN: 2147-3188
VOLUME: 12 NO: 1 PAGE: 247-260 YEAR: 2023
DOI:10.17798/bitlisfen.1232008

Nonlinear Seismic Assessment of Historical Masonry Karaz Bridge Under Different Ground Motion Records

Ömer Faruk NEMUTLU[1,2*], İhsan GÜZEL[1,2], Bilal BALUN[2,3], Mitat ÖZTÜRK[4], Ali SARI[5]

[1]*Department of Civil Engineering, Bingöl University*
[2]*Bingöl University Centre for Energy, Environment and Natural Disasters*
[3]*Department of Architecture, Bingöl University*
[4]*Department of Civil Engineering, Osmaniye Korkutata University*
[5]*Faculty of Civil Engineering, İstanbul Technical University*
(ORCID: 0000-0001-7841-3911) (ORCID: 0000-0002-0746-070X) (ORCID: 0000-0003-0906-4484)
(ORCID: 0000-0003-4685-7088) (ORCID: 0000-0002-6888-1276)

Keywords: Finite element method, Masonry bridges, Nonlinear dynamic analysis, Failure, Earthquake behaviour.

Abstract

The most significant artifacts that transfer the cultural heritage of past civilizations to the present are historical structures. Historical bridges are of great importance in terms of transportation, trade and architecture from past to present. Some of these structures have been destroyed by natural disasters or have suffered significant structural damage. Especially earthquakes cause damage to these structures. In this study, the earthquake behavior of the Historical Karaz Bridge was investigated. The structural elements of the bridge and the materials connecting the bearing elements were evaluated together with the macro modeling approach. For this purpose, a 3D finite element model of the bridge was generated and its seismic behavior under different ground motion records was investigated by nonlinear analysis. Analyzes were carried out using the ground motion records of Bingöl, Elazığ, Erzincan, Van and Gölcük, and the results were evaluated mutually. In the analysis results, the dynamic behavior of the bridge was evaluated over the distribution of displacements and stresses and the earthquake behavior was investigated.

1. Introduction

Bridges have been an important part of transportation routes throughout history. Historical bridges, on the other hand, establish a link between the past and the present, apart from their intended use in their time. It is important to protect these bridges as they reflect their period socially and culturally. Therefore, historical bridges should be preserved and passed on to future generations. It should be kept as far away from environmental influences as possible for durability and sustainability. Climatic conditions, fires, wars and all the situations they are exposed to reduce the useful life of historic bridges. Otherwise, vehicle loads, human loads and earthquake loads cause historical bridges to decrease in strength, to be damaged and to collapse completely as seen in some historical bridges. Historical bridges are one of the historical structures that are accepted as cultural heritage. These structures, which have a history of hundreds of years, should be preserved in the best way and transferred to the future. Earthquakes are one of the most important external factors that cause damage to historical structures. In order for these structures to suffer the least damage from earthquakes and to protect their structural integrity, seismic behavior should be determined, and necessary precautions should be taken accordingly. Most of the historical bridges were built as masonry stone walls. These bridges consist of foundation, arch, side wall and filling material, and the superstructure forming the carrier part was built using stone and binding material [1–3].

*Corresponding author: ofnemutlu@bingol.edu.tr
Received: 01.01.2022, Accepted: 01.06.2022

Vibrations occur during earthquakes and these vibrations cause historic bridges to reach significant levels of damage [4,5]. By design, historical structures are important. Bridges built on different dates in the past were generally built as arches. Arch form is the general structural carrier system of historical bridges [6]. The arch-shaped structure is a suitable design system for passing wide openings due to its positive behavior to pressure forces due to its geometric form. Stone or brick was used as the main building material in the construction of the arches due to their resistance to high pressures [2,3,7]. The importance of historical bridges in terms of engineering as well as social life has encouraged researchers to work in this field. Studies that investigating the seismic behavior of historical masonry bridges with linear and nonlinear finite element models are available in the literature [1, 2, 8-28]. After analyzing 3 historical palaces with the finite element models, Valente ve Milani [18] studied the crack development, earthquake behavior with nonlinear dynamic analysis, and made a general assessment of damage and collapse. Karaton et al. examined the earthquake behavior of historical Malabadi bridge, which was built in the 12th century and located in the east of Turkey, for different earthquake levels [25]. As a result of the study, D1, D2 and D3 are from the lowest to the highest ground motion level, no significant damage occurred at the ground motion levels D1 and D2; it was observed that the historic bridge suffered substantial damage at the D3 ground motion level. Güllü [2] created a finite element model for the Historic Cendere Bridge, using earthquake scenarios suitable for the seismicity of the region where the bridge is located, and performed linear analyzes in the time domain. As a result of the analyzes made, it has been observed that the vulnerability of the historical bridge in possible during an earthquake is high. Özmen ve Sayın [6], created a finite element model for the historical Dutpınar Bridge and investigated its dynamic behavior using the records of the 2003 Bingöl earthquake, one of the most destructive earthquakes that occurred in the region. At the end of the study, the maximum and minimum displacement values for the critical structural members were examined. Bayraktar et al. [24] determined analytical and experimental vibration parameters of a historical two-span bridge built in the 19th century and located in northern Turkey. Comparing the natural frequency, mode shapes, and damping rates for analytical and experimental results, the authors observed slight differences. Pela et al. [17] investigated the earthquake behavior of two different historical bridges by using nonlinear static analysis methods for different modern standards. As a result, they concluded that the nodes at the top of the bridges are an important point in determining seismic capacity. Işık et al. [19] studied the historical Ahlat Emir Bayındır bridge and made observational and analytical seismic evaluations in this study. After the field studies, they explained how similar structures would be evaluated.

In this study, the seismic response of the historical Karaz (Öznü) bridge was modeled and analyzed using the ABAQUS program using different earthquake records reflecting the seismicity of the region. As a result of the study, the stressed areas on the bridge were determined for different earthquake records and the displacements occurred during the earthquake period were obtained.

2. Historical Karaz (Öznü) Bridge

The historical Karaz bridge is located 5 km northeast of the Karaz District (Village), just to the right of the International Erzurum Airport and the ring road. Coordinates of bridge are 39.967-41.147. It was built in the period to provide transportation on the Karasu River. The building does not have an inscription, but it is estimated that it was built in the 16th century when Erzurum joined the Ottoman lands and development activities were concentrated.

The bridge was repaired by the General Directorate of Highways between 1980-1984. In the meantime, the old stones were replaced, and the periphery of the flood splitter was supported with triangular reinforced concrete elements. Then, in 2017, it was restored by the 12th Regional Directorate of Highways. The historical Karaz bridge is 135 m long and 6.6 m wide in the east-west direction and has eight arches. Seven of them were built with low pointed arches where the water flows fast and hard, and the eighth was built with smaller, round arches at the far end. The spans and heights of the bridges are not equal to each other, some of them are arranged with low pointed arches and some with narrower pointed arches. On the upstream side, which is the incoming direction of the water, there are triangular-bottom floods covered with a half-pyramidal cone and six round-bottomed heels in the downstream direction of the water. The bridge reaches the middle point with a slight inclination towards the middle from both ends and the height of the bridge is 7.70 meters from the ground, and it is limited by stone railings on both sides. The materials used in the bridge were smooth cut stone on the facades and rubble stone with plenty of mortar in between. The historical Karaz bridge still continues to provide transportation services especially between the surrounding villages. The

current view and location of the Historical Masonry Karaz bridge are given in Figure 1.

Figure 1. Historical Karaz bridge views and location of Karaz bridge

3. Material and Method

The Historical Masonry Karaz bridge is located in the northeast of Karlıova district of Bingöl is located of the intersection of the North Anatolian Fault (NAF) and East Anatolian Fault (EAF) one of Turkey's active fault zones. Therefore, Karaz bridge, which is within the boundaries of Erzurum province, has a significant earthquake risk potential.

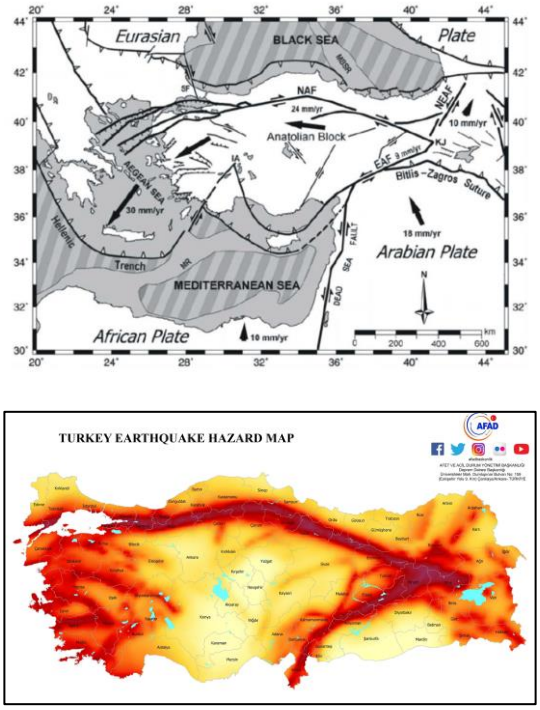

Figure 2. Turkey's active fault map [28] and Turkey earthquake hazard map [29]

The Turkey's active fault map is given in Figure 2. By using Turkey Earthquake Hazard Map, the necessary earthquake parameters are generated for the coordinates of the bridge [29]. Since there is no clear information about the ground properties of the Karasu river and its surroundings, the ground class was accepted as ZC (the middle of the soil classification made according to the TEC 2018) according to the classification used in Turkish Earthquake Code 2018 [30]. Turkey Earthquake Hazard Map overview is given in Figure 2 and the data taken from the earthquake hazard map are given in Table 1. The information about the earthquakes used in the analyzes are given in Table 2, the acceleration spectrum used for scaling the earthquake records in Figure 3, and the ground motion records (acceleration-time) and scaled records of 5 earthquakes considered within the scope of the study are given in Figure 4 and 5.

Table 1. Data from the earthquake hazard map

Earthquake Ground Motion Level	DD-2
Local Soil Class	ZC
Latitude-Longitude	39.967991-41.14791
S_s	0.717
S_1	0.214
PGA	0.3
PGV	18.985

Analyzes were completed using the acceleration records of the Gölcük, Bingöl, Van,

Erzincan and Elazığ earthquakes (only in the z direction) and these analyzes were named as A1, A2, A3, A4 and A5, respectively. First, the horizontal elastic response spectrum was created from the Turkey earthquake hazard map by using the location of the bridge [29]. The reason for choosing these ground motion records is to take into account the earthquakes that occurred in the region where the bridge is located and the Gölcük earthquake that occurred in Turkey, which is frequently used in the literature.

The scaled earthquake records given in Figure 5 were used in the analysis. The earthquake records were scaled by the SeismoMatch [31] program using the horizontal elastic response spectrum in Fig. 9, and the minimum period and maximum period were 0.2T and 1.5T (ASCE7), respectively [32]. In order to shorten the analysis time, specific parts of the records used were taken into account. The first 10 seconds for A1, 10 seconds between 20-30 seconds for A2, 40 seconds between 20-60 seconds for A3, first 30 seconds for A4 and 30-70 seconds for A5.

Table 2. Selected ground motion records

Code	Earthquake	Record Station	Mw	Epicentral Distance (km)	Shear Wave Velocity (m/sn)
A1	Gölcük (1999)	5401	7.2	35.87	412
A2	Bingöl (2003)	1201	6.4	11.80	529
A3	Van (2011)	6503	6.7	42.24	N/A
A4	Erzincan (1992)	2402	6.1	12.82	455
A5	Elazığ (2020)	2308	6.8	23.81	450

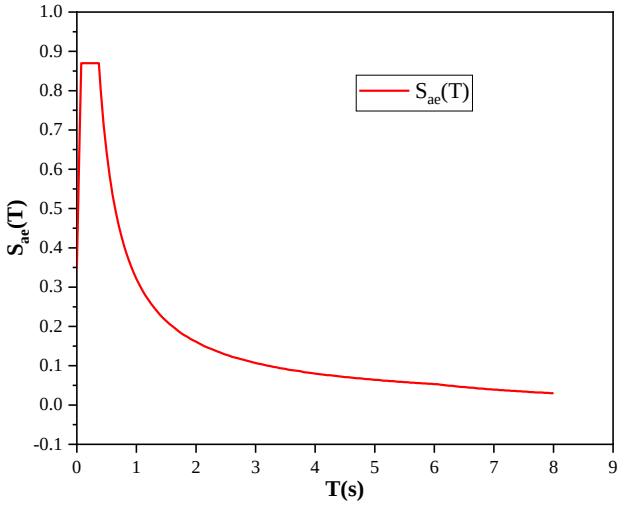

Figure 3. Horizontal Elastic Acceleration Spectrum

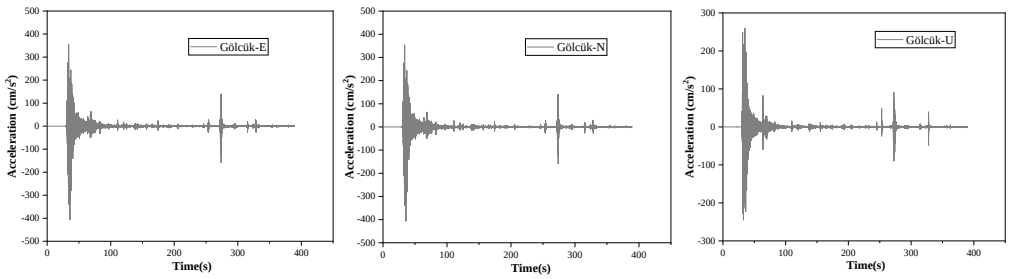

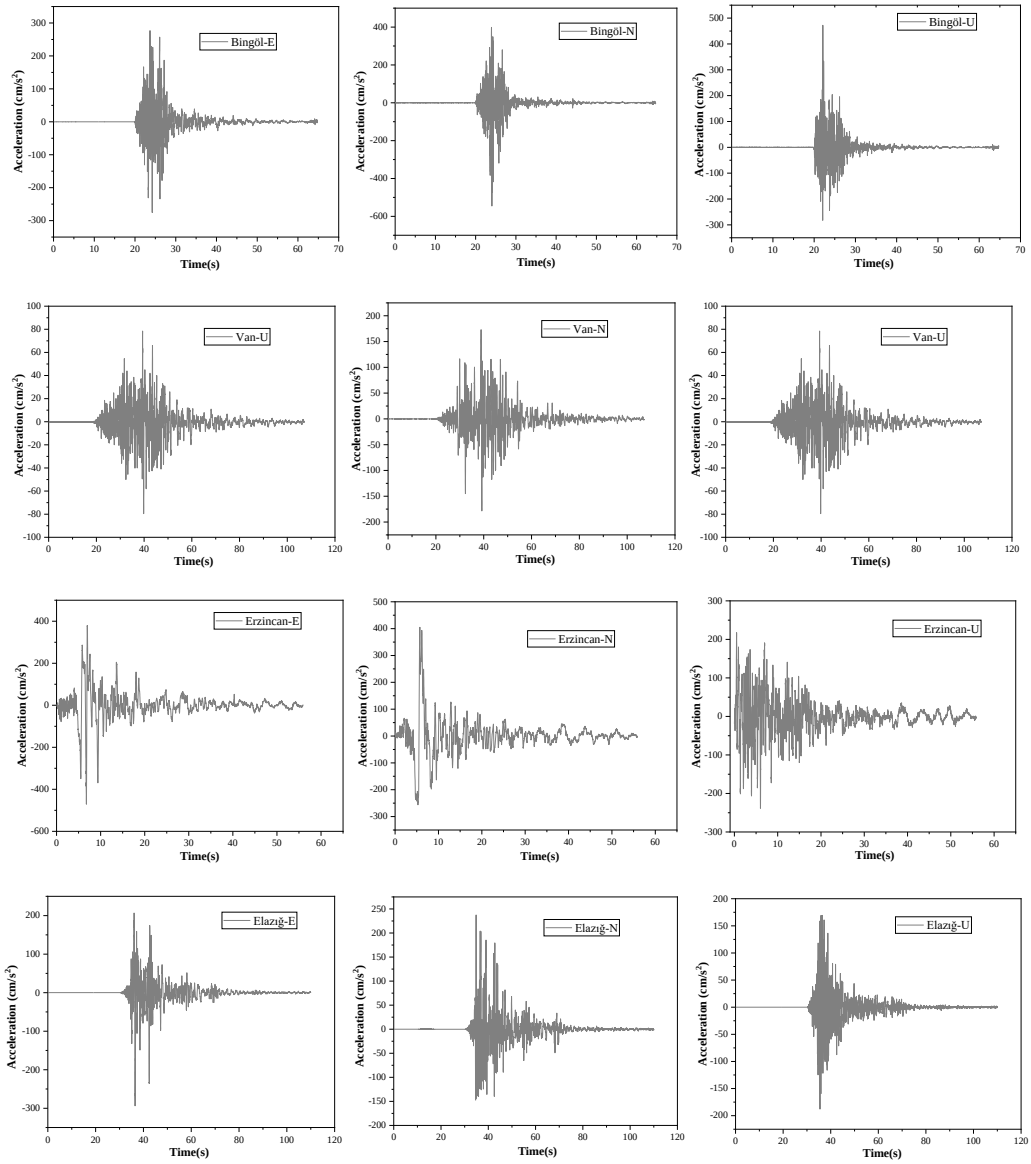

Figure 4. Earthquake acceleration records

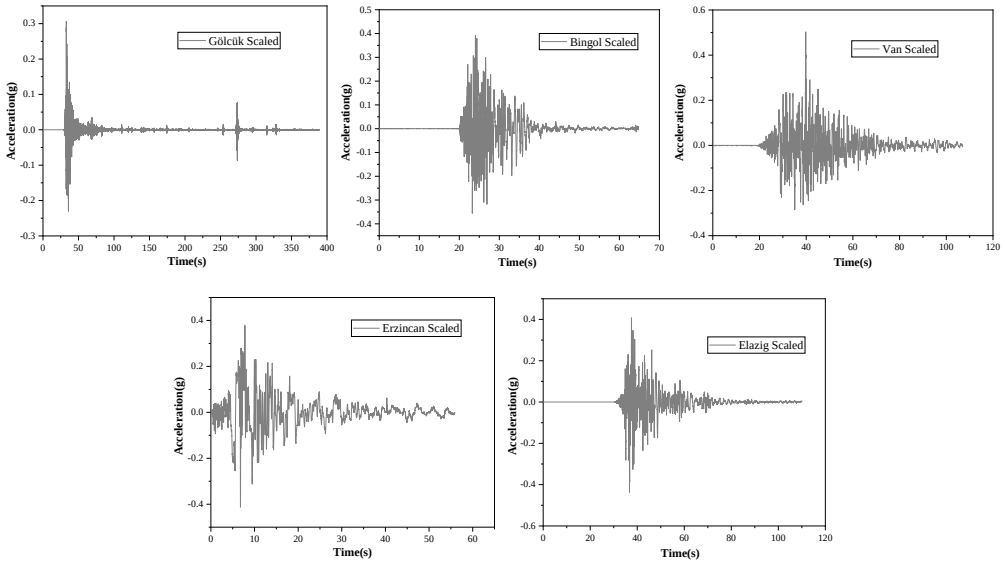

Figure 5. Scaled earthquake records

4. Methodology

In the scope of the study, 3 dimensional 10-node tetrahedral C3D10 finite elements are used as a finite element model. The C3D10 element is a general-purpose tetrahedral element (4 integration points). Shape functions can be found in Figure 6. Node numbering follows the rule in Figure 6. Element behavior is very good and is a good general-purpose element, but the C3D20R element is available in the literature where it gives better results for the same number of degrees of freedom. The C3D10 element may be particularly preferred due to the availability of fully automatic tetrahedral networks [33].

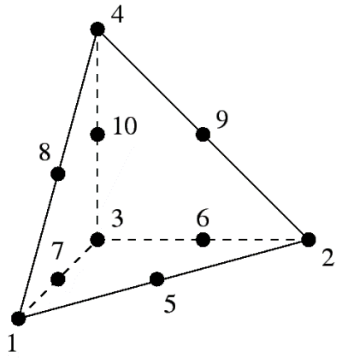

Figure 6. 3-dimensional 10 nodes tetrahedral C3D10 finite element [25]

Whether the finite element network is sufficient for analysis should be considered in the analysis. If the element network is "good enough", it can be said that the analysis results are also acceptable, assuming all other inputs of the model are correct. Finite element density is an important metric used to check the accuracy of the analysis (element type and shape also affect the accuracy of the analysis). Assuming that there is no region of singularity in the model, a high-density network structure will produce results with high accuracy. However, large amounts of computer memory and long runtimes will be required if the network of elements in the model is very dense. This disadvantage is frequently encountered especially for multiple iteration conditions specific to nonlinear and transient analysis. One of the ways to evaluate the quality of a finite element network is to compare the results with test data or theoretical values. Unfortunately, test data and theoretical results are often not available in the early stages of the study. Therefore, other tools are required to assess network quality. The most basic and most accurate method for evaluating the quality of the mesh is to tighten the mesh with smaller elements until the maximum stress convergence at a given location is achieved (mesh convergence). Within the scope of this study, mesh size to be used was determined by making mesh optimization. By comparing the number of elements and frequencies belonging to the 1st mode, the mesh size to be used in the study was selected as 600 mm. In Table 3, mesh size, number of elements and frequencies of the first mode are given. In Figure 7, mesh convergence graph is given.

Table 3. Optimization of meshes

Mesh size (mm)	Number of elements	1.mode frequency (Hz)
400	232506	19.28
500	113770	19.29
600	**79704**	**19.31**
750	36789	19.37
1000	18788	19.42
1250	10255	19.52
1500	8025	19.58
1750	6066	19.66
2000	4587	19.71

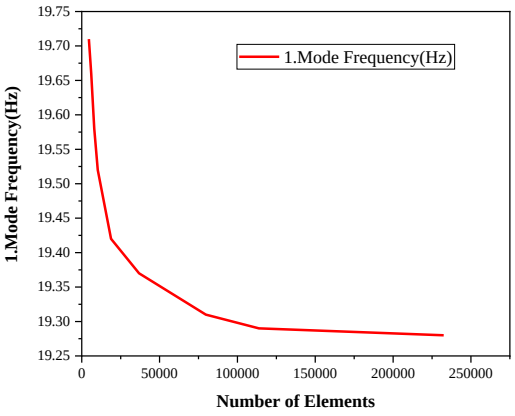

Figure 7. Mesh convergence graph

4.1. Numerical Modeling

Three methods are commonly used in modeling masonry structures. Modeling techniques are given in Figure 8 [6]. In detailed micro modeling, the masonry unit, and the material properties of the mortar i.e., elasticity modulus, Poisson ratio and unit volume weights are evaluated separately. This modeling technique is

one of the best techniques for modeling the behavior of masonry walls. Thus, damage and collapse mechanisms can be simulated properly. However, this method makes the analysis of the entire structure difficult and prolongs the solution time. This modeling technique is particularly suitable for small structures or solving parts of the structure. In simplified micro modeling, the size of the masonry units is expanded by half the thickness of the mortar layer, neglecting the mortar layer. Masonry units are separated from each other by interfacial lines. It is accepted that the cracks that will occur in the system will occur at these interface lines. Macro modeling, on the other hand, is an equivalent material model that accepts the building element as composite and reflects the common feature of these materials, without making any distinction between stone and brick blocks and mortar [34]. This method is generally preferred because it significantly reduces the computer solution time in modeling large systems [26]. The three-dimensional solid model of the Historical Masonry Karaz bridge to be used in this study, prepared in the ABAQUS program, is given in Figure 9 and its geometric properties are given in Figure 10.

Concrete Damage Plasticity (CDP) model is adopted to simulate the nonlinear behavior of the wall. Although originally developed to describe the nonlinear behavior of concrete [35,36], the use of such a model for masonry is widely accepted in the literature after proper adaptation of the main parameters. The CDP model is a damage model based on continuous plasticity, allowing different tensile and compressive strength as in the wall, with different damage parameters in stress and compression. The CDP model considers the effect of closing preformed cracks under cyclic loading conditions, resulting in compression stiffness recovery.

Masonry Bridge material specified as green part is modeled with linear and nonlinear parameters and Base material specified as white part is modeled with linear parameters only. The general analysis procedure and accepted material properties in this study were based on the studies of Valente and Milani [18] and Güllü [2]. In Table 4, material properties for analysis and in Table 5, damage values and stress strain values for the CDP model are given.

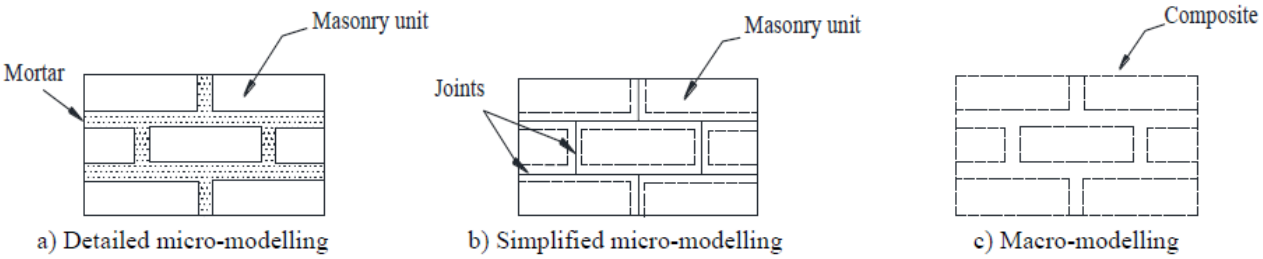

Figure 8. Modeling Approaches [6]

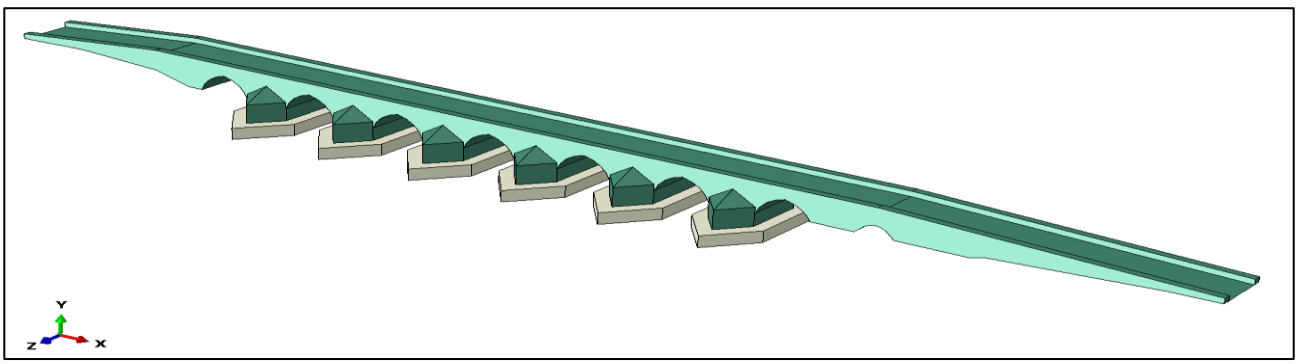

Figure 9. Solid Model of the Karaz bridge

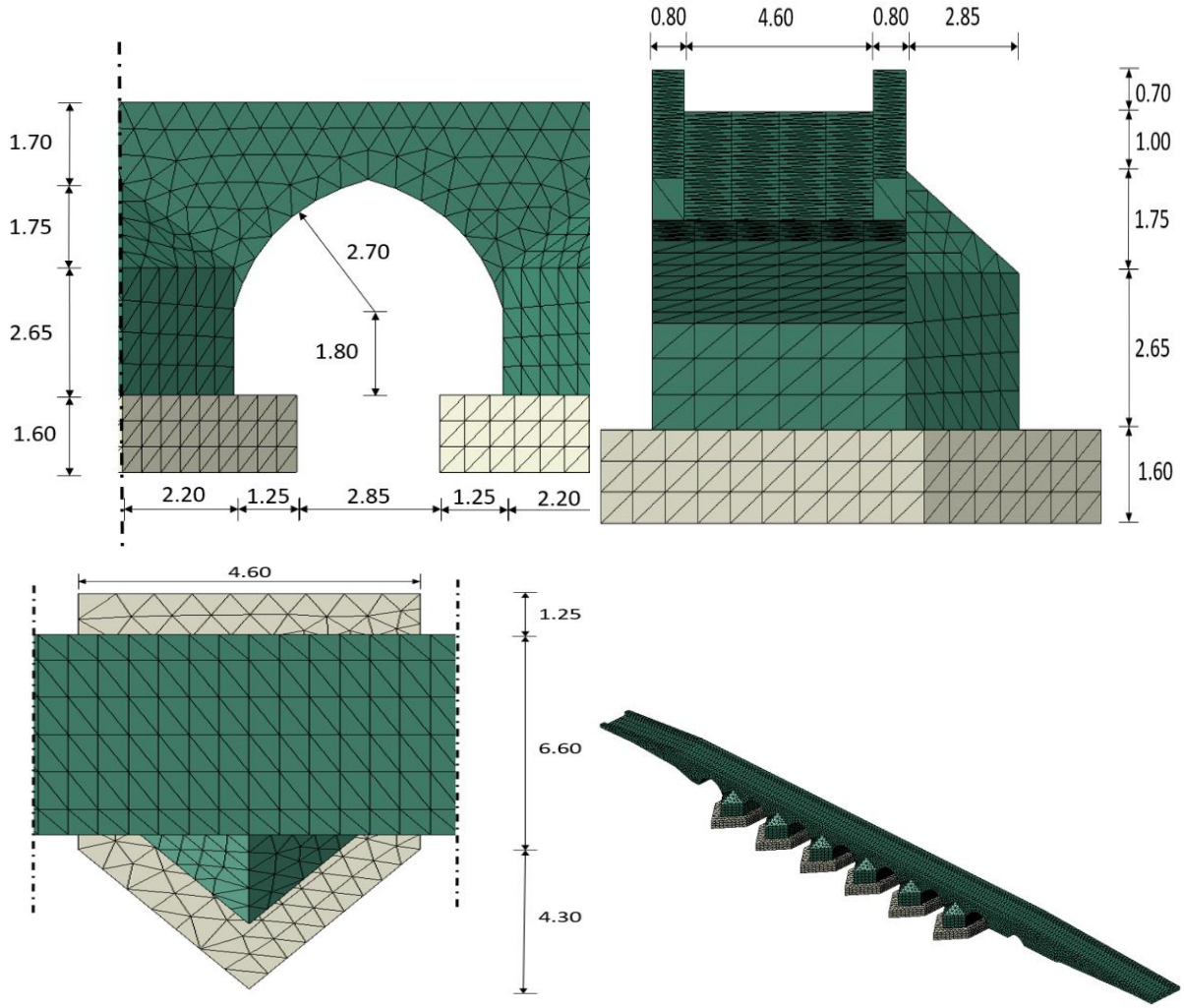

Figure 10. Geometric Properties of the Karaz bridge

Table 4. Linear Material Properties [2,18]

	E (Young Modulus) MPa	ν (Poisson Ratio)	Mass Density (t/mm^3)
Masonry Bridge	3500	0.25	2.20E-09
Base	5000	0.3	2.40E-09

Table 5. Uniaxial stress–strain values and scalar damage values utilized in the CDP model for masonry [18]

Non-linear Material Properties (mansory brigde)										
Concrete Damaged Plasticity					Tensile Behavior				Compressive Behavior (type strain)	
Dil Angle	E_{cc}	f_b/f_c	K	Vis	Yield Stress	Cracking Strain	Damage	Crack strain	Yield Stress	Inelastic Strain
10	0.1	1.16	0.666	0.001	0.15	0	0	0	1.9	0
					0.075	0.00025	0.95	0.00121	2.4	0.0051
					0.018	0.00057			0.96	0.0102
					0.009	0.00121			0.48	0.0307

5. Results

Since the stresses (compression, tensile) caused by its own weight (constant load) are lower than the material strength, no damage is expected in the stone arch bridge under constant load. The unfavorable earthquake motion affecting the bridge has been determined by calculating the stresses due to earthquake-induced loads separately for the maximum (tensile), minimum (pressure) and maximum acceleration of the stress envelope. It can be said that this tensile stress obtained is compatible with the tensile strength/compressive strength ratios (1/20-1/10) proposed by Pela [17] for masonry structures and can be used as a control in the assessment of damage potential. However, it would be appropriate to stay on the safer side due to factors arising from the loading situation (dead, earthquake, and dead+earthquake), analysis type (linear) and lack of experimental data. Therefore, as mentioned before, in this study, the damage potential was evaluated by assuming the tensile strength / compressive strength ratio as 1/20 or 5%. Therefore, it has been predicted that structural strength may decrease, and damage may occur at values greater than 1/20 (> 1 MPa) of tensile stress under earthquake effect. After the analysis, free vibration modes and corresponding frequency values are given in Figure 11 for the first 4 modes.

When the period values of free vibration modes calculated by modal analysis are examined, it is seen that the period values change between 0.052 and 0.048 s for the first 4 modes. If the studies are examined, the mode shapes up to the first 5 modes gain importance in such structures [37]. The study also analyzed the number of modes up to ensure the effective mass of up to 95% participation condition in Turkey Seismic Code [30]. Since these period values remain in the same range with the elastic acceleration spectrum used in the study, the possibility of resonance of the structure under the effect of an earthquake should also be taken into consideration.

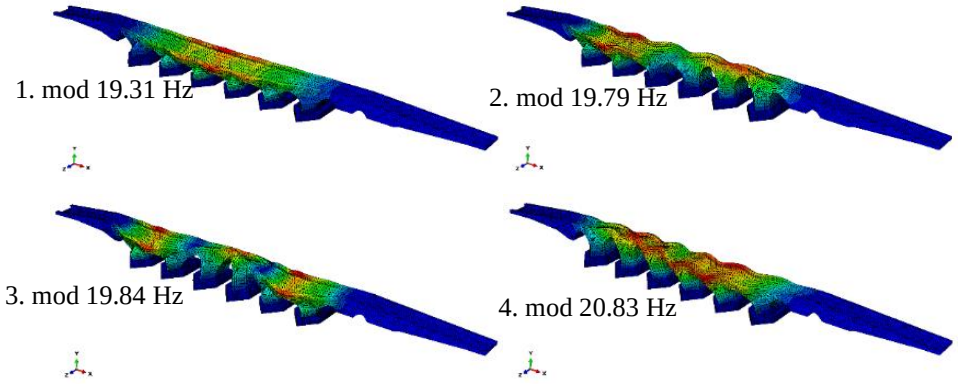

Figure 11. Free vibration modes and frequency values

5.1. Dynamic Analysis Results

As a result of the numerical analysis, it was found that the strength limits were not exceeded according to the stress distributions and damage profiles under constant stresses caused by the self-weight of the structure. The results of the nonlinear dynamic analysis in the time domain performed with 5 different scaled acceleration records were evaluated over the region of the structure that performs the maximum peak displacement and the DAMAGET crack distributions that represent the tensile damage defined in the material model. With the assessment, it has been observed that the acceleration record that causes the most unfavorable results for the building model is A2 (Bingöl) earthquake. For this reason, the damage profiles of the model were evaluated based on the A2 earthquake results. According to this damage profile (Figure 12), the most critical tensile cracks occur both in the heel area and in the middle of the arch. Numerical analyzes by displacement provided detailed information on the seismic behavior of the structure for different acceleration records. In particular, nonlinear dynamic analysis provided evidence about damage distribution and the weakest elements. In Figure 12, the detailed results of the tensile damage on the bridge are given visually for A2 (Bingöl) earthquake recording. As can be seen in Fig. 13, in the analysis made for the Bingöl earthquake(A2), damage has occurred. In Figures 14 and 15, detailed views of the damage mechanisms for the damaged (A2) Bingöl earthquake are given.

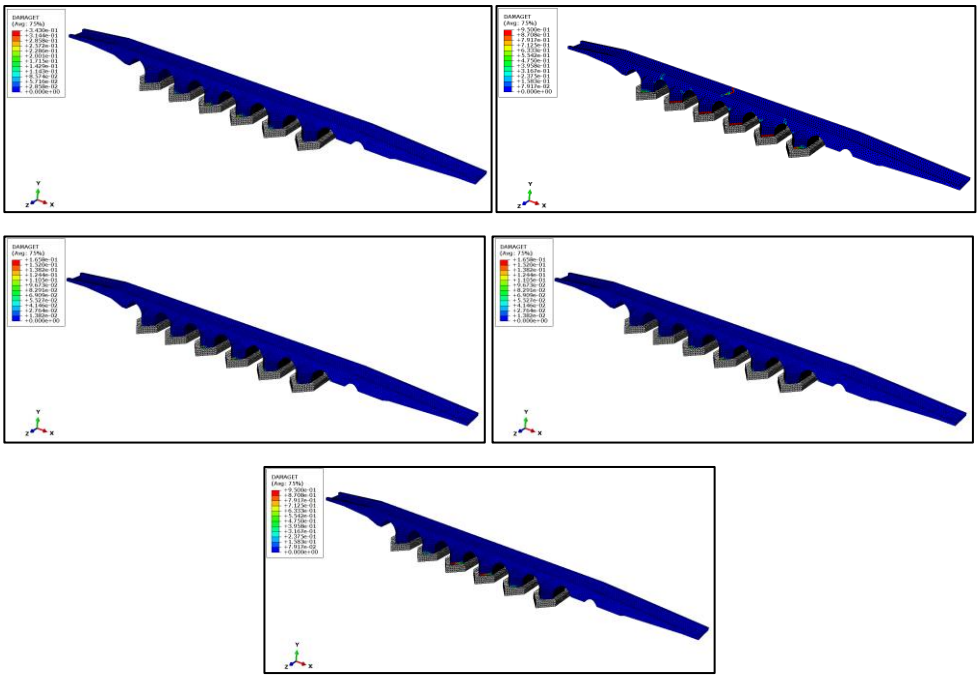

Figure 12. Dynamic analysis results

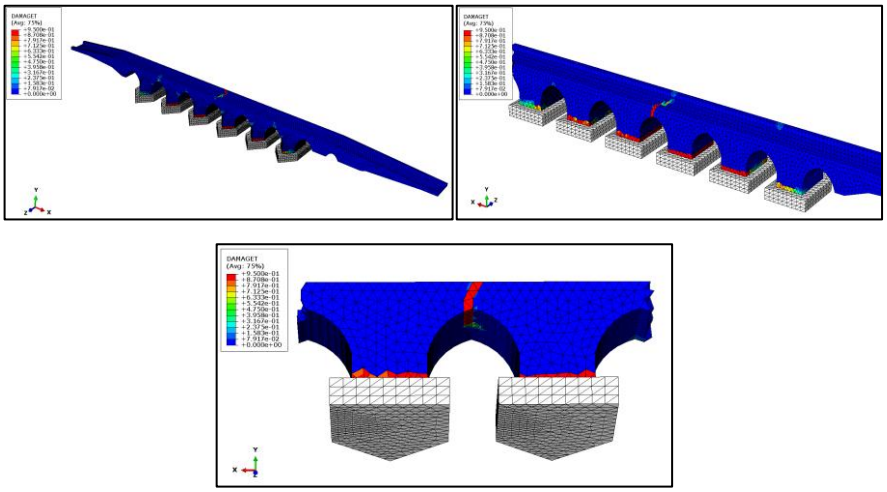

Figure 13. Damages on the bridge for A2 (Bingöl) earthquake

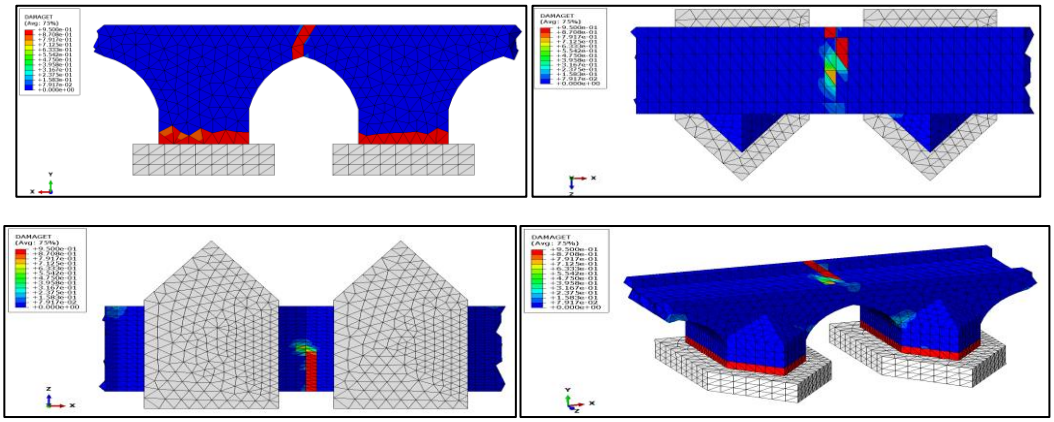

Figure 14. Damage profiles for A2 (Bingöl) earthquake

The maximum displacement point was selected for each analysis from the midpoint of the bridge where the crack occurred in A2 earthquake. According to the damage profile created using the Bingöl earthquake records, it was determined that the most critical tensile cracks occurred both in the heel area and in the middle of the bridge. Therefore, taking these data into consideration, the displacement time graphs in the model were obtained for the finite element number 1624 (Figure 15), which expresses the behavior at the point where the damage occurred for the A2 earthquake. In Figure 16, displacement-time graphs of the same finite element piece are given for each earthquake.

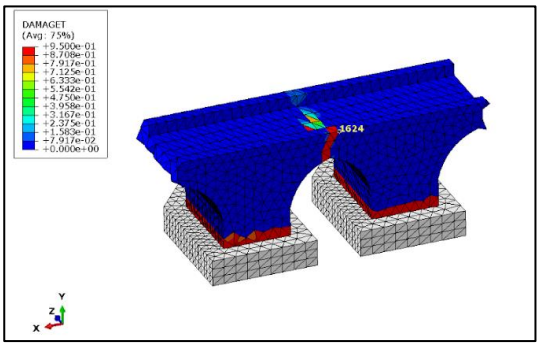

Figure 15. The nodal point considered for the displacement-time graphs (A2 Earthquake)

When we look at the displacement time graphs in Figure 16, a displacement of 0.012 m, 0.16 m, 0.8 m, 3 m and 0.2 m has occurred for the Historical Masonry Karaz bridge, Gölcük, Bingöl, Van, Erzincan and Elazığ earthquake records, respectively.

As we can see in Figures 13 and 14, in the Bingöl earthquake named as A2, damage occurred in the middle part of the bridge. When we look at Fig. 16, in the Erzincan earthquake we named as A4, although the maximum displacement of the node point in Fig. 15 was around 3m, damage occurred in the A2 Bingöl earthquake, where the maximum displacement was around 0.16 m. The most important reason for this is that the impact on the vertical component of the Bingöl earthquake is more destructive than other earthquakes. In addition, Bingöl earthquake can be said to be the best earthquake reflecting the real behavior, considering the location of the bridge.

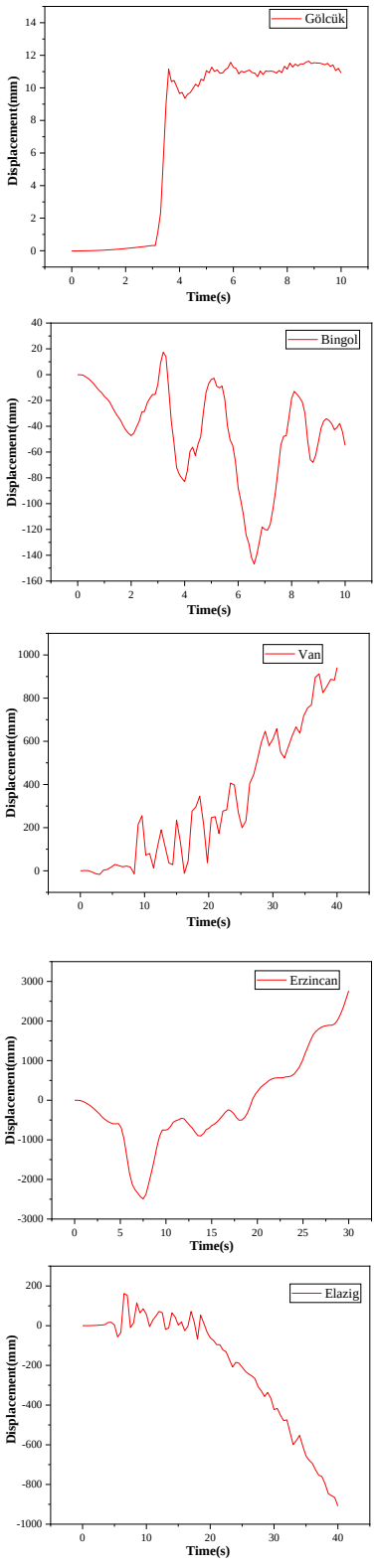

Figure 16. Displacement-time graphs

6. Conclusions

In this study, the three-dimensional finite element model of the Historical Karaz (Öznü) bridge, which has historical masonry and arch form, was created and the

behavior under the effect of earthquake was evaluated with the nonlinear analysis in the time history. The results of the nonlinear dynamic analysis in the time domain performed with 5 different scaled acceleration records were evaluated over the region of the structure that performs the maximum peak displacement and the crack distributions expressing the tensile damage defined in the material model. Detailed information on the seismic behavior of the structure is provided by numerical analysis by using different acceleration records for the displacement values at joint 1624 in the finite element model. In particular, nonlinear dynamic analysis provided evidence about damage distribution and the weakest elements. The following results can be proposed for the historical Karaz bridge, depending on the linear and nonlinear analysis findings obtained with the effect of the finite element behavior model:

•The three-dimensional finite element model of the masonry and arch shaped historical Karaz (Öznü) bridge was created and the behavior under the effect of an earthquake was examined using the nonlinear time history analysis and the damage status was evaluated.

•For this reason, the damage profiles of the model were evaluated based on the A2 earthquake results. According to this damage profile, the most critical tensile cracks occur both in the heel area and in the middle of the arch. The damage potential was found at a critical level in the middle parts of the bridge due to displacement. However, there was no displacement that would cause damage to the remaining parts of the bridge.

•Tensile stresses under earthquake load have reached the permissible tensile strength of masonry stones, especially on the upper sides of the middle belt, upper sides of the arch and the belt side road surface and pose a risk in terms of damage.

•When the periods of the bridge response spectrum obtained by time-history analysis and the natural vibration periods calculated by modal analysis are compared with the earthquake spectrum, the possibility of resonance on the bridge can be mentioned.

•Critical (large) relative displacement levels were not determined along the bridge height.

•Due to the modeling approach used, the behavior (damage, etc.) occurred in the regions where the stresses were concentrated in the elements. It should be noted that different modeling approaches may reveal different damage or collapse mechanisms due to other discontinuities that may exist in bridge elements. In future studies, field observation as well as analytical studies will contribute to the literature.

Conflict of Interest Statement

There is no conflict of interest between the authors.

Statement of Research and Publication Ethics

The study is complied with research and publication ethics

References

[1] A. Özmen and E. Sayın, "Linear Dynamic Analysis of a Masonry Arch Bridge," *in International Conference on Innovative Engineering Applications*, 2018, no. September.

[2] H. Güllü, "Investigation of Earthquake Effect of Historical Masonary Cendere Bridge," Omer Halisdemir Univ. *J. Eng. Sci*., vol. 7, no. 1, pp. 245–259, 2018.

[3] A. Ural, Ş. Oruç, A. Doğangün, and Ö. I. Tuluk, "Turkish Historical Arch Bridges and Their Deteriorations and Failures," *Eng. Fail. Anal*., vol. 15, pp. 43–53, 2008.

[4] Z. Celep and N. Kumbasar, *Betonarme Yapılar*. Istanbul: Beta, 2005.

[5] B. Balun, Ö. F. Nemutlu, A. Benli, and A. Sari, "Estimation of probabilistic hazard for Bingol province, Turkey," *Earthq. Struct*., vol. 18, no. 2, pp. 223–231, 2020.

[6] A. Özmen and E. Sayın, "Seismic Assessment of a Historical Masonry Arch Bridge," *J. Struct. Eng. Appl. Mech*., vol. 1, no. 2, pp. 95–104, 2018.

[7] H. Güllü and H. S. Jaf, "Full 3D Nonlinear Time History Analysis of Dynamic Soil–Structure Interaction for a Historical Masonry Arch Bridge," *Environ. Earth Sci*., vol. 75, no. 21, 2016.

[8] M. Valente and G. Milani, "Damage Assessment and Collapse Investigation of Three Historical Masonry Palaces Under Seismic Actions," *Eng. Fail. Anal*., vol. 98, pp. 10–37, 2019.

[9] B. Sevim, A. Bayraktar, A. C. Altuniik, S. Atamtürktür, and F. Birinci, "Finite Element Model Calibration Effects on the Earthquake Response of Masonry Arch Bridges," *Finite Elem. Anal. Des*., vol. 47, pp. 621–634, 2011.
[10] A. Bayraktar, T. Türker, and A. C. Altunişik, "Experimental Frequencies and Damping Ratios for Historical Masonry Arch Bridges," *Constr. Build. Mater*., vol. 75, pp. 234–241, 2015.
[11] A. Bayraktar, A. C. Altunişik, F. Birinci, B. Sevim, and T. Türker, "Finite-Element Analysis and Vibration Testing of a Two-Span Masonry Arch Bridge," *J. Perform. Constr. Facil*., vol. 24, no. 1, pp. 46–52, 2010.
[12] M. Karaton, H. S. Aksoy, E. Sayın, and Y. Calayır, "Nonlinear Seismic Performance of a 12th Century Historical Masonry Bridge Under Different Earthquake Levels," *Eng. Fail. Anal*., vol. 79, pp. 408–421, 2017.
[13] E. Sayın, Y. Calayır, and M. Karaton, "Nonlinear Seismic Analysis of Historical Uzunok Bridge," *in Seventh National Conference on Earthquake Engineering*, 2021.
[14] D. Proske and P. van Gelder, Safety of Historical Stone Arch Bridges. 2009.
[15] G. Milani and P. B. Lourenço, "3D Non-linear Behavior of Masonry Arch Bridges," *Comput. Struct*., vol. 110–111, pp. 133–150, 2012.
[16] P. Lourenço and D. Oliveira, "Conservation of Ancient Constructions and Application to a Masonry Arch Bridge," in Proceedings of the International Seminar on Theory and Practice in Conservations, 2006.
[17] L. Pelà, A. Aprile, and A. Benedetti, "Seismic assessment of masonry arch bridges," *Eng. Struct*., vol. 31, pp. 1777–1788, 2009.
[18] V. Sarhosis, S. De Santis, and G. de Felice, "A review of experimental investigations and assessment methods for masonry arch bridges," *Struct. Infrastruct. Eng*., vol. 12, no. 11, pp. 1439–1464, 2016.
[19] E. Işık, F. Avcil, E. Harirchian, E. Arkan, H. Bilgin, and H. B. Özmen, "Architectural Characteristics and Seismic Vulnerability Assessment of a Historical Masonry Minaret under Different Seismic Risks and Probabilities of Exceedance," *Buildings*, vol. 12, no. 8, 2022.
[20] E. Işık, E. Harirchian, E. Arkan, F. Avcil, and M. Günay, "Structural Analysis of Five Historical Minarets in Bitlis (Turkey)," *Buildings*, vol. 12, no. 2, 2022.
[21] M. Scamardo, M. Zucca, P. Crespi, N. Longarini, and S. Cattaneo, "Seismic Vulnerability Evaluation of a Historical Masonry Tower: Comparison between Different Approaches," *Appl. Sci*., vol. 12, no. 21, 2022.
[22] E. G. Çubuk, E. Sayın, A. Özmen, "Dynamic Analysis of Historical Masonry Arch Bridges under Different Earthquakes: The Case of Murat Bey Bridge," *Turkish J. Sci. Technol*., vol. 17, no. 2, pp. 461–473, 2022.
[23] F. Avcil, E. Işık, H. Bilgin, H. B. Özmen, "Sahaya Özgü Tasarim Spektrumlarinin Anitsal Yiğma YapSismik DavranişinEtkisi," *Adıyaman Üniversitesi Mühendislik Bilim. Derg*., vol. 16, pp. 165–177, 2022.
[24] R. İzol, O. Türkmen, A. Gürel, and P. Turgut, "Mimar Sinan Camilerinde Sütunların Formları, Dikey ve Yanal Yük Kapasiteleri," *Bitlis Eren Üniversitesi Fen Bilim. Derg*., pp. 649–659, 2022.
[25] F. Avcil and E. Arkan, "Assessment of architectural heritage characteristics and seismic behavior of Ziyaeddin Han Tomb," *Bitlis Eren Univ. J. Sci. Technol*., vol. 12, no. 2, pp. 79–85, 2022.
[26] E. Işık, B. Antep, and İ. B. Karaşin, "Structural Analysis of Ahlat Emir Bayındır Bridge," *Bitlis Eren Univ. J. Sci. Technol*., vol. 8, no. 1, pp. 11–18, 2018.
[27] P. Zampieri, C. D. Tetougueni, and C. Pellegrino, "Nonlinear seismic analysis of masonry bridges under multiple geometric and material considerations: Application to an existing seven-span arch bridge," *Structures*, vol. 34, no. January, pp. 78–94, 2021.
[28] H. Yalçin, L. Gülen, and M. Utkucu, "Active Fault Data Base and Assesment of Earthquake Hazard for Turkey and Surrounding Regions," *Earth Sci*., vol. 34, no. 3, pp. 133–160, 2013.
[29] "Ministry of Interior Disaster and Emergency Management Presidency," 2021. [Online]. Available: https://en.afad.gov.tr/.
[30] TEC, Turkish Earthquake Code. Ankara, Turkey, 2018.
[31] "SeismoMatch Software." 2020.
[32] American Society of Civil Engineers, Minimum Design Loads and Associated Criteria for Buildings and Other Structures. 2017.
[33] O. C. Zienkiewicz and R. L. Taylor, *The Finite Element Mothod*. Butterworth-Heinemann, 2006.

[34] J. Campbell and M. Durán, "Numerical model for nonlinear analysis of masonry walls," *Rev. la Constr.*, vol. 16, no. 2, pp. 189–201, 2017.
[35] J. Lee and G. L. Fenves, "Plastic-Damage Model for Cyclic Loading of Concrete Structures," *J. Eng. Mech.*, vol. 124, no. 8, pp. 892–900, 1998.
[36] J. Lubliner, J. Oliver, S. Oller, and E. Onate, "A Plastic Damage Model for Concrete," *Int. J. Solids Struct.*, vol. 25, no. 3, pp. 299–326, 1989.
[37] N. Bayülke, Depremlerde Hasar Gören Yapıların Onarım ve Güçlendirilmesi. İzmir: İnşaat Mühendisleri Odası İzmir Şubesi, 2010.

Bitlis Eren Üniversitesi Fen Bilimleri Dergisi
BİTLİS EREN UNIVERSITY JOURNAL OF SCIENCE
ISSN: 2147-3129/e-ISSN: 2147-3188
VOLUME: 12 NO: 1 PAGE: 261-271 YEAR: 2023
DOI:10.17798/bitlisfen.1232889

The Effect of Different Heavy Overhang on Structural Performance in Reinforced Concrete Structures

Ercan IŞIK[1*], Fırat AKAT[1]

[1]*Bitlis Eren University, Faculty of Engineering and Architecture, Department of Civil Engineering, BİTLİS (ORCID: 0000-0001-8057-065X) (ORCID: 0000-0002-6645-2363)*

Keywords: Earthquake, Overhang, Performance, Reinforced-concrete, Structural analysis.

Abstract

There are many structural factors that affect the earthquake performance of buildings. Heavy overhang is one of these factors which are made to increase the storey area on the storeys above the ground storey. Within the scope of this study, the effect of different heavy overhangs on the earthquake performance of the building was investigated, which are commonly used in reinforced-concrete (RC) structures. A sample RC building with no heavy overhangs was chosen as the reference building model for numerical analysis. The numerical analyses were carried out for a total of 16 structural models designed by adding heavy overhangs of different lengths to different facades of the reference building model. The obtained results were compared with the results of the reference structure model without heavy overhang to reveal the heavy overhang effect. The period, base shear force, displacement, and performance levels were obtained for each structural model. It has been determined that the base shear force, period, and total mass increase with the increase of heavy overhangs, while the earthquake performance decreases. The obtained results clearly revealed that the earthquake performance was negatively affected by the increase in the amount of closed heavy overhang.

1. Introduction

Different damage levels may occur in engineering structures under the influence of earthquakes due to weak structural features and the magnitude of the earthquake. Damage levels are directly related to structural features. In particular, discontinuities and irregularities in the structures can increase the level and the amount of damage. In this context, in order to keep the loss of life and property at a lower level in the event of possible earthquakes in settlements that are very risky in terms of earthquake hazards, it is of great importance to consider earthquake-resistant building design principles both in the design and construction phases. Therefore, it is obvious that many factors that may adversely affect the earthquake performance of buildings should be taken into account, and studies on these issues will make significant contributions in this area [1], [2], [3], [4], [5].

Significant property and life losses occur due to structural damage as a result of destructive earthquakes [6], [7], [8]. It does not seem possible to predict and prevent earthquakes with today's technology [9], [10]. In this context, the design rules of earthquake-resistant engineering structures have become much more important [11], [12], [13], [14]. These rules, which may differ from country to country, are updated over time. It has carried out the necessary renovations and codes on this issue in Türkiye on different dates and has finalized and implemented the earthquake resistant building design principles with the Türkiye Building Earthquake Code (TBEC-2018) in 2018 [15], [16], [17], [18]. Due to this change in the earthquake code, a change in the rapid assessment method used in the country has become inevitable [19].

Irregularity and negativity parameters in the structures have found their place with their details both in the code and in the rapid assessment methods

*Corresponding author: eisik@beu.edu.tr
Received: 12.01.2023, Accepted: 19.03.2023

that will affect the seismic behaviour. Heavy overhang is one of the factors taken into consideration in RC structures. Heavy overhangs are generally formed by increasing the ground floor area of the building on the upper floors. This subject has been studied in detail by different researchers. Sarı (2010) examined the effects of different structural parameters, which may be encountered in practice, on the seismic behaviour of the heavy overhangs. In the study, static pushover analysis was used for 16 different building models, and the obtained results were compared [20]. Doğangün (2004) stated that heavy overhang was one of the reasons for the structural damage that occurred in May 1, 2003, Bingöl earthquake [21]. İnel et al. (2008) investigated the effects of structural parameters commonly encountered in Türkiye's RC building stock on the seismic performance of the building. One of the parameters they examined is soft-storey irregularity with heavy overhangs [22]. Tesfamariam and Liu (2010) performed reinforcement scaling using different statistical methods. The heavy overhang ratio was included in six different parameters that they used in their study [23]. On the other hand, Saatçi and Vecchio (2009) experimentally investigated the overhang effects of beams on eight different RC beams. The values obtained as a result of 20 different experiments were compared, and the results were interpreted [24]. In his master's thesis study, Öz (2019) performed linear and non-linear time history analyses on the structural models he created with a 1.50 m overhang for three different storeys and revealed the effect of closed heavy overhangs on the seismic behaviour of the building [25]. İnel et al. (2009) investigated the closed overhang irregularity created by beam lifting in the RC structures, depending on the amount of overhang. They stated that the seismic behaviour of the structure was significantly affected by the frame discontinuity that occurred with the removal of the beams [26]. In the study conducted by Meral (2019), for a sample RC building with 3 different storeys, non-linear time history analyses were made and the effect of overhangs on the earthquake behaviour of the building was revealed [27]. Meral and İnel (2016) created a total of 144 building models for 3 different storeys such as 2, 4 and 7-storeys, within the scope of their studies. They used static pushover analyses to reveal the effects of different parameters. Heavy overhang was one of the parameters they took into account [28]. Işık and Tozlu (2015) revealed the effects of different variables on the building performance score, such as heavy overhang, which are taken into account in the rapid assessment method [29]. Işık, et al. (2012) examined the heavy overhangs as one of the causes of structural damage in the Adilcevaz district, based on observation after the 2011 Van earthquake [30]. Özmen (2005) compared the seismic performance of the RC structures for different parameters, including heavy overhangs, which are taken into account in rapid evaluation methods within the scope of his thesis [31].

This study examines the behaviour of heavy overhangs in RC buildings under earthquake effects, which are widely used. The aim of this study is to reveal at what level the closed heavy overhangs affect the earthquake performance of the building with different variations. For this purpose, a sample RC structural model was created, and structural analyses were carried out considering the current seismic design code in Türkiye. First of all, a regular RC building model was designed that does not contain any heavy overhang. In order to reveal the heavy overhang effect, analyses were carried out considering four different overhang lengths on different facades. Four different overhang lengths were taken into account: 0.80 m, 1.0 m, 1.2 m, and 1.5 m. Structural models are grouped into four different categories: 1 facade, 2 facades, 3 facades, and 4 facades. In this study, it is tried to reveal the effects of both the heavy overhang length and the number of facades on the structural analysis and performance results. In addition, the effect of heavy overhang was tried to be revealed by using the rapid scanning method recommended for Türkiye, which was updated with the seismic design code and seismic hazard map. According to TBEC-2018, this study, which is carried out with the details of performance analysis and heavy overhang irregularities, may contribute to this and similar studies. The comparison of the amount of heavy overhangs both on different facades and at different lengths according to TBEC-2018 is what the study differentiates from other studies. In the study, the comparison and interpretation of the heavy overhang results according to the Turkish rapid assessment method that was updated in 2019 also makes the study different from other studies.

2. Material and Method

Engineering structures are exposed to different levels of damage due to their weak structural features and irregularities, and as a result of the structural damage, life and property losses occur on different scales depending on the magnitude of the earthquake. In general, low-strength concrete, insufficient reinforcement, non-usage of materials in accordance with the standards, and workmanship defects, as well as irregularities and negativities in the structures,

directly affect the damage levels in RC structures. These irregularities are included in the seismic design code. The types of irregularities considered in TBEC-2018 are shown in Figure 1.

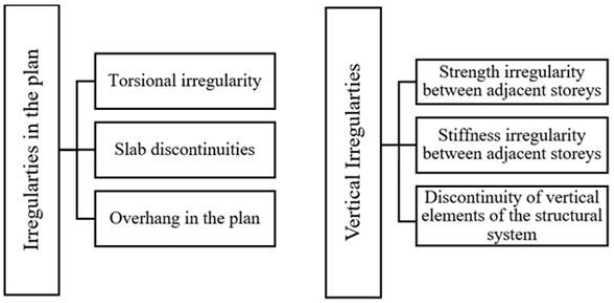

Figure 1. Irregular buildings under earthquake in TBEC-2018

Irregularities in RC structures are also taken into account in the rapid assessment methods, which have been updated with the changes in TBEC-2018 and have been used to determine regional risks in Türkiye since 2019 [32]. The negativity parameters taken into account in this rapid assessment method for the RC buildings are shown in Figure 2.

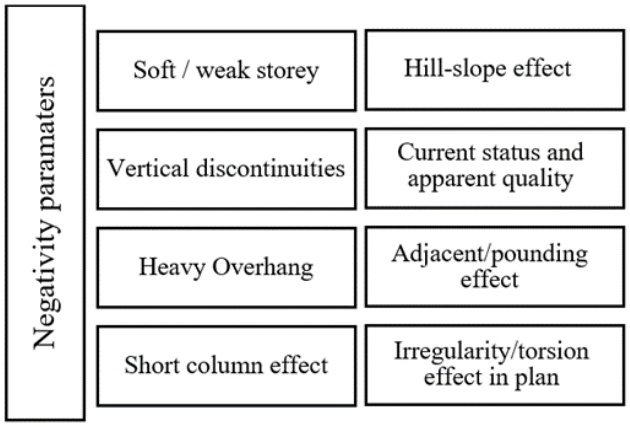

Figure 2. Negativity parameters that specified in Türkiye rapid assessment method

2.1. Heavy Overhang in RC Structures

One of the factors that can affect the earthquake performance of RC structures is the presence of heavy overhangs. This type of heavy overhangs is common in every settlement. In general, such heavy overhang, which are made to increase the building area, are formed by making overhangs on one or more facades of the building. The lower building area, especially on the ground storey, is replaced by larger building areas on the upper storeys. Heavy overhang status is clearly stated within the negativity parameters taken into account in the rapid assessment method [33], [34], [35], [36]. In this method, the presence of heavy overhangs is determined according to Figure 3.

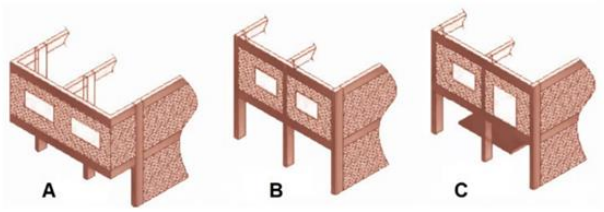

Figure 3. Examples of overhangs (**A**) with overhang, (**B**) no overhangs, and (**C**) balcony with no overhangs.

Some heavy overhangs encountered in practice in RC structures are shown in Figure 4.

Figure 4. Heavy overhangs observed in existing RC structures

In heavy overhangs, the presence of beams negatively affects the aesthetic appearance, and due to architectural needs, beams are often not built in areas with closed overhangs, resulting in a lack of connection between column and beam. Since beam deficiencies cause frame discontinuity, the load transfer mechanism between column and beam is adversely affected [26], [37]. It has been stated by the researchers that especially the closed overhangs made on one side increase the distance between the centre of gravity and stiffness of the structure, and that the increase in weight affects the earthquake behaviour of the structure [21]. It has been understood that buildings with heavy closed overhangs are more damaged during earthquakes than buildings that are regular along the height [38], [39]. In buildings with heavy overhangs, these parts are damaged after earthquakes. Some of the damages caused by heavy overhangs in different earthquakes are shown in Figure 5.

2.2. Structural Models

In this study, a sample RC building was made with no heavy overhangs so that the effects of heavy overhangs could be looked at. The blueprint of the reference building model is shown in Figure 6.

Figure 5. Damages observed in heavy overhangs after different earthquakes in Türkiye

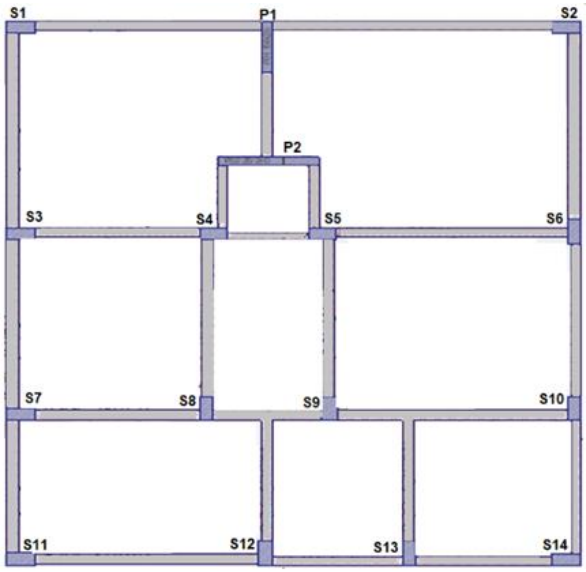

Figure 6. The plan of the reference RC building

Earthquake parameters for the sample RC building were obtained using the Türkiye Earthquake Hazards Map Interactive Web Application (TEHMIWA). The values obtained through this application, depending on the location of the building, are shown in Table 1.

Table 1. Earthquake parameters considered for the reference building

Parameter	Value
Local soil class	ZD
Earthquake ground motion level	DD-2
Spectrum characteristic periods (T_A /T_B)	0.13/0.65
Short period map spectral acceleration coefficient (S_s)	0.274
Map spectral acceleration coefficient for a 1.0 s period (S_1)	0.12
Short period design spectral acceleration coefficient (S_{DS})	0.433
Design spectral acceleration coefficient for a 1.0 s period (S_{D1})	0.283
Peak ground acceleration (g) (PGA) (g)	0.122
Peak ground velocity (PGV) (m/s)	9.31

The structural parameters considered for the sample RC building are shown in Table 2.

Table 2. Structural features for the reference building

Number of storeys	7
Total height of the building (m)	21.90
Maximum storey height (m)	3.40
Building importance coefficient (I)	1
Building usage class (BKS)	3
Ductility level	High
Earthquake design class (DTS)	3
Building height class (BYS)	6
Normal performance target	Controlled Damage
Evaluation / design approach	Design by strength
Material	C25-B420C

In this study, four different structural group models were created to examine the heavy overhang effect. Structural models are grouped into four different categories: only 1 facade, 2 facades, 3 facades, and four facades. The models considered for each group while constructing the structural models are shown in Figure 7.

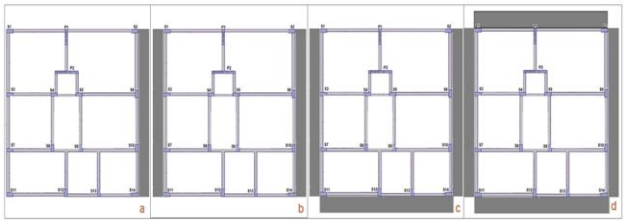

Figure 7. Structural models with heavy overhangs added to their facades a) one facade, b) two facades, c) three facades, d) four facades

Four different overhangs were taken into account in each structural model group, such as 0.80 m, 1.0 m, 1.2 m, and 1.5 m. The groups and the length of overhang of the structural models are shown in Table 3.

Table 3. Structural models considered in the study

Group	Group I	Group II	Group III	Group IV
Length of overhang (m)	0.8	1.0	1.20	1.50
1 facade	Model 1	Model 5	Model 9	Model 13
2 facade	Model 2	Model 6	Model 10	Model 14
3 facade	Model 3	Model 7	Model 11	Model 15
4 facade	Model 4	Model 8	Model 12	Model 16

The values to be obtained for the 16 structural models were compared both with the reference building model without heavy overhangs and within the structural group. The mode superposition method was used in all structural analyses.

3. Results and Discussion

In this study, a total of 17 RC structural models were designed, and one of which is a reference building. Structural analyses were performed with IDECAD software [48] for four different heavy overhang cases for four different structural model groups. The total mass, period, and modal base shear forces obtained for all structural models are shown in Table 4. The percentages of change obtained for structural models with different heavy overhangs compared to the reference building are also given in Table 4.

Table 4. Comparison of total mass, period and shear forces for the structural models

Group No	Model	Total mass (t)	%	Period (s)	%	Modal base shear (tf)	%
Reference	Reference	1525.96	0.00	1.172	0.00	44.62	0.00
Group I	Model 1	1660.22	0.09	1.251	0.07	48.554	0.09
	Model 2	1794.48	0.18	1.299	0.11	48.613	0.09
	Model 3	1910.14	0.25	1.316	0.12	49.987	0.12
	Model 4	2023.64	0.33	1.38	0.18	49.987	0.12
Group II	Model 5	1675.35	0.10	1.264	0.08	48.613	0.09
	Model 6	1824.74	0.20	1.313	0.12	48.748	0.09
	Model 7	1953.86	0.28	1.332	0.14	50.296	0.13
	Model 8	2079.86	0.36	1.406	0.20	52.298	0.17
Group III	Model 9	1690.53	0.11	1.277	0.09	48.425	0.09
	Model 10	1855.05	0.22	1.327	0.13	48.911	0.10
	Model 11	1997.64	0.31	1.349	0.15	50.612	0.13
	Model 12	2136.04	0.40	1.434	0.22	53.236	0.19
Group IV	Model 13	1713.17	0.12	1.298	0.11	47.807	0.07
	Model 14	1900.39	0.25	1.348	0.15	49.117	0.10
	Model 15	2063.17	0.35	1.382	0.18	51.106	0.15
	Model 16	2220.31	0.46	1.478	0.26	54.841	0.23

Figure 8 shows a comparison of the total mass values that were found for all of the structural models that were looked at as part of the study.

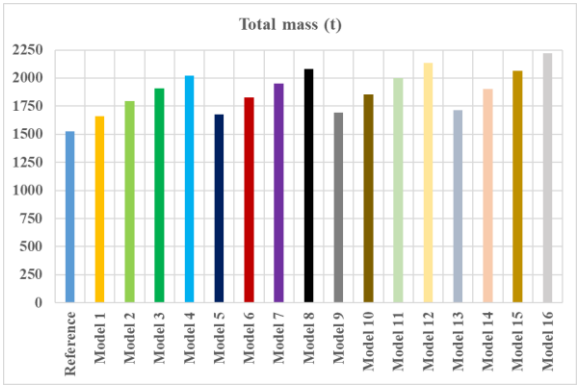

Figure 8. Total mass values obtained for structural models

The comparison of the total masses obtained for Group I (heavy overhang on one side) is shown in Figure 9 as an example.

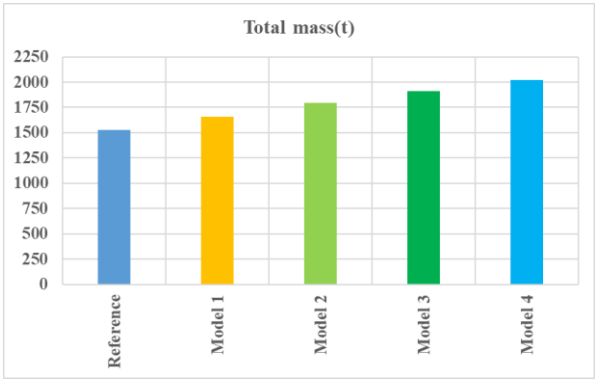

Figure 9. Comparison of total masses for Group I

In order to have the heavy overhang length of 1.50 m, one structural model was selected from each structural group in order to compare the heavy overhangs on different numbers of facades. The total mass values obtained for reference for a single facade (Model 4), two facades (Model 8), three facades (Model 12), and four facades (Model 16) when the heavy overhang is 1.50 m are shown in Figure 10.

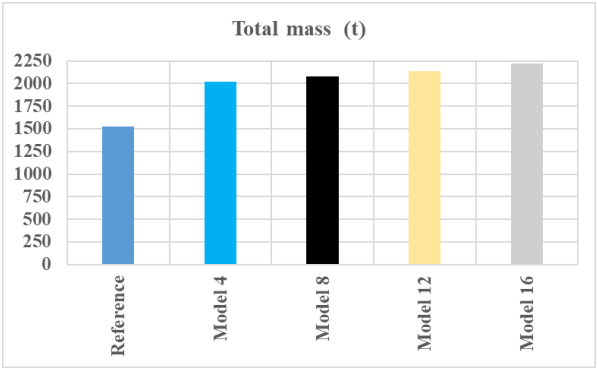

Figure 10. The effect of heavy overhangs on the total mass on different number of facades

The comparison of the period values for selected structural models are shown in Figure 11.

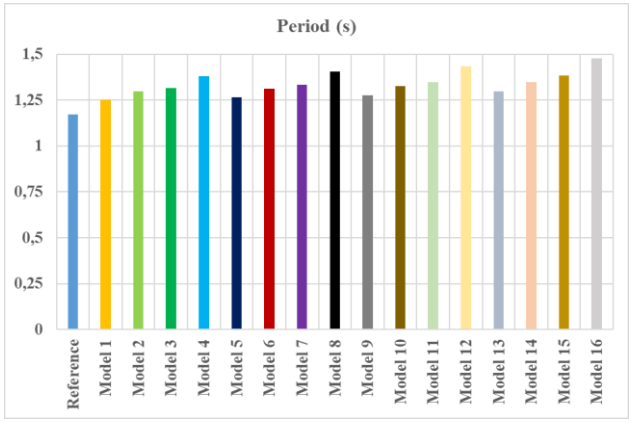

Figure 11. Comparison of the period values for all structural models

The period values obtained for reference for a single facade (Model 4), two facades (Model 8), three facades (Model 12), and four facades (Model 16) when the heavy overhang is 1.50 m are shown in Figure 12.

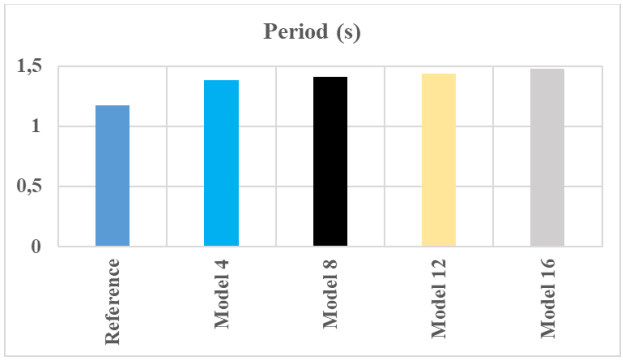

Figure 12. Comparison of periods for different number of facades

The comparison of the period values obtained for Group IV (heavy overhang on all four facades) is shown in Figure 13, as an example.

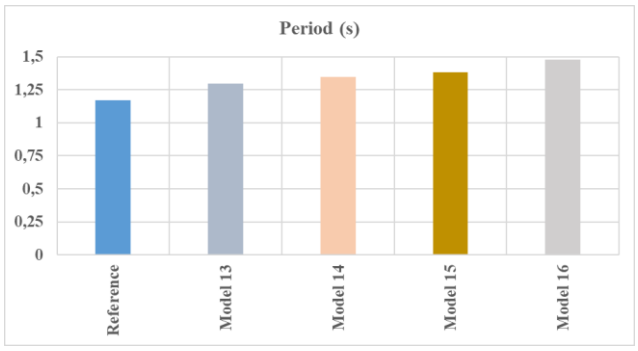

Figure 13. Comparison of periods for group IV

Column plastic rotations and section unit deformation demands for models where the heavy overhang length is constant (1.50 m) but the number of heavy overhangs increases sequentially for each facade are shown in Table 5. As an example, the S7 column on the ground floor was taken as an example.

Table 5. Column plastic rotations and section strain demands

Group No	Model No	ε^C (10^{-3})	ε^s(10^{-3})	θ^p(rad)
Reference	Reference	2.290	5.242	0.00213
Group I	Model 4	3.266	6.370	0.00310
Group II	Model 8	3.422	6.535	0.00322
Group III	Model 12	3.582	6.702	0.00329
Group IV	Model 16	3.782	6.834	0.00345

The displacement values obtained in the X and Y directions for heavy overhangs on equal but different numbers of facades are shown in Table 6.

Table 6. Comparison of displacements

Model	Displacement (mm)	
	X	Y
Reference Model	97.95	93.32
Model 4	110.02	105.18
Model 8	111.69	107.24
Model 12	113.13	109.1
Model 16	115.11	111.59

The earthquake performance results of the models in which the heavy overhang length is constant (1.5 m) and the number of heavy overhangs increases sequentially for each facade are shown in Table 7.

Table 7. Comparison of earthquake performances of some structural models

Criteria	Reference	Model 4	Model 8	Model 12	Model 16
Up to 35% of beams on any storey can pass into the forward Damage Zone	0.00	0.00%	0.00%	0.00%	7.10%
Contribution of vertical elements to the shear force in the Advanced Damage Zone should be less than 20%	0.00	16.10%	16.20%	16.30%	16.40%
The contribution of the vertical elements in the Advanced Damage Zone to the shear force on the top storey should be less than 40%	0.00	0.00%	0.00%	0.00%	0.00%
The ratio of shear force carried by vertical members whose Significant Damage Limit has been exceeded should not exceed 30%.	0.00	0.00%	0.00%	0.00%	8.60%
All other structural elements must be in the Limited or Significant Damage Zone	✓	X	X	X	X
Building performance	Controlled damage	Collapse	Collapse	Collapse	Collapse

In the Turkish Rapid Assessment Method, which was updated in 2019, the effect of heavy overhang was also looked at as part of this study. According to this method, the negativity parameter scores recommended for a heavy overhang in RC structures depending on the number of stories are given in Table 8.

Table 8. Negativity parameter score for overhang

Number of storeys	Heavy overhang
1,2	-10
3	-20
4	-30
5	-30
6,7	-30

In this method that used to determine the regional risk priorities in RC structures, the heavy overhang changes only according to the number of storeys. It has not been taken into account the amount of heavy overhang, its length, or how many facades there are. Within the scope of this study, structural performance scores were calculated for a sample building selected as an example in cases of no heavy overhangs and heavy overhangs for all storeys in the rapid evaluation method. All parameters are taken into account equally for the building with and without heavy overhangs. As a variable, only the presence of a heavy overhang was taken into account. For the selected RC building, the danger zone is selected as I. While selecting the base point, the values were chosen with the assumption that the sample RC structure consisted of

only the frame. A comparison of the obtained results is made in Table 9.

Table 9. The effect of heavy overhang in the rapid assessment method

Number of storeys	Base score	Heavy overhang negativity parameter score	Reference	Heavy overhang
1,2	90	-10	90	80
3	80	-20	80	60
4	70	-30	70	40
5	60	-30	60	30
6,7	50	-30	50	20

As the number of storeys increases, the performance score of the heavy overhang decreases for the building. In the rapid assessment method, the average effect of heavy overhang is 38%. As can be understood from this value, it is an important factor even in the simplified methods used in determining the risk priorities. While heavy overhangs are taken into account in the rapid evaluation method, the number of facades with heavy overhangs and the lengths of heavy overhangs are not taken into account. The result values obtained in this study revealed that the number and amount of facades with heavy overhangs directly affect the structural performance results.

4. Conclusion and Suggestions

Within the scope of this study, the behaviour of heavy overhangs in RC buildings, which are widely used, under earthquake effects was investigated. In future studies, different analyses, including the time-history analysis, will be able to analyse more structural models in different software programs. The data obtained from this study can be a source for such studies.

The results were based on two main situations that show how heavy overhangs on RC buildings can have different effects on the structure. The first of these two main cases is the case where the length of the heavy overhang is kept constant and the heavy overhang is added to all facades, while the second case is the case where the number of heavy overhangs is kept constant and their lengths are applied in variable lengths. As a result of the analyses performed for all structural models within the scope of the study, the following results were obtained;

- With the increase in the number of facades with heavy overhangs, it has been observed that the structural elements have difficulty performing compared to the reference model. Furthermore, the building performance of heavy overhangs on 1, 2, and 3 facades, while controlled damage occurred as in the reference model, was obtained as the collapse state in the model with heavy overhangs on 4 facades.
- The period value increased as the length of the heavy overhang and the number of facades with heavy overhangs increased. The high period value is related to the rigidity of the structure. Therefore, the rigidity of structures with heavy overhangs will be lower than that of structures without heavy overhangs.
- As more heavy overhangs were added to the facades of the sample RC building, the building's weight naturally went up.
- It has been found that the value of the base shear force goes up as more heavy overhangs are added to the facades.
- When compared to the reference model, the number of heavy overhangs added to the facades of the Group IV models caused both the concrete section unit shortening and the reinforcing steel unit strain to go up.
- Plastic rotation has increased compared to the reference model due to the increase in the number of added heavy overhangs.
- It was seen that the length of the heavy overhang made the building less stable during an earthquake.
- Models with heavy overhangs on one side and variable lengths (0.8 m-1m-1.2 m-1.5 m) had the same performance compared to the reference model, and the building performance of 5 models was found to be controlled damage.
- The performance of all models with heavy overhangs on all four facades and variable lengths has been found to collapse. In all models with heavy overhang, the contribution of vertical elements in the forward damage zone to the shear force increased, respectively. In addition, the forward damage zone penetration of the beams in the 16^{th} model increased by percentage.

As a result, it is necessary to avoid, as much as possible, the parameters that will negatively affect the behaviour of structures under the effects of earthquakes. In cases of necessity, it is obligatory to take the necessary preventive measures. This study was carried out by analysing the regular RC structure.

These results can be compared with future studies for irregular buildings.

It can also be suggested that the number of facades with heavy overhangs be integrated into the scoring in the rapid assessment method.

Acknowledgment

This research was produced from master thesis of second author of the article.

Contributions of the authors

All authors contributed equally to the study.

Conflict of Interest Statement

There is no conflict of interest between the authors.

Statement of Research and Publication Ethics

The study is complied with research and publication ethics

References

[1] A. Tabrizikahou, M. Hadzima-Nyarko, M. Kuczma, S. Lozančić, Application of shape memory alloys in retrofitting of masonry and heritage structures based on their vulnerability revealed in the Bam 2003 earthquake. *Materials*, vol.14 (16), 4480, 2021.

[2] G. Dogan, A.S. Ecemis, S.Z. Korkmaz, M.H. Arslan, H.H. Korkmaz HH, Buildings damages after Elazığ, Turkey earthquake on January 24, 2020. *Natural Hazards*, vol.109 (1), pp.161-200, 2021.

[3] O.F. Nemutlu, B. Balun, A. Sari, A. Damage assessment of buildings after 24 January 2020 Elazığ-Sivrice earthquake. *Earthquakes and Structures*, vol. 20(3), pp.325-335, 2021.

[4] E. Çelebi, M. Aktas, N. Çağlar, A. Özocak, M. Kutanis, N. Mert, Z. Özcan, 2013. October 23, 2011 Turkey/Van Ercis earthquake: structural damagesin the residential buildings. Natural Hazards, vol. 65(3), pp.2287-2310, 2013.

[5] R. Pekgökgöz, A. Gürel, F. Avcil, GAP YENEV Binasının Kısmi Göçmesinin İncelenmesi ve Güçlendirme Çalışmaları. *Dicle Üniversitesi Mühendislik Fakültesi Mühendislik Dergisi*, 12(2), pp.389-399, 2021.

[6] M.H. Arslan, H.H. Korkmaz, What is to be learned from damage and failure of reinforced concrete structures during recent earthquakes in Turkey?. *Engineering Failure Analysis*, vol. 14(1), pp.1-22, 2007.

[7] H. Bilgin, N., Shkodrani, M. Hysenlliu, H.B. Ozmen, E. Isik, E. Harirchian, Damage and performance evaluation of masonry buildings constructed in 1970s during the 2019 Albania earthquakes. *Engineering Failure Analysis*, vol.131, 105824, 2022.

[8] N., Ademović, M. Hadzima-Nyarko, N. Zagora, Seismic vulnerability assessment of masonry buildings in Banja Luka and Sarajevo (Bosnia and Herzegovina) using the macroseismic model. *Bulletin of Earthquake Engineering*, vol.18(8), pp.3897-3933, 2020.

[9] B. Özmen, H. Can, Ankara için deterministik deprem tehlike analizi. *Gazi Üniversitesi Mühendislik Mimarlık Fakültesi Dergisi*, vol.31(1), pp.9-18, 2016.

[10] E. Işık, Ç. Sağır, Z. Tozlu, Ü.S. Ustaoğlu, Determination of urban earthquake risk for Kırşehir, Turkey. *Earth Sciences Research Journal*, vol.23(3), pp.237-247, 2019.

[11] A. Yakut, Preliminary seismic performance assessment procedure for existing rc buildings. *Engineering Structures*, vol.26(10), pp.1447-1461, 2004.

[12] E. Işık, Comparative investigation of seismic and structural parameters of earthquakes (M≥ 6) after 1900 in Turkey. *Arabian Journal of Geosciences*, vol.15(10), pp.1-21, 2022.

[13] H. Bilgin, M. Hadzima-Nyarko, E. Isik, H.B. Ozmen, E. Harirchian, (2022). A comparative study on the seismic provisions of different codes for RC buildings. *Structural Engineering and Mechanics*, vol.83(2), pp.195-206, 2022.

[14] B. Yön, O. Onat, M.E. Öncü, A. Karaşin, Failures of masonry dwelling triggered by East Anatolian Fault earthquakes in Turkey. *Soil Dynamics and Earthquake Engineering*, vol.133, 106126, 2020.

[15] M.F. Işık, E. Işık, E. Harirchian, Application of IOS/Android rapid evaluation of post-earthquake damages in masonry buildings. *Gazi Mühendislik Bilimleri Dergisi*, vol.7(1), pp.36-50, 2021.

[16] C. Aksoylu, A. Mobark, M.H. Arslan, İ.H. Erkan, 2020. A comparative study on ASCE 7-16, TBEC-2018 and TEC-2007 for reinforced concrete buildings. *Revista de la Construcción*, vol.19(2), pp.282-305, 2020.

[17] H. Ulutaş H, DBYBHY (2007) ve TBDY (2018) Deprem yönetmeliklerinin kesit hasar sınırları açısından kıyaslanması. *Avrupa Bilim ve Teknoloji Dergisi*, vol.17, pp. 351-359, 2019.

[18] Ö.F. Nemutlu, B. Balun, A. Benli, A. Sarı, Bingöl ve Elazığ illeri özelinde 2007 ve 2018 Türk deprem yönetmeliklerine göre ivme spektrumlarının değişiminin incelenmesi. *Dicle Üniversitesi Mühendislik Fakültesi Mühendislik Dergisi*, vol.11(3), pp.1341-1356, 2020.

[19] E. Işık, A.E. Ulu, M.C. Aydın, A case study on the updates of Turkish rapid visual screening methods for reinforced-concrete buildings. *Bitlis Eren University Journal of Science & Technology*, vol.11(2), pp.97-103, 2021.

[20] H. Sarı, *Mevcut Betonarme Yapılardaki Tasarım Olumsuzluklarının Yapı Performansına Etkisi.* Yüksek Lisans Tezi, Sakarya Üniversitesi, Sakarya, 2010.

[21] A. Doğangün, 2004. Performance of reinforced concrete buildings during the May 1, 2003 Bingöl earthquake in Turkey. *Engineering Structures*, vol.26(6), 841-856, 2004.

[22] M. İnel, H.B. Ozmen, H. Bilgin, Re-evaluation of building damage during recent earthquakes in Turkey. *Engineering Structures*, vol.30(2), 412-427, 2008.

[23] S. Tesfamariam, Z. Liu, Earthquake induced damage classification for reinforced concrete buildings. *Structural Safety*, vol.32(2), pp.154-164, 2010.

[24] S. Saatci, F.J. Vecchio, Effects of shear mechanisms on ımpact behaviorof reinforced concrete beams. *ACI Structural Journal*, vol.106-109, pp. 78-86, 2009.

[25] S.B. Öz, *Kapalı Çıkma Düzensizliğinin Betonarme Yapıların Sismik Davranışına Etkilerinin Doğrusal Elastik Olmayan Analizle Belirlenmesi*. Yüksek Lisans Tezi, Osmaniye Korkut Ata Üniversitesi, Osmaniye, 2019.

[26] M. İnel, M. Bucaklı, H.B. Özmen, Betonarme binalarda çerçeve süreksizliğinin yapı performansı üzerindeki etkileri. *Uluslararası Sakarya Deprem Sempozyumu*; 1-2 Ekim 2009, Sakarya, Türkiye, 2009.

[27] E. Meral, Kapalı çıkmalı betonarme binaların deprem davranışının değerlendirilmesi. *Fırat Üniversitesi Mühendislik Bilimleri Dergisi*, vol.31(2), pp. 309-318, 2019.

[28] E. Meral, M. İnel, Düşük ve orta yükseklikteki betonarme binaların yapısal parametre özelliklerinin değerlendirilmesi. *Pamukkale Üniversitesi Mühendislik Bilimleri Dergisi*, vol. 22(6), pp.468-477, 2016.

[29] E. Işık, Z. Tozlu, Farklı değişkenler kullanılarak yapı performans puanının hesaplanması. *Bitlis Eren Üniversitesi Fen Bilimleri Enstitüsü Dergisi*, vol.4(2), pp.161-172, 2015.

[30] E. Işık, M.H. Özlük, E. Demir, H. Bilici, 23.10. 2011 Van depreminin Adilcevaz ilçesindeki etkilerinin gözleme dayalı incelenmesi. *Bitlis Eren Üniversitesi Fen Bilimleri Dergisi*, vol.*1*(1), pp.1-10, 2012.

[31] H.B. Özmen, 2005. *Hızlı Değerlendirme Yöntemlerinde Kullanılan Parametrelerin Yapı Performansı Üzerindeki Etkilerinin İncelenmesi*, Yüksek Lisans Tezi, Pamukkale Üniversitesi, Denizli, 2005.

[32] PDRB, 2019. *The Principles of Determining Risky Buildings, Turkey Ministry of Environment and Urbanization* Ankara, Turkey

[33] Ö.F. Nemutlu, Ö.F. *2018 Türk Deprem Yönetmeliklerinin ve Amerikan Deprem Yönetmeliğinin Deprem Hesapları Açısından Karşılaştırılması*. Yüksek Lisans Tezi, İstanbul Teknik Üniversitesi Fen Bilimleri Enstitüsü, Türkiye, 2019.

[34] M.A., Bülbül, E. Harirchian, M.F. Işık, S.E. Aghakouchaki Hosseini, E. Işık, A hybrid ANN-GA model for an automated rapid vulnerability assessment of existing RC buildings. *Applied Sciences*, 12(10), 5138, 2022.

[35] Ö.F. Nemutlu, A. Sarı, Comparison of Turkish Earthquake Code in 2007 with Turkish Earthquake Code in 2018. In *International Engineering and Natural Sciences Conference (IENSC 2018), Diyarbakır* (Vol. 568, p. 76), 2018.

[36] Ö.F. Nemutlu, A. Sarı, 2018 Yeni Türk Deprem Yönetmeliği ile Amerikan Deprem Yönetmeliklerinin deprem hesapları açısından karşılaştırılması. *5. Uluslararası Deprem Mühendisliği ve Sismoloji Konferansı,* 8-11 Ekim 2019, Ankara, Türkiye, 2019.

[37] H.B. Özmen, M. İnel, B.T. Çaycı, 2011. Kapalı çıkma düzensizliğinin betonarme yapıların sismik davranışına etkilerinin değerlendirilmesi. *Yedinci Ulusal Deprem Mühendisliği Konferansı;* 30 Mayıs-3 Haziran 2011, İstanbul, Türkiye, 2011.

[38] G. Özcebe, 2004. *Deprem Güvenliğinin Saptanması için Yöntemler Geliştirilmesi*. TÜBİTAK İÇTAG YMAÜ İ574-Araştırma Projesi Sonuç Raporu, Ankara, 2004.
[39] H. Sucuoglu, U. Yazgan, Simple survey procedures for seismic risk assessment in urban building stocks. *Seismic Assessment and Rehabilitation of Existing Buildings*, vol.29, pp:97-118, 2003.
[40] H.B. Özmen, M. İnel, B.T. Çaycı, *23 Ekim ve 9 Kasım 2011 Van Depremleri Yapısal Hasar Değerlendirme Raporu.* Pamukkale Üniversitesi, Mühendislik Fakültesi, İnşaat Mühendisliği, Denizli, 2012.
[41] M, Inel, H.B. Ozmen, E. Akyol E, Observations on the building damages after 19 May 2011 Simav (Turkey) earthquake. *Bulletin of Earthquake Engineering*, vol.11, pp.255-283, 2013.
[42] M. Dogan, E. Unluoglu, H. Ozbasaran, Earthquake failures of cantilever projections buildings. *Engineering Failure Analysis*, vol.14, pp.1458-1465, 2007.
[43] A. Yakut, H. Sucuoğlu, B. Binici, E. Canbay, C. Donmez, A. İlki, B.Ö. Ay, Performance of structures in İzmir after the Samos Island earthquake. *Bulletin of Earthquake Engineering*, vol.*20*, pp.7793-7818, 2022.
[44] M. İnel, H.B. Özmen, B.T. Çaycı, Simav ve Van Depremleri (2011) yapı hasar nedenlerinin değerlendirilmesi. *Pamukkale Üniversitesi Mühendislik Bilimleri Dergisi*, vol.19, pp.256-265, 2013.
[45] E. Isik, M.C. Aydin, A. Buyuksarac, 24 January 2020 Sivrice (Elazığ) earthquake damage sand determination of earth quake parameters in the region. *Earthquakes and Structures,* vol.19, pp.145-156, 2020.
[46] Ö. Yurdakul, B. Duran, O. Tunaboyu, Ö. Avşar Ö, Field reconnaissance on seismic performance of rc building safter the January 24, 2020 Elazığ-Sivrice Earthquake. *Natural Hazards,* vol.105, pp.859-887, 2021.
[47] E. Işık, The effects of 23.10.2011 Van earthquake on near-fieldand damaged on structures. *International Anatolia Academic Online Journal Scientific Science*, vol.2, pp.10-25, 2014.
[48] IdeCAD, 2022, ideYAPI Ltd. www.idestatik.com. Erişim tarihi:15.11.2021.

Bitlis Eren Üniversitesi Fen Bilimleri Dergisi
BİTLİS EREN UNIVERSITY JOURNAL OF SCIENCE
ISSN: 2147-3129/e-ISSN: 2147-3188
VOLUME: 12 NO: 1 PAGE: 272-291 YEAR: 2023
DOI:10.17798/bitlisfen.1238241

Russia-Ukraine Conflict: A Text Mining Approach through Twitter

İbrahim Miraç ELİGÜZEL[1*]

[1] *Gaziantep University, Industrial Engineering, 27310 Gaziantep, Turkey (ORCID:0000-0003-3105-9438)*

Keywords: Fuzzy c-means, Russia, Ukraine, War, Topic modeling, Twitter

Abstract

The focus of this study is to use social media to investigate the Russia-Ukraine conflict. With the assent of the Russian parliament, Russian President Vladimir Putin proclaimed that they will begin invading Ukraine on February 24, 2022. During the Russia-Ukraine conflict, social media, particularly Twitter, has been heavily used. For that reason, it becomes to strong tool for handling processes during the conflict such as political decision making, organizing humanitarian activities, and proving assistance for victims. As a result, social media becomes the most up-to-date, comprehensive, and large information source for current scenario analysis. A total of 65412 tweets are gathered as a dataset for analysis in the proposed study between February 24 and April 5. Then, for each tweet, a topic modeling method called Latent Dirichlet Allocation (LDA) is used to collect significant topics and their probabilities considering each tweets. Then, using the specified probabilities, Fuzzy c-means is utilized to generate clusters for the entire document. Finally, seven unique clusters have been gathered for processing. N-grams and network analysis are used to examine each resulting cluster for a better understanding. As a result of this study, worldwide public opinion, current situation of civilians, course of the conflict, humanitarian issues during the Russia-Ukraine conflict are extracted.

1. Introduction

Following the resignation of Ukraine's then-President, pro-Russian Viktor Yanukovych, in February 2014, Russia annexed Crimea and increased its support for pro-Russian separatists in the Russian-speaking Donbas region in the country's east [1]. Separatists in Donbas declared Donetsk and Luhansk People's Republics and seized state institutions shortly after. This action triggered an armed conflict between the Ukrainian government and separatists [2]. While Russia is not officially involved in the conflict in Ukraine, experts, international organizations, the media, and the Ukrainian government have all stressed Russia's backing for rebels since 2014. Recently, with Russia's recognition of the independence of separatist forces in eastern Ukraine on February 21, tensions in the region rose and Russia invaded Ukraine on February 24. As the war continues to contribute to the ongoing humanitarian and refugee catastrophe in Ukraine, the usage of social media by both sides of the conflict has produced a variety of responses.

The advancement of Web 2.0 technology has made it possible for individuals without programming skills to create content on the Internet [3]. With the social media applications built around the idea of Web 2.0, it has become very easy to reach social or cultural phenomena instantly. Data has been generated by users and shared as a result of the widespread use of available software and hardware to access social media platforms through the Internet. In this way, users have become accustomed to receiving regular updates on major personal or worldwide events. As a result, social media platforms like Twitter and Facebook have become increasingly popular as communication tools around the world. Twitter is the first platform that springs to mind for disseminating information in real-time crisis situations.

User-generated data collected from social media refers to unstructured data such as text, images, and videos. As a result of social media shares

*Corresponding author: miraceliguzel@gmail.com
Received: 17.01.2023, Accepted: 03.03.2023

of many users, huge amounts of data emerge in short time periods. To give an example from Twitter, posts, comments, likes constitute big data. Big data collected from social media is useless unless it is used to drive decision making by converting massive amounts of social data into meaningful information [4]. The fact that the data is large and contains many-to-many interactions, unlike traditional media, has significant potential for researchers. With the popularity of data-driven systems, the analysis of social networks gains importance in understanding various social phenomena.

One of the processes converting data into information, topic modeling [5] has been applied in many social media platforms. It is an attractive tool for detecting hidden text patterns in content. It aids in determining the relevance of a topic based on how often it is mentioned and how it is related with other topics. Topic modeling is important, both from the perspective of individuals, as well as, analyzing the public opinion about ongoing conflicts at local and international levels. Without a prepared text data set with established schemes, the topic modeling can help discover and explain broad subjects of interest on social media. The potential of this method to uncover hidden subjects or patterns in text data on its own without supervision is what makes it popular among scholars in a wide range of areas [6-8].

Russia's attempt to invade Ukraine, as in many social events, attracted great attention in the social media in a short time. This study examines Russia's attempt to invade Ukraine, which is one of the current global issues, through public opinions in tweets. In this regard, this study proposes using machine learning techniques on Twitter data containing tweets related to Russia-Ukraine war. Following contributions are made in the current study: i) a twitter dataset is collected containing #UkraineRussiawar hashtag, ii) topic extraction is performed using LDA, iii) extracted topics are clustered with Fuzzy c-means, another machine learning technique, and iv) clusters are deciphered by using n-gram technique.

The contribution of the proposed paper is to provide a general view of society from different perspectives on the war between Ukraine and Russia via social media analysis. In addition, the proposed study is the first one that analyzes the attitude of society through Twitter by utilizing topic modelling and Fuzzy c-means clustering technique with an n-gram analysis approach. Therefore, it aims to provide a basis for decision processes such as political decisions, humanitarian activities, and effective and efficient support for victims.

The remaining part of the study is organized as follows. Section 2 outlines the extant literature on the topic modeling and its applications on social networks. Section 3 explains the integration of the methodologies of topic modeling, Fuzzy c-means and n-grams. Our experiment is conducted and their results are discussed in Section 4. The paper is concluded with Section 5.

2. Literature Review

Several models for interpreting text data are offered by machine learning-based text analysis. Topic modeling can help identify and explain general interest topics in social media without a textual dataset with predefined schemas. Several works use topic modeling methodologies such as LDA, LSA (Latent Semantic Analysis), and their extensions, since topic modeling has the ability to derive key characteristics of particular topics. Among other approaches, LDA has become a standard tool as it is frequently preferred in topic modeling [9, 10].

During the last decade a considerable amount of literature has been published on topic modeling [11-14]. The development of social media platforms and the ease of access to data also accelerated its pace [15, 16]. In particular, what the data say about social phenomena was frequently examined. Vazquez et al. [17] analyzed online news about Venezuela migration for 4 years period. They applied topic modeling to the news that were decided to be related to migration with the binary classifier. They found that the factors that cause migration are unemployment, medicine and food shortages. Tang et al. [18] grouped the construction industry into four clusters and compared how the industry was perceived in terms of workers, companies, unions and the media over 3200 most recent tweets. Using the ability of text mining, especially in social issues, the view of society can also be revealed. For example, Lee and Jang [19] analyzed how the 2021 Atlanta shooting ignited debates. They explored the emergent topics of Twitter from the first 7 days' data about #StopAsianHate.

Because topic detection in large documents is too challenging to do manually, topic modeling methods are frequently combined with clustering algorithms. The goal is to decompose a group of objects in such a way that objects in the same cluster are more similar to each other than objects in other clusters. The center of each cluster is interpreted as topics in topic modeling [20]. K-means is the most common clustering algorithm because its simplicity and efficiency. According to the k-means algorithm, since each object may belong to a cluster, each

document also belongs to a subject in topic modeling. However, real-world data may belong to more than one topic. For example, a textual data can be a combination of several topics. Fuzzy c-means (FCM) is a clustering method that groups objects into multiple clusters with a membership degree [21]. Since FCM is more suitable than other clustering algorithms, it has been widely used in literature. Abri and Abri [22] integrated FCM and topic modeling to provide a personalized model for a search engine. FCM results random initializations on each run. To avoid randomness, Alatas et al. [23] proposed non-negative double singular value decomposition (NNDSVD) as the initialization method of FCM in topic modeling. Prakoso et al. [24] used eigenspace-based FCM (EFCM) for conducting the clustering process in low dimensional textual data. Fearing that dimension reduction would reduce accuracy, the authors used a kernel trick to improve accuracy. Parlina et al. [25] also used EFCM to characterize the dimensions of smart sustainable cities over the related literature. Sutrisman and Murfi [26] used NNSVD as the initialization method of EFCM and applied it on Indonesian online news for topic modeling. Trupthi et al. [27] and Mandhula et al. [28] took advantage of possibilistic FCM (PFCM) topic modelling for twitter sentiment analysis and amazon customer's opinion prediction, respectively. Taking it a step further, Kolhe et al. [29] proposed a robust system that integrates LDA and modified grey wolf optimizer. Authors first identified optimal keywords through the superior topic modeling, then clustered them into positive and negative forms through quantum inspired FCM.

Table 1 Comparison of literature papers

Study Reference	*Focus of Study*	*Methods*	*Data*
[17]	Migration crisis in Venezuela	Text classification, word	10000 news articles
[18]	Construction industry	Sentiment analysis, topic	3200 Twitter messages
[19]	Hate crimes, racism, and	Topic modelling	- Twitter messages
[24]	Sensing trending topics	Clustering	- Twitter messages
[25]	Smart sustainable city	Topic detection, topic	Scientific literature
[26]	News analysis	Clustering , Topic detection	Online news
[27]	Twitter sentiment analysis	Topic modeling, sentiment	479 Twitter messages
[28]	Customer's opinion on	Topic modeling, Sentiment	Amazon customer review
Proposed study	Russia-Ukraine Conflict	Topic modeling, clustering,	65412 Twitter messages

The following contributions are made by this study as its shown in Table 1: i) a Twitter dataset including the #UkraineRussiawar hashtag is collected, ii) topics are extracted using LDA, iii) retrieved topics are clustered using Fuzzy c-means, another machine learning technique, and iv) clusters are decoded using the n-gram technique.

3. Material and Method

The core idea of proposed paper is to provide a public opinion against war between Ukraine and Russia. To obtain mentioned aim, LDA topic modeling and Fuzzy c-means clustering technique are integrated. The total of 65412 tweets are gathered between February, 24 and April, 5 by using #UkraineRussiawar hashtag. In order to achieve gathering tweets, Snscrape library in Python software is used. After that, some sequential stages are applied in order to obtain different cluster as seen Figure 1. Each cluster can demonstrate different opinions and views against war. First of all, pre-processing technique is used to provide clean data. The right after, LDA topic modeling is used as feature extraction method to obtain a feature vector. Then, Fuzzy c-means model is applied and various clusters are provided. Lastly, each cluster is analyzed by using n-gram technique.

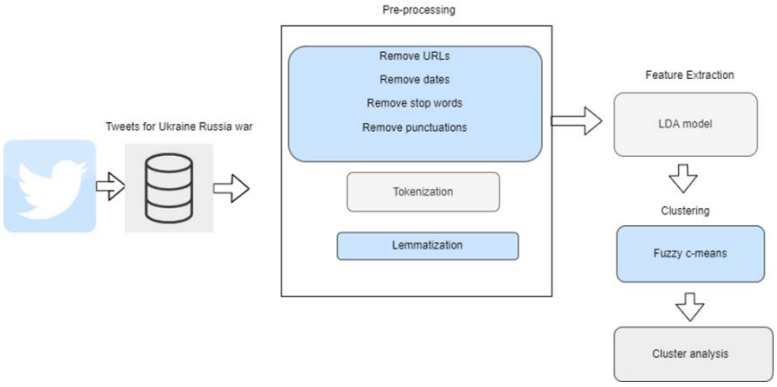

Figure 1. Stages of the proposed study

The gathered tweets are subjected to pre-processing stage. In this level, URLs, dates, stop words, punctuations, and key hashtag (UkraineRussiawar) are removed. After that, tokenization process is implemented. Tokenization is used to split the strings into pieces such as words, symbols, phrases. These pieces are called as token. Tokenization is required before topic process. Lastly, lemmatization is applied in pre-processing stage. Lemmatization is the process of putting together the inflected elements of a word such that they can be identified as a single element, known as the lemma or vocabulary form of the word [30]. After all pre-processing stages are completed, LDA topic modeling is conducted.

3.1. LDA topic modeling

It is called as a generative probabilistic model of a corpus [9]. LDA is utilized to identify underlying topics in a collection of documents and to calculate the probabilities of words in those topics [31]. The key principle is that documents are displayed as random mixtures of latent topics, each of which is described by a word distribution. The structure of LDA model is given in Figure 2, and equation of the probability of a corpus based on this structure is given in Equation (1).

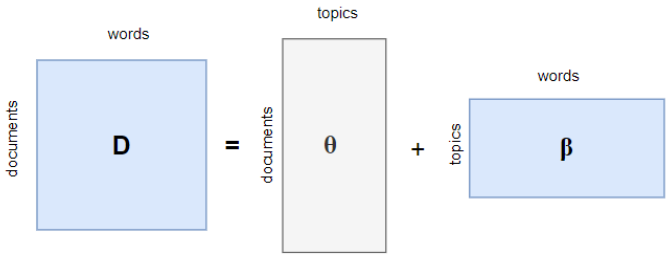

Figure 2. Structure of the LDA model

D refers the document to word matrix. Each document's topic distribution is demonstrated with θ, and each topic-word distribution is demonstrated with β.

$$p(D|\alpha,\beta) = \prod_{d=1}^{M} \int P(\theta_d|\alpha)\left(\prod_{n=1}^{N_d} \sum_{z_{dn}} p(z_{dn}|\theta_d)p(w_{dn}|z_{dn},\beta)\right)d\theta_d \quad (1)$$

M is the number of documents to analyze, D is the corpus of collection M documents, N is the number of words in the document, α refers Dirichlet-previous concentration parameter of each document topic distribution, β refers corpus level parameter, θ_d refers the document-level variable, z_{dn} refers the topic assignment for w_{dn}, w_{dn} refers the n^{th} word in the d^{th} document. To implement LDA process, MATLAB software is used. The number of documents is takes as 65412 and number of topic is determined according to the validation perplexity as seen in Figure 3.

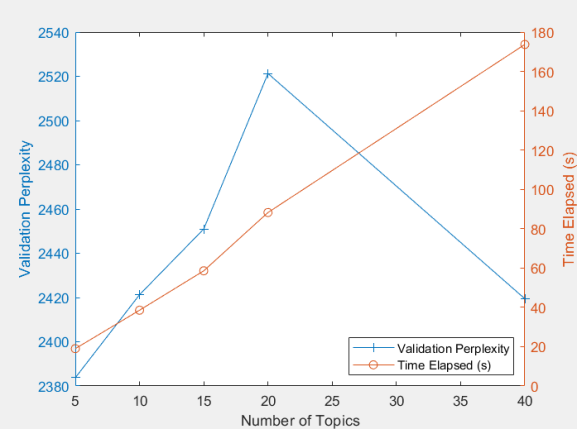

Figure 3. The number of topics for the LDA model

Considering both Figure 3 and the number of topics for text documents in the literature [32], the number of topic for LDA model is considered as 7. Namely, at the end of the LDA process, 65412x7 feature vector is provided. Fuzzy c-means is applied on this vector.

3.2 Fuzzy c-means

Fuzzy c-means clustering technique was first reported by Joe Dunn in 1973 [33], and it was extended by Bezdek [21] in 1984. Fuzzy c-means technique is a popular unsupervised clustering technique. In this technique, objects on the boundaries of many classes are not obliged to fully belong to one of them, but are instead assigned membership degrees ranging from 0 to 1, signifying their partial membership [33]. Fuzzy c-means utilizes fuzzy portioning. The algorithm is demonstrated as follows [33]:

1. ***Initialize*** $U=[u_{ij}]$ matrix, $U^{(0)}$
2. At t step: compute the centers vectors $C^{(t)}=[c_j]$ with $U^{(t)}$

$$C_i = \frac{\sum_{j=1}^{n} u_{ij}^{m} x_j}{\sum_{j=1}^{n} u_{ij}^{m}}$$

3. Update $U^{(t)}$, $U^{(t+1)}$
4.

$$d_{ij} = \sqrt{\sum_{i=1}^{n}(x_i - c_i)}$$

$$u_{ij} = \frac{1}{\sum_{t=1}^{c}(\frac{d_{ij}}{d_{tj}})^{2/(m-1)}}$$

5. If $\| U^{(t+1)}-U^{(t)} \| < \varepsilon$ ***then Stop; otherwise return to step 2.***

According to the Fuzzy c-means algorithm; m is a constant real number called as the fuzzifier, u_{ij} refers the membership degree of x_i in cluster j, x_i is the i^{th} of d-dimensional measured data, c_j is the d-dimension center of the cluster. The algorithm considers the distance between cluster centers and data point and memberships are assigned to related each data point. The number of clusters for Fuzzy c-means algorithm is found by using silhouette score. The clustering quality of each data point is measured by constructing a silhouette for that point [34]. The number of the clusters is found as 7. After the clustering process, 7 clusters are analyzed and interpreted. N-gram analysis is used for each cluster.

3.3 N-gram analysis

An "n-gram" is referred as sequence of n words [35]: a 2-gram is called a bigram which is sequence of two words such as "Ukrainian war", "stop war". In the proposed study, after the application of Fuzzy c-means clustering, each cluster is evaluated by utilizing bigram analysis.

4. Results and Discussions

Following the application of the LDA model, seven topics are obtained, as shown in Figure 4. Each topic

is made up of six words and represents a theme related to the war. Each topic is given a name based on the words that make up the topic.

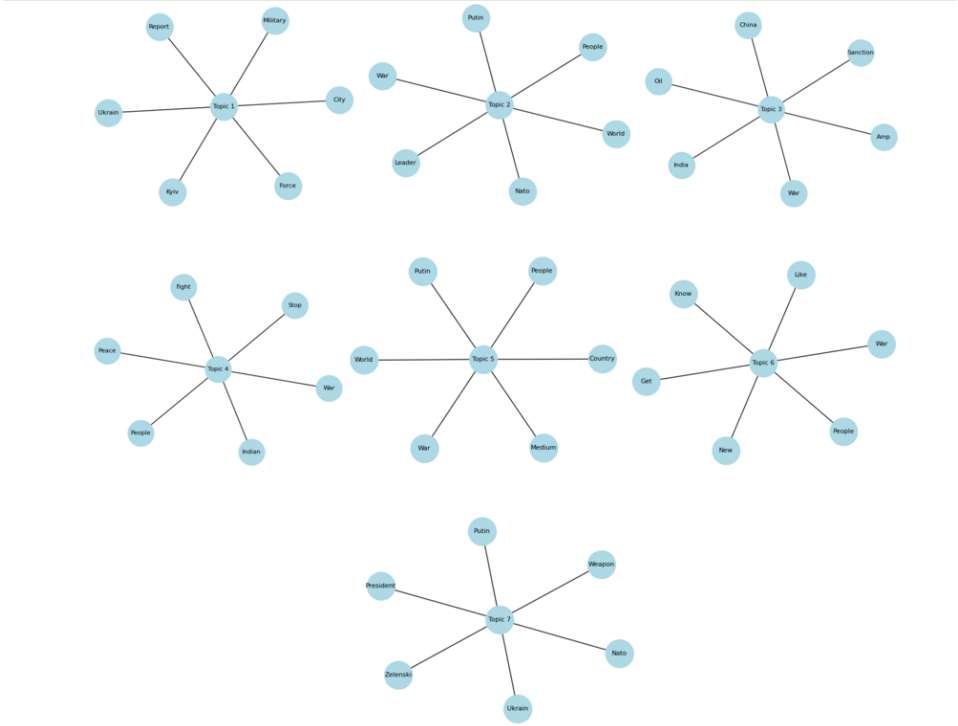

Figure 4. Network visualization of topics

The words Ukraine, city, Kyiv, report, military, and force are all included in the initial topic model. The title of the topic is "Ukraine military force." Words like Putin, leader, conflict, people, world, and NATO appear in the second topic. "Leader Putin" is the title of the second topic. Because of the words China, sanction, India, oil, and war, "Sanction from the World to Russia" can be used as a topic name for the third topic. The most common words in the fourth cluster are peace, people, right, Indian, stop, and conflict. As a result, the fourth topic can be referred to as "end the war." "People in a war" is the title of the fifth topic. The terms people, know, get, news, war, and like appear in Topic 6. The name of topic 6 is "receiving news about the war," as these words illustrate. Finally, by including the words president, Putin, NATO, Ukraine, and Zelensky, topic 7 is referred to as "Putin vs. Zelensky." A matrix of 65412x7 dimensions is generated by examining the seven topics mentioned above. The Fuzzy c-means clustering method is used with the generated matrix. A total of seven clusters is obtained. There are 189, 25, 38471, 2490, 18781, 4803, and 653 tweets in each cluster, correspondingly. The third cluster has the most tweets, with 18781 tweets, and the fifth cluster comes in second with 18781 tweets. There are far fewer tweets in the first and second clusters. The VOSviewer tool is used to evaluate each cluster in the next step. VOSviewer tool demonstrates the connection and number of studies for each selected subject. After that, word frequency and n-gram (bigram) analysis are applied to each cluster. The rest of the discussion section lists all of these applications as well as comments on each cluster.

The following are the applications to the first cluster and analysis: In the first cluster 189 tweets are evaluated. For the evaluation, VOSviewer word frequency and n-gram techniques are utilized. In Figure 5, sub-clusters of cluster 1 are presented through network visualization.

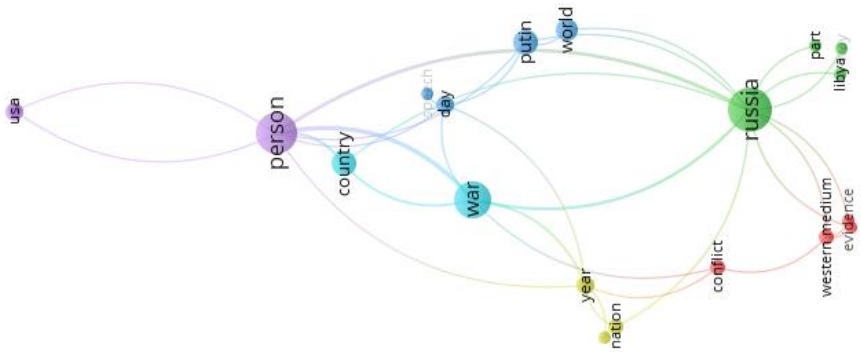

Figure 5. Network visualization of cluster 1 (min. number co-occurrences of a term is 2)

The first cluster is divided into 6 sub-clusters. The red area includes words such as conflict, western media, and evidence. Therefore, it's possible to conclude that there's a lot of uncertainty about the conflict in the Western media. The green area covers words Russia and Libya. Therefore, there can be some political factors between Russia and Libya under the influence of the war. While light blue cluster comprehends words such as country and war, dark blue cluster includes Putin, world, and day words. These areas focus on Russia and president of Russia who is Putin. Lastly, purple cluster includes USA and person words. USA is connected to Putin and Russia. Also, Putin and Russia are connected to Libya. This situation demonstrates that Libya, USA and Russia are focus of first cluster.

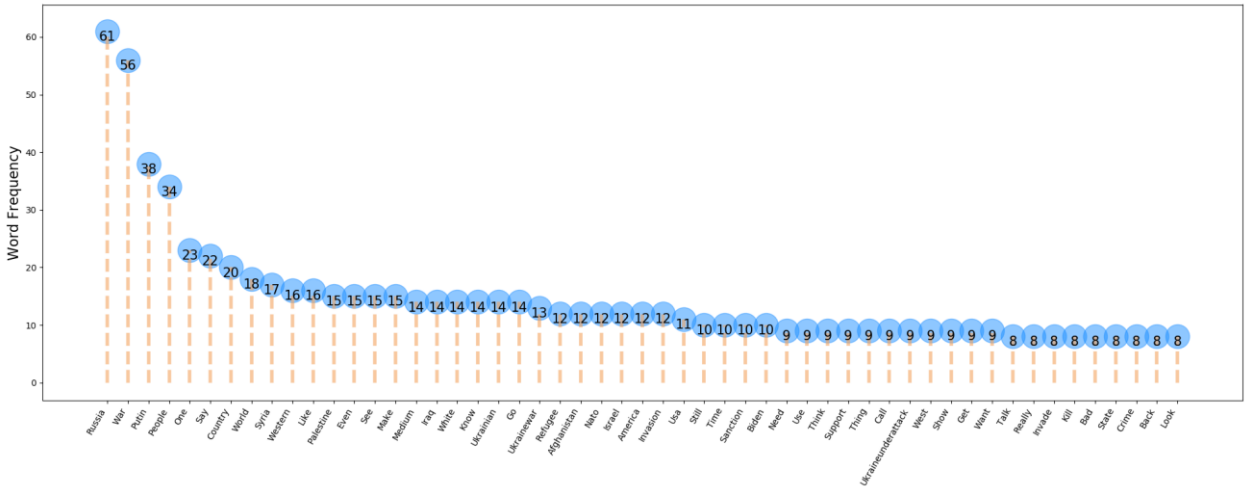

Figure 6. Network Word frequency analysis for cluster 1

As shown in Figure 6, the word Russia is mentioned more frequently on Twitter than the word Ukraine. Some topics such as sanction, invading, crime, and refugee have been debated as a result of this war. Furthermore, discussions concerning NATO are quite common. Syria, Palestine, Iraq, Libya, Yemen, and Afghanistan are among the war-torn countries mentioned. The refugee crisis and an act of war condemnation can both be observed in this cluster.

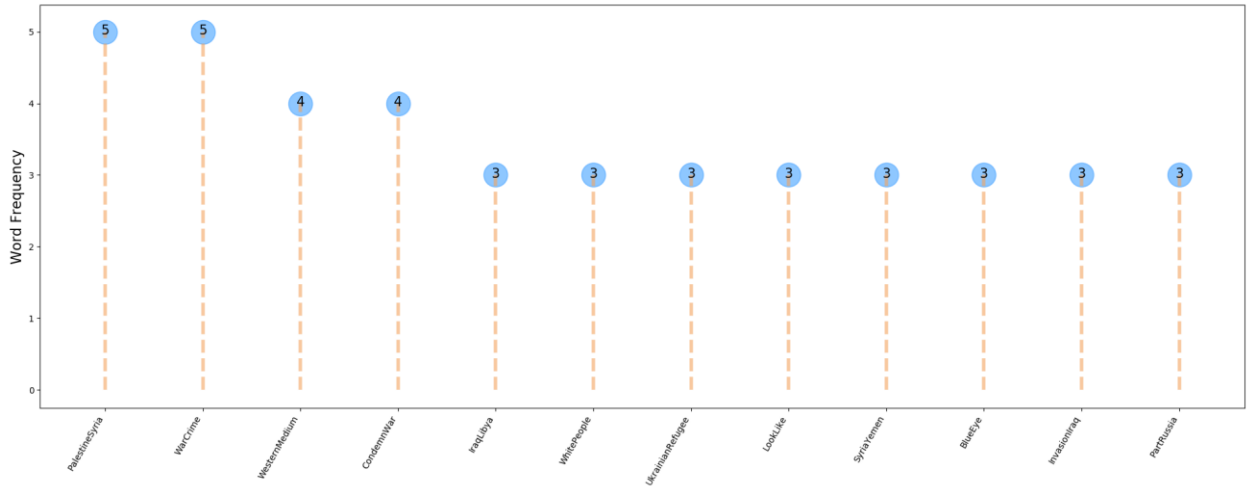

Figure 7. N-gram (bigram) analysis for cluster 1

When n-gram (bigram) analysis is used to look at sequential words, the most regularly used terms are "Palestine Syria" and "War Crime." In the first cluster document, they appear five times. Following that are "Western Media" and "Condemn War." The rest of the sequential terms in the first cluster, such as "Iraq Libya," "White People," "Ukranian Refugee," "Syria Yemen," and "Invasion Iraq," show that the first cluster stresses "war" by considering other nations that have suffered conflict.

After the first cluster analysis, the second cluster is evaluated with the same process as the first cluster. Cluster 2 sub-clusters are seen using network visualization in Figure 8.

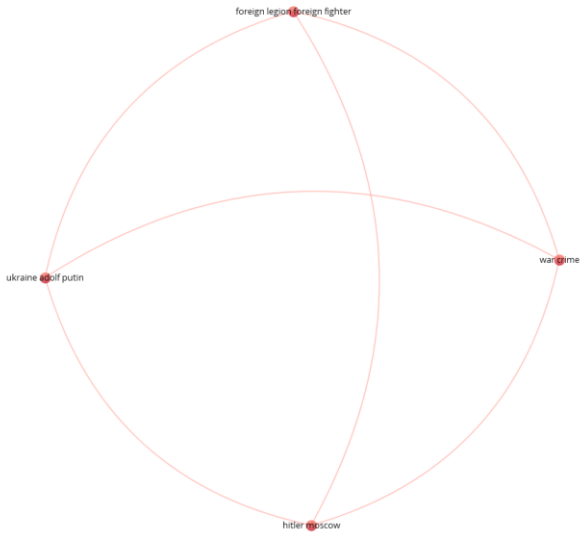

Figure 8. Network visualization of cluster 2 (minimum number co-occurrences of a term is 1)

Twenty-five tweets are analyzed in the second cluster. There are the fewest tweets in this cluster. As a result, there isn't a sub-cluster. In the second cluster, Putin is compared to Adolf Hitler, as shown in Figure 8. Furthermore, war crimes are considered. In Figure 9, word frequency analysis for cluster 2 is demonstrated.

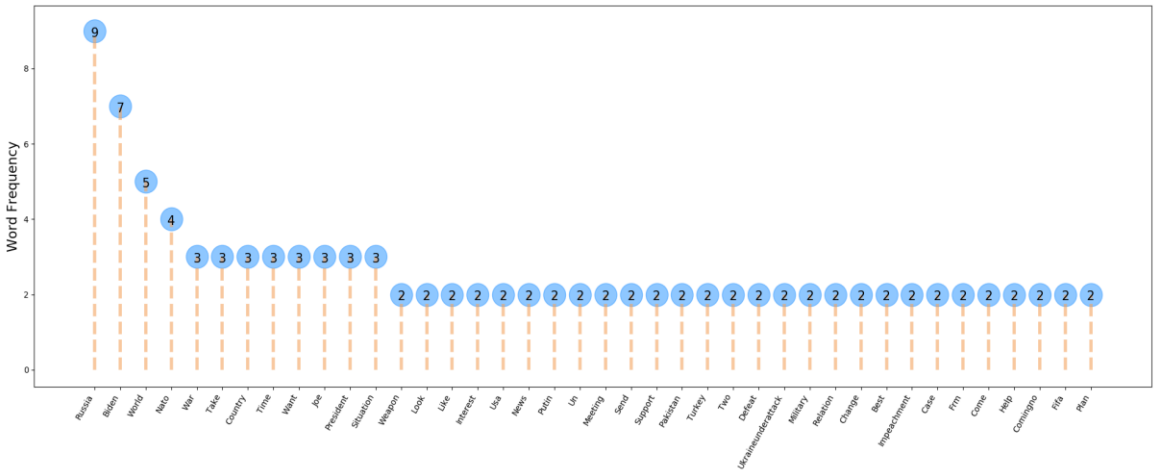

Figure 9. Word frequency analysis for cluster 2

In this cluster, mostly the USA and its president are included. In addition, NATO and weapon can be seen. Besides these points, there are also other words such as "weapon", "military", "send", "help", "meeting", and "support". From the aforementioned words, it can be concluded that tweets under this cluster include the description of the current situation at war in the manner of politics and the army. Figure 10 shows N-gram analysis for cluster 2.

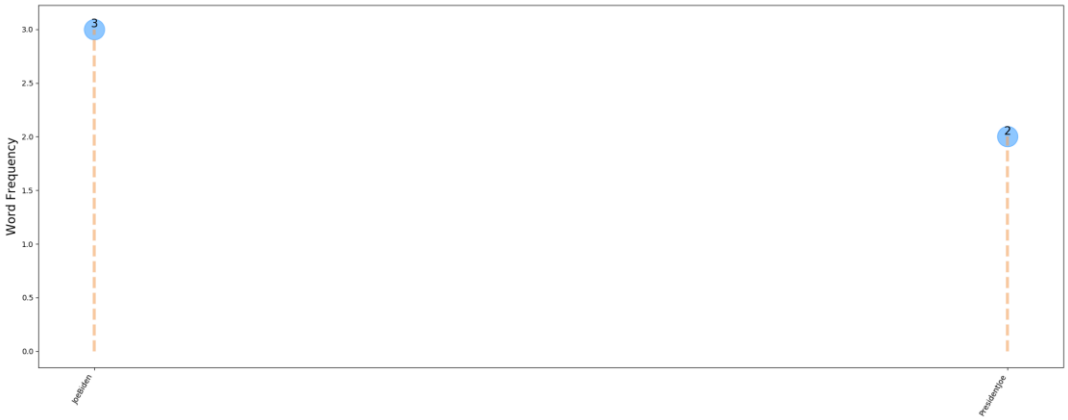

Figure 10. N-gram (bigram) analysis for cluster 2

The second cluster is related to USA president Joe Biden. Since the number of tweets in this cluster is low, mostly Joe Biden is mentioned. All in all, word frequency analysis emphasizes NATO, USA president Joe Biden, weapon and some countries such as Turkey and Pakistan in the second cluster. Figure 10 demonstrates that “Joe Biden” and “President Joe” (USA president) are the most frequently seen sequential words in the cluster. Therefore, it can be said that this cluster includes the tweets related to the USA president. A total of 38471 tweets are analyzed when the third cluster is considered. As a result, this cluster contains the most tweets. The result of network analysis using VOSviewer is shown in Figure 11.

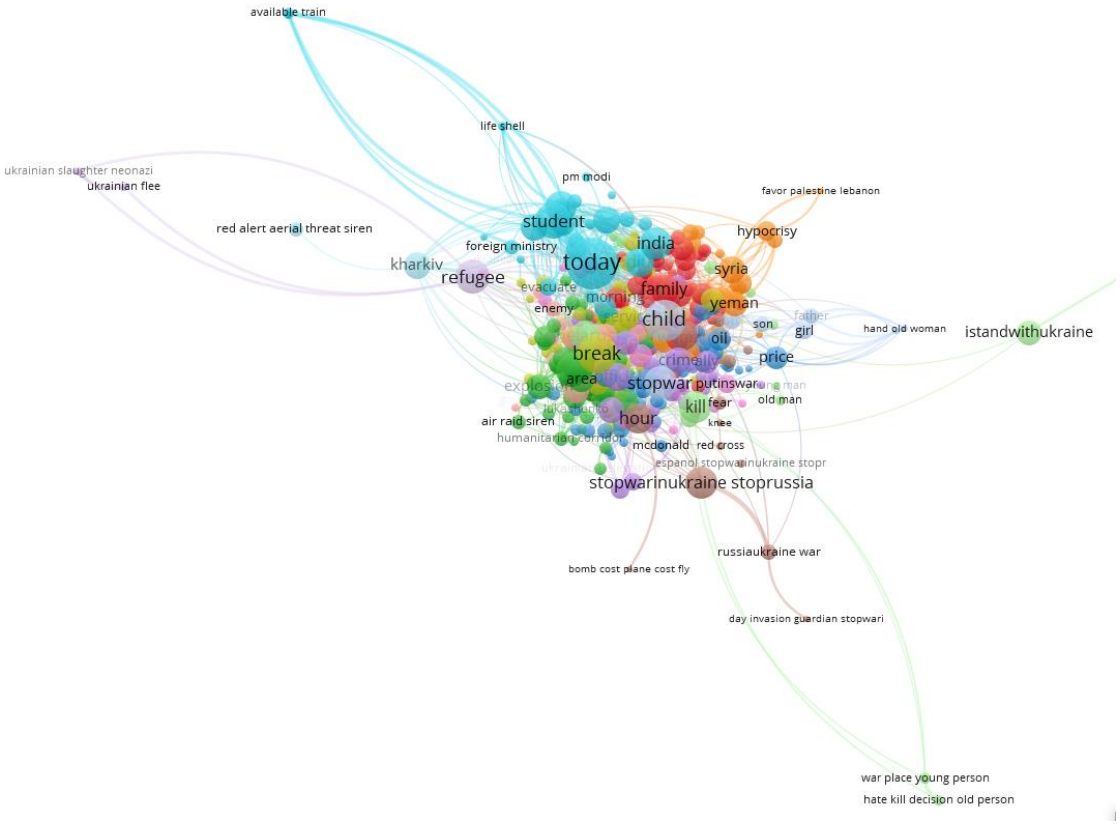

Figure 11. Network visualization of cluster 3 (minimum number co-occurrences of a term is 10)

There are too many sub-clusters in the third cluster since it has the most tweets. The cluster is divided into more than eight sub-clusters. The purple area focuses on the refugee crisis. The light blue area covers Indian students. The red area is related to the family. The orange area includes Syria and Yemen. The light green area focuses on Istanbul and is related to negotiations. The brown area emphasizes stopping the war. In Figure 12, Word frequency analysis for cluster 3 is given.

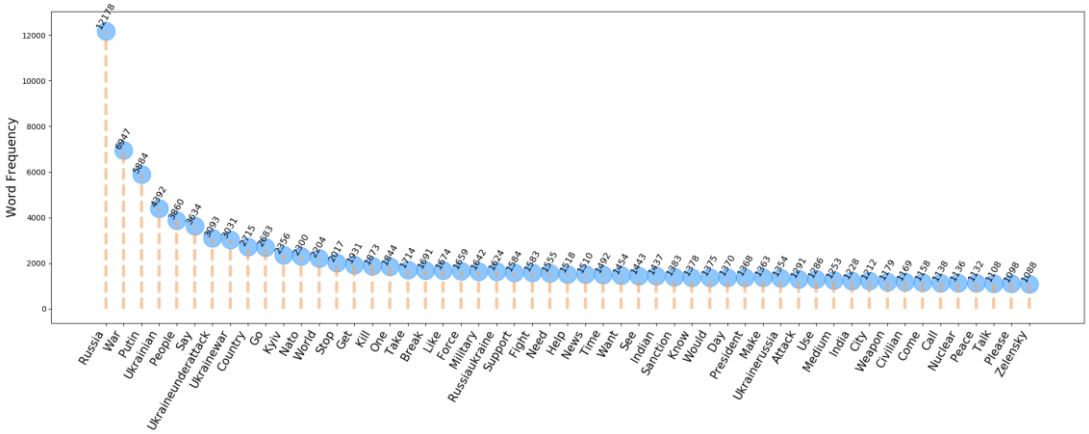

Figure 12. Word frequency analysis for cluster 3

It is true that most people refer to Putin (the Russian President) rather than Zelensky (the President of Ukraine). This indicates that the attacking side is mentioned more than the defending side. As in the other clusters, NATO is included in this one as well. N-gram analysis for cluster 3 is demonstrated in Figure 13.

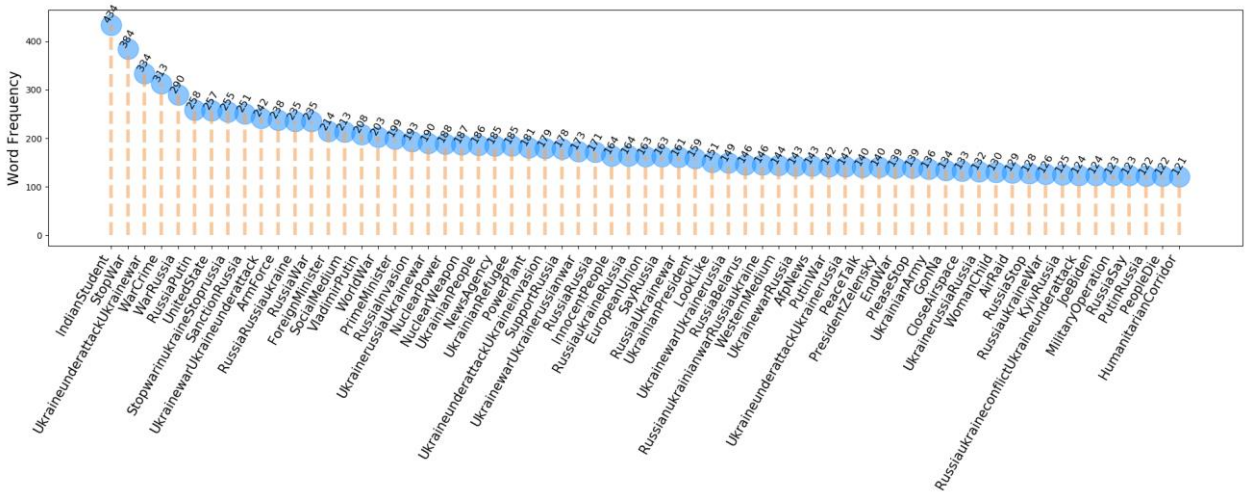

Figure 13. N-gram (bigram) analysis for cluster 3

"Indian students" is the most commonly used term in the third cluster. This demonstrates that Indian students are having difficulties throughout the war. The strikes by Russia, the use of nuclear weapons, the necessity to end the war, and innocent people, women, and children are all discussed in this cluster. To summarize, word frequency analysis reveals that the most usually seen word in terms of being under attack is Ukrainian. "Sanctions on Russia," "Indian students," "war crimes," "power plants," "nuclear weapons," and "United States" are all recognized as consecutive words. The third cluster contains certain sanctions imposed by other countries as well as the weapons employed by Russia in its attacks on Ukraine.

After the third cluster analysis, the standard procedure (same techniques as in the other clusters) is applied to the fourth cluster. A total of 2490 tweets are included in this cluster. Cluster 4 sub-clusters are seen using network visualization in Figure 14.

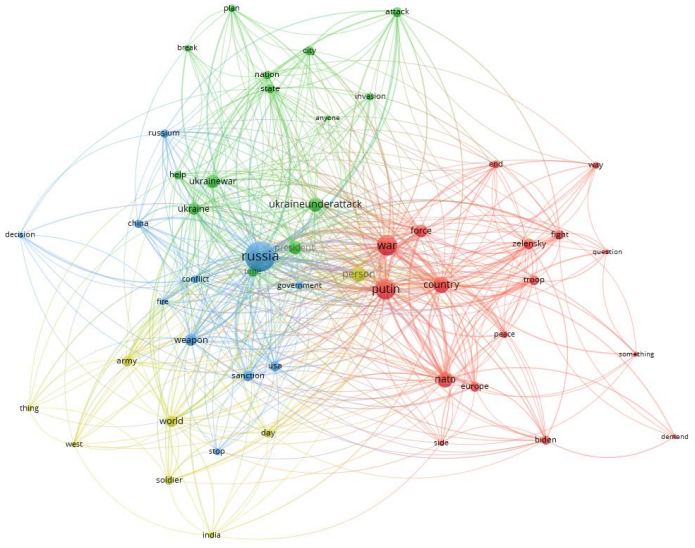

Figure 14. Network visualization of cluster 4 (min. number co-occurrences of a term is 7)

The fourth cluster is divided into four sub-clusters. Also, it can be seen that the network between sub-clusters is more intense compared to the aforementioned clusters. The blue area focuses on sanctions imposed on Russia by other countries such as the United States and China. When it comes to red area, tweets include the efforts of NATO and Europe to provide peace between two sides by referring to

the presidents of both sides. The tweets in the green area focus on the invasion and attack of Russia on Ukraine. Lastly, the yellow area is mostly concerned with the military. Figure 15 demonstrates the word frequency analysis for cluster 4.

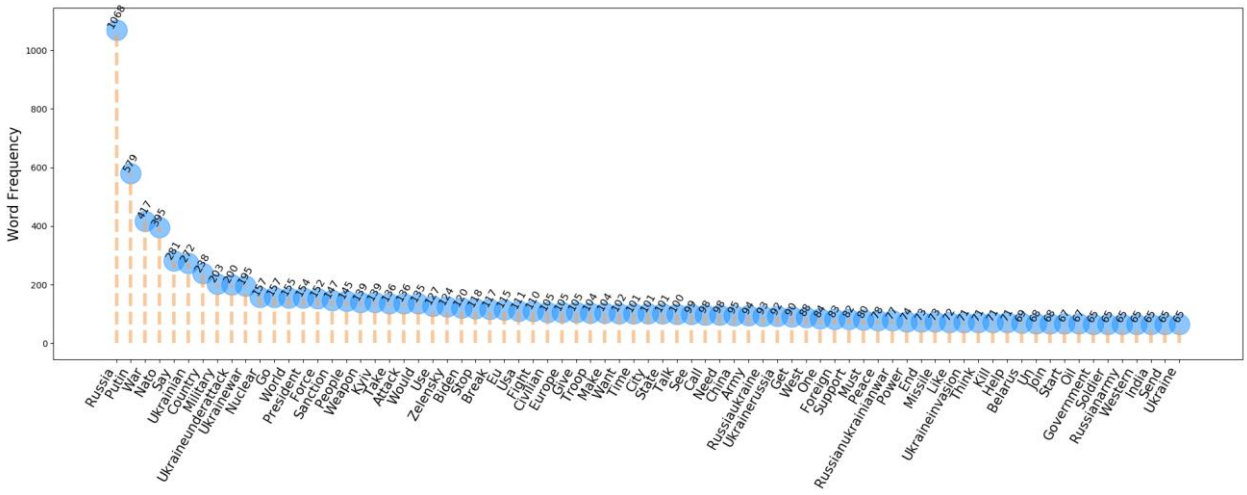

Figure 15. Word frequency analysis for cluster 4

According to the word frequencies indicated in Figure 15, there are several other countries involved in the war from a political standpoint, such as China, Belarus, and the United States. Apart from Russia, Putin, and war, NATO is the most often highlighted word in this cluster, according to the data. Therefore , it can be inferred that NATO's engagement is desirable in order to bring the war to an end as soon as possible. Overall, word frequencies show that nuclear, attack, sanction, and NATO are the most often used terms, as shown in Figure a. As a result, it can be determined that tweets cover issues such as nuclear attack and NATO engagement in the conflict. Figure 16 gives N-gram analysis of cluster 4.

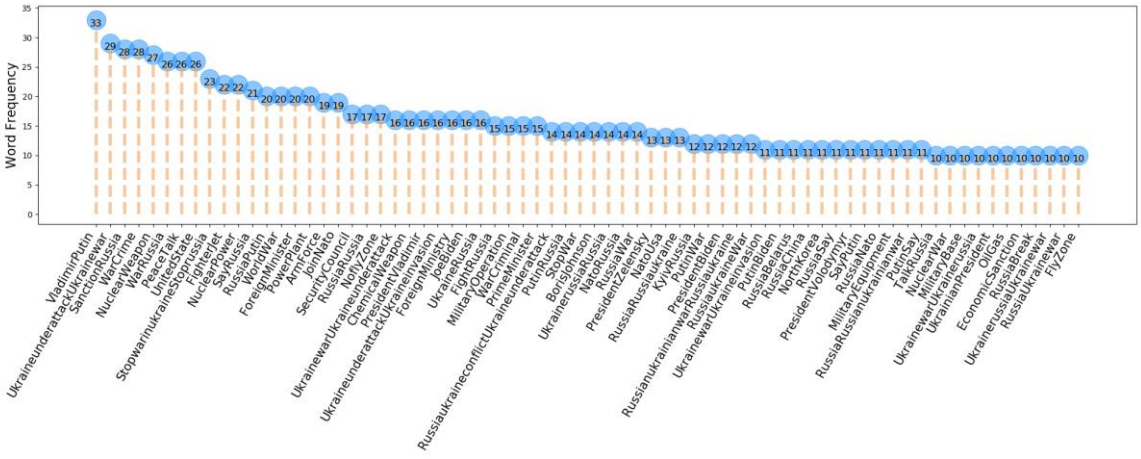

Figure 16. N-gram (bigram) analysis for cluster 4

The most frequently occurring sequence terms, according to bigram analysis, are "Vladimir Putin," "Ukraine under attack," "sanction Russia," "war crime," "nuclear weapon," "war Russia," and "peace talk." The conclusion drawn from the analysis is that there is a widespread desire to avoid conflict, avoid nuclear weapons, and need the participation of foreign ministers.

Cluster 5 has 18781 tweets, making it the second largest cluster out of a total of seven. The majority of tweets in this cluster are about war crimes, Vladimir Putin, and a common desire to end the conflict. Using network visualization, Cluster 5 sub-clusters can be visualized in Figure 17.

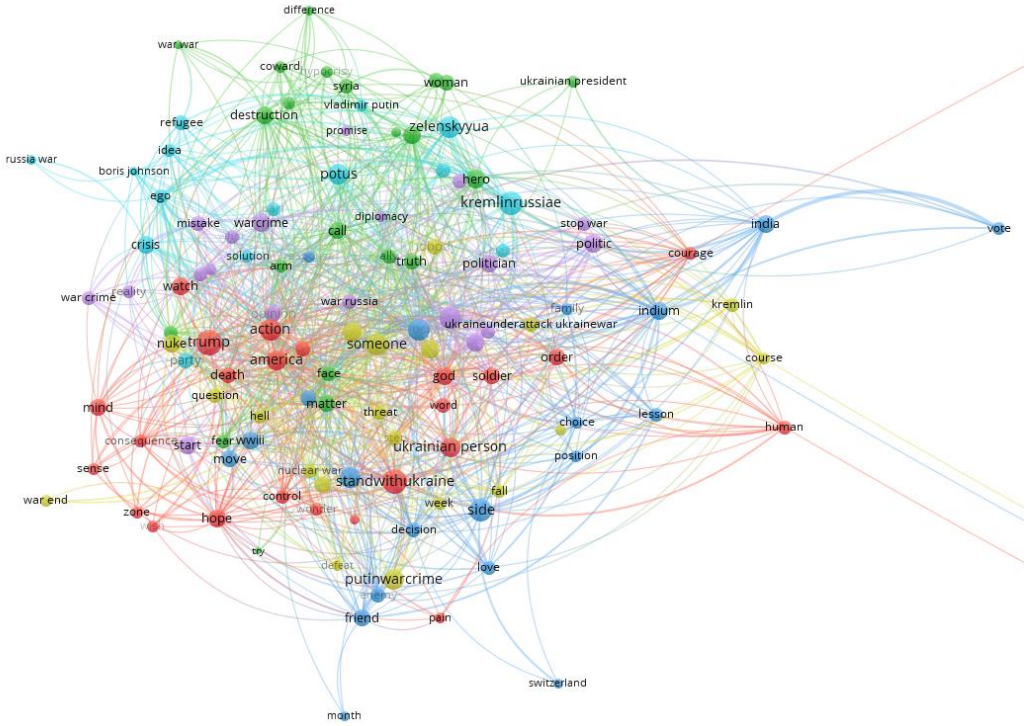

Figure 17. Network visualization of cluster 5 (min. number co-occurrences of a term is 15)

The fifth cluster is divided into 6 sub-clusters indicated by different colors, which are green, light blue, dark blue, purple, red, and yellow. In the sub-cluster referred to by green, tweets related to destruction, women, heroes, and Zelensky. The status of women in the war, the destruction wrought by conflict, and society's perception of Zelensky as a hero may all be inferred from these remarks. The words encountered in the light-blue sub-cluster are Kremlin, Potus, refuge, crisis, and solution. Therefore, it can be concluded that tweets are related to the discourse of America to the Kremlin about the solution to the refugee crisis. The dark-blue sub-cluster consists of words like India, indium, lesson, side, decision, position, and choose. These words demonstrate that decision about the situation of Indian students who are suffering from the ongoing war. Ukraine under attack, war crimes, politicians, politics, and mistakes are the words that are mostly underlined in the purple sub-cluster. These words indicate that the main theme of the sub-cluster is about wrong political decisions and the occurrence of war crimes. The Red sub-cluster includes words that stand with Ukraine, Trump, America, and action. These words demonstrate that the sub-cluster is related to American support for Ukraine by taking some actions such as military support. The last sub-cluster is illustrated by the yellow color, which includes threat, someone, nuclear war, Putin's war crimes, and ending war words. As a result, it can be determined that this sub-cluster is about Russia's threat of using nuclear weapons, which is considered a war crime.

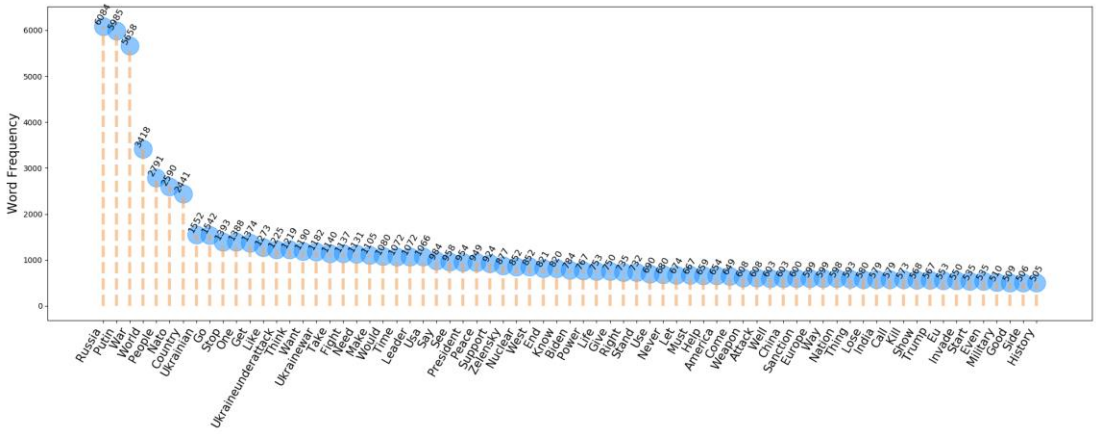

Figure 18. Word frequency analysis for cluster 5

The word frequency analysis of the fifth cluster demonstrates Russia's dominance over Ukraine (Figure 18). People's desires, anti-war sentiments, and peace terms are all part of this cluster. Russia's attacks and the world's reactions to Russia can be seen in this cluster. Figure 19 gives N-gram analysis of cluster 5.

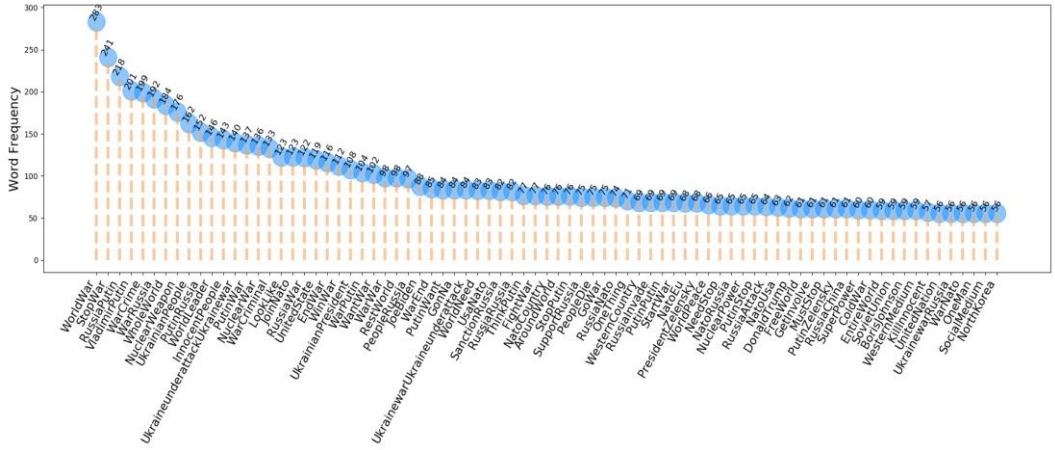

Figure 19. N-gram (bigram) analysis for cluster

The most often occurring sequential term in cluster 5 is "World War", which is followed by the "Stop War" word in the sequence. Therefore, it can be concluded that the war is at an important point for the whole world to overcome, and the general tendency in social media is in favor of ending the war. Also, from the point of war victims, tweets focused on "war crimes" and "innocent people" are observed in this cluster. From the analysis of this cluster, it can be deduced that the other focus of tweets is "nuclear weapons". As a result, bigram analysis depicts Putin's war crimes as well as the rest of the world's judgment on the war.

The sixth cluster includes a total of 4803 tweets. This is the third big cluster. The network visualization of cluster 6 is given in Figure 20.

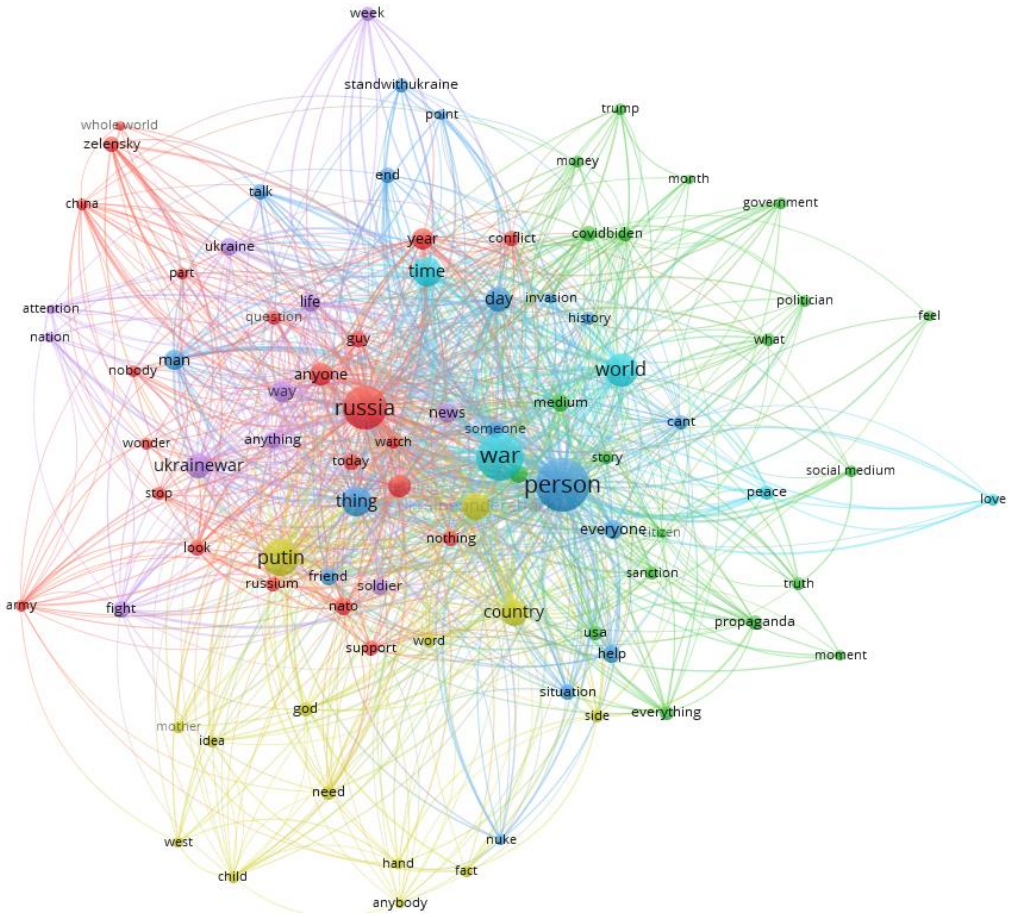

Figure 20. Network visualization of cluster 6 (min. number co-occurrences of a term is 10)

6 sub-clusters are shown in Figure 20 for the cluster 6. Russia, person, war, and Putin are the focus points of this cluster. The green area focuses on social media and propaganda while taking into account political considerations such as the United States and its former and current presidents. The blue area emphasizes people in distress and asks for help. The light blue area reflects the global community's attitude on war and yearning for peace. The red area denotes a conflict, and the war must come to an end. The other area is referred by purple color, that includes military and media terms such as soldier and news with the main focus on Ukraine. Finally, spiritual and emotional concepts such as mother, child, and god are represented in the yellow area. Word frequency analysis for sixth cluster is given in Figure 21.

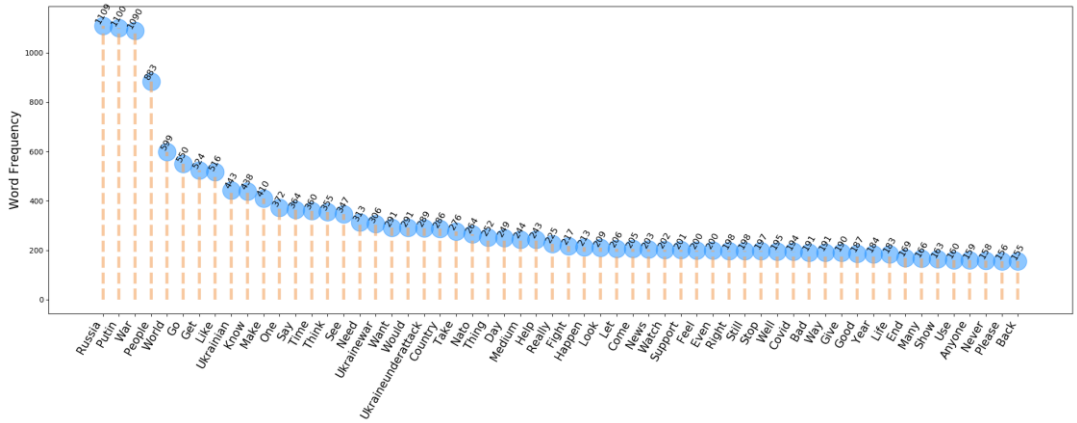

Figure 21. Word frequency analysis for cluster 6

Russia, Putin, and war are seen as the top three words in terms of word frequency analysis. Figure 21 shows that Ukraine is being attacked, and the world talks about it. Therefore, this analysis gives the result that almost same with aforementioned results. Next Figure is Figure 22 which demonstrates the bigram analysis of sixth cluster.

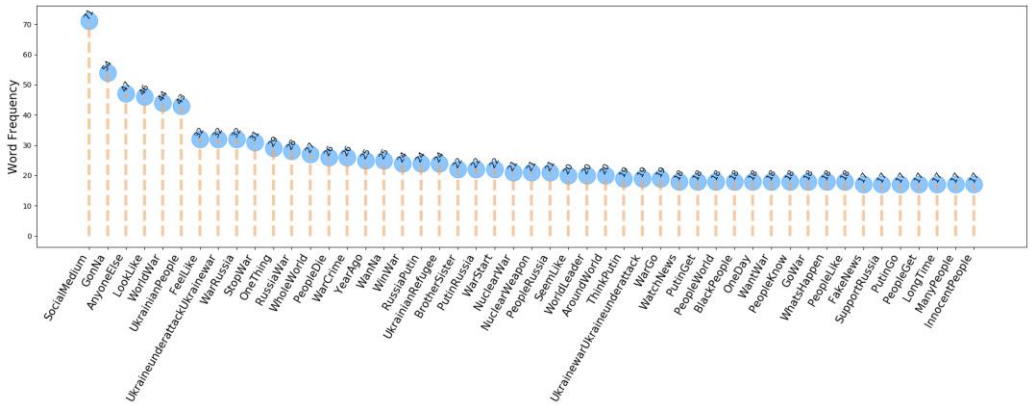

Figure 22. N-gram (bigram) analysis for cluster 6

The first consecutive term in this cluster is “social media”. From the perspective of real-world, this cluster demonstrates the relevance of social media in a war. This analysis demonstrates that the war affects the entire world. Feelings and emotions are included in this cluster. Furthermore, the terms "nuclear war" and "Ukrainian refugee" are significant consecutive words in this cluster. The final cluster contains a total of 653 tweets. Figure 23 depicts the network visualization of cluster 7. Although there are a limited number of tweets in this cluster, the number of sub-clusters is high. However, sub-clusters are not represented in as many tweets.

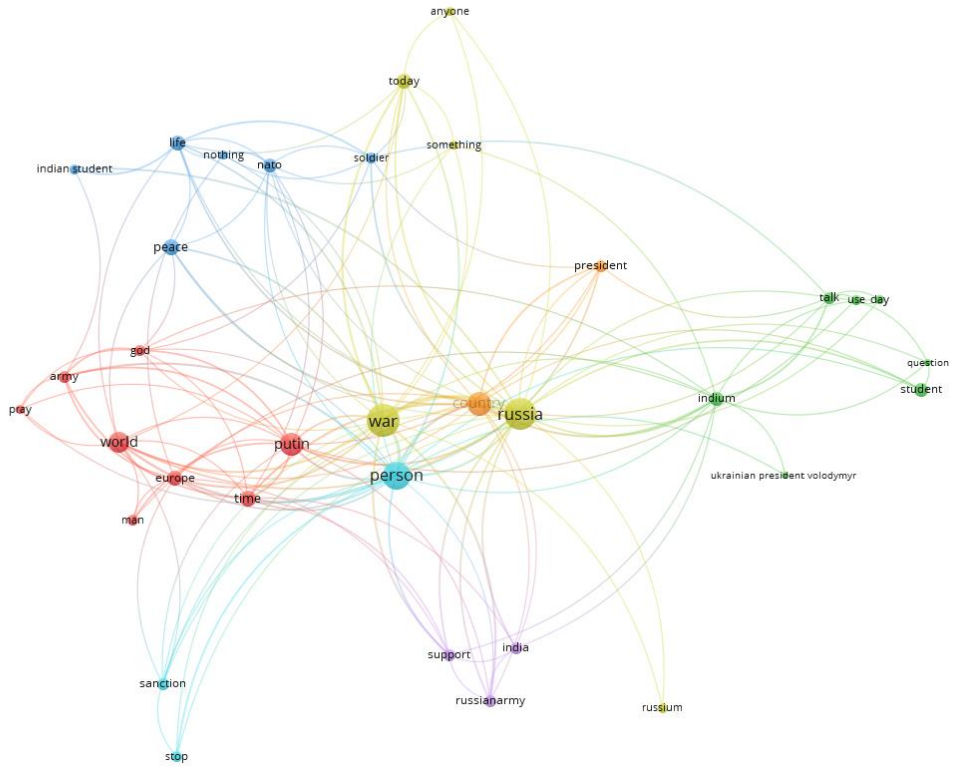

Figure 23. Network visualization of cluster 7 (min. number co-occurrences of a term is 3)

7 sub-clusters are seen in cluster 7. Indian students have an impact across several sub-clusters. The green area represents questions about Indian students. Also, the blue are focuses on Indian students together with peace. The purple area emphasizes Russian army and India. Therefore, it can be concluded that the problem related to the Indian students is discussed in the several sub-clusters. The words encountered in the red sub-cluster are world, Europe, army, god, and time. It illustrates that war is not viewed from afar by the rest of the world or Europe. The light blue area consists of sanctions on Russia. The yellow and orange areas are intersected and focus on Russia and its president. In Figure 24 word frequency analysis of cluster 7 is demonstrated.

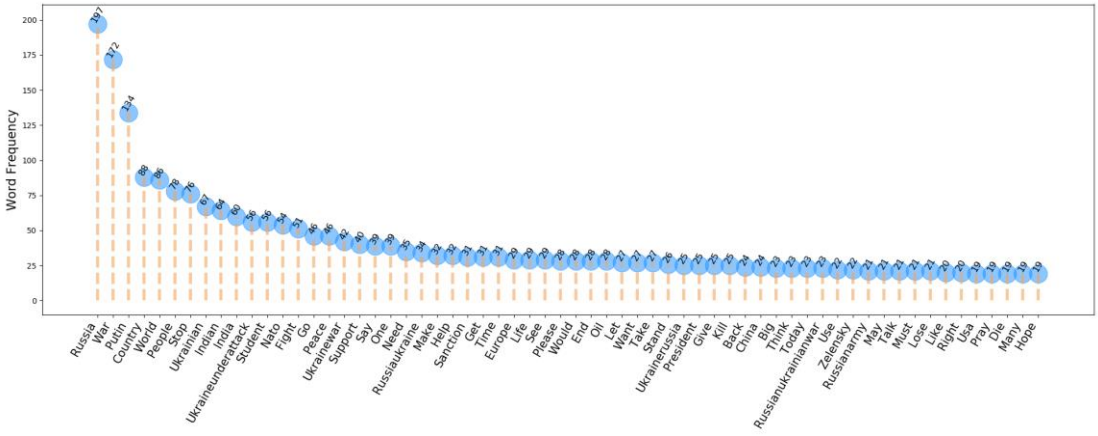

Figure 24. Word frequency analysis for cluster 7

After the top three words, which are "Russia", "war", and "Putin", it is seen that "people", "Ukrainian", "Indian", and "student" are the mostly underlined words from Figure 24. Therefore, the interpretation of this cluster can be expressed as considered tweets mostly focused on war victims and

their issues. On the other hand, words like "NATO", "peace", "support", "please", and "end" lead the interpretation to the concept of ending war, waiting for international support, and seeking peace. Bigram analysis of cluster 7 is given Figure 25.

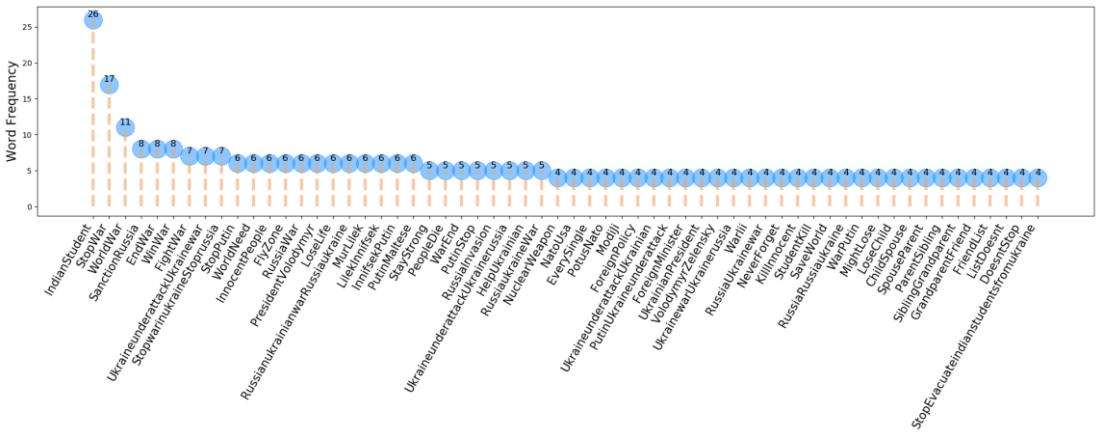

Figure 25. N-gram (bigram) analysis for cluster 7

As given in network visualization of cluster 7, “Indian students” is the most discussed consecutive word. In addition, “stop war”, “world war”, “sanction Russia”, and “end war” are the other popular consecutive words in this cluster. It can be concluded that other nations living in Ukraine are experiencing problems as a result of the war.

4. Conclusion and Suggestions

In a nutshell, the aim of the conducted study is to reveal the objectives of social media during the war. As a result, it can provide a better understanding of society and their general perspective on the issues that have arisen. In that way, some of the decision and assistance processes can be provided with a more accurate and efficient approach. Some of the aforementioned processes can be summarized as: political decisions can be taken with a deeper understanding of the current situation; humanitarian activities can be conducted in accordance with detected needs; and support can be provided to victims in an effective and efficient way. Analysis in the proposed study consists of two main parts. The first part is LDA application and Fuzzy c-means clustering. In detail, LDA is applied to extract topic probabilities in order to define each tweet in accordance. After that, these results are utilized as an input for Fuzzy c-means to gather clusters of retrieved tweets for further analysis. Furthermore, 7 distinct clusters are gathered to be processed. To provide a better understanding, the second part of the analysis evaluates each obtained cluster using n-grams and network analysis. Lastly, the implications of the proposed study are given as follows:

- Putin is discussed more than Zelensky as a leader, and every action taken by Putin has become a social media trend.
- During the war Ukraine has been under attacked heavily and the global public opinion is in the favor of ending war.
- America, China, Europe, and the Western media are the main actors who comment on war across the world.
- Sanctions have been imposed on Russia by other countries.
- Problems related to foreign students are discussed throughout the Indian students.
- The refugee crisis has arisen as a result of people leaving Ukraine.
- Other war-torn nations (such as Syria, Palestine, Iraq, Yemen, and Libya) are referenced in the context of the Ukraine-Russia conflict.
- Situation of women and children who experienced war is underlined.
- According to both cluster analysis and LDA application, the oil problem has arisen as a result of war.
- Assistance from the NATO and other countries are demanded to Ukraine by Ukraine and other people.

Limitations of the proposed study can be underlined as: because it's difficult to analyze tweets in many languages at the same time, only those posted in English are evaluated. The

"#UkraineRussiawar " term and hashtag were used to find tweets. It's possible, however, that there are additional tweets that don't use the hashtag but are nonetheless related to the topic. As a result, the outcomes may be more representative of English-speaking communities. For the future study, the system can be generated to demonstrate the interpretations of tweets on the chosen hashtags. Different text mining approaches can be applied. Integration of the languages rather than English can be investigated and implemented in the analysis.

Conflict of Interest Statement

There is no conflict of interest between the authors.

References

[1] F. Bordignon, I. Diamanti, and F. Turato, "Rally'round the Ukrainian flag. The Russian attack and the (temporary?) suspension of geopolitical polarization in Italy," *Contemporary Italian Politics*, pp. 1-17, 2022.

[2] L. Eras, "War, Identity Politics, and Attitudes toward a Linguistic Minority: Prejudice against Russian-Speaking Ukrainians in Ukraine between 1995 and 2018," *Nationalities Papers*, pp. 1-22, 2022.

[3] N. A. Ghani, S. Hamid, I. A. Targio Hashem, and E. Ahmed, "Social media big data analytics: A survey," *Computers in Human Behavior*, vol. 101, pp. 417-428, 2019/12/01/ 2019.

[4] A. Gandomi and M. Haider, "Beyond the hype: Big data concepts, methods, and analytics," *International Journal of Information Management*, vol. 35, no. 2, pp. 137-144, 2015/04/01/ 2015.

[5] D. M. Blei and J. D. Lafferty, "*Topic models*," in Text mining: Chapman and Hall/CRC, 2009, pp. 101-124.

[6] S. A. Curiskis, B. Drake, T. R. Osborn, and P. J. Kennedy, "An evaluation of document clustering and topic modelling in two online social networks: Twitter and Reddit," *Information Processing and Management*, Article vol. 57, no. 2, 2020, Art no. 102034, doi: 10.1016/j.ipm.2019.04.002.

[7] M. E. Roberts et al., "Structural topic models for open-ended survey responses," *American Journal of Political Science*, Article vol. 58, no. 4, pp. 1064-1082, 2014, doi: 10.1111/ajps.12103.

[8] H. Yuan, R. Y. K. Lau, and W. Xu, "The determinants of crowdfunding success: A semantic text analytics approach," *Decision Support Systems*, Article vol. 91, pp. 67-76, 2016, doi: 10.1016/j.dss.2016.08.001.

[9] D. M. Blei, A. Y. Ng, and M. I. Jordan, "Latent dirichlet allocation," *Journal of machine Learning research*, vol. 3, no. Jan, pp. 993-1022, 2003.

[10] Y. Yang, J. H. Hsu, K. Löfgren, and W. Cho, "Cross-platform comparison of framed topics in Twitter and Weibo: machine learning approaches to social media text mining," *Social Network Analysis and Mining, Article* vol. 11, no. 1, 2021, Art no. 75, doi: 10.1007/s13278-021-00772-w.

[11] P. Hu, W. Liu, W. Jiang, and Z. Yang, "Latent topic model for audio retrieval," *Pattern Recognition, Conference Paper* vol. 47, no. 3, pp. 1138-1143, 2014, doi: 10.1016/j.patcog.2013.06.010.

[12] L. Yao et al., "Concept over time: The combination of probabilistic topic model with wikipedia knowledge," *Expert Systems with Applications*, Article vol. 60, pp. 27-38, 2016, doi: 10.1016/j.eswa.2016.04.014.

[13] M. Pavlinek and V. Podgorelec, "Text classification method based on self-training and LDA topic models," *Expert Systems with Applications*, Article vol. 80, pp. 83-93, 2017, doi: 10.1016/j.eswa.2017.03.020.

[14] S. Xiong, K. Wang, D. Ji, and B. Wang, "A short text sentiment-topic model for product reviews," *Neurocomputing*, Article vol. 297, pp. 94-102, 2018, doi: 10.1016/j.neucom.2018.02.034.

[15] L. Hong and B. D. Davison, "Empirical study of topic modeling in twitter," in Proceedings of the first workshop on social media analytics, 2010, pp. 80-88.

[16] E. Lee, F. Rustam, I. Ashraf, P. B. Washington, M. Narra, and R. Shafique, "Inquest of Current Situation in Afghanistan Under Taliban Rule Using Sentiment Analysis and Volume Analysis," *IEEE Access*, Article vol. 10, pp. 10333-10348, 2022, doi: 10.1109/ACCESS.2022.3144659.

[17] P. Vazquez, J. C. Garcia, M. J. Luna, and C. Vaca, "Temporal topics in online news articles: Migration crisis in Venezuela," in 2020 *7th International Conference on eDemocracy and eGovernment, ICEDEG* 2020, 2020, pp. 106-113, doi: 10.1109/ICEDEG48599.2020.9096804.

[18] L. Tang, Y. Zhang, F. Dai, Y. Yoon, Y. Song, and R. S. Sharma, "Social Media Data Analytics for the U.S. Construction Industry: Preliminary Study on Twitter," *Journal of Management in Engineering, Article* vol. 33, no. 6, 2017, Art no. 04017038, doi: 10.1061/(ASCE)ME.1943-5479.0000554.

[19] C. S. Lee and A. Jang, "Questing for Justice on Twitter: Topic Modeling of #StopAsianHate Discourses in the Wake of Atlanta Shooting," *Crime and Delinquency*, Article 2021, doi: 10.1177/00111287211057855.

[20] J. Allan, *Topic detection and tracking: event-based information organization*. Springer Science & Business Media, 2012.

[21] J. C. Bezdek, R. Ehrlich, and W. Full, "FCM: The fuzzy c-means clustering algorithm," *Computers & Geosciences*, vol. 10, no. 2, pp. 191-203, 1984/01/01/ 1984.

[22] S. Abri and R. Abri, "Providing a Personalization Model Based on Fuzzy Topic Modeling," *Arabian Journal for Science and Engineering*, Article vol. 46, no. 4, pp. 3079-3086, 2021, doi: 10.1007/s13369-020-05048-7.

[23] H. Alatas, H. Murfi, and A. Bustamam, "Topic Detection using fuzzy c-means with nonnegative double singular value decomposition initialization," *International Journal of Advances in Soft Computing and its Applications*, Article vol. 10, no. 2, pp. 206-222, 2018.

[24] Y. Prakoso, H. Murfi, and A. Wibowo, "Kernelized Eigenspace based fuzzy C-means for sensing trending topics on twitter," in *ACM International Conference Proceeding Series*, 2018, pp. 6-10, doi: 10.1145/3239283.3239297.

[25] A. Parlina, K. Ramli, and H. Murfi, "Exposing emerging trends in smart sustainable city research using deep autoencoders-based fuzzy c-means," *Sustainability (Switzerland)*, Article vol. 13, no. 5, pp. 1-28, 2021, Art no. 2876, doi: 10.3390/su13052876.

[26] R. T. Sutrisman and H. Murfi, "Analysis of non-negative double singular value decomposition initialization method on eigenspace-based fuzzy C-Means algorithm for Indonesian online news topic detection," in 2018 *6th International Conference on Information and Communication Technology, ICoICT* 2018, 2018, pp. 55-60, doi: 10.1109/ICoICT.2018.8528791.

[27] M. Trupthi, S. Pabboju, and G. Narsimha, "Possibilistic fuzzy C-means topic modelling for twitter sentiment analysis," *International Journal of Intelligent Engineering and Systems*, Article vol. 11, no. 3, pp. 100-108, 2018, doi: 10.22266/IJIES2018.0630.11.

[28] T. Mandhula, S. Pabboju, and N. Gugulotu, "Predicting the customer's opinion on amazon products using selective memory architecture-based convolutional neural network," *Journal of Supercomputing*, Article vol. 76, no. 8, pp. 5923-5947, 2020, doi: 10.1007/s11227-019-03081-4.

[29] L. Kolhe, A. K. Jetawat, and V. Khairnar, "Robust product recommendation system using modified grey wolf optimizer and quantum inspired possibilistic fuzzy C-means," *Cluster Computing*, Article vol. 24, no. 2, pp. 953-968, 2021, doi: 10.1007/s10586-020-03171-6.

[30] D. Khyani, B. Siddhartha, N. Niveditha, and B. Divya, "An Interpretation of Lemmatization and Stemming in Natural Language Processing," Shanghai Ligong Daxue Xuebao/*Journal of University of Shanghai for Science and Technology*, vol. 22, pp. 350-357, 2020.

[31] N. Eligüzel, C. Çetinkaya, and T. Dereli, "Comparison of different machine learning techniques on location extraction by utilizing geo-tagged tweets: A case study," *Advanced Engineering Informatics*, vol. 46, p. 101151, 2020.

[32] K. Crockett, D. Mclean, A. Latham, and N. Alnajran, "Cluster analysis of twitter data: A review of algorithms," in *Proceedings of the 9th International Conference on Agents and Artificial Intelligence*, 2017, vol. 2: Science and Technology Publications (SCITEPRESS)/Springer Books, pp. 239-249.

[33] J. C. Dunn, "A Fuzzy Relative of the ISODATA Process and Its Use in Detecting Compact Well-Separated Clusters," *Journal of Cybernetics*, vol. 3, no. 3, pp. 32-57, 1973/01/01 1973, doi: 10.1080/01969727308546046.

[34] M. Rawashdeh and A. L. Ralescu, "Fuzzy Cluster Validity with Generalized Silhouettes," in MAICS, 2012.

[35] D. Jurafsky and J. H. Martin, "*N-gram Language Models*," in Speech and Language Processing, 3rd ed. draft ed., 2021.